# X-ray Source Population Study of the Local Group Galaxy M 31


Dissertation der Fakultät für Physik
der Ludwig-Maximilians-Universität München

vorgelegt von

**Holger Stiele**

aus Dachau

München, Februar 2010

1. Gutachter: Prof. Dr. Ralf Bender
2. Gutachter: Prof. Dr. Hans Böhringer

Tag der mündlichen Prüfung: 24. März 2010

# Populationsstudie der Röntgenquellen der Andromeda Galaxie

## Zusammenfassung


Diese Dissertation präsentiert die Analyse einer großen und tiefen Durchmusterung von M 31, der zweiten großen Spiralgalaxie der Lokalen Gruppe, mit dem Röntgenteleskop *XMM-Newton*. Die Beobachtungen der Durchmusterung, welche zwischen Juni 2006 und Februar 2008 aufgenommen wurden, überdecken zusammen mit erneut analysierten Archivbeobachtungen, aufgenommen zwischen Juni 2000 und Juli 2004, die gesamte $D_{25}$ Ellipse von M 31, zum ersten Mal bis zu einer unteren Grenzleuchtkraft von $\sim 10^{35}$ erg s$^{-1}$ im 0.2 – 4.5 keV Bereich.

Das Hauptziel dieser Arbeit war das Studium der verschiedenen Quellklassen in M 31, welche im Röntgenbereich beobachtet werden können. Hierzu wurde ein Katalog aller im 0.2–12.0 keV Bereich detektierter Quellen erstellt, welcher 1 948 Quellen enthält, wobei 961 Quellen zum ersten Mal im Röntgenbereich nachgewiesen wurden. Die Klassifikation und Identifikation der Quellen beruhte auf 'Hardness Ratios', der räumlichen Ausdehnung der Quellen und Korrelationen mit Katalogen im Optischen, Infrarot-, Radio- und Röntgenbereich. Zusätzlich wurde die Langzeitvariabilität der Quellen im Röntgenbereich als weiteres Klassifikationskriterium verwendet, da sie eine Unterscheidung zwischen Röntgendoppelsternen und aktiven galaktischen Kernen ermöglichte. Des Weiteren konnten Supernova Überrest Klassifikationen vorangegangener Studien, welche keine Langzeitvariabilität für die Quellklassifikation verwendet hatten, validiert werden. Unter der Hinzunahme früherer *Chandra* und *ROSAT* Beobachtungen in die Untersuchung der Langzeitvariabilität konnten weitere mögliche 'transient' oder zumindest hochvariable Quellen gefunden werden, welche gute Kandidaten für Röntgendoppelsterne sind.

Vierzehn der 40 Kandidaten für superweiche Quellen (SWQn) korrelierten mit optischen Novae und konnten somit als die superweiche Röntgenstrahlung von optischen Novae angesehen werden. Unter ihnen befindet sich die erste Nova/SWQ, welche in einem Sternhaufen in M 31 nachgewiesen wurde. Korrelationen mit früheren *ROSAT* und *Chandra* Studien offenbarten, dass nur drei SWQn länger als ein Jahrzehnt sichtbar sind. Dieses Ergebnis unterstreicht die starke Langzeitvariabilität der Klasse der SWQn. Zusätzlich zeigten die Korrelationen, dass nur die Anwendung strenger Selektionskriterien eine sichere Auswahl von SWQn erlaubt.

Die Untersuchung der räumlichen Verteilung der 25 Supernova Überreste (SNÜe) und 37 SNÜ Kandidaten zeigte, dass viele dieser Quellen mit dem 10 kpc Staubring und anderen Sternentstehungsgebieten in M 31 korrelieren. Diese Beziehung zwischen SNÜen und Sternentstehungsgebieten impliziert, dass viele der Überreste von Typ II Supernovae stammen.

Die hellsten Quellen von M 31 gehören zur Klasse der Röntgendoppelsterne (RDSe). Es wurden 10 massenarme RDSe (maRDSe) und 26 maRDS Kandidaten auf Grund ihrer zeitlichen Variabilität identifiziert. Zusätzlich wurden 36 maRDSe und 17 maRDS Kandidaten durch Korrelationen mit (möglichen) Sternhaufen identifiziert. Von den letztgenannten Quellen wurde eine als Kandidat für einen maRDS mit Schwarzem Loch und eine andere als Kandidat für einen maRDS mit einem Neutronenstern vorgeschlagen. Aus optischen und Röntgen Zwei-Farben-Diagrammen wurden mögliche Kandidaten für massenreiche Röntgendoppelsterne (mrRDSe) ausgewählt. Zwei dieser Kandidaten zeigten ein Röntgenspektrum, wie es für mrRDSe, welche einen Neutronenstern enthalten, erwartet wird.

Für die Untersuchung der log N-log S Beziehung der Quellen im Feld von M 31 wurde ein Quellkatalog für den 2.0–10.0 keV Energiebereich erstellt. Die Steigung der log N-log S Beziehung der gesamten Galaxie ist mit dem erwarteten Wert für Spiralgalaxien verträglich (Colbert et al. 2004). Nach Abzug der Hintergrund log N-log S Beziehung enthielt das Gebiet jenseits der $D_{25}$ Ellipse noch immer ungefähr 13 Quellen/deg$^2$ von M 31 mit Flüssen oberhalb des Vollständigkeitslimits von $\sim 3.2\times10^{-14}$ erg cm$^{-2}$ s$^{-1}$ ($\hat{=}2.3\times10^{36}$ erg s$^{-1}$ im Abstand von M 31). Die Abstandsabhängigkeit der Quellverteilung in der Scheibe von M 31 konnte für Grenzflüsse von $\sim 3.2\times10^{-14}$ erg cm$^{-2}$ s$^{-1}$ bzw. $10^{-13}$ erg cm$^{-2}$ s$^{-1}$ ($\hat{=}7.3\times10^{36}$ erg s$^{-1}$) gut mit einem exponentiellen Profil angenähert werden. Ungefähr 60% aller Quellen mit Flüssen oberhalb von $3.2\times10^{-14}$ erg cm$^{-2}$ s$^{-1}$ sind Hintergrundquellen. Während der Beitrag an Hintergrundquellen in der inneren Scheibe nur $\sim$20% beträgt, steigt ihr Anteil in den äußeren Regionen von M 31 auf $\gtrsim$80%. Für die Staubringregion stimmte sowohl die Steigung der log N-log S Beziehung, als auch die Anzahl der Quellen und ihre Abhängigkeit von der Sternentstehungsrate mit den theoretischen Betrachtungen der universellen log N-log S Beziehung einer Population massenreicher Röntgendoppelsterne (mrRDSe) überein (Grimm et al. 2003). Dies legt nahe, dass die Staubringregion eine Population mrRDSe beinhaltet. Ein Vergleich der Anzahl der Röntgendoppelsterne (RDSe) gewonnen aus den log N-log S Beziehungen, mit denjenigen, die im Quellkatalog aufgelistet werden zeigte, dass hauptsächlich Quellen im Flussbereich zwischen $10^{-13}$–$3.2\times10^{-14}$ erg cm$^2$ s$^{-1}$, oder solche die in der inneren Scheibe liegen, im Quellkatalog nicht als RDSe klassifiziert werden.

Die im Rahmen dieser Arbeit erzielten Resultate führten zu einem tieferen Verständnis der Eigenschaften der Röntgenquellpopulationen in M 31. Allerdings können ca. 65% aller Quellen im Feld von M 31 lediglich als 'harte' Quellen klassifiziert werden, d. h. es kann nicht entschieden werden, ob es sich bei diesen Quellen um Röntgendoppelsterne oder dem Krebsnebel ähnliche Supernova Überreste in M 31 oder aktive galaktische Kerne handelt. Um diese Quellen zu klassifizieren, sind weitere und tiefere Beobachtungen in sämtlichen Wellenlängenbereichen notwendig.

# X-ray Source Population Study of the Local Group Galaxy M 31

## Abstract

This dissertation presents the analysis of a large and deep *XMM-Newton* survey of the second large Local Group spiral galaxy M 31. The survey observations, taken between June 2006 and February 2008, together with re-analysed archival observations from June 2000 to July 2004 cover, for the first time, the whole $D_{25}$ ellipse of M 31 with *XMM-Newton* down to a limiting luminosity of $\sim 10^{35}$ erg s$^{-1}$ in the 0.2–4.5 keV band.

The main goal of the thesis was a study of the different source populations of M 31 that can be observed in X-rays. Therefore a catalogue was created, which contains all 1 948 sources detected in the 0.2–12.0 keV range. 961 of these sources were detected in X-rays for the first time. Source classification and identification was based on X-ray hardness ratios, spatial extent of the sources, and by cross correlating with catalogues in the X-ray, optical, infrared and radio wavelengths. An additional classification criterion was the long-term temporal variability of the sources in X-rays. This variability allows us to distinguish between X-ray binaries and active galactic nuclei. Furthermore, supernova remnant classifications of previous studies that did not use long-term variability as a classification criterion, could be validated. Including previous *Chandra* and *ROSAT* observations in the long-term variability study allowed me to detect additional transient or at least highly variable sources, which are good candidates for being X-ray binaries.

Fourteen of the 40 supersoft source (SSS) candidates correlated with optical novae and therefore can be considered the supersoft emission of the optical novae. Among them is the first nova/SSS detected in a globular cluster of M 31. Correlations with previous *ROSAT* and *Chandra* studies revealed that only three SSSs are visible for at least one decade. This result underlines the strong long-term variability found for the class of SSSs. In addition the correlations demonstrated that strict selection criteria have to be applied to securely select SSSs.

An investigation of the spatial distribution of the 25 supernova remnants (SNRs) and 37 SNR candidates showed that many of these sources are consistent with the location of the 10 kpc dust ring and other star forming regions in M 31. This connection between SNRs and star forming regions implies that most of the remnants are from type II supernovae.

The brightest sources of M 31 belong to the class of X-ray binaries (XRBs). Ten low mass XRBs (LMXBs) and 26 LMXB candidates were identified based on their temporal variability. In addition 36 LMXBs and 17 LMXB candidates were identified due to correlations with globular clusters and globular cluster candidates. From the LMXBs located in globular clusters one is a black hole candidate and another a neutron star candidate. From optical and X-ray colour-colour diagrams, possible high mass XRB (HMXB) candidates were selected. Two of these candidates have an X-ray spectrum as is expected for an HMXB containing a neutron star primary.

To investigate the log N-log S relations of sources in the field of M 31, a catalogue of sources detected in the 2.0–10.0 keV energy range was created. The slope of the log N-log S relation for the whole galaxy is consistent with the expectation for spiral galaxies (Colbert et al. 2004). Subtracting the background log N-log S relation, the region beyond the $D_{25}$ ellipse still contains about 13 sources/deg$^2$ of M 31 with fluxes above the completeness limit of $\sim 3.2 \times 10^{-14}$ erg cm$^{-2}$ s$^{-1}$ ($\hat{=} 2.3 \times 10^{36}$ erg s$^{-1}$ at the distance of M 31). The radial dependence of the source distribution in M 31's disc can be well fitted with an exponential profile, for limiting fluxes of $\sim 3.2 \times 10^{-14}$ erg cm$^{-2}$ s$^{-1}$ and $10^{-13}$ erg cm$^{-2}$ s$^{-1}$ ($\hat{=} 7.3 \times 10^{36}$ erg s$^{-1}$). About 60% of all sources with fluxes above $3.2 \times 10^{-14}$ erg cm$^{-2}$ s$^{-1}$ are background sources. While the contribution of background sources lies at $\sim$20% in the inner disc region, the fraction increases to $\gtrsim$80% in the outer areas of M 31. For the dust ring region, the slope of the log N-log S relation as well as the number of sources and their dependence on the star forming rate were consistent with the universal log N-log S relation predicted from theoretical considerations of HMXBs (Grimm et al. 2003). These findings propose that the dust ring region contains a population of HMXBs.

A comparison of the number of X-ray binaries (XRBs) obtained from the log N-log S study to the ones listed in the source catalogue showed that many XRBs detected in the log N-log S study with fluxes between $10^{-13}$ erg cm$^{-2}$ s$^{-1}$ and $3.2 \times 10^{-14}$ erg cm$^{-2}$ s$^{-1}$, or (independent from the flux) those XRBs located in the inner disc of M 31, remain without XRB classification in the source catalogue.

The results presented in this thesis gave us deeper insights in the properties of the population of X-ray sources in M 31. Nevertheless, about 65% of all sources detected in the field of M 31 can be classified as "hard" sources only, *i. e.* it is not possible to decide whether these sources are X-ray binaries or Crab-like supernova remnants in M 31, or active galactic nuclei. Deeper observations in the X-ray and at other wavelengths are needed to classify these sources.

# Contents

# Chapter 1

# Introduction

Over the past four decades X-ray source population studies of nearby galaxies have come a long way since the first detections of X-ray emission from the Andromeda galaxy (*e. g.* Bowyer et al. 1974). In the late seventies, the first pioneering imaging X-ray telescope, *Einstein*, opened up the systematic study of the X-ray emission of normal galaxies. The *ROSAT* mission (1990–1999) expanded our knowledge of X-ray properties of galaxies, and widened the observable X-ray window down to lower energies. We are now in the era of third generation X-ray observatories led by the *XMM-Newton* and *Chandra* satellites, which provide unprecedented spatial and energy resolution over a broad energy band down to low fluxes.

Compared to studies of our own Galaxy, the Milky Way, there are some advantages in the study of nearby galaxies.

- First of all, the observed sources of the nearby galaxy, *i. e.* excluding foreground and background objects, are all more or less at the same distance. So if the distance to the galaxy is known, the luminosity of the sources will be known too. Nowadays it is still challenging to determine precise distances to our neighbouring galaxies or even within the Milky Way itself. However compared to the distance estimates available for objects within our own Galaxy, the distances to nearby galaxies are well determined.

- Another advantage is that the field of view of a telescope covers a larger part of the nearby galaxy compared to the Milky Way. It is therefore easier to study source populations. An observation of a nearby galaxy can cover many representatives of a source class, whereas within the Milky Way in general each source must be observed individually.

- In addition observations of nearby galaxies are not so severely affected by absorption as observations within the Milky Way might be, *e. g.* observations to the Galactic centre.

- The study of nearby galaxies also allows us to investigate a wide range of different environments, for instance different types of galaxies, or different galactic components (bulge, disc, spiral arms). From these studies we can derive the relationships between the X-ray properties and the galactic structure and star formation activity.

Compared to more distant galaxies, the radiation observed in nearby galaxies can be resolved into individual sources. From the comparison of the results obtained form nearby galaxies to the observed radiation of more distant galaxies, it is possible to explore the properties of the distant galaxies, like *e. g.* star formation at high redshift (Soria 2003).

Exceptionally well suited for source population studies are the galaxies belonging to the *Local Group*. The dominant members of the Local Group are the Milky Way and the Andromeda galaxy (also known as M 31). These two galaxies each have a system of satellite galaxies (for instance the Large and Small Magellanic Cloud are satellite galaxies of the Milky Way, or M 32 and NGC 205 are satellite galaxies of M 31). In total the Local Group contains more than about 30 galaxies.

Apart from sources in the Milky Way, X-ray sources have been studied for instance in the Large and Small Magellanic Cloud[1] (LMC, SMC; *e. g.* Haberl & Pietsch 1999a; Kahabka et al. 1999), the Triangulum galaxy (also known as M 33; *e. g.* Pietsch et al. 2004; Misanovic et al. 2006) and of course in M 31.

With respect to observations of M 31, the American-led *Chandra* satellite has mainly observed sources in the central field of M 31 and in selected areas of the disc (*e. g.* Kong et al. 2002b, 2003a; Williams et al. 2004a; Di Stefano et al. 2004). *Chandra* is especially well suited to studying crowded fields due to its high spatial resolution. However, a survey of the entire galaxy would be very time consuming because of *Chandra*'s relatively small field of view. A complete catalogue of point-like X-ray sources based on archival *XMM-Newton* observations, which cover mainly the major axis of M 31, can be found in Pietsch et al. (2005b). Combining a high spatial resolution and a large field of view *XMM-Newton* is the satellite choice for X-ray surveys of Local Group galaxies.

Following the interesting results from Pietsch et al. (2005b), the *M 31 Large Program collaboration* (PI: W. Pietsch) was granted a deep homogeneous *XMM-Newton* survey of M 31 as a *large program* that covers the entire galaxy and allows the study of the X-ray point source population down to a limiting luminosity of $\sim 10^{35}$ erg s$^{-1}$ in the 0.2–4.5 keV band.

Sources that are observable in X-rays are supersoft sources (a class of sources discovered by *ROSAT*), supernovae and their remnants, X-ray binaries and so called ultra-luminous X-ray sources. Hot X-ray emitting gas and populations of spatially unresolved X-ray emitting sources are observed as diffuse emission. In addition, surveys of nearby galaxies always contain foreground sources, located within the Milky Way, and background objects, such as other galaxies, active galactic nuclei and galaxy clusters.

M 31 does not contain any ultra-luminous X-ray source. In addition no supernova was observed in X-rays in M 31 up to now. Another interesting fact is that, despite some more or less reliable candidates, not a single, clearly detected high-mass X-ray binary is known in M 31.

The main goal of this thesis is to study the populations of the above mentioned source classes in M 31. It was first necessary to create a catalogue of the sources found in the large program observations. As these observations mainly pointed to the outer regions of M 31, archival[2] data were reanalysed to cover the whole $D_{25}$ ellipse.

For the classification and identification of the sources different methods were used. A very powerful and often used method, which can be applied to every discrete source, are X-ray colour-colour diagrams. They are called hardness ratio diagrams, and are based on the different spectral shapes of the sources of each class. However, there are source classes that have such similar spectral properties that they cannot be separated in hardness ratio diagrams and so other methods are also needed.

Further information about a source and its membership in a source class can be obtained from its temporal behaviour. Phenomena on short time scales are bursts or dips from X-ray binaries, flares from foreground stars or the periodic variability of pulsars. The method used in Misanovic et al. (2006) for M 33 to study variability on long term time scales (several months to years), was adapted to M 31. The results obtained for the sources of the central field of M 31 were published in Stiele et al. (2008b). Those investigations help to separate supernova remnants, which do not show variability on those time scales, from foreground stars. Among the hard X-ray sources mainly X-ray binaries are expected as strongly variable sources (compared

[1] For the SMC an *XMM-Newton* survey (PI: F. Haberl) is underway, where most of the up to now uncovered areas are observed.
[2] observations taken before 2005

to the few known active galactic nuclei with comparable variability).

Another criterion to strengthen specific source classification is the extent of a source. In the Milky Way and the LMC and SMC supernova remnants are observed as spatially resolved sources (*e. g.* Decourchelle et al. 2001; van der Heyden et al. 2004). In M 31 supernova remnants are normally observed as point-like sources, although in *Chandra* observations of M 31, some were found as spatially resolved X-ray sources (*e. g.* Kong et al. 2003b). Galaxy clusters can be found as extended sources, too.

Additional information can be achieved by cross correlating with catalogues in the radio, infra-red and optical wavelengths.

Despite this wealth of classification and identification methods a large fraction of "hard" sources – which comprises X-ray binaries or Crab-like supernova remnants in M 31, or active galactic nuclei – could not be assigned to a single source class. Therefore I developed procedures to study the log N-log S relations (luminosity functions) of the population of "hard" sources of M 31. The methods are based on techniques applied to the sources of the COSMOS field (*e. g.* Cappelluti et al. 2007). In this way the contribution of background sources could be estimated from the results of the COSMOS survey.

This work presents a study of the different source populations of M 31 observable in X-ray light, including the spatial and energetic distributions. Furthermore, detailed comparisons with previous X-ray studies are discussed. For these investigations several source catalogues were created. The full catalogues will only be available in electronic form on the attached CD. Descriptions of the structure and contents of the catalogues (so-called ReadMe files) are given in Appendices C, D and E.

**Thesis outline**

In the next chapter (Chap. 2) I introduce the X-ray emission mechanisms and present the different source classes that can be observed in X-rays in the fields of nearby galaxies. Furthermore, I present the methods used to categorise the sources within these classes.

The main properties of the Andromeda galaxy and a short overview of previous observations and results which are related to the topic of this thesis are given in Chap. 3. The focus lies on previous X-ray studies.

As this thesis is mainly based on the "*XMM-Newton* M 31 Large Program observations" obtained with the ESA *XMM-Newton* X-ray observatory, Chap. 4 introduces the satellite and its instruments.

A detailed presentation of the *XMM-Newton* observations used and a general description of the data analysis can be found in Chap. 5.

The investigation of the temporal variability of the X-ray sources in the centre of M 31, based on archival observations, is presented in Chap. 6. These results are published in Stiele et al. (2008b).

Chapter 7 presents the new source catalogue of the "*XMM-Newton* M 31 Large Program project". In addition the classification criteria are introduced and the flux variability, the distribution of hardness ratios, the extent, and bright sources are investigated.

Form all sources detected in the 2.0–10.0 keV band I created a special catalogue to derive log N-log S relations. The relations were determined for different regions to search for and to examine the spatial dependence within the log N-log S relations. The results of the investigation can be found in Chap. 8. Furthermore possible correlations between the number of sources (especially high mass X-ray binaries) and the star formation rate, claimed in the literature, were investigated for the source population(s) of M 31.

Chapter 9 contains a detailed discussion. Here both source catalogues and cross-correlations with other X-ray catalogues of M 31 are discussed. Furthermore the chapter presents the results found for the sources from each different source class, including the spatial and flux distributions, and the flux variability observed between different satellites (*XMM-Newton*, *Chandra*, *ROSAT*). Sources belonging to M 31 are discussed separately from foreground stars and background sources located in the field of M 31. For the class of

X-ray binaries the number of sources derived from log N-log S relations is compared with the number of sources listed as X-ray binaries or X-ray binary candidates in the source catalogue to estimate the number of unclassified X-ray binaries.

The thesis is concluded in Chap. 10 with the conclusions and an outlook on future developments.

Publications that are included in this thesis are:

Stiele et al. (2007) on "*XMM-Newton* observation of two X-ray transients in M 31"

Stiele et al. (2008a) on "A deep *XMM-Newton* survey of M 31"

Stiele et al. (2008b) on "Time variability of X-ray sources in the M 31 centre field"

Stiele et al. (2010) on "Supersoft sources in M 31: Comparing the XMM-Newton Deep Survey, ROSAT and Chandra catalogues"

Publications that contain results obtained within the framework of this thesis, but which are not, or only in part included in this thesis, are:

Pietsch et al. (2007) on "X-ray monitoring of optical novae in M 31 from July 2004 to February 2005"

Barnard et al. (2008) on "New *XMM-Newton* analysis of three bright X-ray sources in M 31 globular clusters, including a new black hole candidate"

Voss et al. (2008) on "Three X-ray transients in M 31 observed with *Swift*"

Ofek et al. (2008) on "GRB 070201: A possible soft gamma-ray repeater in M 31"

Henze et al. (2009) on "The first two transient supersoft X-ray sources in M 31 globular clusters and the connection to classical novae"

Henze et al. (2010) on "Recent discoveries of supersoft X-ray sources in M 31"

# Chapter 2

# X-rays from fields of nearby galaxies

Astronomers gain information about their research subjects by gathering and analysing the electromagnetic radiation travelling from astronomical objects to the Earth.[1] The energy distribution of the radiation ranges from short gamma rays to long radio waves. Here we are interested in the X-rays, which provide us with information about the high-energy state of matter in the universe. In high-energy astrophysics, photon energies and temperatures are usually given in units of 'electron volts' (eV) or 'kilo electron volts' (keV). $E[\mathrm{keV}] = k_{\mathrm{B}}T[\mathrm{K}]$, where $k_{\mathrm{B}}$ is the Boltzmann constant ($8.62 \times 10^{-5}\mathrm{eV\,K^{-1}}$). 1 keV hence corresponds to a temperature of $1.16 \times 10^7$ K. In general, X-rays in the range from 0.1 to 100 keV are characteristically produced by gas heated to high temperatures (millions of Kelvin), and high-energy particles interacting with magnetic fields (synchrotron radiation) or photons (inverse Compton radiation). Since the X-rays are absorbed in the Earth's atmosphere, it is not possible to observe this radiation with ground-based techniques and one has to use X-ray detectors mounted on balloons, rockets or satellites, to detect the X-ray emission and discover the nature of its sources. That is the reason why X-ray astronomy only became possible in the last century, even though astronomy is one of the oldest sciences of mankind in general.

In the following section the main properties of the X-ray emission mechanisms are summarised (Charles & Seward 1995; Vogel 1995).

## 2.1 X-ray emission mechanisms

- **Synchrotron Radiation:**
  When charged particles move through a magnetic field they are accelerated perpendicular to their instantaneous direction of motion by the magnetic field. Due to the acceleration, the charged particles emit so-called 'synchrotron radiation'. As electrons are the lightest particles, they dominate the emission mechanism. In an astrophysical setting with electrons with a power-law energy spectrum, the superposition of radiation from the entire ensemble can also be characterised by a power-law spectrum:

  $$I(E) = A\,E^{-\alpha} \tag{2.1}$$

  where $\alpha$ is the spectral index. $E$ denotes the energy and $A$ is some constant. In X-ray astronomy, spectra are usually in units of photons per photon energy, and *not* intensity (or flux) per frequency. Thus Eq. 2.1 changes to:

  $$N(E) = B\,E^{-\Gamma} \tag{2.2}$$

[1] Information about astronomical objects is nowadays also obtained from measurements of cosmic rays and neutrinos. In the future, detections of gravitational waves could provide additional information about astronomical objects.

where $\Gamma$ is the photon index and $B$ is a constant. Since the intensity (at energy $E$) is proportional to the number of photons (at energy $E$) times the energy $E$, the photon and spectral indices are related such that $\Gamma = \alpha + 1$. With increasing $\Gamma$ or $\alpha$ the spectrum becomes 'softer'. Supernovae and supernova remnants are typical astrophysical examples for the production of synchrotron radiation. The relativistic electrons released in these processes move through strong magnetic fields within shock fronts in the circumstellar medium. Another example of synchrotron radiation is the relativistic jets emanating from compact objects such as super-massive black holes within AGN.

- **Inverse Compton Radiation:** X-ray radiation scattered by matter loses part of its energy, due to the collisions between X-ray photons and electrons within the scattering material (which are at rest). This is the so-called Compton effect (Compton 1923). The energy loss of an X-ray photon, or its corresponding increase in wavelength, can be derived from:

$$\lambda' - \lambda = 2\frac{h}{mc}\sin^2\frac{\vartheta}{2} \tag{2.3}$$

where $\lambda$ and $\lambda'$ are the wavelength of the photon before and after the collision, respectively, $\vartheta$ is the scattering angle, and

$$\frac{h}{mc} = \lambda_{\rm C} = 0.0243\text{Å} \tag{2.4}$$

is called the Compton wavelength. Here $m$ is the mass of the electron ($9.11\times10^{-31}$ kg), $h$ the Planck constant ($6.63\times10^{-34}$ Js), and $c$ the speed of light ($3.00\times10^{8}$ ms$^{-1}$).
Inverse Compton radiation can be produced when the electron, which has an energy much larger than its rest energy, gives some of its energy to the photon. In this case the photon is scattered up to shorter wavelengths. In X-ray astronomy, inverse Compton scattering occurs in supernovae and in the corona around the accretion disc of active galactic nuclei. In the latter case, it is believed to cause the power-law component in the X-ray spectra of accreting black holes.

- **Thermal Emission from Hot Gas:**
An important emission process for astronomical X-rays is the emission of hot gas. In thermal equilibrium, electrons have a well-determined velocity distribution ('Maxwell distribution'). When an electron passes close to a positive ion, the electrostatic force causes the electron to change its trajectory and subsequently to emit radiation ('bremsstrahlung'). With increasing temperature, $T$, of the electron, its velocity and subsequently the energy, $E$, of its bremsstrahlung radiation rise. Thermal bremsstrahlung radiation can be described by a spectral distribution of the form:

$$I(E,T) = AG(E,T)Z^2 n_{\rm e} n_{\rm i} (k_{\rm B}T)^{-1/2} {\rm e}^{E/k_{\rm B}T}, \tag{2.5}$$

where $k_{\rm B}$ is the Boltzmann constant ($1.38\times10^{-23}$JK$^{-1}$), $G(E,T)$ is the Gaunt factor, $Z$ is the charge of the ions, $n_{\rm e}$ and $n_{\rm i}$ are the electron and ion densities, respectively, and $A$ is a constant. If line emission from ions of heavier elements that have been excited in collisions with electrons is taken into account, the thermal bremsstrahlung continuum emission will be superposed by emission lines. Within galaxies, thermal plasma spectra from hot gas are observed in various emission regions, *e. g.* galactic halos, supernova remnants, H II regions or accretion of material onto a compact object.

- **Blackbody Radiation:**
In the theory of radiation an object that neither reflects nor scatters incident radiation, but absorbs and re-emits the radiation completely, is defined as a black body. Despite the definition being rather idealistic, the radiation emitted by many astrophysical objects can to first order be approximated almost perfectly by a blackbody. The energy distribution of a black body is only dependent on its

temperature, and completely independent of its shape, material or internal structure. The intensity of the radiation from a blackbody is characterised by the Planck spectrum:

$$I(E,T) = 2 \times E^3 \frac{1}{h^2 c^2 \left(\mathrm{e}^{E/k_\mathrm{B}T} - 1\right)}, \tag{2.6}$$

where $h$ is the Planck constant, $k_\mathrm{B}$ is the Boltzmann constant and $c$ is the speed of light. Examples of astrophysical sources often approximated by blackbody spectra are young neutron stars (*e. g.* in the centre of supernova remnants) or white dwarfs in the supersoft phase after a nova outburst.

## 2.2 Sources in the fields of nearby galaxies

In X-rays, the observed fields of nearby galaxies comprise a multitude of different source classes. The sensitivity of current X-ray telescopes allows the detection of point-like sources with luminosities above $\sim 10^{35}$ erg s$^{-1}$ (0.2–4.5 keV) in M 31, in an exposure time of $\sim$60 ks.[2] This limit depends on the distance to the observed galaxy and increases quadratically for larger distances, assuming an unchanged exposure time. X-ray emission from stars and cataclysmic variables located within a nearby galaxy is normally too faint to reach the limiting luminosities. In the following subsection I will describe the different types of observed X-ray sources.

### 2.2.1 Discrete sources

#### 2.2.1.1 X-ray binaries

X-ray binaries (XRBs) are among the brightest objects in the sky at $\sim$ keV energies. They were detected by the first X-ray missions launched into space (Giacconi et al. 1962). As their name already indicates, XRBs consist of a compact object plus a companion star. The compact object can either be a white dwarf (these systems are then also known as cataclysmic variables, CVs), a neutron star (NS), or a black hole (BH). A common feature of all these systems is that a large amount of the emitted X-rays are produced due to the conversion of gravitational energy from the accreted matter into radiation by a mass-exchange from the companion star onto the compact object.

X-ray binaries containing an NS or a BH are divided into two main classes, depending on the mass of the companion star:

**Low mass X-ray binaries (LMXBs)** contain companion stars of low mass ($M \lesssim 1\,\mathrm{M}_\odot$) and late type (type A or later), and have a typical lifetime of $\sim 10^{8-9}$ yr (Fabbiano 2006). LMXBs can be located in globular clusters.

Mass transfer from the companion star into an accretion disc around the compact object occurs via Roche-lobe overflow. The mass transfer can be sustained in two ways, either by the expansion of the low mass star as it evolves off the main sequence, or by the loss of orbital angular momentum due to gravitational radiation and magnetic braking.

In a binary system the gravitational interaction of both objects affects the shape of the stars. The shape follows the equipotential surfaces of the rotating binary. Moving away from the stellar centres the equipotential surfaces become more and more pear-shaped, until the point is reached where the two surfaces touch one another and the gravity of the two stars cancels out. This happens in the so-called first Lagrange point $\mathrm{L}_1$. The equipotential surface touching this point is called the Roche-lobe of the star. When the size of the star is large enough to fill the star's Roche-lobe, matter can flow through $\mathrm{L}_1$ and forms a rotating accretion

[2] The unscreened observations of the Large *XMM-Newton* Survey of M 31 have an exposure time of $\sim$60 ks.

disc around the compact object due to its angular momentum. The size of the Roche-lobe can be described by an average radius $R_{\rm L}$, which is defined as the radius of a sphere that encloses the same volume as the Roche-lobe (Paczyński 1971). The radius $R_{\rm L}$ can be approximated by

$$\frac{R_{\rm L}}{a} = \frac{0.49}{0.6 + q^{2/3} \ln\left(1 + q^{-1/3}\right)} \tag{2.7}$$

where $a$ is the orbital separation of the binary and $q = M_{\rm a}/M_{\rm d}$ is the mass ratio of the two stars ($M_{\rm d}$ being the mass of the donor and $M_{\rm a}$ the mass of the accretor; Eggleton 1983).

In the material that has settled into a disc, viscosity transports angular momentum outwards, thereby allowing matter to be accreted by the central compact object (Shakura & Sunyaev 1973). The energy released during this process is emitted from the surface of the disc. The disc temperature varies as $T \sim R^{-3/4}$ in a stationary viscously heated disc (where $R$ is the radius of the disc) and as $T \sim R^{-1/2}$ in an illuminated disc, and thus the X-rays are predominantly emitted from the inner regions of the disc (*i. e.* the regions closer to the accreting object). This general picture is still valid, even though the theory has advanced significantly. For a comprehensive overview of accretion discs, see Frank et al. (2002).

For very high accretion rates, the radiation pressure produced by the infalling matter limits the accretion rate. If the pressure is stronger than the gravitational attraction of the compact object, the material will be dispersed rather than accreted. For objects with steady, spherically symmetric emission, the limiting luminosity (called the Eddington luminosity) is given by

$$L_{\rm Edd} = \frac{4\pi G M m_{\rm p} c}{\sigma_{\rm T}} \tag{2.8}$$

where $G$ is the gravitational constant ($6.67\times10^{-11}{\rm m^3kg^{-1}s^{-2}}$), $M$ is the mass of the accreting object, $m_{\rm p}$ is the mass of the proton ($1.67\times10^{-27}$ kg), $c$ is the speed of light and $\sigma_{\rm T}$ is the Thomson cross-section ($6.65\times10^{-25}{\rm cm^2}$). Hence a 1.4 $\rm M_\odot$ NS accreting hydrogen rich matter cannot produce a *steady* luminosity greater than $\sim 2\times10^{38}$ erg s$^{-1}$. Since the Eddington limit is proportional to the mass of the accreting object massive BHs can have *steady* luminosities $\gtrsim 2\times10^{38}$ erg s$^{-1}$. Magnetised NSs or massive BHs will reach luminosities above their Eddington limit if the accretion is non-spherical or beaming effects and jet-formation occur.

A very special class of LMXBs are the so-called ultra-compact X-ray binaries, where the donor star is a white dwarf (Deloye & Bildsten 2003; Bildsten & Deloye 2004).

**Variability and emission spectra of LMXBs in different states** At low accretion rates NS and BH LMXBs show rather similar emission spectra and variability (van der Klis 1994). The power density spectrum (PDS) of this low-hard state can be characterised by a broken power-law with spectral index, $\gamma$, changing from $\sim$0 to $\sim$1 at some break frequency. In addition the root mean square (r.m.s.) variability is high ($\sim$10–50%, van der Klis 1994, 1995; McClintock & Remillard 2006). However, at higher accretion rates, the PDS may be described by a simple power-law with $\gamma \sim$1 and the r.m.s. variability is only a few percent (van der Klis 1994, 1995; McClintock & Remillard 2006).

Going from low to high accretion rate we find that the change in variability is accompanied by a change in the emission spectra of LMXBs. The hard spectra of low-state LMXBs are characterised by power-laws with photon indices of $\sim$1.4–1.7, regardless of the primary object (van der Klis 1994; McClintock & Remillard 2006). At higher accretion rates the emission spectra depend on the accretor. For BH LMXBs two states have been identified: a thermally dominated state (also known as the high/soft state) where a 0.7–2 keV disc blackbody contributes $\gtrsim$90% of the 0.3–10 keV flux (McClintock & Remillard 2006) and a "steep power-law" state, where an additional power-law component is observed, with a photon index

$> 2.4$ (McClintock & Remillard 2006). Whereas, NS LMXBs emit predominantly non-thermal spectra. Nevertheless, at higher luminosities an additional blackbody component becomes increasingly important. This blackbody component can contribute up to 50% of the flux (see e.g. White et al. 1988; Church & Bałucińska-Church 1995, 2001; Barnard et al. 2003a, and references within).

Van der Klis (1994) proposed that LMXBs switch from low to high accretion rate behaviour at some constant fraction of the Eddington limit. If this were true, then BH LMXBs would be capable of exhibiting low-state variability and spectra at higher luminosities than neutron star LMXBs, as the Eddington limit is proportional to the mass of the accretor (Barnard et al. 2003c). Barnard et al. (2004) found some empirical evidence for a transition at $\sim$10% of the Eddington luminosity. We would therefore expect an LMXB containing a $\sim 10\,\mathrm{M}_\odot$ BH to exhibit low-state characteristics at $\sim$10 times the maximum luminosity of the low-states observed in $1.4\,\mathrm{M}_\odot$ NS LMXBs.

LMXBs can show intrinsic or apparent periodic or aperiodic flux variations. Sometimes the variations are accompanied by significant spectral variability (Hasinger & van der Klis 1989). One source of the flux variations is the orbital motion of the stars, which causes smooth periodic modulations and periodic dips (see review by White et al. 1995, and references therein). Depending on the viewing angle between the observer and the LMXB, the companion star can cross the line of sight, which results in periodic eclipses. NS LMXBs can exhibit isolated flux increases, with short rise times ($\sim$1 s or even less) and decays lasting up to several minutes, and accompanied by distinct spectral softening (Lewin et al. 1993, and references therein). These aperiodic variabilities are believed to be caused by thermonuclear burning, either, because a sufficient amount of hot, compressed material is accreted onto the neutron star surface (type-I burst), or due to instabilities in the accretion disc (type-II burst). The profiles of the bursts depend on the photon energy, and show much shorter decays at lower energies (Strohmayer & Bildsten 2006). Rotating NSs with strong magnetic fields can show pulsations. Irregularities in the inner accretion disc can cause rapid aperiodic variabilities, which are observed as quasi-periodic oscillations (QPOs) or flickerings in the power density spectra of XRBs.

A special type of variability is the transient behaviour shown by many LMXBs. These sources are sometimes called X-ray novae and go through a phase of greatly increased X-ray flux (by a factor of $10^3$–$10^4$) that can last from less than one month to tens of years or longer (Priedhorsky & Holt 1987; Bradt et al. 2000; Tanaka & Lewin 1995). The reason for the transient behaviour is a thermal-viscous instability in the accretion disc (*e. g.* Lasota 2001; Dubus et al. 2001). As long as the LMXB is in quiescence, the accretion disc is cold and neutral and the accumulated matter, which arrives at the outer edge of the disc, can diffuse inwards. When the surface density of the accreted material exceeds a certain threshold[3], the disc temperature rises above the ionisation temperature of neutral hydrogen ($\sim 10^4\,\mathrm{K}$), which causes a thermal disc instability, since the opacity is related to temperature in the case of partially ionised hydrogen. The instability of the disc triggers the observed X-ray nova outburst (Dubus et al. 2001). Complications, which are not included in the model, can arise if the disc is large enough that it becomes warped in outburst, or shadows the secondary star, or if the mass transfer is increased due to a previous outburst, or if winds cause a significant mass loss.

**High mass X-ray binaries (HMXBs)** contain a massive O or B star companion ($M_{\mathrm{star}} \gtrsim 10\,\mathrm{M}_\odot$, Verbunt & van den Heuvel 1995) and are short-lived with lifetimes of $\sim 10^{6-7}$ yr (Fabbiano 2006). One has to distinguish between two main groups of HMXBs: super-giant and the Be/X-ray binaries.

In the super-giant systems, the compact object mainly accretes mass from radially outflowing stellar winds, since OB stars have significant winds with mass-loss rates between $10^{-6}$–$10^{-10}\mathrm{M}_\odot\ \mathrm{y}^{-1}$. This

[3]The location within the disc where this happens depends on many parameters, for example the accretion rate, the irradiation or the size of the disc. From theory the so-called "inside-out" bursts (type B) should occur more often than the "outside-in" bursts (type A; Dubus et al. 2001).

wind-driven accretion onto the compact object powers the X-ray emission. Mass-accretion via Roche-lobe overflow is less frequent in HMXBs, but is still known to occur in several bright systems (*e. g.* LMC X-4, SMC X-1, Cen X-3). HMXBs, in which the donor has evolved away from the main sequence, are permanently bright X-ray sources. While variability can occur due to absorption in the wind, we can observe pulsations due to the rotation of the NS.

A newly discovered subclass of super-giant HMXBs are Super-giant Fast X-ray Transients (SFXTs) found by *INTEGRAL*, which show short outbursts lasting typically a few hours (*e. g.* Negueruela et al. 2006).

Be-stars not only lose mass in a spherical wind, as other high-mass stars do, but occasionally lose much matter in an equatorial wind, which possibly flows out in a disc-like geometry. In Be/X-ray binaries, the orbit of the compact object, presumably a neutron star, is generally wide and eccentric. Most of the time the neutron star accretes at a low level from the stellar wind and hence radiates at low X-ray luminosity. X-ray outbursts are normally associated with the passage of the neutron star through the circumstellar disc, where accretion onto the compact object is enhanced. As a result, Be/X-ray binaries are highly variable X-ray sources.

Depending on the viewing angle between the observer and the HMXB the companion star can cross the line of sight, which results in periodic eclipses.

Independent of the nature of the donor, HMXBs are potentially good tracers of the very recent star formation activity in a galaxy, because of their rapid evolution (Sunyaev et al. 1978).

#### 2.2.1.2 Supersoft sources

The class of supersoft sources (SSSs) is based on observable characteristics. Classification is afforded to sources showing extremely soft spectra with equivalent blackbody temperatures of ∼15–80 eV. The associated bolometric luminosities are in the range of $10^{36}$–$10^{38}$ erg s$^{-1}$ (Kahabka & van den Heuvel 1997).

Because of the phenomenological definition, this class is likely to include objects of several types. The favoured model for these sources are close binary systems with a white dwarf (WD) primary, burning hydrogen on the surface (*cf.* Kahabka & van den Heuvel 1997). Close binary SSSs include post-outburst, recurrent, and classical novae, the hottest symbiotic stars, and other LMXBs containing a WD (CVs). Symbiotic systems, which contain a WD in a wide binary system, were also observed as SSSs (Kahabka & van den Heuvel 1997). Because matter that is burned can be retained by the WD, some SSS binaries may be progenitors of type-Ia supernovae (*cf.* van den Heuvel et al. 1992, and Sect. 2.2.1.3). It should be mentioned that, indeed, any object more compact than a WD could certainly act as an SSS. Suggestions for these compact objects are neutron stars or intermediate-mass BHs.

Compared to blackbody fits, WD atmosphere models are more sophisticated and more physically representative models of the X-ray spectra observed from SSSs. However, it can be challenging to constrain and interpret the many free parameters of those models. This is especially true for spectra of faint, distant sources with low statistics.

The soft X-ray emission is produced by nuclear burning of the hydrogen accreted onto the white dwarf. Depending on the accretion rate, we either observe a steady nuclear burning of the material on the white dwarf surface ($dM/dt \sim 1 - 4 \times 10^{-7}\,\mathrm{M}_\odot$ yr$^{-1}$), or we observe an irregular burning ($dM/dt \sim 10^{-8}$–$10^{-7}\,\mathrm{M}_\odot$ yr$^{-1}$), which results in outbursts as seen in novae or other cataclysmic variables.

Up to now, several SSSs have been optically identified with close binary systems (Greiner 2000). Prototypical sources are, on the one hand, CAL 83 (Greiner & Di Stefano 2002, and references therein) and CAL 87 (Greiner et al. 2004b, and references therein). Both sources are located in the Large Magellanic Cloud and show eclipses (CAL 87) or rare X-ray off states (CAL 83), but are rather permanent SSSs. On the other hand Pietsch et al. (2005a, 2007) showed that many SSSs in M 31 correlate with classical novae.

These sources are luminous transient SSSs which seem to go through an outburst that can last from weeks to several years[4].

How are classical novae (CNe) connected to SSSs? A WD in a cataclysmic binary accretes hydrogen-rich matter from its companion. The transferred matter accumulates on the surface of the WD until hydrogen ignition starts a thermonuclear runaway in the degenerate matter of the WD envelope. This thermonuclear explosion is called a classical nova. The brightness of the WD can rise by more than nine magnitudes within a few days, and mass can be ejected at high velocities, due to the expansion of the hot envelope of the WD (*cf.* Hernanz 2005; Warner 1995, and references therein). However, a fraction of the hot envelope can remain, burning hydrogen steadily on the surface of the WD, powering an SSS (Starrfield et al. 1974; Sala & Hernanz 2005). Once the ejected envelope becomes sufficiently transparent to X-rays, the SSS can be observed directly. Therefore, the turn-on time depends on the fraction of mass ejected in the outburst (*cf.* Sala & Hernanz 2005; Tuchman & Truran 1998; Hachisu & Kato 2006). The amount of *un*ejected hydrogen-rich material and the luminosity of the WD determine the duration of the supersoft phase. As more massive WDs need to accrete less matter to initiate the thermonuclear runaway (Jose & Hernanz 1998) and, in general, retain less accreted matter after the explosion (Yaron et al. 2005), the duration of the SSS state is inversely related to the mass of the WD. Therefore X-ray lightcurves provide important clues on the physical parameters of the components in a nova outburst.

#### 2.2.1.3 Supernovae

A supernova (SN) is a stellar explosion, during which the gravitational binding energy of the entire star is released. The largest fraction of the binding energy is transported into space by neutrinos ($\sim$99%) and the ejected shell ($\sim$1%), whereas radiation released during the SN explosion only accounts for $\sim$0.01% of the total liberated energy. Nonetheless, SNe are one of the most spectacular events visible in the universe and can reach luminosities of $10^9\,\mathrm{L}_\odot$, a considerable fraction of the total luminosity of a galaxy. With the ejection of the stellar shell, all heavy elements synthesised during the life of the star are released into the interstellar space. In addition all elements heavier than iron are synthesised during the SN explosion. In this respect, SN explosions play an important role in the chemical evolution of the universe. In fact, all heavy elements found on planets, the Earth and even in our own body were produced during consecutive SN explosions, and spread into the interstellar medium (ISM) from which stars and planets form. SNe can effect the birth of stars and planets in a second way, in which the SN blast triggers the collapse of nearby molecular clouds.

Based on their optical spectra, SNe are classified into two different classes: type-I and type-II. SNe of type-I do not show Balmer lines of hydrogen in their spectrum, in contrast to SNe of type-II, and are further subdivided into classes Ia, Ib and Ic. This subdivision is based on the emission lines from SiII ($\lambda = 6\,150\,\text{Å}$). SNe Ia show strong SiII lines, while they are absent in the spectra of SNe Ib and Ic. In SN Ib, c the progenitor star loses its outer shell (or shells in the case of type-Ic) during its evolution. This mass loss can be due to strong stellar winds or ejection of shells during the evolution of the star, but must occur before the SN explosion, or the interaction with a companion. Examples for mass loss due to strong stellar winds or ejection of shells are Wolf-Rayet stars, which are supposed to be progenitors of type-Ib supernovae. Mass loss due to the interaction with a companion is realised in type-Ic supernovae, where the progenitor star loses so much mass, that a bare carbon-oxygen star is left (Nomoto et al. 1994).

Our current understanding of SNe differs from this phenomenological classification. SNe II and Ib, c are linked to a young stellar population, while SNe Ia occur in older stellar populations.

SN II and Ib, c are the final stages in the evolution of massive ($\gtrsim 8\,\mathrm{M}_\odot$) stars. Since the interstellar

[4]Up to now, the shortest known SSS phase of a classical nova is 60 d, while the longest known SSS phase of a classical nova is $\sim$10 yr.

medium from which the star was formed, consists mostly of hydrogen ($\sim$90.8%[5]; Ferrière 2001), the first fusion step turns hydrogen into helium. Once all the hydrogen fuel in the core is used up, the star becomes unstable and leaves the main sequence. If the star is massive enough, it will ignite further fusion steps in its core. The element synthesis goes from helium, through carbon, oxygen, neon, magnesium, silicon, sulphur and ends with nickel. The nickel then decays to iron (see Eq. 2.9). Since the elements of the iron group have the highest binding energy per nucleon, further fusion to heavier elements than iron would use up rather than release energy. Once the core is made up entirely of iron, it is surrounded by many shells, which contain the products of preceding fusion stages. The stage of each shell is dependant on the distance to the core. Once the fuel in the core is exhausted, no more energy can be produced and the radiation pressure, which until then counteracts gravity can no longer be maintained. The whole star starts to collapse, compressing the innermost region to a density of about three times the density of an atomic nucleus. During the compression the iron decays into free protons and neutrons. Due to the extreme pressure, the free protons and electrons combine to neutrons. Thus the core of the star mainly consists of neutrons. At the point when the innermost infalling material of the shell reaches the extremely stiff nucleus the so-called rebounce occurs, where a shockwave travels outwards, heating up the remaining infalling material. The neutrinos that are produced in the collapse additionally power the explosion via neutrino heating and the neutrino-driven baryonic wind (Kitaura et al. 2006). In the centre, a compact object remains (a neutron star or a black hole).

SNe Ia, which are thought to be the explosion of white dwarfs in binary systems, follow a strictly different evolution track. A WD is the final evolutionary stage of a less massive star and is stabilised by the degenerate electron pressure up to the Chandrasekhar mass ($1.44\,\mathrm{M}_\odot$). If the WD has accreted enough mass from its companion to exceed $\sim$$1.3\,\mathrm{M}_\odot$ [6], the temperature and the pressure of the underlying hydrogen layer will reach the thermonuclear ignition point. The WD will be disrupted by either deflagration[7] or detonation[8]. The exact mechanism that leads to the runaway reaction is still unclear (*e. g.* Dursi & Timmes 2006). In contrast to core-collapse SNe (SN II and Ib, c), models predict that in SNe Ia the star is disrupted completely, and no compact object is left behind.

We expect X-ray emission in two phases of an SN explosion (see *e. g.* Immler & Lewin 2003). There should be 'prompt' X-ray emission in addition to a black-body continuum of $\sim$0.02 keV as a result of the high-temperature flash associated with the SN shock wave breaking through the stellar surface. Weeks or months later, 'late' X-ray emission is produced when either the hot expanding shell becomes optically thin to X-rays, or when the outgoing wave runs into the circumstellar material deposited by the progenitor star prior to the explosion. In the first instance the high-energy X-rays are produced by Compton scattering of monoenergetic gamma-rays from the radioactive decay

$$^{56}\mathrm{Ni} \rightarrow ^{56}\mathrm{Co} \rightarrow ^{56}\mathrm{Fe} \tag{2.9}$$

(*e. g.* Sunyaev et al. 1987; Itoh et al. 1987b). In the latter case the interaction produces a fast shock wave in the circumstellar wind and a reverse shock wave into the outer SN ejecta (*e. g.* Itoh et al. 1987a). The temperatures reached in the shocked gas are so high ($10^7\,\mathrm{K} \lesssim T \lesssim 10^9\,\mathrm{K}$) that X-rays are emitted.

#### 2.2.1.4 Supernova remnants

After an SN explosion the interaction between the ejected material and the ISM forms a supernova remnant (SNR). The X-ray luminosities ($L_\mathrm{X}$) typically vary between $10^{35}$ and $10^{37}$ erg s$^{-1}$.

[5] in number density

[6] which is slightly below the Chandrasekhar limit

[7] subsonic speed of the ignition front outward through the layers of the white dwarf

[8] supersonic speed of the ignition front

The evolution of an SNR can be best described in terms of three phases: the first phase is the *free expansion* of the SN ejecta into the ambient ISM. The ejected mass expands with velocities of 5 000–10 000 km s$^{-1}$ into the surrounding medium, which is shock-heated to temperatures of $10^7$–$10^8$ K and hence emits X-rays. This phase lasts until the swept-up material reaches a mass similar to the ejecta. During the next phase, the *adiabatic expansion*, the propagating shock slows down and the remnant adiabatically cools as it sweeps up the cold ISM. While the material behind the shock continues to cool and electrons start to combine with carbon and oxygen ions, most of the internal energy is radiated away. This phase of evolution is hence called the *radiative phase*.

In general, the X-ray emission from SNRs is generated by different mechanisms: most of the observed X-ray emission is thermal line emission which is produced in the forward and reverse shocks. These SNRs appear as ring-like limb-brightened remnants with several hot spots in the interaction regions. Radiative cooling of hot material located behind the shock produces thermal bremsstrahlung emission (irregular or centre-filled SNR). A non-thermal component of the X-ray emission can be observed from synchrotron radiation from electrons that are accelerated in the compressed magnetic fields. In some cases the synchrotron emission from a pulsar may significantly contribute to the overall emission of the SNR.

The cooling time scale of an SNR is of about $10^6$ years. During this period the remnant disperses into the local medium and decreases in brightness until it blends into the surrounding ISM. SNRs reach typical sizes of $\lesssim$100 pc before they dissolve.

#### 2.2.1.5 Ultra luminous X-ray sources

Ultra-luminous X-ray sources (ULXs) are compact X-ray sources in galaxies outside the nucleus with luminosities considerably exceeding the Eddington luminosity for stellar mass X-ray binaries ($L_{\rm Edd} \sim 2\times10^{38}$ erg s$^{-1}$; Makishima et al. 2000). They are preferentially found in star forming galaxies (*e. g.* Fabbiano et al. 2001; Roberts et al. 2002; Gao et al. 2003). As this class is based on a phenomenological definition it may include objects of different types. Currently, there are four preferred models to explain the nature of ULXs and the extreme luminosities produced by these objects. There is the suggestion that ULXs contain intermediate mass black holes (IMBHs: $M_{\rm BH} \sim 10^2$–$10^5 {\rm M}_\odot$). However, it is still unclear whether IMBHs really exist and how they are formed. It also seems that their physical properties disagree with the observed X-ray spectra of ULXs (Roberts 2007; Stobbart et al. 2006). Alternatives are stellar-mass black hole X-ray binaries, preferably HMXBs, which reach super-Eddington luminosities by either photon bubble instabilities (Begelman 2002) or because they anisotropically emit their X-rays (King et al. 2001). A special case of the later possibility are micro-quasars that are observed down the beam of their relativistic jet (*e. g.* Reynolds et al. 1997). Recently, Caballero-García & Fabian (2010) suggested a new model, which assumes that the dominant source of radiation is a power-law continuum produced a few gravitational radii above a rapidly spinning, stellar-mass black hole. The crucial point in this model is whether the magnetic energy extraction works without requiring considerable thermal energy release.

### 2.2.2 Diffuse emission

The origin of truly diffuse X-ray emission is very hot ($T \sim 10^6$–$10^7$ K) gas that is radiatively cooling. It shows a thermal bremsstrahlung spectrum, superimposed with atomic line transitions. This hot gas can originate from massive stars with strong stellar winds that enrich the surrounding medium with heavy elements. Another mechanism producing hot gas is the explosion of supernovae, which also enriches the interstellar medium (ISM). Combined, the stellar winds and the supernovae can create a bubble around them in the ISM that expands due to the higher pressure inside (Chevalier & Clegg 1985). On the surface of this expanding shell the surrounding material is shocked and heated up to temperatures of $\sim 10^8$ K. The preferred direction of expansion of this bubble is perpendicular to the disc plain, as this is the direction with

the least resistance. At some point the bubble breaks out of the disc, and metal enriched, hot gas is fuelled into the halo of the galaxy, forming so called galactic fountains (Shapiro & Field 1976; Bregman 1980). Depending on the kinetic energy of the outflow, the gas can either escape the galactic potential well and escape into the intergalactic medium, or it can rain down again onto the disc.

Alternatively to the truly diffuse emission from a hot interstellar gas component in the disc, the cumulative emission of a large unresolved population of weak stellar-type X-ray sources can also appear as unresolved emission. This was first discovered in the Milky Way's ridge X-ray emission (*e. g.* Revnivtsev et al. 2006, 2009), where evidence was found that the bulk of the Galactic ridge X-ray emission is composed of weak X-ray sources, mostly cataclysmic variables and coronally active stars in binary systems, with an absorption-corrected 2.0–10.0 keV luminosity of most of these sources of less than $10^{31}$ erg s$^{-1}$. Also in other galaxies, Revnivtsev et al. (2007) found evidence that the apparently diffuse emission may partly be consistent with the emission from an old stellar population.

Therefore, caution is necessary in the interpretation of an apparently diffuse emission in a galactic disc, since it can be both due to a hot interstellar gas component and/or an unresolved old stellar population.

### 2.2.3 Foreground and background sources

Apart from the X-ray sources belonging to the nearby galaxy, we also observe X-ray sources which are located along the line of sight and lie either within the Milky Way or (far) behind the nearby galaxy. The foreground objects, sources in our own Galaxy, are mostly stars. Another contribution to the foreground sources can come from CVs. These source classes are too X-ray faint to be observed in external galaxies. The group of background objects, which are of extragalactic origin, consists of more distant galaxies, active galactic nuclei or clusters of galaxies.

#### 2.2.3.1 Stars

X-ray emission has been detected from many late-type[9] stars, as well as from hot OB stars (see review by Schmitt 2000). Hence, X-ray observations of nearby galaxies also reveal a significant fraction of Galactic stars. The foreground stars (fg Stars) are seen as relatively soft X-ray sources homogeneously distributed across the field of view. With typical absorption-corrected luminosities of $L_{2-10\,\mathrm{keV}} < 10^{31}$ erg s$^{-1}$, single stars in other galaxies are too faint to be detected with present instruments. However, concentrations of stars can be detected, but not resolved.

X-ray emission from late-type stars is thought to originate from the coronal activity of the stars, which is similar to that observed in the sun but occurs on a much larger scale in these stars. For example, many M-type stars show significant coronal activity and strong flares. In addition, the fraction of observed X-ray emission in late-type stars is found to be correlated with the rotational period (Schmitt 2000). There is also a strong correlation between relatively strong X-ray and H$\alpha$ emission, which is another indicator of strong coronal activity (Fleming et al. 1989). According to the current understanding, the X-ray emission in the stellar coronae is produced by plasma that is heated up by the interaction of the convective layers with magnetic fields in the star's outer convection zone (*e. g.* Haisch et al. 1991). Recently Jess et al. (2009) claimed the detection of Alfvén waves in the lower solar atmosphere, which have an energy flux that is sufficient to heat the solar corona.

A completely different explanation is necessary for the relatively soft X-ray emission observed from hot stars (Harnden et al. 1979), which do not have an outer convection zone. It has been suggested that X-ray emission from hot OB stars is produced by heating due to hydrodynamic shocks caused by instabilities in strong stellar winds emerging from such stars (Feldmeier et al. 1997).

[9] spectral types F, G, K, and M

X-ray emission has been detected from A-type stars as well, although it is not clear which mechanism is responsible for producing it, since A-type stars do not have strong stellar winds. It is expected that in most cases, X-ray emission from A stars is due to their late-type companions (*e. g.* Schröder & Schmitt 2007). In some cases, dynamo mechanisms result in magnetic activity and lead to X-ray emission (Robrade & Schmitt 2009).

#### 2.2.3.2 Active Galactic Nuclei

The majority of background sources belongs to the class of active galactic nuclei (AGN). This was shown by the recent deepest available surveys of the X-ray background (Mushotzky et al. 2000; Hasinger et al. 2001; Brandt & Hasinger 2005). The class of AGN is divided into many sub-sets, like *e. g.* Seyfert galaxies (Sy 1 and Sy 2), quasars and QSOs (quasi-stellar objects), Narrow/Broad Line Radio Galaxies (NLRG/BLRG), LINERS (Low Ionisation Nuclear Emission Regions), Fanaroff-Riley radio galaxies (FR I and FR II), BL Lac objects, and many others. The common factor in all the sub-sets is that their emission emanates from a small, spatially unresolved galactic core. This small emitting region is implied by the X-ray flux variability observed in many AGN, which is on time scales as short as several minutes (to years). The observed X-ray luminosities range from $10^{39}$ to $10^{46}$ erg s$^{-1}$, sometimes even exceeding $10^{46}$ erg s$^{-1}$.

Although AGN show many different properties, like the amount of radio emission or the emission line strengths and widths, they are believed to be only different facets of one underlying basic phenomenon (*cf.* Urry & Padovani 1995): the accretion of galactic matter onto a supermassive black hole ($\sim 10^6 - 10^9$ M$_\odot$) in the centre of the galaxy. Typical accretion rates are 1–100 M$_\odot$ yr$^{-1}$. Due to the angular momentum of the infalling matter, an accretion disc is formed around the black hole. The central black hole is further surrounded by a thick and dusty torus, sometimes obscuring a direct view onto the nucleus. Broad emission lines are produced in clouds located 2–20$\times 10^{16}$ cm above the disc. Whereas narrow emission lines are observed from clouds much further away from the nucleus ($10^{18-20}$ cm). Further components are a hot corona, which emits hard X-ray continuum emission, and relativistic radio jets. These jets emerge from the nucleus and are observed to be extended on scales from $10^{17}$ to $10^{24}$ cm, a factor of 10 larger than the largest galaxies.

The observed differences between AGN subclasses only depend on the angle of the system to the observer.

The typical X-ray emission of AGN shows a power-law spectrum with a photon index between 1.5 and 2.0 (*e. g.* Mushotzky 1984). It can be explained by the conversion of gravitational energy of matter into non-thermal radiation. Additional spectral components like the Fe K$_\alpha$ line at ∼6.4–6.7 keV, soft excess, etc, are believed to be due to reflection and reprocessing of the power-law emission in the optically thick accretion disc. The recent detection of an iron L emission line in the X-ray spectrum of an AGN supports the reflection model (Fabian et al. 2009).

#### 2.2.3.3 Galaxies

It is difficult and, to some extent, arbitrary to distinguish between active and normal galaxies, since most galaxies are believed to host a black hole at the position of their kinetical centre (Bender et al. 2005). In normal galaxies the accretion rate of the central supermassive BH is so low, that only weak activity can be detected – if at all. Rapid flares in X-rays (Baganoff et al. 2001; Porquet et al. 2003) and infrared (Eckart et al. 2004; Dodds-Eden et al. 2009) have been observed from the BH in the Galactic centre. The absorption corrected 2–10 keV luminosity changes from $\sim 2.2\times 10^{33}$ erg s$^{-1}$ in the quiescent state to a few times $10^{35}$ erg s$^{-1}$ at the peak of the flaring state emission (Baganoff et al. 2001; Porquet et al. 2003). Garcia et al. (2000) has reported a possible detection of X-ray emission ($L_{\mathrm{X,unabs}} \approx 4\times 10^{37}$ erg s$^{-1}$ in the 0.3–7.0 keV band) from the central supermassive BH in M 31.

The overall thermal emission of the nuclear region is due to bremsstrahlung from hot gas. The total X-ray luminosities of normal galaxies can reach some $10^{41}$ erg s$^{-1}$, at maximum. It consists of all of the components mentioned above (XRBs, SSSs, SNs, SNRs and diffuse emission), apart from emission from an active central region. With increasing distance to the galaxy, fewer and fewer of the individual sources can be resolved and only the overall emission of the galaxy is observable.

#### 2.2.3.4 Galaxy Clusters

Galaxy clusters (GCls) are by far the largest and most massive virialised objects in the Universe. Their masses lie in the range of $10^{14}$–$10^{15}$M$_\odot$ and they have sizes of a few Mega parsecs (Mpc). A mass-to-light ratio of $M/L \simeq 200\,(\mathrm{M}_\odot/\mathrm{L}_\odot)$ indicates that galaxy clusters are clearly dominated by their dark matter content. On the other hand, clusters allow us to study the baryonic matter component, as they define the only large volumes in the Universe from which the majority of baryons emit detectable radiation. About 90% of all baryons in the Universe reside in intergalactic space, but X-ray emitting gas temperatures are only reached in the deep potential wells of galaxy clusters. This baryonic gas, the *hot intracluster medium* (ICM), is extremely thin, with electron densities of $n_\mathrm{e} \simeq 10^2$–$10^5\,\mathrm{m}^{-3}$, and fills the whole cluster volume. Thus galaxy clusters can be considered as extraordinary plasma physics laboratories, which provide environments that are unattainable in the laboratory. Owing to the plasma temperatures of $k_\mathrm{B}\,T \simeq 2$–$10\,\mathrm{keV}$, the thermal ICM emission gives rise to X-ray luminosities of $L_\mathrm{X} \simeq 10^{43}$–$3\times10^{45}\,\mathrm{erg\,s}^{-1}$. Therefore galaxy clusters are the most X-ray luminous objects in the Universe next to AGN.

The dominant X-ray emission mechanism for Galaxy clusters at temperatures of $T \gtrsim 10^7\,\mathrm{K}$ ($k_\mathrm{B}T \gtrsim 1\,\mathrm{keV}$) is *thermal bremsstrahlung* (free-free radiation). The intracluster medium is a collisionally ionised, optically thin plasma, which implies that essentially every emitted photon will escape from the cluster volume. At temperatures of $T \lesssim 2\,\mathrm{keV}$, recombination radiation (free-bound) and line emission radiation (bound-bound) become important as the ionisation levels of the ICM metals decrease. The most important X-ray line feature for massive clusters is the K-shell line complex of hydrogen-like iron Fe XXVI around 6.7 keV. For other ionisation states the energy is slightly shifted. At lower temperatures, additional important line features originate from the Fe L line complex at $\sim 1\,\mathrm{keV}$ and ions of O, Mg, Si, S, Ar, Ca, and Ne.

X-ray observations of the intracluster medium of nearby clusters nowadays allow precise measurements of the ICM structure, its thermodynamic state, and elemental abundances. Furthermore, the ICM enables studies of hydrodynamical and plasma physical processes on the largest scales such as shock fronts, contact discontinuities, propagation of sound waves, turbulence, heat conduction, and diffusion processes.

More details can be found in Sarazin (1986), Biviano (2000) or in the review of Voit (2005).

## 2.3 Source classification methods

After introducing the different source classes, which can be observed in fields of nearby galaxies, I want to present the methods that are used to distinguish the X-ray sources between the different classes.

### 2.3.1 Hardness ratio diagrams

The most general method, which can be applied to all sources and which is based on their X-ray spectral properties, is the analysis of *hardness ratios* (HR). The hardness ratios and errors are defined as:

$$\mathrm{HR}i = \frac{B_{i+1} - B_i}{B_{i+1} + B_i} \text{ and } \mathrm{EHR}i = 2\frac{\sqrt{(B_{i+1}EB_i)^2 + (B_iEB_{i+1})^2}}{(B_{i+1} + B_i)^2}, \tag{2.10}$$

for $i = 1$ to 4, where $B_i$ and $EB_i$ denotes count rates and corresponding errors in energy band $i$.[10] A hardness ratio can be seen as a kind of normalised *X-ray colour*.

In theory, the position of each class of objects in the HR diagram is determined by the unique spectral shape of the sources belonging to a specific class. However, the position is also affected by the foreground absorption. The advantage of the hardness ratio diagrams, compared to an in-detail spectral analysis of the sources, is that it can also be used when only a limited number of photons is detected, and allows large numbers of sources to be classified rather quickly. However, the results obtained with different detectors cannot be directly compared, as the HR diagrams must be calibrated for each instrument separately.

The method was developed for classifying the SMC and LMC (*e. g.* Kahabka et al. 1999; Haberl & Pietsch 1999a) sources observed with *ROSAT*. Since then HR diagrams have been successfully applied to many nearby galaxies, like *e. g.* M 33 (*e. g.* Pietsch et al. 2004) and M 31 (*e. g.* Pietsch et al. 2005b), and have allowed the distinction of SSSs, SNRs and foreground stars from intrinsically hard sources like XRBs and AGN. However XRBs and AGN occupy the same region in the diagram and, hence, cannot be separated (Colbert et al. 2004).

Figure 2.1 shows, as an example, the HR2 versus HR1 diagram for sources of the catalogue of Pietsch et al. (2005b). The HRs were derived from the following energy bands: 0.2–0.5 keV, 0.5–1.0 keV, 1.0–2.0 keV. Three distinct regions of sources can be clearly seen. In the lower left corner SSSs can be found (HR1$< 0$ and HR2$\sim -1$). SNRs and foreground stars are located in the lower right corner of the hardness ratio plot (HR1$> -0.1$ and HR2$< -0.2$). All "hard" sources (AGN, XRBs and Crab-like SNRs) can be found in the upper right part of the diagram.

### 2.3.2 Time variability

To further distinguish between source classes that occupy (partially) overlapping areas in an HR diagram, an investigation of their X-ray time variability is important. Misanovic et al. (2006) showed, for a source population study of M 33, that the X-ray flux variability on different time scales allows us to further distinguish between different source classes. Phenomena such as bursts from X-ray binaries, flares from stars or the periodic variability of pulsars occur on short time scales and can therefore be observed during one single observation. On the other hand there is long term variability. These time scales can be covered, by comparing different observations of the same source.

### 2.3.3 Source extent

Within our own Galaxy and in observations of the SMC and LMC the X-ray emission of SNRs is spatially resolved and the SNR is detected as an extended source. With increasing distance to the observed galaxy, the threshold of spatial resolution is shifted to objects of larger and larger absolute diameter, due to the limited spatial resolution of the X-ray telescopes. Nevertheless, in *Chandra* observations of M 31, SNRs can be found as spatially resolved X-ray sources (*e. g.* Kong et al. 2003b). Therefore, the extent of an X-ray source can be an additional criterion for an SNR classification.

Other X-ray sources that can appear as extended objects are H II-regions and superbubbles, which contain hot, X-ray emitting gas and are located within the nearby galaxy (Chu & Mac Low 1990), or background galaxy clusters.

### 2.3.4 Cross correlations

In the subsections before, only X-ray properties of the sources have been used for source classification. Additional information can be achieved using cross correlations with catalogues in the radio, infra-red and

[10] assuming that five energy bands are in use, as is the case in the studies presented in this thesis

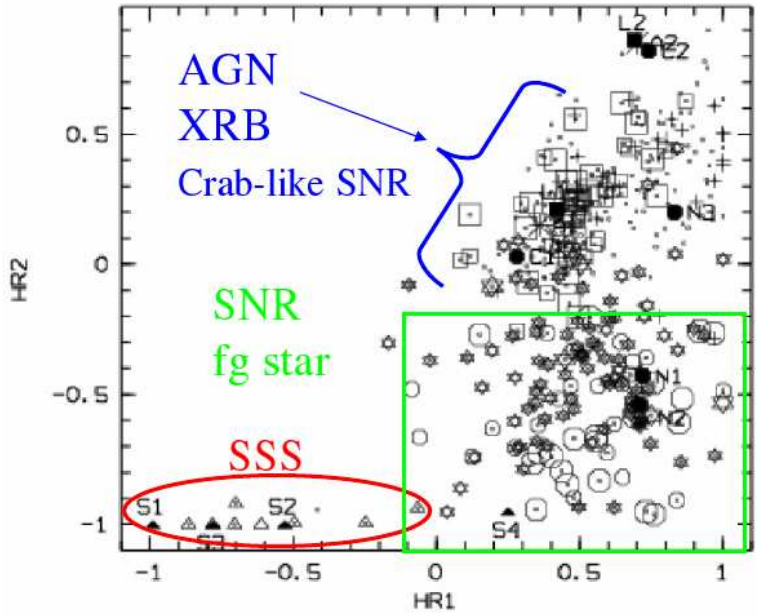


**Figure 2.1:** Hardness ratio plot HR2 versus HR1 for sources from the catalogue of Pietsch et al. (2005b). Three regions are marked, which are clearly distinct from each other. Source classification is indicated: foreground stars and candidates are marked as big and small stars, AGN candidates as small crosses, SSS candidates as triangles, SNR and candidates as big and small hexagons, XRBs and candidates (including those sources located in globular clusters) as big and small squares. Taken from Stiele et al. (2008a).

optical wavelengths. From identifications in the Milky Way, we know that bright X-ray sources, which correlate with optical globular clusters, are most likely low mass X-ray binaries. Optical information can also be helpful to distinguish between foreground stars and SNRs. Correlations with radio counterparts can support AGN and SNR classifications. For the classification of AGN optical spectra can also be helpful.

## 2.4 Luminosity functions

In statistical studies of nearby galaxies in X-rays the method of cumulative luminosity functions is often used. The X-ray cumulative luminosity function (CLF) is defined as the number of sources (usually normalised per unit area) with luminosities higher than a certain threshold luminosity. The CLF provides information about the formation, evolution and physical properties of the X-ray source population (Fabbiano & White 2006). Bulges of spiral galaxies and elliptical galaxies normally have broken power-law log N-log S curves, with generally steeper slopes at their bright ends. Whereas CLFs for sources in galactic discs are generally flatter single power-laws (Soria & Wu 2002, and references therein).

Grimm et al. (2003) found that CLFs of populations of HMXBs can be roughly described as a power-law with a slope of $\alpha \sim 0.6$, where $N(> S) \propto S^{-\alpha}$. This result is independent of the examined galaxy. In addition they showed that the collective luminosity of HMXBs can be used to estimate the star formation rate (SFR) in distant galaxies. A discussion of luminosity functions of LMXBs and their connection to the star formation rate can be found in Gilfanov (2004). The average CLF of LMXBs has a more complex shape than that of HMXBs. At low luminosities it follows a rather flat power-law, steepens at $\log(L_{\rm X}[{\rm erg/s}]) \gtrsim 37.0$–$37.5$ and has a rather abrupt cut-off at $\log(L_{\rm X}[{\rm erg/s}]) \gtrsim 39.0$–$39.5$.

# Chapter 3

# The Andromeda Galaxy

The Andromeda Galaxy, also known as M 31, or NGC 224 (Dreyer 1888) is the nearest large spiral galaxy (SA(s)b)[1] to our own. With a distance of 780 kpc [2] (Holland 1998; Stanek & Garnavich 1998) and its moderate Galactic foreground absorption ($N_{\rm H} = 6.6{\times}10^{20}$ cm$^{-2}$, Stark et al. 1992) M 31 is well suited to study the X-ray source population of a nearby spiral galaxy similar to the Milky Way. The optical extent of M 31 can be approximated by an inclination-corrected $D_{25}$ ellipse with a large diameter of $153\farcm3$ and an axial ratio of 3.09 (de Vaucouleurs et al. 1991; Tully 1988). The $D_{25}$ ellipse gives an elliptical representation of the dimension of a galaxy at the 25 mag/arcsec$^2$ isophote in blue light. Throughout this thesis the corrected $D_{25}$ ellipse is used, which is adjusted for the effects of projection and obscuration (Tully 1988, and references therein). A summary of the main properties of M 31 is given in Table 3.1. For a comparison of M 31 with the Milky Way see Yin et al. (2009).

**Table 3.1:** Properties of M 31.

| | | reference |
|---|---|---|
| Type | SA(s)b | Tully (1988) |
| Assumed distance | 780 kpc | Holland (1998); Stanek & Garnavich (1998) |
| Systemic velocity | -59 km s$^{-1}$ | Tully (1988) |
| Position of centre | $\alpha_{2000} = 0^{\rm h}42^{\rm m}\ 44\fs31$, $\delta_{2000} = +41\degr16\arcmin09\farcs4$ | Cotton et al. (1999) |
| $D_{25}$ | $193\farcm2$ | Tully (1988) |
| Corrected $D_{25}$ | $153\farcm3$ | Tully (1988) |
| Axial ratio | 3.09 | Tully (1988); de Vaucouleurs et al. (1991) |
| Position angle | 38° | Huchtmeier & Richter (1989); Huchtmeier et al. (2008) |
| Inclination | 78° | Tully (1988) |
| Galactic foreground $N_{\rm H}$ | $6.6{\times}10^{20}$ cm$^{-2}$ | Stark et al. (1992) |

It would be far beyond the scope of this thesis to summarise the enormous amount of literature related to M 31. Hence I only give a short overview of the historical observations of M 31 and highlight a few (recent) findings, related to the topic of the thesis. The main emphasis is on X-ray observations and especially previous X-ray surveys of M 31.

[1] de Vaucouleurs-Sandage classification of spiral galaxies: SA: ordinary spiral; (s): S-shaped spiral; b: intermediate stage (de Vaucouleurs 1959)

[2] *i. e.* $1\farcs$corresponds to 3.8 pc and the flux to luminosity conversion factor is $7.3{\times}10^{49}$ cm$^{-2}$

## 3.1 History

Since the Andromeda galaxy can be seen without the aid of a telescope, it has been mentioned in texts and marked on maps for over a thousand years. One of the first recorded instances of the recognition of the unusual nature of the faint smudge of light that makes up the Andromeda galaxy as it is seen with the naked eye, is found in the *Book on the Constellations of the Fixed Stars* by the famous Islamic author Abu I-Husain al-Sufi (A.D. 903-986).

The first telescopic observation of the Andromeda galaxy was reported by Simon Marius in 1612 (Coddington 1898). In the eighteenth century, the first systematic catalogues of non-stellar objects were prepared. The best known of these is the Messier catalogue (Messier 1781), which listed over 100 nebulous objects; the 31st of which is the Andromeda galaxy.

In August 1885 a "new star" (called S And) – a truly variable object – was discovered (see review of de Vaucouleurs & Corwin 1985, 1986). Showing characteristics similar to those of ordinary Galactic novae, it was concluded that S And must be a nova and hence M 31 must be within the Milky Way system.

The modern history of M 31 is dominated by the pioneering work of Edwin Hubble. Based on previous observations by other astronomers at Mt. Wilson observatory, Hubble began his systematic study of M 31 and by 1929 had found 85 objects that were confirmed to be novae similar to Galactic examples, based on their light curves and for one, also by its spectrum. In this way Hubble showed that S And was an object which did not behave like a Galactic nova. Today we know that S And was the first recorded observation of a supernova in M 31.

Furthermore, Hubble used a population of 40 Cepheids, detected by himself, to derive a distance to M 31 of 275 kpc, which is less than half the distance presently derived. Nevertheless Hubble showed for the very first time that M 31 is an external galaxy; similar to our Milky Way, but not belonging to it.

Walter Baade discovered that the Cepheids located in Galactic globular clusters belonged to the class of Population II stars, while the Cepheids in the spiral arms of M 31 or in the main disc of our Galaxy were found only among Population I stars. Baade also found that the Population II Cepheids are on average intrinsically four times fainter than normal Cepheids of the same period. Thus, the normal Cepheids studied by Hubble in M 31 must be twice as far as had been thought. With this discovery Baade doubled the estimate of the size of the universe at that time.

## 3.2 Radio, infra-red, optical and ultra violet observations of M 31

With the help of optical observations, astronomers study the stellar and globular cluster population of M 31. An optical image of M 31 is shown in Fig. 3.1. As part of their "Local Group Galaxies Survey" (LGS) Massey et al. (2006) obtained optical photometry down to at least 21 (23) mag[3] for the stars in the field of M 31. While colour magnitude diagrams are dominated by foreground dwarfs and giants at intermediate colours, at extreme colours the diagrams are populated with blue and red supergiants (Massey et al. 2009) belonging mostly to M 31. Drout et al. (2009) used the large negative systematic velocity of M 31 to separate the population of yellow supergiants from foreground stars. The Andromeda galaxy was also observed in the framework of all-sky surveys in the optical (*e. g.* Monet et al. 2003, USNO-B1) and infra red (*e. g.* Skrutskie et al. 2006, 2MASS).

Accurate distance measurements to the Local Group galaxies are crucial to calibrate the cosmic distance scale. The distance to M 31 has been estimated using a variety of methods. Stanek & Garnavich (1998) used red clump stars observed with the *Hipparcos* satellite in the Milky Way and with the *Hubble Space Telescope*

[3] with an accuracy of 1–2% (<10%)

**Figure 3.1:** The Andromeda galaxy in the optical, with two of their companion galaxies. M 32 is the bright yellow spot in the lower part of the image, while NGC 205 is located in the upper right part. North is at the top and east to the left hand side of the image. The image was taken with the Schmitt telescope at the Tautenburg observatory. Source: Thüringer Landessternwarte Tautenburg; `http://www.tls-tautenburg.de/research/gallery/english/galaxien_neu.html`

*(HST)* in M 31. Red clump stars are the metal-rich equivalent of the horizontal-branch stars. Theoretical models predict that their absolute luminosity depends only weakly on their age and chemical composition. The determined distance modulus is $(m-M)_o = 24.471 \pm 0.035 \pm 0.045$ ($\hat{=}784\pm13\pm17$ kpc). The first uncertainty is statistical and the second uncertainty is systematic. Based on fitting theoretical isochrones to the observed red giant branches of 14 globular clusters in M 31, Holland (1998) derived a distance modulus ($(m-M)_o = 24.47 \pm 0.07$) that is in excellent agreement with the value reported by Stanek & Garnavich (1998). Ribas et al. (2005) used an eclipsing binary to determine the distance to M 31. From their spectral analysis, they obtained a distance modulus of $(m-M)_o = 24.44 \pm 0.12$ ($\hat{=}772\pm44$ kpc). Other distance estimates are based for instance on the location of the tip of the red giant branch, which acts as a standard candle in old, metal-poor stellar populations (McConnachie et al. 2005, $(m-M)_o = 24.47 \pm 0.07$), or on fitted period-luminosity relations of Cepheids (Macri et al. 2001).

Williams (2003) investigated the star formation history of M 31, using six fields of the LGS observations. For the total disc of M 31 he estimated a star formation rate of $\sim$1 $M_\odot$ yr$^{-1}$. In addition the analysis routine used also gives distances to the examined parts of M 31. The distance examination provides a hint that the disc southeast of the major axis is more distant. This finding is in agreement with the spatial orientation determined from the location of the absorbing dust lanes (Simien et al. 1978) and from the differential reddening among globular clusters (Iye & Ozawa 1999). In summary, the northwestern side of the disc of M 31 is nearer to us than its southeastern side.

Studies of the globular clusters of M 31 revealed two subpopulations, associated with the halo and bulge of the galaxy. Perhaps the main difference between the globular cluster systems of M 31 and the Milky Way is that the former are more populous, with an estimated total of $\sim 450$ members and may contain a significant population of intermediate age (3–6 Gyr) globular clusters (Alves-Brito et al. 2009, and references therein). Recent discoveries are that of a metal-poor stellar halo in M 31 (Kalirai et al. 2006; Chapman et al. 2006), and that of outer halo globular clusters beyond a projected radius of 70 kpc from the centre of M 31 (Alves-Brito et al. 2009).

The globular cluster population of M 31 was also studied in the near and far ultraviolet (NUV/FUV) using the *Galaxy Evolution Explorer (GALEX)*. Rey et al. (2007) analysed the UV properties of the globular cluster population of M 31 and compared them with the Milky Way globular cluster population. Figure 3.2 presents a UV image of M 31, which clearly shows the star forming regions in the spiral arms of the galaxy (*cf.* Kang et al. 2009).

Surveys of hydrogen lines (Brinks & Shane 1984; Pellet et al. 1978), CO (Dame et al. 1993), molecular gas (Nieten et al. 2006) and of the 20 cm radio continuum emission (Beck et al. 1998) detected and confirmed an outer ring of star formation at a radius of ten kiloparsecs, whose centre is offset from the M 31 nucleus. In addition, the outer galaxy disc is warped, as seen in both optical (Ibata et al. 2001) and radio (Braun 1991) wavelengths. A second, inner dust ring, whose centre is offset by about half a kpc from the centre of M 31, was detected in an 8 $\mu$m image – after subtraction of a scaled 3.6 $\mu$m image – taken with the Infrared Array Camera (IRAC) on-board the *Spitzer Space Telescope* (Block et al. 2006, Fig. 3.3). Both rings appear to be density waves propagating in the disc. Based on numerical simulations Block et al. (2006) propose that the rings result from a companion galaxy that plunged through the centre of the disc of M 31, about 210 million years ago. The most likely candidate for that interloper is M 32.

Using *HST* spectroscopy of the centre of M 31 Bender et al. (2005) showed that the core of M 31 is a triple. In addition to the previously known double brightness peaks P1 and P2 they found that the blue nucleus embedded in P2 consists of a hot star population (P3). The kinematics of P3 are consistent with a circular stellar disc in Keplerian rotation around a supermassive black hole. The derived properties of the

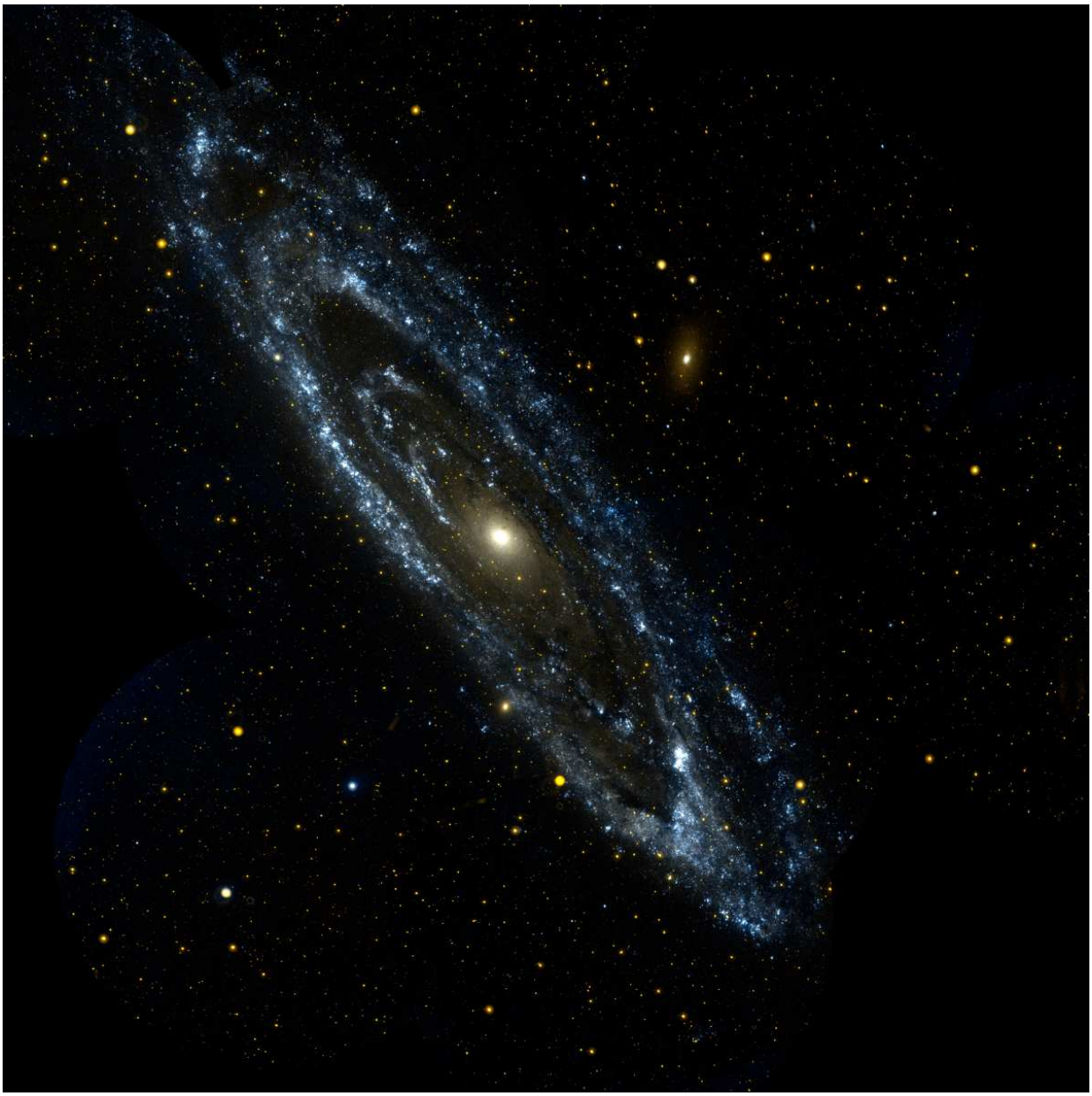

**Figure 3.2:** A UV image of M 31. The mosaic is composed of NUV (red) and FUV (blue) observations taken with *GALEX*. The spiral arms, with their star forming regions, are clearly visible in blue. Taken from Thilker et al. (2005).

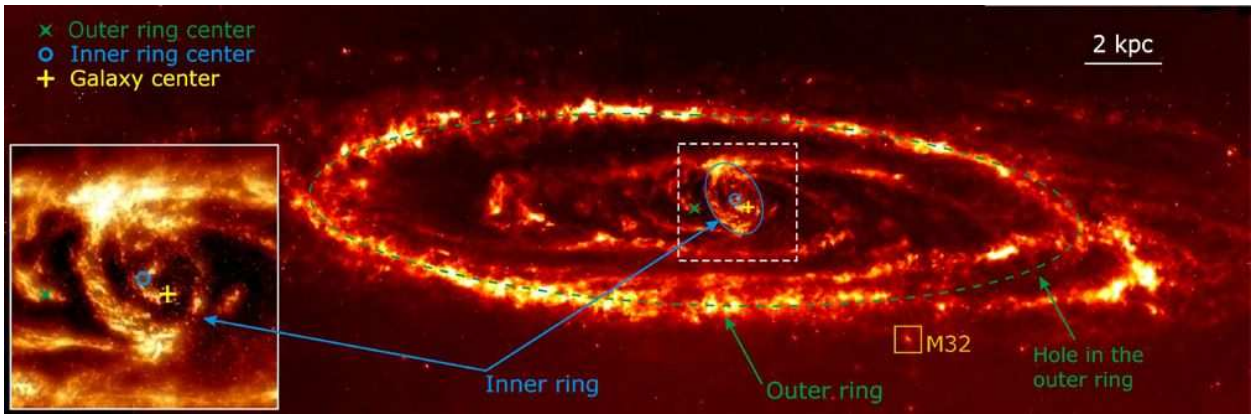


**Figure 3.3:** Infrared view of M 31, obtained with the IRAC on-board *Spitzer*. The image clearly shows the inner and outer dust ring of M 31. North is on the left hand side and east at the bottom side. From Block et al. (2006).

P3 disc and the central black hole mass are in agreement with previous results based on studies of P1 and P2. Therefore astrophysical arguments strongly favour the conclusion that the dynamically detected central dark object in M 31 is a black hole.

## 3.3 X-ray observations of M 31

Early X-ray observations of M 31 were obtained with X-ray detectors mounted on rockets (*e. g.* Bowyer et al. 1974) and the *Uhuru* satellite (US, 12 December 1970-March 1973, energy range: 2-20 keV; Giacconi et al. 1974, and references therein). The detectors available at that time had a poor spatial resolution, which only allowed the detection of the X-ray emission of the whole galaxy, without being able to resolve individual sources. It was thus possible to determine only the integrated flux and the spectral distribution of the flux. Comparison with Galactic sources allowed provisional conclusions on the nature of the individual sources of M 31.

The first satellite to allow individual sources to be resolve in M 31 was the *Einstein* X-ray observatory (US, 12 November 1978–April 1981, energy range: 0.2–4.5 keV; Giacconi et al. 1979). The increase in sensitivity by a factor of $\sim 1\,000$ compared to *Uhuru* (Trümper 1982) was achieved by employing *imaging X-ray optics*. For a historical review on the development of *observational techniques in X-ray astronomy* see Giacconi et al. (1968). In the entire set of *Einstein* imaging observations of M 31 performed in the years 1979 and 1980, Trinchieri & Fabbiano (1991, hereafter TF91) found 108 individual X-ray sources brighter than $\sim 6.4{\times}10^{36}$ erg s$^{-1}$ in the 0.2–4.0 keV band. These observations have a total exposure of 300 ks and cover $\sim 86\%$ of the uncorrected $D_{25}$ diameter of M 31 (Supper et al. 1997). Many of the detected point-sources have positions accurate to about $3''$. Fourteen sources were bright enough to examine their X-ray spectra. Sixteen sources showed variability (van Speybroeck et al. 1979; Collura et al. 1990, TF91). The sources were identified to young stellar associations, globular clusters (*i. e.* LMXBs) and supernova remnants (Blair et al. 1981; Crampton et al. 1984). The spatial distribution of the sources revealed two regions of enhanced concentration: a highly confused bulge region and an outer region approximately following the spiral arms.

To provide an all-sky survey with similar or better sensitivity and angular resolution than the *Einstein* observatory, extending to photon energies below 1 keV, the joint German/UK/US *ROSAT* (ROentgen SATellite[4]) X-ray mission (1 June 1990–12 February 1999, energy range: 0.1–2.4 keV; Trümper 1982) was built.

[4]Named in honour of Wilhelm Conrad Röntgen (∗1845,†1923 in Munich), who won the Nobel Prize in Physics in 1901 for the

In July 1990 the bulge region of M 31 was observed with the *ROSAT* High Resolution Imager (HRI) for ∼48 ks. Primini et al. (1993, hereafter PFJ93) reported 86 sources brighter than $\sim 1.8\times10^{36}$ erg s$^{-1}$ (0.2–4.0 keV) in this observation. Of the *ROSAT* HRI sources located within 7.′5 of the nucleus, ∼42% were found to vary when compared to previous *Einstein* observations and ∼6% of the sources were possible "transients". Two deep PSPC (Position Sensitive Proportional Counter) surveys of M 31 were performed with *ROSAT*, the first in July 1991 (Supper et al. 1997, hereafter SHP97), and the second in July/August 1992 (with a few follow-up observations in January 1993; Supper et al. 2001, hereafter SHL2001). Both surveys consisted of a number of observations arranged in such a way that the whole area of M 31 was covered. The higher sensitivity of the *ROSAT* telescope, together with the total observation time of 200 ks for each survey, pushed the limiting flux to a factor of 10–100 lower than for the *Einstein* observatory. This led to the detection of 560 X-ray sources in the field of M 31. Of these 560 sources, 55 were identified with foreground stars, 33 with globular clusters, 16 with supernova remnants and 10 with radio sources and galaxies. *ROSAT* detected 491 sources, which had not been detected in previous *Einstein* observations. In addition, a comparison with the results of the *Einstein* survey revealed 11 long term variable, and seven possible transient sources. Comparing the two *ROSAT* surveys, 34 long term variable sources and eight transient candidates were detected. The observed luminosities of the detected M 31 sources ranged from $5\times10^{35}$ erg s$^{-1}$ to $5\times10^{38}$ erg s$^{-1}$ in the 0.1–2.0 keV band. Another important result obtained with *ROSAT* was the establishment of super soft sources as a new class of M 31 X-ray sources (*cf.* Kahabka 1999) and the identification of the first SSS with an optical nova in M 31 (Nedialkov et al. 2002).

In 1999 two new X-ray satellites, with a much improved spatial and energetic resolution compared to their predecessors, were launched: the American-led *Chandra* mission (launch: 23 July 1999, energy range: 0.1–10 keV; Weisskopf et al. 2000) and the European X-ray mission *XMM-Newton* (for an in detail discussion see Chap. 4).

Shirey et al. (2001) analysed an *XMM-Newton* Performance Verification observation (25 July 2000), which pointed to the centre of M 31. They detected 116 sources down to a limiting unabsorbed luminosity of $6.3\times10^{35}$ erg s$^{-1}$ (0.3–12.0 keV) and used hardness ratios to distinguish between source classes. In addition they examined the diffuse emission and the cumulative luminosity function of the central region of M 31. For sources that lie within 30′ of the centre of M 31 (total observed field) they found a power-law index of $0.47 \pm 0.03$ for $36.2 < \log L_{\rm x} < 37.4$ and $1.79 \pm 0.26$ for $37.4 < \log L_{\rm x} < 38.1$. Taking only the innermost 5′ into account, the power-law indices change to $0.43 \pm 0.04$ and $1.77 \pm 0.35$, respectively. They found no significant differences in the shapes of the analysed source distributions.

Osborne et al. (2001) used *XMM-Newton* observations from 25 July and 27 December 2000 to study the variability of X-ray sources in the central 30′ of M 31. They found that at least 15% of the ∼60 brightest sources are variable on a time scale of several months. In addition they detected a new bright transient source, which is located ∼2.′9 from the nucleus, and an SSS with a pulsation period of ∼865 s, which might be the counterpart of an optical nova.

Kong et al. (2002b) report on eight *Chandra* ACIS-I observations taken between 1999 and 2001, which cover the central $\sim 17' \times 17'$ region of M 31. They detected 204 sources, of which 22 were identified with globular clusters, two with supernova remnants, nine with planetary nebulae, and nine with supersoft sources. About 50% of the sources are variable on timescales of months and 13 sources were classified as transients. The spectra of the brightest sources were examined. In addition, X-ray luminosity functions (XLFs) were studied. This analysis of XLFs was extended by Kong et al. (2003a) to fields located in the disc of M 31. They found differences in the luminosity functions among the fields, but could not definitively relate them to the stellar content of the fields.

Kaaret (2002) analysed a 47 ks *Chandra* High Resolution Camera (HRC) observation of the central region of M 31. He detected 142 point sources ($L_X = 2\times10^{35}$ to $2\times10^{38}$ erg s$^{-1}$ in the 0.1–10 keV band),

discovery of a new kind of rays he denoted X-rays.

of which 14 sources are coincident with globular clusters, one is coincident with the nucleus of M 31 and another one is likely to be the counterpart of an optical nova. A comparison with a *ROSAT* observation taken 11 years earlier, showed that 46±26% of the sources with $L_X > 5{\times}10^{36}$ erg s$^{-1}$ are variable. The source density radial profile follows a power-law distribution with an exponent of 1.25±0.10. This is not consistent with the optical brightness profile. The luminosity function is well fitted by a differential broken power-law, with a slope of ∼0.3 below and ∼1.5 above the break. The power-law breaks at a luminosity of $4.5^{+1.1}_{-2.2}{\times}10^{37}$ erg s$^{-1}$.

Using *Chandra* HRC observations, Williams et al. (2004a) measured the mean fluxes and long-term time variability of 166 sources detected in these data. By cross-correlating their sources with published optical and radio catalogues, they found counterpart candidates for 55 sources. In addition 17 sources appeared to be transients. For two of these transient sources optical follow-up observations were analysed.

Pietsch et al. (2005b, hereafter PFH2005) prepared a complete catalogue of M 31 point-like X-ray sources, analysing all observations available at that time in the *XMM-Newton* archive which overlapped at least in part with the optical $D_{25}$ extent of the galaxy. In total, they detected 856 sources. Of these sources 21 were classified as SNRs, 23 as SNR candidates, 18 as SSS candidates, seven as XRBs, nine as XRB candidates, 27 as X-ray sources located in globular clusters, and ten as globular cluster source candidates. Of the sources not associated to M 31, they found six foreground stars, 90 foreground star candidates, one BL Lac-type AGN, 36 AGN candidates, one source which coincides with M 32, one with a background galaxy cluster and one classified as a galaxy cluster candidate. In follow-up work (i) Pietsch & Haberl (2005, hereafter PH2005) searched for X-ray burst sources in globular cluster (GlC) sources and candidates and identified two X-ray bursters and a few more candidates, and (ii) Pietsch et al. (2005a, hereafter PFF2005) searched for correlations with optical novae. They identified seven SSSs from the list from PFH2005 with optical novae, and identified one additional *XMM-Newton* source with an optical nova. Another source that showed a transition from a supersoft state to a hard state was suggested as a symbiotic nova candidate. This work was continued and extended on archival *Chandra* HRC-I and ACIS-I observations in Pietsch et al. (2007, hereafter PHS2007).

Trudolyubov et al. (2006b) examined the spectral properties of 123 bright X-ray sources found in the centre of M 31. The spectral distribution of M 31 X-ray sources, based on the spectral fitting with a power-law model, is clearly bimodal with a main peak corresponding to a photon index $\Gamma \sim 1.75$ and a shoulder at $\Gamma \sim 2.0$–$2.2$ extending to the soft spectral region. In addition they found that more than 80% of sources observed in two or more observations show significant variability on time scales of days to years. From cross correlations with data at other wavelengths, and based on the similarity of the properties of M 31 X-ray sources and their Galactic counterparts, they expect most of the M 31 X-ray sources in their sample to be accreting binary systems with neutron star or black hole primaries.

Voss & Gilfanov (2007) found 263 X-ray sources within a maximum distance of 12′ to the centre of M 31. Their study is based on 26 archival *Chandra* observations. The limiting luminosity is $\sim 10^{35}$ erg s$^{-1}$ in the 0.5–8.0 keV band. Based on the spatial distribution and the luminosity function of the X-ray sources, they showed that the distribution of primordial LMXBs is consistent with the distribution of the *K*-band light and that the luminosity function of primordial LMXBs flattens below $\sim 10^{37}$ erg s$^{-1}$ to a $dN/dL \propto L^{-1}$ law. In the examined region the luminosity function is independent of the distance to the centre of M 31. The LMXBs located in GCls and within ∼1′ from the centre of M 31 are presumably created via dynamical interaction. This is strongly suggested by their radial distribution, which follows the square of the stellar density rather than the *K*-band light distribution. In addition they found 28 transient sources that varied by a factor larger than 20 and showed that their spatial distribution follows the distribution of the persistent LMXBs.

Shaw Greening et al. (2009, hereafter SBK2009) presented the results of a complete spectral survey of the 335 X-ray point sources they detected in five *XMM-Newton* observations located along the major axis

of M 31. They obtained background subtracted spectra and lightcurves for each of the 335 X-ray sources. The spectra for sources with more than 50 source counts were fitted individually. This allowed the derivation of the first cumulative luminosity functions, created using the best fit spectral model. The luminosity functions show a statistically significant flattening in the X-ray luminosity interval $37.0 \lesssim \log L_{\rm X} \lesssim 37.5$. Above $L_{\rm X} \sim 1.5{\times}10^{36}$ erg s$^{-1}$ (0.3–10.0 keV) the observed population is statistically dominated by the point source population of M 31. In addition they selected 18 HMXB candidates, based on a power-law photon index of $0.8 \leq \Gamma \leq 1.2$.

There are a lot of studies dedicated to specific classes of sources within M 31:

**Sources with soft spectrum:** Di Stefano et al. (2004, hereafter DKG2004) examined three fields located in the disc of M 31 and the central region of M 31 with *Chandra* ACIS-S. They developed an algorithm which allows the selection of SSSs and quasi-soft sources (QSSs)[5], despite their low count rates and an a priori unknown nature. With the help of this algorithm they detected 33 VSSs that were not foreground stars, and two sources were associated with SNRs. Comparisons to *ROSAT* and *XMM-Newton* observations revealed the high variability of VSSs (Greiner et al. 2004a). Di Stefano et al. (2004) suggested that variable VSSs are XRBs. Based on *XMM-Newton* observations Orio (2006) studied the population of SSSs and QSSs in M 31. She also examined the spectra and time variability characteristics of these sources and searched for counterparts at other wavelengths. Many of the sources can be associated with SNRs or novae, but for some of them it cannot be excluded that they are LMXBs containing a WD, foreground neutron stars or even anomalous X-ray pulsars. Trudolyubov & Priedhorsky (2008) detected X-ray pulsations with a period of ∼217.7 s from the supersoft source XMMU J004252.5+411540. They suggested this source to be a rotating white dwarf with a strong magnetic field that burns hydrogen-rich material on its surface. The work of PFF2005 and PHS2007, which demonstrated that classical novae are an important class of counterparts for supersoft X-ray sources, have been presented before.

**Supernova remnants:** Kong et al. (2002a) reported on the discovery of a spatially resolved SNR in M 31 with *Chandra*. In other studies they also analysed the radio and optical emission of SNRs, in addition to the X-ray (Kong et al. 2003b; Williams et al. 2004b).

**X-ray binaries:** Within this class, which includes very bright X-ray sources, one has to distinguish between "field XRBs" and those located in globular clusters. Di Stefano et al. (2002) investigated three fields in the disc of M 31 observed with *Chandra* and explored possible explanations for the high X-ray luminosities of the brightest sources. In addition they examined the X-ray luminosity function of sources located in globular clusters and found that the peak X-ray luminosity is higher than in the Milky Way and that also systems with $L_{\rm X} > 10^{37}$ erg s$^{-1}$ (0.5–7 keV) constitute a larger fraction of all globular cluster sources. Trudolyubov & Priedhorsky (2004) examined the spectra and variability of M 31 globular cluster sources observed with *XMM-Newton* and *Chandra*. They found that ∼80% of their sources with multiple flux measurements available showed significant variability on timescales from days to years. They also investigated the connection between bright X-ray sources and the optical brightness and metal content of globular clusters. The remarkable similarities between the properties of the M 31 globular cluster X-ray sources and those of Galactic neutron star LMXBs led them to expect most of the persistent M 31 globular cluster X-ray sources to be LMXB systems with neutron star primaries.

Within the class of XRBs, many sources are transient (*cf.* Sect. 2.2.1.1). Williams et al. (2006b) compiled a catalogue of 45 transient X-ray sources in M 31 observed with *Chandra* and *XMM-Newton*

[5]Both source classes are put together to the class of very soft sources (VSSs).

between October 1999 and August 2002. They performed a spectral analysis of all *XMM-Newton* and *Chandra* ACIS detections of these sources, and studied their temporal behaviour. The absorption-corrected peak luminosities are distributed in the range from $\sim 10^{36}$ to $\sim 10^{39}$ erg s$^{-1}$ (0.3–7.0 keV). Five sources are potential ultra-compact X-ray binaries and another two sources have possible periodic outbursts and hard spectra consistent with HMXBs. In addition there are a lot of publications reporting on one or a few new found X-ray transients, like *e. g.* Trudolyubov et al. (2001), Williams et al. (2005b), Williams et al. (2005a), Trudolyubov et al. (2006a, hereafter TPC06), Williams et al. (2006a, hereafter WGM06) and Voss et al. (2008). Detections of new transient sources are also reported in "The Astronomer's Telegram"[6] or in "IAU Circulars"[7].

Mangano et al. (2004) searched for periodicities in *XMM-Newton* archival observations and discovered the dipping X-ray source XMMU J004308.6+411247. In three *XMM-Newton* and one *Chandra* observation the source showed dips with a 107 min period. If the source belongs to M 31 its properties are consistent with those of dipping low mass X-ray binaries.

## 3.4 Summary

The X-ray observations and studies presented in this chapter are "limited" in the following ways:

- The *ROSAT* PSPC detector had a rather low resolution compared with nowadays available X-ray detectors. Therefore the positions of the sources listed in the *ROSAT* PSPC survey catalogues have rather large errors. In addition the *ROSAT* observations were limited to the 0.1-2.0 keV band.
- With *XMM-Newton* and *Chandra*, which both have a much improved spatial and energy resolution compared to *ROSAT*, only parts of M 31 (mainly the bulge) have been studied.

The "Deep *XMM-Newton* survey of M 31 ", which is presented in this thesis, allows for the first time to obtain a source catalogue of the whole galaxy (defined by the extend of the corrected $D_{25}$ ellipse) that is based on observation with high spatial and energy resolution in the 0.2–10.0 keV flux range. Therefore source classification and identification is simplified (*cf.* Sect. 7.2), and the properties of source classes can be studied over the whole galaxy (*cf.* Chaps. 8 and 9).

[6] http://www.astronomerstelegram.org
[7] http://www.cfa.harvard.edu/iau/services/IAUC.html

# Chapter 4

# The XMM-Newton observatory

*XMM-Newton* (Jansen et al. 2001), the X-ray Multi-Mirror Mission, was launched on 10 December 1999 by the European Space Agency (ESA) as the second of ESAs four cornerstone missions of the *Horizon 2000* program. With a length of more than 10 m and a weight of almost 4 tons, *XMM-Newton* was the largest scientific satellite ever built in Europe (see Fig. 4.1).

The observatory was launched into a highly elliptical orbit with a perigee of 6 000 km and an apogee[1] of 115 000 km. The eccentricity of the orbit is $\sim 0.60$ and one orbit takes $\sim 47.9$ hours. Because of the radiation belt around the Earth, X-ray observations are only carried out when the satellite elevation is above 46 000 km, allowing about 130 ksec of uninterrupted science observations per revolution. Below this elevation the radiation background is too high to carry out measurements with an acceptable signal-to-noise ratio (S/N). Even at higher elevations, observations can often be seriously affected by the background radiation or particles.

## 4.1 X-ray telescopes

The main scientific payload consists of three co-aligned X-ray mirror systems made up of 58 nested mirror shells each. This large number of Wolter type-1 X-ray mirrors (Wolter 1952) provide an unprecedented effective geometric[2] area of 1 550 cm$^2$ (at 1.5 keV energy) per module. A sketch of the telescopes is shown in Fig. 4.2. The total gathering power is shared by five simultaneously operating focal plane X-ray instruments, which will be presented in the following sections.

In addition *XMM-Newton* carries a co-aligned 30 cm optical/UV telescope and hence allows simultaneous observations in the X-ray and optical/UV regime.

## 4.2 European Photon Imaging Camera

The European Photon Imaging Camera (EPIC) consists of three CCD cameras with a field of view (FoV) of about 30 arcmin diameter. The relative astrometry between the three cameras is calibrated to better than 1 – 2″ across the full FoV.

[1] An orbital manoeuvre in February 2003 changed the orbital parameters to the current perigee and apogee values of 27 830 km and 106 030 km (Ehle et al. 2008).

[2] The combined area, *i. e.* the sum of all thin shell-like regions from where (on-axis) photons are focussed onto the detector, is equivalent to the area of a circle with a diameter of 44.4 cm.

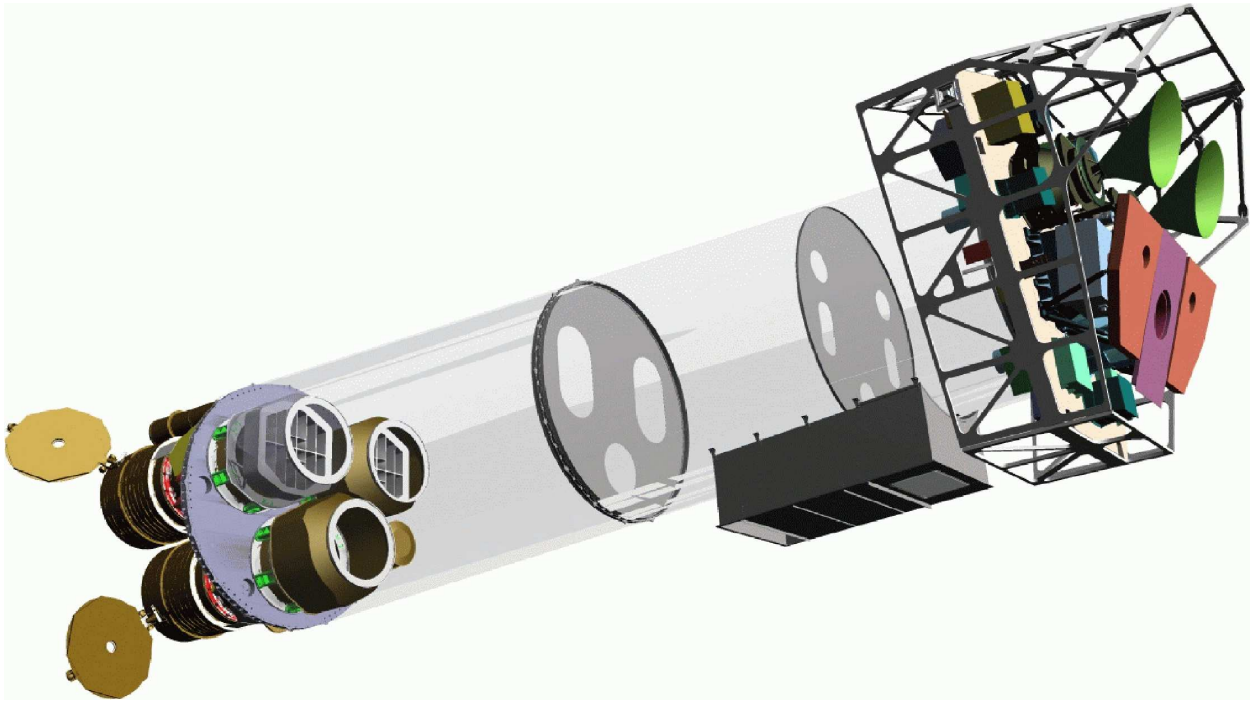

**Figure 4.1:** Sketch of the *XMM-Newton* payload. At the lower left end the mirror modules, two of which are equipped with Reflection Grating Arrays, are visible. At the right end of the assembly, the focal X-ray instruments are shown: The EPIC MOS cameras with their radiators (black/green "horns"), the radiator of the EPIC PN camera (violet) and those of the (light blue) RGS detectors (in pink). The OM telescope is obscured by the lower mirror module. From Ehle et al. (2008).

### 4.2.1 EPIC MOS

Two of the EPIC cameras are Metal Oxide Semi-conductor (MOS) CCD arrays (Turner et al. 2001), which are rotated by 90° with respect to each other.

They share two of the three X-ray telescopes with the Reflection Grating Spectrometers (RGS, see Sect. 4.3). The incident photons are focused by the mirrors and then pass through the grating where about half of the telescope incident flux is diverted to the RGS detectors (see Fig. 4.2). Taking the structural obscuration into account, about 44% of the incoming photons reach the MOS detectors.

Each of the two identical MOS detectors is composed of seven separate front-side illuminated CCDs with a frame store region that acts as data buffer. The CCDs are arranged in a non co-planar way, where six CCDs surround the CCD in the centre (see Fig. 4.3(a)). Thus they follow closely the slight curvature of the focal surface of the Wolter telescopes and leave space for the connection to the central CCD. Each of the seven CCDs has $600 \times 600$ pixels and one pixel (40 micron square) covers $1\farcs1 \times 1\farcs1$ of the FoV.

While the outer ring of 6 CCDs remains in the standard imaging mode, the central CCD can be operated separately. This allows the following modes: full frame, large window, small window and timing. As all observations considered in this thesis were taken in full frame mode, I do not discuss the different modes further.

After a micrometeoroid impact on 09 March 2005 CCD 6 of the MOS 1 detector had to be switched off.

The intrinsic energy resolution of the EPIC MOS camera is $\sim$70 eV at 1 keV. Its time resolution is 2.6 s in full frame mode. (The maximum time resolution is 1.75 ms in timing mode.)

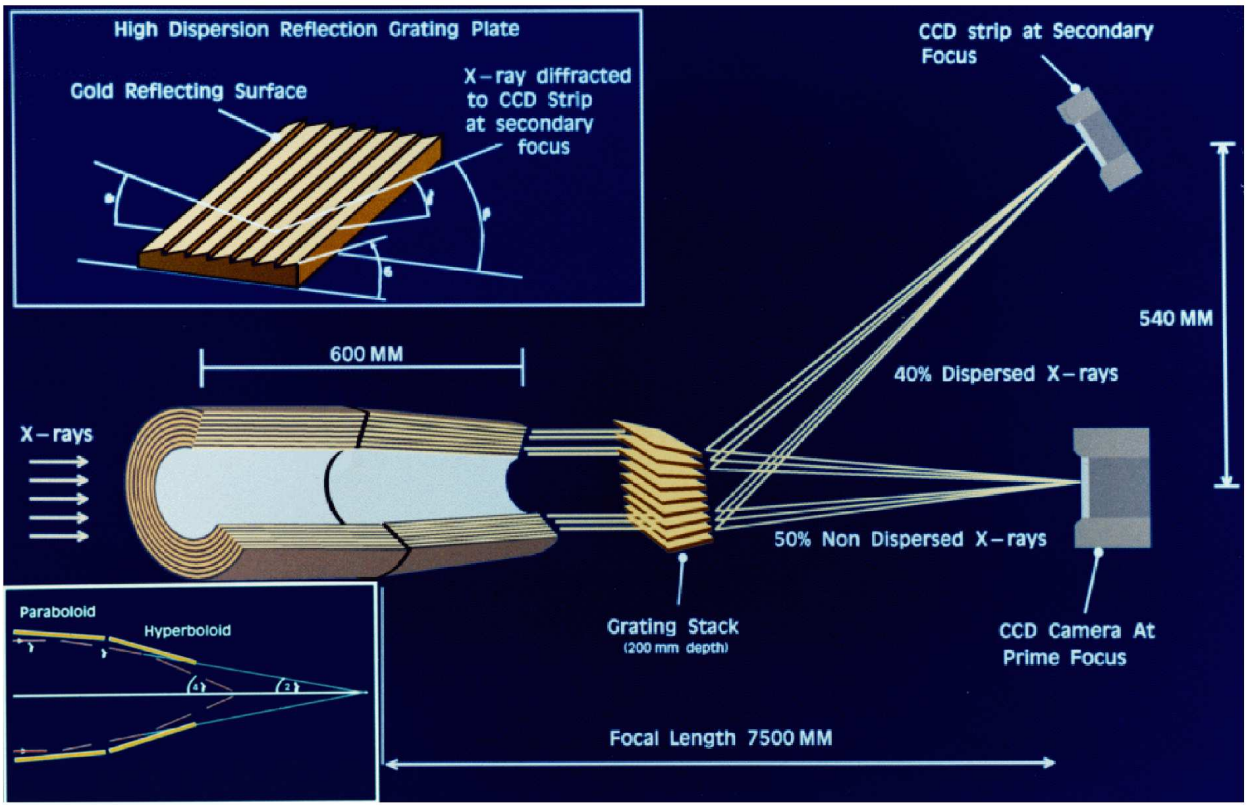


**Figure 4.2:** X-ray path through the X-ray mirror shells and gratings onto the EPIC MOS detector at the primary focus and the RGS camera at the secondary focus (not to scale). The EPIC PN camera is in the focus of an X-ray telescope without gratings. The inlay in the lower left corner shows one of the Wolter type-1 mirror shells, which consists of two mirrors, one a paraboloid and the second a hyperboloid. From Ehle et al. (2008).

(a) EPIC MOS (b) EPIC PN

**Figure 4.3:** Photographies of the focal planes of the (a) EPIC MOS and the (b) PN cameras that show the arrangement of the CCDs. Taken from Turner et al. (2001) and from the ESA *XMM-Newton* Image Gallery (Image courtesy of MPI-semiconductor laboratory, MPE, Astronomisches Institut Tübingen, Germany and ESA).

### 4.2.2 EPIC PN

The PN detector[3] (Strüder et al. 2001) is in the focal plane of the third X-ray telescope. It is a back-side illuminated CCD and consists of 12 CCDs on a single silicon wafer that are aligned in two rows (see Fig. 4.3(b)). One of the CCDs has $200 \times 64$ pixels, where each pixel (150 micron square) covers $4\farcs1 \times 4\farcs1$.

The EPIC PN camera allows several modes of data acquisition. These are: full frame, extended full frame, large window, small window, timing and burst mode. In small window, timing and burst mode, only CCD 4 is active. As for the MOS cameras, all observations used in the thesis were taken in full frame mode.

The intrinsic energy resolution of the EPIC PN camera is $\sim$80 eV at 1 keV. Its time resolution is 73.4 ms in full frame mode. (The maximum time resolution is 7 $\mu$s in burst mode.)

Compared to MOS, the PN camera is characterised by a higher sensitivity at energies $\lesssim$1 keV and $\gtrsim$5 keV. The PN CCDs have a higher quantum efficiency ($\mathrm{QE_{PN}} > 90\%$) than the MOS detectors ($\mathrm{QE_{MOS}} \sim$ 40–85%), and allow higher frame rates through the integration of readout nodes for each individual pixel column. The PN chips lack frame store buffers, which in practice has the consequence of so-called out-of-time events (OoT). These OoT events are generated since the pixels still register incoming X-ray events during the column readout phase, which lasts a few percent of the full integration cycle.[4] Sources will imprint a smeared event streak over the full pixel column (Y direction) due to falsely identified photon positions during readout.

### 4.2.3 EPIC filters and background

Since the EPIC CCDs are also sensitive to IR, visible and UV light, there is a possibility that the X-ray signal of a source with a high optical flux becomes contaminated by the aforesaid photons. To reduce these effects, each camera has three aluminised optical blocking filters, named *thick*, *medium* and *thin*. The use of a blocking filter, especially the thick one, will necessarily limit the softest X-ray energy response.

In addition to the optical blocking filters, internal "offset tables" are used to subtract the constant level of (optical) light or other systematic shifts of the zero level of charge measurements. For the MOS, the offset table values are fixed. For the PN camera, an offset map is computed before the beginning of each observation.

The EPIC background[5] can be divided into two components: a cosmic X-ray background (*e. g.* Gilli et al. 2007), and an instrumental background. The latter one may be further divided into a detector noise component, which becomes important at energies below 300 eV, and a particle induced component, which becomes important at energies above a few keV.

One component of the particle induced background is an external "flaring" component, which is characterised by strong and rapid variability. It is produced by protons with energies less than a few 100 keV, which are funnelled towards the detectors by the X-ray mirrors. The current understanding is that soft protons are most likely organised in clouds populating the Earth's magneto sphere. The number of such clouds encountered by *XMM-Newton* in its orbit depends upon many factors, such as the altitude of the satellite, its position with respect to the magneto sphere, and the amount of solar activity.

The second component of the particle induced background is "normally" much less variable and originates from the interaction of high-energy particles ($E \gtrsim 100$ MeV) with the structure surrounding the detectors and possibly the detectors themselves. As the particles have high energies they can penetrate the satellite from any side, *i. e.* they do not only enter through the telescopes like the soft protons. The intensity of

[3] PN is derived from the pn-junction of the silicon semiconductor technology used in the detectors. For easier readability, the capitalised form PN, instead of pn, is used throughout the thesis.

[4] The out-of-time fraction is 6.3% for full frame mode.

[5] An overview table of the different background components is provided at `http://www.star.le.ac.uk/~amr30/BG/BGTable.html`

the background component induced by high-energy particles during any given observation is within mostly $\sim 10\%$ of the mean. Exceptions are periods close to the Earth's radiation belts (begin and end of an orbit) or those affected by solar flares (during which the satellite is switched off). During these periods the contribution of that background component can be significantly enhanced ($\sim$ a factor ten, see also Fig. 5.2). The spectra are quite flat and present a number of spectral features due to fluorescence from the detectors and the structures surrounding them. In the MOS spectrum Al-K$\alpha$ and Si-K$\alpha$ are clearly visible. In case of the PN detector Al-K$\alpha$ and an intense complex due to Cu-K$\alpha$, Ni-K$\alpha$ and Zn-K$\alpha$ lines around 8 keV is visible. An important point is that the intensity of this complex is not constant over the PN detector (Freyberg et al. 2004).
An additional background component at low energies ($<$1.5 keV), which is neither related to the instrumental background nor to the cosmic X-ray background is the emission from solar wind charge exchange. It originates from charge exchange between solar wind ions and either interstellar neutral material in the heliosphere or material from Earth's exosphere (*e. g.* Snowden et al. 2004).
An important contribution to the detector noise component can occure during the PN offset map calculation. Occasionally (mainly during high particle background) the offset calculation leads to a slight underestimate of the offset in some pixels, which can result in blocks of pixels ($\approx 4\times4$) with enhanced low energy signal.

Table 4.1 summarizes the most important *XMM-Newton* EPIC imaging (full frame) mode characteristics. All data analysed in this thesis were obtained with the *XMM-Newton* European Photon Imaging Camera. In the following sections of this chapter I will briefly describe the remaining instruments of *XMM-Newton*.

## 4.3 Reflection Grating Spectrometer

In addition to the imaging camera, there are two co-aligned Reflection Grating Spectrometers (RGS, den Herder et al. 2001) on-board *XMM-Newton*. Each of them consists of an array of reflection gratings located in the light path of the X-ray telescopes with EPIC MOS cameras at their primary focus (see Fig. 4.2). The incoming light strikes the gratings at an angle of incidence, $\alpha$, with respect to the plane of the grating, and emerges at an angle $\beta$ given by the dispersion equation,

$$\cos\beta = \cos\alpha + \frac{m\lambda}{d}, \tag{4.1}$$

**Table 4.1:** *XMM-Newton* EPIC full frame imaging-mode characteristics. From Ehle et al. (2008)

| Characteristic | XMM Performance |
|---|---|
| number of telescopes and imaging detectors | 3 |
| total effective area at 1keV | $\sim$2 500 cm$^2$ |
| field-of-view | 30′ diameter $\simeq$ 0.2 deg$^2$ |
| spatial resolution (FWHM) | 5″–15″ |
| half-energy width (HEW) | 14″–20″ |
| time resolution PN / MOS | 73.4 ms / 2.6 s |
| pixel scale PN / MOS | 4.″1 / 1.″1 per pixel |
| energy resolution at 1keV | $\sim$80 eV |
| point source sensitivity in 10 ksec (all cameras; 0.15–15.0 keV) | $\sim 5\times10^{-15}$ erg s$^{-1}$cm$^{-2}$ |

where $\lambda$ is the radiation wavelength, $d$ the grating spacing and $m$ the spectral order. The RGS is designed to be used with negative orders, $\beta > \alpha$. About 58% of the incident flux is intercepted by the grating, which diffracts the X-rays onto a linear array of nine CCD detectors. The chips are similar to those of the EPIC MOS cameras. To maximise the soft energy response the chips are back-illuminated. On their exposed side they are aluminium-coated to suppress optical and UV light. Each CCD contains $1024 \times 768$ pixels with a pixel size of 27 micron square, half ($1024 \times 384$) exposed to the sky and half used as a storage area.

The RGS resolving power is 150 to 800 over a range from 5 to 35 Å [2.5 to 0.35 keV][6] (in the first spectral order). The RGS does not have an entrance slit, thus the whole field of view is mapped onto the detector plane. The field of view in the cross-dispersion direction is determined by the width of the CCDs ($5'$), and the spatial resolution in this direction is largely determined by the imaging properties of the mirrors. In the dispersion direction, the aperture of RGS covers the entire FoV of the mirrors, although the effective area decreases significantly for off-axis sources.

## 4.4 Optical Monitor

The *XMM-Newton* payload not only consists of the X-ray telescopes and instruments described above, but also includes an optical/UV telescope (called Optical Monitor (OM); Mason et al. 2001) with a wavelength coverage between 180 and 600 nm, which is co-aligned with the X-ray telescopes. The diameter of its Cassegrain telescope is 30 cm and it covers a field of view of $17' \times 17'$ with an angular resolution of $\sim 1''$. It can detect sources down to a magnitude of 20.7 with a time resolution of 0.5 s. The OM provides different filters (V, B, U, UVW1, UVM2, and UVW2) for imaging and two grisms to obtain low-resolution optical or UV spectra.

## 4.5 Support instruments

*XMM-Newton* also carries two "non-science" instruments. The first one is the EPIC Radiation Monitor Subsystem, which registers the total count rate and also basic spectral information on the background radiation impinging on *XMM-Newton* and its science instruments. When the level of radiation intensity exceeds a certain threshold, the system issues a warning to the ground for the Spacecraft Operator to safe the instruments.

The second one is the Attitude and Orbit Control Subsystem, which determines the attitude of the *XMM-Newton* spacecraft while in orbit.

[6] conversion of wavelength into energies: $\lambda\,(\text{Å}) \times E\,(\text{keV}) = 12.3985$

# Chapter 5

# Observations and data analysis

## 5.1 Observations

In this thesis I analysed the observations of the "Deep *XMM-Newton* Survey of M 31" (PI Pietsch). This survey is the follow-up project of the "Major Axis Survey of M 31" (Pietsch et al. 2005b). These two surveys provide, for the first time, a full coverage of the whole $D_{25}$ ellipse of this galaxy with *XMM-Newton* (see Fig. 5.1). To treat all data in the same way, I re-analysed all archival *XMM-Newton* observations of M 31 which were used in Pietsch et al. (2005b). In addition I included an *XMM-Newton* target of opportunity (ToO) observation of source CXOM31 J004059.2+411551 and four observations of source RX J0042.6+4115 (PI Barnard).

All observations of the "Deep *XMM-Newton* Survey of M 31" and the ToO observation were taken in *XMM-Newton* AO5, AO6 and AO7, respectively, between June 2006 and February 2008. All other observations were available via the *XMM-Newton* Data Archive[1] and were taken between June 2000 and July 2004.

The journal of observations is given in Table 5.1. It gives the M 31 field name (Column 1), the identification number (2) and date (3) of the observation and the pointing direction (4, 5). Column 6 contains the systematic offset (see Sect. 5.2.5). For each EPIC camera, the filter used and the exposure time after screening for high background is given (see Sect. 5.2.2).

Table 5.2 gives similar information as in Table 5.1 for five *XMM-Newton* observations of the *XMM-Newton*/*Chandra* M 31 nova monitoring project[2], which were only used to examine spectral properties and time variability of selected XRBs (see Sects. 9.4.3 and 9.4.4). In addition I included four *Chandra*/HRC observations of the M 31 nova monitoring project in the variability studies in Sects. 9.4.3 and 9.4.4. Table 5.3 gives the identification number (1), date (2) and duration (3) of these *Chandra*/HRC observations and the pointing direction (4, 5).

The observations given in Tables 5.2 and 5.3 are not part of the Deep *XMM-Newton* Survey of M 31 and are therefore not included in the overall analysis of the survey data. They are only used for the investigation of individual sources discussed in Sects. 9.4.3 and 9.4.4.

[1] `http://xmm.esac.esa.int/xsa/`

[2] `http://www.mpe.mpg.de/~m31novae/xray/index.php`

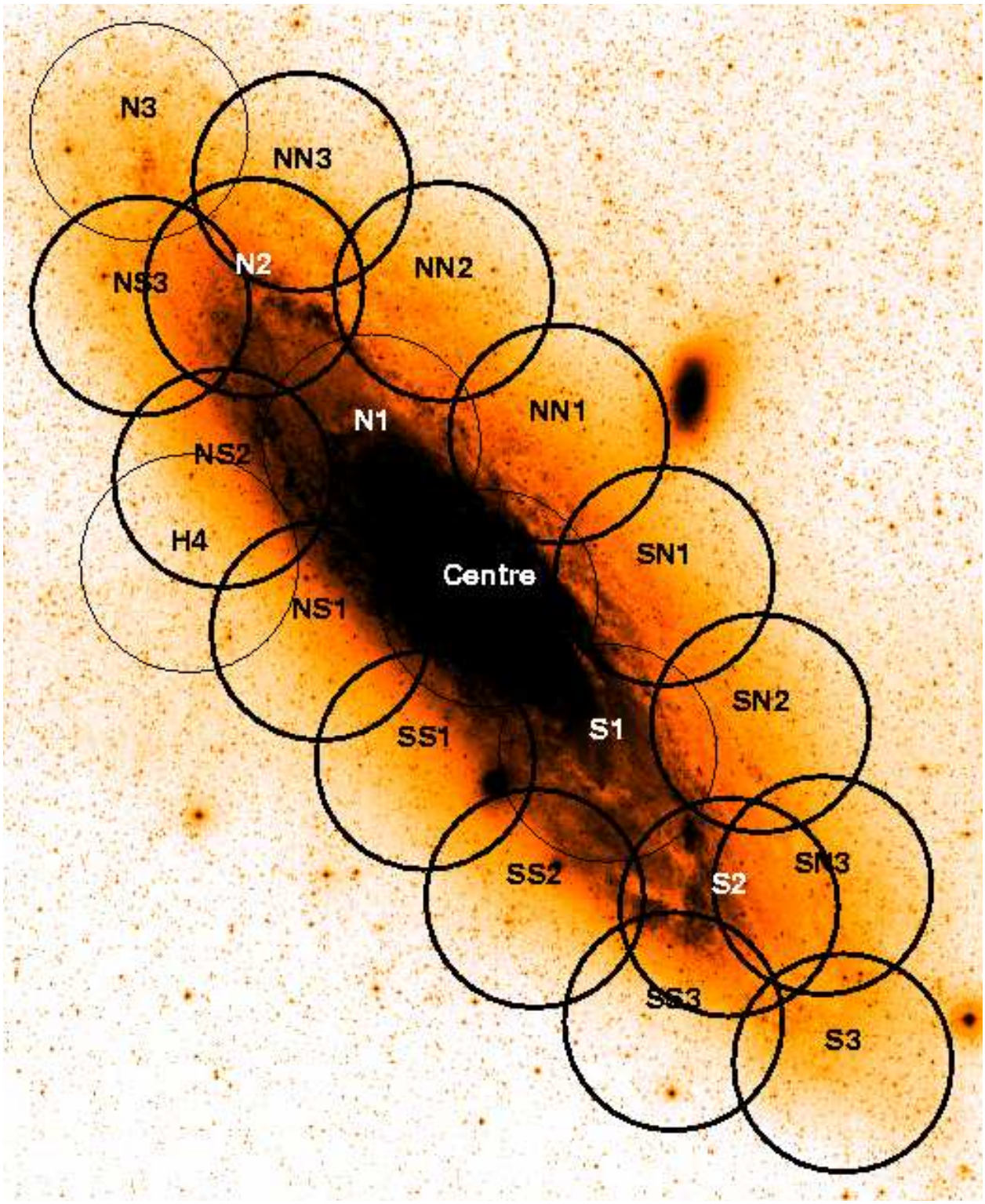


**Figure 5.1:** A deep optical image of M 31 overplotted with the *XMM-Newton* fields of the survey. The area covered by individual EPIC observations is approximately marked by circles with 14 arcmin radius. Fields observed in the "Deep *XMM-Newton* Survey of M 31" are marked as bold. For clarity the ToO observation (coinciding with the position of SN1) and the observations of RX J0042.6+4115 (centre) are omitted.

**Table 5.1:** *XMM-Newton* log of the *Deep Survey* and archival M 31 observations overlapping with the optical $D_{25}$ ellipse.

| M 31 field | | Obs. id. | Obs. dates | Pointing direction RA/Dec (J2000) | | Offset * | EPIC PN | | EPIC MOS1 | | EPIC MOS2 | |
|---|---|---|---|---|---|---|---|---|---|---|---|---|
| | | | | | | | Filter$^+$ | $T^\dagger_{\rm exp}$ | Filter$^+$ | $T^\dagger_{\rm exp}$ | Filter$^+$ | $T^\dagger_{\rm exp}$ |
| (1) | | (2) | (3) | (4) | (5) | (6) | (7) | (8) | (9) | (10) | (11) | (12) |
| Centre 1 | (c1) | 0112570401 | 2000-06-25 | 0:42:36.2 | 41:16:58 | $-1.9, +0.1$ | medium | 23.48(23.48) | medium | 29.64(29.64) | medium | 29.64(29.64) |
| Centre 2 | (c2) | 0112570601 | 2000-12-28 | 0:42:49.8 | 41:14:37 | $-2.1, +0.2$ | medium | 5.82( 5.82) | medium | 6.42( 6.42) | medium | 6.42( 6.42) |
| Centre 3 | (c3) | 0109270101 | 2001-06-29 | 0:42:36.3 | 41:16:54 | $-3.2, -1.7$ | medium | 21.71(21.71) | medium | 23.85(23.85) | medium | 23.86(23.86) |
| N1 | (n1) | 0109270701 | 2002-01-05 | 0:44:08.2 | 41:34:56 | $-0.3, +0.7$ | medium | 48.31(48.31) | medium | 55.68(55.68) | medium | 55.67(55.67) |
| Centre 4 | (c4) | 0112570101 | 2002-01-06/07 | 0:42:50.4 | 41:14:46 | $-1.0, -0.8$ | thin | 47.85(47.85) | thin | 52.87(52.87) | thin | 52.86(52.86) |
| S1 | (s1) | 0112570201 | 2002-01-12/13 | 0:41:32.7 | 40:54:38 | $-2.1, -1.7$ | thin | 46.75(46.75) | thin | 51.83(51.83) | thin | 51.84(51.84) |
| S2 | (s2) | 0112570301 | 2002-01-24/25 | 0:40:06.0 | 40:35:24 | $-1.1, -0.3$ | thin | 22.23(22.23) | thin | 24.23(24.23) | thin | 24.24(24.24) |
| N2 | (n2) | 0109270301 | 2002-01-26/27 | 0:45:20.0 | 41:56:09 | $-0.3, -1.5$ | medium | 22.73(22.73) | medium | 25.22(25.22) | medium | 25.28(25.28) |
| N3 | (n3) | 0109270401 | 2002-06-29/30 | 0:46:38.0 | 42:16:20 | $-2.3, -1.7$ | medium | 39.34(39.34) | medium | 43.50(43.50) | medium | 43.63(43.63) |
| H4 | (h4) | 0151580401 | 2003-02-06 | 0:46:07.0 | 41:20:58 | $+0.3, +0.0$ | medium | 10.14(10.14) | medium | 12.76(12.76) | medium | 12.76(12.76) |
| RX 1 | (b1)$^\ddagger$ | 0202230201 | 2004-07-16 | 0:42:38.6 | 41:16:04 | $-1.3, -1.2$ | medium | 16.32(16.32) | medium | 19.21(19.21) | medium | 19.21(19.21) |
| RX 2 | (b2) | 0202230301 | 2004-07-17 | 0:42:38.6 | 41:16:04 | $-1.0, -0.9$ | medium | 0.0(0.0) | medium | 0.0(0.0) | medium | 0.0(0.0) |
| RX 3 | (b3)$^\ddagger$ | 0202230401 | 2004-07-18 | 0:42:38.6 | 41:16:04 | $-1.7, -1.5$ | medium | 12.30(12.30) | medium | 17.64(17.64) | medium | 17.68(17.68) |
| RX 4 | (b4)$^\ddagger$ | 0202230501 | 2004-07-19 | 0:42:38.6 | 41:16:04 | $-1.4, -1.8$ | medium | 7.94(7.94) | medium | 10.12(10.12) | medium | 10.13(10.13) |
| S3 | (s3) | 0402560101 | 2006-06-28 | 0:38:52.8 | 40:15:00 | $-3.1, -3.0$ | thin | 4.99(4.99) | medium | 6.96(6.96) | medium | 6.97(6.97) |
| SS1 | (ss1) | 0402560201 | 2006-06-30 | 0:43:28.8 | 40:55:12 | $-4.4, -3.7$ | thin | 14.07(9.57) | medium | 24.56(10.65) | medium | 24.58(10.66) |
| SN1 | (sn1) | 0402560301 | 2006-07-01 | 0:40:43.2 | 41:17:60 | $-2.7, -1.5$ | thin | 41.23(35.42) | medium | 47.60(39.40) | medium | 47.64(39.44) |
| SS2 | (ss2) | 0402560401 | 2006-07-08 | 0:42:16.8 | 40:37:12 | $-1.2, -1.3$ | thin | 21.64(9.92) | medium | 25.59(11.04) | medium | 25.64(11.05) |
| SN2 | (sn2) | 0402560501 | 2006-07-20 | 0:39:40.8 | 40:58:48 | $-0.8, -0.7$ | thin | 48.79(21.45) | medium | 56.13(23.85) | medium | 56.17(23.86) |
| SN3 | (sn3) | 0402560701 | 2006-07-23 | 0:39:02.4 | 40:37:48 | $-0.9, -2.0$ | thin | 23.80(15.43) | medium | 28.02(17.16) | medium | 28.04(17.17) |
| SS3 | (ss3) | 0402560601 | 2006-07-28 | 0:40:45.6 | 40:21:00 | $-1.8, -1.7$ | thin | 27.77(20.22) | medium | 31.92(22.49) | medium | 31.94(22.5) |
| S2 | (s21) | 0402560801 | 2006-12-25 | 0:40:06.0 | 40:35:24 | $-1.6, -0.7$ | thin | 39.12(39.12) | medium | 45.19(45.19) | medium | 45.21(45.21) |
| NN1 | (nn1) | 0402560901 | 2006-12-26 | 0:41:52.8 | 41:36:36 | $-1.5, -1.5$ | thin | 37.9(37.9) | medium | 43.08(43.08) | medium | 43.1(43.1) |
| NS1 | (ns1) | 0402561001 | 2006-12-30 | 0:44:38.4 | 41:12:00 | $-1.0, -1.3$ | thin | 45.11(45.11) | medium | 50.9(50.9) | medium | 50.93(50.93) |
| NN2 | (nn2) | 0402561101 | 2007-01-01 | 0:43:09.6 | 41:55:12 | $-0.0, -1.2$ | thin | 41.73(41.73) | medium | 46.45(46.45) | medium | 46.47(46.47) |
| NS2 | (ns2) | 0402561201 | 2007-01-02 | 0:45:43.2 | 41:31:48 | $-2.3, -1.7$ | thin | 34.96(34.96) | medium | 40.55(40.55) | medium | 40.58(40.58) |
| NN3 | (nn3) | 0402561301 | 2007-01-03 | 0:44:45.6 | 42:09:36 | $-1.4, -0.7$ | thin | 31.04(31.04) | medium | 34.81(34.81) | medium | 34.81(34.81) |
| NS3 | (ns3) | 0402561401 | 2007-01-04 | 0:46:38.4 | 41:53:60 | $-2.1, +0.3$ | thin | 39.41(39.41) | medium | 45.50(45.50) | medium | 45.52(45.52) |
| N2 | (n21) | 0402561501 | 2007-01-05 | 0:45:20.0 | 41:56:09 | $-2.6, -1.3$ | thin | 37.18(37.18) | medium | 41.98(41.98) | medium | 42.03(42.03) |
| SS1 | (ss11) | 0505760201 | 2007-07-22 | 0:43:28.8 | 40:55:12 | $-2.5, -2.6$ | thin | 30.07(23.90) | medium | 34.01(26.70) | medium | 34.02(26.72) |
| S3 | (s31) | 0505760101 | 2007-07-24 | 0:38:52.8 | 40:15:00 | $-1.8, -1.0$ | thin | 21.86(15.74) | medium | 24.74(17.65) | medium | 24.74(17.65) |
| TOO | (sn11)$^\diamond$ | 0410582001 | 2007-07-25 | 0:40:59.2 | 41:15:51 | $-1.2, -0.3$ | thin | 11.27(11.27) | medium | 14.01(14.01) | medium | 14.02(14.02) |
| SS3 | (ss31) | 0505760401 | 2007-12-25 | 0:40:45.6 | 40:21:00 | $-1.0, +0.1$ | thin | 23.56(22.82) | medium | 28.18(25.8) | medium | 28.2(25.82) |
| SS2 | (ss21) | 0505760301 | 2007-12-28 | 0:42:16.8 | 40:37:12 | $+1.3, -0.1$ | thin | 35.28(35.28) | medium | 40.00(40.00) | medium | 40.01(40.01) |
| SN3 | (sn31) | 0505760501 | 2007-12-31 | 0:39:02.4 | 40:37:48 | $-1.6, -1.3$ | thin | 24.26(24.26) | medium | 28.77(28.77) | medium | 28.78(28.78) |
| S3 | (s32) | 0511380101 | 2008-01-02 | 0:38:52.8 | 40:15:00 | $-1.7, -3.3$ | thin | 38.31(38.31) | medium | 44.92(44.92) | medium | 44.95(44.95) |
| SS1 | (ss12) | 0511380201 | 2008-01-05 | 0:43:28.8 | 40:55:12 | $-0.9, -1.4$ | thin | 8.85( 8.85) | medium | 11.28(11.28) | medium | 11.29(11.29) |
| SN2 | (sn21) | 0511380301 | 2008-01-06 | 0:39:40.8 | 40:58:48 | $-0.2, -0.4$ | thin | 24.79(24.79) | medium | 29.28(29.28) | medium | 29.29(29.29) |
| SS1 | (ss13) | 0511380601 | 2008-02-09 | 0:43:28.8 | 40:55:12 | $-0.8, -1.8$ | thin | 13.35(13.35) | medium | 15.07(15.07) | medium | 15.08(15.08) |

Notes:

* : Systematic offset in RA and Dec in arcsec determined from correlations with 2MASS, USNO-B1, LGS and *Chandra* catalogues

$^{+}$ : All observations in full frame imaging mode

$^{\dagger}$ : Exposure time in units of ks after screening for high background used for detection, for colour image in brackets

$^{\ddagger}$ : Combination of the three observations is called b, RX denotes RX J0042.6+4115

$^{\diamond}$ : TOO denotes the target of opportunity observation pointed on CXOM31 J004059.2+411551

**Table 5.2:** Journal of additional *XMM-Newton* observations of M 31. (only used in Sects. 9.4.3 and 9.4.4)

| M 31 field | Obs. id. | Obs. dates | Pointing direction RA/Dec (J2000) | | Offset * | EPIC pn | | EPIC MOS1 | | EPIC MOS2 | |
|---|---|---|---|---|---|---|---|---|---|---|---|
| | | | | | | Filter$^{+}$ | $T^{\dagger}_{\rm exp}$ | Filter$^{+}$ | $T^{\dagger}_{\rm exp}$ | Filter$^{+}$ | $T^{\dagger}_{\rm exp}$ |
| (1) | (2) | (3) | (4) | (5) | (6) | (7) | (8) | (9) | (10) | (11) | (12) |
| Centre 5 (c5) | 0405320501 | 2006-07-02 | 0:42:44.3 | 41:16:09 | $-1.8, -2.3$ | thin | 9.26 | medium | 9.24 | medium | 9.26 |
| Centre 6 (c6) | 0405320601 | 2006-08-09 | 0:42:44.3 | 41:16:09 | $-1.2, -2.7$ | thin | 7.20 | medium | 7.19 | medium | 7.19 |
| Centre 7 (c7) | 0405320701 | 2006-12-31 | 0:42:44.3 | 41:16:09 | $-0.6, -0.9$ | thin | 14.04 | medium | 15.61 | medium | 15.62 |
| Centre 8 (c8) | 0405320801 | 2007-01-16 | 0:42:44.3 | 41:16:09 | $-0.1, -0.9$ | thin | 12.04 | medium | 13.42 | medium | 13.42 |
| Centre 9 (c9) | 0405320901 | 2007-02-05 | 0:42:44.3 | 41:16:09 | $+0.5, -2.2$ | thin | 15.04 | medium | 16.42 | medium | 16.42 |

Notes:

* : Systematic offset in RA and Dec in arcsec determined from correlations with *Chandra* catalogues

$^{+}$ : All observations in full frame imaging mode

$^{\dagger}$ : Exposure time in units of ks after screening for high background used for detection

**Table 5.3:** *Chandra*/HRC observations of the central field of M 31. (only used in Sects. 9.4.3 and 9.4.4)

| Obs. id. | Obs. dates | duration | Pointing direction RA/Dec (J2000) | |
|---|---|---|---|---|
| | | ks | | |
| (1) | (2) | (3) | (4) | (5) |
| 7283 | 2006-06-06 | 19.9 | 00:42:44.8 | 41:16:23 |
| 7284 | 2006-10-01 | 20.0 | 00:42:43.1 | 41:16:17 |
| 7285 | 2006-11-14 | 18.5 | 00:42:43.3 | 41:15:59 |
| 7286 | 2007-03-12 | 18.7 | 00:42:45.2 | 41:15:58 |

## 5.2 Data analysis

In this section, the basic concepts of the X-ray data reduction and source detection processes are introduced.

The analysis of the data is based upon the available tools of the *XMM-Newton* Science Analysis Software[3] (SAS), which is the mission software package used to reduce and analyse *XMM-Newton* data.[4] The SAS provides software tools to extract the basic data products, like event files and exposure information, and to produce more sophisticated products, such as images, spectra, light curves, etc. The data presented in the following was analysed using versions 6.5 to 8.0 of the SAS, together with the most recent calibration files available at the time of the analysis. In particular, for the critical source detection procedure, the performance of the SAS tasks impose a 'boundary condition' for the survey outcome. Additionally, I used existing software such as ds9 (Joye & Mandel 2003), ftools[5] (Blackburn 1995), the EURO-VO tools[6] Aladin and TOPCAT, as well as perl and shell scripts, and sophisticated programs in idl that were developed within our research group.

### 5.2.1 Pipeline products

The raw *XMM-Newton* data for each observation are organised in a so-called Observation Data File (ODF), a directory with a collection of $\sim 200$ files containing the uncalibrated data of all instruments, satellite attitude files, and calibration information. ODFs have unique identification numbers (Obs. ids.) and can be considered as the basic starting data set from which all science products can be derived. After downloading the ODFs from the archive, the files have to be processed with the latest version of the SAS tasks and calibration before they can be used to extract scientific products. This is achieved with a few SAS procedures. odfingest extracts and organises the satellite housekeeping data necessary to accurately reconstruct the observations. The task cifbuild matches the input data with the appropriate calibration files, which are accessible through the so-called Calibration Access Layer (CAL). The instrument specific processing chains epchain for the EPIC PN and emchain for the MOS cameras generate calibrated photon event lists, *i. e.* tables with entries for each detected photon, for the complete observation.

Such a table contains the detection time of the event, the CCD pixel where it was detected, the energy of the photon after correcting for gain and charge transfer inefficiency (CTI), and several diagnostic values. Also, via the attitude information of the spacecraft, the sky position for each event is calculated. An example of one of the diagnostic values is the pattern of the detection, *i. e.* whether a photon was detected in only one, two, three, four or more pixels, and the arrangement of these pixels.

### 5.2.2 Screening for high background

In Chap. 4 the different components of the background, which can affect observations, were described. To reduce the background contamination, science observations are only conducted at a satellite elevation larger than $46\,000$ km. Nevertheless, observations can contain additional times of increased background, especially if they are located at the start or end of an orbital window. Severe background screening is especially important for the detection of faint point sources, the investigation of diffuse emission and for colour images (see Sect. 5.2.3).

The first step was to investigate the effect of soft proton flares on the observations. Hence, for each observation, a high energy (7 to 15 keV) background light curve was produced (some examples are shown in Fig. 5.2). I used these light curves to select time intervals with low background, the so-called good time

[3] The SAS homepage can be found at http://xmm.esac.esa.int/sas.

[4] SAS tasks such as eboxdetect are set in typewriter font for easy identification.

[5] http://heasarc.gsfc.nasa.gov/ftools/

[6] http://www.euro-vo.org/pub/fc/software.html

intervals (GTIs). The GTIs were determined from the higher statistic PN light curves and were also used for the MOS cameras. Outside of the PN time coverage, GTIs were determined from the combined MOS light curves. For each observation the limiting thresholds in the count rate, were adjusted individually. That way I avoided having to cut out short periods (up to a few hundred seconds) of marginally increased background. Short periods of low background, which were embedded between longer periods of high background, were also omitted. For most observations, the PN count rate thresholds are two for the lower limit and eight for the higher limit. As many of the observations were affected by strong background flares (mostly at the beginning or end of the observation), the net exposure time that could be used for our analysis was strongly reduced. The sum of GTIs after high energy background screening ranges from 6 ks to about 56 ks, apart from observation b2 which had to be rejected because it shows high background throughout the observation. The exact values for each observation for all three EPIC instruments are given in Cols. 8, 10 and 12 of Table 5.1. The observations taken during the summer visibility window of M 31 (*i. e.* the observations taken in June and July) were affected more strongly by background radiation than those taken during the winter window. The most affected observations of the deep survey were re-approved in *XMM-Newton* AO6 or AO7 and the new observations were added to the analysis.[7]

After screening for times of enhanced particle background, the second step was to examine the influence of solar wind charge exchange (SWCX). This was done by producing soft energy ($< 2$ keV) background light curves. In only 10 observations did these light curves show periods of increased count rates due to SWCX, requiring additional screening (GTI values after this additional screening are given in brackets in Cols. 8, 10 and 12 of Table 5.1). For the creation of colour images, the screening of enhanced background due to SWCX was applied to the observations. It was not used for source detection.

The third and last step includes the study of the background due to detector noise. The processing chains take into account all known bad or hot pixels and columns, and flag the affected pixels in the event lists. To search for additional warm or hot pixels and columns, each observation was checked by eye. The decision whether a suspicious pixel was flagged as warm or hot, and at which lower energy cut-off an affected column was set, was aided by shell scripts developed by ourselves. To avoid background variability over the PN images I omitted the energy range form 7.2–9.2 keV where strong fluorescence lines cause higher background in the outer detector area (Freyberg et al. 2004). An additional background component can occur during the EPIC PN offset map calculation. At the beginning of each observation the deviation of the nominally zero signal level for each pixel is determined. This requires about 0.5–1.5 h for the EPIC PN.[8] If this period is affected by high particle background the offset calculation will lead to a slight underestimate of the offset in some pixels, which can result in blocks of pixels ($\approx 4 \times 4$) with enhanced low energy signal.[9] These blocks will be found by the `SAS` detection tools and appear as sources with extremely soft spectrum (so called supersoft sources, see Sect. 2.2.1.2). To reduce the number of false detections in this source class, I decided to include the task `eproject` in `epchain`, which locates the pixels with a slight underestimate of the offset and corrects this underestimate. To ensure that `eproject` produces the correct results, difference images of the event lists obtained with and without `eproject` were created. Only events with energies above 200 eV were used. I checked whether `eproject` removed all pixels with an enhanced low energy signal. Only in observation ns1 does the difference image still show a block of pixels with enhanced signal. As this block is also visible at higher energies (PHA[10]$>$30) it cannot be corrected with `eproject`. Additionally I checked that all the pixels unaffected during the offset map calculation have a value consistent with zero in the difference images. The two exceptions found are discussed in Sect. 7.2.

[7] That is why the fields S3, SS1, SS2, SS3, SN2 and SN3 appear more than once in Table 5.1. For the same reason the fields S2 and N2 were observed once more in the context of the deep survey.

[8] For the EPIC MOS instruments a predefined offset table is uploaded, which takes about 10 min. The more sensitive PN camera hence achieves on average about 1 h less on-target time than the MOS instruments.

[9] See also `http://xmm2.esac.esa.int/docs/documents/CAL-TN-0050-1-0.ps.gz`

[10] The column denoted by PHA in the event file contains the measured photon energy in units of uncalibrated spectral channel.

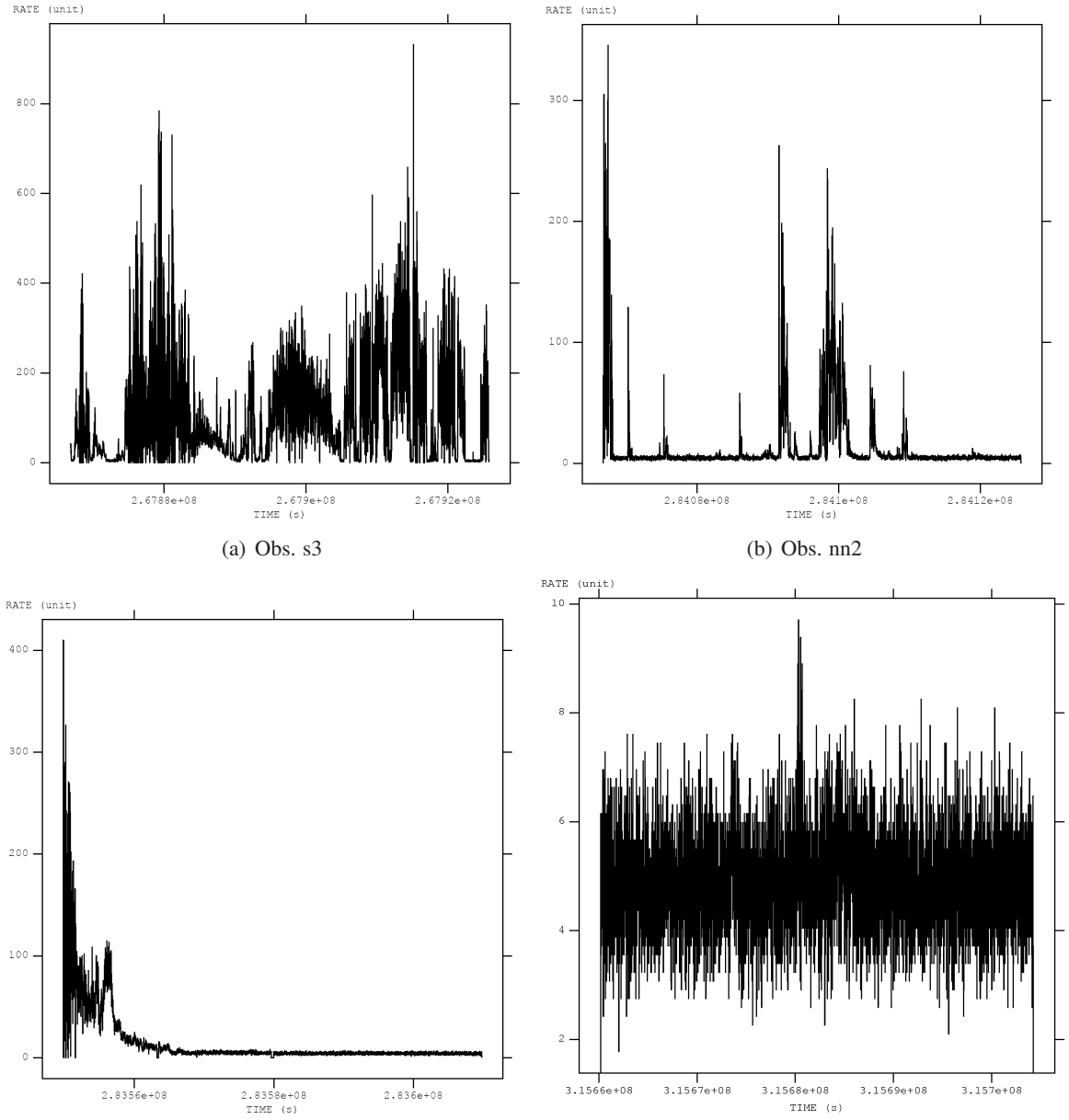


(a) Obs. s3

(b) Obs. nn2

(c) Obs. nn1

(d) Obs. s32

**Figure 5.2:** High energy (7–15 keV) EPIC PN light curves of observations s3 (a), nn2 (b), nn1 (c) and s32 (d). Figure (a) shows the observation which is most strongly affected by enhanced background radiation. For most of the observation, the detected rate is about a factor 40 to 160 over the quiescence rate. The other extreme, an observation which is hardly affected by background flaring is shown in Fig. (d). Please note that the scale is reduced by a factor of $\sim$100 compared to Fig. (a). Figures (b) and (c) show observations that are affected by strong background flares during and at the beginning of the observation, respectively.

**Different data reduction in Chap. 6**

For the analysis of temporal variability in the central field of M 31, we used the images, background images, exposure maps and masks of PFH2005. We adapted the same background screening as in PFH2005 for the July 2004 monitoring observations. Differences between the background screening for the Large *XMM-Newton* survey and PFH2005 are: a more relaxed background screening in PFH2005, the renunciation of the `epreject` task in PFH2005, as it was only available with shortened functionality at that time, and of course the versions of the `SAS` software used.

### 5.2.3 Images

For each observation, the data were split into five energy bands: (0.2–0.5) keV, (0.5–1.0) keV, (1.0–2.0) keV, (2.0–4.5) keV, and (4.5–12) keV. For the PN data I used only "single" events (PATTERN == 0) in the first energy band and for the other bands "singles and doubles" were selected (PATTERN <= 4). In the MOS cameras "single" to "quadruple" events (PATTERN <= 12) were used. I created images, background images and exposure maps (with and without vignetting correction) for PN, MOS 1 and MOS 2 in each of the five energy bands mentioned above and masked them for acceptable detector area. The image bin size is $2''$.

The background images are created in a two step process. In the first step a so called "cheese image" is produced by cutting out all individual sources. In the second step the "holes" (positions where sources were located) in the cheese image have to be filled with appropriate background values that are determined from the measured background in the area surrounding the hole. The source detection is done with the `SAS` task `eboxdetect`. This tool runs a sliding cell detection algorithm with detection box sizes of $5 \times 5$, $10 \times 10$ and $20 \times 20$ pixels ($10'' \times 10''$, $20'' \times 20''$and $40'' \times 40''$). To create background images, `eboxdetect` runs in a local mode, where it determines the background from the pixels surrounding the sliding box. The detection threshold is set to `likemin = 15`, which is a good compromise between cutting out most of the sources and leaving enough area from which the background at the positions of the sources can be derived. For the background calculation a two dimensional spline is fit to a rebinned and exposure corrected image (task `esplinemap`). The number of bins used for rebinnig is controlled by the parameter `nsplinenodes`, which is set to 16 for all but the observations of the central region, where it was set to 20 (maximum value). For PN the background maps contain the contribution from the "out of time (OoT)" events (parameter `withootset=true` in task `esplinemap`).

For the colour images the X-ray energies were colour-coded as follows: red: 0.2–1.0 keV, green: 1.0–2.0 keV and blue: 2.0–12.0 keV. Observations which were affected by soft proton flares have an increased background in the high energy (*i. e.* blue) band. If they are combined with other, unaffected observations into a colour mosaic image, the observations with enhanced background will appear with a tinge of blue. The reason for that tinge is a uniform count rate threshold, which is applied to all observations of the mosaic image. To create colour mosaic images that are not affected by any tinge, a severe background screening is needed. If observations are affected by solar wind charge exchange they will appear in the mosaic image with a tinge of red. To avoid this, a second screening step (in the low energy band) was necessary.

### 5.2.4 Source detection

Source detection was performed simultaneously on $5 \times 3$ images (5 energy bands for each EPIC camera), using the XMM-`SAS` detection tasks `eboxdetect` and `emldetect`. In the following I describe the detection procedure used.

The source detection procedure consists of two consecutive detection steps. An initial source list is created with the task `eboxdetect` (*cf.* Sect. 5.2.3). To select source candidates down to a low statistical

significance level a low likelihood threshold (`likemin = 5` in Chap. 6, `likemin = 4` in Chap. 7) was used. The background was estimated from the previously created background images (see Sect. 5.2.3).

This list is the starting point for the XMM-SAS task `emldetect` (v. 4.44.19 in Chap. 6, v. 4.60.1 in Chap. 7). The `emldetect` task performs a Maximum Likelihood fit of the distribution of source counts (based on a Cash C-statistics approach; Cash 1979), using a point spread function model obtained from ray tracing calculations. If $P$ is the probability that a Poissonian fluctuation in the background is detected as a spurious source, the likelihood of the detection is then defined as $\mathcal{L} = -\ln(P)$.[11] The fit is performed simultaneously in all energy bands for all three cameras by summing the likelihood contribution from each band and each camera. Sources exceeding the detection likelihood threshold in the full band (combination of the 15 bands) are regarded as detections; the catalogue is thus full band selected. The detection threshold used is six (in Chap. 6) and seven (in Chap. 7 as in PFH2005). Some other parameters also differ from the values used in PFH2005, since in this thesis a parameter setting optimised for the detection of extended sources (G. Lamer; private communication) was used. The parameters in question are the event cut-out (`ecut = 30.0`) and the source selection (`scut = 0.9`) radius for multi-source fitting, the maximum number in which one input source can be split (`nmulsou = 2`) and the maximum number of sources to be fit simultaneously (`nmaxfit = 2`). Multi-PSF fitting was performed in a two stage process (`withtwostage = true`) for objects with a detection likelihood larger than ten. All the sources were also fitted with a convolution of a $\beta$-model cluster brightness profile (`extentmodel = beta`; Cavaliere & Fusco-Femiano 1976) with the *XMM-Newton* point spread function, in order to detect any possible extension in the detected signal (`fitextent = true`). Sources which have a core radius significantly larger than the PSF are flagged as extended. The free parameters of the fit are the source location, the source extent and the source counts in each energy band of each telescope.

To derive the X-ray flux of a source from its measured count rate, one uses the so-called energy conversion factors (ECFs):

$$\mathrm{Flux} = \frac{\mathrm{Rate}}{\mathrm{ECF}} \tag{5.1}$$

These factors are calculated from the *Response Matrix File*, and depend on the filter used, the energy band in question, and the spectrum of the source. As I want to apply the conversion factors to all sources found in the survey, I assume a power-law model with photon index $\Gamma = 1.7$ and a foreground absorption of $N_\mathrm{H} = 7 \times 10^{20}\,\mathrm{cm}^{-2}$ (PFH2005) to be the universal source spectrum for the ECF calculation. The ECF values used are given in Chap. 6, and in Chap. 7, respectively.

For most sources, band 5 just adds noise to the total count rate. If converted to fluxes this noise often dominates the total flux due to the small ECF. To avoid this problem I calculated count rates and fluxes for detected sources in the "XID" (0.2–4.5) keV band (bands 1 to 4 combined). While for most sources this is a good solution, for extremely hard or soft sources there may still be bands just adding noise. This then may lead to rate and flux errors that seem to wrongly indicate a lower source significance. A similar effect occurs in the combined rates and fluxes if a source is detected primarily in one instrument (*e. g.* soft sources in PN).

I rejected spurious detections in the vicinity of bright sources. In regions with a highly structured background, the SAS detection task `emldetect` registered some extended sources. I also rejected these "sources" as spurious detections. In an additional step I checked whether each object had visible contours in at least one image out of the five energy bands. The point-like or extended nature, which was determined with `emldetect`, was taken into account. In this way, "sources" that are fluctuations in the background, but which were not fully modelled in the background images, are detected. In addition, objects located on hot pixels, or bright pixels at the rim or in the corners of the individual CCD chips (which were missed during the background screening) were recognised and excluded from the source catalogue.

[11] This is a simplified description, as `emldetect` transforms the derived likelihoods to equivalent likelihoods, corresponding to the case of two free parameters. This allows a comparison between detection runs with different numbers of free parameters.

### 5.2.5 Astrometrical corrections

To obtain astrometrically-corrected positions for the sources of the five central fields I used the SAS-task eposcorr with *Chandra* source lists (Kong et al. 2002b; Kaaret 2002; Williams et al. 2004a). For the other fields I selected sources from the USNO-B1 (Monet et al. 2003), 2MASS (Skrutskie et al. 2006) and the Local Group Survey (LGS; Massey et al. 2006) catalogues[12].

#### 5.2.5.1 Astrometry of optical/infrared catalogues

In a first step I compared the various optical catalogues used to check whether the source positions were consistent with each other. The optical catalogues, as well as the catalogue of the Deep *XMM-Newton* Survey, are composed of individual observations of sub-fields of M 31. For each of the X-ray fields I compared this field in each of the optical catalogues to each other.[13]. In this way systematic offsets between different parts of the whole M 31 field would be found. A close examination of the shifts obtained, showed significant differences between the positions given in the individual catalogues. However no systematic offsets, related to different parts of the observed field were found. In summary, between the USNO-B1 and LGS catalogues I found an offset of $0\farcs197$ in R.A. and $0\farcs067$ in Dec[14], and between the USNO-B1 and 2MASS catalogues I found an offset of $0\farcs108$ in R.A. and $0\farcs204$ in Dec. I chose the USNO-B1 catalogue as a reference, since it covers the whole field observed in the Deep *XMM-Newton* survey, and in addition provides values of the proper motion of the optical sources.

The offsets found between the USNO-B1 and 2MASS catalogues can be explained by the independent determination of astrometry for each of the two catalogues. Given that the positions given in the LGS catalogue are corrected with respect to the USNO-B1 catalogue (see Massey et al. 2006), the offset found in right ascension was totally unexpected and cannot be explained.

#### 5.2.5.2 Corrections of the X-ray observations

From the positionally corrected catalogues, I selected sources which either correlate with globular clusters from the Revised Bologna Catalogue (V.3.4, January 2008; Galleti et al. 2004, 2005, 2006, 2007) or with foreground stars, characterised by their optical to X-ray flux ratio (Maccacaro et al. 1988) and their hardness ratio (see source selection criteria given in Table 7.3 and Stiele et al. 2008b). For sources selected from the USNO-B1 catalogue, I used the proper motion corrected positions. I then used the SAS-task eposcorr to derive the offset in the X-ray aspect solution. Four observations did not have enough optical counterparts to apply this method. The lack of counterparts is due to too short exposure times after screening for high background (obs. s3, ss12, ss13) and the location of the observation (obs. sn11). In these cases I used bright persistent X-ray sources which I correlated with another observation of the same field. I checked the remaining systematic uncertainty in the source positions and found it to be well characterised by the conservative $1\sigma$ value of $0\farcs5$. This uncertainty is due to the positional errors of the optical sources as well as the inaccuracy in the process of the determination of the offset between optical and X-ray sources, and is called a systematic positional error. The appropriate offset, given in Col. 6 of Table 5.1, was applied to the event file from each pointing, and images and exposure maps were then reproduced with the corrected astrometry.

[12]For the remainder of the subsection I will call all three catalogues "optical catalogues" for easier readability, although the 2MASS catalogue is an infrared catalogue.

[13]From the LGS catalogue only sources brighter than 21 mag were used in order to be comparable to the brightness limit of the USNO-B1 catalogue.

[14]the offset in declination is negligible

Fields that were observed two times or more are treated in a special way, which is described in the following section.

### 5.2.6 Multiple observed fields

The fields that were observed more than once were the central field, the fields pointing on RX J0042.6 +4115[15], two fields located on the major axis of M 31 (S2, N2) and all fields of the "Large Survey" located in the southern part of the galaxy (SS1, SS2, SS3, S3, SN3, SN2, SN1). To reach higher detection sensitivity I merged the images, background images and exposure maps, respectively, of observations which have the same pointing direction and were obtained with the same filter setting. After that, source detection, as described in Sect. 5.2.4, was repeated on the merged data. For the S2 field there are two observations with different filter settings. In this case source detection was performed simultaneously on all 15 bands of both observations, *i. e.* on 30 bands simultaneously. The N2 field was treated in the same way. For the central field images, background images and exposure maps of observations c1, c2 and c3 were merged. This merged data together with the data from observation c4 were used to search for sources simultaneously. In this way it was possible to take into account the different ECFs for the different filters. The same method was used for observations sn1 and sn11, which were of the same field, but with slightly different pointings.

### 5.2.7 Variability calculation

To examine the time variability of each source listed in the total source catalogue, I determined the XID flux at the source position in each observation or at least an upper limit for the XID flux. I used the task `emldetect` (v. 4.60), setting the parameter `xidfixed=true`, which forced `emldetect` to not alter the source positions when calculating the total flux. To get fluxes and upper limits for all sources in the input list I set the detection likelihood threshold to 0.

A starting list was created, which only contains the number and position of each source located in the examined field (see Chaps. 6 and 7). To give correct results, the task `emldetect` has to process the sources from the brightest one to the faintest one. I, therefore, had to first order the sources in each observation by the detection likelihood. For sources not visible in the observation in question I set the detection likelihood to 0. This list was used as input for a first `emldetect` run. In this way I achieved an output list in which a detection likelihood was allocated to every source. For a final examination of the sources in order of detection likelihood, a second `emldetect` run was necessary.

I only accepted XID fluxes that are at least three times larger than their $1\sigma$ errors. Otherwise the triplicated error was used as an upper limit. To compare the XID fluxes between the different observations, I calculated the significance of the difference,

$$S = \frac{F_{\max} - F_{\min}}{\sqrt{\sigma_{\max}^2 + \sigma_{\min}^2}} \tag{5.2}$$

and the ratio of the XID fluxes $V = F_{\max}/F_{\min}$, where $F_{\max}$ and $F_{\min}$ are the maximum and minimum (or upper limit) source XID flux, and $\sigma_{\max}$ and $\sigma_{\min}$ are the errors of the maximum and minimum flux, respectively. This calculation was not done in these cases where $F_{\max}$ was an upper limit. Finally, the largest XID flux of each source was derived, excluding upper limits.

### 5.2.8 Spectral investigations

To extract the X-ray spectrum of individual sources, I selected an extraction region and a corresponding background region, where the background region was at least as large as the source region, was located on

[15]The combination of observations b1, b3 and b4 is called b.

the same CCD, at a similar off axis angle as the source, and did not contain any point sources or extended emission. For EPIC PN I only accepted single events (PATTERN == 0) for the spectra of supersoft sources, while for all other spectra single and double events (PATTERN <= 4) were used. For the EPIC MOS detectors single through to quadruple events (PATTERN <= 12) were always used. Additionally, I only kept events with FLAG == 0, for all three detectors. For each extraction region, I produced the corresponding response matrix files and ancillary response files.

For each source the spectral fit was obtained by fitting all three EPIC spectra simultaneously, using the tool `Xspec`[16](v. 11.3.2). For the absorption I used the `TBabs` model, with abundances of Wilms et al. (2000) and the photoelectric absorption cross-sections of Bałucińska-Church & McCammon (1992) with a new He cross-section based on Yan et al. (1998).

### 5.2.9 Cross correlations

Sources are regarded as correlating if their positions overlap within their $3\sigma$ (99.73%) position errors, defined as (Watson et al. 2009):

$$\Delta\mathrm{pos} \leq 3.44 \times \sqrt{\sigma_{\mathrm{stat}}^2 + \sigma_{\mathrm{syst}}^2} + 3 \times \sigma_{\mathrm{ccat}} \tag{5.3}$$

where $\sigma_{\mathrm{stat}}$ is the statistical and $\sigma_{\mathrm{syst}}$ the systematic error of the X-ray sources detected in the present study. The statistical error is derived by `emldetect`. The determination of the systematic error is described in Sect. 5.2.5. I use a value of $0\farcs5$, for all sources. The positional error of the sources in the catalogue used for cross-correlation is given by $\sigma_{\mathrm{ccat}}$. The values of $\sigma_{\mathrm{ccat}}$ (68% error) used for the different X-ray catalogues can be found in Table 5.4. Exceptions to Eq. 5.3 are sources that are listed in more than one catalogue or that are resolved into multiple sources with *Chandra*. The first case is restricted to catalogues with comparable spatial resolution and hence positional uncertainty.

To identify the X-ray sources in the field of M 31 I searched for correlations with catalogues in other wavelength regimes. The *XMM-Newton* source catalogue was correlated with the following catalogues and public data bases:

**Globular Clusters:** Bologna Catalogue (V.3.5, March 2008; Galleti et al. 2004, 2005, 2006, 2007, $\sigma_{\mathrm{ccat}} = 0\farcs2$; RBV 3.5), Caldwell et al. (2009, $\sigma_{\mathrm{ccat}} = 0\farcs2$), Hodge et al. (2009, $\sigma_{\mathrm{ccat}} = 0\farcs5$), Krienke & Hodge (2008, $\sigma_{\mathrm{ccat}} = 0\farcs2$), Krienke & Hodge (2007, $\sigma_{\mathrm{ccat}} = 0\farcs2$), Fan et al. (2005), Magnier (1993, $\sigma_{\mathrm{ccat}} = 1''$)

**Novae:** Nova list of the M 31 Nova Monitoring Project[17] ($\sigma_{\mathrm{ccat}}$ is given for each individual source)

**Supernova Remnants:** Dodorico et al. (1980), Walterbos & Braun (1992) and Braun & Walterbos (1993), Magnier et al. (1995); An X-ray source is considered as correlating with an SNR if the X-ray source position (including $3\sigma$ error) lies within the extent given for the SNR.

**Radio Catalogues:** Gelfand et al. (2005, $\sigma_{\mathrm{ccat}}$ is given for each individual source), Gelfand et al. (2004, $\sigma_{\mathrm{ccat}}$ is given for each individual source), Kimball & Ivezić (2008, $\sigma_{\mathrm{ccat}} = 3''$), Braun (1990, $\sigma_{\mathrm{ccat}}$ is given for each individual source), NVSS (NRAO/VLA Sky Survey[18]; Condon et al. 1998, $\sigma_{\mathrm{ccat}}$ is given for each individual source)

**H II Regions, H $\alpha$ Catalogue:** Walterbos & Braun (1992, $\sigma_{\mathrm{ccat}}$ is given for each individual source), Massey et al. (2007, $\sigma_{\mathrm{ccat}} = 0\farcs2$)

[16] `http://heasarc.gsfc.gov/docs/xanadu/xspec`
[17] `http://www.mpe.mpg.de/~m31novae/opt/m31/M31_table.html`
[18] `http://www.cv.nrao.edu/nvss/NVSSlist.shtml`

**Optical Catalogues:** USNO-B1 (Monet et al. 2003, $\sigma_{\rm ccat}$ is given for each individual source), Local Group Survey (LGS; Massey et al. 2006, $\sigma_{\rm ccat} = 0\farcs2$)

**Infrared catalogues:** 2MASS (Skrutskie et al. 2006, $\sigma_{\rm ccat}$ is given for each individual source), Mould et al. (2008, $\sigma_{\rm ccat} = 0\farcs8$, for Table 2: $\sigma_{\rm ccat} = 0\farcs5$)

**Data bases:** the SIMBAD catalogue[19] (Centre de Données astronomiques de Strasbourg; hereafter SIMBAD) , the NASA Extragalactic Database[20] (hereafter NED)

[19] http://simbad.u-strasbg.fr/simbad
[20] http://nedwww.ipac.caltech.edu

**Table 5.4:** X-ray source catalogues used for cross-correlation and the used positional errors

| X-ray catalogue‡ | $\sigma^{\dagger}_{\rm ccat}$ | X-ray catalogue‡ | $\sigma^{\dagger}_{\rm ccat}$ |
|---|---|---|---|
| TF91 | $*$ | DKG2004 | $0\farcs3$ |
| PFJ93 | $*$ | TP2004 | $1''$ |
| SHP97 | $*$ | PFH2005 | $*$ |
| SHL2001 | $*$ | O2006 | $1''$ |
| OBT2001 | $3''$ | WNG2006 | $0\farcs3$ |
| D2002 | $0\farcs5$ | VG2007 | $0\farcs4$ |
| KGP2002 | $*$ | SPH2008 | $*$ |
| Ka2002 | $0\farcs3$ | SBK2009 | $3''^{+}$ |
| WGK2004 | $1''^{+}$ | | |

Notes:
$^{\dagger}$ : $*$ indicates that the catalogue provides $\sigma_{\rm ccat}$ values for each source individually
$^{+}$ : value taken from indicated paper
‡ : TF91: Trinchieri & Fabbiano (1991), PFJ93: Primini et al. (1993), SHP97: Supper et al. (1997), SHL2001: Supper et al. (2001), OBT2001: Osborne et al. (2001), D2002: Di Stefano et al. (2002), KGP2002: Kong et al. (2002b), Ka2002: Kaaret (2002), WGK2004: Williams et al. (2004a), DKG2004: Di Stefano et al. (2004), TP2004: Trudolyubov & Priedhorsky (2004), PFH2005: Pietsch et al. (2005b), O2006: Orio (2006), WNG2006: Williams et al. (2006b), VG2007: Voss & Gilfanov (2007), SPH2008: Stiele et al. (2008b), SBK2009: Shaw Greening et al. (2009)

# Chapter 6

# Time variability of X-ray sources in the M 31 centre field

The results presented in this chapter are published in Stiele et al. (2008b, hereafter SPH2008). Therefore this chapter is a copy of SPH2008, apart from the "Introduction" and "Observations and analysis" section therein, which have been expanded on and are presented in the first few chapters of this thesis.

## 6.1 Observations and analysis

The overall description of the observations and data analysis was given in Chap. 5.

For our analysis we used the archival *XMM-Newton* observations of the central region of M 31, obtained from June 2000 to January 2002 (from observations s1 and n1 only sources which lie in the intersection with at least one of the other observations are included). In addition, we analysed the July 2004 monitoring observations of the low mass X-ray binary RX J0042.6+4115 (PI Barnard), which are pointed $1\farcm1$ to the west of the M 31 nucleus position. Thus we have a time span of about four years for examining time variability. To achieve comparable images and results we adapted the same background screening as in PFH2005 for the newly added observations. This results in longer exposures compared to the ones given in Table 5.1. The exposures used in this chapter are given in Table 6.1. In addition the `epreject` task was not applied to the data.

We searched for sources in b, which were not visible in the X-ray wavelength regime about 2.5 years earlier. In addition we reexamined observations c1, c2, c3 and c4 individually, to search for sources not included in the PFH2005 catalogue, which – besides source 856 – was based on an analysis of the merged images of observations c1 to c4.

Two sources were added manually. Source 871 was first detected as nova WeCAPP-N2001-12 and in the POINT-AGAPE variable star catalogue (An et al. 2004). An et al. (2004) proposed the hard X-ray transient [OBT2001] 3 (Osborne et al. 2001) as a counterpart, which is source 287 in the PFH2005 catalogue. PFF2005 showed that several points speak against this identification and that a faint SSS close to the position of [PFH2005] 287, which was only visible during observation c4, is a more reliable counterpart. Source 885 (see Table 6.3) was clearly visible in observation b (see Fig. 6.2) and we could not find any reason, why `emldetect` did not automatically find it. As the source was already reported with *Chandra* (Kong et al. 2002b, r2-41), we took the *Chandra* position to derive the source parameters, using `emldetect` with fixed position.

Our source catalogue extension only contains sources not already found by PFH2005. These sources were ordered according to increasing right ascension for each observation individually. Finally we merged

**Table 6.1:** *XMM-Newton* log of archival observation of M 31's central field

| M 31 field | | EPIC PN | EPIC MOS 1 | EPIC MOS 2 |
|---|---|---|---|---|
| | | $T^{\dagger}_{\rm exp}$ | $T^{\dagger}_{\rm exp}$ | $T^{\dagger}_{\rm exp}$ |
| Centre 1 | (c1) | 26.40 | 29.92 | 29.91 |
| Centre 2 | (c2) | 9.81 | 12.24 | 12.24 |
| Centre 3 | (c3) | 27.65 | 27.65 | 27.65 |
| N1 | (n1) | 54.78 | 57.31 | 57.30 |
| Centre 4 | (c4) | 60.79 | 63.31 | 63.32 |
| S1 | (s1) | 53.45 | 53.76 | 53.73 |
| RX 1 | (b1)$^{\ddagger}$ | 18.30 | 19.40 | 19.40 |
| RX 2 | (b2) | 0.0 | 0.0 | 0.0 |
| RX 3 | (b3)$^{\ddagger}$ | 13.80 | 17.90 | 17.90 |
| RX 4 | (b4)$^{\ddagger}$ | 8.90 | 10.20 | 10.20 |

Notes:

$^{\dagger}$ : Exposure time in units of ks after screening for high background used for detection

$^{\ddagger}$ : Combination of the three observations is called b

the source lists and numbered the sources consecutively. If a source was detected in more than one observation, we took the source parameters from the first observation in which it was detected. As this catalogue is an extension of the source list of PFH2005, new sources start with number 857.

The data analysis was performed using tools in the *XMM-Newton* Science Analysis System (`SAS`) v6.6.0 and v7.0.0, EXSAS/MIDAS 03OCT_EXP, and FTOOLS v6.0.6 software packages, the imaging application DS9 v4.0b7 together with the funtools package, the mission count rate simulator WebPIMMS v3.6a and the spectral analysis software `Xspec` v11.3.1.

Figure 6.1 shows logarithmically scaled *XMM-Newton* EPIC low background images of the M 31 central observations integrated in $1'' \times 1''$ pixels, and combining data from the PN, MOS 1 and MOS 2 cameras in the (0.2–4.5) keV XID band. The data are smoothed with a 2D-Gaussian of FWHM $5''$, which corresponds to the point spread function in the centre of the field of view (FoV). Figure 6.2 shows a zoom-in of the crowded centre region.

To classify the source spectra we computed four hardness ratios from the source count rates. These hardness ratios and errors were derived from Eq. 2.10, using the five energy bands defined in Sect. 5.2.3. The identification and classification criteria are given in Table 6.2. The source catalogue extension is presented in Sect. 6.2 (see Table 6.3).

We generated a starting list for our variability analyses by merging the source catalogue extension (see Sect. 6.2) with the source catalogue of PFH2005.

## 6.2 Source catalogue

PFH2005 reported 265 sources in the central field of M 31. Our catalogue extension contains 39 sources. Four are detected in observation c1, eight in observation c3, thirteen in c4 and twenty one in b.

The source parameters are summarised in Table 6.3[1] (EPIC combined products and products for EPIC

[1]Table 6.3 is only available in electronic form either via the CDS (`http://vizier.cfa.harvard.edu/viz-bin/VizieR?-source=J/A+A/480/599`) or on the attached CD. A description of the content of this table can be found in Appendix C.

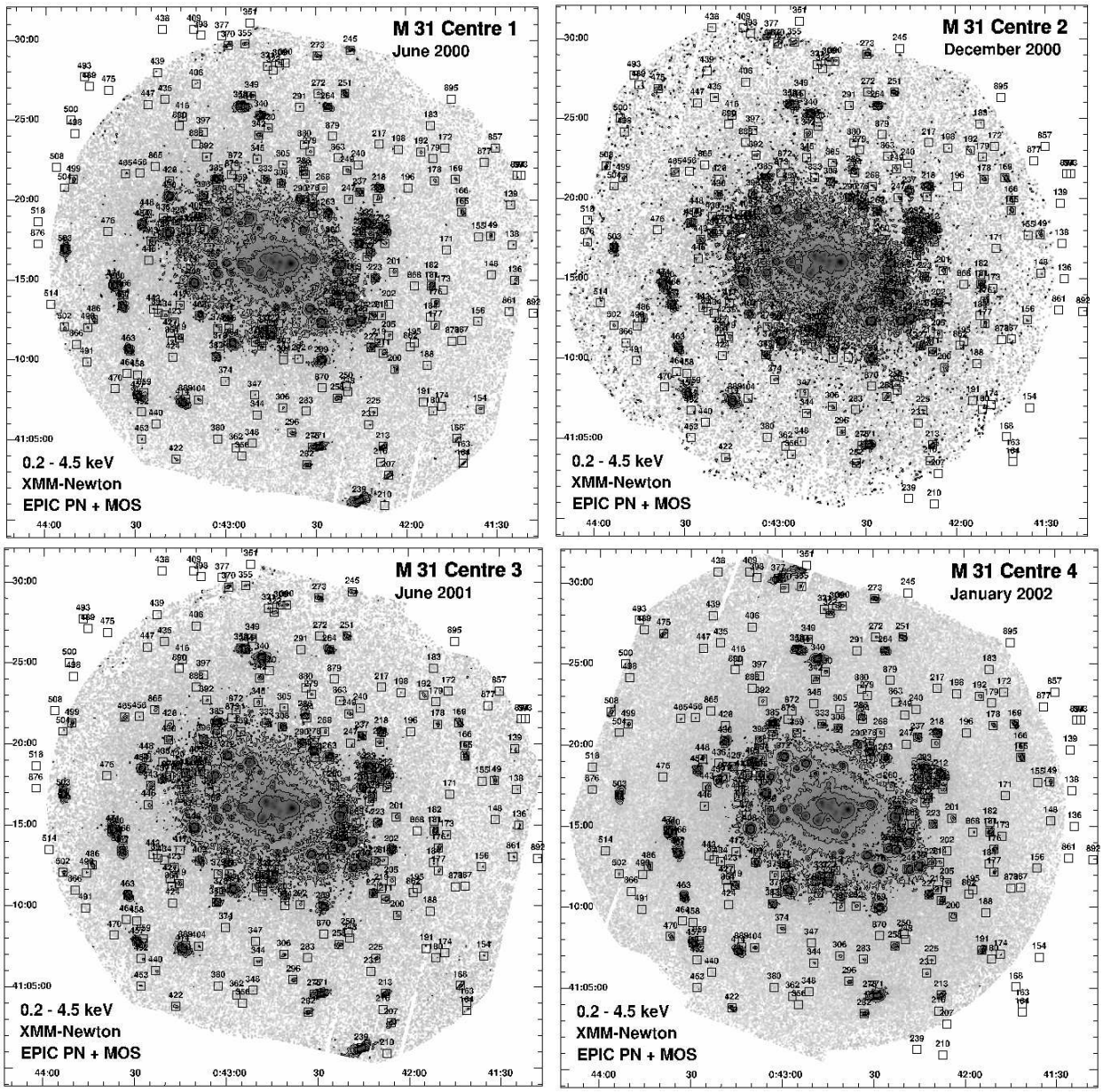


**Figure 6.1:** Logarithmically scaled *XMM-Newton* EPIC low background images integrated in $1'' \times 1''$ pixels of the M 31 central observations, combining PN and MOS 1 and MOS 2 cameras in the (0.2–4.5) keV XID band. The data are smoothed with a 2D-Gaussian of FWHM $5''$, which corresponds to the point spread function in the central area. The images are corrected for unvignetted exposures. Contours are at $(2, 4, 8, 16, 32) \times 10^{-6}$ ct s$^{-1}$ pix$^{-1}$ including a factor of two smoothing. Sources from the combined catalogue are marked in the outer area. The inner area is shown in detail in Fig. 6.2.

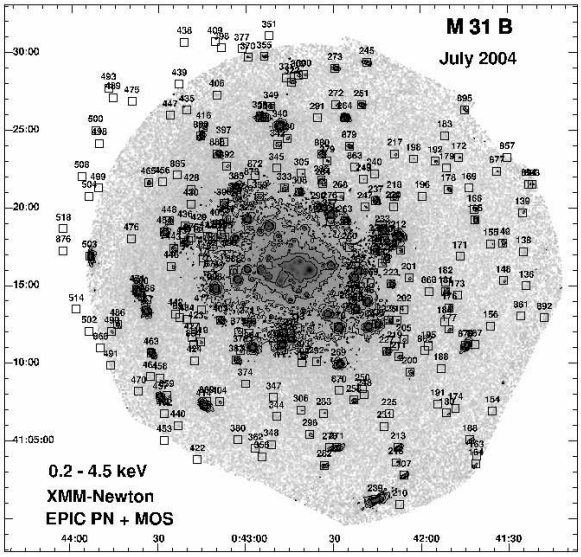


**Figure 6.1:** (continued) Logarithmically scaled *XMM-Newton* EPIC low background images integrated in $1'' \times 1''$ pixels of the M 31 central observations, combining PN and MOS 1 and MOS 2 cameras in the (0.2–4.5) keV XID band.

PN, MOS 1 and MOS 2, summarised separately).

With the exception of the newly added *XMM-Newton* source name (column 77, see below), Table 6.3 is structured in the same way as Table 2 from PFH2005. It gives the source number (Col. 1), detection field from which the source was entered into the catalogue extension (2), source position (3 to 9) with $1\sigma$ uncertainty radius (10), likelihood of existence (11), integrated PN, MOS 1 and MOS 2 count rate and error (12,13) and flux and error (14,15) in the (0.2–4.5) keV XID band, and hardness ratios and errors (16–23). Hardness ratios are calculated only for sources for which at least one of the two band count rates has a significance greater than $2\sigma$. Errors are the properly combined statistical errors in each band and can extend beyond the range of allowed values of hardness ratios as defined previously (–1.0 to 1.0). The EPIC instruments contributing to the source detection, are indicated by the three characters in the "Val" parameter (Col. 24, first character for PN, second MOS 1, third MOS 2), where "T" indicates if the source is inside the FoV, and "F", if it lies outside of the FoV. There are eight sources at the periphery of the FoV where only part of the EPIC instruments contribute to the source detection. The positional error (10) does not include intrinsic systematic errors, which amount to $0\farcs5$ (see PFH2005), and should be quadratically added to the statistical errors.

Table 6.3 then gives for EPIC PN, exposure (25), source existence likelihood (26), count rate and error (27, 28) and flux and error (29, 30) in the (0.2–4.5) keV XID band, and hardness ratios and errors (31–38). Columns 39 to 52 and 53 to 66 give the same information corresponding to Cols. 25 to 38, but for the EPIC MOS 1 and MOS 2 instruments. Hardness ratios for the individual instruments were again screened as described above. From the comparison of the hardness ratios derived from integrated PN, MOS 1 and MOS 2 count rates (Cols. 16–23) and the hardness ratios of the individual instruments (Cols. 31–38, 45–52 and 59–66), it is clear that combining the instrument count rate information yields significantly more hardness ratios above the chosen significance threshold.

Column 67 shows cross correlations with M 31 X-ray catalogues in the literature.

Our catalogue extension contains 23 until now unknown X-ray sources in M 31. The discussion of the

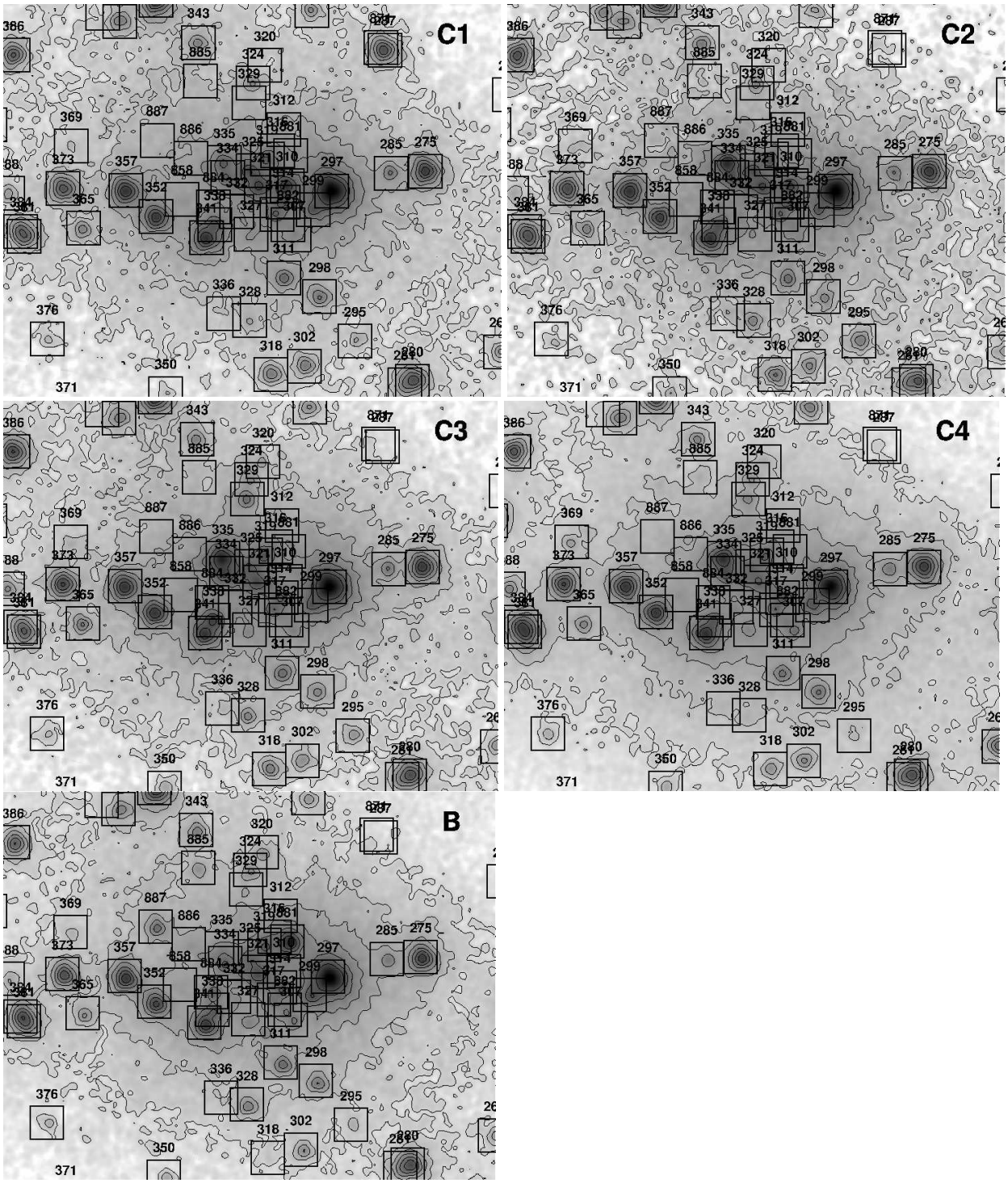


**Figure 6.2:** Inner area of M 31 enlarged from Fig. 6.1. Contours are at $(4, 8, 16, 32, 64, 128, 256)\times10^{-6}$ ct $s^{-1}$ $pix^{-1}$ including a factor of two smoothing. Sources from the combined catalogue are marked as $30''\times30''$ squares. The images are ordered as follows: Centre 1 (upper left), Centre 2 (upper right), Centre 3 (middle left), Centre 4 (middle right) and Centre B (lower left).

results of the cross correlation is in Sect. 6.4.

In the remaining columns of Table 6.3, we give cross correlation information with sources in other wavelength ranges.

To identify the X-ray sources in the M 31 field we searched for correlations with sources in other wavebands within $3\sigma$ of the total X-ray source position error in the SIMBAD and NED archives and within several catalogues. In columns 68 to 73 of Table 6.3, we give extraction information from the USNO-B1 catalogue (name, number of objects within search area, distance, B2, R2 and I magnitude of the brightest object). To improve the reliability of identifications we used the B and R magnitudes to calculate

$$\log\left(\frac{f_{\rm x}}{f_{\rm opt}}\right) = \log\left(f_{\rm x}\right) + \frac{m_{\rm B2} + m_{\rm R2}}{2 \times 2.5} + 5.37, \tag{6.1}$$

following Maccacaro et al. (1988, see Col. 74).

The X-ray sources in the catalogue extension are identified or classified based on properties in the X-ray band (HRs, variability), and of the correlated objects in other wavelength regimes (Table 6.3, Cols. 75, 76). For classified sources, the class name is given in angled brackets. Identification and classification criteria are summarised in Table 6.2. The criteria are discussed in detail in Sect. 6 of PFH2005. As we have no clear hardness ratio criteria to select XRBs, Crab-like supernova remnants (SNRs) or AGN we introduced a class <hard> for those sources. If such a source shows strong variability (*i. e.* V$\geq$ 10) on the examined time scales, it is likely to be an XRB. Fifteen sources are classified as <hard>. Five sources remain unidentified or without classification.

The last column (77) of Table 6.3 contains the *XMM-Newton* source name as registered to the IAU Registry. Source names consist of the acronym XMMM31 and the source position as follows: XMMM31 Jhhmmss.s+ddmmss, where the right ascension is given in hours (hh), minutes (mm) and seconds (ss.s) truncated to decimal seconds, and the declination is given in degrees (dd), arc minutes (mm) and arc seconds (ss) truncated to arc seconds, for equinox 2000.

Only two sources from our catalogue extension (869, 863) are found as extended sources (see Table 6.4 and Sect. 6.4).

**Table 6.2:** Summary of identifications and classifications.

| Source class† | Selection criteria | Identified | Classified |
|---|---|---|---|
| fg Star | $\log(\frac{f_{\rm x}}{f_{\rm opt}}) < -1.0$ and HR2$-$EHR2$<0.3$ and HR3$-$EHR3$<-0.4$ or not defined | | 1 |
| AGN | Radio source and not classification as SNR from HR2 or optical/radio | | |
| Gal | optical id with galaxy | | |
| GCl | X-ray extent and/or spectrum | | |
| SSS | HR1$< 0.0$, HR2$-$EHR2$<-0.99$ or HR2 not defined, HR3, HR4 not defined | | 3 |
| SNR | HR1$>-0.1$ and HR2$<-0.2$ and not a fg Star, or id with optical/radio SNR | 1 | 6 |
| GlC | optical id | | 1 |
| XRB | optical id or X-ray variability | 3 | 4 |
| hard | HR2$-$EHR2$>-0.2$ or only HR3 and/or HR4 defined, and no other classification | | 15 |

Notes:

† : fg Star: foreground star, AGN: active galactic nuclei, Gal: galaxy, GCl: galaxy cluster, SSS: supersoft source, SNR: supernova remnant, GlC: globular cluster, XRB: X-ray binary

**Table 6.4:** Extension properties of sources 863 and 869

| Source | Extent arcsec* | Ext. err.† arcsec* | MELH‡ |
|---|---|---|---|
| 863 | 6.71 | 2.14 | 4.70 |
| 869 | 6.39 | 1.12 | 5.05 |

Notes:
† : Extent error
‡ : Maximum extent likelihood
* : 1″corresponds to 3.8 pc at the assumed distance of M 31

## 6.3 Variability

Table 6.5[2] contains all information necessary to examine time variability. The sources are taken from the combined catalogue (*i. e.* PFH2005 and Sect. 6.2). Sources are only included in the table, if they are in the FoV for at least two observations. Column 1 gives the source number. Columns 2 and 3 contain the flux and error in the (0.2–4.5) keV XID band. The hardness ratios and errors are given in columns 4 to 11. Column 12 shows cross correlations with M 31 X-ray catalogues in the literature. The next two columns contain the class of the source (13) and cross correlation information with sources in other wavelength ranges (14). The EPIC instruments contributing to the source detection in the c1 observation, are indicated by three characters in the "c1_val" parameter (Col. 15, first character for PN, second MOS 1, third MOS 2) each one either a "T" if the source is inside the FoV, or "F" if it is outside the FoV. Then the count rate and error (16,17) and flux and error (18,19) in the (0.2–4.5) keV XID band, and hardness ratios and error (20–27) of the c1 observation are given. Corresponding information is given for observation c2 (cols. 28–40), c3 (41–53), n1 (54–66), c4 (67–79), s1 (80–92) and b (93–105).

Column 106 indicates the number of observations in which the source is covered in the combined EPIC FoV. The maxima of the significance of variation and flux ratio (fvar_max) are given in columns 107 and 108. As described in Sect. 5.2.7 we only used detections with a significance greater $3\sigma$. Otherwise the $3\sigma$ upper limit was used. Column 109 indicates the number of observations where we could only gain an upper limit. The maximum flux (fmax) and its error are given in columns 110 and 111. In a few cases we could not derive the maximum flux, because every observation only gave an upper limit. This can have two reasons. The first reason is that PFH2005 merged observations c1 to c4 for source detection. Hence a faint source may not be detectable at the $3\sigma$ limit in the individual observations. The second reason is, that in cases where the significance of detection is not much above the $3\sigma$ limit, it can become smaller than the $3\sigma$ limit when the source position is fixed. The source name, according to the IAU naming convention (see Sect. 6.2), can be found in column 112.

In Fig. 6.3 we plotted the variability factor (Col. fvar_max) of each source as function of its maximum flux (Col. fmax) in the XID band. Identified sources are marked with big symbols, whereas classified sources are indicated by small symbols. Source numbers from PFH2005 and Sect. 6.2 are indicated for sources with flux variability above 5 or maximum XID flux above $8\times10^{-13}$ erg cm$^{-2}$ s$^{-1}$. In this region only, can variability help distinguish between foreground stars or SNRs, or to decide if a source classified

[2]Table 6.5 is only available in electronic form either via the CDS (`http://vizier.cfa.harvard.edu/viz-bin/VizieR?-source=J/A+A/480/599`) or on the attached CD. A description of the content of this table can be found in Appendix C.

as hard is an AGN or an XRB. Sources with a statistical significance on the variability below 3 are marked in green.

Figure 6.3 clearly shows that most of the variable sources are XRBs or XRBs in GlCs or candidates of these source classes. In addition there are a few SSS candidates, and even some SNR candidates showing pronounced temporal variability. These SNR candidates are discussed in Sect. 6.4, as they should not show time variability. The sources classified or identified as AGN or foreground stars all show $F_{\rm var} < 4$, except for the new foreground star candidate [PFH2005] 295, which is discussed later.

We found 149 sources with a significance for variability $> 3.0$ out of the 300 examined sources. There is a bias towards bright variable sources, because for bright sources it is much easier to detect variability

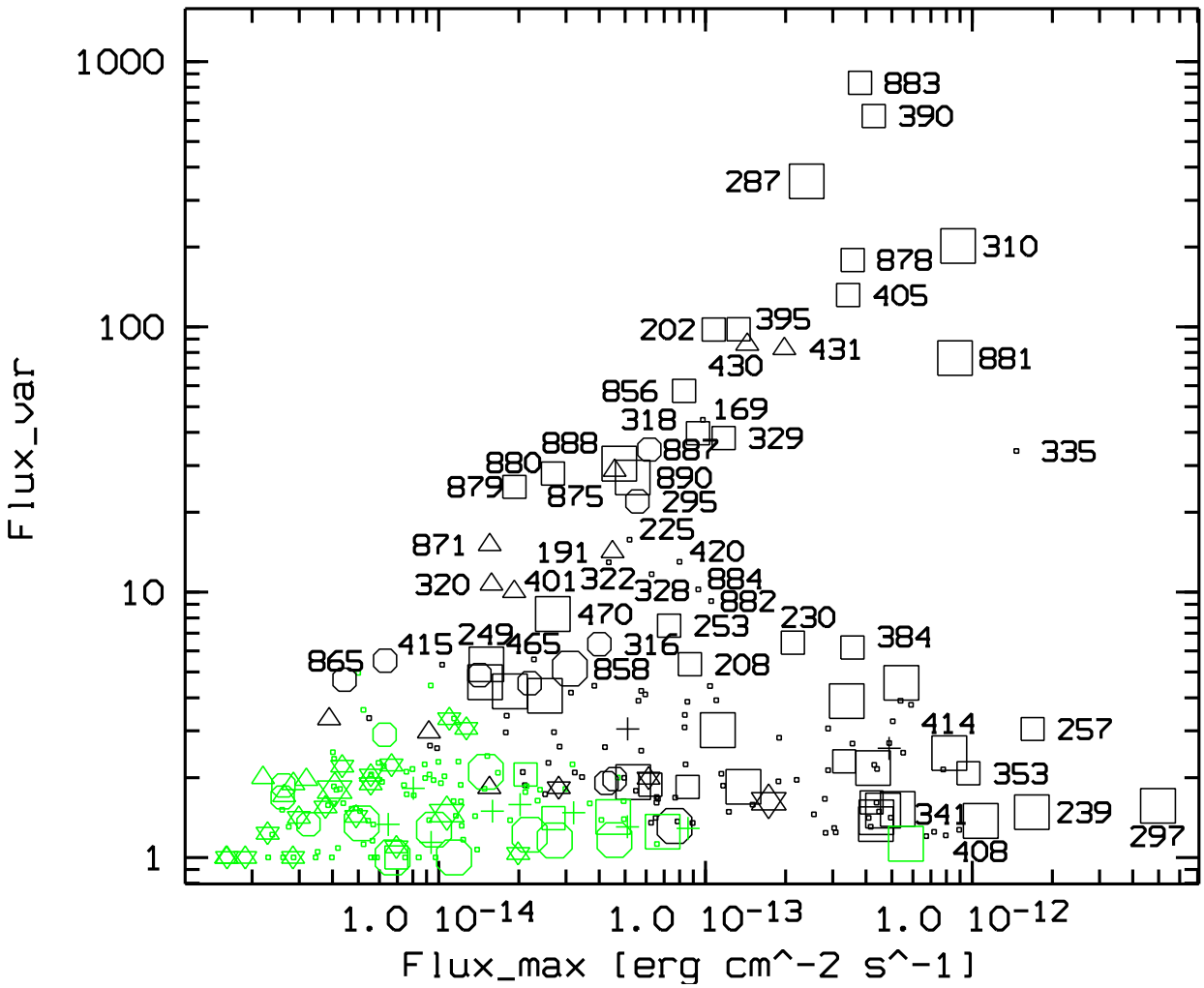


**Figure 6.3:** Variability factor of M 31 central sources from PFH2005 and Sect. 6.2 in the 0.2–4.5 keV band derived from average fluxes of the *XMM-Newton* EPIC observations from June 2000 to July 2004 plotted versus maximum detected XID flux (erg cm$^{-2}$ s$^{-1}$). Source classification from PFH2005 is indicated: Foreground stars and candidates are marked as big and small stars, AGN candidates as small crosses, SSS candidates as triangles, SNRs and candidates as big and small hexagons, GlCs and XRBs as big squares, and their candidates as small squares. Sources with a statistical significance for the variability below 3 are marked in green. Source numbers from PFH2005 and Sect. 6.2 are indicated for sources with flux variability above 5 or maximum XID flux above $8\times10^{-13}$ erg cm$^{-2}$ s$^{-1}$.

**Table 6.6:** Variable sources with flux variability larger than 5, ordered by variability.

| Source | Name XMMM31 J | fvar | svar | fmax‡ | class+ | Comment† |
|---|---|---|---|---|---|---|
| (1) | (2) | (3) | (4) | (5) | (6) | (7) |
| 883 | 004247.8+411113 | 831.10 | 54.75 | 38.02 | <GlC> | 1(r), 2(t, 92.2), 12, 17 |
| 390 | 004305.7+411703 | 624.05 | 79.83 | 42.71 | <XRB> | 1(t), 2(t, 954.2), 3(t, 2163), 20, 21(t), 23 |
| 287 | 004234.3+411810 | 353.67 | 43.26 | 23.95 | XRB | 1(t), 2(t, 370.5), 15(t, BH-XRN), 21(t), 22(v,t) |
| 310 | 004242.1+411608 | 201.71 | 62.44 | 88.47 | XRB | 1(t), 2(t, 468.8), 3(t, 285), 15(v,t, BH-XRT), 19(t), 22(v,t) |
| 878 | 004144.7+411111 | 178.79 | 40.20 | 35.61 | <XRB> | 1(t,sv), 4(t) |
| 405 | 004309.8+411900 | 131.73 | 57.22 | 34.25 | <XRB> | 1(sv, <AGN>), 2(t, 96.3), 3(t, 107), 10, 12(v), 13, 14(v), 20, 22(v,t) |
| 202 | 004205.8+411329 | 97.89 | 22.41 | 13.32 | <XRB> | 1(r), 2(t, 20.8), 3(t, 93), 12, 15(t), 21(t) |
| 395 | 004307.1+411810 | 97.65 | 25.27 | 10.75 | <XRB> | 1(t), 2(t, 46.1), 3(t, 155), 20, 21(t), 24 |
| 430 | 004318.8+412017 | 85.93 | 40.54 | 14.35 | <SSS> | 1(r), 2, 3(t, 96), 10, 13, 14(v), 15(v), 20(v), 22(v) |
| 431 | 004319.5+411756 | 82.68 | 40.17 | 19.76 | <SSS> | 1(t), 3(t, 694), 15(v,t), 21(t) |
| 881 | 004241.8+411635 | 76.27 | 79.68 | 86.17 | XRB | 1(t,r,sv), 4(t), 6(t, LMXB), 10, 22(v) |
| 856 | 004256.7+411843 | 57.41 | 12.69 | 8.32 | <XRB> | 2(t, 79.0), 3(t, 260), 15(t), 19, 21(t), 22(v,t) |
| 169 | 004143.4+412118 | 44.67 | 20.22 | 9.77 | <XRB> | former class: <hard>; 1, 14, 24 |
| 887 | 004252.4+411649 | 39.69 | 20.28 | 9.39 | <XRB> | 2(t, 64.6) |
| 329 | 004245.1+411723 | 38.07 | 24.24 | 11.71 | <XRB> | 1(r,sv), 2(t, 99.5), 3(t, 158), 22(v,t) |
| 318 | 004243.3+411319 | 34.47 | 21.30 | 6.17 | | former class: <SNR>; 2(t), 20, 22, 24 |
| 335 | 004247.1+411629 | 34.02 | 84.69 | 146.44 | <XRB> | former class: <hard>; 1(sv), 2, 10, 12, 13, 14, 20, 22(v) |
| 888 | 004309.9+412332 | 30.50 | 18.26 | 4.75 | XRB | 1(t), 2(t), 4(t), 7(t, LMXB) |
| 875 | 004318.7+411804 | 28.78 | 10.70 | 4.57 | <SSS> | |
| 880 | 004233.9+412331 | 28.02 | 10.39 | 2.68 | <XRB> | 2(t, 65.2) |
| 890 | 004315.4+412440 | 27.06 | 20.07 | 5.34 | XRB | 1(t), 4(t) |
| 879 | 004224.5+412401 | 24.95 | 9.75 | 1.92 | <XRB> | 2 |
| 295 | 004236.7+411349 | 21.97 | 11.77 | 5.56 | <fgStar> | former class: <SNR>; 2, 13, 14, 20, 22, 24 |
| 225 | 004210.9+410647 | 15.76 | 8.30 | 5.20 | <XRB> | former class: <hard>; 2, 22(v) |
| 871 | 004234.6+411812 | 15.09 | 3.67 | 1.55 | <SSS> | 18 |
| 191 | 004154.3+410724 | 14.18 | 14.03 | 4.48 | <SSS> | 1(t) |
| 420 | 004316.0+411842 | 13.01 | 17.55 | 7.99 | <XRB> | former class: <hard>; 1, 2, 13, 20, 22(v) |
| 322 | 004244.2+412809 | 12.96 | 11.83 | 4.34 | <XRB> | former class: <hard>; 1, 2, 13, 14 |
| 328 | 004245.0+411407 | 11.69 | 19.22 | 6.29 | <XRB> | former class: <hard>; 1, 2, 12 ,13, 20, 22 |
| 320 | 004243.8+411756 | 10.70 | 13.89 | 1.58 | <SSS> | 3(t, 51), 20 , 24 |
| 884 | 004247.9+411549 | 10.24 | 25.85 | 9.41 | | 2, 20, 22, 24 |
| 401 | 004308.5+411820 | 10.05 | 12.08 | 1.92 | <SSS> | 3(t, 38) |
| 882 | 004242.0+411533 | 9.26 | 14.38 | 10.50 | | 2, 20, 22(v) |
| 470 | 004336.6+410812 | 8.27 | 8.54 | 2.68 | GlC | 5 |
| 253 | 004221.6+411418 | 7.48 | 17.56 | 7.31 | <GlC> | 1(sv,burst), 2, 8, 20 , 22(v) |
| 230 | 004212.1+411757 | 6.45 | 27.71 | 21.25 | <GlC> | 1(sv), 2, 5, 12, 15(v),16, 20, 22(v) |
| 316 | 004242.8+411639 | 6.37 | 8.01 | 4.00 | | former class: <SNR>; 10, 12(v), 20, 22(v) |
| 384 | 004303.3+411527 | 6.19 | 37.24 | 35.54 | <XRB> | 1(sv), 2(t, 58.6), 3(t, 33), 5, 10, 12(v), 13, 14, 20, 22(v,t) |
| 465 | 004333.4+412140 | 5.58 | 5.13 | 2.28 | <hard> | 2 |
| 865 | 004323.4+412208 | 5.52 | 3.57 | 0.63 | <SNR> | |
| 208 | 004207.0+410017 | 5.35 | 5.10 | 8.75 | <GlC> | 5, 13, 14, 16, 21 |
| 249 | 004219.6+412153 | 5.35 | 10.47 | 1.51 | GlC | 2, 5, 16, 22 |
| 415 | 004314.5+411649 | 5.33 | 5.21 | 1.03 | | 2, 22, 24 |
| 858 | 004250.4+411556 | 5.14 | 9.69 | 3.10 | SNR | 2, 9, 22, 24 |

Notes:
‡ : maximum XID flux in units of $1\times10^{-14}$ erg cm$^{-2}$ s$^{-1}$ or maximum (absorbed 0.2–4.5 keV) luminosity in units of $7.3\times10^{35}$ erg s$^{-1}$
+ : class according to Table 6.2, partly changed as mentioned in the comment column
† : 1: Trudolyubov et al. (2006b), 2: Voss & Gilfanov (2007), 3: Williams et al. (2006b), 4: Trudolyubov et al. (2006a), 5: Trudolyubov & Priedhorsky (2004), 6: Williams et al. (2006a), 7: Williams et al. (2005b), 8: Pietsch & Haberl (2005), 9: Kong et al. (2003b), 10: Trinchieri & Fabbiano (1991), 11: Collura et al. (1990), 12: Primini et al. (1993), 13: Supper et al. (1997), 14: Supper et al. (2001), 15: Osborne et al. (2001), 16: Di Stefano et al. (2002), 17: Fan et al. (2005), 18: Pietsch et al. (2007), 19: Garcia et al. (2000), 20: Kaaret (2002), 21: Williams et al. (2004a), 22: Kong et al. (2002b), 23: Williams et al. (2005a), 24: Di Stefano et al. (2004), 25: Barnard et al. (2003b); t: transient, v: variable, sv: spectrally variable, r: recurrent, d: dipping, z: Z-source candidate; BH: black hole, XRN: X-ray nova, XRT: X-ray transient, LMXB: low mass X-ray binary, NS: neutron star; numbers indicate the variability given by the corresponding paper

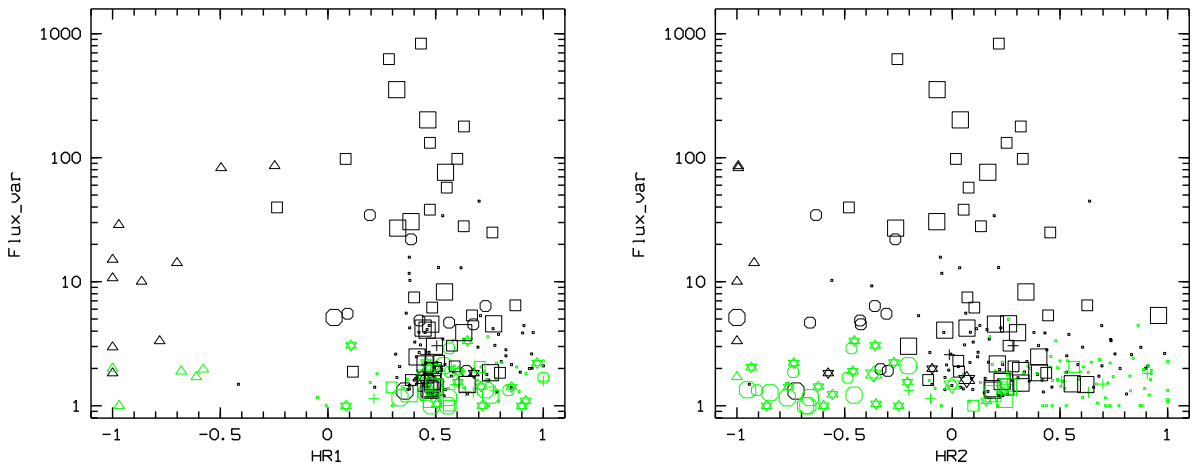


**Figure 6.4:** Variability factor of M 31 central sources from PFH2005 and Sect. 6.2 in the 0.2–4.5 keV band comparing average fluxes of the *XMM-Newton* EPIC observations from June 2000 to July 2004 plotted versus HR1 in the left panel and HR2 in the right panel. For source classification see Fig. 6.3. Sources with a statistical significance on the variability below 3 are marked in green.

**Table 6.7:** Sources with maximum XID flux larger than $8\times10^{-13}$ erg cm$^{-2}$ s$^{-1}$, a statistical significance of variability larger than 10 and a flux variability smaller than 5, ordered by flux.

| Source | Name | fvar | svar | fmax‡ | class+ | Comment† |
|---|---|---|---|---|---|---|
| | XMMM31 J | | | | | |
| (1) | (2) | (3) | (4) | (5) | (6) | (7) |
| 297 | 004238.5+411603 | 1.56 | 47.20 | 49.71 | XRB | 1(sv,z), 2, 10(v), 12(v), 13, 14, 20, 22(v), 25(LMXB) |
| 257 | 004223.0+411534 | 3.05 | 51.35 | 16.84 | <XRB> | 1(sv), 2, 10(v), 12(v), 13, 14, 20(v), 22(v) |
| 239 | 004215.7+410115 | 1.48 | 10.70 | 16.73 | GlC | 10, 11(v), 12, 13, 14(v), 16, 20, 21(v) |
| 408 | 004310.6+411451 | 1.37 | 12.81 | 10.77 | GlC | 1(sv), 2, 5, 10, 12, 13, 14, 16, 20, 22(v) |
| 353 | 004252.5+411854 | 2.07 | 29.97 | 9.68 | <XRB> | 1(sv), 2, 10, 12, 13, 14, 20(v, NS-LMXB), 22(v) |
| 341 | 004248.5+411522 | 1.27 | 10.99 | 8.94 | <hard> | 1(sv), 2, 10, 12, 13, 14, 20, 22(v,sv) |
| 414 | 004314.3+410722 | 2.47 | 26.89 | 8.21 | GlC | 1(d,sv), 2(t, 53.4), 5, 10, 12, 13, 14, 16, 20, 22 |

Notes:

‡ : maximum XID flux in units of $1\times10^{-13}$ erg cm$^{-2}$ s$^{-1}$ or maximum (absorbed 0.2–4.5 keV) luminosity in units of $7.3\times10^{36}$ erg s$^{-1}$

+ : class according to Table 6.2

† : for comment column see Table 6.6

than for faint sources.

Table 6.6 lists all sources with a variability factor larger than five in descending order. The source number (Col. 1), source name (2), maximum flux variability (3) and maximum significance parameter (4) are given in the same way as in Table 6.5 (Cols. 1, 152, 148 and 147). The next column (5) indicates the class of the source. If $F_{\rm var} \geq 10$, sources formerly classified as <hard> are now classified as <XRB>. Time variability can also be helpful to distinguish between foreground star candidates and SNR candidates. In some cases we had to change the source class with respect to PFH2005. This is indicated in the comment column (6). Column 6 also contains references to the individual sources in the literature. In some cases the reference provides information on the temporal behaviour and a more precise classification (see brackets). The numbers given in connection with Voss & Gilfanov (2007) and Williams et al. (2006b) are the *Chandra* derived variability factors obtained in these papers. From the 44 sources listed in Table 6.6, six show a flux variability larger than 100. With a flux variability factor $>830$ source 883 is the most variable source in our sample. Source 335 has the largest significance of variability, with a value of $\approx$85. In only ten sources was the significance of the variability below 10, for two it was below 5. Twenty-eight sources are XRBs or XRB candidates and seven are SSS candidates.

Table 6.7 lists all "bright" sources with maximum XID flux larger than $8\times10^{-13}$ erg cm$^{-2}$ s$^{-1}$ and a flux variability smaller than five, giving the same information as in Table 6.6. All seven sources listed in Table 6.7 have a significance of variability $> 10$. Apart from source 341, they are XRBs (three in globular clusters) or XRB candidates. The most luminous source in our sample is source 297 with an absorbed 0.2–4.5 keV luminosity of $\approx 3.6\times10^{38}$ erg s$^{-1}$.

Figure 6.4 shows the relationship between the variability factor and the hardness ratios HR1 and HR2. We used the hardness ratios of the observation from which the source entered the catalogue of variable sources. The HR1 plot shows that the sample of highly variable sources includes SSS and XRB candidates, which occupy two distinct regions in this plot (see also Haberl & Pietsch 1999b, for the LMC). The SSSs marked by triangles, appear on the left hand side, while the XRBs or XRB candidates have much harder spectra, in agreement with their classification. In the HR2 plot the highly variable XRBs and XRB candidates are separated from the bulk of the less variable sources by sources classified as <hard>, with the exception of the two sources with $F_{\rm var} > 10$ and classified as <SNR>. Due to the distinct temporal variability of these sources and the strong absorption in the central region of M 31, it is very unlikely that they are AGN. So only <fg star> or <XRB> are left as possible classifications. In accordance with the hardness ratios, we propose sources 169, 225, 322, 328, 335 and 420 to be XRB candidates.

Individual sources are discussed in the next section.

## 6.4 Discussion

In each of the following subsections, we discuss the sources described in the catalogue extension (Sect. 6.2). In addition we reclassify some sources from PFH2005 based on the results from our time variability study and on recent papers in the literature.

We classified the sources described in the catalogue extension into different classes of X-ray emitting objects: foreground stars (fg Star), galaxies (Gal), AGN, supersoft sources (SSS), supernova remnants (SNR) and X-ray binaries (XRB), using the X-ray properties together with information from catalogues at other wavelengths. The selection criteria for these classes are given in Table 6.2. Additionally, we use the time variability to classify sources. In the field of M 31, it is mainly XRBs or SSSs that can show very strong variability ($F_{\rm var} \geq 10$) on time scales of years. In only a few cases were we able to identify an X-ray source with a source already classified from optical, infrared or radio data. We have no well-defined hardness ratio criteria to differentiate between <hard> sources (XRBs, Crab-like SNRs or AGN). Fifteen sources from the catalogue extension are classified as <hard> (see Table 6.2). Three of them were found with *Chandra*

(Kong et al. 2002b; Voss & Gilfanov 2007). Five sources remain unidentified or without classification. Two of the five are already known from *Chandra* observations (see Table 6.6). Kong et al. (2002b) classified source 884 as an SSS.

### 6.4.1 Foreground stars

Foreground stars are a class of X-ray sources which are homogeneously distributed over the field of M 31. The good positioning of *XMM-Newton* and the available catalogues USNO-B1 and 2MASS allow us to effectively select this type of source. We found one foreground star candidate (877) in our source catalogue extension. From the optical colours in the USNO-B1 catalogue we estimate the type to be A3 III or A5 III, based on the stellar spectral flux library from Pickles (1998). Another possible foreground star candidate (859) is a USNO-B1 and 2MASS source. From the USNO-B1 magnitudes we derived $f_{\rm x}/f_{\rm opt} \approx -0.87$ and $f_{\rm x}/f_{\rm opt,R} \approx -1.27$, where $f_{\rm opt,R}$ is the flux in the R-band. The $f_{\rm x}/f_{\rm opt}$ value is too large to satisfy our foreground star selection criterion. However, it is possible for very red foreground stars to have such a large $f_{\rm x}/f_{\rm opt}$ value, in which case $f_{\rm x}/f_{\rm opt,R}$ must be $< -1$. Therefore, the source could be a foreground star, in agreement with the values we found for source 295 (see below). However Kim et al. (2007b) presented this optical source as a possible globular cluster. This classification would also be in agreement with our hardness ratios, $f_{\rm x}/f_{\rm opt}$ values, and USNO-B1 magnitudes (see Fan et al. 2005). We therefore cannot distinguish between a foreground star or an XRB, and we thus classify source 859 as <hard>.

PFH2005 classified source 295 as an SNR. This classification has to be rejected due to the distinct time variability we found. We created light curves in the 0.2–2.0 keV range for the different observations. In some observations, especially in c3 (see Fig. 6.5) and in c4, the source showed strong flares. The observation c2 consisted of the decaying wing of a strong flare, while the source remained rather quiet in b. In addition we carefully checked the 2MASS and Local Group (LG) survey R-band images (Massey et al. 2006) and we found a faint point-like source, at the X-ray position in both images. Equation (6.1) gives $f_{\rm x}/f_{\rm opt} \approx -0.66$ and $f_{\rm x}/f_{\rm opt,R} \approx -1.28$ using brightnesses given in the LG survey photometric catalogue. The $f_{\rm x}/f_{\rm opt}$ values derived from the catalogue by Haiman et al. (1994, $f_{\rm x}/f_{\rm opt} \approx -0.60$ and $f_{\rm x}/f_{\rm opt,R} \approx -1.44$) are in good agreement with the values derived form the LG Survey and are reasonable for a red star. Considering all those points, we classify this source as a foreground star.

### 6.4.2 Supersoft sources

Our catalogue extension contains three SSSs. Two of them (871, 886) correlate with optical novae and have been investigated in more detail in PFF2005 and PHS2007.

The third one (875) lies near source [PFH2005] 431 (distance $\approx 12''$). As source 431 is brightest in observation c1 and source 875 is detected in observation c4, we can exclude the possibility that they are the same source. From the time variability and the positional errors it would be possible that source 875 corresponds to the nova M31N1923-12b (= [H29] N28; distance $\approx 7''$), which was reported in the optical wavelength regime by Hubble (1929, see also Nova list of PHS2007). However supersoft X-ray emission from novae up to now has only been observed up to ten years after the optical outburst (see *e. g.* PHS2007). So if source 875 really coincides with M31N1923-12b, the X-ray emission we found would have to be connected with an unreported optical outburst that occurred during the last ten years, making the source a recurrent nova. Another possibility is that source 875 corresponds to yet another nova, not reported in the optical. But we cannot exclude that source 875 is not a nova at all.

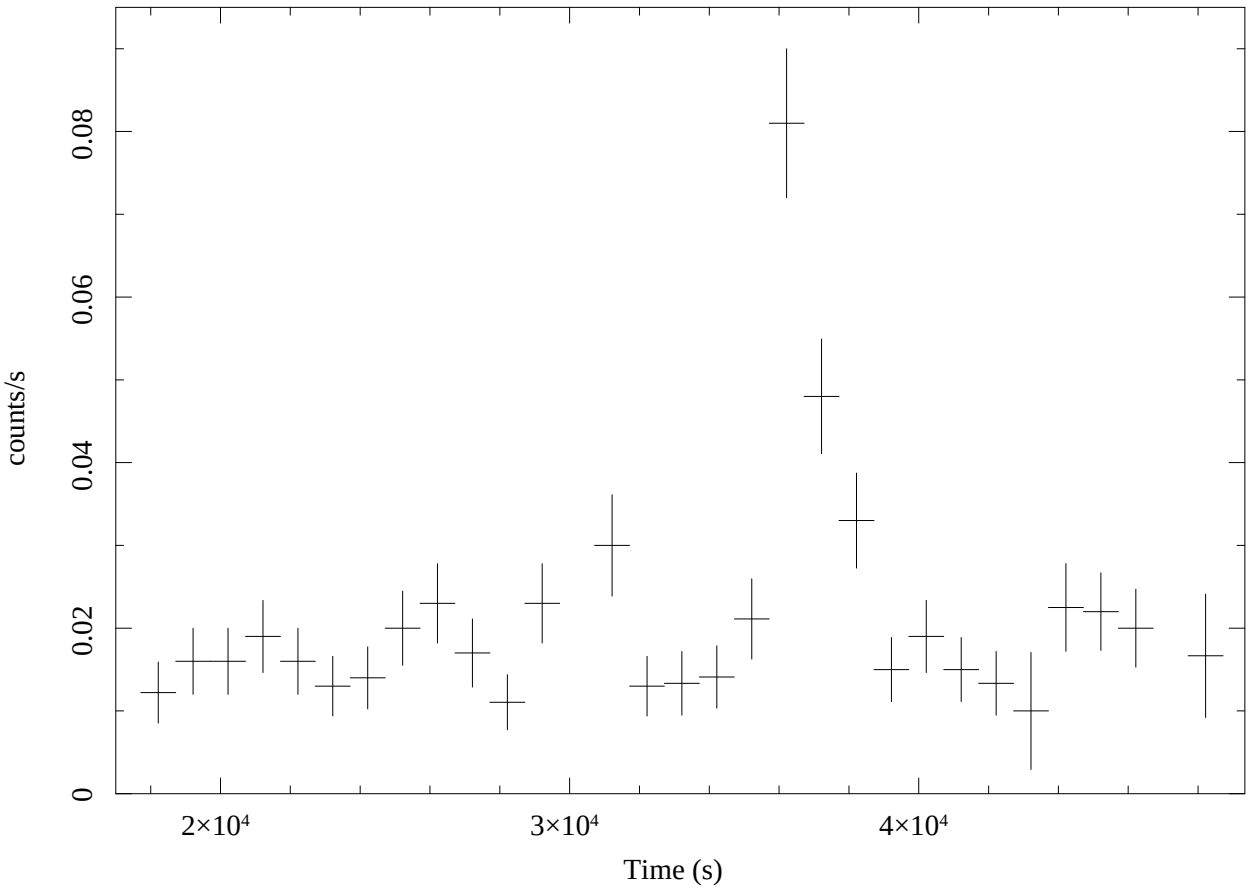


**Figure 6.5:** Summed EPIC PN, MOS 1 and MOS 2 0.2–2.0 keV light curve of source 295 in the c3 observation binned with 1000 s and without background subtraction. The zero time corresponds to 2001-06-29 07:53:36 (UTC).

### 6.4.3 Supernova remnants

SNRs can be separated into sources where thermal components dominate the X-ray spectrum below 2 keV, and so-called "plerions" with power-law spectra. The former are located in areas of the X-ray colour/colour diagrams which only overlap with foreground stars. If we assume that we have identified all foreground star candidates from optical correlations and the inspection of the optical images, the remaining sources can be classified as SNR candidates using the criteria given in Table 6.2.

We thus identified six SNR candidates in our catalogue extension. One of them (885) had been previously observed with *Chandra* (Kong et al. 2002b; Kaaret 2002), but was not classified. A second source (858) coincides with a source reported as a ring-like extended object from *Chandra* observations, and was also detected in the optical and radio wavelength regimes and thus identified as an SNR (Kong et al. 2003b).

Two sources from our catalogue extension, which are classified as SNRs are listed in Table 6.6. Source 858 lies next to source 875, the latter of which was first detected in observation b. Therefore the flux from source 858 is underestimated in b and the source appears variable. There is thus no need to change the class of this source. For source 865 we can only gain upper limits on the flux, apart from in observation c3 ($L_{\mathrm{X,\,abs}} \approx 4.6 \times 10^{35}$ erg s$^{-1}$; 0.2–4.5 keV), which leads to a significance of variability of only 3.57, not much above the $3\sigma$ limit. So the source can still be classified as an SNR candidate, despite the alleged time variability.

We now discuss the SNR candidates in PFH2005, that show time variability:

Source 318 shows significant variability. We therefore have to reject the classification given in PFH2005 of <SNR>. Fig. 6.6 shows that in observation b the source is about a factor of 10 to 35 less luminous than in the other observations. We checked carefully whether the source lies at the rim of a CCD or on a CCD gap. Neither is the case. In the following we discuss possible source classifications: the hardness ratios are in agreement with our foreground star criterion, however, the duration of the outburst of about two years seems much too long for a stellar flare (Fig. 6.6). Since we also did not find an optical counterpart in the images of the LG survey (Massey et al. 2006), we can exclude a foreground star identification. The behaviour on long-term time scales suggests an X-ray nova as a possible source classification (Haberl & Pietsch 1999b; Tanaka & Shibazaki 1996; Chen et al. 1997). We used the data from observation c2, in which the source is most luminous, to produce an EPIC PN spectrum. A disc blackbody model fitted to the spectrum gives a temperature at the inner edge of the accretion disc of ≈190 eV, which seems too small for an X-ray Nova or LMXB. We also fitted a blackbody spectrum. The temperature of ≈160 eV is too high for an SSS, but would be in agreement with a QSS (Orio 2006; Fabbiano 2006). A power-law fit gives a photon index of ≈4.7. Photon indices of XRBs and AGN are much smaller than this value. The nature of this source therefore remains unclear.

For source 316 the variability factor we found is based on observation b (without b: $F_{\rm var} = 3.07$ and

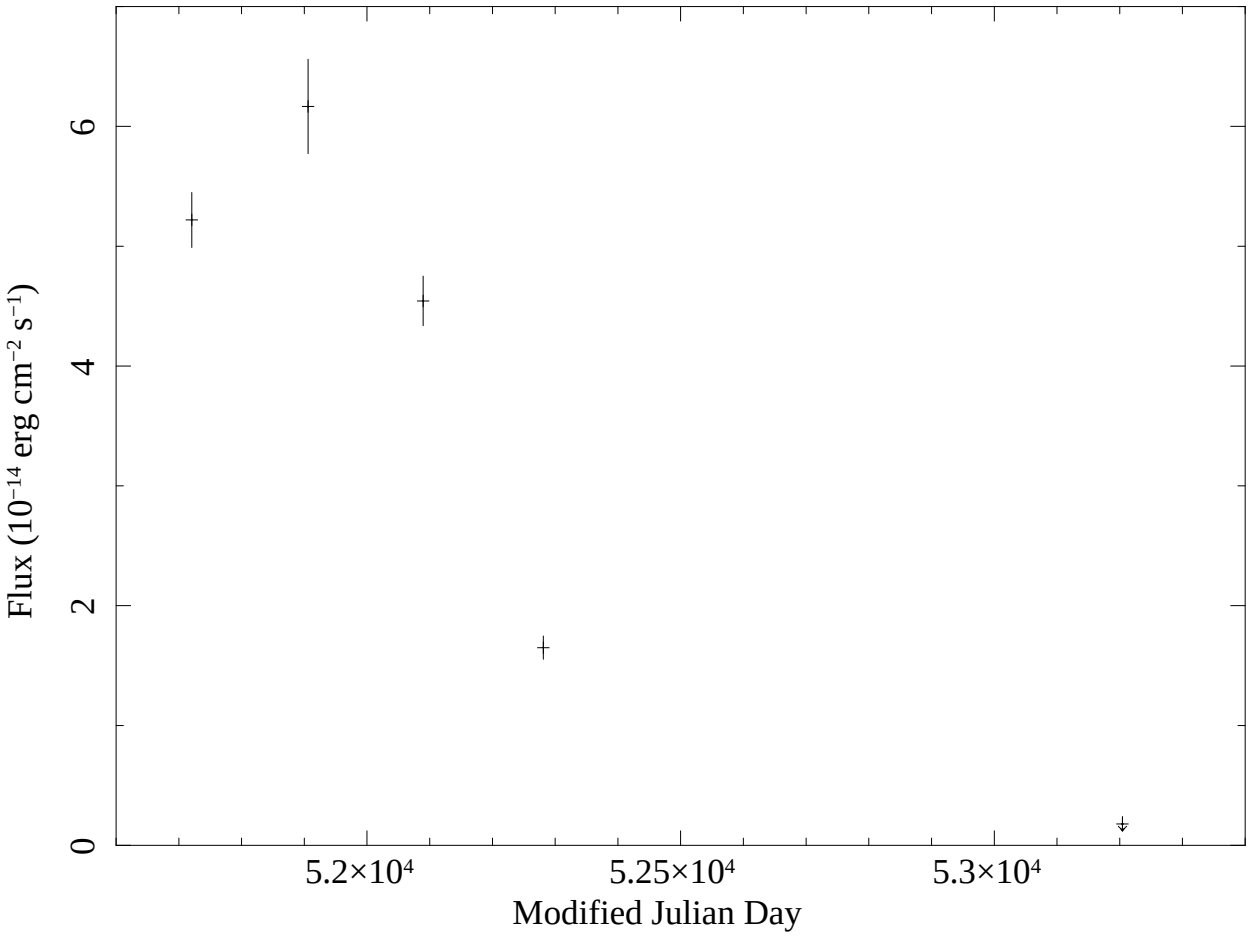


**Figure 6.6:** The EPIC long-term light curve of source 318. We used XID fluxes. The arrow marks a $3\sigma$ upper limit.

$S_{\rm var} = 4.75$). Since the source lies next to the bright transient source 881, which was first detected in observation b, the flux of source 316 may be underestimated and the source could appear as variable. However due to the variability reported in the literature (see Table 6.6), the SNR classification has to be rejected.

### 6.4.4 Globular cluster sources and X-ray binaries

A significant part of the luminous X-ray sources in the Milky Way and M 31 are found in globular clusters. We correlated our catalogue extension with that of Galleti et al. (2004).

All <hard> sources from our source catalogue extension that have a variability factor larger than ten are classified as XRBs. References for these sources can be found in Table 6.6. TPC06 report on four bright X-ray transients which they detected in the observations of July 2004 and suggest them to be XRB candidates. We also detected these sources, and classified source 878 and identified sources 881, 888, 890 as XRBs. One of the identified XRBs (890) shows a very soft spectrum. Williams et al. (2005b) observed source 888 with *Chandra* and *HST*. From the location and X-ray spectrum they suggest it to be an LMXB. They propose the optical counterpart to be a star within the X-ray error box that shows a change in optical brightness ($\Delta B$) of $\approx$1 mag. Source 881 was first detected in January 1979 by TF91 with the *Einstein* observatory. WGM06 rediscovered it in *Chandra* observations from 2004. Their coordinated *HST* ACS imaging does not reveal any variable optical counterpart. Based on the X-ray spectrum and the lack of a bright star, WGM06 suggest this source to be an LMXB with a black hole.

In PFH2005, sources 169, 225, 322, 328, 335 and 420 were classified as <hard>. We found that they all have a time variability factor larger than ten and therefore re-classified them as XRB candidates.

Sources 257 and 384 were proposed to be stellar mass black hole candidates by Barnard et al. (2003c) and Barnard et al. (2004), respectively. Recently, it was shown that the aperiodic variability of these sources has an artificial origin (Barnard et al. 2007b). So there is no longer clear evidence supporting a black hole nature for these objects (Barnard et al. 2007a). We now classify sources 257 and 384 as XRB candidates, based on their time variability (see Tables. 6.6 and 6.7).

Source 883 is a transient, only detected in the July 2004 observations (obs. b) from our study. It stands out in Fig. 6.3 and Table 6.6 as the source with the highest variability ($F_{\rm var} \approx 830$). The EPIC PN data of source 883 during observation b can be well fitted with an absorbed power-law model ($N_{\rm H} = 1.1 \pm 0.2 \times 10^{21}$ cm$^{-2}$, photon power-law index $= 1.61 \pm 0.08$ , unabsorbed 0.5–8.0 keV luminosity $= 3.7 \times 10^{37}$ erg s$^{-1}$). The source correlates with the GlC candidate Bo 128 (*e. g.* Galleti et al. 2004). Based on its variability, luminosity and absorbed power-law spectrum Trudolyubov et al. (2006b) classify this source as a neutron star XRB candidate (# 77 in their list of bright X-ray sources detected in the central part of M 31). During the *Chandra* monitoring of the centre area of M 31, the transient was detected at a similar luminosity 2 months earlier in May 2004 (source 136 in Voss & Gilfanov 2007), most likely during the same outburst. No additional *Chandra* detections of the source have been reported. No source was detected at the position of this bright transient with the Einstein Observatory 1979/80 (*e. g.* TF91), during the ROSAT PSPC surveys (Jul 2001, Jul/Aug 2002, Dec 2002/Jan 2003, Jul 2003; see Supper et al. 1997, 2001) and during ROSAT HRI observations in Jul 2004 and Jan 2006 (see source catalogues of the pointed HRI observations 1RXH). However, two additional outbursts of the transient were detected with the ROSAT HRI in July 1990 (source 51 in PFJ93) and in Jul/Aug 1995 (see 1RXH). The luminosity derived for these outbursts is remarkably similar to the luminosity of the outburst in 2004, if we assume that the X-ray spectrum of this recurrent transient can be described by the same model applied during the 2004 outburst (see Table 6.8).

**Table 6.8:** Outbursts of source 883 = [PFJ93] 51 = [VG2007] 136 = [TPC2006] 77

| Satellite | Time of observation | $L_{\rm x}$ $^{+}$ | Reference$^{\dagger}$ |
|---|---|---|---|
| ROSAT HRI | Jul 1990 | 4.7 | 1 |
| ROSAT HRI | Jul/Aug 1995 | 4.6 | 2 |
| *Chandra* ACIS-I | May 2004 | 3.3 | 3 |
| *XMM-Newton* EPIC | Jul 2004 | 3.7 | 4, this work |

Notes:
$^{+}$ : 0.5–8.0 keV unabsorbed luminosity in units of $10^{37}$ erg s$^{-1}$, assuming $N_{\rm H} = 1.1 \times 10^{21}$ cm$^{-2}$ and a photon index of 1.6
$^{\dagger}$ : 1: Primini et al. (1993), 2: 1RXH catalogue, 3: Voss & Gilfanov (2007), 4: Trudolyubov et al. (2006b)

## 6.5 Conclusion

In this chapter we present an updated source list of the central area of the bright Local Group spiral galaxy M 31, using the observations from June 2000 to July 2004 available from the *XMM-Newton* archive. We extended the source catalogue in PFH2005, which is based on the merged images from the observations taken between 2000 and 2002, by searching for sources in the observations of 2004 and reexamining the observations used in PFH2005 individually. To classify or identify a greater number of sources, we examined their long term time variability.

We obtained 39 sources in addition to the 265 reported by PFH2005 in the same field. The identification and classification of these sources is based on properties in the X-ray wavelength regime: hardness ratios and temporal variability. In addition, information from cross correlations with M 31 catalogues in the radio, infra-red, optical and X-ray wavelength regimes are used.

We detected three SSS candidates, one SNR and six SNR candidates, one GlC candidate, three XRBs and four XRB candidates. Additionally we identified one foreground star candidate and classified fifteen sources as <hard>, which may either be XRBs or Crab-like SNRs in M 31 or background AGN. The remaining five sources remain unidentified and without classification. Two sources were found to be extended. One of them was classified as <hard>. The other remains without a classification.

To examine the time variability, we calculated the flux, or at least an upper limit, at the source position in each observation. We determined the variability factor and significance parameter for each source, comparing the XID flux ratios of the different observations with each other. The time variability helped us to decide if a source classified as <hard> in PFH2005 could be an XRB candidate. In addition we used the time variability to distinguish between foreground star candidates and SNR candidates.

Six sources from PFH2005 that were classified as <hard>, show distinct time variability. Based on this variability, their hardness ratios and the strong absorption in the centre of M 31, we propose these sources to be XRB candidates. The SNR classification from source 295 was changed to a foreground star classification due to the distinct time variability we found, and its identification with a faint stellar object. Other SNR classifications (sources 316, 318) were rejected due to the time variability of these sources.

To verify our suggested classifications, further investigations, in the X-ray and at other wavelengths, will be necessary.

# Chapter 7

# *XMM-Newton* Large Program: Source catalogue

## 7.1 Observations and data analysis

This chapter presents the source catalogue of the "Deep *XMM-Newton* survey of M 31" (in the following called XMM LP-total catalogue). To cover the whole $D_{25}$ ellipse of M 31 archival *XMM-Newton* observations were re-analysed and the detected sources were included in the XMM LP-total catalogue. As the archival observations, which cover, at least in parts, the central field of M 31, were used already for the time variability study presented in Chap. 6, the overall description of the observations and data analysis was given in Chap. 5. There you will also find the journal of observations (Table 5.1), which contains all observations used.

### 7.1.1 Images

Figure 7.1 shows the combined, exposure corrected, EPIC PN, MOS 1 and MOS 2 RGB mosaic image of the Deep Survey and archival data. The colours represent the X-ray energies as follows: red: 0.2–1 keV, green: 1–2 keV and blue: 2–12 keV. The optical extent of M 31 is indicated by the $D_{25}$ ellipse and the boundary of the observed field is given by the green contour. The image is smoothed with a 2D-Gaussian of $20''$ FWHM. In some observations individual noisy MOS 1 and MOS 2 CCDs are omitted.
The colour of the sources reflects their class. Supersoft sources appear in red. Thermal SNRs and foreground stars are orange to yellow. "Hard" sources (background objects (mainly AGN) and X-ray binaries or Crab-like SNRs) are blue to white.

Logarithmically scaled *XMM-Newton* EPIC low background images made up of the combined images from the PN, MOS 1 and MOS 2 cameras in the (0.2–4.5) keV XID band for each M 31 observation can be found in Appendix B. The images also show X-ray contours, and the sources from the XMM LP-total catalogue are marked with boxes (size: $30'' \times 30''$).

### 7.1.2 Source detection

The principle detection algorithm is described in Sect. 5.2.4. Here I shortly explain the ECF values used for the Large *XMM-Newton* (XMM LP-total) catalogue and how they were derived. In addition, the selection criteria used to include sources in the XMM LP-total catalogue are summarised.

The ECFs (see Table 7.1) were derived with `Xspec` (command `fakeit`) using response matrices, avail-

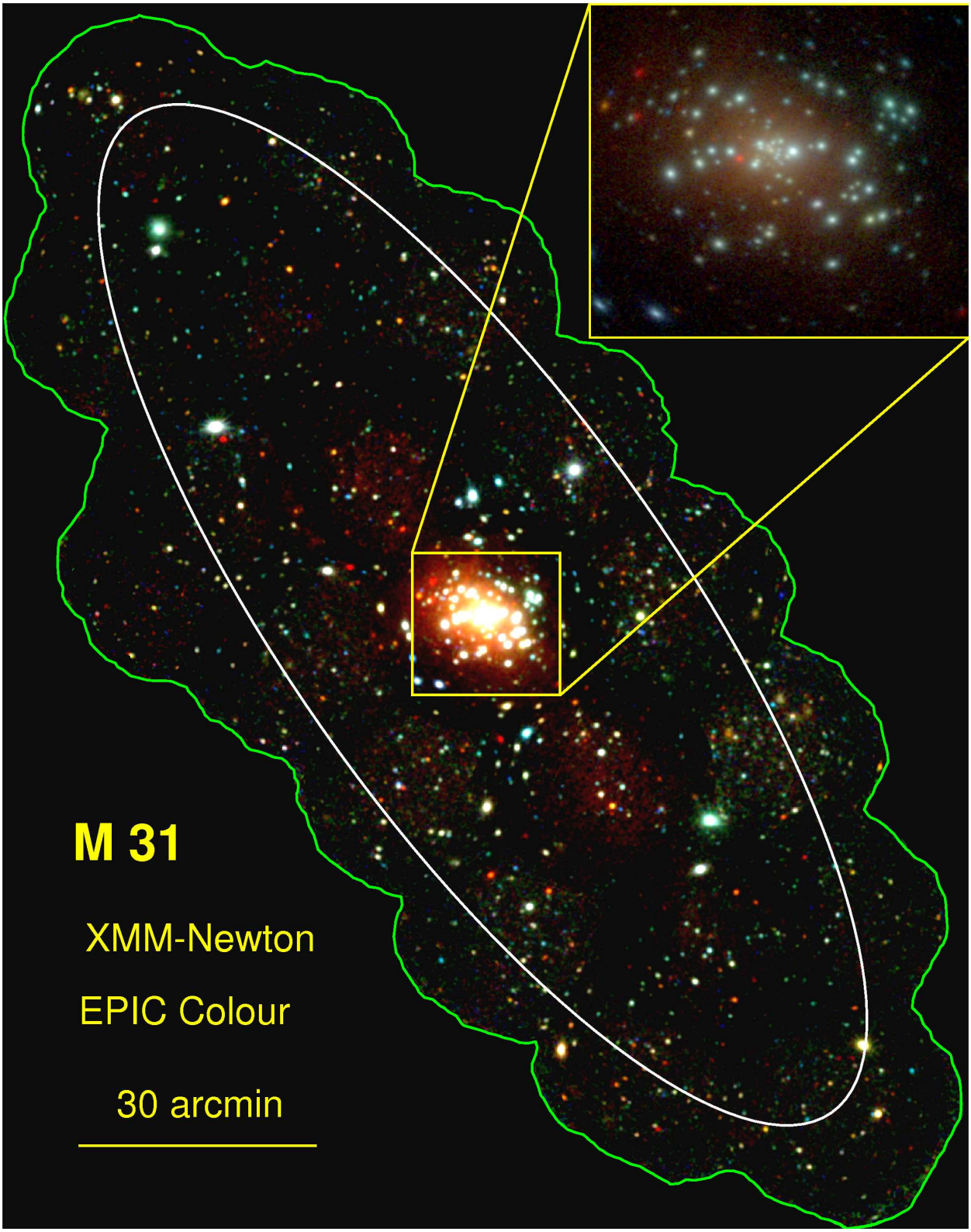


**Figure 7.1:** Combined EPIC PN, MOS 1 and MOS 2 RGB image of the Deep Survey and archival data. The central region, marked with the yellow square, is shown in higher resolution in the upper right corner. For more details see Sect. 7.1.1.

able from the *XMM-Newton* calibration homepage[1]. As all necessary corrections of the source parameters (*e. g.* vigneting corrections) are included in the image creation and source detection procedure[2] described in Sects. 5.2.3 and 5.2.4, the *on axis* ECF values were derived (*cf.* Watson et al. 2009). The fluxes determined with the ECFs given in Table 7.1 are absorbed (*i. e.* observed) fluxes and hence correspond to the observed count rates, which are derived in the `emldetect` task.

During the mission lifetime, the MOS energy distribution behaviour has changed. Near the nominal boresight position, where most of the detected photons hit the detectors, there has been a decrease in the low energy response of the MOS cameras (Read et al. 2006). To take this effect into account, different response matrices for observations obtained before and after the year 2005 were used. The ECFs used for observations obtained before 2005 are marked with "OLD" in Table 7.1.

I accepted sources with a likelihood above seven in the combined fit. Sources enter the XMM LP-total catalogue from the observation in which the highest source detection likelihood is obtained (either combined or single observations). For variable sources this means that the source properties given in the XMM LP-total catalogue (see Sect. 7.2 and Table 7.2) are those observed during their bright state.

To allow for a statistical analysis, the source catalogue only contains sources detected with the `SAS` tasks `eboxdetect` and `emldetect` as described in Sect. 5.2.4, *i. e.* the few sources that were not detected by the analysis program, despite being visible in the X-ray images, are not added by hand as was done for the examination presented in Chap. 6.

To classify the source spectra I computed four hardness ratios, applying Eq. 2.10 to the source count rates in the five energy bands defined in Sect. 5.2.3.

For fields which were observed more than once, I generated a starting list for the variability analysis from the XMM LP-total catalogue.

## 7.2 Source catalogue

The source catalogue of the Deep *XMM-Newton* survey of M 31 contains 1 948 X-ray sources. Of these sources 961 are detected for the first time in X-rays.

The source parameters are summarised in Table 7.2[3], which gives the source number (Col. 1), detection field from which the source was entered into the catalogue (2), source position (3 to 9) with $3\sigma$ (99.73%) uncertainty radius (10), likelihood of existence (11), integrated PN, MOS 1 and MOS 2 count rate and error (12,13) and flux and error (14,15) in the (0.2–4.5) keV XID band, and hardness ratios and errors (16–23). Hardness ratios are calculated only for sources for which at least one of the two band count rates has a significance greater than $2\sigma$. Errors are the properly combined statistical errors in each band and can extend beyond the range of allowed values of hardness ratios as defined previously (–1.0 to 1.0; Eq. 2.10). The EPIC instruments contributing to the source detection are indicated by the three characters in the "Val" parameter (Col. 24, first character for PN, second MOS 1, third MOS 2) where "T" indicates if the source is inside the FoV, and "F", if it lies outside of the FoV.

Table 7.2 also gives the exposure (25), source existence likelihood (26), the count rate and error (27, 28) and the flux and error (29, 30) in the (0.2–4.5) keV XID band, and hardness ratios and errors (31–38) for the EPIC PN. Columns 39 to 52 and 53 to 66 give the same information corresponding to Cols. 25 to 38, but for the EPIC MOS 1 and MOS 2 instruments. Hardness ratios for the individual instruments were again screened as described above. From the comparison between the hardness ratios derived from the integrated

[1] `http://xmm2.esac.esa.int/external/xmm_sw_cal/calib/epic_files.shtml`

[2] especially in the `emldetect` task

[3] Table 7.2 is only available in electronic form on the attached CD. A description of the content of this table can be found in Appendix D.

**Table 7.1:** Count rate to energy conversion factors for the PN, MOS 1 and MOS 2 thin and medium filters, derived from a power-law model fit, assuming a photon index of $\Gamma = 1.7$ and a foreground absorption of $N_{\rm H} = 7 \times 10^{20}\,{\rm cm}^{-2}$. The ECFs used for the observations obtained before revolution 534 are marked with "OLD".

| Detector | Filter | B1 | B2 | B3 | B4 | B5 |
|---|---|---|---|---|---|---|
| | | $(10^{11}{\rm cts\,cm^2\,erg^{-1}})$ | | | | |
| EPIC PN | thin | 11.33 | 8.44 | 5.97 | 1.94 | 0.58 |
| | medium | 10.05 | 8.19 | 5.79 | 1.94 | 0.58 |
| EPIC MOS 1 | thin | 2.25 | 1.94 | 2.06 | 0.76 | 0.14 |
| | medium | 2.07 | 1.90 | 2.07 | 0.75 | 0.15 |
| EPIC MOS 2 | thin | 2.29 | 1.98 | 2.09 | 0.78 | 0.15 |
| | medium | 2.06 | 1.90 | 2.04 | 0.75 | 0.15 |
| EPIC MOS 1 OLD | thin | 2.59 | 2.04 | 2.12 | 0.76 | 0.15 |
| | medium | 2.33 | 1.98 | 2.09 | 0.76 | 0.15 |
| EPIC MOS 2 OLD | thin | 2.58 | 2.04 | 2.13 | 0.76 | 0.15 |
| | medium | 2.38 | 1.99 | 2.09 | 0.75 | 0.16 |

PN, MOS 1 and MOS 2 count rates (Cols. 16–23) and the hardness ratios of the individual instruments (Cols. 31–38, 45–52 and 59–66), it is clear that the combined count rates from all instruments yielded significantly larger fraction of hardness ratios above the chosen significance threshold.

Column 67 shows cross correlations with the M 31 X-ray catalogues in the literature (*cf.* Sect. 5.2.9). I discuss the results of the cross correlation in Chap. 9.

In the remaining columns of Table 7.2, I give information extracted from the USNO-B1, 2MASS and LGS catalogues (*cf.* Sect. 5.2.9). The information from the USNO-B1 catalogue (name, number of objects within search area, distance, B2, R2 and I magnitude of the brightest[4] object) is given in Cols. 68 to 73. The 2MASS source name, the number of objects within search area, and the distance can be found in Cols. 74 to 76. Similar information from the LGS catalogue is given in Cols. 77 to 82 (name, number of objects within search area, distance, V magnitude, V-R and B-V colours of the brightest[5] object). To improve the reliability of identifications I used the USNO-B1 B2 and R2 magnitudes to calculate $\log\left(\frac{f_{\rm x}}{f_{\rm opt}}\right)$ using Eq. 6.1 and the LGS V magnitude to calculate

$$\log\left(\frac{f_{\rm x}}{f_{\rm opt,\,v}}\right) = \log\left(f_{\rm x}\right) + \frac{m_{\rm V}}{2.5} + 5.37, \tag{7.1}$$

following Maccacaro et al. (1988, see Cols. 83–86).

The X-ray sources in the XMM LP-total catalogue are identified or classified based on properties in the X-rays (HRs, variability, extent) and of the correlated objects in other wavelength regimes (Cols. 87 and 88 in Table 7.2). For classified sources the class name is given in angle brackets. Identification and classification criteria are summarised in Table 7.3. The hardness ratio criteria are based on model spectra. As we have no clear hardness ratio criteria to select XRBs, Crab-like supernova remnants (SNRs) or AGN we introduced a class <hard> for those sources. If such a source shows strong variability (*i. e.* V$\geq$10) on the examined time scales it is likely to be an XRB. Compared with Table 6.2 the HR2 selection criterion for

[4] in B2 magnitude

[5] in B magnitude

SNRs was tightened (from HR2$< -0.2$ to HR2+EHR2$< -0.2$) to exclude questionable SNR candidates from the class of SNRs. Applying the selection criterion that is given in Table 6.2 to the survey data, $\sim$35 sources would be classified as SNRs in addition to the classified SNRs listed in Table 7.3. Most of the 35 sources are located outside the $D_{25}$ ellipse, and none of them correlates with an SNR, a radio source, or an HII region. In addition, the errors in HR2 are of the same order as the HR2 values. It is therefore very likely that these sources do belong to other classes, since the strip between $-0.3 <$HR2$<0$ is populated by foreground stars, XRBs, background objects, and candidates of these three classes, apart from a few SNRs. Outcomes of the identification and classification process are discussed in detail in Sects. 9.3 and 9.4.

The last column (89) of Table 7.2 contains the *XMM-Newton* source name as registered to the IAU Registry. Details on the source name were given in Sect. 6.2. For sources that have counterparts in Tables 6.3 or 6.5 the source name stayed the same. In the following I refer to individual sources by their source number (Col. 1 of Table 7.2), which is marked with an "Nº" at the front of the number.

Of the 1 948 sources, 1 263 can only be classified as <hard> sources, while 139 sources remain without classification. Two of them (Nº 482, Nº 768) are highly affected by optical loading. Both "X-ray sources" coincide spatially with very bright optical foreground stars (USNO-B1 R2 magnitudes of 6.76 and 6.74 respectively). The spectrum of source Nº 482 is dominated by optical loading. This becomes evident from the hardness ratios which indicate an SSS. For Nº 768 the hardness ratios would allow a foreground star classification. The obtained count rates and fluxes of both sources are affected by the usage of `epreject`, which neutralises the corrections applied for optical loading. Therefore residuals are visible in the difference images created from event lists obtained with and without `epreject`. As I cannot exclude the possibility that some of the detected photons are true X-rays – especially for source Nº 768 –, I decided to include them in the XMM LP-total catalogue, but without a classification.

### 7.2.1 Flux distribution

The faintest sources have an XID band flux of $\sim(5.7\text{–}5.8)\times10^{-16}$ erg cm$^{-2}$ s$^{-1}$. The source with the highest XID Flux (Nº 966, XID band flux of $3.75\times10^{-12}$ erg cm$^{-2}$ s$^{-1}$) is located in the centre of M 31 and identified as a Z-source LMXB (Barnard et al. 2003b). This source has an absorbed XID luminosity of $\sim2.74\times10^{38}$ erg s$^{-1}$.

Figure 7.2 shows the distribution of the XID (0.2–4.5 keV) source fluxes. Plotted are the number of sources in a certain flux bin. We see from the inlay that the number of sources starts to decrease in the bin from 2.6 to $2.8\times10^{-15}$ erg cm$^{-2}$ s$^{-1}$. This XID flux roughly determines the completeness limit of the survey and corresponds to an absorbed 0.2–4.5 keV limiting luminosity of $\sim2\times10^{35}$ erg s$^{-1}$.

Previous X-ray studies (Williams et al. 2004a, and references therein) noticed a lack of bright sources

**Table 7.3:** Summary of identifications and classifications.

| Source class | Selection criteria | identified | classified |
|---|---|---|---|
| fg Star | $\log(\frac{f_x}{f_{opt}}) < -1.0$ and HR2$-$EHR2$<0.3$ and HR3$-$EHR3$<-0.4$ or not defined | 39 | 227 |
| AGN | Radio source and not classification as SNR from HR2 or optical/radio | 11 | 49 |
| Gal | optical id with galaxy | 4 | 19 |
| GCl | X-ray extent and/or spectrum | 1 | 5 |
| SSS | HR1$<0.0$, HR2$-$EHR2$<-0.96$ or HR2 not defined, HR3, HR4 not defined | | 40 |
| SNR | HR1$>-0.1$ and HR2+EHR2$<-0.2$ and not a fg Star, or id with optical/radio SNR | 25 | 37 |
| GlC | optical id | 36 | 17 |
| XRB | optical id or X-ray variability | 10 | 26 |
| hard | HR2$-$EHR2$>-0.2$ or only HR3 and/or HR4 defined, and no other classification | | 1 263 |

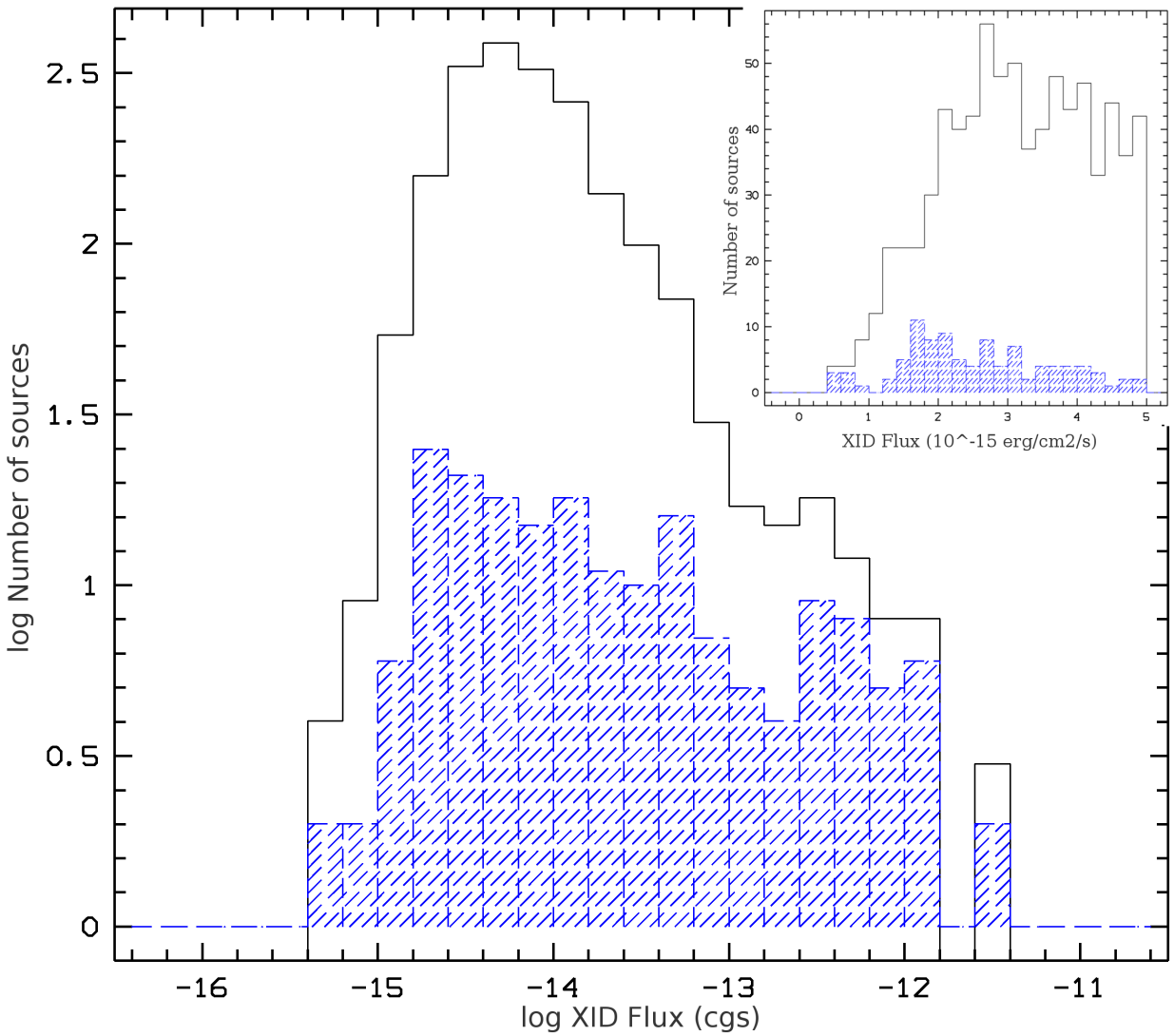


**Figure 7.2:** Distribution of the source fluxes in the 0.2–4.5 keV (XID) band. The diagram shows the number of sources at each flux bin, plotted versus the flux, using logarithmic scales. The inlay shows the number of sources for XID fluxes smaller than $5\times10^{-15}$ erg cm$^{-2}$ s$^{-1}$, on linear scales. The blue histogram gives the distribution of sources classified or identified either as SSSs, SNRs, XRBs or GlCs.

($L_{\rm X} \gtrsim 10^{37}$ erg s$^{-1}$; 0.1–10 keV) in the southern half of the disc compared to the northern half. This finding is not supported in the present study. Excluding the pointings to the centre of M 31, we found in the observations of both the northern half and the southern half of the disc, 13 sources in each hemisphere that were brighter than $L_{\rm X,\,abs} \gtrsim 10^{37}$ erg s$^{-1}$.[6] In the central field of M 31 a total of 41 sources brighter than $L_{\rm X,\,abs} \gtrsim 10^{37}$ erg s$^{-1}$ (0.2–4.5 keV) were found.

Figure 7.3 shows the spatial distribution of the bright sources. Striking features are the two patches located north and south of the centre. The southern one seems to point roughly in the direction of M 32 (N$^{\underline{o}}$ 995), while the northern one ends in the globular cluster B 116 (N$^{\underline{o}}$ 947). However there is no association to any known spatial structure of M 31, like *e. g.* the spiral arms. A possible explanation for these features is the transit of M 32 through the disc of M 31.

### 7.2.2 Exposure map

The exposure map, which is shown in Fig. 7.4, was used to create the colour image of all *XMM-Newton* Large Survey and archival observations (Fig. 7.1). For source detection, only the exposures from the observations of one field were used, as the available random access memory does not allow to search on more than about 30 images simultaneously in a detection run (remember that each band of each camera contributes one image). That means that in regions where different fields overlap, the shown exposure map (Fig. 7.4) over estimates the exposure available for source detection.

From Fig. 7.4 we see that the exposure of most of the surveyed area is rather homogeneous. Exceptions are the central area, overlapping regions and observation h4.

### 7.2.3 Hardness ratio diagrams

I plot X-ray colour/colour diagrams based on the HRs (see Fig. 7.5). Sources are plotted as dots if the error in both contributing HRs is below 0.2. Classified and identified sources are plotted as symbols even if the error in the contributing HRs is greater than 0.2. Symbols including a dot therefore mark the well-defined HRs of a class.

From the HR1-HR2 diagram (upper left panel in Fig. 7.5) we see that the class of SSSs is the only one that can be defined based on hardness ratios alone. In the part of the HR1-HR2 diagram that is populated by SNRs, most of the foreground stars and some background objects and XRBs also are found. Foreground star candidates can be selected from the HR2-HR3 diagram (upper right panel in Fig. 7.5), where most of them are located in the lower left corner. However, we need additional information from correlations with sources at other wavelengths or on the source variability to classify the sources.

## 7.3 Extended sources

The XMM LP-total catalogue contains 12 sources which are fitted as extended sources with a likelihood of extension larger than 15. This value was chosen on the one hand to minimise the number of spurious detections of extended sources (H. Brunner; private communication), and on the other hand to keep all sources that already can be seen as extended sources in the X-ray images. A convolution of a $\beta$-model cluster brightness profile (Cavaliere & Fusco-Femiano 1976) with the *XMM-Newton* point spread function was used to determine the extent of the sources (*cf.* Sect. 5.2.4). This model describes the brightness profile of galaxy clusters. Since previous studies showed that extended sources that were detected with *XMM-Newton* in the field of M 31 are most likely galaxy clusters (PFH2005), the $\beta$-model was chosen.

[6] The luminosity is based on XID Fluxes. Using the total 0.2–12 keV band the result does not change (23 in the northern half and 24 in the southern half).

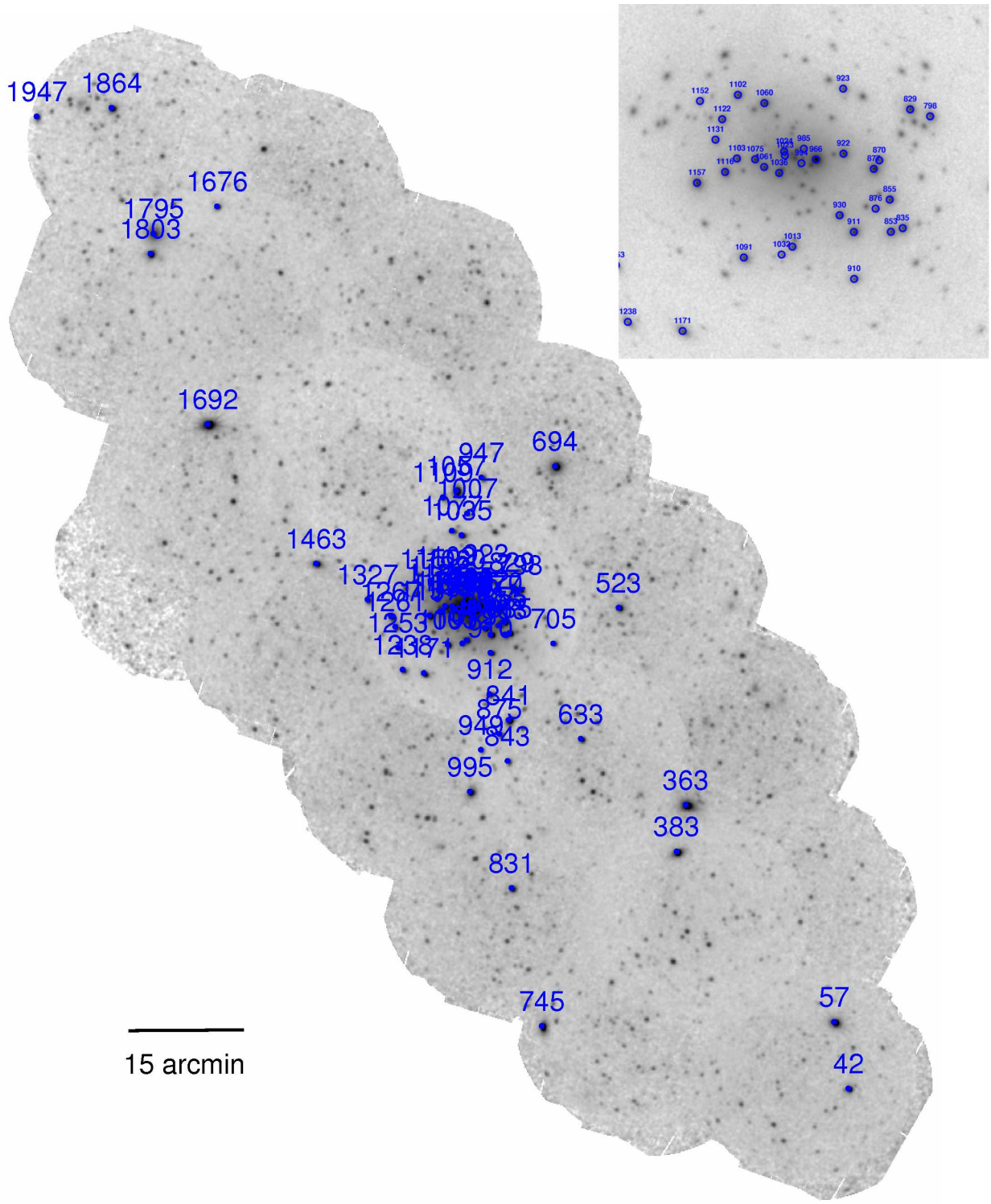


**Figure 7.3:** *XMM-Newton* Deep Survey image over plotted with sources that have an absorbed 0.2–4.5 keV luminosity larger than $10^{37}$ erg $s^{-1}$. Striking features are the two patches located north and south of the centre. The central region (same as in Fig. 7.1) is shown with higher resolution in the upper right corner.

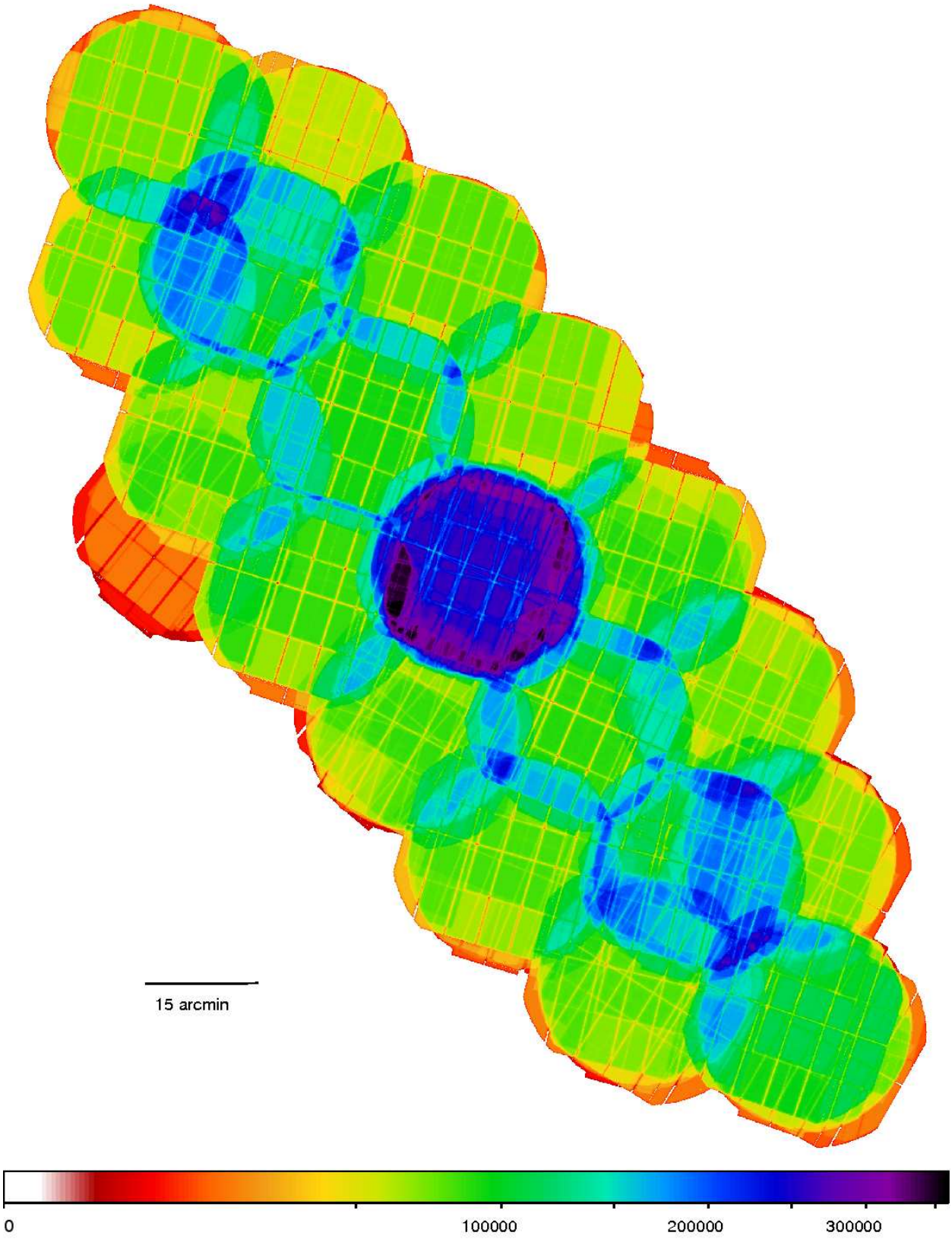


**Figure 7.4:** Exposure map of all fields of the XMM LP-total catalogue. For details see Sect. 7.2.2.

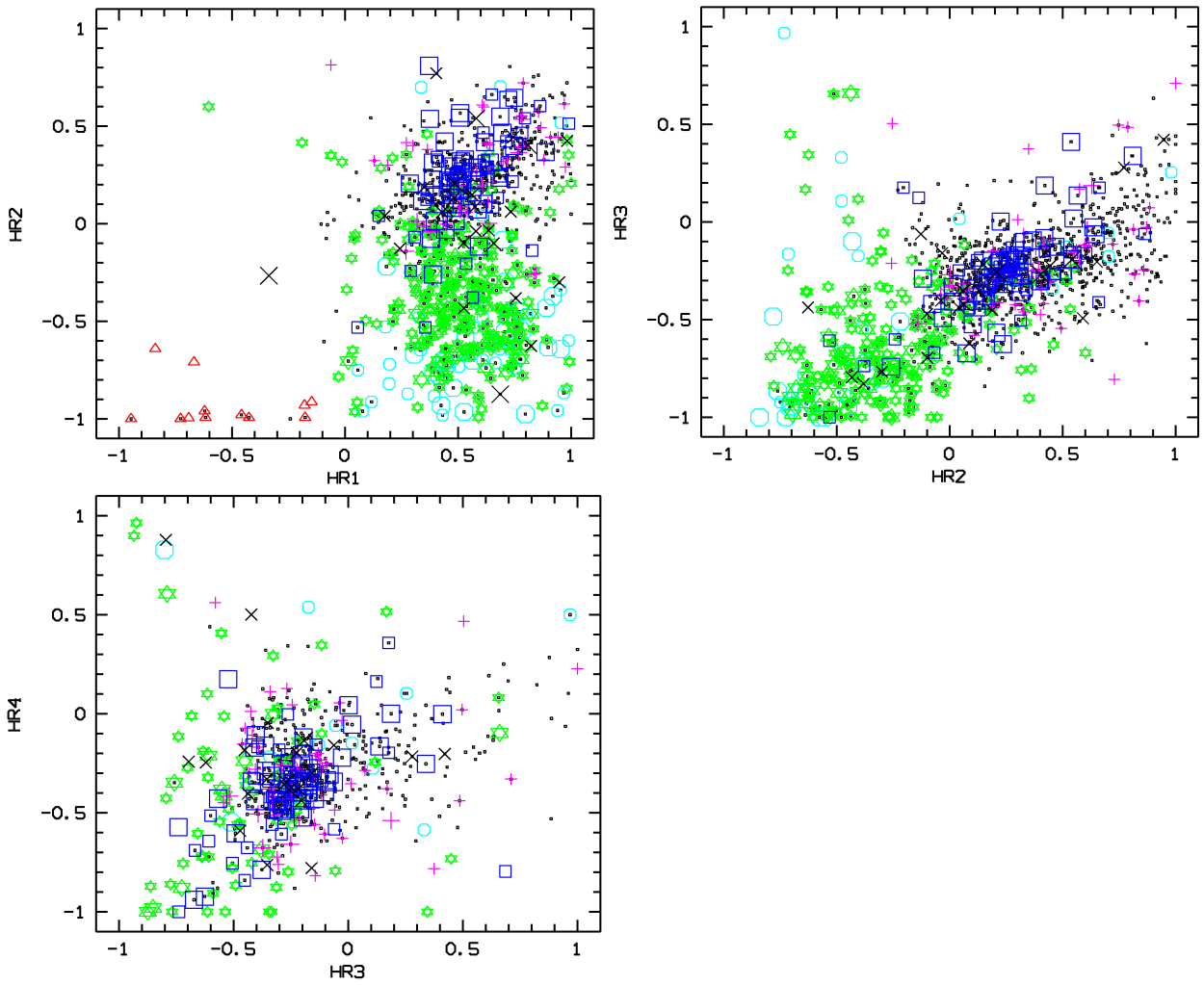


**Figure 7.5:** Hardness ratios of sources detected by *XMM-Newton* EPIC. Sources with HR errors smaller then 0.20 on both HR$(i)$ and HR$(i+1)$ are shown as dots. Foreground stars and candidates are marked as big and small stars, AGN and candidates as big and small crosses, background galaxies and galaxy clusters as big"X" and their candidates as small "X", SSS candidates as triangles, SNRs and candidates as big and small hexagons, GlCs and XRBs as big squares and their candidates as small squares.

**Table 7.4:** Extended sources in the XMM LP-total catalogue

| SRC (1) | DET_ML (2) | EXT$^{+}$ (3) | EEXT$^{+}$ (4) | EXT_ML (5) | XFLUX$^{*}$ (6) | XEFLUX$^{*}$ (7) | class (8) | comment$^{\dagger}$ (9) |
|---|---|---|---|---|---|---|---|---|
| 141 | 65.08 | 11.22 | 1.29 | 23.68 | 1.45 | 0.20 | <GCl> | GLG127(Gal), 37W 025A (IR, RadioS; NED) |
| 199 | 275.16 | 17.33 | 1.05 | 174.73 | 4.33 | 0.29 | <hard> | |
| 252 | 222.05 | 14.64 | 1.12 | 81.60 | 4.40 | 0.49 | <GCl> | 5 optical objects in error box |
| 304 | 299.75 | 15.10 | 0.92 | 133.62 | 2.20 | 0.18 | <GCl> | B242 [CHM09]; RBC3.5: <GlC> |
| 442 | 33.76 | 11.60 | 1.71 | 15.44 | 1.62 | 0.28 | <hard> | |
| 618 | 271.08 | 6.20 | 0.73 | 42.86 | 3.17 | 0.21 | <hard> | |
| 718 | 77.75 | 7.18 | 1.23 | 21.47 | 0.58 | 0.07 | Gal | B052 [CHM09], RBC3.5 |
| 1 130 | 168.31 | 10.80 | 0.97 | 44.23 | 3.28 | 0.31 | <hard> | |
| 1 543 | 70.49 | 11.87 | 1.37 | 28.63 | 1.51 | 0.19 | <GCl> | [MLA93] 1076 PN (SIM,NED) |
| 1 795 | 11 416.36 | 18.79 | 0.29 | 4 169.74 | 99.17 | 1.43 | GCl | GLG253 (Gal), [B90] 473, $z = 0.3$ [KTV2006] |
| 1 859 | 107.09 | 13.73 | 1.40 | 43.89 | 1.23 | 0.19 | <hard> | |
| 1 912 | 332.06 | 23.03 | 1.23 | 213.90 | 5.40 | 0.37 | <GCl> | cluster of galaxies candidate |

Notes:

$^{+}$ : Extent and error of extent in units of $1''$; $1''$ corresponds to 3.8 pc at the assumed distance of M 31

$^{*}$ : XID Flux and flux error in units of $1 \times 10^{-14}$ erg cm$^{-2}$ s$^{-1}$

$^{\dagger}$ : Taken from Table 7.2

Table 7.4 gives the source number (Col. 1), likelihood of detection (2), the extent found (3) with error (4) in arcsec, the likelihood of extension (5), and the classification of the source (6, see Sect. 9.3.2) for each of the 12 extended sources. Additional comments taken from Table 7.2 are provided in the last column.

The extent found for the sources ranges from $6\farcs2$ (23.56 pc) to $23\farcs03$ (87.51 pc; see Fig. 7.6).

The brightest source (N$^{\underline{o}}$ 1 795), which has the highest likelihood of extension and the second largest extent, was identified from its X-ray properties as a galaxy cluster located behind M 31 (Kotov et al. 2006). The iron emission lines in the X-ray spectrum yield a cluster redshift of $z = 0.29$.

For further discussion see Sect. 9.3.2.

## 7.4 Variability between *XMM-Newton* observations

To examine the long-term time variability of each source, I determined the XID flux at the source position in each observation or at least an upper limit for the XID flux. The XID fluxes were used to derive the variability factor and the significance of variability (*cf.* Sect. 5.2.7).

The sources are taken from the XMM LP-total catalogue (Table 7.2). Table 7.5[7] contains all information necessary to examine time variability. Sources are only included in the table if they are observed at least twice. Column 1 gives the source number. Columns 2 and 3 contain the flux and error in the (0.2–4.5) keV XID band. The hardness ratios and errors are given in columns 4 to 11. Column 12 contain the type of the source. All this information was taken from Table 7.2. The then-following 140 columns provide information related to individual observations in which the position of the source was observed. Column 13 gives the name of one of these observations, which I will call observation 1. The EPIC instruments contributing to the source detection in observation 1, are indicated by three characters in the "obs1_val" parameter (Col. 14, first character for PN, second MOS 1, third MOS 2), each one either a "T" if the source is inside the FoV, or "F" if it lies outside the FoV. Then the count rate and error (15,16) and flux and error (17,18) in the (0.2–4.5) keV XID band, and hardness ratios and error (19–26) of observation 1 are given.

[7] Table 7.5 is only available in electronic form on the attached CD. A description of the content of this table can be found in Appendix D.

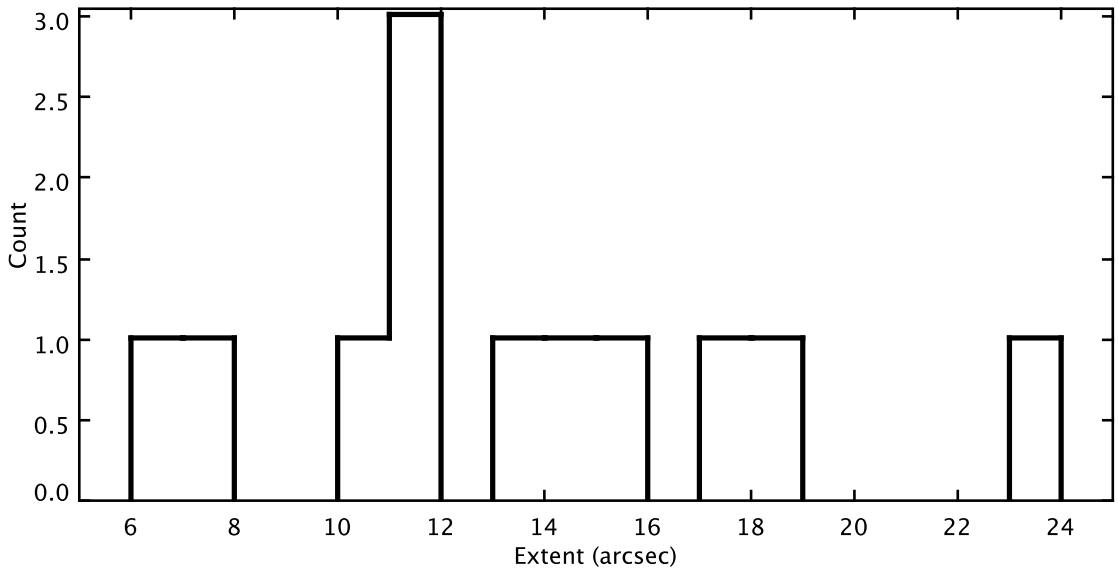


**Figure 7.6:** Distribution of extent.

Corresponding information is given for the remaining observations which cover the position of the source: obs. 2 (cols. 27–40), obs. 3 (41–54), obs. 4 (55–68), obs. 5 (69–82), obs. 6 (83–96), obs. 7 (97–110), obs. 8 (111–124), obs. 9 (125–138), obs. 10 (139–152). Whether the columns corresponding to obs. 3 – obs. 10 are filled in, depends on the number of observations in which the source is covered in the combined EPIC FoV. This number is indicated in column 153. The maximum significance of variation and the maximum flux ratio (fvar_max) are given in columns 154 and 155. As described in Sect. 5.2.7, only detections with a significance greater than $3\sigma$ were used, otherwise the $3\sigma$ upper limit was used. Column 156 indicates the number of observations that provide only an upper limit. The maximum flux (fmax) and its error are given in columns 157 and 158. In a few cases I could not derive the maximum flux, because each observation only gave an upper limit. This can have two reasons: The first reason is that faint sources detected in merged observations may not be detected in the individual observations at the $3\sigma$ limit. The second reason is, that in cases where the significance of detection was not much above the $3\sigma$ limit, it can become smaller than the $3\sigma$ limit when the source position is fixed.

**Table 7.6:** Variable sources with flux variability larger than 5, ordered by variability.

| Source | fvar | svar | fmax‡ | efmax‡ | class+ | Comment† |
|---|---|---|---|---|---|---|
| (1) | (2) | (3) | (4) | (5) | (6) | (7) |
| 523 | 692.64 | 63.33 | 106.61 | 1.68 | XRB | |
| 1 032 | 660.61 | 54.21 | 33.89 | 0.62 | <GlC> | 1(r), 2(t, 92.2), 12, 17, 28(831.10) |
| 57 | 644.03 | 96.796 | 147.76 | 1.52 | XRB | |
| 1 131 | 558.48 | 80.18 | 38.93 | 0.48 | <XRB> | 1(t), 2(t, 954.2), 3(t, 2163), 20, 21(t), 23, 27, 28(624.05) |
| 944 | 236.47 | 44.74 | 24.24 | 0.54 | XRB | 1(t), 2(t, 370.5), 15(t, BH-XRN), 21(t), 22(v,t), 27, 28(353.67) |
| 705 | 185.02 | 39.85 | 32.52 | 0.81 | <XRB> | 1(t,sv), 4(t), 28(178.79) |
| 1 007 | 161.84 | 42.33 | 44.30 | 1.04 | <XRB> | 1, 2, 13, 14, 27, 28(12.96) |
| 1 195 | 144.47 | 36.95 | 28.51 | 0.76 | <SSS> | 1(t), 3(t, 694), 15(v,t), 21(t), 27, 28(82.68) |
| 1 152 | 123.95 | 55.31 | 31.86 | 0.56 | <XRB> | 1(sv, <AGN>), 2(t, 96.3), 3(t, 107), 10, 12(v), 13, 14(v), 20, 22(v,t), 27, |

**Table 7.6:** continued.

| Source (1) | fvar (2) | svar (3) | fmax‡ (4) | efmax‡ (5) | class+ (6) | Comment† (7) |
|---|---|---|---|---|---|---|
| | | | | | | 28(131.73) |
| 788 | 117.83 | 20.99 | 12.27 | 0.58 | <XRB> | 1(r), 2(t, 20.8), 3(t, 93), 12, 15(t), 21(t), 27, 28(97.89) |
| 1 136 | 87.84 | 25.00 | 9.79 | 0.39 | <XRB> | 1(t), 2(t, 46.1), 3(t, 155), 20, 21(t), 24, 27, 28(97.65) |
| 934 | 84.94 | 28.35 | 21.26 | 0.90 | <SSS> | |
| 949 | 80.16 | 25.55 | 17.75 | 0.68 | <XRB> | 3(t, 13), 21, 26, 27 |
| 1 194 | 75.22 | 39.69 | 12.79 | 0.31 | <SSS> | 1(r), 2, 3(t, 96), 10, 13, 14(v), 15(v), 20(v), 22(v), 27, 28(85.93) |
| 1 416 | 72.25 | 21.00 | 10.51 | 0.49 | <SSS> | 27, 29 |
| 1 084 | 59.11 | 8.70 | 6.64 | 0.75 | <XRB> | 2(t, 79.0), 3(t, 260), 15(t), 19, 21(t), 22(v,t), 27, 28(57.41) |
| 985 | 51.66 | 80.00 | 80.46 | 0.97 | XRB | 1(t,r,sv), 4(t), 6(t, LMXB), 10, 22(v), 28(76.27) |
| 1 017 | 49.85 | 20.73 | 9.64 | 0.45 | <XRB> | 1(r,sv), 2(t, 99.5), 3(t, 158), 22(v,t), 27, 28(38.07) |
| 990 | 48.90 | 61.77 | 82.16 | 1.28 | XRB | 1(t), 2(t, 468.8), 3(t, 285), 15(v,t, BH-XRT), 19(t), 22(v,t), 27, 28(201.71) |
| 1 059 | 48.10 | 23.64 | 9.16 | 0.37 | <XRB> | 2(t, 64.6), 28(39.69) |
| 698 | 41.20 | 18.73 | 9.33 | 1.37 | <XRB> | 1, 14, 24, 27, 28(44.67) |
| 884 | 32.88 | 9.59 | 2.84 | 0.61 | <XRB> | 2, 28(24.95) |
| 1 153 | 31.06 | 17.96 | 4.22 | 0.22 | XRB | 1(t), 2(t), 4(t), 7(t, LMXB), 28(30.50) |
| 1 000 | 26.86 | 20.17 | 5.75 | 0.48 | | 2(t), 20, 22, 24, 27, 28(34.47) |
| 1 024 | 25.66 | 78.46 | 144.02 | 1.89 | <XRB> | 1(sv), 2, 10, 12, 13, 14, 20, 22(v), 27, 28(34.02) |
| 1 177 | 24.00 | 19.31 | 4.59 | 0.22 | XRB | 1(t), 4(t), 28(27.06) |
| 939 | 22.48 | 10.13 | 2.20 | 0.20 | <XRB> | 2(t, 65.2), 28(28.02) |
| 960 | 21.56 | 9.497 | 5.51 | 0.55 | <fg Star> | 2, 13, 14, 20, 22, 24, 27, 28(21.97) |
| 1 180 | 16.48 | 17.16 | 7.53 | 0.40 | <XRB> | 1, 2, 13, 20, 22(v), 27, 28(13.01) |
| 378 | 16.21 | 9.39 | 6.83 | 0.98 | <XRB> | 26, 27 |
| 714 | 14.89 | 13.77 | 10.35 | 0.68 | <fg Star> | |
| 748 | 14.45 | 13.86 | 3.62 | 0.23 | <SSS> | 1(t), 26, 27, 28(14.18) |
| 92 | 14.23 | 5.73 | 1.86 | 0.30 | <SSS> | |
| 814 | 13.66 | 7.98 | 4.94 | 0.56 | <XRB> | 2, 22(v), 26, 27, 28(15.76) |
| 1 006 | 11.30 | 14.34 | 1.44 | 0.08 | <SSS> | 3(t, 51), 20 , 24, 27, 28(10.70) |
| 542 | 10.90 | 3.26 | 2.50 | 0.69 | <XRB> | |
| 1 016 | 10.46 | 20.66 | 6.37 | 0.26 | <XRB> | 1, 2, 12 ,13, 20, 22, 27, 28(11.69) |
| 1 144 | 10.23 | 10.53 | 1.54 | 0.12 | <SSS> | 3(t, 38), 27, 28(10.05) |
| 1 034 | 10.11 | 28.93 | 9.81 | 0.28 | <XRB> | 2, 20, 22, 24, 28(10.24) |
| 1 099 | 9.95 | 4.50 | 5.12 | 1.01 | <hard> | 26, 27 |
| 904 | 9.16 | 8.65 | 8.55 | 0.84 | <hard> | 13, 27 |
| 872 | 9.13 | 17.16 | 7.31 | 0.38 | <GlC> | 1(sv,burst), 2, 8, 20 , 22(v), 27, 28(7.48) |
| 1 422 | 9.06 | 2.99 | 1.87 | 0.55 | <hard> | |
| 1 183 | 7.66 | 11.93 | 8.43 | 0.57 | <hard> | 1, 13, 14, 27 |
| 422 | 7.23 | 9.65 | 2.10 | 0.16 | <hard> | 14 |
| 823 | 7.16 | 28.29 | 20.25 | 1.30 | <GlC> | 1(sv), 2, 5, 12, 15(v),16, 20, 22(v), 27, 28(6.45) |
| 1 250 | 6.94 | 2.80 | 0.89 | 0.27 | <SSS> | |
| 398 | 6.79 | 2.93 | 1.79 | 0.52 | <hard> | 14, 27 |
| 1 266 | 6.67 | 7.54 | 2.37 | 0.24 | GlC | 5, 27, 28(8.27) |
| 975 | 6.58 | 7.98 | 1.76 | 0.35 | GlC | 1, 2, 5, 14, 16, 20, 21, 22(v), 27 |
| 522 | 6.47 | 6.62 | 2.21 | 0.26 | <hard> | |
| 805 | 6.22 | 3.66 | 0.96 | 0.21 | <hard> | |
| 916 | 6.21 | 3.73 | 2.00 | 0.44 | <hard> | |
| 862 | 6.17 | 5.33 | 1.38 | 0.20 | GlC | 2, 5, 16, 22, 27, 28(5.35) |
| 1 124 | 6.04 | 12.93 | 5.73 | 0.23 | <GlC> | 1, 2, 20, 21, 22(v), 27 |
| 430 | 5.98 | 4.95 | 1.01 | 0.16 | <hard> | |
| 1 825 | 5.57 | 6.11 | 2.97 | 0.39 | fg Star | 14, 27 |
| 1 494 | 5.55 | 4.06 | 0.95 | 0.18 | <hard> | 27 |
| 624 | 5.54 | 7.58 | 1.49 | 0.13 | <fg Star> | |
| 1 167 | 5.44 | 7.69 | 3.22 | 0.57 | <hard> | 1, 2, 20, 21, 22(v), 27 |
| 1 450 | 5.44 | 6.51 | 2.24 | 0.24 | <hard> | |
| 66 | 5.39 | 3.80 | 2.31 | 0.49 | <hard> | |
| 1 655 | 5.34 | 4.72 | 1.50 | 0.24 | <hard> | |
| 964 | 5.30 | 6.36 | 1.09 | 0.12 | <hard> | |
| 226 | 5.28 | 3.29 | 0.56 | 0.13 | <hard> | |
| 244 | 5.27 | 9.08 | 3.33 | 0.28 | <hard> | 14, 26, 27 |
| 1 361 | 5.21 | 3.12 | 1.36 | 0.34 | <hard> | 28 |
| 933 | 5.19 | 4.99 | 8.73 | 1.30 | GlC | 1(sv), 5, 12, 13, 26, 27 |
| 1 366 | 5.13 | 3.02 | 1.05 | 0.27 | <hard> | |

Notes:

‡ : maximum XID flux and error in units of $1\times10^{-14}$ erg cm$^{-2}$ s$^{-1}$ or maximum absorbed 0.2–4.5 keV luminosity and error in units of $7.3\times10^{35}$ erg s$^{-1}$

+ : class according to Table 7.3

† : 1: Trudolyubov et al. (2006b), 2: Voss & Gilfanov (2007), 3: Williams et al. (2006b), 4: Trudolyubov et al. (2006a), 5: Trudolyubov & Priedhorsky (2004), 6: Williams et al. (2006a), 7: Williams et al. (2005b), 8: Pietsch & Haberl (2005), 9: Kong et al. (2003b), 10: Trinchieri & Fabbiano (1991), 11: Collura et al. (1990), 12: Primini et al. (1993), 13: Supper et al. (1997), 14: Supper et al. (2001), 15: Osborne et al. (2001), 16: Di Stefano et al. (2002), 17: Fan et al. (2005), 18: Pietsch et al. (2007), 19: Garcia et al. (2000), 20: Kaaret (2002), 21: Williams et al. (2004a), 22: Kong et al. (2002b), 23: Williams et al. (2005a), 24: Di Stefano et al. (2004), 25: Barnard et al. (2003b), 26: Shaw Greening et al. (2009), 27: Pietsch et al. (2005b), 28: Stiele et al. (2008b), 29: Trudolyubov et al. (2002a) ; t: transient, v: variable, sv: spectrally variable, r: recurrent, d: dipping, z: Z-source candidate; BH: black hole, XRN: X-ray nova, XRT: X-ray transient, LMXB: low mass X-ray binary, NS: neutron star; numbers indicate the variability given by the corresponding paper

Figure 7.7 shows the variability factor plotted versus maximum detected XID flux. Apart from XRBs or XRBs in GlCs or candidates of these source classes, which were selected based on their variability, there are a few SSS candidates showing pronounced temporal variability. The sources classified or identified as AGN, background galaxies or galaxy clusters all show $F_{\rm var} < 4$. Most of the foreground stars show $F_{\rm var} < 4$.

Out of the 1 443 examined sources, I found 317 sources with a significance for variability $> 3.0$. These are 182 additional sources compared with Chap. 6. For bright sources it is much easier to detect variability than for faint sources, because the range between the maximum observed flux and the detection limit is larger. Therefore the significance of the variability declines with decreasing flux. This can be seen from the sources that are marked in green in Fig. 7.7.

Table 7.6 lists all sources with a variability factor larger than five. The sources are sorted in descending order with respect to their variability factors. Table 7.6 gives the source number (Col. 1), maxima of flux variability (2) and maxima of the significance parameter (3). The next columns (4, 5) indicate the maximum observed flux and its error. Column 6 contains the class of the source. Sources with $F_{\rm var} \geq 10$ that are not already classified as SSSs or foreground stars, are classified as XRBs. Time variability can also be helpful to double check an SNR candidate classification. In case of variability the SNR classification must be rejected, and if an optical counterpart is detected, the source will be re-classified as foreground star candidate. Column 7 contains references to the individual sources in the literature. In some cases the

**Table 7.7:** Sources with maximum XID flux larger than $8\times10^{-13}$ erg cm$^{-2}$ s$^{-1}$, a statistical significance of variability larger than 10 and a flux variability smaller than 5, ordered by flux.

| Source | fvar | svar | fmax‡ | efmax‡ | class+ | Comment† |
|---|---|---|---|---|---|---|
| (1) | (2) | (3) | (4) | (5) | (6) | (7) |
| 966 | 1.63 | 49.01 | 46.73 | 0.59 | XRB | 1(sv,z), 2, 10(v), 12(v), 13, 14, 20, 22(v), 25(LMXB), 27, 28(1.56) |
| 877 | 3.13 | 49.13 | 16.06 | 0.20 | <hard> | 1(sv), 2, 10(v), 12(v), 13, 14, 20(v), 22(v), 27, 28(3.05) |
| 745 | 2.43 | 26.89 | 12.65 | 0.18 | AGN | 13, 14 |
| 1 157 | 1.32 | 11.10 | 9.87 | 0.25 | GlC | 1(sv), 2, 5, 10, 12, 13, 14, 20, 21, 22(v), 27, 28(1.37) |
| 1 060 | 2.13 | 30.00 | 9.04 | 0.14 | <XRB> | 1(sv), 2, 10, 12, 13, 14, 20(v, NS-LMXB), 22(v), 27 |
| 1 171 | 4.14 | 18.86 | 9.02 | 0.41 | GlC | 1(d,sv), 2(t, 53.4), 5, 10, 12, 13, 14, 16, 20, 22, 27, 28(2.47) |
| 1 116 | 3.76 | 51.98 | 8.16 | 0.10 | GlC | 1(sv), 2(t, 58.6), 3(t, 33), 5, 10, 12, 13, 14, 16, 20, 21, 22(v,t), 27 |

Notes:

‡ : maximum XID flux and error in units of $1\times10^{-13}$ erg cm$^{-2}$ s$^{-1}$ or maximum absorbed 0.2–4.5 keV luminosity and error in units of $7.3\times10^{36}$ erg s$^{-1}$

+ : class according to Table 7.3

† : for comment column see Table 7.6

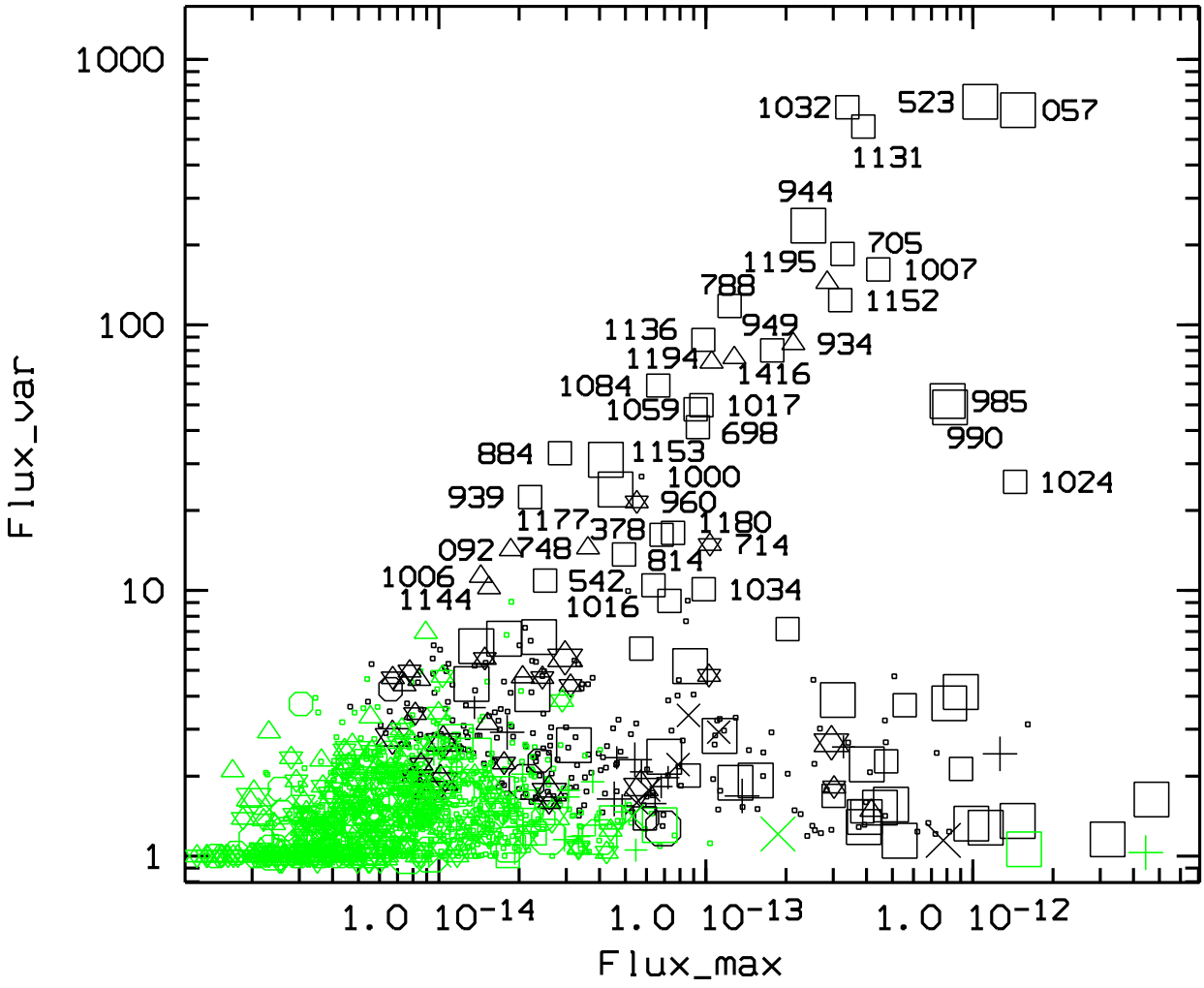


**Figure 7.7:** Variability factor of sources from the XMM LP-total catalogue in the 0.2–4.5 keV band derived from average fluxes of the *XMM-Newton* EPIC observations plotted versus maximum detected XID flux (erg $cm^{-2}$ $s^{-1}$). Source classification is indicated: Foreground stars and candidates are marked as big and small stars, AGN and candidates as big and small crosses, background galaxies and galaxy clusters as big "X" and their candidates as small "X", SSS candidates as triangles, SNRs and candidates as big and small hexagons, GlCs and XRBs as big squares and their candidates as small squares. Sources with a statistical significance for the variability below 3 are marked in green.

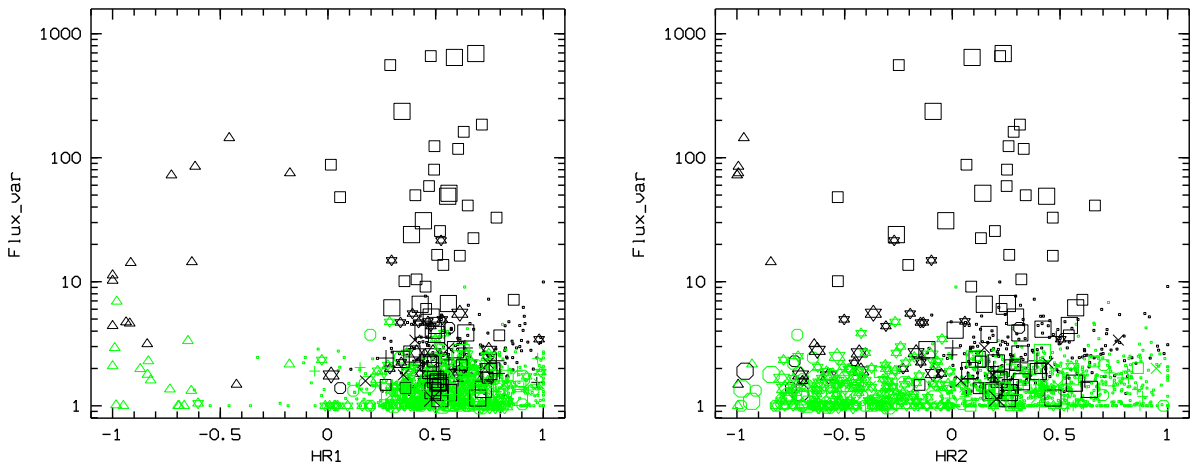


**Figure 7.8:** Variability factor of sources from the XMM LP-total catalogue in the 0.2–4.5 keV band (derived from the average fluxes of the *XMM-Newton* EPIC observations) plotted versus HR1 in the left panel, and HR2 in the right panel. For source classification see Fig. 7.7. Sources with a statistical significance of the variability below 3 are marked in green.

reference provides information on the temporal behaviour and a more precise classification (see brackets). The numbers given in connection with Voss & Gilfanov (2007) and Williams et al. (2006b) are the *Chandra* derived variability factors obtained in these papers. From the 69 sources listed in Table 7.6 (34 in addition to Table 6.6), ten show a flux variability larger than 100. With a flux variability factor $>690$ source N$^{\underline{o}}$ 523 is the most variable source in our sample. Source N$^{\underline{o}}$ 57 has the largest significance of variability, with a value of $\approx$97. In only 33 sources is the significance of variability below 10, for 15 of them it is even below 5. Thirty-three sources are classified as XRBs or XRB candidates, eight of them are located in globular clusters. Nine are SSS candidates.

Table 7.7 lists all "bright" sources with a maximum XID flux larger than $8\times10^{-13}$ erg cm$^{-2}$ s$^{-1}$ and a flux variability smaller than five, giving the same information as in Table 7.6. All seven sources listed in Table 7.7 (three in addition to Table 6.7) have a significance of variability $>10$. Apart from two sources, they are XRBs (three in globular clusters) or XRB candidates. The most luminous source in our sample is source N$^{\underline{o}}$ 966 with an absorbed 0.2–4.5 keV luminosity of $\approx3.3\times10^{38}$ erg s$^{-1}$.

Figure 7.8 shows the relationship between the variability factor and the hardness ratios HR1 and HR2, respectively. The hardness ratios are taken from Table 7.2. The HR1 plot shows that the sample of highly variable sources includes SSS and XRB candidates, which occupy two distinct regions in this plot (see also Haberl & Pietsch 1999b, for the LMC). The SSSs marked by triangles, appear on the left hand side, while the XRBs or XRB candidates have much harder spectra, and appear on the right.

Individual sources are discussed in the Chap. 9.

# Chapter 8

# *XMM-Newton* Large Program: Log N-Log S relation

## 8.1 Introduction

Compared to number counts analyses in deep fields, like the COSMOS field (Scoville et al. 2007; Hasinger et al. 2007) or the Lockman hole (*cf.* Brunner et al. 2008), the number counts analysis of a nearby galaxy is complicated by absorption and extinction of radiation within the galaxy. To quantify these effects I derived the fraction of X-ray absorption in the 0.5–2.0 keV and 2.0–10.0 keV energy bands using WebPIMMS

**Table 8.1:** Absorption of X-ray radiation (percentage) for different column densities, spectral models and energy bands.

| | 0.5-2.0 keV | | | | 2.0-10.0 keV | | | |
|---|---|---|---|---|---|---|---|---|
| $N_{\rm H}$ | $\Gamma = 1.7$ | | $k_{\rm B}T = 2.2\,{\rm keV}$ | | $\Gamma = 1.7$ | | $k_{\rm B}T = 2.2\,{\rm keV}$ | |
| $[{\rm cm}^{-2}]$ | PN | MOS | PN | MOS | PN | MOS | PN | MOS |
| 5.00E+19 | 1.8 | 1.4 | 1.8 | 1.3 | 0.1 | 0.1 | 0.1 | 0.1 |
| 8.00E+19 | 2.9 | 2.2 | 2.8 | 2.1 | 0.1 | 0.1 | 0.2 | 0.2 |
| 1.00E+20 | 3.6 | 2.7 | 3.5 | 2.6 | 0.2 | 0.1 | 0.2 | 0.2 |
| 2.00E+20 | 7.1 | 5.3 | 6.9 | 5.1 | 0.3 | 0.3 | 0.4 | 0.4 |
| 4.00E+20 | 13.4 | 10.1 | 13.1 | 9.8 | 0.6 | 0.6 | 0.8 | 0.8 |
| 7.00E+20 | 21.7 | 16.5 | 21.2 | 16.1 | 1.1 | 1.1 | 1.5 | 1.4 |
| 8.00E+20 | 24.2 | 18.5 | 23.7 | 18.0 | 1.2 | 1.2 | 1.7 | 1.6 |
| 1.00E+21 | 28.8 | 22.2 | 28.2 | 21.7 | 1.6 | 1.5 | 2.1 | 2.0 |
| 2.00E+21 | 46.3 | 37.0 | 45.4 | 36.2 | 3.1 | 3.1 | 4.1 | 3.9 |
| 4.00E+21 | 65.3 | 55.3 | 64.3 | 54.3 | 6.0 | 5.9 | 8.0 | 7.7 |
| 6.00E+21 | 75.1 | 66.2 | 74.2 | 65.2 | 8.8 | 8.7 | 11.7 | 11.2 |
| 8.00E+21 | 81.0 | 73.4 | 80.2 | 72.5 | 11.4 | 11.3 | 15.2 | 14.5 |
| 1.00E+22 | 85.0 | 78.5 | 84.2 | 77.8 | 14.0 | 13.8 | 18.5 | 17.7 |
| 2.00E+22 | 93.9 | 91.1 | 93.6 | 90.7 | 24.9 | 24.8 | 32.6 | 31.3 |
| 4.00E+22 | 98.5 | 97.8 | 98.4 | 97.7 | 40.4 | 40.6 | 51.9 | 50.2 |
| 6.00E+22 | 99.5 | 99.3 | 99.5 | 99.3 | 50.7 | 51.3 | 63.8 | 62.3 |

(v3.9j), and the HI column densities given in Braun et al. (2009). A copy of Braun et al.'s corrected HI map is shown in Fig. 8.1. As background objects I assume either an AGN, modelled by a power-law spectrum with $\Gamma = 1.7$, or a "normal" galaxy, modelled by a thermal bremsstrahlung spectrum with $k_{\mathrm{B}}T = 2.2\,\mathrm{keV}$ (Fabbiano & Trinchieri 1987). The results are shown in Table 8.1. From Fig. 8.1, we see that most parts of M 31 have an $N_{\mathrm{H}} \lesssim 10^{22}\,\mathrm{cm}^{-2}$, and thus the absorption in the 2.0–10.0 keV (hard) band is small to modest, with values of about 15% (AGN) to $\sim$20% (galaxy). However, in the 0.5–2.0 keV (soft) band, absorptions of about 80% are reached. There are a few exceptions of regions of high HI column density ($N_{\mathrm{H}} > 10^{22}\,\mathrm{cm}^{-2}$), which are located in star forming regions in the 10 kpc dust ring of M 31. In these regions absorption of $\sim$50%–60% in the hard band and nearly 100% in the soft band is found.

In summary, absorption effects are especially crucial in the soft energy band ($\lesssim 2\,\mathrm{keV}$). To minimise these effects the following analyses and considerations are limited to the 2–10 keV range, where mainly X-ray binaries and AGN are observed.

To study the population of XRBs in M 31, I assume that the contribution of background objects to the log N-log S relations can be obtained from the corresponding relations of the COSMOS survey (Cappelluti et al. 2007). As the distribution of galaxies is not homogeneous over the sky the log N-log S relation from the COSMOS survey is an approximation to the log N-log S relation of the background objects located in the field of M 31 (Gilfanov 2004).

**Figure 8.1:** Column density of HI in M 31. Those lines of sight with insufficient fit quality were assumed to have negligible opacity. For details see Braun et al. (2009). Taken from Braun et al. (2009).

## 8.2 Data analysis

To be able to use the log N-log S relation from the COSMOS field for the 2–10 keV band to estimate the contribution of background objects to the log N-log S relation from the M 31 field, the data analysis, presented in this section, followed the method described by Cappelluti et al. (2007) in their analysis of the COSMOS field.

The cleaning of the data is done in the same way as described in Sect. 5.2.2. It consists of screening for times of increased background, screening for additional bad or hot pixels and columns, and excluding the 7.2–7.6 keV and 7.8–8.2 keV energy bands[1] in the PN data. I started from astrometrically corrected event files, obtained from the procedure described in Sect. 5.2.5. To have a homogeneous sample, especially in terms of exposure time, the observations pointing on RX J0042.6+4115 and the short observation to the halo region (h4) were excluded from the analyses.

The next step was the creation of images, background images and exposure maps. Here the images were created in the 2–10 keV energy band with a pixel size of $4''$. For the PN detector, single and double events (PATTERN <= 4) were used, while for the MOS cameras all valid event patterns (PATTERN <= 12) were included. The images obtained from the PN detector are affected by the OoT events (*cf.* Sect. 4.2.2). That is why I created artificial OoT event files, which were filtered in the same way as the event files. Then OoT images were produced and subtracted from the PN event images. The reason for using this "subtraction" method here, is that it allows me to add the images of the PN and of both MOS detectors together. The images and background images were added using the `ftool` task `farith`. The exposure maps were added in a spectrally weighted way, applying the following formula:

$$\mathrm{EXP_{spw}} = \frac{\mathrm{EXP_{M1}} \times \mathrm{ECF_{M1}} + \mathrm{EXP_{M2}} \times \mathrm{ECF_{M2}} + \mathrm{EXP_{PN}} \times \mathrm{ECF_{PN}}}{\mathrm{ECF_{PN}} + \mathrm{ECF_{M1}} + \mathrm{ECF_{M2}}} \tag{8.1}$$

The ECF values for the three cameras were calculated in the same way as in Sect. 7.1.2 and can be found in Table 8.2. $\mathrm{EXP_{PN}}$, $\mathrm{EXP_{M1}}$, $\mathrm{EXP_{M2}}$ and $\mathrm{EXP_{spw}}$ denotes the PN, M1, M2 and spectrally weighted exposure maps, respectively.

As mentioned above I used a single energy band and added the images, background images and exposure maps of the three EPIC cameras to run the source detection algorithm simultaneously on all observations. In this way the contribution of flux from different observations to the same source is automatically taken into account. That allows us to detect fainter sources in the overlapping regions of two or more fields compared with the XMM LP-total catalogue. On the other hand, we have to accept that for transient sources we obtain an averaged flux determined over the whole exposure time at the position of the source, which is lower than the actual flux the source reaches during its bright state. The detection procedure is the same as in Sect. 5.2.4, but the detection threshold was set to six. All detected objects located on the diffraction spikes of bright sources were excluded from further investigations. To allow for statistical analyses, sources that were not detected by the analysis program were ignored, even if the sources were visible in the X-ray images.

## 8.3 Catalogue of hard sources (XMM LP-hard)

The catalogue of hard sources found in the field of M 31 (XMM LP-hard) is given in Table 8.3[2]. It contains 1 254 sources, including 24 sources flagged as foreground stars and seven extended sources.

Table 8.3 gives the source number (Col. 1), position of the source (2 to 8) with $3\sigma$ (99.73%) uncertainty radius (9), likelihood of existence (10) and integrated PN, MOS1 and MOS2 count rate and error (11,12)

[1] There is an intense complex due to Cu-K$\alpha$, Ni-K$\alpha$ and Zn-K$\alpha$ lines in the PN background (*cf.* Sect. 4.2.3).

[2] Table 8.3 is only available in electronic form on the attached CD. A description of the content of this table can be found in Appendix E.

**Table 8.2:** Count rate to energy conversion factors for PN, MOS 1 and MOS 2 thin and medium filters, derived for a power-law model, assuming a photon index of $\Gamma = 1.7$ and a foreground absorption of $N_{\rm H} = 7 \times 10^{20} {\rm cm}^{-2}$.

| Detector | Filter | B6 $(10^{11} {\rm cts\,cm^2\,erg^{-1}})$ |
|---|---|---|
| EPIC PN | thin | 1.25 |
| | medium | 1.25 |
| EPIC MOS1 | thin | 0.43 |
| | medium | 0.43 |
| EPIC MOS2 | thin | 0.45 |
| | medium | 0.44 |

and flux and error (13,14) in the 2.0–10.0 keV band. The integrated exposure (*i. e.* integrating the exposures of PN, MOS 1 and MOS 2) is given in Col. 15. Column 16 contains a flag, which indicates whether a source is extended (flag = 8) or identified as a foreground star or a foreground star candidate (flag = 4). The last column (17) gives the XMMM31 source name, which is identical with the one given in Table 7.2 if the source has a counterpart listed in that table. For those sources found to be extended, the extent (2) with error (3), and the likelihood of extent (4) is given in Table E.2. For the derivation of the log N-log S relations (see Sect. 8.4) only sources with flag = 0 were used.

The faintest source (#1 090) has a 2.0–10.0 keV band flux of $2.64 \times 10^{-15}$ erg cm$^{-2}$ s$^{-1}$, while the brightest source (#5) has a flux of $6.73 \times 10^{-12}$ erg cm$^{-2}$ s$^{-1}$. A distribution of the source fluxes is shown in Fig. 8.2.

A comparison of the XMM LP-hard catalogue to the XMM LP-total catalogue is provided in Sect. 9.1.5.

## 8.4 Log N-log S relations

### 8.4.1 Definition of examined regions

To examine the dependence of the log N-log S relation from the distance to the centre of M 31, five regions were defined, as shown in Fig. 8.3. The innermost region has a radius of 5.′0 and corresponds to the bulge of M 31 (SHP97). The second region roughly corresponds to the inner disc of M 31, excluding the bulge. The third region is defined in a way, that on one hand the region roughly follows the dust ring of M 31, located at about 10 kpc – well visible at *e. g.* 60 $\mu$m –, and on the other hand corresponds to the inner part of the outer disc of M 31. The fourth region comprises the remaining area of the outer disc that is located within the corrected $D_{25}$ ellipse (de Vaucouleurs et al. 1991). The outermost (fifth) region contains the observed area located beyond the $D_{25}$ ellipse. All regions have the common centre RA = $00^h\,42^m\,44\overset{\rm s}{.}326$, Dec = $+41^\circ\,16'\,08\overset{''}{.}54$ and, apart from the bulge region, a position angle of 38° (Huchtmeier & Richter 1989; Huchtmeier et al. 2008). Table 8.4 gives the lower and upper limits of the semi-major ($a$) and semi-minor ($b$) axis, respectively, for each region. For instance the inner disc region is defined as the elliptical annulus that is limited by the following two ellipses: an outer one with $a = 0\overset{\circ}{.}48$ and $b = 0\overset{\circ}{.}154$, and an inner one with $a = 0\overset{\circ}{.}083$ and $b = 0\overset{\circ}{.}083$. For the bulge region no lower limit is present (*i. e.* it reaches till the centre of the galaxy), while for the region beyond the $D_{25}$ ellipse the upper limit is given by the rim of the observed field.

In addition I also divided M 31 along the minor axis (in a southern and a northern part) and along the

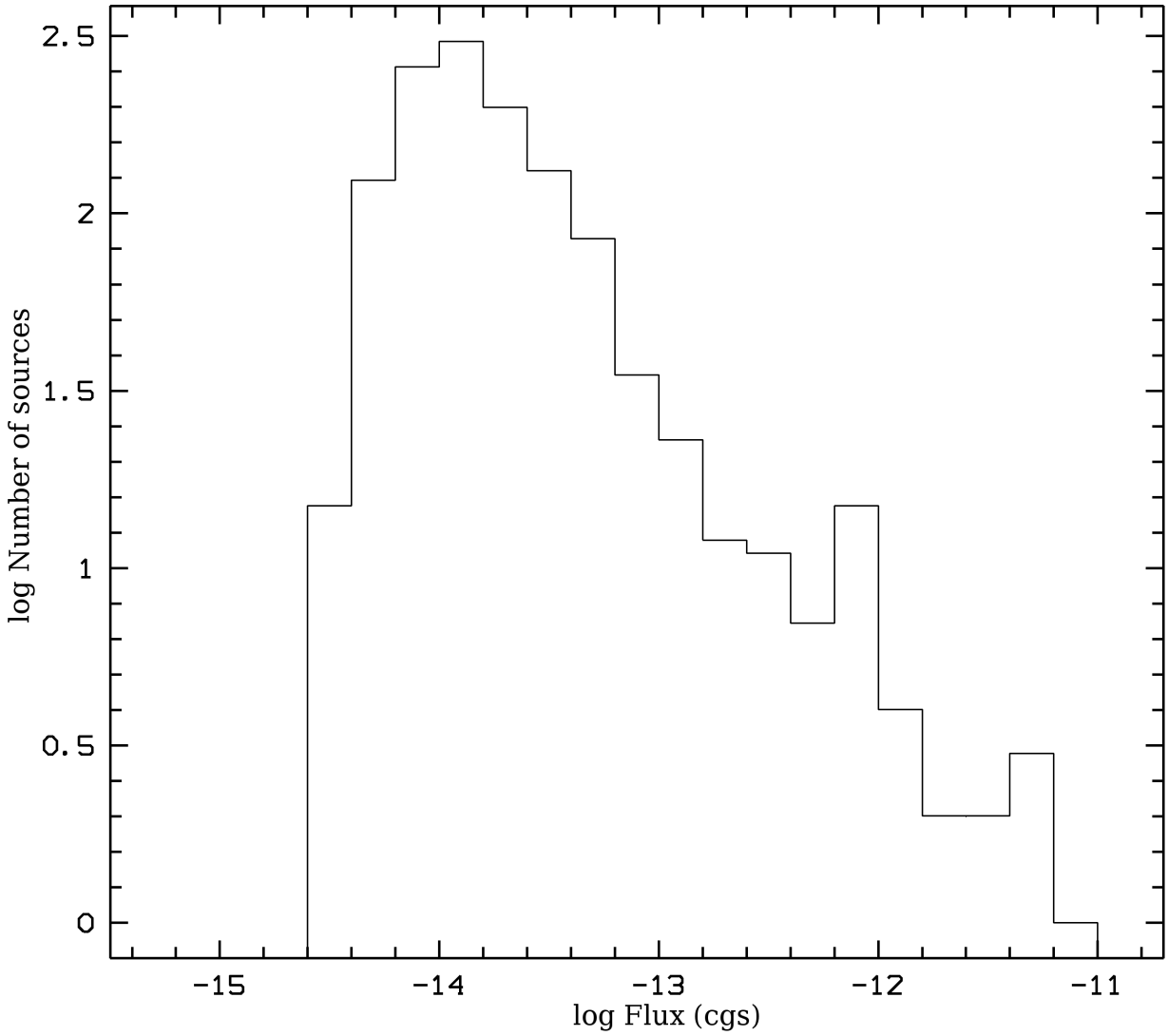


**Figure 8.2:** Distribution of the source fluxes in the 2.0–10.0 keV band. The diagram shows the number of sources per flux bin, plotted versus the flux, using logarithmic scales.

**Table 8.4:** Log N-log S regions

| Region | | semi-major axis ($a$) | semi-minor axis ($b$) |
|---|---|---|---|
| No. | Name | deg | deg |
| I | bulge | $a < 0.083$ | $b < 0.083$ |
| II | inner disc | $0.083 < a < 0.480$ | $0.083 < b < 0.154$ |
| III | dust ring | $0.480 < a < 0.906$ | $0.154 < b < 0.290$ |
| IV | outer disc | $0.906 < a < 1.278$ | $0.290 < b < 0.413$ |
| V | beyond $D_{25}$ | $a > 1.278$ | $b > 0.413$ |

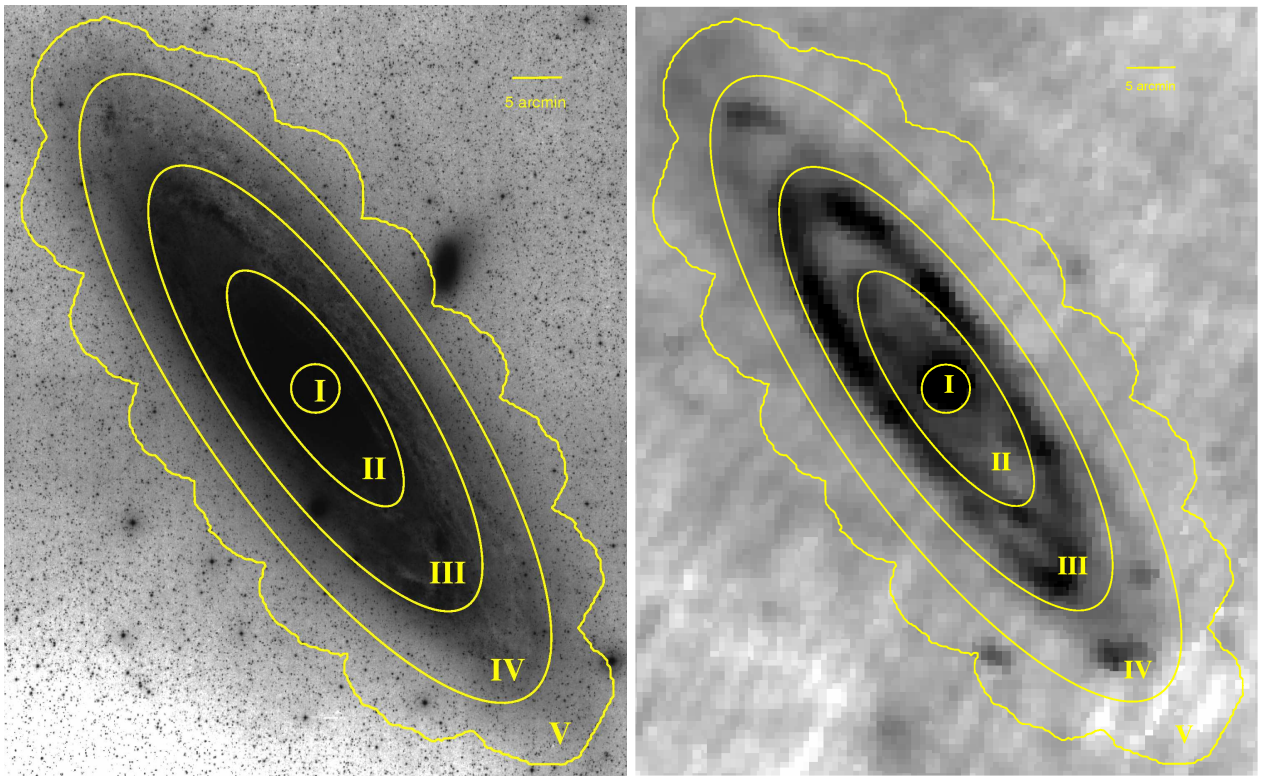


**Figure 8.3:** The five regions defined to examine the dependence of the log N-log S relation from the distance to the centre of M 31. They are over-plotted on an optical (left panel) and an IRAS 60 $\mu$m (right panel) image, respectively. The innermost region (bulge) has a radius of 5′, the outermost ellipse is the $D_{25}$ ellipse of M 31.

major axis (in an eastern part and a western part), respectively, to examine the dependence of the log N-log S relation from those regions (excluding the bulge).

### 8.4.2 Analysis

In essence the derivation of a log N-log S relation merely requires taking all the objects above a certain flux in the sample and dividing them by the volume surveyed for these objects. Unfortunately, the procedure is more complex than it might at first seem, because the volume depends on the limiting flux and hence exposure time. Therefore it is first necessary to estimate the completeness function of our survey, known also as the sky coverage. I constructed the sky coverage ($\Omega$) versus flux relation (Fig. 8.4) from the EPIC sensitivity map, calculated with the `SAS` task `esensmap`. Input files are the exposure maps, background images and detection masks created and used for source detection.

Once the sky coverage is known, the cumulative source number counts can be computed using the equation

$$N\,(>S) = \sum_{i=1}^{N_s} \frac{1}{\Omega_i} \mathrm{deg}^{-2}, \tag{8.2}$$

where $N_s$ is the total number of detected sources in the field with fluxes greater than $S$, and $\Omega_i$ is the sky

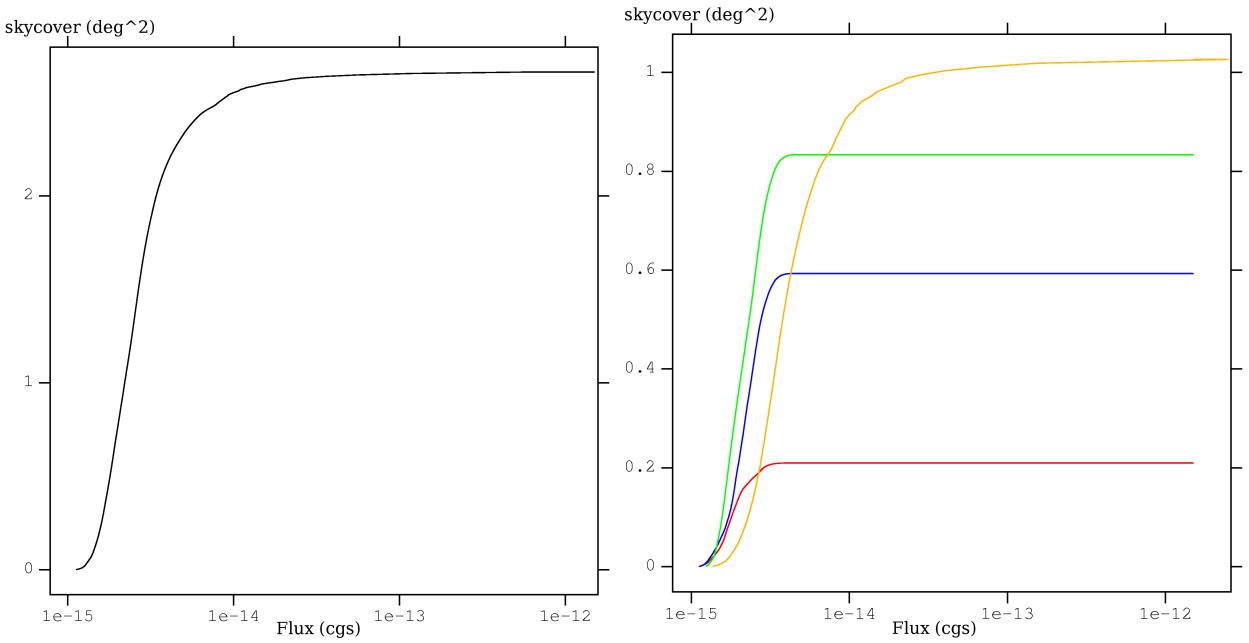


**Figure 8.4:** Sky coverage versus flux relation for the whole field (without bulge), and the regions defined in Fig. 8.3. The left panel shows the relation for the whole field without bulge, while the right panel shows the relation for the inner disc (red), dust ring (blue), outer disc (green) and beyond $D_{25}$ (orange) regions.

coverage associated with the flux of the $i$th source. The variance of the source number counts is defined as

$$\sigma_i^2 = \sum_{i=1}^{N_s} \left( \frac{1}{\Omega_i} \right)^2. \tag{8.3}$$

In this way I obtained the cumulative log N-log S relations (CNCs) for all sources located in the observed field. These sources are the sources belonging to M 31, as well as the background sources located behind the galaxy. Remember that we have excluded the foreground stars. Hence the contribution of foreground sources to the CNCs should be negligible. To obtain the CNCs for the sources of M 31 it is necessary to subtract the CNC of the background sources. The background log N-log S relation was taken from the COSMOS survey (Cappelluti et al. 2009) and extrapolated to higher fluxes, assuming

$$N\left(>S\right) = AS^{-\alpha}, \tag{8.4}$$

where $\alpha = 1.43 \pm 0.10$ and $A = 266 \pm 11$ (Cappelluti et al. 2007, 2009).

The background corrected cumulative log N-log S relations can be obtained from

$$N\left(>S\right)_{\rm m31} = N\left(>S\right) - N\left(>S\right)_{\rm bg} \tag{8.5}$$

where $N\left(>S\right)_{\rm bg}$ is the assumed number of background sources with fluxes greater than $S$, and $N\left(>S\right)_{\rm m31}$ is the obtained number of sources of M 31 with fluxes greater than $S$.

From Eq. 8.5 the background corrected differential log N-log S relations can be derived with (Kim et al. 2007a):

$$\left.\frac{dN_{\rm m31}}{dS}\right|_i = -\frac{N_{\rm m31\,i+1} - N_{\rm m31\,i}}{S_{i+1} - S_i}. \tag{8.6}$$

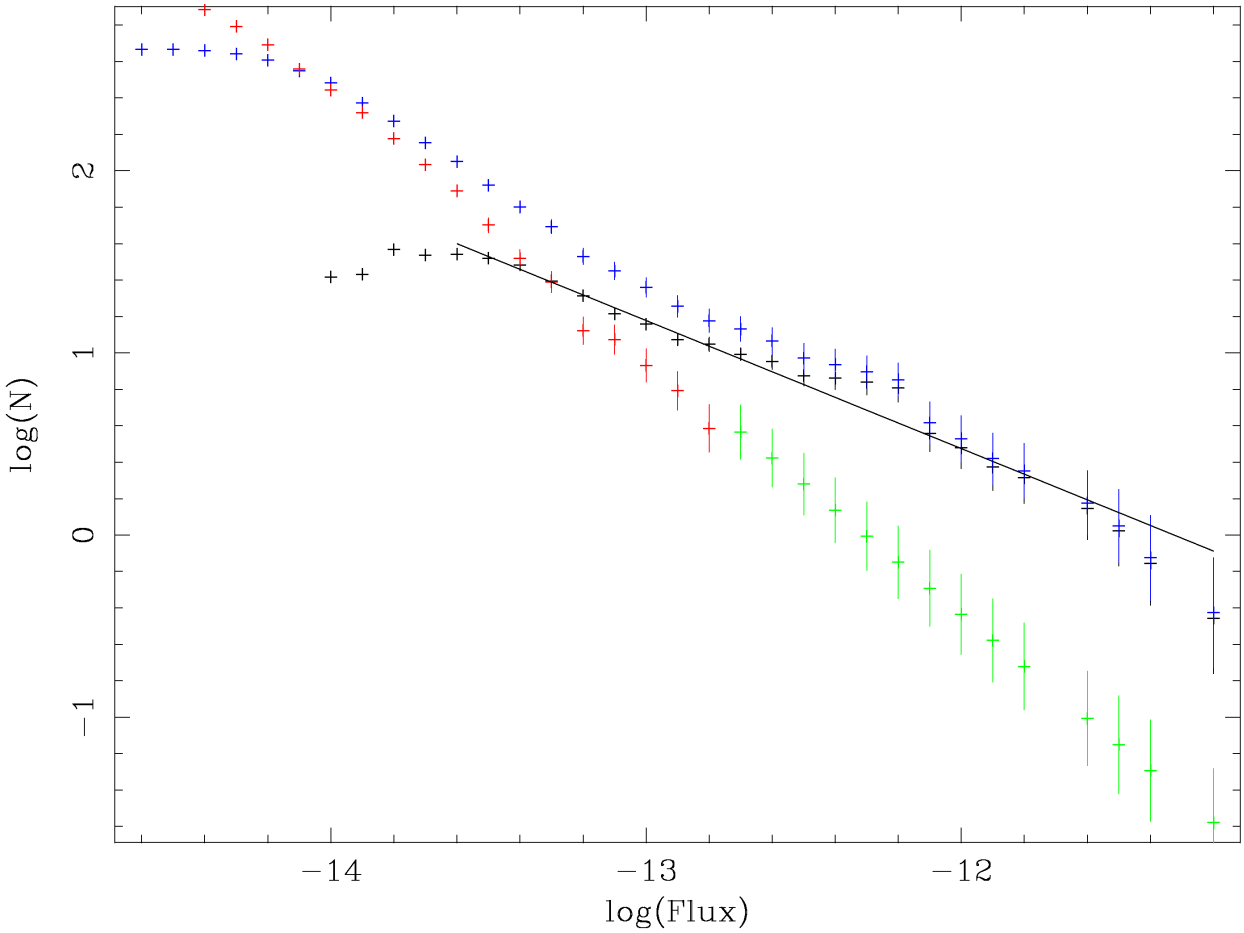


**Figure 8.5:** Cumulative X-ray log N-log S relation (blue), background CNC (red (observed) and green (extrapolated)) and the background corrected CNC (black) for the whole galaxy. The solid line displays the fit to the background corrected CNC. The slope is 0.70±0.03.

Assuming that the cumulative log N-log S relation can be described with Eq. 8.4, the differential log N-log S relation is given by:

$$\frac{dN}{dS} = -A\alpha S^{-\alpha-1}. \tag{8.7}$$

In the following section the slopes of the cumulative log N-log S relations are given.

### 8.4.3 Results

In the analysis of the log N-log S relations, the bulge region was omitted. A comparison of *Chandra* and *XMM-Newton* observations of that region shows that, due to the larger point spread function, *XMM-Newton* cannot resolve all individual sources. Thus the number of sources and the derived source fluxes are biased.

Figure 8.5 shows the derived CNC (blue), background CNC (red (observed) and green (extrapolated)) and the background corrected CNC (black) for the whole galaxy. From the intersection of the derived CNC with the background CNC we can estimate the flux below which the derived CNC becomes incomplete. This limit is $\sim 8\times10^{-15}$ erg cm$^{-2}$ s$^{-1}$ or $\sim 6\times10^{35}$ erg s$^{-1}$ (2.0–10.0 keV). Assuming the source spectrum used to derive the ECF values (*cf.* Table 8.2), this limiting luminosity corresponds to $\sim 1\times10^{36}$ erg s$^{-1}$ in the 0.3–10.0 keV band. Completeness limits of previous studies, which only covered selected parts of M 31, but

also included source fluxes below 2 keV, are $\sim 10^{36}$ erg s$^{-1}$ (Trudolyubov et al. 2002b; Kong et al. 2003a, SBK2009). The energy range used for source detection was 0.3–7 keV in Kong et al. (2003a), 0.3–10 keV in SBK2009, and not given in Trudolyubov et al. (2002b), who stated that they followed the analysis method described in Shirey et al. (2001), where the 0.3–12 keV band was used. This means that the completeness limits of my study is comparable with the limits of these previous studies, which is not surprising as the previous studies are also based on *Chandra* and *XMM-Newton* observations. The studies by SBK2009 and Trudolyubov et al. (2002b), who used *XMM-Newton* observations that cover (part of) the major axis of M 31, had similar integration times as used in my study. Each of the fields studied in Kong et al. (2003a) was observed three times with *Chandra* ACIS-S, where one observation had an exposure of $\sim$15 ks. The difference in my study compared to previous studies, is the large spatial coverage of M 31. The background corrected CNC flattens in the range of 3–4$\times 10^{-14}$ erg cm$^{-2}$ s$^{-1}$ or 2–3$\times 10^{36}$ erg s$^{-1}$. At even lower fluxes the cumulative number of sources decreases with decreasing flux. This behaviour is totally unexpected for a cumulative log N-log S relation. Assuming that the number of background sources as well as the number of sources of M 31 increase with decreasing flux the cumulative number of sources should keep raising with fainter and fainter limiting flux. A flattening could imply that most of the sources of M 31 in our sample emit radiation at fluxes above 3–4$\times 10^{-14}$ erg cm$^{-2}$ s$^{-1}$, which means that the examined source sample starts to be dominated by background sources below that flux. The decreasing number of sources clearly indicates that the contribution of background sources is overestimated at these fluxes. There are several possible explanations for the discrepancy between the assumed and the actual number of background sources. First, the normalisation of the background CNC from the COSMOS field might differ from that of the local background CNC in the field of M 31. Unfortunately, it is not possible to determine the actual value for the field of M 31, as such a determination will always be affected by the presence of the galaxy. The estimation of the background log N-log S relation might be improved by using deep observations of fields close to M 31 that only contain background sources and foreground stars to adjust the normalisation from the COSMOS field. However it is a demanding task to select these fields, as the globular cluster system of M 31 is very extended. It is also questionable whether $\gtrsim$100 ks of observation time would be approved to observe those fields, as the background contribution derived from these fields would still be only an approximation of the real background behind M 31. Second, the effects of absorption of X-rays from background objects by the interstellar medium of M 31, which were neglected so far as they reduce the flux in the 2.0–10.0 keV band by a few percent only (*cf.* Table 8.1), might become important for fluxes near the detection limit. There, a small reduction of the flux can bring the source flux below the detection threshold and hence the source is not detected. Third, faint background sources located close to bright sources of M 31 or behind regions of X-ray emitting gas might not be detected, due to the limiting conditions imposed by the detectors. To minimise the effects of the uncertainty in the number of background sources the following considerations are limited to fluxes above the flattening.

Going from faint to brighter luminosities, the background corrected CNC flattens at $\sim$2.3$\times 10^{37}$ erg s$^{-1}$ ($\sim$3.2$\times 10^{-13}$ erg cm$^{-2}$ s$^{-1}$) and steepens again at $\sim$5.8$\times 10^{37}$ erg s$^{-1}$ ($\sim$8$\times 10^{-13}$ erg cm$^{-2}$ s$^{-1}$). This feature was also reported in SBK2009 (*cf.* Fig. 3 of their paper). Given that SBK2009 determined the source fluxes from spectral fits to the individual sources, whereas I used fluxes derived with `emldetect` and assuming the same spectrum for all sources, the observed "bump" in the CNC seems not to be an artefact resulting from the adopted method, but an inherent property of the source population of M 31. Possible explanations for this "bump" are: (1) an independent source population, which only contains sources in the flux range $\sim$3.2–8$\times 10^{-13}$ erg cm$^{-2}$ s$^{-1}$, or (2) an excess of sources in the XRB population of M 31 in that flux range.

To estimate the slope of the background corrected CNC I fitted the differential log N-log S relation. The best fit slope (of the CNC above 3.2$\times 10^{-14}$ erg cm$^{-2}$ s$^{-1}$) is $\sim$0.7, which lies in the range expected for spiral galaxies ($\alpha \sim$0.6–0.8 Colbert et al. 2004, *cf.* also Sect. 2.4).

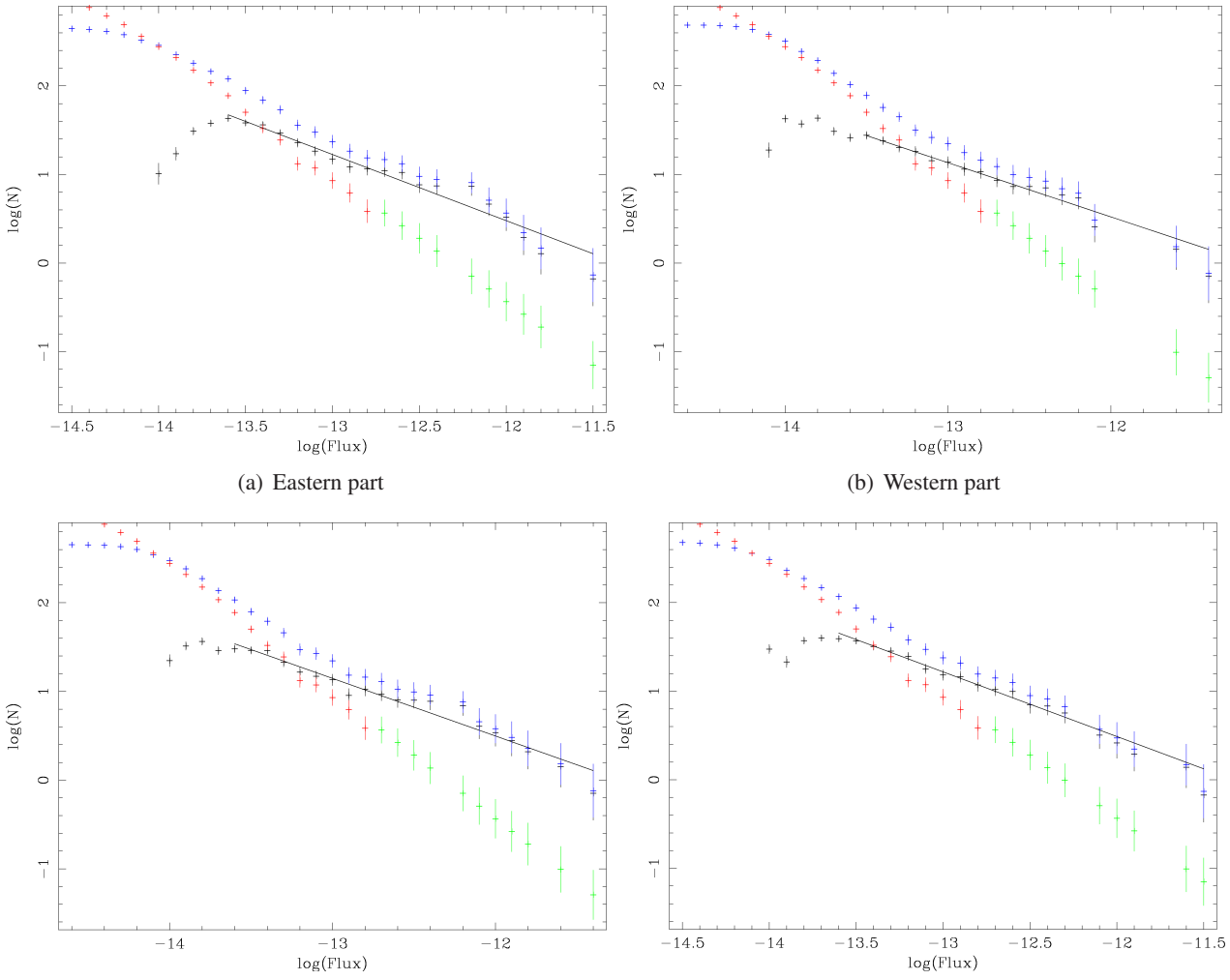


(a) Eastern part

(b) Western part

(c) Northern part

(d) Southern part

**Figure 8.6:** Cumulative X-ray log N-log S relation (blue), background CNC (red (observed) and green (extrapolated)) and the background corrected CNC (black) for the (a) eastern, (b) western, (c) northern and (d) southern part of the galaxy. The solid lines display the fits to the background corrected CNCs. The slopes are given in Table 8.5.

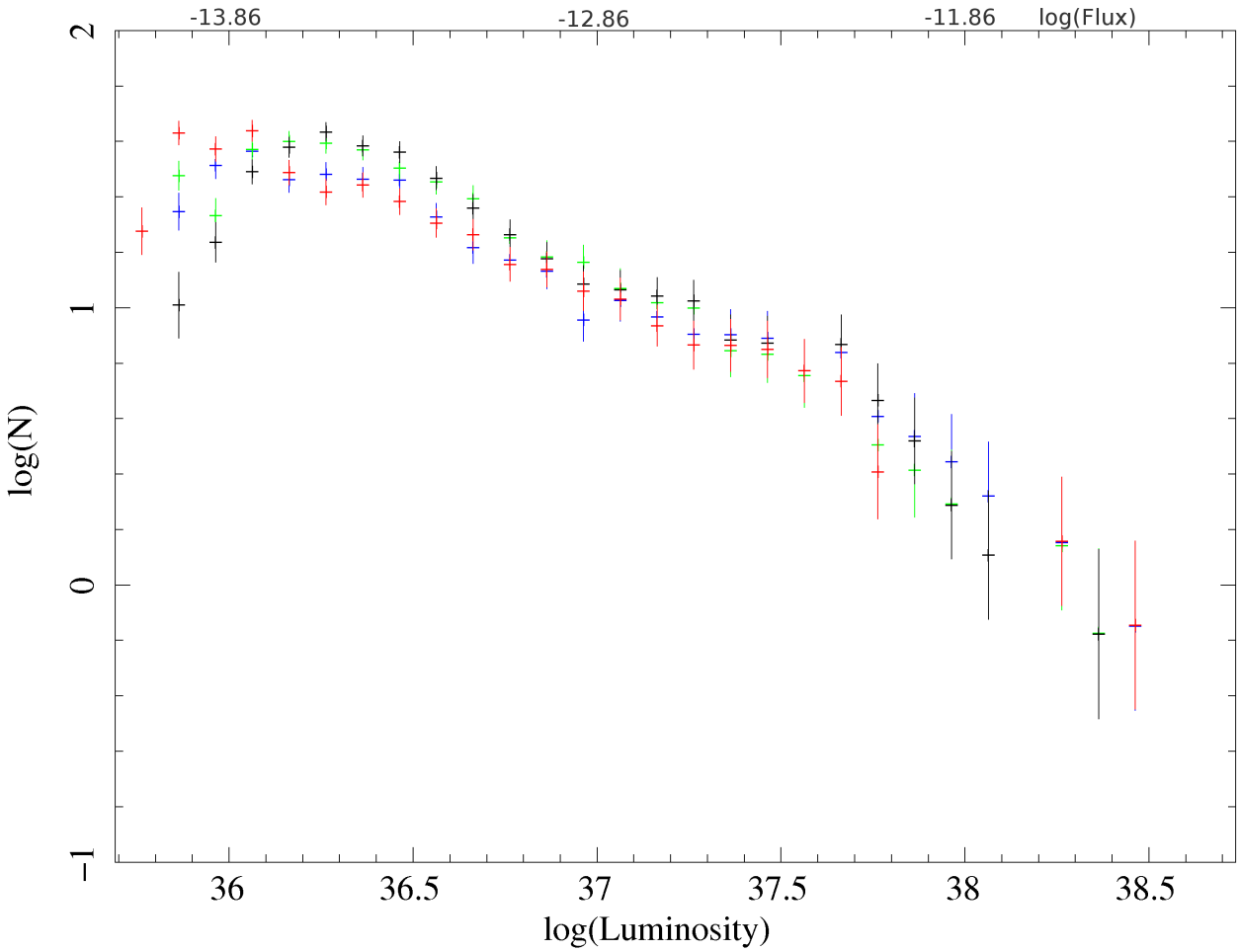


**Figure 8.7:** A comparison of the cumulative luminosity functions for the northern (blue) and southern (green) part and the eastern (black) and western (red) part of the disc.

Figure 8.6 shows the CNCs for the southern and northern part and for the eastern and western part of M 31. The solid lines display the fits to the background corrected CNCs of these four regions. Only data points with fluxes above $3.2\times10^{-14}$ erg cm$^{-2}$ s$^{-1}$ were used in the fits. The best fit slopes are given in Table 8.5. For the western and northern part, the slopes seem to be flatter than for the southern and eastern part. However the slopes of all four parts are consistent (within the errors) among each other and with the slope derived for the whole galaxy. Interestingly, the number of sources per deg$^2$ detected at the same flux limit (for fluxes above $3.2\times10^{-14}$ erg cm$^{-2}$ s$^{-1}$) is higher in the southern and eastern part compared with the northern and western part, although at higher fluxes the differences in the CNCs are within the errors (see Table 8.5). The "bump" that was detected in the CNC of the whole galaxy is also present in the CNCs of the eastern and northern part, while it is not visible in the western and southern parts. A comparison of the background corrected CNCs or cumulative luminosity functions (CLFs) of the four regions is shown in Fig. 8.7.

The cumulative log N-log S relations for the regions with increasing distance to the centre of M 31 are shown in Fig. 8.8. The best fit slopes are given in Table 8.6. Again, only data points with fluxes above $3.2\times10^{-14}$ erg cm$^{-2}$ s$^{-1}$ were used, where for the outer disc region and the region beyond the $D_{25}$ ellipse the data points for fluxes larger than $10^{-13}$ erg s$^{-1}$ were ignored. Grimm et al. (2003) discovered that populations of HMXBs can be characterised by a universal log N-log S relation with a slope of $\sim$0.6. In

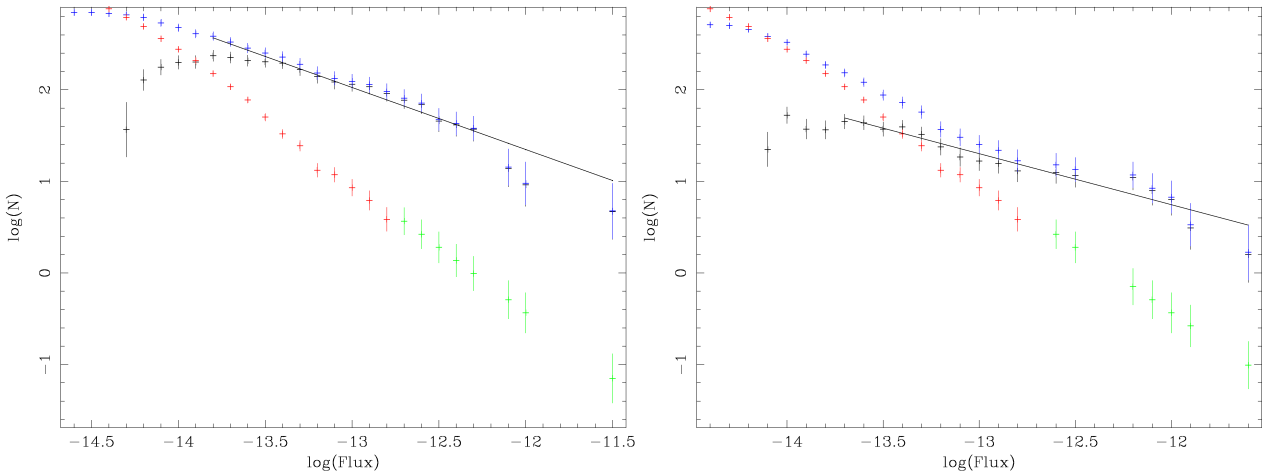


(a) Inner disc

(b) Dust ring

(c) Outer disc

(d) Beyond $D_{25}$

**Figure 8.8:** Cumulative X-ray log N-log S relation (blue), background CNC (red (observed) and green (extrapolated)) and the background corrected CNC (black) for the (a) inner disc, (b) dust ring, and (c) outer disc regions and (d) for the region beyond the $D_{25}$ ellipse. The solid lines display the fits to the background corrected CNCs. The slopes are given in Table 8.6.

**Table 8.5:** Number counts in the northern, southern, eastern and western part of M 31 for two different limiting fluxes

| | | | flux>$3.2\times10^{-14}$ erg cm$^{-2}$ s$^{-1}$ | | | | flux>$10^{-13}$ erg cm$^{-2}$ s$^{-1}$ | | | |
|---|---|---|---|---|---|---|---|---|---|---|
| Region | slope | err | srcs | err | srcs | err | srcs | err | srcs | err |
| | | | deg$^{-2}$ | | area$^{-1}$ | | deg$^{-2}$ | | area$^{-1}$ | |
| Northern disc | 0.65 | 0.07 | 29.11 | 2.03 | 37.99 | 3.82 | 13.54 | 2.11 | 17.75 | 2.77 |
| Southern disc | 0.73 | 0.06 | 37.08 | 3.22 | 49.43 | 4.29 | 15.22 | 2.21 | 20.41 | 2.96 |
| Eastern disc | 0.75 | 0.07 | 38.32 | 3.24 | 51.62 | 4.36 | 15.00 | 2.17 | 20.34 | 2.94 |
| Western disc | 0.61 | 0.07 | 27.72 | 2.91 | 35.73 | 3.75 | 13.76 | 2.15 | 17.83 | 2.79 |
| sum (N+S) | | | | | 87.42 | 4.06 | | | 38.16 | 2.87 |
| sum (E+W) | | | | | 87.35 | 4.06 | | | 38.17 | 2.87 |
| all | 0.70 | 0.03 | 33.14 | 0.76 | 87.5 | 2 | 14.39 | 0.95 | 38.1 | 2.5 |

later studies the range of slopes for HMXB populations was extended to 0.5–0.7, as long as the slope and its error was consistent with 0.6 (Grimm et al. 2005; Shtykovskiy & Gilfanov 2005). From the study of the log N-log S relations of the different radial regions it follows that the slopes of the inner disc and dust ring regions are consistent with the slope expected for an HMXB population. This is an interesting finding as up-to-now, not a single HMXB in M 31 is known for sure (for a discussion of HMXB candidates see Sect. 9.4.3.2). However, the slope, by itself, may not be a good indication of the underlying X-ray source population (Kong et al. 2003a).

Prestwich (2002) showed that flatter slopes indicate higher star formation rates. Applying this finding to the slopes of the different radial regions, we should expect the highest star formation rate (SFR) for the dust ring region, followed by the inner disc region. In the outer disc region and the region beyond the $D_{25}$ ellipse the star formation rate should decrease. These results are in agreement with the SFRs derived from *GALEX* observations (Boissier et al. 2007). The quantitative analysis of the correlation between HMXBs and SFRs, and a detailed discussion about HMXBs and log N-log S relations is presented in Sect. 8.4.3.1.

A comparison of the different background corrected CNCs or CLFs can be found in Fig. 8.9. Going from the inner disc region to the region beyond the $D_{25}$ ellipse, the CNC keeps raising till $F_X \sim 1.6\times10^{-14}$ erg cm$^{-2}$ s$^{-1}$, $\sim4\times10^{-14}$ erg cm$^{-2}$ s$^{-1}$, $\sim2\times10^{-14}$ erg cm$^{-2}$ s$^{-1}$, $\sim3\times10^{-14}$ erg cm$^{-2}$ s$^{-1}$, respectively. In the outer disc region the number of background sources is larger than the number of M 31 sources for fluxes smaller $\sim2\times10^{-13}$ erg cm$^{-2}$ s$^{-1}$. In the outermost region the source population is clearly dominated by the background sources, but we still expect M 31 to have about 13 sources/deg$^2$ with fluxes above $\sim3\times10^{-14}$ erg cm$^{-2}$ s$^{-1}$.

In the range between $\sim1.6\times10^{-13}$ erg cm$^{-2}$ s$^{-1}$ and $\sim8\times10^{-13}$ erg cm$^{-2}$ s$^{-1}$, where the CNC of the whole observed field showed the "bump", we find evidence of such a bump in the CNC of the dust ring region, while the CNC of the inner disc region is rather flat. For the outer disc region and the region beyond the $D_{25}$ ellipse, the statistics are not good enough above $\sim3.2\times10^{-13}$ erg cm$^{-2}$ s$^{-1}$ to decide whether the "bump" is visible or not.

The number of "hard" X-ray sources of M 31 at limiting fluxes of $3.2\times10^{-14}$ erg cm$^{-2}$ s$^{-1}$ and $10^{-13}$ erg cm$^{-2}$ s$^{-1}$ are given in Table 8.6. The sum of all sources obtained from the individual regions (row "sum" of Table 8.6) is in agreement with the values derived from the number counts of the whole field (row "all" of Table 8.6). A graphical illustration of Table 8.6 is given in Fig. 8.10, where the number of sources depending on the distance to the centre is shown. For limiting fluxes of $3.2\times10^{-14}$ erg cm$^{-2}$ s$^{-1}$ and $10^{-13}$ erg cm$^{-2}$ s$^{-1}$, the source distributions in the regions covering the disc of M 31 (*i. e.* omitting the bulge region), can be fitted

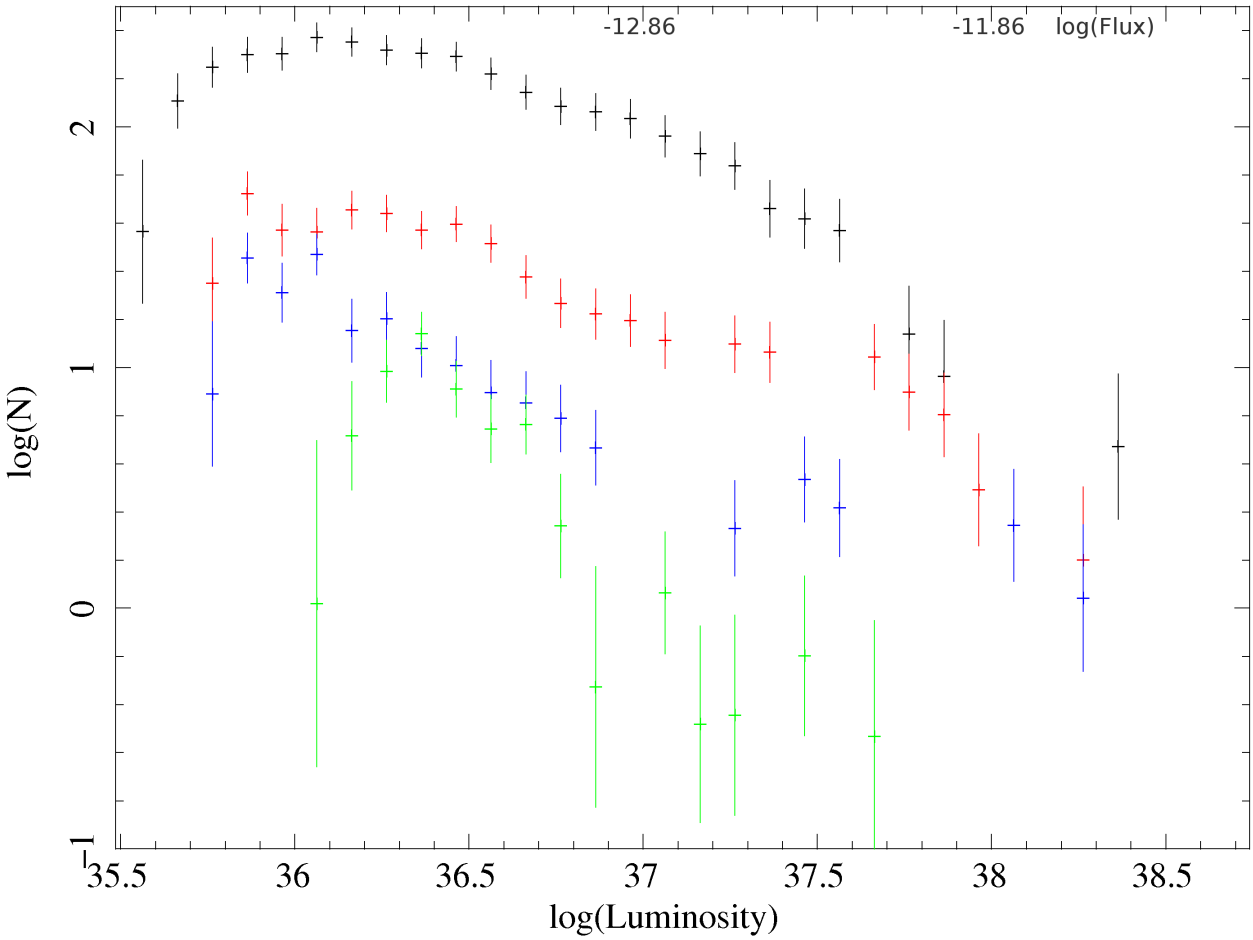


**Figure 8.9:** A comparison of the CLFs for the inner disc (black), dust ring (red), and outer disc (blue) regions and the region beyond the $D_{25}$ ellipse (green).

by an exponential profile:

$$I = I_0 \times \mathrm{e}^{-\frac{a}{a_0}} \tag{8.8}$$

where $a$ is the major axis of the elliptical regions and $a_0$ is the scale length. The best fit values are given in Table 8.7. Exponential profiles are known to describe the (optical) luminosity distribution of spiral galaxy discs. Comparing the best-fit values for the scale length shows that the number of brighter sources decreases faster with increasing distance than the number of faint sources.

I also compared the number of M 31 sources to the number of background sources for the total field (without bulge) at a limiting flux of $3.2{\times}10^{-14}$ erg cm$^{-2}$ s$^{-1}$. The result is that about 60% of all sources brighter than $3.2{\times}10^{-14}$ erg cm$^{-2}$ s$^{-1}$ are background sources. Determining the number of background sources for different radial distances results in a contribution of 20% of background sources for the inner disc region, 57% in the dust ring region and about 80% each in the outer disc region and the region beyond the $D_{25}$ ellipse. For a limiting flux of $10^{-13}$ erg cm$^{-2}$ s$^{-1}$ these values change to 7%, 34%, 65% and 95% going from the inner disc region to the region located beyond the $D_{25}$ ellipse. These numbers, once more, illustrate that the fraction of sources belonging to M 31 decreases with increasing distance to the centre of the galaxy.

**Table 8.6:** Number counts in the inner disc, dust ring, outer disc and beyond $D_{25}$ regions for two different limiting fluxes

| | | | flux>$3.2\times10^{-14}$ erg cm$^{-2}$ s$^{-1}$ | | | | flux>$10^{-13}$ erg cm$^{-2}$ s$^{-1}$ | | | |
|---|---|---|---|---|---|---|---|---|---|---|
| Region | slope | err | srcs deg$^{-2}$ | err | srcs area$^{-1}$ | err | srcs deg$^{-2}$ | err | srcs area$^{-1}$ | err |
| inner disc | 0.68 | 0.09 | 202 | 30 | 42 | 6 | 115.4 | 22.3 | 24.3 | 4.7 |
| dust ring | 0.56 | 0.11 | 37 | 7 | 22 | 4 | 16.7 | 4.5 | 9.9 | 2.7 |
| outer disc | 0.82 | 0.36 | 12 | 4 | 10 | 3 | 4.6 | 2.0 | 3.8 | 1.7 |
| beyond $D_{25}$ | 1.69 | 0.65 | 13 | 3 | 13 | 3 | 0.28 | 0.95 | 0.3 | 1.0 |
| sum | | | | | 87 | 4 | | | 38.3 | 2.5 |
| all | 0.70 | 0.03 | 33.14 | 0.76 | 87.5 | 2 | 14.39 | 0.95 | 38.1 | 2.5 |

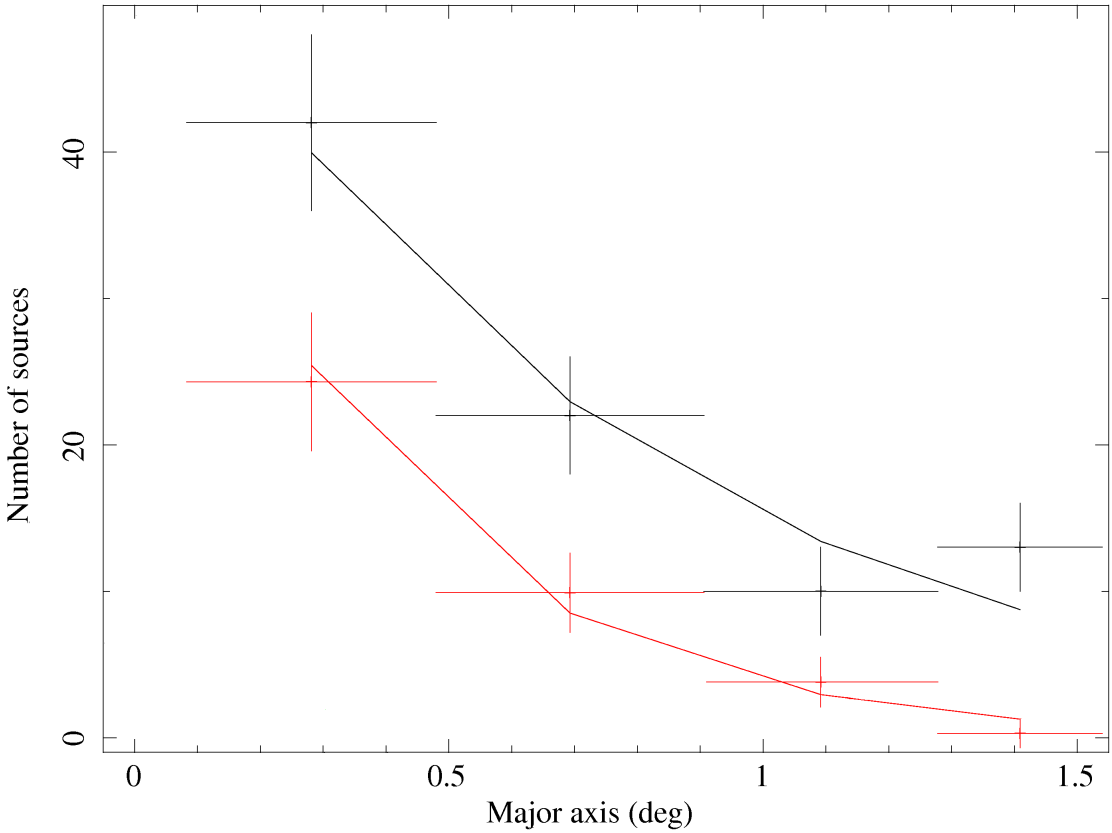


**Figure 8.10:** Number of sources detected in the 2.0–10 keV band depending on the distance to the centre of M 31. The colours illustrate different flux limits: black for a limit of $3.2\times10^{-14}$ erg cm$^{-2}$ s$^{-1}$ and red for a limit of $10^{-13}$ erg cm$^{-2}$ s$^{-1}$.

**Table 8.7:** Fit parameters for the distance distribution shown in Fig. 8.10

| flux limit | $I_0$ | $a_0$ (deg) | $a_0$ (kpc) | $\chi^2$ | d.o.f. |
|---|---|---|---|---|---|
| $3.2\times10^{-14}$ erg cm$^{-2}$ s$^{-1}$ | $58.37^{+21.7}_{-17.9}$ | $0.74^{+0.36}_{-0.20}$ | $10.1^{+4.9}_{-2.7}$ | 3.47 | 2.0 |
| $10^{-13}$ erg cm$^{-2}$ s$^{-1}$ | $53.74^{+28.2}_{-20.2}$ | $0.38^{+0.12}_{-0.10}$ | $5.2^{+1.6}_{-1.4}$ | 1.51 | 2.0 |

#### 8.4.3.1 High mass X-ray binaries and the luminosity function

Grimm et al. (2003) give the following relation between the number of sources (HMXBs) which are brighter than $2\times10^{38}$ erg s$^{-1}$ in the 2.0–10.0 keV band and the SFR:

$$N(L > 2 \times 10^{38}\,\mathrm{erg\ s^{-1}}) = (2.9 \pm 0.23)\,\mathrm{SFR}(\mathrm{M_\odot yr^{-1}}) \tag{8.9}$$

(Eq. 5 of Grimm et al. 2003). Taking the SFRs from Boissier et al. (2007) and the HI surface density of Chemin et al. (2009), we can compare the SFRs to the CLFs for the inner disc and dust ring region. In addition, we can compare those quantities for the whole disc of M 31, by applying an SFR of $\sim$1.0 $\mathrm{M_\odot}$/yr (Williams 2003).

Figure 8.11 shows the number of sources brighter than $2\times10^{38}$ erg s$^{-1}$ and the SFR for different galaxies (taken from Grimm et al. 2003) and in addition the values for the inner disc, the dust ring region, and for the whole disc of M 31. Shown are the number of sources derived from the CLFs (red, green) as well as the values reduced by the amount of known LMXBs (blue). We assumed a poissonian distribution to determine the errors in the numbers of sources. All data points agree within their errors with the values expected from Eq. 8.9. For the outer disc region and the region beyond the $\mathrm{D_{25}}$ ellipse the low statistics do not allow to derive a meaningful number of sources with luminosities brighter than $2\times10^{38}$ erg s$^{-1}$. As M 31 contains only a small amount of sources that are brighter than $2\times10^{38}$ erg s$^{-1}$ (2.0–10.0 keV band; $\sim 4$ sources), the above results does not allow to decide whether the inner disc or dust ring region contain an unknown HMXB population.

Grimm et al. (2003) also provides an expression for a universal cumulative luminosity function for HMXB populations, namely:

$$N(> L_{38}) = \left(5.4^{+2.1}_{-1.7}\right)\,\mathrm{SFR}\left(L_{38}^{-0.61\pm0.12} - 210^{-0.61\pm0.12}\right) \tag{8.10}$$

(Eq. 19 of Grimm et al. 2003), where $L_{38} = L/10^{38}$ erg s$^{-1}$ (2.0–10.0 keV), *i. e.* the luminosity is given in units of $10^{38}$ erg s$^{-1}$, and SFR denotes the star formation rate. Comparing the number of sources derived from Eq. 8.10 with the CLFs of the inner disc and dust ring region, where I used the same values for the star formation rate as in Fig. 8.11, shows that in the inner disc region (Fig. 8.12(a)) HMXBs make up only for a fraction of the observed CLF. This implies that the inner disc region contains a large population of LMXBs.

The CLF of the dust ring region is in agreement (within the errors) with the number of sources expected for an HMXB population (Fig. 8.12), although it looks like for most of the data points the expected CLF is higher than the measured CLF. This could imply that the number of background sources was overestimated for the dust ring region, which seems plausible since the dust ring region is the part of the disc of M 31 were the highest $N_\mathrm{H}$ values have been measured (*cf.* Fig. 8.1). Taking the values listed in Table 8.1 we should expect that the flux from the background sources is reduced by $\sim$20%–30% in the dust ring region. This absorption effect was included in the determination of the number of background sources in the following way. For a given flux $F_\mathrm{g}$ the "absorption-corrected" flux $F_\mathrm{ac} = F_\mathrm{g}/\,(1-a)$ was determined, where $a$ is the fraction by which the flux is reduced due to absorption. With this "absorption-corrected" flux the number of

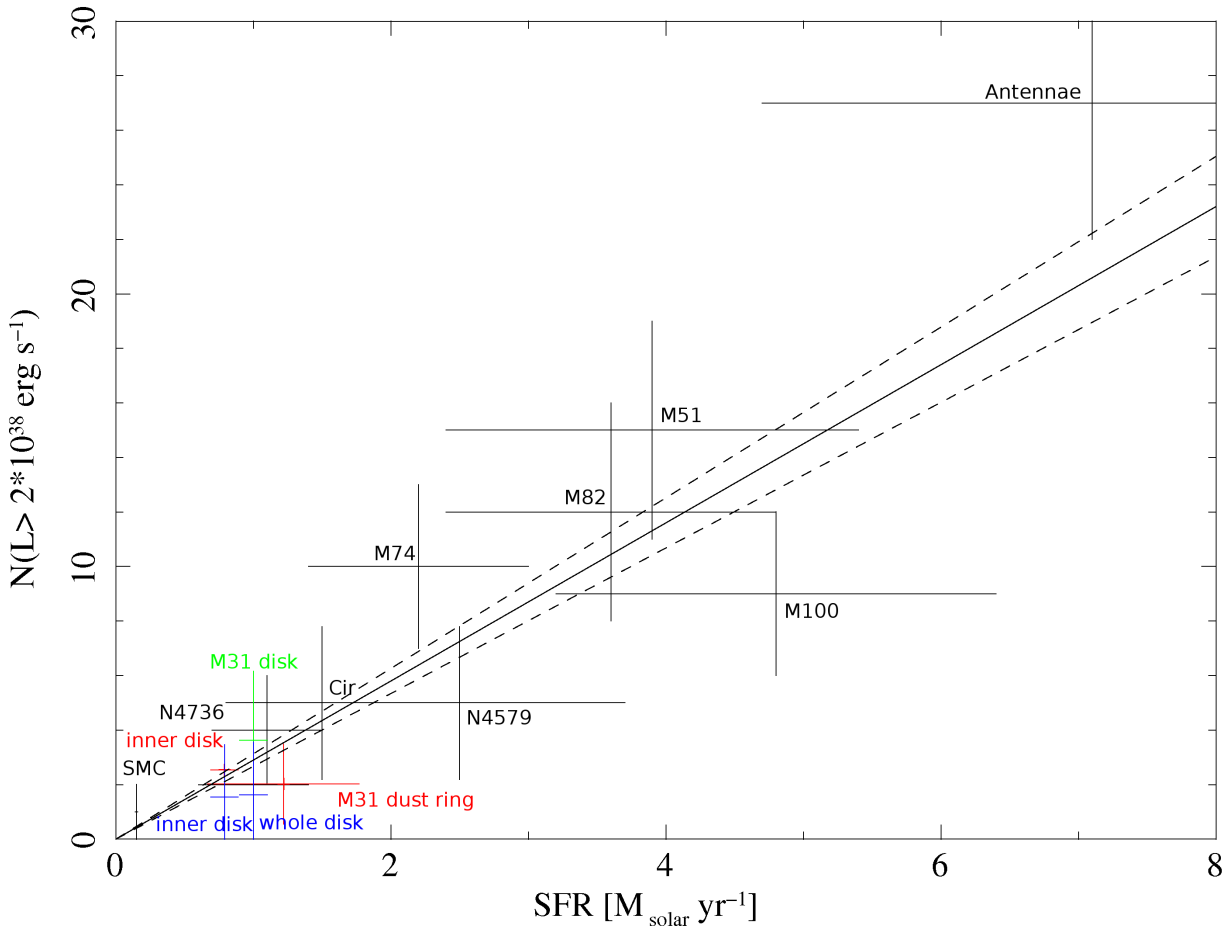


**Figure 8.11:** Star formation rate versus number of sources with luminosities above $2{\times}10^{38}$ erg s$^{-1}$ for different star forming galaxies from Grimm et al. (2003) and for the whole disc (green) and inner disc and dust ring region (red) of M 31. For the whole disc and inner disc region additional number of sources that are reduced by the amount of known LMXBs (blue) are given. Also shown is the relation between the SFR and the CLFs (lines) derived in Grimm et al. (2003).

background sources were derived, using:

$$N(>F_{\rm ac}) = \begin{cases} A\,F_{\rm ac}^{-\alpha_1}, & F_{\rm ac} > S_{\rm b}, \\ B\,F_{\rm ac}^{-\alpha_2}, & F_{\rm ac} \leq S_{\rm b}, \end{cases} \tag{8.11}$$

where $\alpha_1 = 1.43 \pm 0.10$, $\alpha_2 = 0.59 \pm 0.33$, $S_{\rm b} = 1.02^{+0.25}_{-0.19}{\times}10^{-14}$ erg cm$^{-2}$ s$^{-1}$, $A = 266 \pm 11$, and $A = B\,S_{\rm b}^{\alpha_1-\alpha_2}$ (Cappelluti et al. 2007).

Figure 8.13 shows the CLFs of the dust ring region for an absorption of 0%, 20%, and 30%. In addition, the expected number of HMXBs for the SFR measured in the dust ring region (Eq. 8.10) is plotted. We see that the number of sources detected in the dust ring region is in agreement with the values predicted by Eq. 8.10, and that this finding is independent from the absorption used. With the absorption included there are less data points where the expected CLF is higher than the measured CLF.

In summary, the comparison of the measured CLF with the number of sources predicted from theoretical considerations suggests that the dust ring region contains an up to now unknown population of HMXBs. Nevertheless, the results of the source identification and classification (*cf.* Chap. 9) shows that, from all

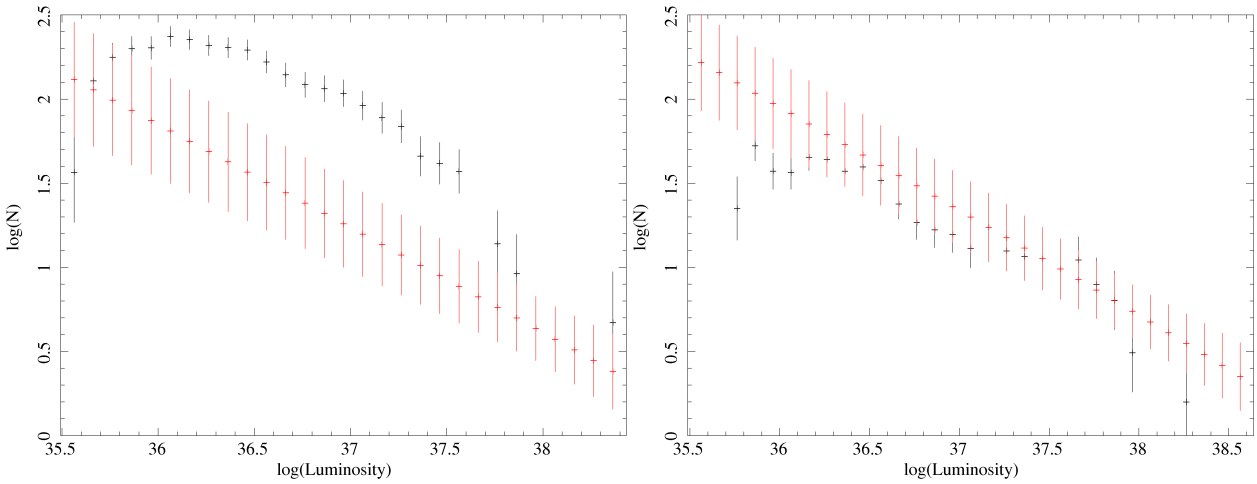


(a) Inner disc (b) Dust ring

**Figure 8.12:** Cumulative X-ray luminosity function (black) and expected CLF of an HMXB population (red), derived from Eq. 8.10, for the (a) inner disc and (b) dust ring regions. The errors of the expected CLF increases with decreasing luminosity, as they also contain the uncertainties in the normalisation and slope of the luminosity function given in Eq. 8.10.

sources located in the dust ring region and detected in the 2.0–10.0 keV band, five source are identified as SNRs or SNR candidates, and a further 14 sources are identified as XRBs or GlCs or as candidates for these two classes. From the five sources identified as SNRs or SNR candidates four sources have 2.0–10.0 keV fluxes below $2.6\times10^{-14}$ erg cm$^{-2}$ s$^{-1}$. This means that from the $\sim$100 sources/deg$^2$ (assuming an absorption of 20%) with a flux larger than $10^{-14}$ erg cm$^{-2}$ s$^{-1}$ we expect $\sim$24 sources to be LMXBs and about seven to be SNRs. Taking into account the corrections for the absorption, and for the numbers of identified or classified sources, the relation given in Eq. 8.10 overestimates still the number of HMXBs in the dust ring region. This can have several reasons. First of all, there is still the possibility that the number of background sources estimated is too high. The second reason can be that the universal log N-log S relation for HMXBs is not enough accurate for low star forming rates. From the Small Magellanic Cloud it is known that the number of observed HMXBs depends not only on the value of the SFR. In addition, it is also important how long ago the star formation took place. Furthermore, we used an averaged value for the SFR of the dust ring region in Eq. 8.10 which therefore does not include the spatial dependence of the SFR within this region.

This analysis showed that the measured CLF of the dust ring region seems to agree with the number of sources predicted from theoretical considerations for a population of HMXBs. However, additional refinement in the theoretical prediction of the luminosity function for HMXBs at low star forming rates is needed to confirm a population of HMXBs in the dust ring of M 31.

#### 8.4.3.2 Comparison with previous studies

The possible comparisons with previous studies of the log N-log S relation of M 31 are very limited, as the analysis presented in this thesis is novel with respect to the covered area in the 2.0–10.0 keV band and the treatment of the contribution of background sources. As earlier mentioned, the previous *XMM-Newton* and *Chandra* studies only cover selected parts of M 31 and do not include corrections for the contribution of background sources. Comparisons are also complicated by the fact that those studies included sources which

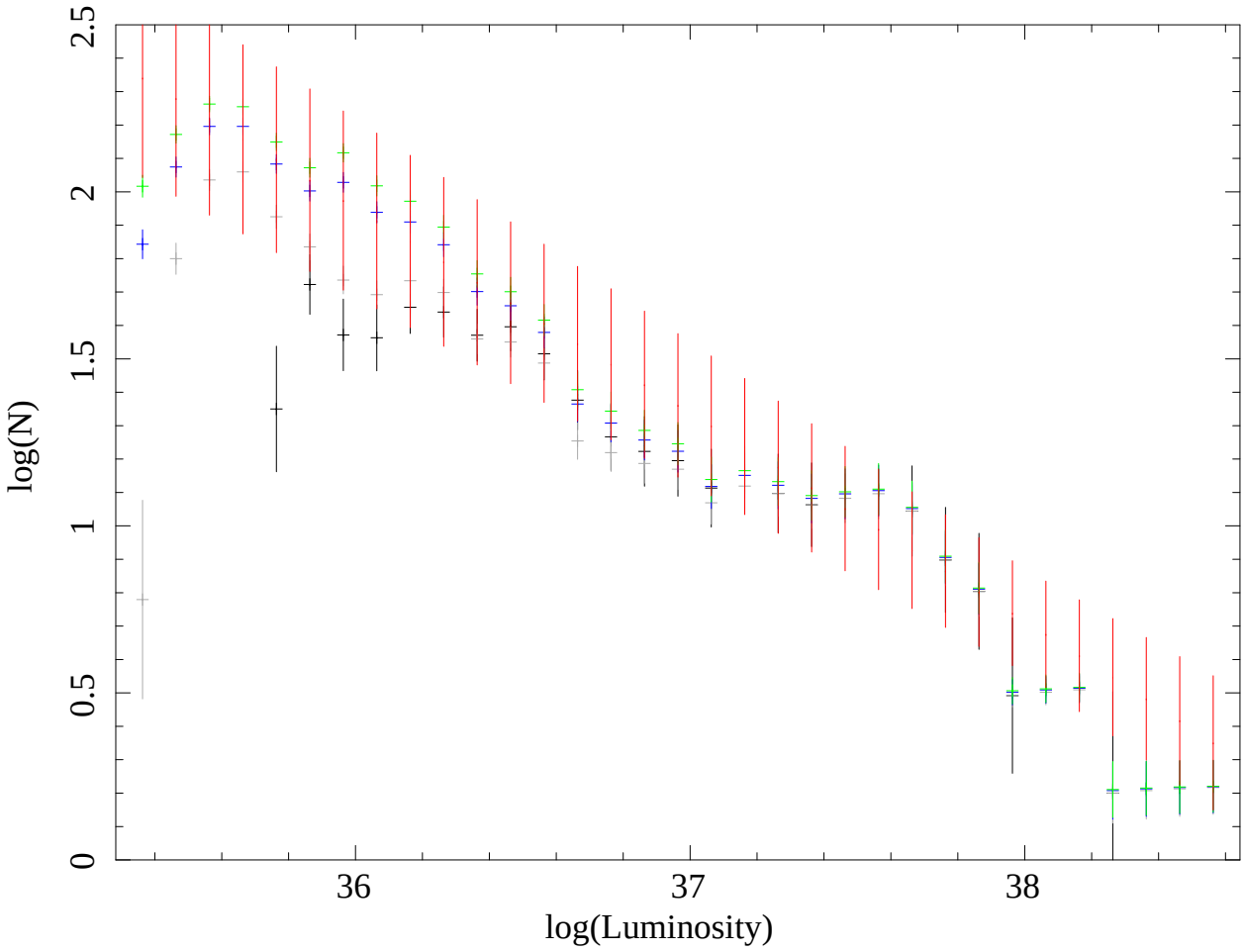


**Figure 8.13:** Cumulative X-ray luminosity function and expected CLF of an HMXB population (red), derived from Eq. 8.10, for the dust ring region. Shown are the CLF from Fig. 8.12(b) (black), as well as CLFs that include corrections for the fraction of the flux from background sources that is absorbed by the ISM in M 31. For the "absorption-corrected" CLFs, the number of background sources was derived from Eq. 8.11. The different colours represent absorption of 0% (grey), 20% (blue), and 30% (green). The black and grey crosses both represent the CLFs without correction for the absorption. To derive the black crosses the *measured* number of sources from the COSMOS field were used to determine the number of background sources, while for the grey crosses the *fitted* number of sources from the COSMOS field were used.

were detected in the ∼0.3–2.0 keV range. With respect to background sources, these studies are certainly incomplete in the aforesaid energy range, as the absorption within M 31 is very large for those energies (see Sect. 8.1). In other words, the previous studies are somehow "background corrected" for sources detected in the ∼0.3–2.0 keV range, but are severely affected by background objects in the 2.0–10 keV range.

To allow comparisons with previous studies, the best fit slopes of the uncorrected CNCs were derived, determined from the unbinned, differential log N-log S relations. These are 0.6, 0.9, 1.2 and 1.5 going from the inner disc region to the region beyond the $D_{25}$ ellipse. The largest deviations from the background corrected slopes can be found for the outer disc and dust ring regions. A comparison of the slopes found in this thesis to the slopes from the *Chandra* study of Kong et al. (2003a) shows that the slopes of the outer disc region ($\alpha = 1.2$) and of field 3B ($\alpha = 1.1^{+0.20}_{-0.10}$) from Kong et al. (2003a), which mainly covers (a small part of) the same region, are in good agreement. The slope found for field 2A ($\alpha = 0.9^{+0.16}_{-0.12}$ Kong et al. 2003a) is consistent with the *XMM-Newton* value for the dust ring region ($\alpha = 0.9$), but field 2A is located in the outskirts of the inner disc region. A possible explanation is that the source population of field 2A (not background corrected) is similar to the population found in the dust ring region (without background correction), and that the slope found for the inner disc region is dominated by sources located closer to the centre, or in parts of the inner disc region not covered by field 2A. Colbert et al. (2004) found that log N-log S relations are dominated by the bright sources. In the inner disc region most of the brighter sources are located outside field 2A. The biggest part of field 1 (Kong et al. 2003a) is located outside the $D_{25}$ ellipse[3]. Although Kong et al. (2003a) found a somewhat steeper slope ($\alpha = 1.7^{+0.34}_{-0.15}$), the *Chandra* and *XMM-Newton* values are consistent within their errors. One should also take the low statistic in the region outside the $D_{25}$ ellipse into account. In summary the slopes derived in this work are compatible with the slopes found by Kong et al. (2003a).

The slope derived in SBK2009 for the whole galaxy agrees with value determined in the present study.

For a single power-law fit to the slope of the disc population of M 31 (*i. e.* sources with a distance of $>7\farcm0$ to the centre of M 31) in the 0.1–10 keV band Williams et al. (2004a) obtained a best fit value of $0.9 \pm 0.1$ for the slope. This again agrees with the slope found for the dust ring region, which is not really surprising as most of the *Chandra* sources used by Williams et al. (2004a) for the fit are located in that region or in the southern most part of the inner disc region, similar to the field 2A of Kong et al. (2003a). The slope of the population of field 2A was $0.9^{+0.16}_{-0.12}$ (Kong et al. 2003a).

Trudolyubov et al. (2002b) used the *XMM-Newton* observations of the N1 and N2 field available at that time to examine their population. They obtained a slope of ∼1.3. A comparison with the slopes of the regions used to study the radial dependence of the log N-log S relation is difficult as the two fields (N1 and N2) cover parts of the inner disc, dust ring and outer disc regions. For the whole northern part of M 31 (bulge excluded) the uncorrected log N-log S data gives a best fit slope of ∼0.9, which is inconsistent with the value of Trudolyubov et al. (2002b). Apart from the differences in the used energy bands, this suggests that the two fields located along the major axis of M 31 do not represent well the whole population of the northern disc of M 31, as was expected.

Comparing the number of detected sources at different limiting fluxes between the individual studies (including the present one) is not feasible, since the previous studies (Trudolyubov et al. 2002b; Kong et al. 2003a; Williams et al. 2004a, SBK2009), apart from including background sources and fluxes from the <2.0 keV band, which is highly affected by absorption, only gave the number of sources in the examined region, and did not indicate the number of sources per square degree (or any other unit area), which would be needed for a comparative study. To determine the area covered in each study one has to derive the sky coverage, as was described in Sect. 8.4.2. Therefore it is not enough to know the geometrical area covered by the observation(s), but one also has to know the sensitivity of the observations (instrument) for different

[3]Please note that in Fig. 1 of Kong et al. (2003a) the observed $D_{25}$ ellipse is shown, while throughout this thesis the corrected $D_{25}$ ellipse was used.

fluxes. Another difficulty arises from the fact that different parts of the disc of M 31 seem to be populated by sources which show individual log N-log S relations, as was detected in the present study. Therefore one could not expect that the properties derived from a log N-log S curve of a small part of the galaxy are a good representation for the properties of the whole galaxy.

A comparison with previous *ROSAT* studies, namely SHP97, is not meaningful as *ROSAT* only examined the source population of M 31 which is detectable in the 0.1–2.0 keV range. This is the energy range that was excluded in the present study, as it is highly affected by absorption.

# Chapter 9

# Discussion

In the first two sections of this chapter correlations with other X-ray catalogues and with catalogues at other wavelengths are presented. The discussion of the X-ray correlations focuses on the sources that were found in previous studies, but not contained in the XMM LP-total catalogue.

I then (in Sects. 9.3 and 9.4) discuss the source identifications and classifications and comment on the XMM LP-total catalogue.

## 9.1 Cross-correlations with other M 31 X-ray catalogues

Cross-correlations were determined by applying Eq. 5.3 to the sources of the XMM LP-total catalogue and to sources reported in earlier X-ray catalogues. The list of X-ray catalogues used is given in Table 5.4.

### 9.1.1 Previous *XMM-Newton* catalogues

Previous source lists based on archival *XMM-Newton* observations were presented in Osborne et al. (2001), PFH2005, Orio (2006), Trudolyubov et al. (2006b), SPH2008, and SBK2009. From these four studies, PFH2005 covers the largest area of M 31. Table 9.1 lists all sources from previous *XMM-Newton* studies that are not detected in the present investigation.

In ten observations, covering the major axis and a field in the halo of M 31, PFH2005 detected 856 X-ray sources, with a detection likelihood threshold of seven (*cf.* Sects. 5.2.4 and 3.3). Of these 856 sources 755 sources are also present in the XMM LP-total catalogue, *i. e.* 101 sources of PFH2005 are not detected. Figure 9.1 shows the distribution of the detection likelihood for all sources in PFH2005 as well as the 101 sources undetected in the XMM LP-total catalogue. Six of these 101 sources, were detected with $\mathcal{L} > 50$ in PFH2005. These six sources are all located in the centre of M 31. Four of them ([PFH2005] 312, 316, 327, 332) are located in the innermost central region of M 31 where source detection is complicated by the bright diffuse X-ray emission. The other two sources ([PFH2005] 281 and 384) lie in the immediate vicinity of two bright sources ([PFH2005] 280 and 381; distance: $7\farcs7$ and $5\farcs5$, respectively). The reason why these six sources were found in PFH2005, is that the search strategy of PFH2005 was optimised to detect sources located close to each other in crowded fields. To achieve this result, PFH2005 used, amongst other things, a detection likelihood threshold of three in the task `eboxdetect`. In the central region of M 31 `eboxdetect` mistakes residuals in the background of the diffuse emission as sources. These residuals are the differences between the background calculated with the task `esplinemap`, and the diffuse emission. Due to the high source density the task `esplinemap` cuts out a rather large fraction of the central region. In the then-following fit `esplinemap` extrapolates the background in the missing region from the background that is left at the outer edge of that region. Hence, there are severe differences between the reconstructed

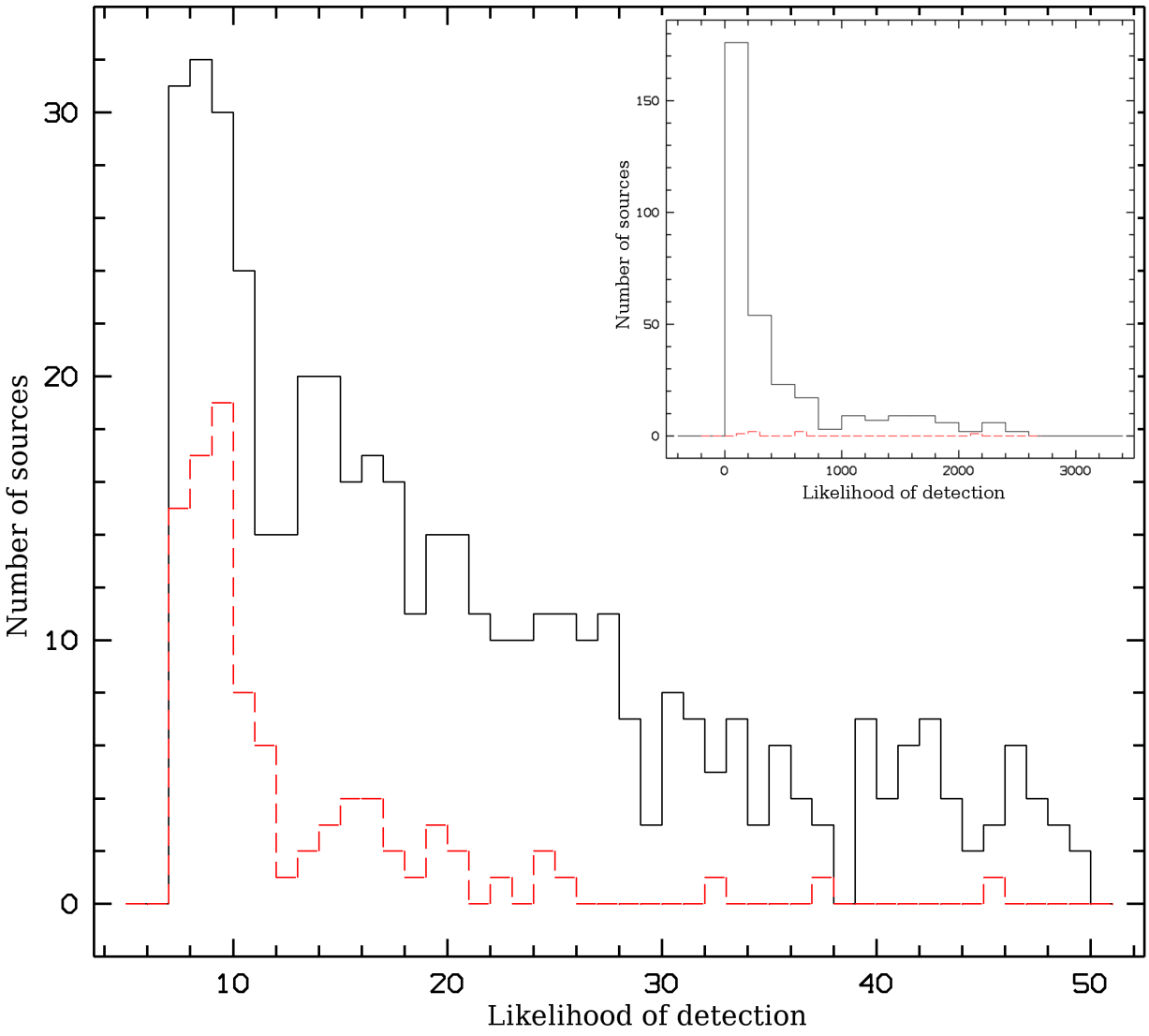


**Figure 9.1:** Distribution of detection likelihoods for all sources in PFH2005 (black) as well as the 101 undetected sources (red). The inlay shows all sources with a detection likelihood larger than 50 and smaller than 2 500. Of these sources six were not found in the present study. All sources with detection likelihoods even higher than 2 500 are detected. Reasons for none detections of previously found sources are discussed in Sect. 9.1.1.

**Table 9.1:** Sources from previous *XMM-Newton* studies that are not listed in the XMM LP-total catalogue.

| | |
|---|---|
| PFH2005 856 sources | |
| 101 not detected | |
| 6 not detected, LH>100: | 327 (<SNR>,LH=2140.0), 384 (XRB,667.0), 332 (<SNR>,654.0), 316 (<SNR>,259.0), 312 (<SNR>,241.0), 281(<hard>,160.0) |
| 10 not detected, 20≤LH<50: | 75 (<SSS>), 423 (<fg Star>), 120 (<hard>), 505 (<hard>), 220 (<SNR>), 304 (<fg Star>), 819 (<hard>), 799 (<SSS>), 413 (<SNR>), 830 (<hard>) |
| 14 not detected, 15≤LH <20: | 427(<hard>), 734 (<hard>), 424 (<hard>), 518 (<SSS>), 232 (<hard>), 339 (<hard>), 446 (<SSS>), 219 (<fg Star>), 567 (<hard>), 256 (<fg Star>), 356 (<hard>), 248 (<hard>), 160 (<hard>), 399 () |
| 20 not detected, 10≤LH<15: | 375 (<hard>), 17 (<hard>), 195 (<hard>), 417 (<SNR>), 783 (<hard>), 803 (<hard>), 829 (<hard>), 135 (<hard>), 151 (<hard>), 131 (<hard>), 426 (<hard>), 593 (<fg Star>), 526 (<hard>), 250 (<hard>), 62 (<hard>), 67 (<hard>), 188 (<hard>), 186 (<AGN>), 510 (<hard>), 754 (<hard>) |
| 51 not detected, LH<10: | 599 (<hard>), 439 (<hard>), 809 (<hard>), 14 (<SNR>), 743 (<hard>),433 (<hard>), 5 (), 210 (<hard>), 97 (<hard>), 708 (<hard>), 476 (), 534 (<hard>), 501 (), 170 (<hard>), 146 (SNR), 769 (), 838 (<hard>), 571 (<hard>), 816 (<hard>, 554 (), 627 (<hard>), 464 (<fg Star>), 811 (<hard>), 655 (<hard>), 184 (<hard>), 447 (<hard>), 380 (<hard>), 566 (<hard>), 137 (<fg Star>), 63 (), 48 (), 152 (<fg Star>), 291 (<hard>), 559 (<hard>), 102 (<hard>), 740 (<hard>), 540 (<fg Star>), 240 (<hard>), 485 (), 668 (<hard>), 44 (), 560 (<hard>), 836 (<hard>), 436 (<hard>), 484 (<fg Star>), 216 (<hard>), 527 (<>), 179 (<hard>), 834 (<hard>), 86 (<hard>), 455 () |
| SPH2008 39 sources | |
| 14 not detected | |
| 3 not detected, 50≤LH<100: | 874 (<SNR>,LH=85.5), 895 (<hard>,75.9), 882 ( ,56.4) |
| 5 not detected, 10≤LH<50: | 869 (), 885 (<SNR>), 863 (<hard>), 875 (<SSS>), 893 (<hard>) |
| 6 not detected, LH<10: | 870 (<SNR>), 891 (<hard>), 889 (<hard>), 872 (<SNR>), 867 (<hard>), 862 (<SNR>) |
| SBK2009 335 sources | |
| 31 not detected | |
| | 4 (<hard>), 18 (<hard>), 29 (<hard>), 32 (<hard>), 34 (<hard>), 45 (<SSS>), 67 (<hard>), 102 (<hard>), 106 (<hard>), 117 (<hard>), 149 (<hard>), 152 (<hard>), 179 (<hard>), 183 (<hard>), 184 (<hard>), 188 (<hard>), 191 (<hard>), 192 (<AGN>), 202 (<hard>), 204 (<fg star>), 217 (<hard>), 249 (<hard>), 250 (<hard>), 260 (<hard>), 274 (<hard>), 279 (<hard>), 285 (<hard>), 295 (<hard>), 306 (<hard>), 325 (<hard>), 333 (<hard>) |

background and the diffuse emission. To achieve reliable detection results in the subsequent `emldetect` run, it was necessary to thin out the preliminary source list. The decision on which of the preliminary sources to include in the starting list of `emldetect` was based not only on visible structures in the contour plots, but also on sources reported in earlier X-ray catalogues (W. Pietsch, private communication). To allow for statistical analyses of the sources found, the detection strategy and parameter setting described in Sect. 5.2.4 was also applied to the archival observations. I want to state clearly, that the six sources ([PFH2005] 281, 312, 316, 327, 332, 384) are real sources, as they were also found in *Chandra* observations. Concerning the remaining 95 undetected sources, some of them are also located in regions of enhanced source density. For these sources similar arguments as those given above are valid. Further differences to PFH2005 can be found in the parameter setting used in the `emldetect` run; in the determination of the extent of a source for the XMM LP-total catalogue; in the more sever screening for GTIs for the XMM LP-total catalogue, which led to shorter exposure times; in the use of the `epreject` task and last but not least in the `SAS` versions and calibration files used. The changes in the `SAS` versions and the GTIs, in particular, affect sources with small detection likelihoods ($\mathcal{L} < 10$). The improvements in the `SAS` detection tools and calibration files should reduce the number of spurious detections, which increase with decreasing detection likelihood. However this does not necessarily imply that *all* the undetected sources with $\mathcal{L} < 10$ of PFH2005 are spurious detections. The changes in the `SAS` versions, calibration files and GTIs do not only affect the source detection tasks,

but also can cause changes in the background images. These changes may increase the assumed background value at the position of a source, which would result in a lower detection likelihood. Going from `mlmin = 7` to `mlmin = 6`, but leaving everything else unchanged, I found an additional nine sources from PFH2005. One of the undetected sources ([PFH2005] 75) was classified as <SSS>, but correlates with blocks of pixels with an enhanced low energy signal in the PN offset map and was corrected by `epreject`. Another source classified as <SSS> ([PFH2005] 799) is only detected in the MOS 1 camera, but not in MOS 2. From an examination by eye, it seems that source [PFH2005] 799 is the detection of some noisy pixels at the rim of the MOS 1 CCD 6 and not a real X-ray source.

SPH2008 (see Chap. 6) extended the source catalogue of PFH2005 by re-analysing the data of observations to the central region of M 31 and included data of monitoring observations of LMXB RX

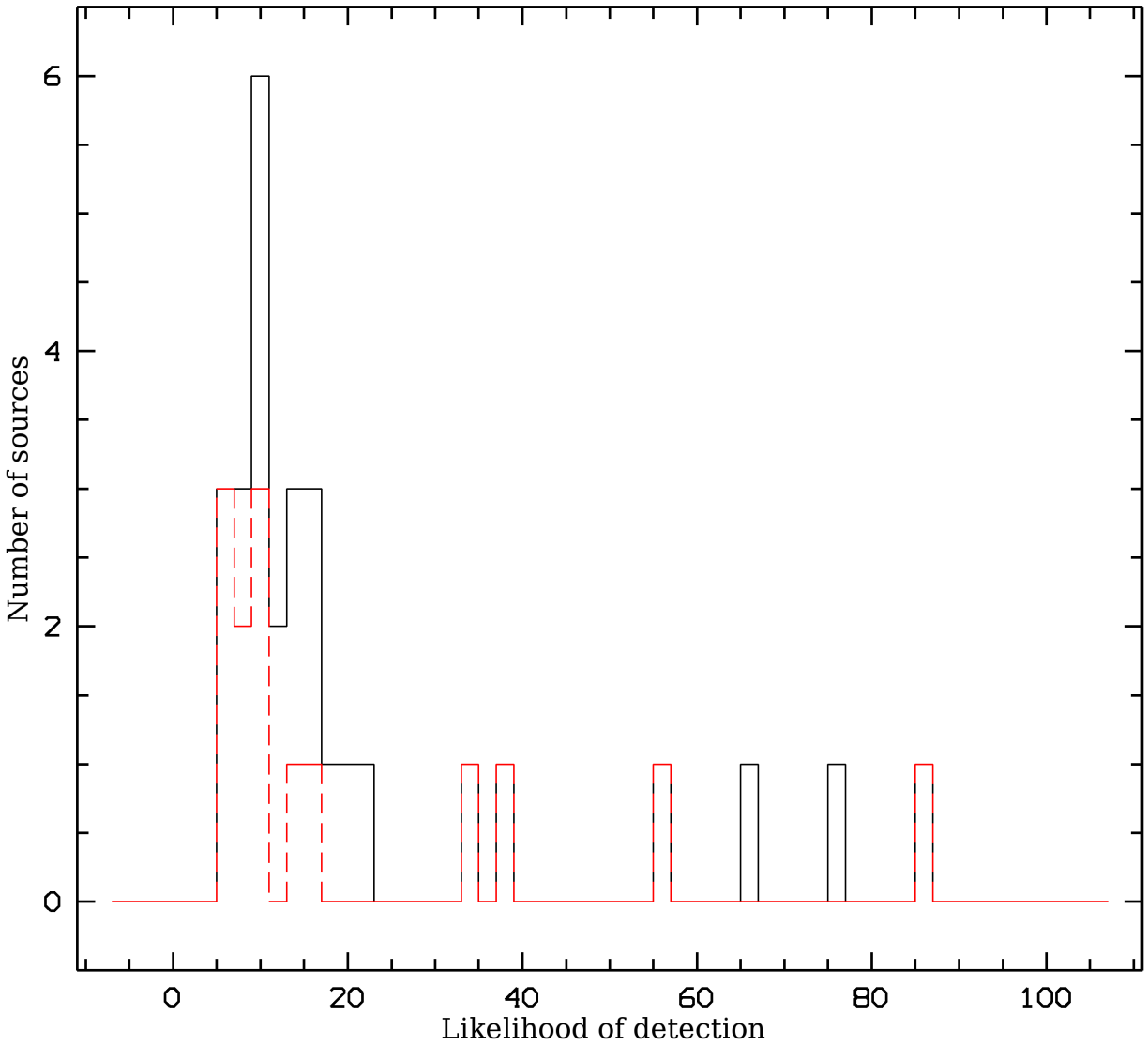


**Figure 9.2:** Distribution of detection likelihoods for all sources in SPH2008 (black) with a detection likelihood smaller than 100 and for the 14 undetected sources (red). All sources with higher detection likelihoods were detected in my work. Reasons for non-detections of previously found sources are discussed in Sect. 9.1.1.

J0042.6+4115. From the 39 additional sources presented in Chap. 6, 25 are also listed in the XMM LP-total catalogue, *i. e.* 14 sources of SPH2008 are not detected. Differences between both studies are the detection likelihood thresholds used for `eboxdetect` (SPH2008: `likemin` = 5) and `emldetect` (SPH2008: `mlmin` = 6), the lower limit for the likelihood of extention (SPH2008: `dmlextmin` = 4; XMM LP-total: 15), the screening for GTIs, the use of the `epreject` task and the `SAS` versions and calibration files used. Concerning the GTIs, images, background images and exposure maps, SPH2008 followed the same procedures as in PFH2005. The arguments given above are therefore also valid here. From the 14 undetected sources, three sources were detected in SPH2008 with `mlmin` $< 7$ (Fig. 9.2). One source ([SPH2008] 882) was added by hand to the final source list, as SPH2008 could not find any reason why `emldetect` did not automatically find it. The two extended sources ([SPH2008] 863, 869) detected with extent likelihoods between 4.7 and 5.1 in SPH2008, are neither detected as extended nor as pointlike sources in the present study, where the extent likelihood has to be larger than 15.

SBK2009 re-analysed the *XMM-Newton* observations located along the major axis of M 31, ignoring all observations pointing to the centre of the galaxy. They used a detection likelihood threshold of ten. Of the 335 sources detected by SBK2009, 304 sources are also contained in the XMM LP-total catalogue, *i. e.* 31 sources are not detected. Of the 304 re-detected sources, two sources ([SBK2009] 298, 233) are found with a detection likelihood below ten. Of the 31 undetected sources, 27 sources were also undetected in PFH2005. The remaining four sources correlate with PFH2005 sources, which were not detected in the present study. SBK2009 state that they find 34 sources not present in the source catalogue of PFH2005. A possible reason for this may be that SBK2009 used different energy bands for source detection. They also had five bands, but on the one hand combined bands two and three from PFH2005 into one band in the range 0.5–2 keV, and on the other hand split band five of PFH2005 into two bands from 4.5–7 keV and from 7–12 keV, respectively. This might also explain why most of the additionally found sources were classified as <hard>.

Trudolyubov et al. (2006b) re-analysed eight observations from the centre of M 31, including the observations centred on RX J0042.6+4115. They found 123 sources, each with more than 300 source counts. Of these sources all but two ([TPC2006] 70, 72) were listed in the XMM LP-total catalogue. These two sources correlate with sources [PFH2005] 327 and 332, respectively, which were already discussed above.

In addition, there is the study of Orio (2006) which addresses the population of SSSs and QSSs and is based on the same archival observations as PFH2005. Orio (2006) detected 15 SSSs, 18 QSSs and ten SNRs of which one ([O2006] Tab. 4, Src. 3) is also listed as SSS ([O2006] Tab. 2, Src. 13). Of these sources two SSSs, four QSSs and two SNRs (among them is the source [O2006] Tab. 4, Src. 3) are not contained in the XMM LP-total catalogue. These seven sources are also not present in the PFH2005 catalogue.

The nine bright variable sources from Osborne et al. (2001) were all detected.

### 9.1.2 *Chandra* catalogues

The *Chandra* catalogues used for cross-correlations were presented in Sect. 3.3 (see also Table 5.4).

Details of the comparison between the XMM LP-total catalogue and different *Chandra* catalogues can be found in Table 9.2. Here I only give a few general remarks. A non-negligible number of the *Chandra* sources not reported in the XMM LP-total catalogue are already classified as transient or variable sources. Thus, it is not surprising that those sources were not detect in the *XMM-Newton* observations (parts of: Voss & Gilfanov 2007; Williams et al. 2006b, DKG2004). One *Chandra* source (n1-66) lies outside the field of M 31 covered by the *XMM-Newton* observations. For the innermost central region of M 31 the point spread function of *XMM-Newton* causes source confusion and therefore only *Chandra* observations are able to resolve the individual sources, especially if they are faint compared to the diffuse emission or nearby bright sources (Kong et al. 2002b; Kaaret 2002; Williams et al. 2004a; Di Stefano et al. 2004; Williams

et al. 2006b; Voss & Gilfanov 2007). This explaines why a certain number of these sources are not detected in *XMM-Newton* observations.

Of the 28 bright X-ray sources located in globular clusters (Di Stefano et al. 2002), two were not found in the *XMM-Newton* data (see Table 9.2). They are also not part of the source catalogue of PFH2005 and SPH2008. Hence, both objects are good candidates for transient or at least highly variable sources (*cf.* Sect. 9.4.4.2). Another study of the globular cluster population of M 31 is presented by Trudolyubov & Priedhorsky (2004). Their work is based on *XMM-Newton* and *Chandra* data and contains 43 X-ray sources. Of these sources three were not found in the present study. One of them ([TP2004] 1) is located far outside

**Table 9.2:** Sources detected in previous *Chandra* studies that are not present in the XMM LP-total catalogue.

| | |
|---|---|
| Kong et al. (2002b) 204 sources | |
| 58 not detected | |
| 5 transient: | r3-46,r3-43,r2-28,r1-23,r1-19 |
| 20 variable: | r3-53,r3-77,r3-106,r3-76,r2-52,r2-31,r2-23,r1-31,r2-20,r1-24,r1-28,r1-27,r1-33,r1-21,r1-20,r1-7,r2-15,r1-17,r1-16,r2-47 |
| 33 unclassified: | r3-102,r3-92,r3-51,r3-75,r3-91,r3-89,r3-101,r3-88,r2-44,r2-55,r2-54,r3-32,r2-53,r1-30,r3-99,r1-22,r1-26,r1-18,r3-26, r2-41,r2-40,r3-71,r2-50,r2-49,r2-38,r3-97,r2-46,r3-12,r3-66,r3-104,r3-82,r3-5,r3-4 |
| Kaaret (2002) 142 sources | |
| 26 not detected | |
| 3 transient: | J004217.0+411508,J004243.8+411604,J004245.9+411619 |
| 7 variable: | J004232.7+411311,J004242.0+411532,J004243.1+411640,J004244.3+411605,J004245.2+411611,J004245.5+411608, J004248.6+411624 |
| 16 unclassified: | J004207.3+410443,J004229.1+412857,J004239.5+411614,J004239.6+411700,J004242.5+411659,J004242.7+411503, J004243.1+411604,J004244.2+411614,J004245.0+411523,J004246.1+411543,J004247.4+411507,J004249.1+411742, J004251.2+411639,J004252.3+411734,J004252.5+411328,J004318.5+410950 |
| Williams et al. (2004a) 166 sources | |
| 28 not detected | |
| 12 transient: | s1-79,s1-80,s1-82,r3-46,r2-28,r1-23,r1-19,r2-69,r1-28,r1-35,r1-34,n1-85 |
| 7 variable: | r2-31,r1-31,r1-24,r1-20,r1-7,r1-17,r1-16 |
| 9 unclassified: | s1-81,r2-68,s1-85,r1-30,r1-22,r1-26,r1-18,n1-77,n1-84 |
| Voss & Gilfanov (2007) 261 sources | |
| 104 not detected | |
| 11 transient: | 6,12,29,32,41,51,59,84,118,130,146 |
| 15 variable: | 3,5,8,9,18,22,24,27,44,63,92,96,99,149,169 |
| 78 unclassified: | 4,19,21,25,26,30,37,39,40,42,48,49,53,56,57,58,60,62,65,70,73,75,76,77,80,82,84,86,87,89,91,94,97,98,104,109,114, 115,117,119,122,124,129,133,138,141,143,144,145,150,152,158,162,164,167,171,173,182,183,188,189,191,193,194, 197,202,205,206,210,213,217,219,220,225,256,257,263 |
| Williams et al. (2006b) 45 sources | |
| 25 not detected | |
| 25 transient: | n1-26,n1-85,n1-86,n1-88,n1-89,r1-19,r1-23,r1-28,r1-34,r1-35,r2-28,r2-61,r2-62,r2-66,r2-69,r2-72,r3-43,r3-46,s1-18, s1-27,s1-69,s1-79,s1-80,s1-82,s2-62 |
| DKG2004 43 sources | |
| 15 not detected | |
| 9 transient: | s2-62,s1-27,s1-69,s1-18,n1-26,r2-62,r1-35,r2-61,r2-66 |
| 5 unclassified: | s2-27,s2-10,n1-29,n1-46,r2-54 |
| 1 not in FoV: | n1-66 |
| Di Stefano et al. (2002) 28 sources | |
| 2 not detected | |
| 2 unclassified: | 17 ($\hat{=}$ r2-15), 28 ($\hat{=}$ r3-71) |

Notes:

Variability information (transient, variable) is taken from the papers. "Unclassified" denotes sources which are not indicated as transient or variable sources in the papers.

the field of M 31 covered by the Deep *XMM-Newton* Survey[1]. The second source ([TP2004] 21) correlates with r3-71, which is discussed above (see Di Stefano et al. (2002) in Table 9.2). The transient nature of the third source ([TP2004] 35), and the fact that it was not observed in any *XMM-Newton* observation taken before 2004, was already reported by Trudolyubov & Priedhorsky (2004). The source was first detected with *XMM-Newton* in the observation from 31 December 2006 (see Sect. 9.4.4).

### 9.1.3 *ROSAT* catalogues

Of the 86 sources detected with *ROSAT* HRI in the central $\sim 34'$ of M 31 (PFJ93), all but eight sources ([PFJ93] 1,2,31,33,40,48,63,85) are detected in the *XMM-Newton* observations. Six of these eight sources ([PFJ93] 1,2,31,33,63,85) were already discussed in PFH2005 and classified as transients. The sources [PFJ93] 40 and 48 correlate with [PFH2005] 312 and 332, respectively, which are discussed in Sect. 9.1.1. In addition to these eight sources PFH2005 did not detect source [PFJ93] 51. This source was detected in the *XMM-Newton* observations centred on RX J0042.6+4115 and thus classified as a recurrent transient (see Sect. 6.4.4).

In each of the two *ROSAT* PSPC surveys of M 31, 396 individual X-ray sources were detected (SHP97 and SHL2001). From the SHP97 catalogue 129 sources were not detected. Of these sources 48 are located outside the FoV of our *XMM-Newton* M 31 survey. From the SHL2001 catalogue 92 sources are not detected. Sixty sources lie outside the *XMM-Newton* FoV. For information on individual sources see Table 9.3.

Forty-four (out of 302) sources from SHP97 and 27 (out of 293) sources from SHL2001, respectively, have *ROSAT* detection likelihoods larger than 15 but are not listed in the XMM LP-total catalogue. These sources have to be regarded as transient or at least highly variable.

### 9.1.4 *Einstein* catalogue

The list of *Einstein* X-ray sources in the field of M 31 reported by TF91 contains 108 sources, with 81 sources taken from the *Einstein* HRI data with an assumed positional error of $3''$ (reported by Crampton et al. 1984), and 27 sources based on *Einstein* IPC data with a $45''$ positional error. Applying the above mentioned correlation procedure to the *Einstein* HRI sources, 64 of these sources are also detected in this work and listed in the XMM LP-total catalogue, *i. e.* 17 sources are not detected ([TF91] 29, 31, 35, 39, 40, 43, 46, 50, 53, 54, 65, 66, 72, 75, 78, 93, 96). For the *Einstein* IPC sources only the one $\sigma$ positional error was used to search for counterparts among the *XMM-Newton* sources. Of the 27 *Einstein* IPC sources six remain without a counterpart ([TF91] 15, 99, 100, 106, 107, 108), where [TF91] 15 and 108 are located outside the field of M 31 covered by the observations used for the XMM LP-total catalogue. The sources [TF91] 50 and 54 correlate with [PFH2005] 312 and 316, respectively. Both sources were already discussed in Sect. 9.1.1. Apart from [TF91] 106 which is suggested as a possible faint transient by SHL2001, the remaining 18 sources are also non detected by PFH2005. They classified those sources as transient.

### 9.1.5 Catalogue used for Log N–Log S calculation

In this subsection I discuss the correlation between the XMM LP-total catalogue and the catalogue that was created to analyse the luminosity functions (XMM LP-hard catalogue; see Sect. 8.3).

The cross-correlations are presented in Table 9.4[2]. That table gives the source number from the XMM LP-hard catalogue (Col. 1), the source number of the correlating source from the XMM LP-total catalogue

[1] The source was observed with *XMM-Newton* on 11 January 2001. Obs. id.: 0065770101

[2] Table 9.4 is only available in electronic form on the attached CD. A description of the content of this table can be found in Appendix E.

**Table 9.3:** Sources from the *ROSAT* PSPC catalogues that are not present in the XMM LP-total catalogue.

| | |
|---|---|
| SHP97 396 sources | |
| 129 not detected | |
| 48 outside FoV: | 1,2,3,4,5,7,8,14,31,41,72,91,98,104,120,125,159,202,209,271,276,285,286,290,300,312,314, 320,342,350,363,367,371,374,383,385,386,387,388,389,390,391,392,393,394,395,396 |
| 1 transient: | 69 |
| 21 not detected, LH<12: | 19,24,27,33,46,52,59,63,68,71,133,149,161,264,273,275,307,329,330,358,377 |
| 15 not detected, 12≤LH<15: | 12,15,49,82,93,113,114,128,196,230,283,334,364,372,376 |
| 44 not detected, LH≥15: | 16(LH=26.6),32(30.2),43(18.2),45(51.2),60(20.1),66(36.2),67(4536.2),78(20.5),80(16.3),81(26.6), 88(33.7),95(548.0),102(16.4),126(217.3),141(843.3),145(46.9),146(673.7),166(17.4),167(90.0), 171(54.3),182(454.4),186(39.8),190(113.0),191(54.5),192(54.3),203(103.3),214(400.2),215(251.0), 232(104.4),245(26.0),260(54.6),263(38.1),265(24.6),268(54.3),270(40.4),277(15.6),309(81.8), 319(23.4),331(19.5),335(51.2),340(27.5),341(28.1),365(22.4),373(69.5) |
| SHL2001 396 sources | |
| 92 not detected | |
| 60 outside FoV: | 1,2,3,4,5,6,7,8,9,10,11,12,14,15,16,21,22,32,39,58,67,69,75,77,81,83,85,90,93,125,141,146, 160,164,192,202,243,260,282,296,298,302,325,326,328,355,371,372,378,379,383,388,389,390, 391,392,393,394,395,396 |
| 3 not detected, LH<12: | 62,96,238 |
| 2 not detected, 12≤LH<15: | 231,361 |
| 27 not detected, LH≥15: | 51(LH=28.4),104(901.2),121(94.1),126(46.2),143(34.7),168(131.9),171(43.0),173(317.8),190(215.8), 207(98.0),208(298.8),226(73.1),230(75.6),232(1165.6),240(218.4),246(39.9),248(219.6),256(60.0), 267(22.2),271(52.8), 322(2703.3),324(147.7),344(40.7),356(15.3),365(19.0),380(17.4),384(15.8) |

(2), the spatial distance between both sources (3) and the source type from the XMM LP-total catalogue (4). The last column, (5), flags sources that are listed more than once. The table is sorted according to the source numbers of the XMM LP-hard catalogue.

In total 1 107 sources of the 1 254 sources of the XMM LP-hard catalogue have counterparts in the XMM LP-total catalogue. Three of them have two correlations with sources of the XMM LP-total catalogue (flagged with "2" in Col. 5 of Table 9.4). There is only one source of the XMM LP-total catalogue (N$^{o}$ 745) that correlates with two sources in the XMM LP-hard catalogue (flagged with "3" in Col. 5 of Table 9.4).

Table 9.5 gives the number of classified and identified sources for individual source classes using the classification from the XMM LP-total catalogue. The identified foreground stars and foreground star candidates were excluded from the analysis on the luminosity functions. No SSS and only ∼10% of the soft sources (foreground stars and SNRs) from the XMM LP-total catalogue were found. This is expected since these sources mostly emit in the energy bands below 2 keV. Of the remaining sources in the XMM LP-total catalogue >70% were found in the XMM LP-hard catalogue. There are several reasons why the remaining ∼30% are not detected. One reason is that the class of <hard> sources, due to its definition, still contains sources that have a significant flux contribution below 2 keV.[3] Therefore we cannot expect that all sources listed as <hard> in the XMM LP-total catalogue will also be detected in the 2.0–10.0 keV band, since the missing flux contribution can reduce the detection likelihood below the limiting threshold. A second reason is that in "crowded fields", like in the centre of M 31, or in case of two or more sources located next to each other, sources are not detected because of the reduced resolution (factor of 4) of the images, background images and the exposure maps used for the creation of the XMM LP-hard catalogue. A third, but somewhat minor reason, is that observation b (which contains some transients; *cf.* Chap. 6) and h4 are not included in the XMM LP-hard catalogue. Hence, sources that are only visible in these observations cannot appear in the XMM LP-hard catalogue.

[3] In the hardness ratio diagrams an overlap exists with the class of foreground stars and candidates. As shown before we only detected ∼10% of the sources of the latter class in the 2.0–10.0 keV band.

**Table 9.5:** Summary of identified and classified sources.

| Source class | identified | classified |
|---|---|---|
| fg Stars | 5 | 19 |
| AGN | 11 | 37 |
| Gal | 2 | 10 |
| GCl | 1 | 2 |
| SNR | 1 | 7 |
| XRB | 6 | 17 |
| GlC | 33 | 13 |

147 sources of the XMM LP-hard catalogue remain without a counterpart from the XMM LP-total catalogue. For 15 of these 147 sources, counterparts can be found in the catalogue of PFH2005. In PFH2005, most of the counterparts are classified as hard (12), while one is suggested to be an SNR candidate and two have no classification.

In summary, these comparisons show that the catalogue created for the study of luminosity functions contains mainly sources identified/classified as XRBs, GlCs, background objects or <hard>, as was expected. Therefore the log N-log S studies presented in Chap. 8, do really probe a population mainly consisting of X-ray binaries and (a few) Crab-like SNRs of M 31.

## 9.2 Cross-correlations with catalogues at other wavelengths

The XMM LP-total catalogue was correlated with the catalogues and public data bases given in Sect. 5.2.9. Two sources (from the XMM LP-total and from the reference catalogues, respectively) will be considered as correlating if their positions match within the $3\sigma$ uncertainty (see Eq. 5.3).

However, the correlation of an X-ray source with a source from the reference catalogue does not necessarily imply that the two sources are counterparts. To confirm that a source from the reference catalogue is a counterpart of an X-ray source, additional information is needed, like corresponding temporal variability of both sources or corresponding spectral properties. We should also take the possibility into account, that the counterpart of the examined X-ray source is not even listed in the reference catalogue used.

The whole correlation process will get even more challenging if an X-ray source correlates with more than one source from the reference catalogue. In this case we need a method to decide which of the correlating sources is the most likely to correspond to the X-ray source in question. Therefore, the used method should indicate how likely the correlation is with each of the sources from the reference catalogue. Based on these likelihoods one can define criteria to accept a source from the reference catalogue as being the most likely source to correspond to the X-ray source. The simplest method uses the spatial distance between the X-ray source and the reference sources to derive the likelihoods. In other words, the source from the reference catalogue that is located closest to the X-ray source is regarded as the most likely source corresponding to the X-ray source. An improved method is a "likelihood ratio" technique, where an additional source property (*e. g.* an optical magnitude in deep field studies) is used to strengthen the correlation selection process. This technique was applied successfully to deep fields to find optical counterparts of X-ray sources (*e. g.* Brusa et al. 2007). A drawback of this method is that one has to know the expected probability distribution of the optical magnitudes of the sources belonging to the studied object a priori. In our case, this means that we have to know the distribution function for all optical sources of M 31 that can have

X-ray counterparts, *without* including foreground and background sources. Apart from the fact that such distribution functions are unknown, an additional challenge would be the time dependence of the magnitude of the optical sources (*e. g.* of novae) and of the connection between optical and X-ray sources (*e. g.* optical novae and SSSs). Therefore it is not possible to apply this "likelihood ratio" technique to the sources in the Deep *XMM-Newton* survey.

The whole correlation selection process becomes even more challenging if more than one reference catalogue is used.

To be able to take all available information into account, we decided not to automatise the selection process, but to select the class and most likely correlations for each source by hand (as it was done *e. g.* in PFH2005). Therefore the source classification, and thus the correlation selection process, is based on the cross correlations between the different reference catalogues, on the X-ray properties (hardness ratios, extent and time variability), and on the criteria given in Table 7.3. For reasons of completeness I give for each X-ray source the number of correlations found in the USNO-B1, 2MASS and LGS catalogues in Table 7.2. The caveat of that method is that it cannot quantify the probability of the individual correlations.

## 9.3 Foreground stars and background objects

### 9.3.1 Foreground stars

Foreground stars are a class of X-ray sources which are homogeneously distributed over the field of M 31 (Fig. 9.3). The good positioning of *XMM-Newton* and the available catalogues USNO-B1, 2MASS and LGS allow us to effectively select this type of source. The selection criteria are given in Table 7.3. Exceptions are very red foreground stars, with an LGS colour $\mathrm{V} - \mathrm{R} > 1$ or USNO-B1 colour $\mathrm{B2} - \mathrm{R2} > 1$. They are classified as foreground star candidates, if $f_\mathrm{x}/f_\mathrm{opt} < -0.65$ and $f_\mathrm{x}/f_\mathrm{opt,R} < -1.0$. If the position of the foreground star candidate lies within the field covered by the Local Group Survey (LGS) I then checked its visibility in the images of the LGS. Otherwise DSS2 images were used. Correlations with bright optical sources from the USNO-B1 catalogue, with an $f_\mathrm{x}/f_\mathrm{opt}$ in the range of foreground stars, that were not visible in the optical images were rejected. I found 227 foreground star candidates. Thirty-nine sources were identified as foreground stars, either because they are listed in the globular cluster catalogues as spectroscopically confirmed foreground stars or because a spectral type is indicated in the literature (Bonfini et al. 2009; Hatzidimitriou et al. 2006, SIMBAD).

Two of the foreground star candidates close to the centre of M 31 (№ 828, № 1 112) have no entry in the USNO-B1 and LGS catalogues, and one has no entry in the USNO-B1 R2 and B2 columns (№ 978). However they are clearly visible on LGS images, they are 2MASS sources and they fulfil the X-ray hardness ratio selection criteria. Therefore, I also classify them as foreground stars.

The following 19 sources were selected as very red foreground star candidates: № 54, № 118, № 384, № 391, № 393, № 585, № 646, № 651, № 711, № 1 038, № 1 119, № 1 330, № 1 396, № 1 429, № 1 506, № 1 605, № 1 695, № 1 713 and № 1 747. A further 11 sources (№ 79, № 210, № 269, № 278, № 310, № 484, № 714, № 978, № 1 591, № 1 908 and № 1 930) fulfil the hardness ratio criteria, but violate the $f_\mathrm{x}/f_\mathrm{opt}$ criteria and are therefore marked as "foreground star candidates" in the comment column of Table 7.2.

Six sources (№ 473, № 780, № 1 551, № 1 585, № 1 676, № 1 742) classified as foreground star candidates, have X-ray light curves that in a binning of 1 000 s showed flares (see Fig. 9.4). These observations strengthen the foreground star classification. A seventh source (№ 714) is classified as a foreground star candidate, since its hardness ratios and its $f_\mathrm{x}/f_\mathrm{opt}$ ratio in the quiescent state fulfil the selection criteria of foreground star candidates. In addition the source shows a flare throughout observation ss3. Hence, the $f_\mathrm{x}/f_\mathrm{opt}$ ratio for this observation, in which the source is brightest, is too low to be consistent with the value

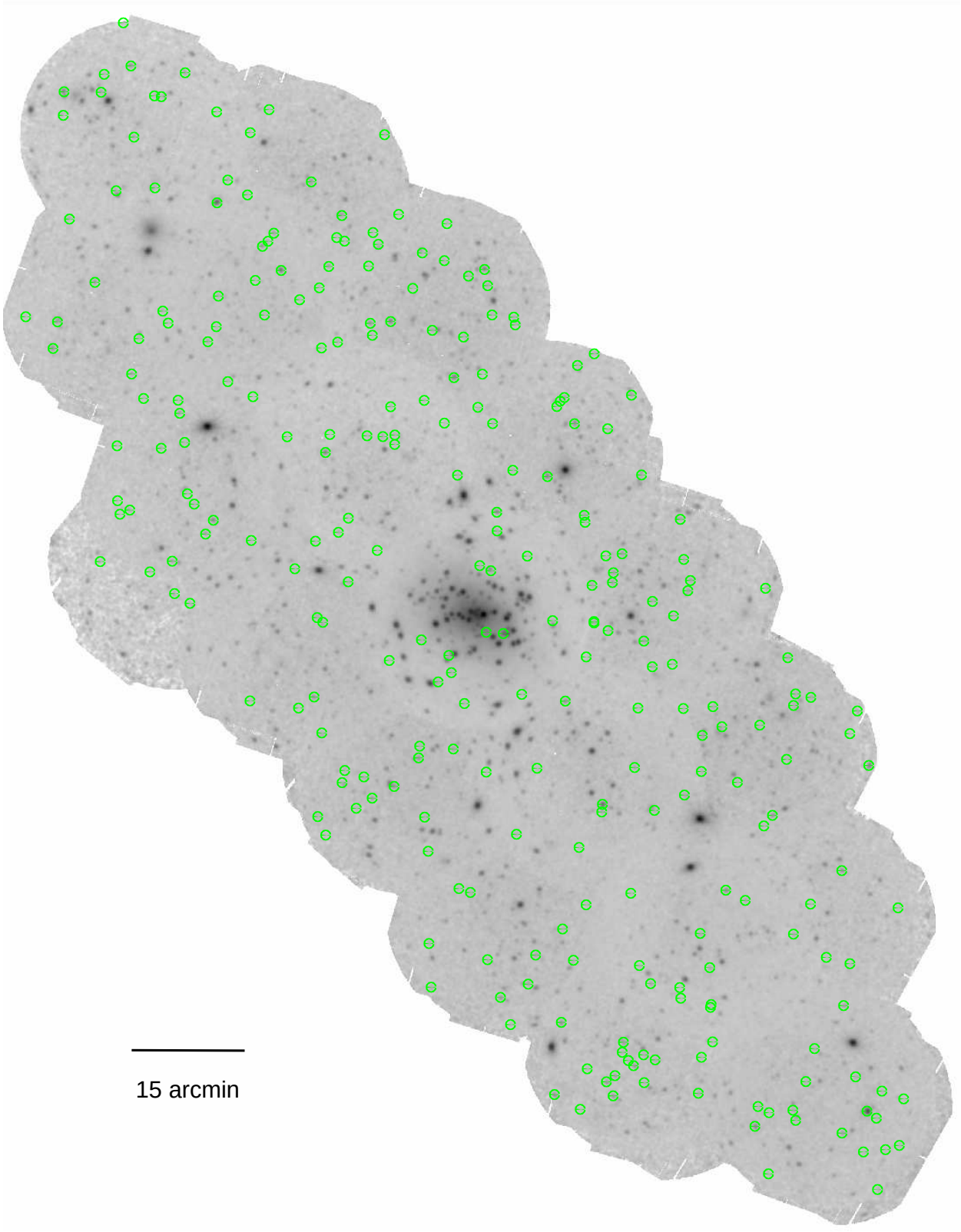


**Figure 9.3:** The spatial distribution of foreground stars and candidates, classified in the XMM LP-total catalogue. The image shows the homogeneous distribution of the sources over the covered field (marked with green dots).

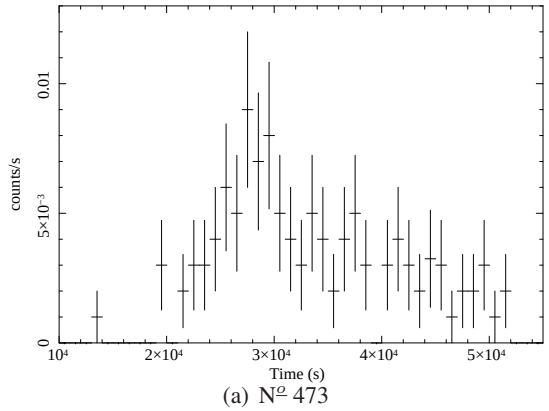


(a) N$^{o}$ 473

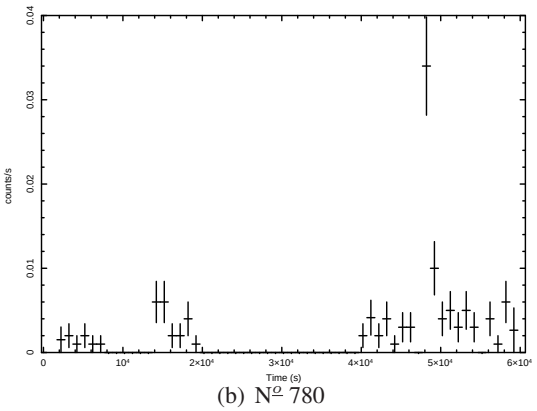


(b) N$^{o}$ 780

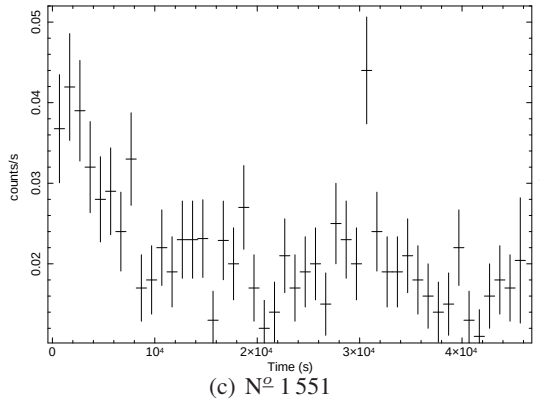


(c) N$^{o}$ 1 551

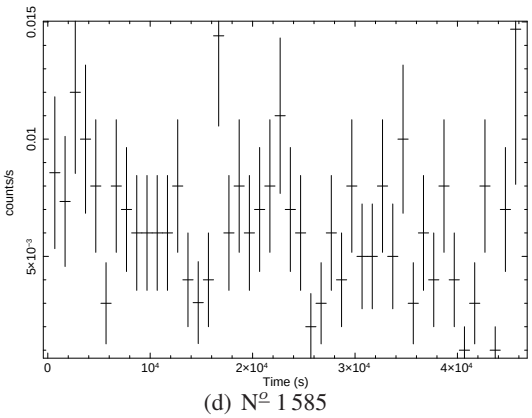


(d) N$^{o}$ 1 585

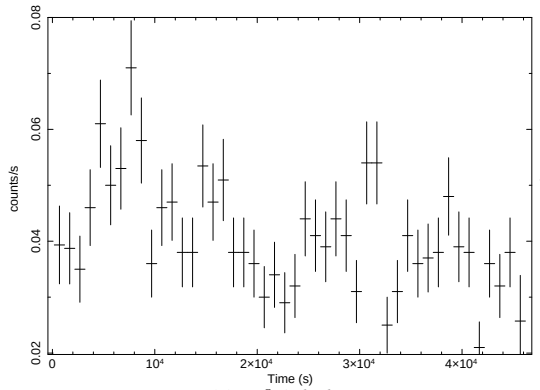


(e) N$^{o}$ 1 676

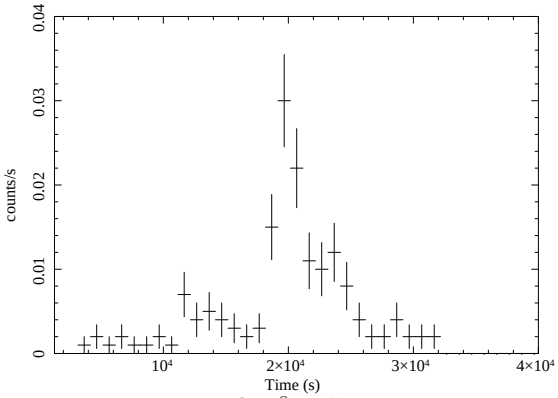


(f) N$^{o}$ 1 742

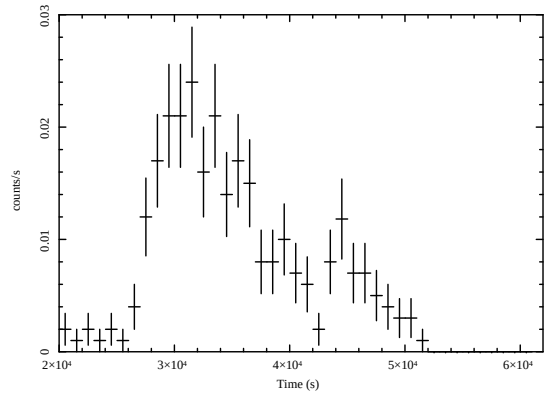


(g) N$^{o}$ 714

**Figure 9.4:** X-ray light curves of foreground stars and candidates that, with a binning of 1000 s, show flares.

range expected for foreground stars.

Figure 9.5 shows the XID flux distribution for foreground stars and foreground star candidates, which ranges from $6.8\times10^{-16}$ erg cm$^{-2}$ s$^{-1}$ to $2.0\times10^{-13}$ erg cm$^{-2}$ s$^{-1}$. Most of the foreground stars and candidates (260 sources) have fluxes below $5\times10^{-14}$ erg cm$^{-2}$ s$^{-1}$.

#### 9.3.1.1 Comparing *XMM-Newton*, *Chandra* and *ROSAT* catalogues

In the combined *ROSAT* PSPC survey (SHP97, SHL2001) 55 sources were classified as foreground stars. Of these sources 14 remain without counterparts in the present *XMM-Newton* survey. Five of these 14 sources are located outside the field observed with *XMM-Newton*. Forty-one *ROSAT* foreground star candidates have counterparts in the XMM LP-total catalogue. Of these counterparts 16 were classified as foreground star candidates and four were identified as foreground stars (spectral type from Bonfini et al. 2009; Hatzidimitriou et al. 2006, or SIMBAD). In addition 12 sources were listed as <hard>, two as AGN candidates and

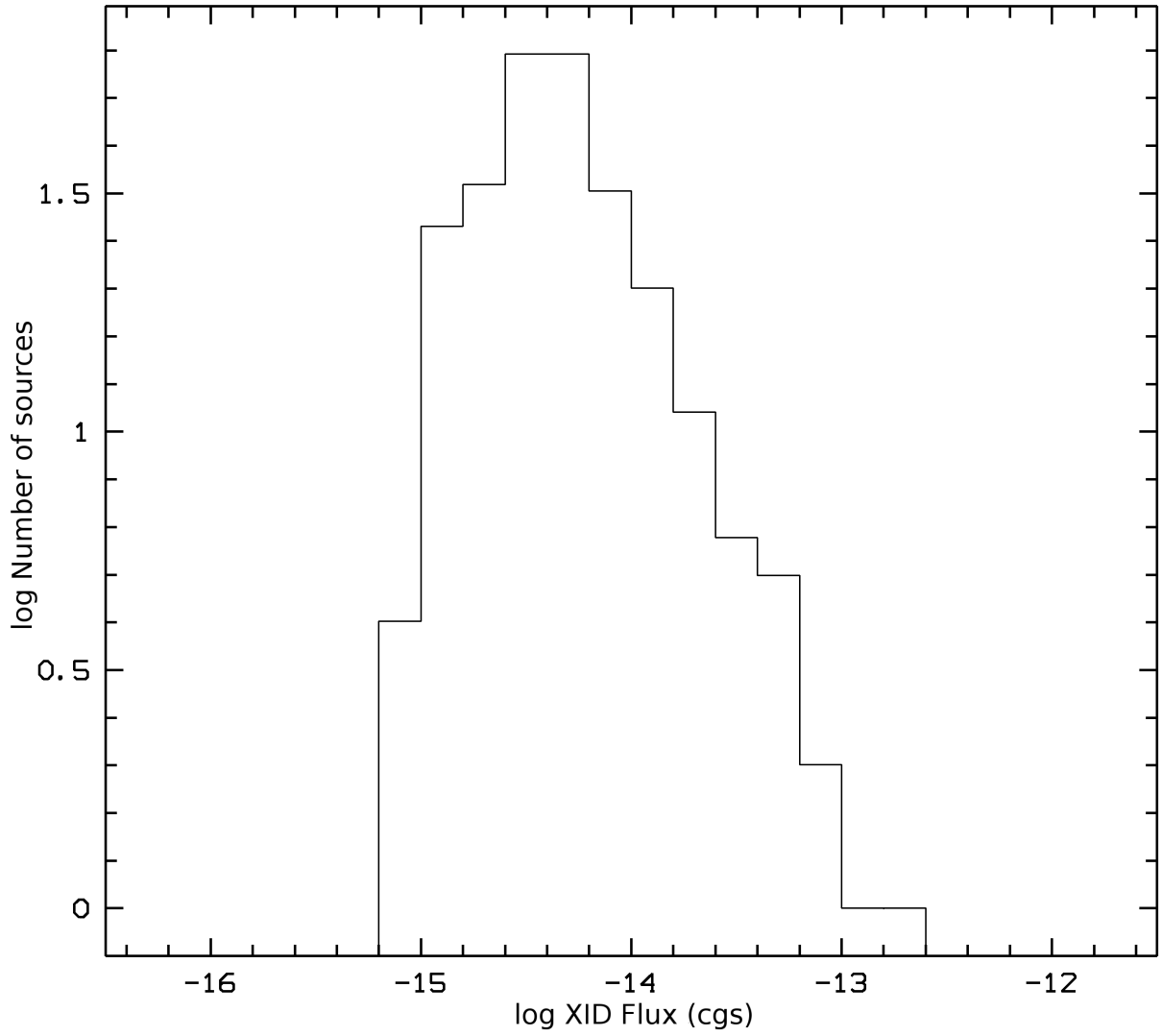


**Figure 9.5:** Distribution of the source fluxes in the 0.2–4.5 keV (XID) band. The diagram shows a histogram of the number of foreground stars and candidates per flux bin, in logarithmic scales.

one as globular cluster candidate in the XMM LP-total catalogue. The counterparts of three *ROSAT* sources remain without classification in the XMM LP-total catalogue. Another three *ROSAT* sources have more than one counterpart in the *XMM-Newton* data. Source [SHP97] 109 correlates with sources Nº 597, Nº 604, Nº 606, and Nº 645. The former three are classified as <hard>, while source Nº 645 is classified as a foreground star candidate. However source Nº 645 has the largest distance to the position of [SHP97] 109 from the four *XMM-Newton* counterparts. Furthermore that source had a flux below the *ROSAT* detection threshold (about a factor 2.6) in the *XMM-Newton* observations and is about a factor 3–34 fainter than the three other possible *XMM-Newton* counterparts. Thus it is very unlikely that [SHP97] 109 represents the X-ray emission of a foreground star. Source [SHL2001] 156 has two *XMM-Newton* counterparts and is discussed in Sect. 9.4.1.3. The third source ([SHL2001] 374) correlates with sources Nº 1 922 and Nº 1 924. The two *XMM-Newton* sources are classified as <hard> and as a foreground star candidate, respectively. In the source catalogue of SHL2001 source [SHP97] 369 is listed as counterpart of [SHL2001] 374. The source in the first *ROSAT* survey has a smaller positional error and only correlates with source Nº 1 924. Although this seems to indicate that source Nº 1 924 is the counterpart of [SHL2001] 374, we cannot exclude the possibility that [SHL2001] 374 is a blend of both *XMM-Newton* sources, as these two sources have similar luminosities in the *XMM-Newton* observations.

Kong et al. (2002b) classified four sources as foreground stars. For two sources (Nº 960≙r2-42 and Nº 976≙r3-33) the classification is confirmed by our study. The third source (Nº 1000≙r2-19) remained without classification in the XMM LP-total catalogue, as it is too soft to be classified as <hard> and the optical counterpart found in the LGS catalogue does not fulfil the $f_{\rm x}/f_{\rm opt}$ criteria. The fourth source (r2-46) was not detected in the *XMM-Newton* observations.

The foreground star classification of three sources (s1-74, s1-45, n1-82) in Williams et al. (2004a) is confirmed from the *XMM-Newton* Deep Survey study (Nº 289, Nº 603, Nº 1 449). For source Nº 289 the spectral type F0 was determined (Hatzidimitriou et al. 2006).

The source list of DKG2004 contains six sources (s2-46, s2-29, s2-37, s1-45, s1-20, r3-122) that are classified as foreground stars. All six sources are confirmed as foreground star candidates by our *XMM-Newton* study (*cf.* Table 9.13). For source Nº 696 (≙s1-20) Hatzidimitriou et al. (2006) obtained the spectral type G0.

Of the four sources listed as foreground stars in Voss & Gilfanov (2007) only one source (Nº 936≙ [VG2007] 168) was confirmed as a foreground star, based on the entry in the RBC V3.5 and Caldwell et al. (2009). The second source (Nº 1 118≙[VG2007] 180) is listed in the RBC V3.5 and Caldwell et al. (2009) as a globular cluster. The third source (Nº 829≙[VG2007] 181) does not have a counterpart in the USNO-B1, 2MASS or LGS catalogues, nor does it fulfil the hardness ratio criteria for foreground stars. Hence the source is classified as <hard>. The fourth source ([VG2007] 81) is not spatially resolved from its neighbouring source [VG2007] 79 in our *XMM-Newton* observations (source Nº 1 078). Hence source Nº 1 078 is classified as <hard>.

### 9.3.2 Galaxies, galaxy clusters and AGN

I identified four sources as background galaxies and 11 as AGN, and classified 19 galaxy and 49 AGN candidates. The classification is based on SIMBAD and NED correlations and correlations with sources listed as background objects in the globular cluster catalogues (RBC V3.5 and Caldwell et al. 2009). Sources are classified as AGN candidates, if they have a radio counterpart (NVSS; Braun 1990; Gelfand et al. 2004) with the additional condition of being neither an SNR nor an SNR candidate from X-ray hardness ratios, as well as not being listed as a "normal" background galaxy in Gelfand et al. (2004).

One (Nº 995) of the four identified galaxies is M 32. An overview of former X-ray observations of this galaxy is given in PFH2005. They also discuss the fact that *Chandra* resolved the X-ray emission of M 32 into several distinct point sources (maximum separation of the three central *Chandra* sources $8\farcs3$).

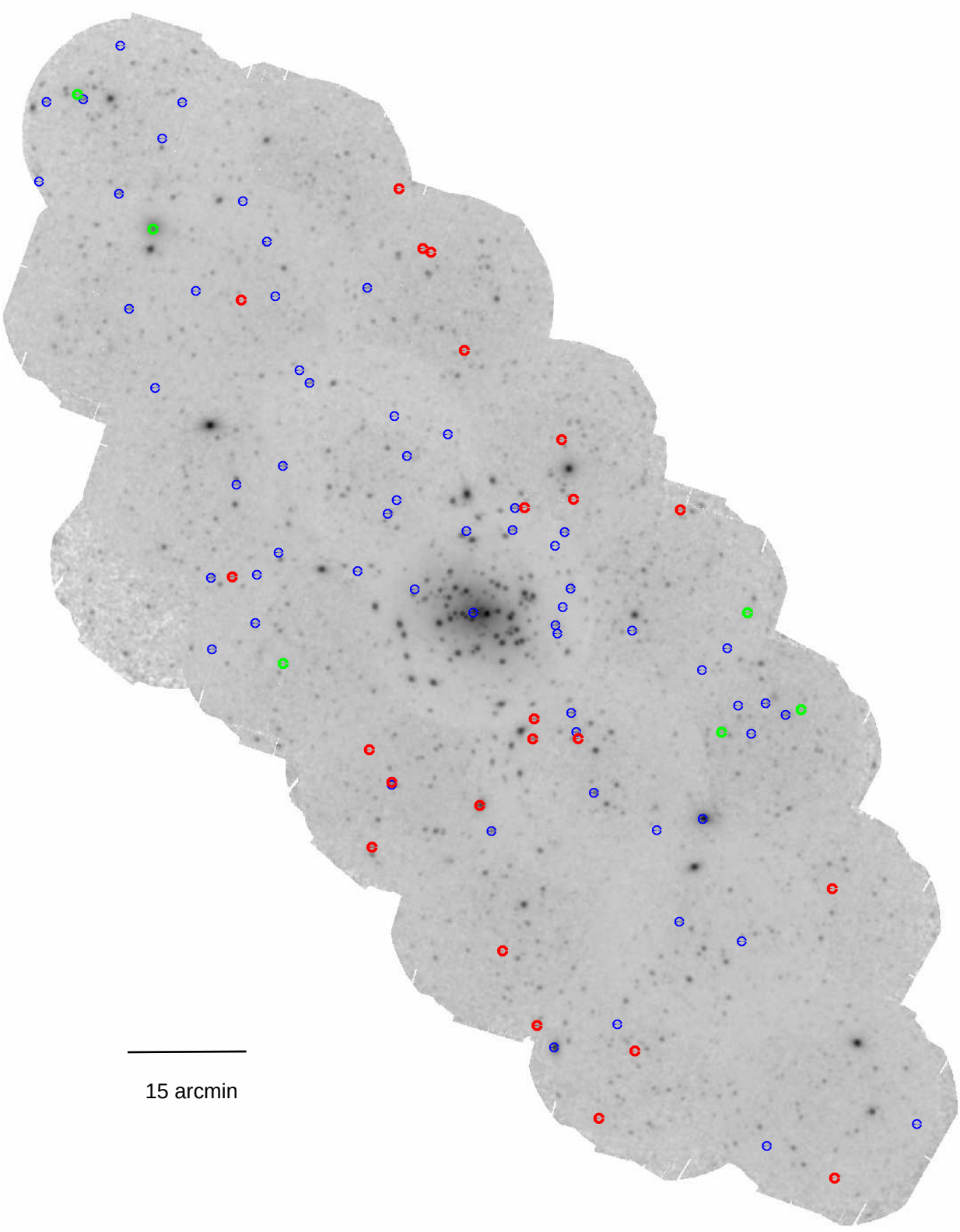


**Figure 9.6:** The spatial distribution of background sources and candidates, classified in the XMM LP-total catalogue. AGN are marked with blue dots, "normal" galaxies with red dots and galaxy clusters with green dots.

Although M 32 is located closer to the centre of the FoV in the Deep Survey observations of field SS1, than it was in the s1 observation used in PFH2005, *XMM-Newton* still detects only one source. The remaining three sources (№ 88, № 403, № 718) are identified as galaxies, because they are listed as background galaxies in both the RBC V3.5 and Caldwell et al. (2009). For source № 403 (B 007) NED gives a redshift of $0.139692 \pm 0.000230$ (Kim et al. 2007b).

Eleven X-ray sources are identified as AGN. The first one (№ 363) correlates with a BL Lac object located beyond M 31 (NED, see also PFH2005). The second source (№ 745) correlates with a Seyfert 1 galaxy (5C 3.100), which has a redshift of $\approx 0.07$ (SIMBAD). The remaining sources were spectroscopically confirmed (from our optical follow-up observations) to be AGN (D. Hatzidimitriou, private communication).

In Sect. 7.3 the 12 extended sources were presented. Kotov et al. (2006) showed that the brightest of these sources (№ 1795) is a galaxy cluster located at a redshift of $z = 0.29$.

For the remaining 11 sources, X-ray spectra were created and fitted with the `MEKAL` model in `Xspec`. Unfortunately, for most of the examined sources the spectral parameters (foreground absorption, temperature and redshift) are not very well constrained. Nevertheless four sources (№ 141, № 252, № 304, № 1543) with temperatures in the range of $\sim$ 1–2 keV and proposed redshifts between 0.1 – 0.6 were found (Table 9.6). Inspection of optical images (DSS 2 images and if available LGS images) revealed an agglomeration of optical sources at the positions of these four extended X-ray sources. Thus they are classified as galaxy cluster candidates.

Although, B242 (the optical counterpart of source № 304) is listed as a globular cluster candidate in the RBC3.5 catalogue, Caldwell et al. (2009) classified this source as a background object. My findings from the X-rays strengthen the background object classification. Hence a globular cluster classification for this source seems to be excluded.

Source № 1 912 was already classified as a galaxy cluster candidate in PFH2005. The spectrum confirms this classification. The best fit parameters are $N_{\rm H} = 1.29^{+0.53}_{-0.41} \times 10^{21}$ cm$^{-2}$, $T = 2.8^{+0.8}_{-0.5}$ keV and redshift of $0.06^{+0.03}_{-0.04}$.

A plot of the spatial distribution of the classified / identified background sources is given in Fig. 9.6, which shows that these sources are rather homogeneously distributed over the observed field. However, in the fields located along the major axis of M 31 we mainly see AGN, which are bright enough to be visible through M 31, while most of the galaxies and galaxy clusters are detected in the outer fields.

#### 9.3.2.1 Comparing *XMM-Newton*, *Chandra* and *ROSAT* catalogues

Of the ten *ROSAT* PSPC survey sources classified as background galaxies one is located outside the field of the Deep *XMM-Newton* Survey. The remaining objects are confirmed to be background sources and are classified or identified as galaxies or AGN. The only case which is worth discussing in more detail is the source pair [SHP97] 246 and [SHL2001] 252. From the *XMM-Newton* observations it is evident that this

**Table 9.6:** Spectral fit parameters for extended sources

| Src ID | $N_{\rm H}/10^{21}$ cm$^{-2}$ | $k_{\rm B}T$/keV | redshift | $\chi^2$/dof |
|---|---|---|---|---|
| 141 | $1.19^{+1.63}_{-0.88}$ | $2.17^{+2.30}_{-0.68}$ | $0.24^{+1.24}_{-0.11}$ | 78.5/53 |
| 252 | $0.61^{+1.16}_{-0.43}$ | $1.95^{+0.64}_{-0.29}$ | $0.22^{+0.15}_{-0.07}$ | 56.4/151 |
| 304 | $2.68^{+2.64}_{-1.85}$ | $0.95^{+3.32}_{-1.95}$ | $0.12^{+0.07}_{-0.05}$ | 50.9/57 |
| 1543 | $2.74^{+6.91}_{-1.76}$ | $2.08^{+2.31}_{-1.11}$ | $0.61^{+1.11}_{-0.26}$ | 32.9/34 |

source pair is not one source, as indicated in the combined *ROSAT* PSPC source catalogue (SHL2001), but consists of three individual sources (№ 1 269, № 1 279 and № 1 280). [SHL2001] 252 correlates spatially with all three *XMM-Newton* sources, while [SHP97] 246 correlates only with source № 1 269, which is identified as a foreground star of type K2 (SIMBAD). The two other *XMM-Newton* counterparts of [SHL2001] 252 are classified as a galaxy and an AGN candidate, respectively. In summary, [SHL2001] 252 is most likely a blend of both background sources and maybe even a blend of all three *XMM-Newton* sources, while [SHP97] 246 seems to be the X-ray counterpart of the foreground star mentioned above.

Kong et al. (2002b) classified source r3-83 (№ 1 132) as an extragalactic object, as it is listed in SIMBAD and NED as an emission line object. Following PFH2005, we classified source № 1 132 as <hard>. The BL Lac object (№ 363) was also detected in *Chandra* observations (Williams et al. 2004a).

## 9.4 M 31 sources

### 9.4.1 Supersoft sources

The XMM LP-total catalogue contains 40 SSS candidates that were selected from their hardness ratios (see Fig. 7.5 and Table 7.3).

#### 9.4.1.1 Spatial and flux distribution

Figure 9.7 shows the spatial distribution of the SSSs. Clearly visible is a concentration of sources in the central field. There are two explanations for that central enhancement. The first is that the central region was observed more often than the remaining fields and therefore there is a higher chance of catching a transient SSS in outburst. The second reason is that the major class of SSSs in the centre of M 31 are optical novae (PFF2005, PHS2007).

Figure 9.8 gives the distribution of 0.2–1.0 keV source fluxes for all SSSs (black) and for those correlating with optical novae (blue). The unabsorbed fluxes were determined assuming a 50 eV blackbody model (PFF2005). The two brightest SSSs ($F_{\rm X}$ $>10^{-12}$ erg cm$^{-2}$ s$^{-1}$) are firstly a persistent source with 217 s pulsations (№ 1 061; Trudolyubov & Priedhorsky 2008) and the second is nova M31N 2001-11a (№ 1 416; Smirnova et al. 2006). A large fraction of SSSs are rather faint with fluxes below $5\times10^{-14}$ erg cm$^{-2}$ s$^{-1}$. Nine sources have absorbtion-corrected luminosities below $10^{36}$ erg s$^{-1}$ (0.2–1.0 keV), which was indicated as the limiting luminosity for SSSs (*cf.* Sect. 2.2.1.2). That does not necessarily imply that those sources are not SSSs, since it is possible that the chosen blackbody fit does not represent well the properties of these sources. A higher absorption or a lower temperature would lead to increased unabsorbed luminosities. We also have to take into account that we might have observed the source during a phase of rising or decaying luminosity, *i. e.* not at maximum luminosity.

#### 9.4.1.2 Correlations with optical novae

By cross-correlating with the nova catalogue indicated in Sect. 5.2.9, 14 of the 40 sources can be classified as X-ray counterparts of optical novae. Of these 14 novae, eight (№ 748, № 993, № 1 006, № 1 046, № 1 051, № 1 076, № 1 100, and № 1 236) are already discussed in PFF2005 and PHS2007. Nova M31N 2001-11a was first detected as a supersoft X-ray source. Triggered by that SSS detection, Smirnova et al. (2006) found an optical nova at the position of the SSS in archival optical plates which was overlooked in previous nova searches. The remaining five novae are discussed individually in more detail below. As was shown in the *XMM-Newton*/*Chandra* M 31 nova monitoring project[4], it is absolutely necessary to have

[4] http://www.mpe.mpg.de/~m31novae/xray/index.php

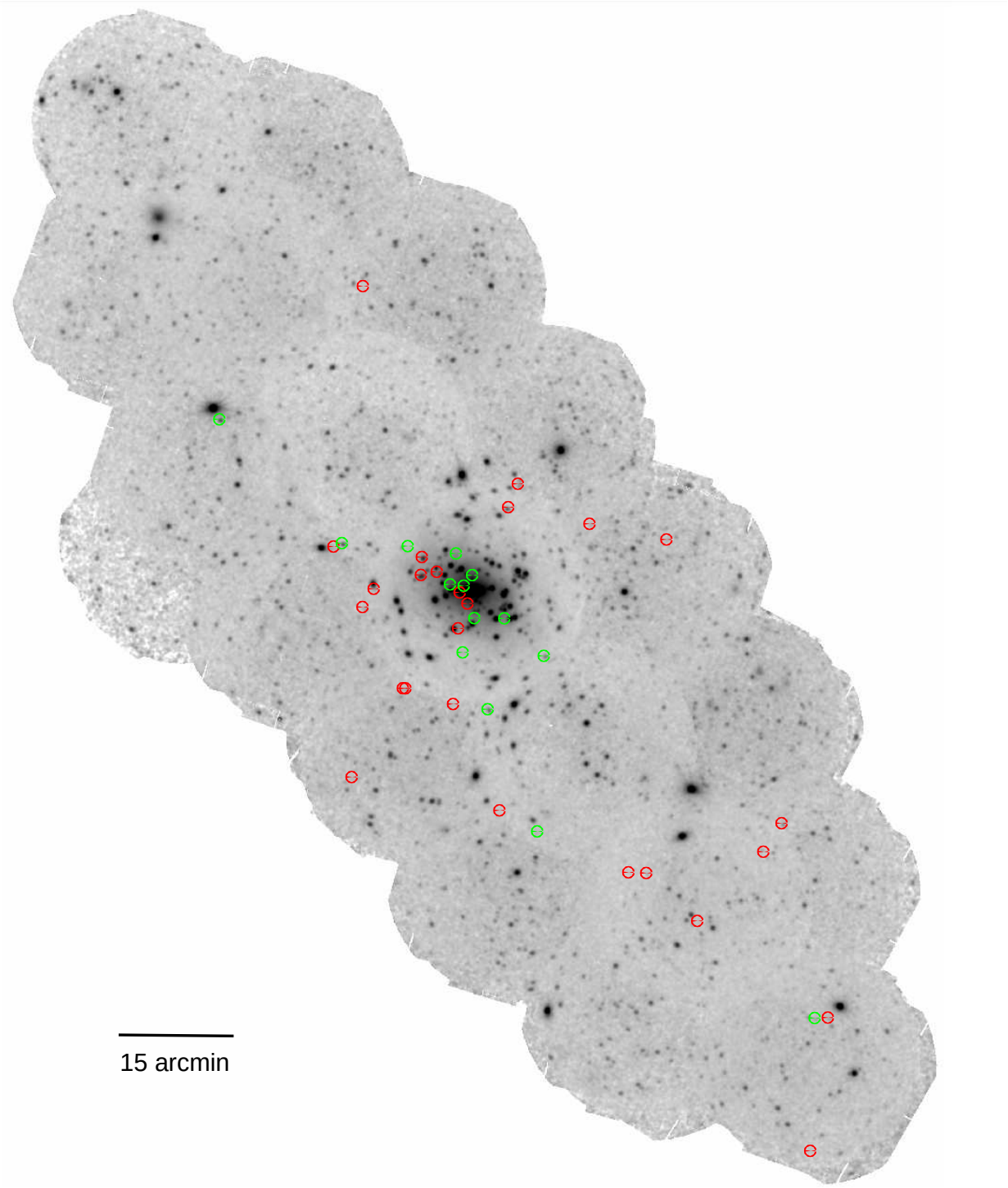


**Figure 9.7:** The spatial distribution of SSSs classified in the XMM LP-total catalogue. The positions of the SSSs are marked with red and green dots. Sources that correlate with optical novae are given in green. An enhancement of sources in the central field is clearly visible.

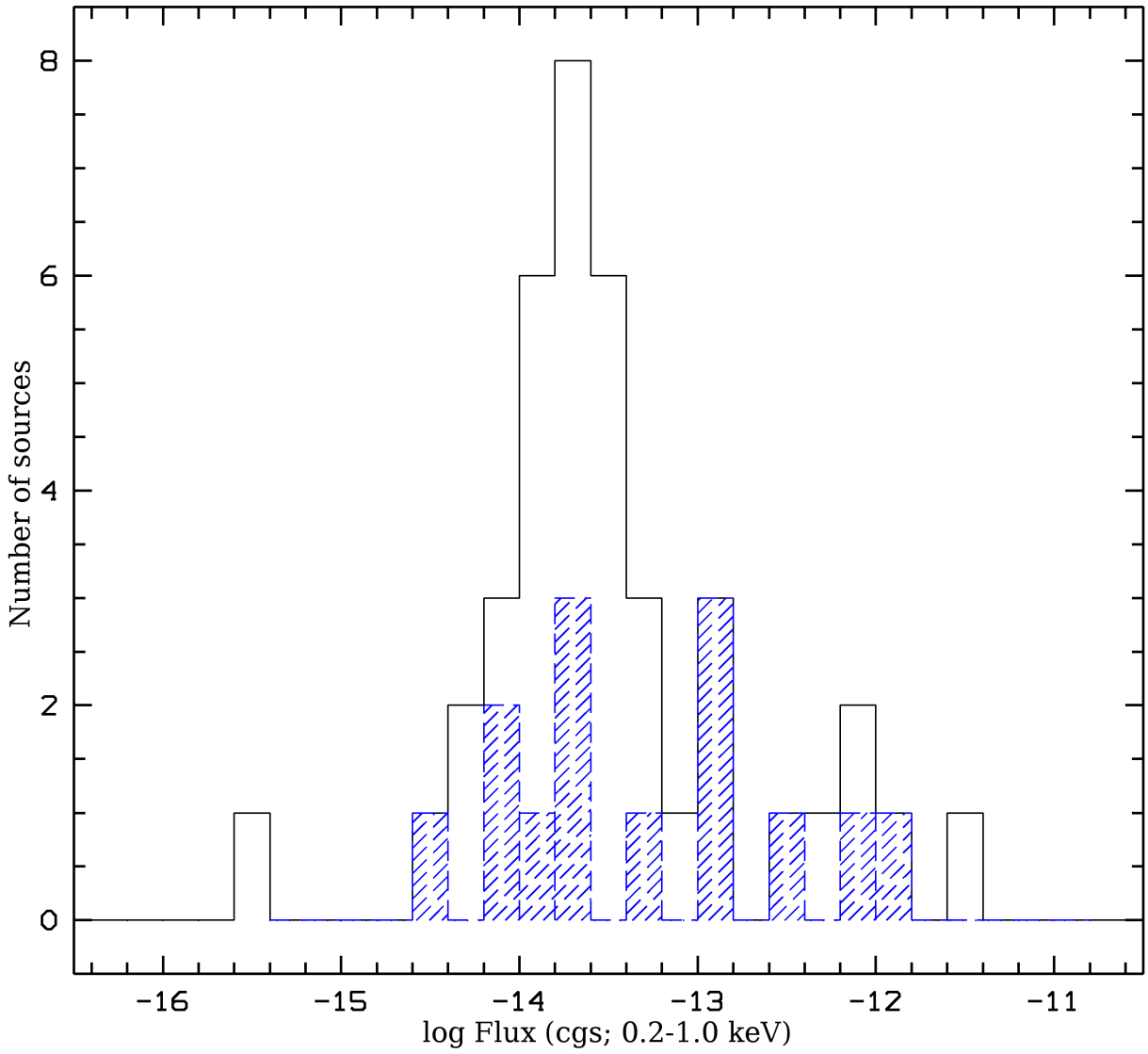


**Figure 9.8:** Distribution of the source fluxes in the 0.2–1.0 keV band. The diagram shows the number of SSSs per flux bin plotted versus the flux in logarithmic scale. The blue histogram gives the distribution of SSSs correlating with optical novae.

a homogeneous and dense sample of deep optical and X-ray observations in order to study optical novae and their connections to supersoft X-ray sources. In the optical, the outer regions of M 31 are regularly observed down to a limiting magnitude of $\sim$17 mag (Texas Supernova Search (TSS); Quimby 2006), while in X-rays only "snapshots" are available. Hence, the correlations of optical novae with detected SSSs have to be regarded as lucky coincidences. That also means that the identified nova counterparts are detected at a random stage of their SSS evolution which does not allow the exact start or end point of the SSS phase, nor the maximum luminosity of the SSS to be constrained. We also cannot exclude the possibility that some of the SSSs observed in the outer parts of M 31 are the supersoft phase of optical novae for which the optical outburst was missed. In the outer regions of M 31, the sample of optical novae and X-ray SSSs are certainly incomplete due to the rather high luminosity limit in the optical monitoring, and the missing monitoring in the X-rays, respectively.[5] So one should be cautious in deriving properties of the disc nova population of M 31 from the available data.

**Nova M31N 1997-10c** was detected on 02 October 1997 at a B-band magnitude of 16.6 (ShA 58; Sharov & Alksnis 1998). An upper limit of 19 mag on 29 September 1997 was reported by the same authors. They classified this source as a very fast nova. In the *XMM-Newton* observation c1 (25 June 2000), an SSS (№ 871), located within $\sim$1.″9 of the optical nova, was detected. The source was fitted with an absorbed blackbody model. The formal best fit parameters of the *XMM-Newton* EPIC PN spectrum are: absorption $N_{\rm H} \approx 3.45{\times}10^{21}$ cm$^{-2}$ and $k_{\rm B}T \approx 41$ eV. The unabsorbed luminosity in the 0.2–1 keV band is $\approx 5.9{\times}10^{37}$ erg s$^{-1}$. Confidence contours for absorption column density and blackbody temperature are show in Fig. 9.9. In the next *XMM-Newton* observation of that region taken about half a year later (c2; 27 December 2000) the source is not detected. Although the source position is covered in observations c3 (29 June 2001), c4 (6/7 January 2002) and b (16–19 July 2004), the source was not re-detected. Using the count rates derived for the variability study (see Sect. 7.4) and assuming the same spectrum for the source as in observation c1, upper limits of the source luminosity can be derived, which are given in Table 9.7.

**Nova M31N 2005-01b** was discovered on 19 January 2005 at a white light magnitude of 16.3 by R. Quimby.[6] An SSS (№ 764) that correlates with the optical nova (distance: 4.″3; 3$\sigma$ error: 5.″5) was found in observation ss2 taken on 8 July 2006, which is 535 days after the discovery of the optical nova.

Due to the severe background screening applied to observation ss2, there are not enough bins available from the *screened* data with sufficiant statistics to obtain a spectrum of the X-ray source. To get an estimate of the spectral properties of that source I created a spectrum in the 0.2–0.8 keV range of the *unscreened* data. Although the spectrum was background corrected, I cannot totally exclude a contribution from background flares. The spectrum is best fitted by an absorbed blackbody model with an absorption of $N_{\rm H} \approx 1.03{\times}10^{21}$ cm$^{-2}$ and a blackbody temperature of $k_{\rm B}T \approx 45$ eV.

In another *XMM-Newton* observation taken 1 073 days after the optical outburst (ss21; 28 December 2007) the X-ray source is no longer visible. The 3$\sigma$ upper limit of the absorbed source flux is $\sim$2.0$\times10^{-15}$erg cm$^{-2}$ s$^{-1}$ in the 0.2–4.5 keV band, assuming the spectral model used for source detection.

**Nova M31N 2005-01c** was discovered on 29 January 2005 at a white light magnitude of 16.1 by R. Quimby.[7] In the *XMM-Newton* observation from 02 January 2007 (ns2, 703 days after optical outburst) an SSS

[5] X-ray monitoring of the outer parts of M 31 is far beyond the scope of the Large Survey project and would either need a large amount of observing time, or an X-ray telescope with a larger field of view. In the optical, the up-coming PANDROMEDA project plans to observe the whole galaxy "every" night, down to limiting luminosity of 24 mag.

[6] http://www.supernovae.net/sn2005/novae.html

[7] http://www.supernovae.net/sn2005/novae.html

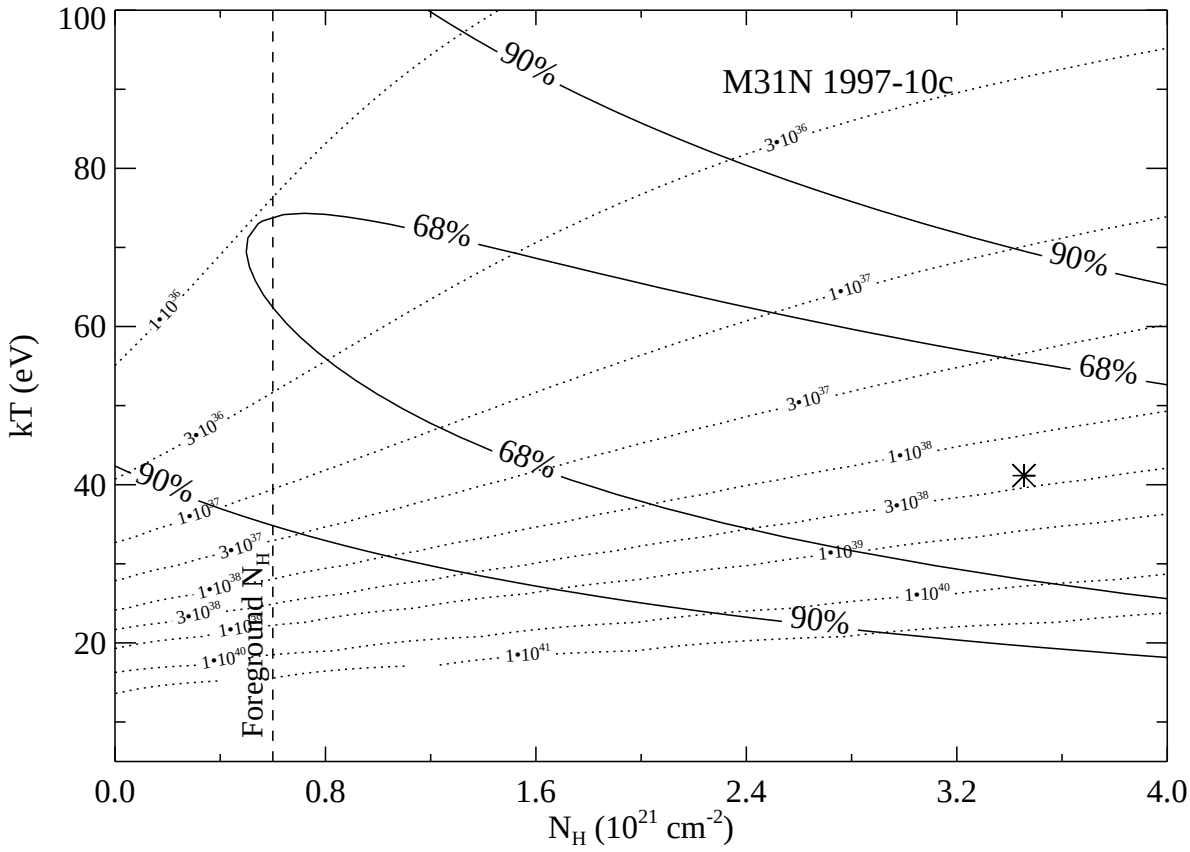


**Figure 9.9:** Column density-temperature confidence contours inferred from the fit to the *XMM-Newton* EPIC PN spectrum of M31N1997-10c. The formal best fit parameters are indicated by the star. Also drawn are lines of constant bolometric luminosity (in erg $s^{-1}$). The vertical dashed line indicates the Galactic foreground absorption in the direction of M 31.

was detected (№ 1 675) at a position consistent with that of the optical nova (distance: $0\farcs9$). The X-ray spectrum (Fig. 9.10(a)) can be well fitted by an absorbed blackbody model with the following best fit parameters: absorption $N_{\rm H} = 1.58^{+0.65}_{-0.45}\times10^{21}$ cm$^{-2}$ and $k_{\rm B}T = 40.23^{+0.60}_{-0.64}$ eV. The unabsorbed 0.2–1 keV luminosity is $L_{\rm X}$ $\sim$1.2$\times10^{38}$ erg s$^{-1}$. Confidence contours for the absorption column density and blackbody temperature are show in Fig. 9.10(b).

**Nova M31N 2005-09b** was discovered in optical images taken on 01 and 02 September 2005 with a white light magnitude of $\sim$ 18.0 and $\sim$ 16.5, respectively. From 31 August 2005, an upper limit of $\sim$ 18.7 mag was reported (Quimby et al. 2005). The nova was spectroscopically confirmed (Pietsch et al. 2006) and suggested as an Fe II or hybrid nova[8].

An X-ray counterpart (№ 92) was detected in the *XMM-Newton* observation s3 (299 days after the optical outburst). Its position is consistent with that of the optical nova (distance: $0\farcs57$). As observation s3 was heavily affected by background flares, I only could estimate the spectral parameters from the *unscreened* data (see also paragraph about Nova M31N 2005-01b). A blackbody fit of the 0.2–0.8 keV gives $N_{\rm H}$ $\approx$

[8] http://cfa-www.harvard.edu/iau/CBAT_M31.html

**Table 9.7:** $3\sigma$ upper limits for the absorbtion-corrected luminosities for Nova M31N 1997-10c

| observation | $L_X/10^{37}$ erg s$^{-1}$ (0.2–1.0 keV) |
|---|---|
| c2 | $10.8^{+}$ |
| c3 | 1.9 |
| c4 | 1.0 |

Notes:
$^{+}$ : The count rate detected in observation c2 gives a luminosity of $2.4\pm2.8\times10^{37}$ erg s$^{-1}$, which results in the upper limit given in the Table. The fact that this upper limit is higher than the luminosity detected in observation c1 is, at least in part, attributed to the very short effective observing time of less than 6 000 s.

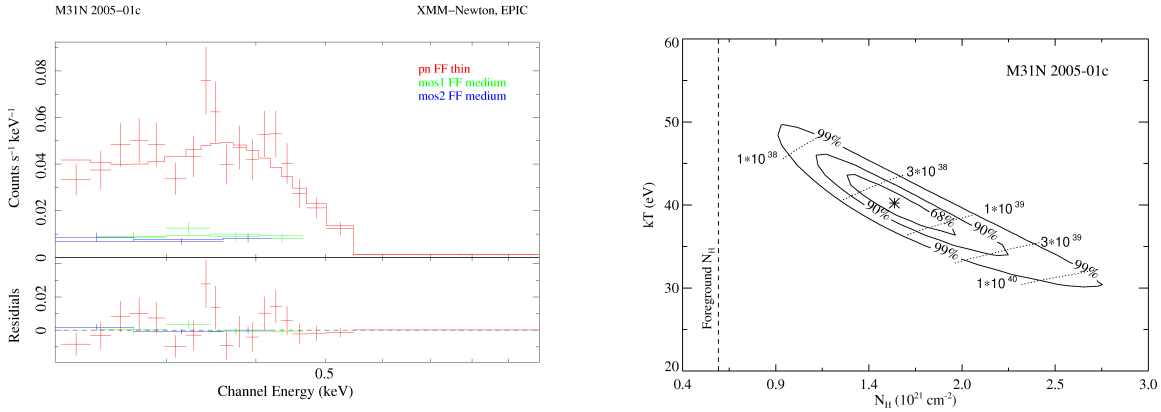


(a) Spectrum (b) Contour plot

**Figure 9.10:** Figure (a) shows the *XMM-Newton* EPIC spectrum of nova M31N 2005-01c. The absorbed black body fit to the data is shown in the upper panel. In Fig. (b) the column density ($N_{\rm H}$) - temperature ($k_{\rm B}T$) confidence contours inferred from the blackbody fit to the *XMM-Newton* EPIC spectrum of M31N 2005-01c (see Fig. (a)) are shown. The formal best fit parameters are indicated by the star. Also drawn are lines of constant bolometric luminosity and the vertical dashed line indicates the Galactic foreground absorption (see Fig 9.9).

$2.7\times10^{21}$ cm$^{-2}$ and k$T \approx 35$ eV.

The X-ray source was no longer visible in observation s31, which was taken 391 days after observation s3.

**Nova M31N 2007-06b** was first detected on 19 June 2007 in the optical (Shafter & Quimby 2007). A supersoft X-ray source (Nº 934) that correlates spatially with the optical nova was detected on 07 November 2007 (141 days after the optical outburst) in a *Chandra* observation of the M 31 nova monitoring campaign (source SS1 in Henze et al. 2009). The X-ray source remained active during the following *Chandra* monitoring observations in November and December 2007. We followed the light curve with *Swift* ToO observations and also found the source to be still visible in two of the *XMM-Newton* Large Program observations in January and February 2008. Details on the individual observations are given in Table 9.8.

An outstanding factor is the location of this source in the globular cluster Bol 111 (Caldwell et al. 2009, RBC V3.5). This makes M31N 2007-06b the first nova and SSS found in an M 31 GlC.

**Table 9.8:** X-ray observations of source N$^{\underline{o}}$ 936 in Bol 111. Table taken from Henze et al. (2009).

| Telescope/Instrument[a] | Obs. id. | Exp. time[b] [ks] | Date[c] [UT] | Offset[d] [d] | Count Rate[e] [ct $s^{-1}$] | $L_{0.2-1.0}$ [e] [erg $s^{-1}$] |
|---|---|---|---|---|---|---|
| *XMM-Newton* EPIC PN | 0505760201 | 49.2 | 2007-07-22.55 | 33 | $< 1.1 \times 10^{-3}$ | $<1.4 \times 10^{36}$ |
| *Chandra* HRC-I | 8526 | 18.7 | 2007-11-07.64 | 141 | $> (1.9 \pm 0.4) \times 10^{-2}$ | $>(5.3 \pm 1.1) \times 10^{38}$ |
| *Chandra* HRC-I | 8527 | 20.0 | 2007-11-17.76 | 151 | $(2.5 \pm 0.2) \times 10^{-2}$ | $(7.0 \pm 0.7) \times 10^{38}$ |
| *Chandra* HRC-I | 8528 | 20.0 | 2007-11-28.79 | 162 | $(2.2 \pm 0.2) \times 10^{-2}$ | $(6.0 \pm 0.6) \times 10^{38}$ |
| *Chandra* HRC-I | 8529 | 18.9 | 2007-12-07.57 | 171 | $(2.8 \pm 0.3) \times 10^{-2}$ | $(7.7 \pm 0.7) \times 10^{38}$ |
| *Chandra* HRC-I | 8530 | 19.9 | 2007-12-17.49 | 181 | $(2.5 \pm 0.3) \times 10^{-2}$ | $(7.1 \pm 0.7) \times 10^{38}$ |
| *Swift* XRT | 00031017001/2 | 7.1 | 2007-11-18.40 | 152 | $(1.18 \pm 0.15) \times 10^{-2}$ | $(11.6 \pm 1.4) \times 10^{38}$ |
| *Swift* XRT | 00031017003 | 3.0 | 2007-12-13.02 | 177 | $(0.8 \pm 0.2) \times 10^{-2}$ | $(8.1 \pm 1.9) \times 10^{38}$ |
| *Swift* XRT | 00031017004 | 3.0 | 2007-12-14.02 | 178 | $(1.1 \pm 0.2) \times 10^{-2}$ | $(10.6 \pm 2.2) \times 10^{38}$ |
| *Swift* XRT | 00031017005 | 3.2 | 2007-12-15.03 | 179 | $(1.1 \pm 0.2) \times 10^{-2}$ | $(11.1 \pm 2.1) \times 10^{38}$ |
| *Swift* XRT | 00031017006 | 2.2 | 2007-12-20.25 | 184 | $(1.1 \pm 0.3) \times 10^{-2}$ | $(11.1 \pm 2.6) \times 10^{38}$ |
| *Swift* XRT | 00031017007 | 2.1 | 2007-12-22.39 | 186 | $(0.5 \pm 0.2) \times 10^{-2}$ | $(5.1 \pm 1.9) \times 10^{38}$ |
| *Swift* XRT | 00031017008 | 2.3 | 2007-12-24.33 | 188 | $(0.9 \pm 0.2) \times 10^{-2}$ | $(9.1 \pm 2.4) \times 10^{38}$ |
| *Swift* XRT | 00031017009 | 2.3 | 2007-12-30.15 | 194 | $(1.0 \pm 0.2) \times 10^{-2}$ | $(10.0 \pm 2.4) \times 10^{38}$ |
| *Swift* XRT | 00031017010 | 2.0 | 2008-01-03.44 | 198 | $(1.2 \pm 0.3) \times 10^{-2}$ | $(12.2 \pm 2.8) \times 10^{38}$ |
| *Swift* XRT | 00031017011 | 1.9 | 2008-01-06.25 | 201 | $(0.4 \pm 0.3) \times 10^{-2}$ | $(4.0 \pm 2.8) \times 10^{38}$ |
| *Swift* XRT | 00031017012 | 1.7 | 2008-01-10.00 | 205 | $(1.1 \pm 0.3) \times 10^{-2}$ | $(11.1 \pm 1.3) \times 10^{38}$ |
| *XMM-Newton* EPIC PN | 0511380201 | 23.0 | 2008-01-05.99 | 200 | $(8.2 \pm 0.2) \times 10^{-2}$ | $(10.6 \pm 0.2) \times 10^{38}$ |
| *XMM-Newton* EPIC PN | 0511380601 | 24.0 | 2008-02-09.31 | 235 | $(7.5 \pm 0.2) \times 10^{-2}$ | $(12.2 \pm 0.4) \times 10^{38}$ |
| *Swift* XRT | 00037718001 | 4.8 | 2008-05-26.29 | 342 | $(0.5 \pm 0.1) \times 10^{-2}$ | $(4.6 \pm 1.3) \times 10^{38}$ |
| *XMM-Newton* EPIC PN | 0560180101 | 17.4 | 2008-07-18.26 | 395 | $(3.0 \pm 0.2) \times 10^{-2}$ | $(8.9 \pm 0.5) \times 10^{38}$ |

Notes: [a]: Telescope and instrument used for observation.

[b]: Dead time corrected exposure time of the observation.

[c]: Start date of the observation.

[d]: Time in days after the discovery of nova M31N 2007-06b in the optical (Shafter & Quimby 2007) on 2007 June 19.38. (JD = 2454271).

[e]: Source count rates, X-ray luminosities (unabsorbed, blackbody fit, 0.2 - 1.0 keV) and upper limits were estimated as explained in the text. For *Chandra* Obs. id. 8526 the source is right on the detector edge, therefore we give lower luminosity limits.

In order to perform spectral analysis of this source, we used the *XMM-Newton* Large Program observations obtained on 2008-01-05.99 UT and 2008-02-09.31 UT (Obs. ss12 and ss13). The source spectra were extracted from the PN detector data because of the better sensitivity in the soft band compared to both MOS detectors. We fitted black body spectra to both observations simultaneously to increase the statistics. The temperature and foreground $N_{\rm H}$ were both assumed to be the same during the two observations and only the respective normalisations were allowed to vary independently from each other. The blackbody fit yields an acceptable $\chi^2_r = 1.39$ for the best fit values of $k_{\rm B}T = 48^{+2}_{-3}$ eV and $N_{\rm H} = 2.3 \pm 0.1 \times 10^{21}$ cm$^{-2}$. This fit and the associated contour plot are shown in Fig. 9.12.

The relative stability of the spectral parameters was confirmed by an *XMM-Newton* ToO observation on 2008-07-18.26 UT (160 days later than ss13), from which we extracted a spectrum of source N$^{\underline{o}}$ 936 that can be fitted by a black body spectrum with similar parameters.

We computed the unabsorbed EPIC PN X-ray luminosities in the range 0.2–1.0 keV from the best fit model in `Xspec`, and we used the best fit values to create fake spectra within `Xspec` (command `fakeit`) and thus infer the energy conversion factors (ECF) for the *Swift* XRT ($\rm ECF_{XRT}$) and the *Chandra* HRC-I ($\rm ECF_{HRC-I}$) observations. The ECF values are given in Table 9.9 and were used to convert our *Swift* XRT and *Chandra* HRC-I count rates to unabsorbed luminosities, which are presented in Table 9.8. Note, that for our first detection of M31N 2007-06b in the *Chandra* HRC-I observation 8 526 no photometry is possible due to the location of the source on the edge of the detector. The blackbody fit parameters and derived values

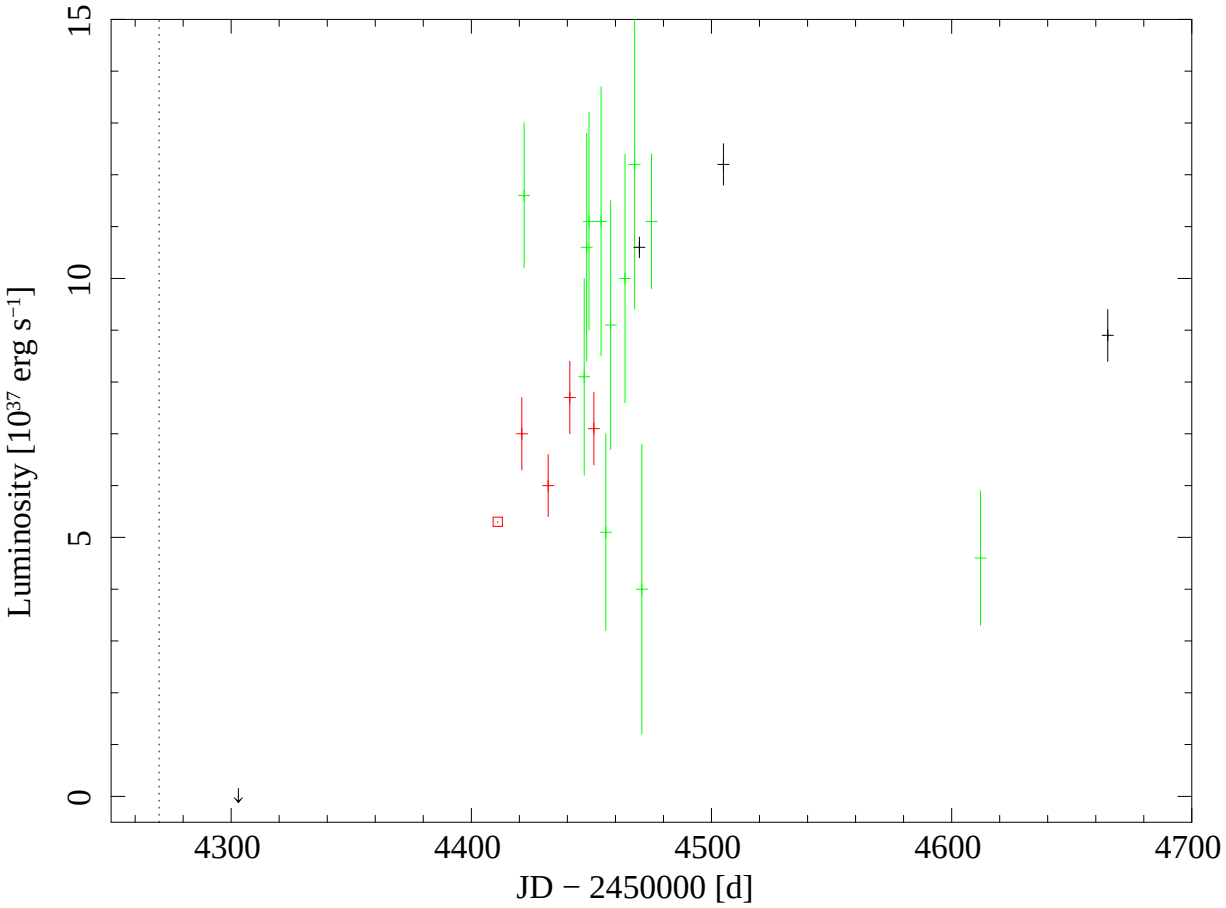


**Figure 9.11:** X-ray light curve of source Nº 936 (0.2–1.0 keV) obtained from *XMM-Newton* (black), *Chandra* HRC-I (red), and *Swift* XRT (green) (see also Table 9.8). The upper limit is indicated by a down-pointing arrow. An open square indicates the lower limit luminosity on *Chandra* Obs. id. 8 526. Crosses symbolise the luminosity of the detections. The vertical dotted line indicates the day of the first detection of nova M31N 2007-06b in the optical (Shafter & Quimby 2007). Adapted from Henze et al. (2009).

(*e. g.* luminosities) for Obs. ss12, are given in Table 9.9. The X-ray light curve of the source is shown in Fig. 9.11.

For a comparison of the blackbody spectral fits to more sophisticated WD atmosphere model fits and a discussion of a second SSS in an M 31 globular cluster, as well as the results obtained on the M 31 nova rate in globular clusters, see Henze et al. (2009).

#### 9.4.1.3 Comparing *XMM-Newton*, *Chandra* and *ROSAT* catalogues

To study the long-term variability of the SSS population of M 31, we performed cross-correlations with the *ROSAT* PSPC surveys (SHP97, SHL2001) and with the *Chandra* source catalogues. The analysis was carried out in two stages. In the first stage we selected all SSS candidates from the XMM LP-total catalogue and cross-correlated them with the full source catalogues obtained from *ROSAT* and *Chandra* observations. With this we were able to investigate whether the *XMM-Newton* sources had been detected in previous studies and how variable they were. The results are presented in the first two subsections (I., II.). In the

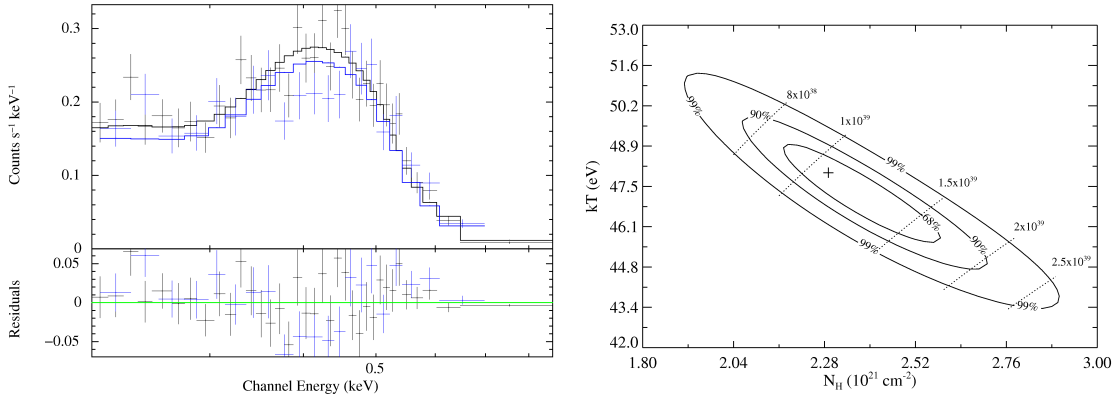


(a) Spectrum (b) Contour plot

**Figure 9.12:** Figure (a) shows the *XMM-Newton* EPIC PN spectra of source N$^{\underline{o}}$ 936 (crosses) from observations 0511380201 (black) and 0511380601 (blue) fitted with an absorbed blackbody (solid lines). In Fig. (b) the column density ($N_{\rm H}$) - temperature ($k_{\rm B}T$) contours inferred from the blackbody fit to the *XMM-Newton* EPIC PN spectra of source N$^{\underline{o}}$ 936 are given. The normalisation has been adjusted. Indicated are the formal best fit parameters (cross) and the lines of constant X-ray luminosity (0.2-1.0 keV, dotted lines). From Henze et al. (2009).

**Table 9.9:** Spectral best fit parameters and derived parameters for a blackbody model.

| Model (energy range [keV]) | Blackbody $(0.2-0.8)$ |
|---|---|
| $k_{\rm B}T$ (eV) | $48^{+2}_{-3}$ |
| $N_{\rm H}(10^{21}$ cm$^{-2})$ | $2.3 \pm 0.1$ |
| $\chi^2_r$ | 1.39 |
| dof | 53 |
| $L_x$ ($10^{38}$ erg s$^{-1}$) | $10.6 \pm 0.2$ |
| $L_{bol}$ ($10^{38}$ erg s$^{-1}$) | $28.7^{+0.2}_{-0.1}$ |
| $R$ ($10^9$ cm) | $7.0^{+1.6}_{-0.7}$ |
| ecf$_{PN}$ (ct cm$^2$ erg$^{-1}$) | $5.0\times10^9$ |
| ecf$_{HRC-I}$ (ct cm$^2$ erg$^{-1}$) | $2.6\times10^9$ |
| ecf$_{XRT}$ (ct cm$^2$ erg$^{-1}$) | $7.4\times10^8$ |

Notes: Luminosities and WD radii refer to the *XMM-Newton* observation 0511380201. The unabsorbed X-ray luminosity $L_x$ is for the 0.2–1.0 keV range. Adapted from Henze et al. (2009).

second step all sources classified as supersoft in the *ROSAT* PSPC surveys and as very soft in *Chandra* observations (DKG2004) were selected and cross-correlated with the full XMM LP-total catalogue. These correlations not only allow us to study the variability of SSSs once more, but also to ascertain the selection power of the method used in *ROSAT* and *Chandra* studies to separate different source classes. The results

of these correlations are presented in the third (III.) and fourth (IV.) subsection. Of course, sources that are classified as supersoft in the XMM LP-total catalogue and also in either the *ROSAT* catalogue or *Chandra* catalogue, are found in both steps of the cross-correlation process. These sources are discussed in the first two subsections (I., II.). In the third (III.) and fourth (IV.) subsection they are only mentioned for reasons of completeness. Our results are discussed and summarised in the fifth subsection (V.).

Table 9.10 overviewes all the examined sources and their correlations and is structured as follows: Column 2 indicates from which source list the examined source is taken, while Col. 3 provides the number (name) of the source in that list. The next three columns (4–6) give information on corresponding sources from the other catalogues (and in some cases provide additional information obtained from studies with the same instrument). Sources that are observed as SSSs with more than one instrument are only listed once, reducing the *ROSAT* and *Chandra* lists to 31 and 38, respectively. The next to last column (7) provides correlations with the *XMM-Newton* SSSs listed in Table 2 of Orio (2006), while in the last column (8) additional remarks are given. The positions of the sources are indicated in Fig. 9.13.

Before we go to compare the different catalogues in detail, we want to mention that three of the 40 *XMM-Newton* SSSs are detected by all three missions. Two of them are located in the central field of M 31. The first one is source Nº 1 194, which correlates with [SHL2001] 235 and r3-8 (Kong et al. 2002b; Williams et al. 2006b). It was classified as SSS by Greiner (2000), but not by SHP97 or SHL2001 and has been visible for at least 25 years. The second is source Nº 1 061, which correlates with [SHL2001] 203 and r2-12 and has been known since the *Einstein* observations. This means that the source has been visible for more than 25 yr. Trudolyubov & Priedhorsky (2008) found that this source varies with a period of 217 s. The third source (Nº 69) is located in the S3 field and correlates with [SHL2001] 27 and s2-26 (DKG2004). [SHL2001] 27 was detected in the *ROSAT* PSPC surveys with $F_{\rm x,SHP97} \approx 5.19\times10^{-14}$ erg cm$^{-2}$ s$^{-1}$ (0.1–2.4 keV) and $F_{\rm x,SHL2001} \approx 4.56\times10^{-14}$ erg cm$^{-2}$ s$^{-1}$ (0.1–2.0 keV), which is a factor $\sim$22 – 25 higher than the fluxes of Nº 69 during the *XMM-Newton* observations. DKG2004 detected s2-26 in only one of three *Chandra* observations obtained between 2000 and 2001 and hence classified the source as variable. In our *XMM-Newton* observations Nº 69 did not show any variability. It was detected in all three observations[9] covering the position of the source. The fact that we found the source in our survey, means that it is, despite its variability, visible for about 20 years.

**Table 9.10:** Overview of SSS candidates detected with *ROSAT*, *Chandra* and *XMM-Newton*.

| Num (1) | I[&] (2) | Corr[&] (3) | *XMM-Newton* [+] (4) | *ROSAT* [◇] (5) | | *Chandra* [#] (6) | | [O2006][♮] (7) | Remarks[‡] (8) |
|---|---|---|---|---|---|---|---|---|---|
| 1 | X | 69 | <SSS> | SI 18, SII 27 | <SSS> | s2-26 (D,v) | <SSS> | | |
| 2 | X | 92 | <SSS> | | | | | | M31N 2005-09b |
| 3 | X | 97 | <SSS> | | | | | | |
| 4* | X | 147 | <SSS> | | | | | | no Chandra |
| 5 | X | 183 | <SSS> | | | | | | |
| 6 | X | 342 | <SSS> | | | | | | |
| 7 | X | 408 | <SSS> | | | | | | no Chandra |
| 8 | X | 454 | <SSS> | | | | | | |
| 9 | X | 511 | <SSS> | | | | | | |
| 10 | X | 617 | <SSS> | | | | | | no Chandra |
| 11* | X | 748 | <SSS> | | | | | 3 | M31N 2001-10f |
| 12 | X | 764 | <SSS> | | | | | | M31N 2005-01b |
| 13 | X | 821 | <SSS> | | | | | | |
| 14 | X | 857 | <SSS> | SII 156[†] | <fg Star> | | | | |
| 15 | X | 871 | <SSS> | SI 160[†] | | | | | M31N 1997-10c |
| 16 | X | 887 | <SSS> | | | | | | |
| 17* | X | 934 | <SSS> | | | | | | M31N 2007-06b |
| 18 | X | 993 | <SSS> | | | Ka 55 | | 5 | M31N 1994-09a |
| 19* | X | 1 006 | <SSS> | | | Ka 67, r2-60 (D,t, W6) | <SSS> | 10 | M31N 2000-07a |
| 20 | X | 1 025 | <SSS> | | | Ka 86, r2-65 (D,t, W6) | <SSS> | 6 | |
| 21 | X | 1 046 | <SSS> | | | | | | M31N 1999-10a |
| 22 | X | 1 051 | <SSS> | | | | | | M31N 1997-08b |
| 23* | X | 1 061 | <SSS> | SI 208, SII 203 | <SSS> | Ka 100, r2-12 (K,r,v, W, D,v), VG 46 | <SSS> | 7 | 217s period[♣], TF 69 |
| 24 | X | 1 069 | <SSS> | | | | | | |
| 25 | X | 1 076 | <SSS> | | | Ka 106 | | 15 | M31N 1996-08b |

[9] Observations s3, s31, and s32 from 28 June 2006, 24 July 2007, and 2 January 2008, respectively.

**Table 9.10:** continued.

| Num (1) | I[&] (2) | Corr[&] (3) | *XMM-Newton* [+] (4) | | *ROSAT* [◇] (5) | | *Chandra* [#] (6) | | [O2006][♯] (7) | Remarks[‡] (8) |
|---|---|---|---|---|---|---|---|---|---|---|
| 26 | X | 1 087 | | <SSS> | | | | | | |
| 27 | X | 1 100 | | <SSS> | | | Ka 111, r2-63 (W, D,t, W6), | <SSS> | 9 | M31N 1995-11c |
| 28 | X | 1 144 | | <SSS> | | | r3-128 (W6) | | 12 | |
| 29[*] | X | 1 194 | | <SSS> | SI 235, SII 235 | <SSS> | Ka 135, r3-8 (K,v, W, W6), VG 214 | <SSS> | 14 | [∞], TF 87 |
| 30[*] | X | 1 195 | | <SSS> | | | r3-126 (W, W6) | | 11 | 865.5s period[♠] |
| 31 | X | 1 236 | | <SSS> | | | | | | M31N 1998-06a |
| 32 | X | 1 242 | | <SSS> | | | | | | |
| 33[*] | X | 1 250 | | <SSS> | | | | | | time variable |
| 34 | X | 1 325 | | <SSS> | | | | | | |
| 35 | X | 1 355 | | <SSS> | SI 262[†], SII 269[†] | <SNR> | | | | |
| 36 | X | 1 356 | | <SSS> | | | | | | no Chandra |
| 37[*] | X | 1 381 | | <SSS> | | | | | | no Chandra |
| 38[*] | X | 1 416 | | <SSS> | | | | | | |
| 39 | X | 1 435 | | <SSS> | | | | | | |
| 40[*] | X | 1 675 | | <SSS> | | | | | | M31N 2005-01c |
| 41 | R | SI 3 | | | | <SSS> | | | | outside FoV |
| 42 | R | SI 12 | | | | <SSS> | | | | |
| 43 | R | SI 35 | 188 | <fg Star> | SII 43 | <SSS> | | | | |
| 44 | R | SI 39 | 240 | <hard> | | <SSS> | | | | |
| 45 | R | SI 45 | | | SII 51 | <SSS> | | | | |
| 46 | R | SI 58 | 304 | <GCl> | SII 60 | <SSS> | | | | |
| 47 | R | SI 62 | 325 | <fg Star> | | <SSS> | | | | |
| 48 | R | SI 78 | | | | <SSS> | | | | |
| 49 | R | SI 88 | | | | <SSS> | | | | |
| 50 | R | SI 114 | | | | <SSS> | | | | |
| 51 | R | SI 128 | | | | <SSS> | | | | |
| 52 | R | SI 129 | 737 | <fg Star> | SII 123 | <SSS> | | | | |
| 53 | R | SI 156 | 842 | <fg Star> | SII 151 | <SSS> | | | | |
| 54 | R | SI 171 | | | | <SSS> | | | | |
| 55 | R | SI 183 | 10 XMM ctps[ℵ] | | SII 185 | <SSS> | | | | |
| 56 | R | SI 185 | 969 | <SNR> | SII 186 | <SSS> | s1-84 (W) | | | |
| 57 | R | SI 245 | | | | <SSS> | | | | |
| 58 | R | SI 252 | 1 297 | <hard> | SII 258 | <SSS> | | | | |
| 59 | R | SI 259 | 1 331 | <fg Star> | | <SSS> | | | | |
| 60 | R | SI 268 | | | | <SSS> | | | | M31N 1990-09a[♡] |
| 61 | R | SI 271 | | | SII 282 | <SSS> | | | | outside FoV |
| 62 | R | SI 280 | 1 442 | fg Star | SII 287 | <SSS> | | | | |
| 63 | R | SI 307 | | | | <SSS> | | | | |
| 64 | R | SI 309 | | | SII 324 | <SSS> | | | | |
| 65 | R | SII 322 | | | | <SSS> | | | | |
| 66 | R | SI 330 | | | | <SSS> | | | | |
| 67 | R | SI 335 | | | | <SSS> | | | | |
| 68 | R | SI 341 | | | | <SSS> | | | | |
| 69 | R | SI 342 | | | | <SSS> | | | | outside FoV |
| 70 | R | SI 374 | | | | <SSS> | | | | outside FoV |
| 71 | R | SI 376 | | | | <SSS> | | | | |
| 72 | C | s2-7 | 52 | <fg Star> | | | (D) | <SSS> | | |
| 73 | C | s2-10 | | | | | (D) | <QSS> | | |
| 74 | C | s2-27 | | | | | (D) | <QSS> | | |
| 75 | C | s2-28 | 32 | | | | (D) | <QSS> | | |
| 76 | C | s2-29 | 23 | <fg Star> | | | (D) | <fg Star> | | ♯ |
| 77 | C | s2-37 | 237 | <fg Star> | SI 40, SII 47 | | (D) | <fg Star> | | ♭ |
| 78 | C | s2-46 | 13 | <fg Star> | | | (D,v) | <fg Star> | | ♯ |
| 79 | C | s2-62 | | | | | (D,t) | <QSS> | | |
| 80 | C | s1-18 | | | | | (D,v,t) | <SSS> | | |
| 81 | C | s1-20 | 696 | fg Star | SI 121, SII 112 | <fg Star> | (D) | <fg Star> | | ♭ |
| 82 | C | s1-27 | | | | | (D,v,t) | <QSS> | | |
| 83 | C | s1-41 | 673 | <Gal> | | | (D) | <GlC> | | ♭ |
| 84 | C | s1-42 | 668 | SNR | SI 116 | SNR | (D) | SNR | | ♯ |
| 85 | C | s1-45 | 603 | <fg Star> | SI 107, SII 99 | <fg Star> | (D,W) | <fg Star> | | ♭ |
| 86 | C | s1-69 | | | | | (D,t) | <SSS> | | |
| 87 | C | r3-11 | 1 172 | <hard> | | | (K, D), VG 161 | <QSS> | | |
| 88 | C | r3-115 | 1 136 | <XRB> | | | (W, D,t, W6), Ka 125, VG 128 (t) | <SSS> | | |
| 89 | C | r3-122 | 826 | <fg Star> | SI 147 | <fg Star> | (D) | <fg Star> | | ♯ |
| 90 | C | r2-19 | 1 000 | | | | (K,f, W, D), Ka 63, VG 72 (t) | <QSS> | | |
| 91 | C | r2-42 | 960 | <fg Star> | SI 181, SII 182 | | (K,f, W, D), Ka 43, VG 69 | <QSS> | | |
| 92 | C | r2-54 | | | | | (D) | <SSS> | | |
| 93 | C | r2-56 | 1 050 | SNR | | | (K,p, D), VG 36, | SNR | | ♯ |
| 94 | C | r2-61 | | | | | (D,t) | <SSS> | | M31N2000-08a[♡] |
| 95 | C | r2-62 | | | | | (D,t) | <QSS> | | |
| 96 | C | r2-66 | | | | | (D,t) | <QSS> | | |
| 97 | C | r1-9 | 1 010[†] | <XRB> | | | (K,r,v,t, W, D,v,t, W6) | <QSS> | | unresolved |
| 98 | C | r1-25 | 1 034 | <XRB> | | | (K, W, D), Ka 89, VG 23 (t) | <SSS> | | |
| 99 | C | r1-35 | | | | | (D,t) | <SSS> | | M31N1995-09b[♡] |
| 100 | C | n1-2 | 1 806 | <fg Star> | | | (D) | <SSS> | | |
| 101 | C | n1-8 | 1 773 | <fg Star> | | | (D) | <QSS> | | |
| 102 | C | n1-13 | 1 747 | <fg Star> | | | (D) | <QSS> | | |
| 103 | C | n1-15 | 1 742 | <fg Star> | SI 327 | | (D) | <QSS> | | |
| 104 | C | n1-26 | | | | | (D,v,t) | <QSS> | | |
| 105 | C | n1-29 | | | | | (D) | <QSS> | | |
| 106 | C | n1-31 | 1 721 | <hard> | | | (D) | <QSS> | | |
| 107 | C | n1-46 | | | | | (D) | <QSS> | | |

**Table 9.10:** continued.

| Num (1) | I[&] (2) | Corr[&] (3) | *XMM-Newton* [+] (4) | *ROSAT* [◇] (5) | *Chandra* [#] (6) | [O2006][♮] (7) | Remarks[‡] (8) |
|---|---|---|---|---|---|---|---|
| 108 | C | n1-48 | 1 741 <SNR> | (D) | <SSS> | | |
| 109 | C | n1-66 | | (D) | <QSS> | | outside FoV |

Notes:

[&] : Correlated SSSs taken from the XMM LP-total catalogue, *ROSAT* SSS lists of Greiner (2000), Kahabka (1999) (given is the source name from SHP97 or SHL2001) and very soft sources from Table 1 of DKG2004; The used lists are marked in the instrument column (I): X: *XMM-Newton*, C: *Chandra*, R: *ROSAT*

[+] : Sources and classification from Table 7.2

[#] : Sourecs from *Chandra* catalogues: D: Di Stefano et al. (2004), K: Kong et al. (2002b), VG: Voss & Gilfanov (2007), W: Williams et al. (2004a), W6: Williams et al. (2006b), Ka: Kaaret (2002), v: variable, t: transient, r: *ROSAT* HRI source, f: foreground star, p: planetary nebula; and classification of *Chandra* sources from DKG2004; [∞] : apart from r3-8 which was classified as SSS by Kong et al. (2002b); [♯] : listed as <SSS> or [♭] : <QSS> in Table 1 of DKG2004

[◇] : Sourecs from *ROSAT* catalogues SI: Supper et al. (1997), SII: Supper et al. (2001) and classification of *ROSAT* sources from Greiner (2000), Kahabka (1999), SHP97 and SHL2001

[‡] : "outside FoV" means *ROSAT* or *Chandra* source is located outside the area covered by the Deep *XMM-Newton* Survey of M 31; "no Chandra" means that the location of the source was not covered by any *Chandra* observation (included in the used literature), TF: Trinchieri & Fabbiano (1991)

[*] : *XMM-Newton* SSSs with 0.2–4.5 keV flux above *ROSAT* PSPC detection threshold

[†] : chance coincidence; [♣] :Trudolyubov & Priedhorsky (2008); [♠] :Osborne et al. (2001); [♡] : more details in PFF2005 or PHS2007; [♮] : from Table 2 of Orio (2006); [ℵ] : counterparts

**I. Correlating *XMM-Newton* SSSs to the *ROSAT* PSPC surveys** Of the 40 SSSs found in the *XMM-Newton* observations, 12 are detected with an XID flux above the *ROSAT* PSPC detection threshold of $\sim 5.3\times10^{-15}$ erg cm$^{-2}$ s$^{-1}$. Only two of these brightest 12 sources correlate with *ROSAT* SSSs (№ 1 061, № 1 194; *cf.* last paragraph). The remaining 10 sources were not detected by *ROSAT*, which implies that these sources are transient or at least strongly variable. Further information on the individual sources is provided in Table 9.11.

The remaining 28 *XMM-Newton* SSSs have fluxes below the *ROSAT* detection threshold. Nevertheless we found four correlations with *ROSAT* sources (№69, № 871, № 1 351, № 857). One of them is source

**Table 9.11:** *XMM-Newton* SSSs with fluxes above *ROSAT* detection limit but without a *ROSAT* counterpart

| Source № | remarks |
|---|---|
| 147 | 3 detections and 1 upper limit with *XMM-Newton* |
| 748 | correlate with Nova M31N2001-10f |
| 934 | correlate with Nova M31N2007-06b |
| 1 006 | correlate with Nova M31N2000-07a |
| 1 195 | supersoft transient; periodicity of 865.5 s (Osborne et al. 2001) |
| 1 250 | supersoft transient; variable by a factor of $F_{\rm var}\sim6.94$ ($\sigma=2.8$, see Fig. 9.14) |
| 1 381 | 1 detection and 3 upper limits with *XMM-Newton* |
| 1 416 | correlate with Nova M31N2001-11a |
| 1 675 | correlate with Nova M31N2005-01c |

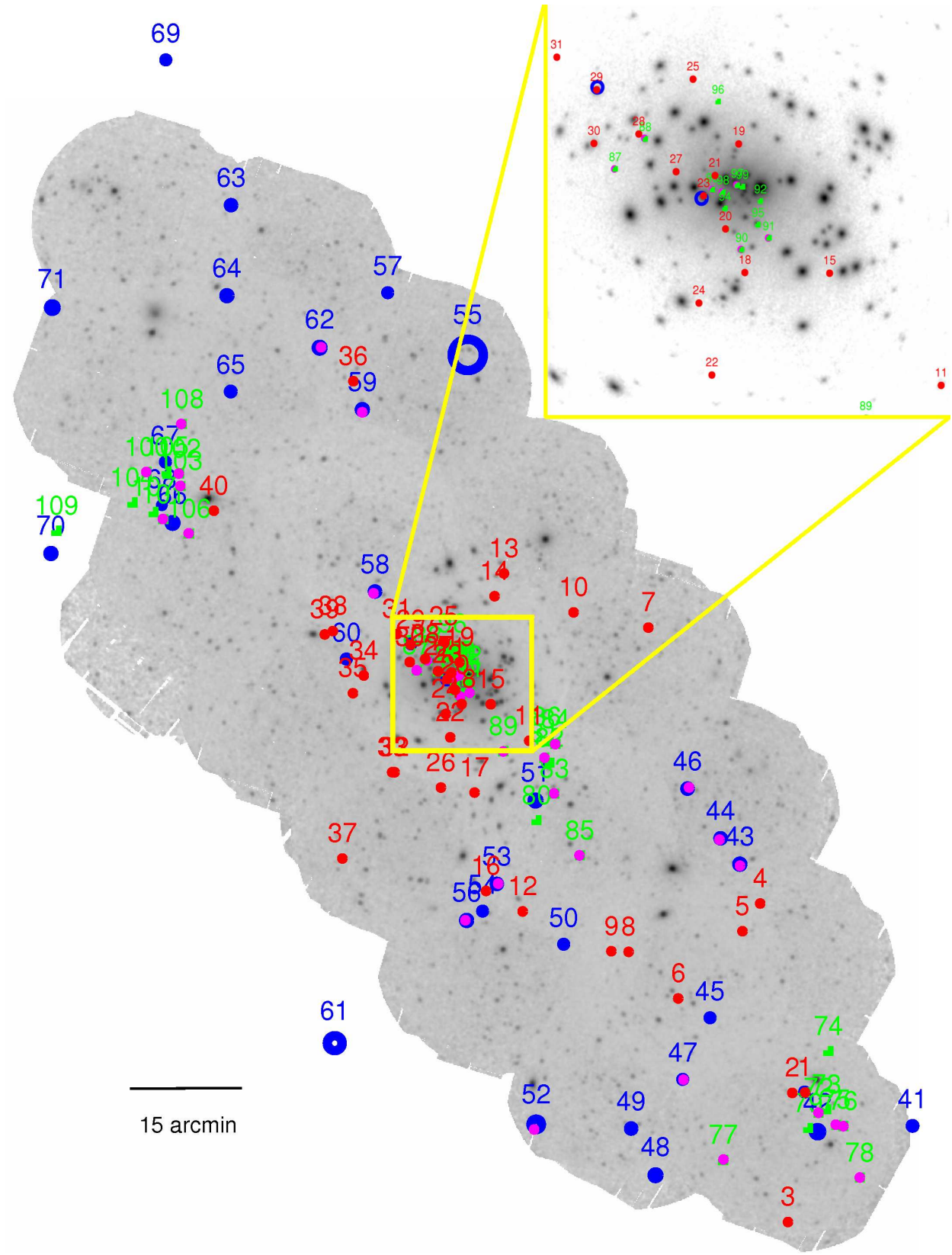


**Figure 9.13:** Image of the deep *XMM-Newton* survey of M 31 with the sources from Table 9.10 over plotted. SSSs from the XMM LP-total catalogue are marked in red, those from DKG2004 in green and those from the *ROSAT* PSPC surveys in blue. *Chandra* and *ROSAT* SSSs with *XMM-Newton* counterparts not classified as SSS are marked in magenta. The image in the upper right corner shows a zoom-in of the central region of M 31 marked by the yellow box.

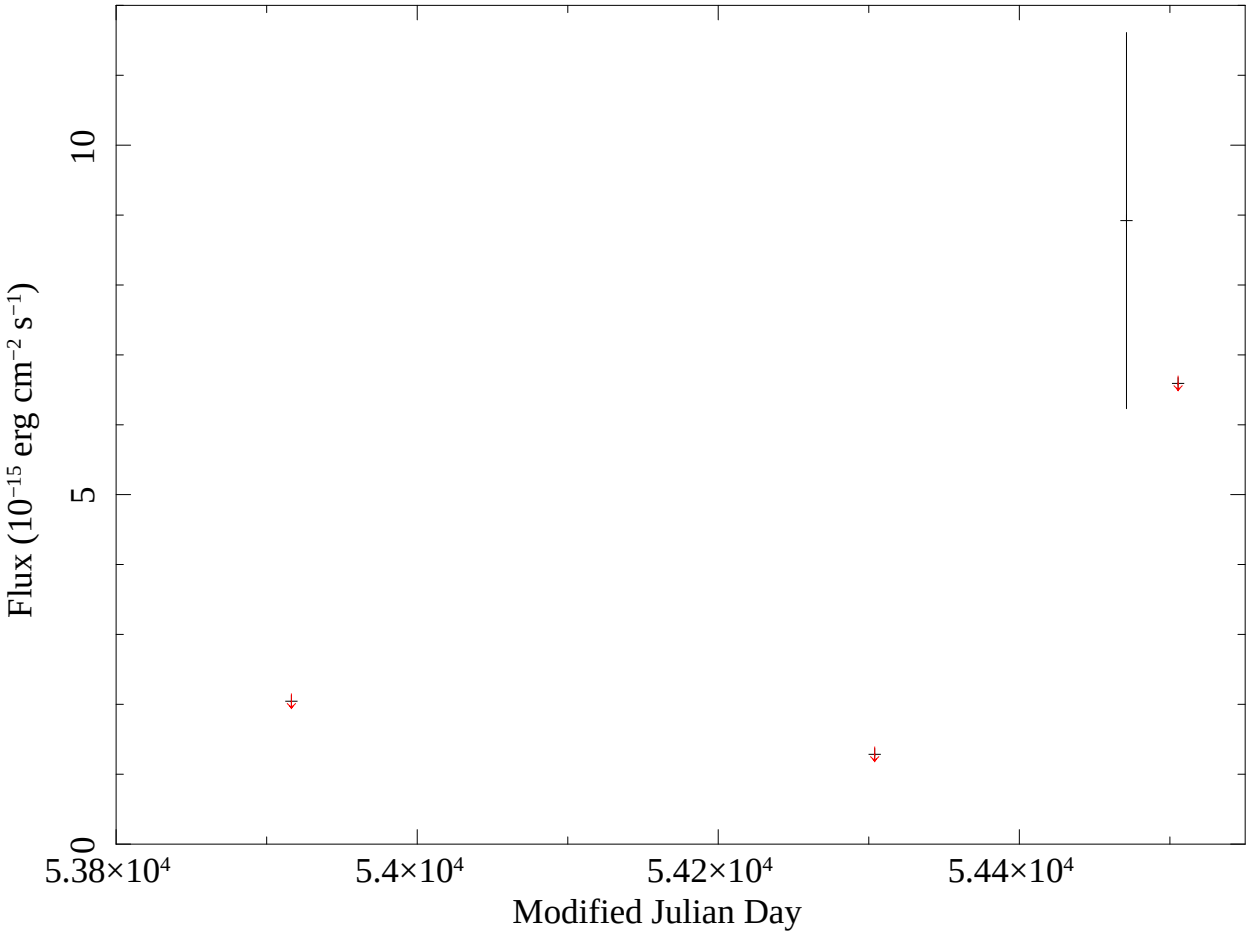


**Figure 9.14:** X-ray light curve of source Nº 1 250. The source was only once detected with a flux above the $3\sigma$ limit. For the other observations $3\sigma$ upper limits (arrows) are given.

Nº 69 which has already been discussed above. The remaining three correlations have to be considered as chance coincidences. The brightest of the four *ROSAT* sources ([SHP97] 160) is detected with $F_{\rm x} \approx 3.37{\times}10^{-13}$ erg cm$^{-2}$ s$^{-1}$ (0.1–2.4 keV) in the first *ROSAT* PSPC survey (SHP97), and has hardness ratios indicating consistent with being a hard source. The source is not detected in the second *ROSAT* PSPC survey (SHL2001). It correlates with *XMM-Newton* source Nº 871, but the spatial distance between both sources is $16\farcs6$. Furthermore, this correlation of the *ROSAT* and the *XMM-Newton* X-ray source has to be considered as chance coincidence, since source Nº 871 a has supersoft hardness ratio in the *XMM-Newton* observations and it correlates with the optical nova M31N 1997-10c (see Sect. 9.4.1.2), which was detected in the optical about six years after the *ROSAT* observations. SSS Nº 1 355 is located within $25\farcs5$ to source Nº 1 351 and is about 8.4 times fainter than Nº 1 351. Both sources correlate spatially with [SHL2001] 269, which might therefore be a blend of the two *XMM-Newton* sources. Given the flux ratio found for Nº 1 355 and Nº 1 351, and the fact that [SHL2001] 269 is classified as an SNR whereas only Nº 1 351 correlates with that SNR ([Ma1995] 2-038, [Br1992] 252), it seems more likely that source Nº 1 351 is the counterpart of [SHL2001] 269. In the case of source Nº 857 the corresponding *ROSAT* source [SHL2001] 156 also correlates with source Nº 864, which is about 6.7 times brighter than Nº 857 during the *XMM-Newton* observations. Source Nº 864 is classified as an AGN candidate. From the brightness ratio, the classification and the fact that the *ROSAT* hardness ratio of [SHL2001] 156 also indicates a hard source (SHL2001), Nº 864 has to be regarded

as the counterpart of [SHL2001] 156. Of the 28 *XMM-Newton* SSSs with fluxes below the *ROSAT* detection threshold, seven (№ 92, № 764, № 993, № 1 051, № 1 076, № 1 100, № 1 236) correlate with recent optical novae, which is an additional reason for why they were not detected by *ROSAT*. One source (№ 1 025) is classified as a transient (DKG2004).

**II. Correlating *XMM-Newton* SSSs to *Chandra* catalogues** Of the 40 *XMM-Newton* SSSs ten have counterparts in the *Chandra* catalogues (*cf.* Table 9.10). Five of them are also classified as *Chandra* SSSs in the very soft source list of DKG2004 (D in Table 9.10). Source № 1 194 correlates with r3-8, which was classified as a *Chandra* SSS by Kong et al. (2002b). Based on spectral examinations, especially of *XMM-Newton* data, Williams et al. (2006b) suggest this source to be a foreground polar. M. Orio[10] proved them wrong. Source № 1 144 was detected with *XMM-Newton* (Shirey 2001). Williams et al. (2006b) included the source as r3-128 in their catalogue of transient sources, although *Chandra* observations only give upper limits for that source, *i. e.* the source was not detected with *Chandra*.

Of the remaining 30 *XMM-Newton* SSSs, five lie in regions that were not covered in the *Chandra* catalogues (№ 147, № 408, № 617, № 1 356, № 1 381). Another ten sources correlate with optical novae. Four of these novae (№ 92, № 764, № 934, № 1 675) had their optical outburst after the *Chandra* observations were taken (so they could not be visible during the *Chandra* observations). For a further four novae (№ 748, № 1 046, № 1 051, № 1 236) PFF2005 and PHS2007 showed that the novae were not detected in *Chandra* observations. The remaining two novae (№ 871, № 1 416) are also not visible in *Chandra* observations (see M31N 1997-10c in Sect. 9.4.1.2 and Smirnova et al. 2006). In addition one source (№ 1 250) was found to be variable (*cf.* Table 7.6).

**III. Correlating *ROSAT* SSSs to the *XMM-Newton* Deep Survey catalogue** As the *ROSAT* PSPC observations were taken more than ∼10 yr earlier than the *XMM-Newton* observations (*cf.* Sect. 3.3), a comparison between the *ROSAT* and the *XMM-Newton* results probes the long term variability of SSSs. Lists of the SSSs detected in the *ROSAT* PSPC surveys are given by Greiner (2000) and Kahabka (1999). The selection of these *ROSAT* SSSs was based on similar selection criteria as those used for the *XMM-Newton* data, since the separation energies of the *ROSAT* bands were ∼0.5 keV and ∼1.0 keV. We ignored all sources from the complimentary sample of Kahabka (1999), which were already classified as foreground stars or SNRs by SHP97. Thus our *ROSAT* sample contains 34 SSSs, where four are located outside the field of M 31 covered with *XMM-Newton* observations. Three sources correlate with *XMM-Newton* SSSs (№ 69, № 1 061, № 1 194, see I.) while 11 sources correlate with XMM LP-total sources with other classifications.

Table 9.12 gives the *XMM-Newton* (Col. 3, 4) and *ROSAT* (Col. 5, 6) fluxes with errors, the flux variability (Col. 7) and its significance (Col. 8), and the classification of the *XMM-Newton* source from the XMM LP-total catalogue (Col. 9) for 13 *ROSAT* sources which have counterparts in the XMM LP-total catalogue. The flux variability and its significance is derived following the procedure described in Sect. 5.2.7. From Table 9.12, we see that two sources (№ 69, № 1 331) show variability between the *ROSAT* and *XMM-Newton* observations with much more than a factor of ten difference in flux. The first one (№ 69) was discussed above (I.). For source [SHP97] 259 it is rather difficult to decide whether source № 1 331 is the correct counterpart or not. The *ROSAT* source was only found in the first *ROSAT* PSPC survey (SHP97), but not in the second survey (SHL2001). Although this indicates strong variability or perhaps even a transient nature of the source, [SHP97] 259 is not discussed as a variable source in SHL2001. Factors that weaken the correlation between the *ROSAT* and *XMM-Newton* source are a rather large spatial distance between the two sources of ∼22″, and the low luminosity of the *XMM-Newton* source, which is about a factor three below the detection threshold of the *ROSAT* PSPC survey. On the other hand the correlation is supported by the

[10] http://xmm.esac.esa.int/external/xmm_science/workshops/2009_science/presentations/morio.ppt

fact that foreground stars can show flares, varying in flux by a factor of ∼20 (see Sect. 9.3.1). The remaining 11 sources in Table 9.12 show rather low variability, with the exception of source Nº 1 061, which has a low ($F_{\rm var} = 3.24$), but very significant ($\sigma_{\rm var} = 26.14$) variability. For source Nº 240 ([SHP97] 39) no variability can be determined because the *ROSAT* catalogue only provides an upper limit for the flux in the B band and that upper limit is higher than the flux observed in the *XMM-Newton* observations. Source [SHP97] 39 was only detected in the soft band with *ROSAT*. This may indicate a transition from a (super)soft state at the time of the *ROSAT* observation to a harder state in the *XMM-Newton* observation. The persistence in the X-ray luminosity of most of the sources listed in Table 9.12 supports the *XMM-Newton* classifications, since SNRs, most foreground stars (those without flares), and background galaxies are not expected to be variable (see Sect. 7.4).

*ROSAT* source [SHP97] 183 has a $3\sigma$ positional error of $42''$, and thus correlates with ten *XMM-Newton* sources. Hence it is not included in Table 9.12.

In summary, – of the XMM LP-total sources with *ROSAT* supersoft counterparts – three sources were classified in the XMM LP-total catalogue as supersoft source candidates, five as foreground star candidates, one as a foreground star, one as an SNR candidate and one as a background galaxy candidate. For source [SHP97] 183 we cannot give a concretely classified *XMM-Newton* counterpart, since [SHP97] 183 correlates with ten *XMM-Newton* sources, due to its large position error. The remaining two *ROSAT* source counterparts can only be classified as <hard>. Due to the large *ROSAT* position errors, it is not clear whether the correlations of the *ROSAT* SSS candidates with sources of another class in the XMM LP-total catalogue are just chance coincidences, or indicative of a change in the spectral state of the sources, or a wrong classification in the *ROSAT* catalogues.

Sixteen *ROSAT* SSSs are left without a corresponding source from the *XMM-Newton* survey. One source ([SHP97] 268) correlates with the optical nova M31N 1990-09a (PFF2005). The remaining 15 sources have to be classified as transient or at least highly variable and may well represent the SSS phase of optical novae

**Table 9.12:** *ROSAT* SSSs in *XMM-Newton* catalogue

| XSRC$^{+}$ (1) | RSRC$^{*}$ (2) | XFLUX$^{+}$ (3) | XEFLUX$^{+}$ (4) | RFLUX$^{*\dagger}$ (5) | REFLUX$^{*\dagger}$ (6) | fvar (7) | svar (8) | type$^{\ddagger}$ (9) |
|---|---|---|---|---|---|---|---|---|
| 69 | 18 | 0.21 | 0.032 | 5.19 | 0.87 | 25.14 | 5.72 | <SSS> |
| 188 | 35 | 1.83 | 0.092 | 8.79 | 1.08 | 4.79 | 6.42 | <fg Star> |
| 240 | 39 | 0.27 | 0.059 | 1.32 | 0.00 | | | <hard> |
| 304 | 58 | 2.20 | 0.177 | 6.12 | 0.96 | 2.78 | 4.01 | <Gal> |
| 325 | 62 | 0.59 | 0.071 | 1.38 | 0.57 | 2.34 | 1.38 | <fg Star> |
| 737 | 129 | 2.90 | 0.196 | 9.54 | 1.74 | 3.29 | 3.79 | <fg Star> |
| 842 | 156 | 0.67 | 0.070 | 1.74 | 0.72 | 2.56 | 1.47 | <fg Star> |
| 969 | 185 | 5.35 | 0.135 | 4.65 | 0.93 | 1.15 | 0.75 | <SNR> |
| 1061 | 208 | 37.13 | 0.201 | 120.42 | 3.18 | 3.24 | 26.14 | <SSS> |
| 1194 | 235 | 7.01 | 0.108 | 20.22 | 1.86 | 2.88 | 7.09 | <SSS > |
| 1297 | 252 | 0.56 | 0.096 | 3.36 | 0.96 | 5.99 | 2.90 | <hard> |
| 1331 | 259 | 0.18 | 0.051 | 3.87 | 1.08 | 22.12 | 3.42 | <fg Star> |
| 1442 | 280 | 1.10 | 0.095 | 3.51 | 0.93 | 3.18 | 2.58 | fg Star |

Notes:

$^{+}$ : XSRC: *XMM-Newton* source identification number, XFLUX: *XMM-Newton* XID Flux, XEFLUX: Error of *XMM-Newton* XID Flux; fluxes and errors are given in units of $1\times10^{-14}$ erg cm$^{-2}$ s$^{-1}$

$^{*}$ : RSRC: *ROSAT* source identification number from SHP97, RFLUX: *ROSAT* B-Band Flux from SHP97, XEFLUX: Error of *ROSAT* B-Band Flux; fluxes and errors are given in units of $1\times10^{-14}$ erg cm$^{-2}$ s$^{-1}$

$^{\dagger}$ : The B-Band Flux was derived from the B-Band count rates given by SHP97 and assuming a conversion factor of $1\,\mathrm{cts\,ksec^{-1}} = 3\times10^{-14}$ erg cm$^{-2}$ s$^{-1}$ (SHL2001)

that have never been detected in the optical. A possible reason for this could be the lack of systematic searches or monitoring campaigns for optical novae in M 31 in the years before the *ROSAT* observations, which resulted in a low detection rate of optical novae (Pietsch 2010).[11]

**IV. Correlating very-soft *Chandra* sources to the *XMM-Newton* Deep Survey catalogue** In this subsection we discuss the results of a cross-correlation between very soft *Chandra* sources (from Table 1 of DKG2004) and the XMM LP-total catalogue. DKG2004 used only *Chandra* ACIS-S S3 data (which are more sensitive to SSSs) and selected SSSs based on the count rates found in the three energy bands: S, 0.1–1.1 keV; M, 1.1–2 keV; and H, 2–7 keV. From these bands they considered two hardness ratios and imposed the criterion that:

$$\mathrm{HR1_{ch}} = \frac{B_\mathrm{M} - B_\mathrm{S}}{B_\mathrm{M} + B_\mathrm{S}} < -0.8 \tag{9.1}$$

and

$$\mathrm{HR2_{ch}} = \frac{B_\mathrm{H} - B_\mathrm{S}}{B_\mathrm{H} + B_\mathrm{S}} < -0.8. \tag{9.2}$$

where $B_\mathrm{S}$, $B_\mathrm{M}$ and $B_\mathrm{H}$ are the count rates in the three energy bands. These conditions can be re-written as: $B_\mathrm{S} > 9B_\mathrm{M}$, and $B_\mathrm{S} > 9B_\mathrm{H}$. Sources fulfilling conditions (9.1) and (9.2) are designate as "SSS-3$\sigma$". Sources in addition satisfying $(B_\mathrm{S} + \Delta B_\mathrm{S}) > 9\,(B_\mathrm{M} + \Delta B_\mathrm{M})$, and $(B_\mathrm{S} + \Delta B_\mathrm{S}) > 9\,(B_\mathrm{H} + \Delta B_\mathrm{H})$ are denoted by "SSS-HRs", where $\Delta B_\mathrm{S}$, $\Delta B_\mathrm{M}$ and $\Delta B_\mathrm{H}$ are the errors of the count rates measured in the S, M and H energy bands. For sources with count rates above 1.1 keV or even 2 keV, DKG2004 defined a hierarchical algorithm containing a further seven steps. Sources selected by these steps are called QSSs. Details on the selection of the QSSs can be found in Di Stefano & Kong (2003). Possible scenarios for QSSs are WD systems where hot coronae or interactions with a dense ISM could produce a small hard component, or NS or BH systems that may occasionally emit harder radiation or even exhibit a power-law tail that carries a small fraction of the energy. The most important difference to our *XMM-Newton* study is the usage of only *one* energy band below $\sim$1 keV. This means that to select SSSs DKG2004 only used hardness ratio cuts corresponding to cuts in HR2 (and not HR1) for *XMM-Newton*. From Fig. 7.5 it is clearly visible, that an HR2 cut – no matter how low the HR2 cut-off threshold chosen is– always selects foreground stars and SNRs as well.

The catalogue of very soft sources detected with *Chandra* contains 43 sources of which 20 are classified as SSSs. Five of these have SSS counterparts in the XMM LP-total catalogue (*cf.* Table 9.13) and another five remain without an *XMM-Newton* counterpart. From the remaining ten *Chandra* SSSs, five have counterparts in the XMM LP-total catalogue classified as foreground star candidates, one as an SNR candidate and two as XRB candidates. Two sources (s1-42, r2-56) correlate with known SNRs. The correlations with SNRs are also given in Table 3 of DKG2004. For three of the five foreground star candidates, correlations with foreground stars are indicated in Table 3 of DKG2004. The first of the *Chandra* SSSs that was classified as an XRB candidate in XMM LP-total (r3-115) has been noted to have a rather uncommon behaviour and was discussed in detail in PFF2005. In early X-ray observations[12] this transient source showed a supersoft spectrum. Later, its luminosity increased and the source showed a hard spectrum (in *XMM-Newton* observation c4). Based on its hard spectrum and transient behaviour the source was classified as an XRB candidate. The soft to hard transition suggests a BH primary (PFF2005). However the alternatives of it being an optical nova or a symbiotic star as counterpart cannot be excluded. The second *Chandra* SSS (r1-25) with an *XMM-Newton* counterpart classified as an XRB candidate showed a very similar behaviour. It was detected with an unabsorbed X-ray 0.3 – 7 keV luminosity of $\sim 5{\times}10^{35}$ erg s$^{-1}$, and the hardness ratios,

[11] That changed dramatically when amateur astronomers acquired the technology to observe optical novae in nearby galaxies.

[12] which include *XMM-Newton* observation c3 and the *Chandra* observations analysed in DKG2004

which have similar definitions to Eqs. 9.1 and 9.2, indicate a supersoft spectrum (Kong et al. 2002b)[13]. The source was not visible in *XMM-Newton* observations c1, c2, c3 and c4 (2000–2002). A correlating source was detected in observation b (2004) with an XID luminosity of $\sim 3.7\times10^{36}$ erg s$^{-1}$ and a hard spectrum. The long-term variability analysis gives a maximum variability factor of $F_{\rm var}=9.35$ and $\sigma_{\rm var}=28.02$. Voss & Gilfanov (2007) reported a *Chandra* detection of a correlating source ([VG2007] 23) in observation 4 682, taken on 23 May 2004, which is about two months before the *XMM-Newton* observation b, at a luminosity of $1.26\times10^{37}$ erg s$^{-1}$ (0.5–8.0 keV) and found a variability factor of 50.3. An optical source located within $1\farcs2$ of the *XMM-Newton* source position is listed as a '*regular or semi-regular red variable*' in Fliri et al. (2006).

*XMM-Newton* counterparts of the *Chandra* SSSs r2-54, s1-69, s1-18, r1-35, and r2-61 were neither detected in the present study nor in PFH2005. Four of the *Chandra* SSSs (s1-69, s1-18, r1-35, r2-61) are classified as transient sources (DKG2004). Sources r1-35, and r2-61 correlate with the optical novae M31N 1995-09b and M31N 2000-08a, respectively (PFF2005, PHS2007).

From the 23 QSSs of DKG2004, 13 correlate with *XMM-Newton* sources. The correlation with r1-9 has to be regarded as a chance coincidence, since *XMM-Newton* cannot resolve this source, which is located within $\lesssim2''$ of the central source of M 31 and a nearby XRB. In XMM LP-total we classified six correlating sources as foreground star candidates and one as a background galaxy candidate, one source is identified with a foreground star, two sources are classified as hard, and two remain without classification. The correlation of s1-45, s1-20, and s2-37 with foreground stars were already given in Table 3 of DKG2004. In the same table the correlation of s1-41 with the globular cluster candidate B 251 (RBC V3.5) is indicated. Caldwell et al. (2009) found that B 251 is more likely to be a background galaxy than a globular cluster candidate.

The following *Chandra* QSSs have no *XMM-Newton* counterparts: s2-27, s2-10, n1-29, n1-46, n1-66, s2-62, s1-27, n1-26, r2-62, r2-66. Five of them (s2-62, s1-27, n1-26, r2-62, r2-66) are classified as transients (DKG2004). Source n1-66 is not in the field observed with *XMM-Newton*.

**V. Discussion** Of the 40 SSSs detected with *XMM-Newton* only three sources are visible for at least one decade. The additional six sources that were visible in both *XMM-Newton* and *Chandra* observations were all located in the central area of M 31. The *Chandra* and *XMM-Newton* observations of that area were taken at about the same time (within several weeks to a few months of each other), whereas in the outer region there is at least a five year gap between the *Chandra* and *XMM-Newton* observations. From all *XMM-Newton* SSSs 12 have a flux above the *ROSAT* detection threshold. Nevertheless only two were detected in the *ROSAT* PSPC surveys. These findings underline the *long* term variability of the class of SSSs (*cf.* Greiner et al. 2004a).

From the 34 *ROSAT* SSSs (selected from Greiner 2000 and Kahabka 1999) four are outside the field observed with *XMM-Newton*. Eleven sources have *XMM-Newton* counterparts with other source types and may be chance coincidences. Subtracting the three SSSs that were confirmed by *XMM-Newton* and the one correlating with an optical nova, there are 15 sources left which must be considered as transient or at least highly variable. Due to the few optical novae, observed in the years before the *ROSAT* observations, several of the *ROSAT* SSSs may be the X-ray counterpart of a nova, where the optical outburst has been missed (see IV.).

DKG2004 report on 20 *Chandra* SSSs, of which three are classified as foreground stars and two as SNRs. From the remaining sources two *XMM-Newton* counterparts are classified as foreground star candidates, one

[13] In Kong et al. (2002b) *Chandra* ACIS-I data were used and the energy bands are defined as: S, 0.3–1.0 keV; M, 1–2 keV; and H, 2–7 keV. So only the H band is exactly the same as in DKG2004. Hence the selection conditions for SSSs change to: $\mathrm{HR2_{kong}}+\sigma_{\mathrm{HR2_{kong}}}\leq-1$ and $\mathrm{HR1_{kong}}<0$, or $\mathrm{HR1_{kong}}+\sigma_{\mathrm{HR1_{kong}}}\leq-0.8$. For r1-25 the hardness ratios are $\mathrm{HR1_{kong}}=-0.79\pm0.22$ and $\mathrm{HR2_{kong}}=-1.00\pm0.01$.

**Table 9.13:** *Chandra* VSSs in the XMM LP-total catalogue

| XSRC$^{+}$ (1) | CSRC$^{*}$ (2) | Cflag$^{*}$ (3) | Ccat$^{*}$ (4) | type$^{\ddagger}$ (5) | comment$^{\ddagger}$ (6) |
|---|---|---|---|---|---|
| 13 | s2-46 | v | SSS-3 sig | <fg Star> | |
| 23 | s2-29 | | SSS-3 sig | <fg Star> | |
| 32 | s2-28 | | QSS-FNOH | | |
| 52 | s2-7 | | SSS-3 sig | <fg Star> | |
| 69 | s2-26 | v | SSS-HR | <SSS> | |
| 237 | s2-37 | | QSS-MNOH | <fg Star> | TYC 2788-215-1, [KPM2002] G120.4916-22.6317 IR-S (SIM) |
| 603 | s1-45 | | QSS-sig | <fg Star> | [SK98] 152 |
| 668 | s1-42 | | SSS-3 sig | SNR | DO80(11),[Ma1995]3-041, LGS Ha image, [B90] 14 |
| 673 | s1-41 | | QSS-NOH | <Gal> | B251 [CHM09] |
| 696 | s1-20 | | QSS-HR1 | fg Star | G0 [HPM06], [MLV92] 189885 (SIM) |
| 826 | r3-122 | | SSS-HR | <fg Star> | about 11.8 arcmin from centre, [SK98] 196 (SIM) |
| 960 | r2-42 | | QSS-SNOH | <fg Star> | time variable, [FRS2006] WeCAPP V07979 (SIM) |
| 1 000 | r2-19 | | QSS-sig | | RadioS, time variable, [MLV92] 235849 (SIM) |
| 1 006 | r2-60 | t | SSS-HR | <SSS> | M31N 2000-07a, supersoft X-ray transient, [PFF2005], [PHS2007] |
| 1 010 | r1-9 | v,t | QSS-sig | <XRB> | recurrent X-ray transient; nucleus |
| 1 025 | r2-65 | t | SSS-3 sig | <SSS> | supersoft X-ray transient |
| 1 034 | r1-25 | | SSS-HR | <XRB> | X-ray transient, time variable, [FRS2006] WeCAPP V11736 (SIM) |
| 1 050 | r2-56 | | SSS-HR | SNR | [B90] 101 |
| 1 061 | r2-12 | v | SSS-HR | <SSS> | supersoft transient, 217s period [TP2008] |
| 1 100 | r2-63 | t | SSS-HR | <SSS> | M31N 1995-11c, [PFF2005], [PHS2007] |
| 1 136 | r3-115 | t | SSS-HR | <XRB> | X-ray transient, no SSS as stated in [WGK2004], [PFF2005] |
| 1 172 | r3-11 | | QSS-FNOH | <hard> | |
| 1 721 | n1-31 | | QSS-FNOH | <hard> | |
| 1 741 | n1-48 | | SSS-3 sig | <SNR> | EmO [MLA93] 1505 |
| 1 742 | n1-15 | | QSS-SNOH | <fg Star> | flare |
| 1 747 | n1-13 | | QSS-SNOH | <fg Star> | |
| 1 773 | n1-8 | | QSS-sig | <fg Star> | |
| 1 806 | n1-2 | | SSS-3 sig | <fg Star> | |

Notes:

$^{+}$ : XSRC: *XMM-Newton* source identification number

$^{*}$ : CSRC: *Chandra* source identification number from DKG2004, Cflag: *Chandra* variability (v) or transient (t) flag, Ccat: source category of DKG2004

$^{\ddagger}$ : from the XMM LP-total catalogue (see Table 7.2)

as an SNR candidate and two as XRB candidates. The latter two sources are very interesting as they were detected as SSSs in *Chandra* observations, but showed a "hard" spectrum in *XMM-Newton* observations. This indicates a transition from a supersoft to a hard spectral state, which is consistent with the behaviour known to occur in BH XRBs. However, other source types like *e. g.* symbiotic stars cannot be excluded yet. Five *Chandra* sources do not have counterparts in the *XMM-Newton* observations. The fact that half of the *Chandra* SSSs are not *XMM-Newton* SSSs underlines the missing selection sensitivity in the *Chandra* studies, as only one band below $\sim$1 keV was used. Of the 23 *Chandra* quasi-soft sources (DKG2004), about half (12) have counterparts in the *XMM-Newton* Deep Survey observations. However none of these 12 *XMM-Newton* sources had hardness ratios consistent with SSSs.

A short summary of the main results is also provided in Table 9.14.

In conclusion, our comparative study of SSS candidates in M 31 detected with *ROSAT*, *Chandra* and *XMM-Newton* demonstrates that strict selection criteria have to be applied to securely select SSSs. It also underlined the high variability of the sources in this class and the connection between SSSs and optical novae.

**Table 9.14:** Summary of *ROSAT*, *Chandra* and *XMM-Newton* comparison of SSSs

| | |
|---|---|
| 40 | total number of *XMM-Newton* SSSs (this work) |
| 3 | SSSs detected by all three missions as SSSs |
| 31 | SSSs only detected by *XMM-Newton* |
| 3 | SSSs also identified as SSSs by *Chandra* |
| 3 | SSSs detected with *Chandra*, but not classified as SSSs |
| 34 | total number of *ROSAT* SSSs (Greiner 2000, Kahabka 1999) |
| 3 | SSSs detected by all three missions as SSSs |
| 11 | *ROSAT* SSSs have *XMM-Newton* counterparts with other classifications |
| 16 | *ROSAT* SSSs that were not detected in *XMM-Newton* observations |
| 4 | *ROSAT* SSSs that were not in the field of *XMM-Newton* |
| 20 | total number of *Chandra* SSSs (DKG2004) |
| 3 | SSSs detected by all three missions as SSSs |
| 2 | SSSs also identified as SSSs in the XMM LP-total catalogue |
| 3 | already classified as foreground stars by DKG2004 |
| 2 | already classified as SNRs by DKG2004 |
| 2 | new foreground star candidates |
| 1 | new SNR candidate |
| 2 | XRB candidates showing soft/hard transition |
| 5 | *Chandra* SSSs not listed in the XMM LP-total catalogue |
| 23 | total number of *Chandra* QSSs (DKG2004) |
| 3 | already classified as foreground stars by DKG2004 |
| 1 | classified as GlC by DKG2004, now background galaxy |
| 3 | new foreground star candidates |
| 1 | new foreground star |
| 2 | new <hard> sources |
| 2 | sources detected with *XMM-Newton*, but no classification |
| 11 | *Chandra* QSSs not listed in the XMM LP-total catalogue |

### 9.4.2 Supernova remnants

SNRs can be separated into sources where thermal components dominate the X-ray spectrum below 2 keV, and so-called "plerions" or Crab-like SNRs with power-law spectra. The former are located in areas of the X-ray colour/colour diagrams that only overlap with foreground stars. If I assume that I have identified all foreground star candidates from the optical correlation and inspection of the optical images, the remaining sources can be classified as SNR candidates using the criteria given in Table 7.3.

I thus identified 25 SNRs and 37 SNR candidates in the XMM LP-total catalogue. An X-ray source will be classified as an SNR candidate if it either fulfils the hardness ratio criterion given in Table 7.3 (these are 31 sources), or if it correlates with a known optical or radio SNR candidate (six sources). The sources allocated membership in the SNR candidate class based on the latter condition are marked in the comment column of Table 7.2 with the add on '*only correlation*'. As these six SNR candidates would be classified as <hard> from their hardness ratios, they are good candidates for "plerions".

The XID fluxes range between $5.9\times10^{-14}$ erg cm$^{-2}$ s$^{-1}$ for source Nº 1 234 and $1.5\times10^{-15}$ erg cm$^{-2}$ s$^{-1}$ for source Nº 419. These fluxes correspond to luminosities of $4.3\times10^{36}$ erg s$^{-1}$ to $1.1\times10^{35}$ erg s$^{-1}$. A

diagram of the flux distribution of the detected SNRs and candidates is shown in Fig. 9.15.

Among the 25 identified SNRs are 20 SNRs from the PFH2005 catalogue. Source [PFH2005] 146, which correlates with the radio source [B90] 11 and the SNR candidate BA146, was not found in the present study. Source [SPH2008] 858, which coincides with a source reported as a ring-like extended object from *Chandra* observations that was also detected in the optical and radio wavelength regimes and identified as SNR (Kong et al. 2003b), was re-detected (№ 1 050). Of the 37 SNR candidates ten have been reported by PFH2005.

In the following I first discuss the four remaining identified SNRs in more detail:

**XMMM31 J003923.5+404419** (№ 182) was classified as an SNR candidate from its [S II]:H$\alpha$ ratio. It appears as an *'irregular ring with southerly projection'* (Dodorico et al. 1980, and Fig. 9.16) and correlates

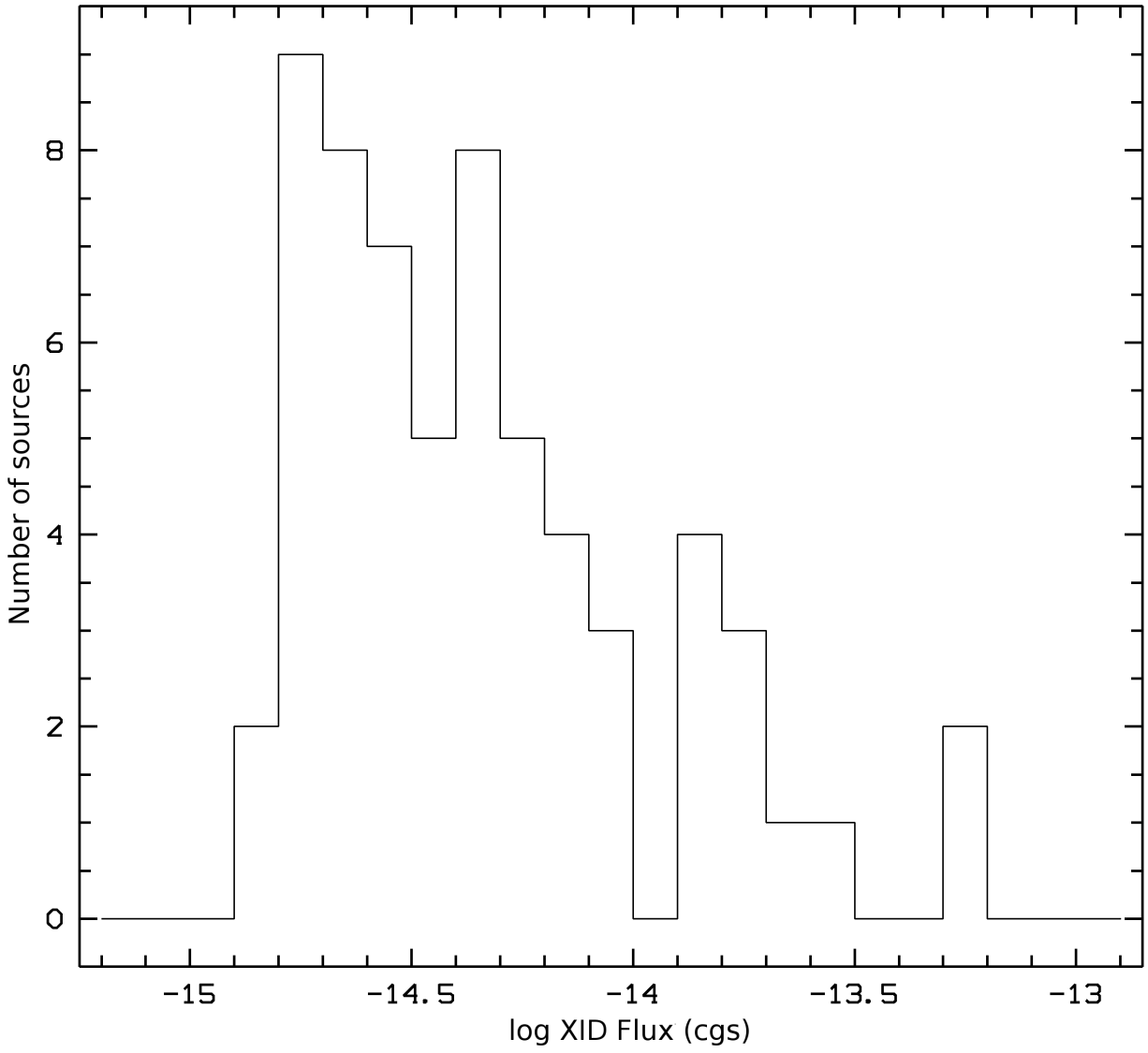


**Figure 9.15:** Distribution of the source fluxes in the 0.2 – 4.5 keV (XID) band. The diagrams show the number of identified and classified SNRs at each flux bin, plotted versus the flux.

with a radio source (Pooley 1969). X-ray radiation of that source was first detected in the present study.

**XMMM31 J004413.5+411954** (№ 1 410) was classified as an SNR candidate from its [S II]:H$\alpha$ ratio (Braun & Walterbos 1993; Magnier et al. 1995). From Fig. 9.17 we can see that the source *'appears as a bright knot'*, as was already reported by Braun & Walterbos (1993). The source has counterparts in the radio (Braun 1990) and X-ray (SHP97) range. It was reported as an SNR by SHP97.

**XMMM31 J004510.5+413251 and XMMM31 J004512.3+420029** Sources № 1 587 and № 1 593, respectively, are new X-ray detections and correlate with the radio sources #354 and #365 in the list of Braun (1990). Source № 1 587 also correlates with source 37W209 from the catalogue of Walterbos et al. (1985). No optical counterparts were reported in the literature.

In the following, I discuss two SNR candidates in more detail:

**XMMM31 J004434.8+412512** (№ 1 481) lies in the periphery of a super-shell with [S II]:H$\alpha$ >0.5 (Braun & Walterbos 1993, src 490). Located next to this source is an SNR candidate reported in Magnier et al. (1995, src 3-086), which has a radio counterpart form the NVSS catalogue. № 1 481 also correlates with *ROSAT* source [SPH97] 284, which was identified as an SNR in SPH97 due to its spatial correlation with

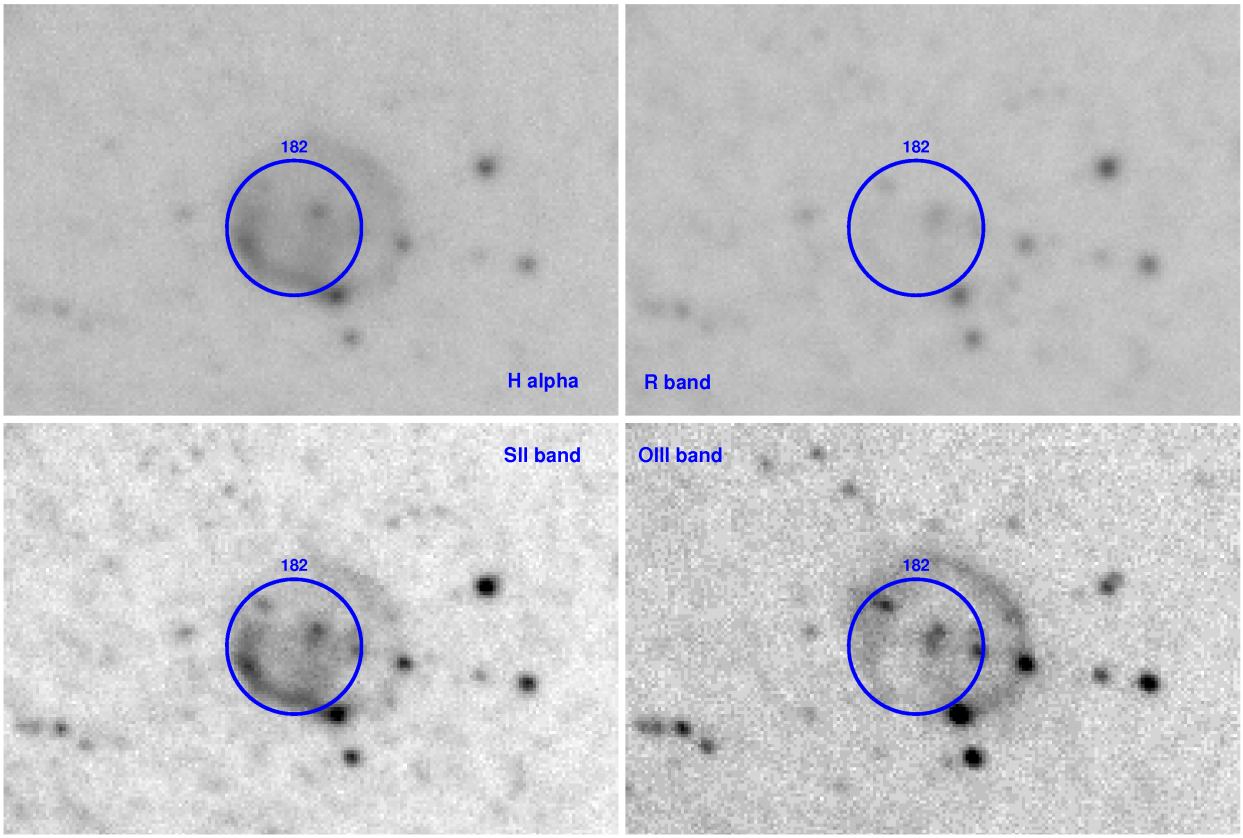


**Figure 9.16:** R, H$\alpha$, S II and O III images, taken from the LG Survey. Over-plotted is a circle at the position of source XMMM31 J003923.5+404419 with a radius of 5.″5 (3$\sigma$ positional error of the X-ray source). The ringlike SNR is clearly visible in the H$\alpha$ and S II bands.

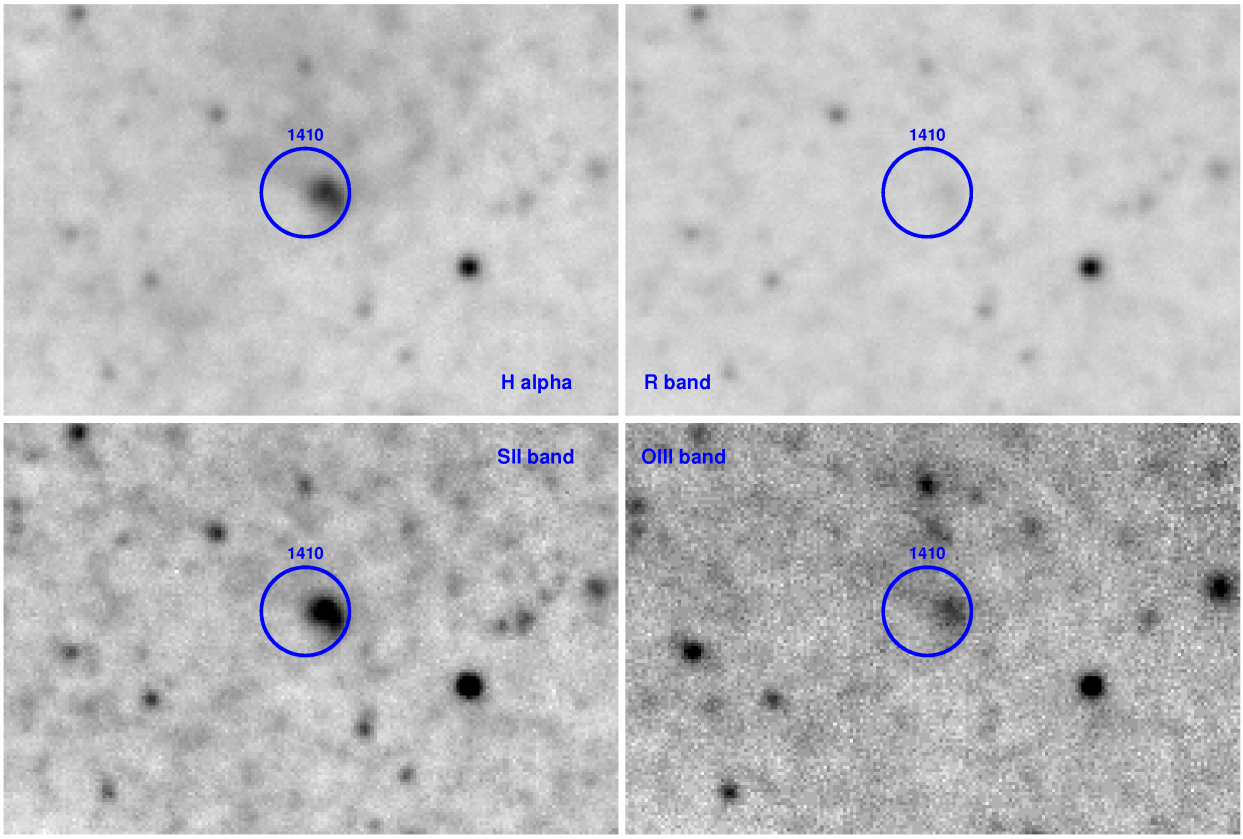


**Figure 9.17:** R, H$\alpha$, S II and O III images, taken from the LG Survey. Over-plotted is a circle at the position of source XMMM31 J004413.5+411954 with a radius of 3.″6 (3$\sigma$ positional error of the X-ray source). The SNR 'appears as a bright knot'.

source 3-086. Figure 9.18 shows the *XMM-Newton* source over-plotted on LGS images. From the *XMM-Newton* source position it looks more like the X-rays are emitted from the H II-region than being the X-ray counterpart of the SNR candidate visible in the optical and radio wavelengths. Nevertheless the detected *XMM-Newton* source is point-like and its hardness ratios lie in the range expected for SNRs. If the X-ray emission originated from the H II-region, it should be detected as spatially extended emission. Thus, Nº 1 481 is classified as an SNR candidate. A puzzling fact, however, is the pronounced variability between *ROSAT* and *XMM-Newton* observations of $F_{\rm var} = 9.82$ with a significance of $S_{\rm var} \approx 4$ (see Table 9.15), which is not consistent with the long term behaviour of SNRs. There is still the possibility that the detected X-ray emission does not belong to the H II-region or an SNR at all.

**XMMM31 J004239.8+404318** (Nº 969) was already observed with *ROSAT* (SHP97, SHL2001) and *Chandra* (Williams et al. 2004a, s1-84). In the images of the LGS no optical counterpart is visible. The X-ray spectrum, which is shown in Fig. 9.19, is well fitted by an absorbed non-equilibrium ionisation model with the following best fit values: an absorption of $N_{\rm H} = 1.76^{+0.46}_{-0.60}\times10^{21}$ cm$^{-2}$, a temperature at the inner edge of the disc of $k_{\rm B}T = 219^{+32}_{-19}$ eV, and an ionisation timescale of $\tau = 1.75^{+0.82}_{-1.75} \times 10^{8}$ s cm$^{-3}$. The unabsorbed 0.2–5 keV luminosity is $L_{\rm X} \sim 6.5\times10^{37}$ erg s$^{-1}$. The soft spectrum with the temperature of $\sim$200 eV is in good agreement with spectra of old SNRs in the SMC (Filipović et al. 2008). Although the unabsorbed luminosity is rather high for an old SNR, it is still in the range found for other SNRs (*cf.* Kong et al. 2002a; Gaetz et al. 2007). Hence, XMMM31 J004239.9+404318 is classified as an SNR candidate.

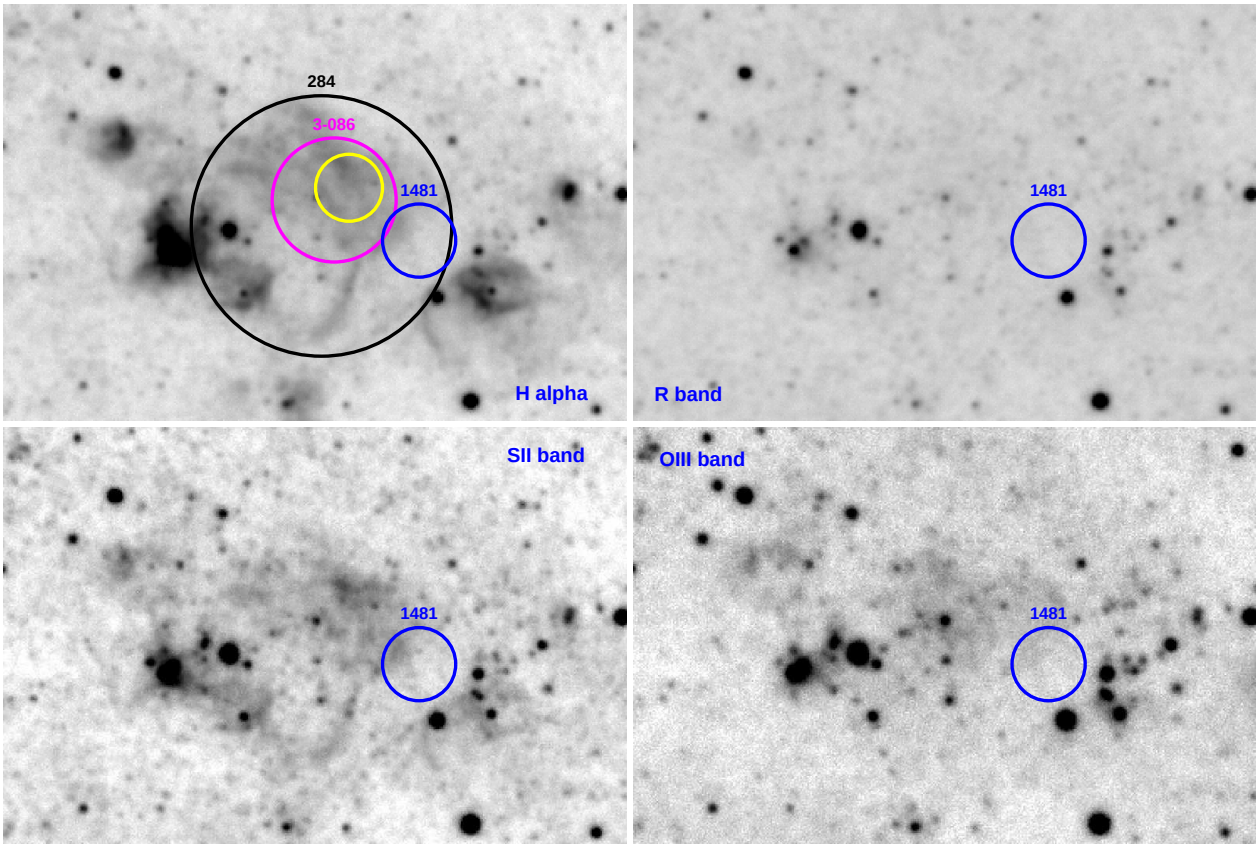


**Figure 9.18:** R, H$\alpha$, S II and O III images, taken from the LG Survey. Over-plotted is a blue circle at the position of source XMMM31 J004434.8+412512 with a radius of $5\farcs9$ ($3\sigma$ positional error of the X-ray source). Source [SPH97] 284 is given by a black circle with a radius of $21''$($3\sigma$ positional error), source 3-086 by the magenta circle with a radius of $10''$; the position of the radio counterpart is marked by the yellow circle.

#### 9.4.2.1 Comparing SNRs and candidates in *XMM-Newton*, *Chandra* and *ROSAT* catalogues

The second *ROSAT* PSPC catalogue (SHL2001) contains 16 sources classified as SNRs. The counterparts of 12 of these sources are also classified as SNRs or SNR candidates in the XMM LP-total catalogue.

Table 9.15 lists the *XMM-Newton*, *ROSAT*, and *Chandra* fluxes of all SNRs and SNR candidates from the XMM LP-total catalogue that have counterparts classified as SNRs in *ROSAT* or *Chandra* source lists. In addition the maximum flux variability and the maximum significance of the variability (following the variability calculation of Sect. 5.2.7) are given. Three SNRs that have *ROSAT* counterparts show variability changing in flux by more than a factor of five. The most variable source (№ 1 066) is discussed in the next paragraph, the second source was discussed in Sect. 9.4.2 (XMMM31 J004434.8+412512), and the third source is embedded in the diffuse emission of the central area of M 31. In this environment the larger PSF of *ROSAT* results in an overestimate of the source flux, since the contribution of the diffuse emission could not be totally separated from the emission of the point source.

The remaining four *ROSAT* sources classified as SNRs and their *XMM-Newton* counterparts are discussed in the following paragraph.

SHP97 report that [SHP97] 203 and [SHP97] 211 ($\hat{=}$[SHL2001] 206) correlate with the same SNR ([DDB80] 1.13), have the same spectral properties and have luminosities within the range of SNRs. A

**Table 9.15:** Variability of SNRs and SNR candidates from the XMM LP-total catalogue with counterparts classified as SNRs in *ROSAT* and *Chandra* catalogues

| Nº | XLPt | SHP97 | SHL2001 | KGP2002$^+$ | WGK2004$^+$ | fvar | svar |
|---|---|---|---|---|---|---|---|
| | | XID Flux with error in $10^{-15}$ erg cm$^{-2}$ s$^{-1}$ | | | | | |
| 474 | $5.27 \pm 0.56$ | $21.18 \pm 4.46$ | | | | 4.01 | 3.54 |
| 668 | $7.94 \pm 1.36$ | $26.30 \pm 6.69$ | | | | 3.31 | 2.69 |
| 883 | $2.83 \pm 0.33$ | | | $3.33 \pm 0.83$ | | 1.18 | 0.56 |
| 1 040 | $7.12 \pm 0.47$ | | | $12.49 \pm 1.67$ | | 1.75 | 3.11 |
| 1 050 | $8.25 \pm 0.70$ | | | $2.50 \pm 0.83$ | | 3.30 | 5.28 |
| 1 066 | $28.35 \pm 1.16$ | | $256.16 \pm 16.19$ | $39.13 \pm 3.33$ | $25.29 \pm 5.32$ | 10.13 | 14.06 |
| 1 234 | $59.12 \pm 1.10$ | $152.91 \pm 13.82$ | $268.98 \pm 17.09$ | $54.11 \pm 3.33$ | $109.13 \pm 11.31$ | 4.97 | 12.34 |
| 1 275 | $23.88 \pm 1.08$ | $53.50 \pm 8.47$ | $79.39 \pm 9.90$ | | | 3.32 | 5.58 |
| 1 328 | $9.25 \pm 0.74$ | | 26.99 | | | 1.00 | 0.00 |
| 1 351 | $4.96 \pm 0.68$ | $24.96 \pm 8.92$ | 17.77 | | | 1.00 | 0.00 |
| 1 372 | $2.12 \pm 0.84$ | | 29.91 | | | 1.00 | 0.00 |
| 1 410 | $7.40 \pm 0.94$ | $29.87 \pm 7.13$ | | | | 4.04 | 3.12 |
| 1 481 | $3.43 \pm 0.97$ | $33.66 \pm 7.36$ | | | | 9.82 | 4.07 |
| 1 535 | $14.73 \pm 1.31$ | $53.94 \pm 9.14$ | $34.41 \pm 7.20$ | | | 3.66 | 4.25 |
| 1 599 | $16.08 \pm 0.92$ | $54.39 \pm 10.03$ | $33.51 \pm 6.97$ | | | 3.38 | 3.80 |
| 1 637 | $12.72 \pm 1.33$ | | 27.21 | | | 1.00 | 0.00 |

Notes:

$^+$ : KGP2002: Kong et al. (2002b),WGK2004: Williams et al. (2004a)

*ROSAT* and *Chandra* count rates are converted to 0.2–4.5 keV fluxes, using WebPIMMS and assuming a foreground absorption of $N_{\rm H} = 6.6\times10^{20}$ cm$^{-2}$ and a photon index of $\Gamma = 1.7$: ECF$_{\rm SHP97} = 2.229\times10^{-14}$ erg cm$^{-2}$ cts$^{-1}$, ECF$_{\rm SHL2001} = 2.249\times10^{-14}$ erg cm$^{-2}$ cts$^{-1}$, and ECF$_{\rm KGP2002} = 8.325\times10^{-14}$ erg cm$^{-2}$ cts$^{-1}$. For WGK2004 the luminosity given in Table 2 of WGK2004 was converted to XID flux using $F_{\rm XID}$[erg cm$^{-2}$ s$^{-1}$] $= 6.654\times10^{-15} \times L_{\rm WGK2004}$[$10^{36}$erg s$^{-1}$].

**Table 9.16:** Variability of SNRs and SNR candidates from the XMM LP-total catalogue which have counterparts in *ROSAT*, and/or *Chandra* catalogues that are not classified as SNRs

| Nº | XLPt | Chandra | PFJ93 | SHP97 | SHL2001 | fvar | svar | remark$^‡$ |
|---|---|---|---|---|---|---|---|---|
| | | XID Flux with error in $10^{-15}$ erg cm$^{-2}$ s$^{-1}$ | | | | | | |
| (1) | (2) | (3) | (4) | (5) | (6) | (7) | (8) | (9) |
| 294 | $18.50 \pm 0.85$ | | | $53.27 \pm 6.69$ | $46.78 \pm 7.87$ | 2.88 | 5.16 | |
| 472 | $3.15 \pm 0.69$ | | | | $26.09 \pm 6.07$ | 8.28 | 3.76 | 468 brt |
| 969 | $53.51 \pm 1.35$ | $84.51 \pm 15.97^+$ | | $34.55 \pm 6.91$ | $89.06 \pm 11.92$ | 2.58 | 3.96 | |
| 1 079 | $4.19 \pm 0.59$ | | | $20.06 \pm 6.24$ | | 4.79 | 2.53 | brt |
| 1 291 | $14.55 \pm 0.75$ | 16.04* | >24.0 | $35.22 \pm 8.47$ | $40.93 \pm 7.87$ | 2.81 | 3.33 | |
| 1 741 | $4.12 \pm 0.65$ | $4.17^\dagger$ | | | | 1.01 | — | brt |
| 1 793 | $3.70 \pm 0.52$ | | | $26.08 \pm 6.46$ | | 7.06 | 3.46 | 1 799 brt |

Notes:

$^‡$ : Source number (from XMM LP-total catalogue) of another (brighter) XMM LP-total source which correlate with the same *ROSAT* source as the XMM LP-total source given in Col. 1; brt: XMM LP-total flux is below the *ROSAT* detection threshold ($5.3\times10^{-15}$ erg cm$^{-2}$ s$^{-1}$).

*ROSAT* and *Chandra* count rates are converted to 0.2–4.5 keV fluxes, using WebPIMMS and assuming a foreground absorption of $N_{\rm H} = 6.6\times10^{20}$ cm$^{-2}$ and a photon index of $\Gamma = 1.7$: ECF$_{\rm SHP97} = 2.229\times10^{-14}$ erg cm$^{-2}$ cts$^{-1}$, ECF$_{\rm SHL2001} = 2.249\times10^{-14}$ erg cm$^{-2}$ cts$^{-1}$, ECF$_{\rm HRI} = 6.001\times10^{-14}$ erg cm$^{-2}$ cts$^{-1}$, $^\dagger$ : ECF$_{\rm DKG2004} = 5.56\times10^{-12}$ erg cm$^{-2}$ cts$^{-1}$. $^+$ : For WGK2004 the luminosity given in Table 2 of WGK2004 was converted to XID flux using $F_{\rm XID}$[erg cm$^{-2}$ s$^{-1}$] $= 6.654\times10^{-15}\times L_{\rm WGK2004}$[$10^{36}$erg s$^{-1}$]. * : For VG2007 the luminosity given in Table 2 of VG2007 was converted to XID flux using $F_{\rm XID}$[erg cm$^{-2}$ s$^{-1}$] $= 9.433\times10^{-15} \times L_{\rm VG2007}$[$10^{36}$erg s$^{-1}$].

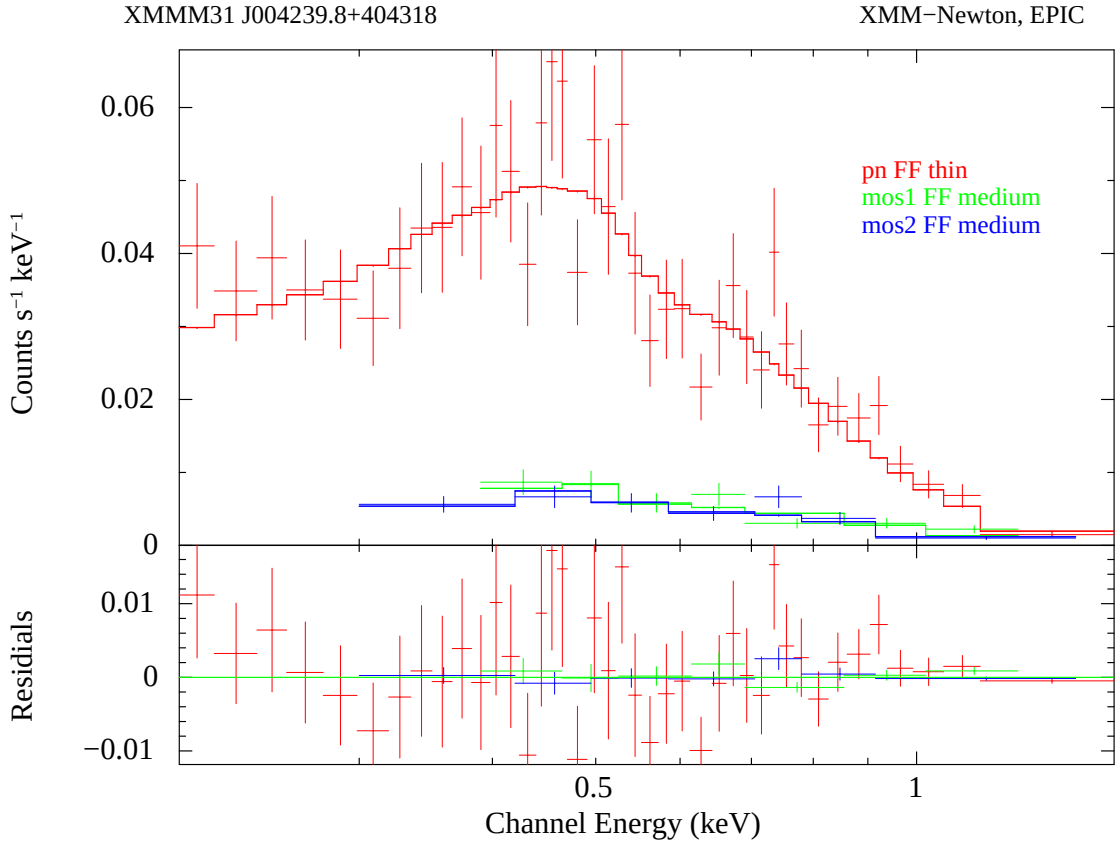


**Figure 9.19:** 0.2–3.0 keV EPIC spectrum of XMMM31 J004239.9+404318. The best fit absorbed non-equilibrium ionisation model is indicated by the solid lines.

correlation with the *ROSAT* HRI catalogue (PFJ93) reveals that the true X-ray counterpart of [DDB80] 1.13 is located between the two *ROSAT* PSPC sources. Furthermore, PFJ93 report that this SNR is located '*within 19″ of a brighter X-ray source*' which matches positionally with [SHP97] 211. These findings are confirmed by *XMM-Newton* and *Chandra* observations. The X-ray counterpart of [DDB80] 1.13 is source Nº 1 066 in the XMM LP-total catalogue (or [PFH2005] 354 or r3-69 in Kong et al. 2002b). The second source, which correlates with [SHP97] 211, is the *XMM-Newton* source Nº 1 077, which has a "hard" spectrum and is $\sim 6.7$ times brighter than Nº 1 066. Hence, [SHP97] 211 is a blend of the two *XMM-Newton* sources Nº 1 066 and Nº 1 077. This also explains the pronounced variability between [SHL2001] 206 and Nº 1 066 given in Table 9.15. Comparing the *Chandra* detections of the SNR counterpart with the *XMM-Newton* flux gives a variability factor of $F_{\rm var} \approx 1.12$. What do we know about [SPH97] 203? The distance between [SPH97] 203 and [DDB80] 1.13 is $\gtrsim 20''$. In addition [SPH97] 203 was detected only in the first *ROSAT* PSPC catalogue. It was not visible during the observations of the second *ROSAT* PSPC catalogue or in any *XMM-Newton* or *Chandra* observation of that region taken up to now. Thus it seems very likely that [SPH97] 203 was either a transient source or a false detection. In both cases [SPH97] 203 cannot be an SNR. As the field of [DDB80] 1.13 was observed many times with *Chandra*, and as *Chandra* had detected weak SNRs in the central part of M 31 (Kong et al. 2003b), *Chandra* should have detected this source if it really was an SNR.

The remaining two *ROSAT* SNRs correlate with *XMM-Newton* sources, which were not classified as SNRs or SNR candidates. Source [SHP97] 258 correlates with source Nº 1 337 and has a $3\sigma$ positional

error of 30″. From the improved spatial resolution of *XMM-Newton* the total positional error reduces to 2.″3. Hence we can see that the X-ray source belongs to a foreground star candidate (*cf.* Table 7.2) and not to the very nearby SNR. Source [SHL2001] 129 correlates with sources Nº 743 and Nº 761, which are classified as a GlC and a GlC candidate, respectively. The SNR candidate listed as the counterpart of [SHL2001] 129 is located between these two *XMM-Newton* sources. In addition PFH2005 gives a third source which lies within the error circle of [SHL2001] 129 and which is classified as an AGN candidate. Thus it is very likely that [SHL2001] 129 is a blend of these three *XMM-Newton* sources and that the correlation with the SNR candidate has to be considered as a chance coincidence.

From the sources listed as SNRs in the different *Chandra* studies, many are re-detected. Nevertheless two SNRs from *Chandra* were not detected in the *XMM-Newton* observations. Source n1-85 is reported as an SNR in Williams et al. (2004a), but was not found in the study of PFH2005. Despite a new *XMM-Newton* observation of the field in which the source is located[14], and the hence a much increased exposure, I did not detect this source in the *XMM-Newton* data. This implies the source to have a variable or even transient nature, which contradicts the SNR classification. Source CXOM31 J004247.8+411556 (Kong et al. 2003b), which correlates with the radio source [B90] 95, is located in the vicinity of two bright sources and close to the centre of M 31. Due to *XMM-Newton*'s larger point spread function this source cannot be resolved by *XMM-Newton* in this environment. The larger PSF of *XMM-Newton* is also the reason why source Nº 1 050 has a significant variability in Table 9.15, since this source is located in the central diffuse emission of M 31.

Finally, we want to investigate how many of our SNRs and SNR candidates were observed in previous X-ray studies if at all, and not classified as SNRs. In total there are seven sources. One (Nº 1741) of them is classified as an SNR candidate based on its *XMM-Newton* hardness ratios, and correlates with source n1-48, which was detected with *Chandra* (DKG2004). The fluxes obtained with *XMM-Newton* and *Chandra* are in good agreement (see Table 9.16) and below the *ROSAT* detection threshold ($5.3 \times 10^{-15}$ erg cm$^{-2}$ s$^{-1}$). That is why no corresponding source was detected with *ROSAT*. For a further four sources, there are only corresponding sources detected with *ROSAT*. One of them (Nº 1 793≙[SHP97] 347) also correlates with a radio source (source 472 of Braun 1990) and is therefore identified as an SNR. The rather high flux variability between the *ROSAT* and *XMM-Newton* observations (see Table 9.16) can be attributed to source Nº 1 799, which is located within 19.″9 of Nº 1 793. This suggests that [SHP97] 347 is a combination of both *XMM-Newton* sources, but as [SHP97] 347 was not detected in SHL2001 we cannot exclude a transient source or false detection as an explanation for the *ROSAT* source. Source Nº 472 (≙[SHL2001] 84), source Nº 294 (≙[SHP97] 53≙[SHL2001] 56) and source Nº 1 079 (≙[SHP97] 212) are SNR candidates based on their hardness ratios. The pronounced flux variability of source Nº 472 is due to source Nº 468, which is located within 18.″5 of Nº 472 and is ∼8.6 times brighter than Nº 472. The variability of source Nº 1 079 between the *ROSAT* and *XMM-Newton* observations, the fact that in the *XMM-Newton* observation the source flux is below the *ROSAT* detection threshold and the classification of the source as an SNR candidate in SHP97 whereas this classification was rejected in SHL2001, due to no source being detected at that position, may indicate that the *ROSAT* SHP97 detection belongs to a transient source unassociated with the SNR. Thus [SHP97] 212 would be a blend of the unknown transient source and source Nº 1 079. Sources corresponding to the remaining two *XMM-Newton* sources were detected with *ROSAT* and *Chandra*. Source Nº 969 has counterparts in both *ROSAT* PSPC surveys ([SHP97] 185≙[SHL2001] 186) and correlates with *Chandra* source s1-84 (Williams et al. 2004a). It is classified as an SNR candidate due to its hardness ratios and X-ray spectrum (see XMMM31 J004239.8+404318). Counterparts for source Nº 1 291 were reported in the literature as [PFJ93] 84, [SHP97] 251, [SHL2001] 255, [VG2007] 261, and source 4 in Table 4 of Orio (2006). Based on the *XMM-Newton* hardness ratios and the correlation with radio source [B90] 166 (Braun 1990), the source was identified as an SNR. For sources Nº 294, Nº 969, and Nº 1 291 the variability between different observations does not contradict the SNR classification.

[14] n1-85 lies in the N2 field

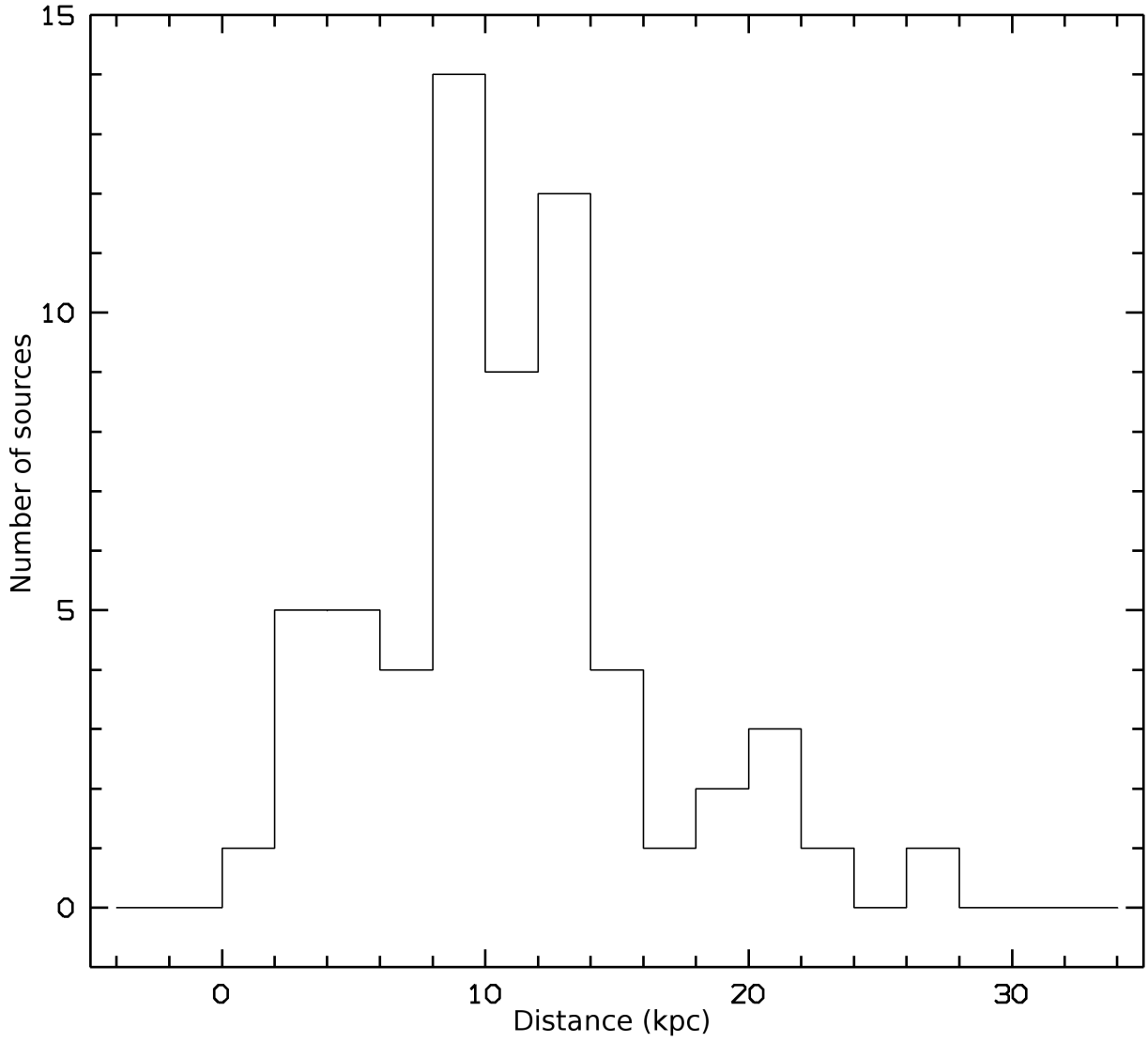


**Figure 9.20:** Projected radial distribution of SNRs and SNR candidates from the XMM LP-total catalogue. An enhancement in the source distribution corresponding to the 10 kpc dust ring of M 31 is visible.

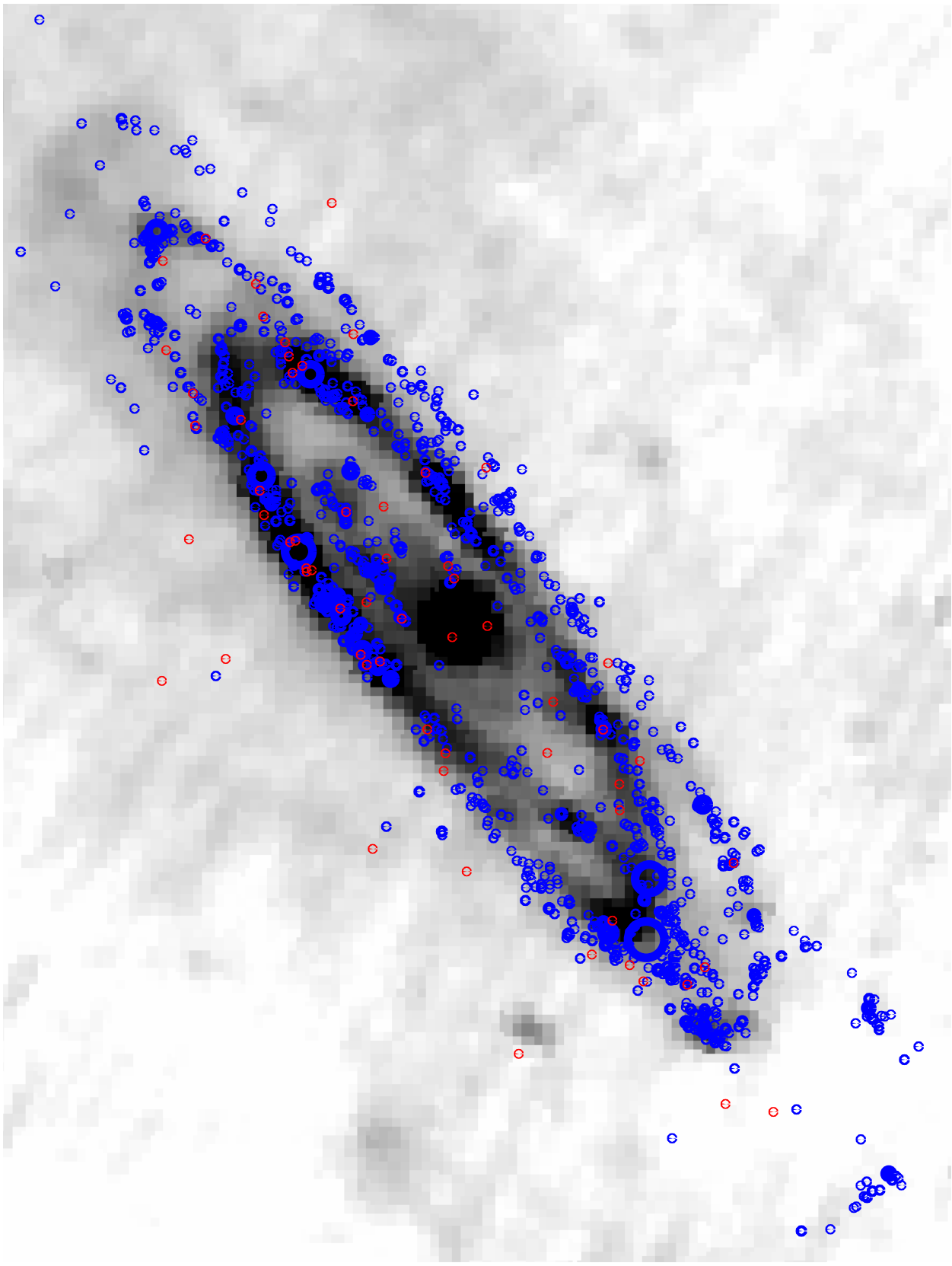

**Figure 9.21:** An IRAS 60$\mu$m image, which clearly shows the dust ring located at $\sim$ 10 kpc, overplotted with the location of SNRs and candidates (red dots) from the XMM LP-total catalogue. The coincidence between the SNRs and candidates and the structures of the image is visible. In addition the locations of star forming regions, which were obtained from GALEX data (Kang et al. 2009), are indicated by blue dots.

#### 9.4.2.2 The spatial distribution

To examine the spatial distribution of the *XMM-Newton* SNRs and SNR candidates, I determined projected distances from the centre of M 31. Their distribution, as can be seen in Fig. 9.20, shows an enhancement of sources around $\sim$10 kpc. This corresponds with the well known dust ring or star formation ring of M 31 (Block et al. 2006). Only a few sources are located in the region beyond this ring. Figure 9.21 shows the spatial distribution of the SNRs and SNR candidates from the XMM LP-total catalogue plotted over the IRAS 60$\mu$m image. We see that most of the SNRs and SNR candidates are located on features that are visible in the IRAS image. This again demonstrates that SNRs and SNR candidates are coincident with the dust ring at $\sim 10$ kpc. In addition, the locations of star forming regions obtained from *GALEX* data (Kang et al. 2009, and private communication) are indicated in Fig. 9.21. We see that many of the SNRs and SNR candidates are located within or next to star forming regions in M 31.

### 9.4.3 X-ray binaries

XRBs are the main contribution to the population of "hard" X-ray sources in M 31. Depending on the mass of the companion star one distinguishes between LMXBs and HMXBs. Despite some more or less reliable candidates, not a single, definitely detected HMXB is known in M 31. The results of a new search for HMXB candidates are presented in Sect. 9.4.3.2. The LMXBs can be separated into two sub-classes: the field XRBs (like the HMXBs; and discussed in this section) and those located in globular clusters. Sources belonging to the latter sub-class are discussed in Sect. 9.4.4. In Sect. 9.4.5 I compare the number of sources found from the log N-log S study (see Chap. 8) to the number of identified and classified XRBs (including sources in GlCs).

The sources presented here are classified as XRBs, because they have HRs indicating a <hard> source and are either transient or show a variability factor larger than ten (see Sect. 7.4).

In total 10 sources are identified and 26 are classified as XRBs. Apart from source Nº 57 (XMMM31 J003833.2+402133, see below), the identified XRBs have been reported as X-ray binaries in the literature (see comment column of Table 7.2). Figure 9.22 shows the flux distribution of XRBs. We see that this class only contains rather bright sources. This is not surprising as the classification criterion for XRBs is based on their variability, which is more easily detected for brighter sources (*cf.* Sect. 7.4). The XID fluxes range from $1.4\times10^{-14}$ erg cm$^{-2}$ s$^{-1}$ (Nº 378) to $3.75\times10^{-12}$ erg cm$^{-2}$ s$^{-1}$ (Nº 966), which correspond to luminosities from $1.0\times10^{36}$ erg s$^{-1}$ to $2.7\times10^{38}$ erg s$^{-1}$.

It is clear from Fig. 9.23, which shows the spatial distribution of the XRBs, that nearly all sources classified or identified as XRBs are located in fields that were observed more than once. One reason for this is that variability factors were determined for sources only located in these fields. For sources located in the remaining fields, especially the northern part of the disc, the transient nature must have been reported in the literature to mark them as an XRB. In addition, an increasing number of observations of the same field enlarges the probability to detect transient sources. Another reason is that the source density of LMXBs, which follows the overall stellar density, is higher in the centre than in the disc of M 31.

References for the sources, selected from their temporal variability, are given in Table 7.6. TPC06 report on four bright X-ray transients, which they detected in the observations of July 2004 and suggested to be XRB candidates. We also found these sources and classified source Nº 705 and identified sources Nº 985, Nº 1 153, Nº 1 177 as XRBs. One of the identified XRBs (Nº 1 177) shows a very soft spectrum. Williams et al. (2005b) observed source Nº 1 153 with *Chandra* and *HST*. From the location and X-ray spectrum they suggest it to be an LMXB. They propose a star within the X-ray error box, which shows a change in optical brightness ($\Delta B$) of $\approx$1 mag, to be the optical counterpart. Source Nº 985 was first detected in January 1979 by TF91 with the *Einstein* observatory. WGM06 rediscovered it in *Chandra* observations from 2004. Their coordinated *HST* ACS imaging does not reveal any variable optical counterpart. From the X-ray spectrum

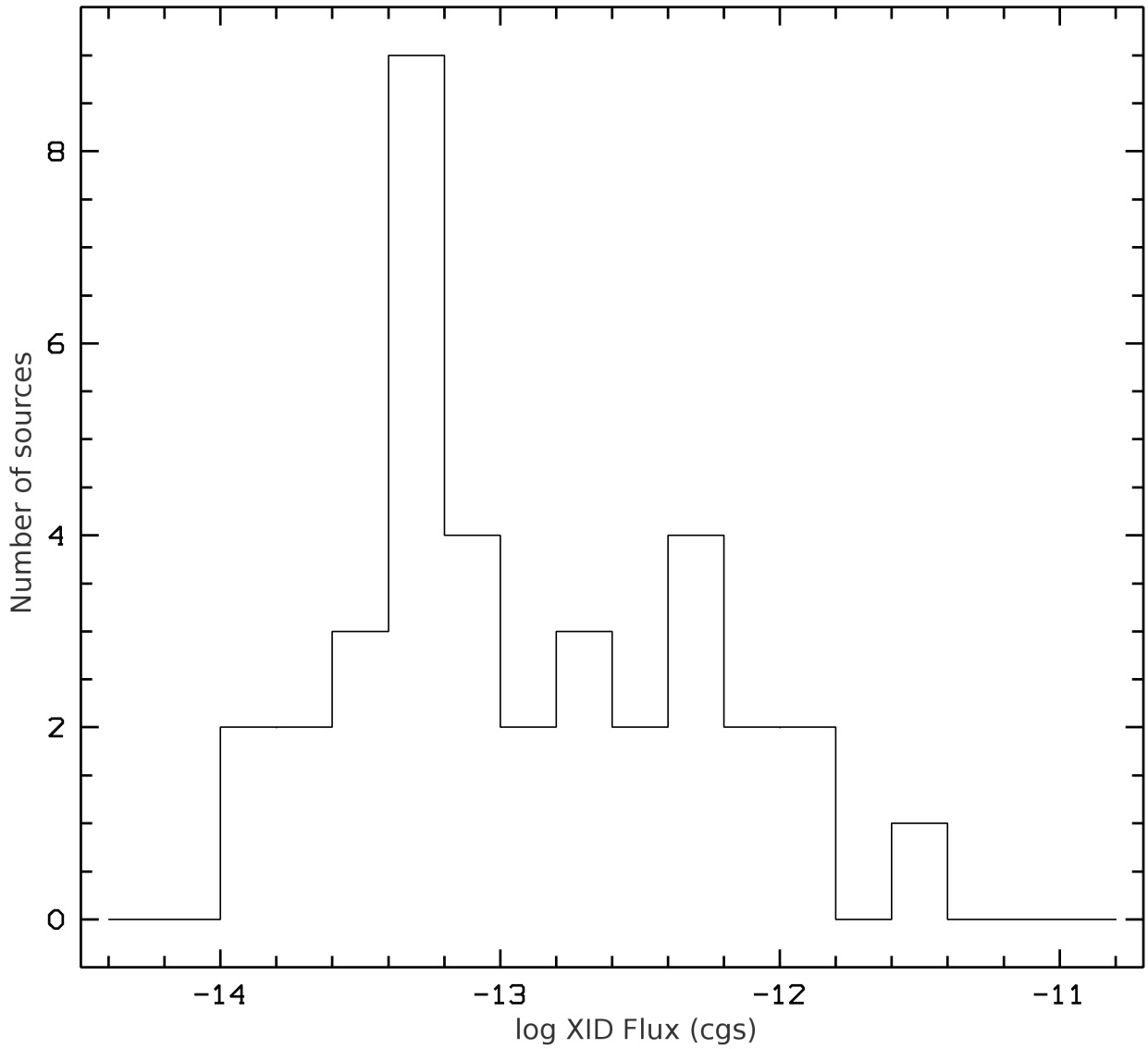


**Figure 9.22:** Distribution of the source fluxes in the 0.2–4.5 keV (XID) band. The diagram shows the number of identified and classified XRBs at each flux bin, plotted versus the flux.

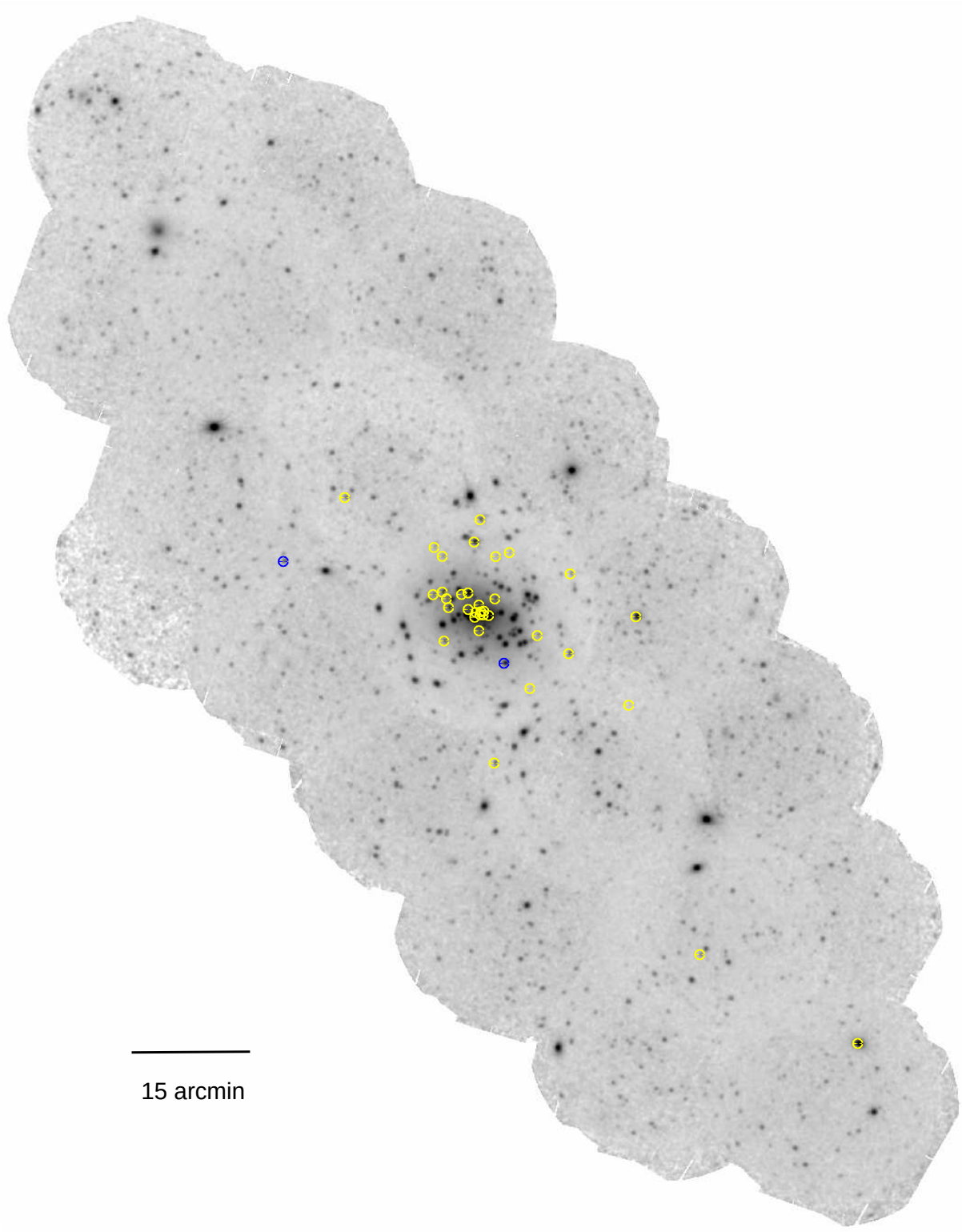


**Figure 9.23:** The spatial distribution of XRBs and candidates from the XMM LP-total catalogue. The positions of the XRBs and candidates are marked with yellow dots; the two XRB candidates classified from their variability compared with *ROSAT* observations are marked with blue dots. An enhancement of sources in the central field is clearly visible.

and the lack of a bright star WGM06 suggest this source to be an LMXB with a black hole.

In the following subsections I discuss three of the sources in more detail.

**XMMM31 J003833.2+402133** (№ 57) was first detected in the *XMM-Newton* observation from 02 January 2008 (s32) at an unabsorbed 0.2 – 10 keV luminosity of $\sim 2\times10^{38}$ erg s$^{-1}$. From two observations, taken about half a year (s31) and one and a half years (s3) earlier, I derived upper limits for the fluxes, which were more than a factor of 100 below the values from January 2008 (see Fig. 9.24(a)).

The combined EPIC spectrum, from observation s32 (Fig. 9.25(a)), is best fitted with an absorbed disc blackbody plus power-law model, with $N_{\rm H} = 1.68^{+0.42}_{-0.48}\times10^{21}$ cm$^{-2}$, temperature at the inner edge of the disc $k_{\rm B}T_{\rm in} = 0.462 \pm 0.013$ keV and power-law index of $2.55^{+0.33}_{-1.05}$. The contribution of the disc blackbody luminosity to the total luminosity is $\sim 59\,\%$. Formally acceptable fits are also obtained from an absorbed disc blackbody model and an absorbed bremsstrahlung model (see Table 9.17).

I did not find any significant feature in an FFT periodicity search. The combined EPIC light curve during observation s32 was consistent with a constant value.

To identify possible optical counterparts I examined the LGS images and the images taken with the *XMM-Newton* optical monitor during the X-ray observation (UVW1 and UVW2 filters). The absence of optical/UV counterparts and of variability on short timescales, as well as the spectral properties suggest this source to be a black hole LMXB in the steep power-law state (McClintock & Remillard 2006).

**CXOM31 J004059.2+411551** Galache et al. (2007) reported on the detection of a previously unseen X-ray source in a 5 ks *Chandra* ACIS-S observation from 05 July 2007. In an *XMM-Newton* ToO observation (sn11, Stiele et al. 2007) taken about 20 days after the *Chandra* detection, the source (№ 523) was still bright. The position agrees with that found by *Chandra*. We detected the source at an unabsorbed 0.2 – 10 keV luminosity of $\sim 1.1\times10^{38}$ erg s$^{-1}$.

The combined EPIC spectrum (Fig. 9.25(b)) can be well fitted with an absorbed disc blackbody model with $N_{\rm H} = (2.00 \pm 0.16)\times10^{21}$ cm$^{-2}$ and with a temperature at the inner edge of the disc of $k_{\rm B}T_{\rm in} = 0.538 \pm 0.017$ keV (Table 9.17). The spectral parameters and luminosity did not change significantly compared to the *Chandra* values of Galache et al. (2007).

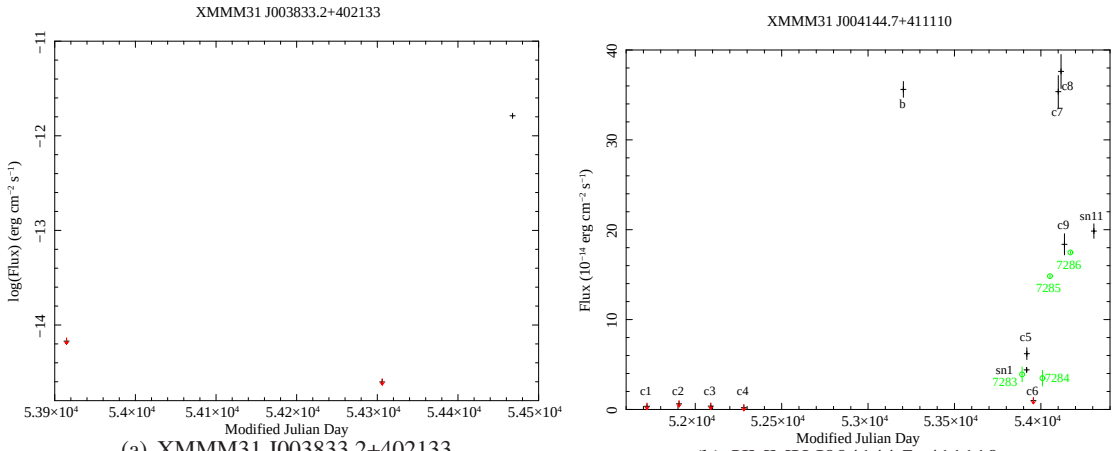


(a) XMMM31 J003833.2+402133 (b) XMMU J004144.7+411110

**Figure 9.24:** Long-term light curves of the transient sources (a) XMMM31 J003833.2+402133 and (b) XMMU J004144.7+411110, containing data from *XMM-Newton* (black crosses) and *Chandra* (green circles) observations. $3\sigma$ upper limits of non detections are indicated by red arrows.

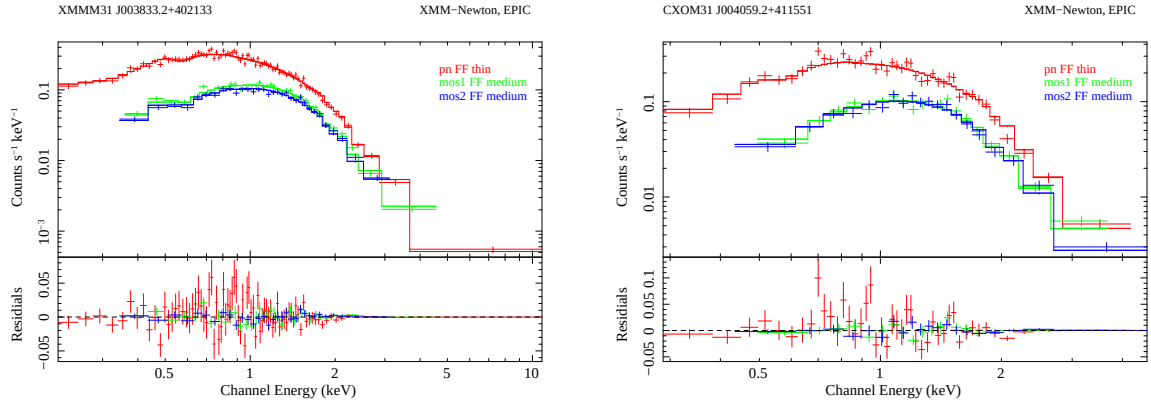


(a) XMMM31 J003833.2+402133




(b) CXOM31 J004059.2+411551

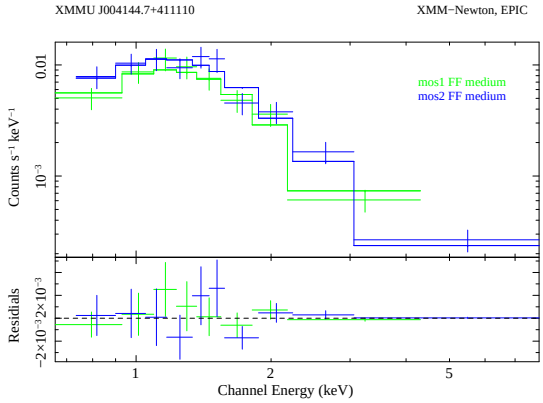


(c) XMMU J004144.7+411110

**Figure 9.25:** EPIC spectra of the transient sources (a) XMMM31 J003833.2+402133, (b) CXOM31 J004059.2+411551 and (c) XMMU J004144.7+411110. The histograms show the best-fit model.

We did not find any significant feature in an FFT periodicity search. The combined EPIC light curve was consistent with a constant value.

The examination of LGS images and of images taken with the *XMM-Newton* optical monitor (UVW1 and UVW2 filters) during the X-ray observation did not reveal any possible optical/UV counterparts.

The lack of bright optical counterparts and the X-ray parameters (X-ray spectrum, lack of periodicity, transient nature, luminosity) are consistent with this source being a black hole X-ray transient, as already mentioned in Galache et al. (2007).

**XMMU J004144.7+411110** (N$^{\underline{o}}$ 705) was detected by Trudolyubov et al. (2006a) in *XMM-Newton* observations b (July 2004) at an absorbed luminosity of $\sim 31.1 \times 10^{36}$ erg s$^{-1}$ in the 0.3–7 keV band. We detected the source in observation sn11 (25 July 2007) at a significantly lower luminosity. Checking additional observations of the centre of M 31 (see Table 5.2), we found another outburst of the source in observations c7 (31 Dec. 2006) and c8 (16 Jan. 2007) (Fig. 9.24(b)). In observations sn1 (01 July 2006) and c5 (02 July 2006) the flux was rather low and for observation c6 (09 August 2006) we only obtained an upper limit (red arrow on the right hand side of Fig. 9.24(b)).

In observations c7 (Fig. 9.25(c)), c8, c9, and sn11 the source was bright enough to allow spectral analysis. Note that in all three observations of the centre of M 31, the source was not in the field of view

**Table 9.17:** Spectral parameters of the transient sources.

| M 31 field | Model | $N_{\rm H}$ ($\times 10^{21}$ cm$^{-2}$) | $k_{\rm B}T$ (keV) | $R_{in}\sqrt{\cos i}^{*}$ (km) | Photon Index | $\chi^2$ (d.o.f) | $L_X^{\dagger}$ | Instrument |
|---|---|---|---|---|---|---|---|---|
| XMMM31 J003833.2+402133 | | | | | | | | |
| s32 | PL+DISCBB | $1.68^{+0.42}_{-0.48}$ | $0.462 \pm 0.013$ | $106^{+9}_{-10}$ | $2.55^{+0.33}_{-1.05}$ | 173.89(145) | 2.04 | PN+M1+M2 |
| s32 | DISCBB | $1.06 \pm 0.06$ | $0.511 \pm 0.009$ | $95 \pm 4$ | | 270.01(147) | 1.46 | PN+M1+M2 |
| s32 | BREMSS | $1.91 \pm 0.07$ | $1.082^{+0.029}_{-0.030}$ | | | 208.65(147) | 2.12 | PN+M1+M2 |
| CXOM31 J004059.2+411551 | | | | | | | | |
| sn11 | DISCBB | $2.00 \pm 0.16$ | $0.538 \pm 0.017$ | $75 \pm 6$ | | 97.70(79) | 1.12 | PN+M1+M2 |
| sn11 | BREMSS | $3.13 \pm 0.19$ | $1.097^{+0.060}_{-0.056}$ | | | 93.17(79) | 1.72 | PN+M1+M2 |
| XMMU J004144.7+411110 | | | | | | | | |
| sn11 | DISCBB | $2.32^{+1.03}_{-0.87}$ | $0.586^{+0.100}_{-0.087}$ | $26^{+13}_{-8}$ | | 29.74(23) | 0.18 | PN+M1+M2 |
| sn11 | BREMSS | $3.72^{+1.14}_{-1.00}$ | $1.216^{+0.373}_{-0.269}$ | | | 29.48(23) | 0.29 | PN+M1+M2 |
| sn11 | PL | $6.17^{+1.72}_{-1.47}$ | | | $3.23^{+0.46}_{-0.40}$ | 31.57(23) | 1.12 | PN+M1+M2 |
| c7 | DISCBB | $1.60^{+1.70}_{-1.51}$ | $0.731^{+0.151}_{-0.127}$ | $21^{+12}_{-7}$ | | 14.95(14) | 0.30‡ | M1+M2 |
| c7 | BREMSS | $3.60^{+1.77}_{-1.62}$ | $1.596^{+0.625}_{-0.407}$ | | | 12.30(14) | 0.47‡ | M1+M2 |
| c7 | PL | $6.80^{+2.48}_{-2.21}$ | | | $3.04^{+0.49}_{-0.42}$ | 10.42(14) | 1.72‡ | M1+M2 |
| c8 | DISCBB | $1.81^{+1.68}_{-1.40}$ | $0.743^{+0.173}_{-0.123}$ | $21^{+12}_{-8}$ | | 12.22(15) | 0.32‡ | M1+M2 |
| c8 | BREMSS | $3.41^{+1.91}_{-1.56}$ | $1.815^{+0.991}_{-0.542}$ | | | 13.25(15) | 0.47‡ | M1+M2 |
| c9 | PL | $5.22^{+2.86}_{-2.07}$ | | | $2.60^{+0.57}_{-0.44}$ | 15.00(15) | 0.99‡ | M1+M2 |
| c9 | DISCBB | $0.00^{+1.92}_{-0.00}$ | $0.746^{+0.166}_{-0.174}$ | $13^{+11}_{-4}$ | | 4.35(7) | 0.13‡ | M1+M2 |
| c9 | BREMSS | $1.35^{+2.55}_{-1.35}$ | $1.897^{+1.774}_{-0.779}$ | | | 3.78(7) | 0.19‡ | M1+M2 |
| c9 | PL | $3.74^{+3.66}_{-3.07}$ | | | $2.69^{+0.82}_{-0.65}$ | 3.39(7) | 0.46‡ | M1+M2 |

Notes:

$^{*}$ : effective inner disc radius, where $i$ is the inclination angle of the disc

$^{\dagger}$ : unabsorbed luminosity in the $0.2-10.0$ keV energy range in units of $10^{38}$ erg s$^{-1}$

$^{\ddagger}$ : derived from model flux given for MOS 1

of the EPIC-PN detector. The spectra can be well fitted with an absorbed power-law, disc blackbody or bremsstrahlung model (Table 9.17). Taking the errors into account, the power-law indices of all four observations agree with each other. Due to the reduced number of source counts and hence the number of bins in observation c9 the absorption column density is not well constrained, but still agrees within the errors with the values from the other observations. The obtained parameters are in good agreement with the values of Trudolyubov et al. (2006a).

An FFT periodicity search did not reveal any significant periodicities in the 0.3 s to 2 000 s range.

No optical counterparts were evident in the images taken with the *XMM-Newton* optical monitor UVW1 and UVW2 during the sn11 observation, non in the LGS images. The lack of a bright optical counterpart and the X-ray parameters support this source to be a black hole X-ray transient, as classified by Trudolyubov et al. (2006a).

#### 9.4.3.1 Sources from the XMM-LP total catalogue that were not detected by *ROSAT*

To search for additional XRB candidates, I selected all sources from the XMM LP-total catalogue, that were classified as <hard> and which, in addition, did not correlate with a source listed in the *ROSAT* catalogues (PFJ93, SHP97 and SHL2001). The flux distribution of the selected sources is shown in Fig. 9.26, and Table 9.18 gives the number of sources brighter than the indicated flux limit.

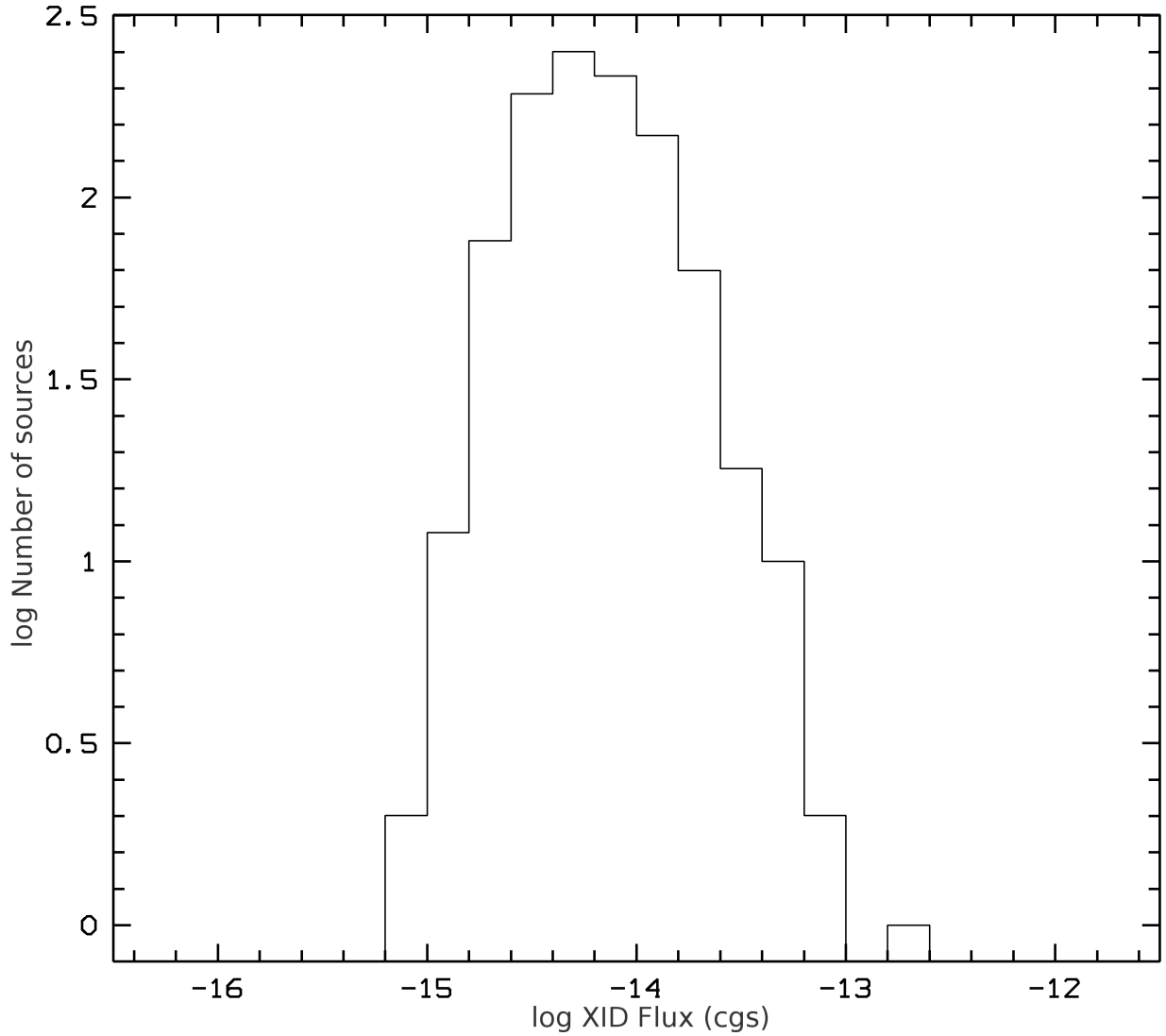


**Figure 9.26:** Distribution of the source fluxes in the 0.2 – 4.5 keV (XID) band. The diagram shows the number of sources from the XMM LP-total catalogue that were classified as <hard>, and in addition do not correlate with a source listed in the *ROSAT* catalogues at each flux bin plotted versus the flux, using logarithmic scales.

**Table 9.18:** Cumulative number of sources for four different limiting fluxes.

| XID flux limit erg cm$^{-2}$ s$^{-1}$ | # of sources |
|---|---|
| 5.5 E-15 | 541 |
| 1 E-14 | 242 |
| 5 E-14 | 7 |
| 1 E-13 | 1 |

Possible, new XRB candidates are sources that have an XID flux that lies at least a factor of ten above the *ROSAT* detection threshold ($5.3\times10^{-15}$ erg cm$^{-2}$ s$^{-1}$). These sources fulfil the variability criterion used to classify XRBs (*cf.* Sect. 7.4). The XMM LP-total catalogue lists five sources without *ROSAT* counterparts that have XID fluxes above $5.3\times10^{-14}$ erg cm$^{-2}$ s$^{-1}$. These are: N$^{\underline{o}}$ 239, N$^{\underline{o}}$ 365, N$^{\underline{o}}$ 910, N$^{\underline{o}}$ 1 164, and N$^{\underline{o}}$ 1 553. Between the *ROSAT* and *XMM-Newton* observations have passed more than ten years. On this time scale AGN can also show strong variability. To estimate the number of AGN among the five sources listed above, I investigated how many sources of the identified and classified background objects from the XMM LP-total catalogue with an XID flux larger than $5.3\times10^{-14}$ erg cm$^{-2}$ s$^{-1}$ were not detected by *ROSAT*. The result is that *ROSAT* detected all background sources with an XID flux larger than $5.3\times10^{-14}$ erg cm$^{-2}$ s$^{-1}$ that are listed in the XMM LP-total catalogue. Thus, the possibility that any of the five sources listed above are background objects is very small, in particular if the source is located within the $D_{25}$ ellipse of M 31. Therefore, the two sources located within $D_{25}$ ellipse are listed in the XMM LP-total catalogue as XRB candidates while the remaining three sources, which are located outside the $D_{25}$ ellipse, are classified as <hard>. All five sources are marked in the comment column of Table 7.2 with 'XRB cand. from *ROSAT* corr.'.

#### 9.4.3.2 Detection of high mass X-ray binaries

As already mentioned, up-to-now not a single secure HMXB in M 31 is known. The reason for this is that the detection of HMXBs in M 31 is difficult. Colbert et al. (2004) showed that the hardness ratio method is very inefficient in selecting HMXBs in spiral galaxies. The selection process is complicated by the fact, that the spectral properties of BH HMXBs, which have power-law spectra with indices of $\sim$1– $\sim$2 are similar to LMXBs and AGN. Therefore the region in the HR diagrams where BH HMXB are located is contaminated by other hard sources (LMXBs, AGN, and Crab like SNRs). For the NS HMXBs, which have power-law indices of $\sim$1, and thus should be easier to select, the uncertainties in the hardness ratios in the best case lead to an overlap – in the worst case to a fusion – with the area occupied by other hard sources (Colbert et al. 2004).

Based on the spectral analysis of individual sources of M 31, SBK2009 identified 18 HMXB candidates with power-law indices between 0.8 and 1.2. One of these sources ([SBK2009] 123) correlates with a globular cluster, and hence is more likely an LMXB in a very hard state than an HMXB (*cf.* Trudolyubov & Priedhorsky 2004). Four of their sources ([SBK2009] 34, 106, 149, and 295) do not have counterparts in the XMM LP-total catalogue.

Eger (2008) developed a selection algorithm for HMXBs in the SMC, which also uses properties of the optical companion. X-ray sources will be selected as HMXB candidates if they have HR2+EHR2>0.1 as well as an optical counterpart within $2\farcs5$ of the X-ray source, with $-0.5$ <B-V< $0.5$ mag, $-1.5$ <U-B< $-0.2$ mag and V<17 mag.

I tried to transfer this SMC selection algorithm to M 31 sources. In doing so, I met two problems. The first problem is that the region of the U-B/B-V diagram is also populated by globular clusters (LMXB candidates) in M 31. The second problem is that due to the much larger distance to M 31, the range of detected V magnitudes of HMXBs in the SMC of $\sim$13<V<17 mag translates to a $\sim$19<V<23 mag criterion for M 31. Thus the V magnitude of optical counterparts of possible HMXB candidates lies in the same range as the optical counterparts of AGN. Therefore the V mag criterion, which provided most of the discriminatory power in the case of the SMC, fails totally in the case of M 31.

A few of the sources selected from the optical colour-colour diagram and HR diagrams are bright enough to allow the creation of X-ray spectra. That way two additional (*i. e.* not given in SBK2009) HMXB candidates were found.

**XMMM31 J004557.0+414830** (№ 1 716) has an USNO-B1 (R2=18.72 mag), a 2MASS and an LGS (V=20.02 mag) counterpart. The EPIC spectrum is best fitted ($\chi^2_{red}=0.93$) by an absorbed power-law with $N_{\rm H}=7.4^{+6.0}_{-3.9}\times10^{21}$ cm$^{-2}$ and photon index $\Gamma=1.2\pm0.4$.

**XMMM31 J004506.4+420615** (№ 1 579) has an USNO-B1 (B2=20.87 mag), a 2MASS and an LGS (V=20.77 mag) counterpart. The EPIC PN spectrum is best fitted ($\chi^2_{red}=1.6$) by an absorbed power-law with $N_{\rm H}=0.48^{+2.4}_{-1.0}\times10^{21}$ cm$^{-2}$ and photon index $\Gamma=1.0^{+0.7}_{-0.5}$.

To strengthen these classifications, spectroscopic optical follow-up observations of the optical counterparts are needed. An FFT periodicity search did not reveal any significant periodicities for either of the two sources and the light curves do not show eclipses.

From the sources reported as HMXB candidates in SBK2009, three sources ([SBK2009] 21, 236, and 256) are located in the region of the U-B/B-V diagram, that I used. Another three sources ([SBK2009] 123, 172, and 226) are located outside that region. The remaining sources of SBK2009 have either no counterparts with a U-B colour entry in the LGS catalogue ([SBK2009] 99, 234, 294, and 302) or have no optical counterpart from the LGS catalogue at all ([SBK2009] 9, 160, 197, and 305).

### 9.4.4 Globular cluster sources

A significant number of the luminous X-ray sources in the Galaxy and in M 31 are found in globular clusters. X-ray sources corresponding to globular clusters are identified by cross-correlating with globular cluster catalogues (see Sect. 5.2.9). Therefore changes between the XMM LP-total catalogue and the catalogue of PFH2005 in the classification of sources related to globular clusters are based on the availability of, and modifications in, recent globular cluster catalogues.

In total 53 sources of the XMM LP-total catalogue correlate with (possible) globular clusters. Of these sources 36 are identified as GlCs because their optical counterparts are listed as globular clusters in the catalogues given in Sect. 5.2.9, while the remaining 17 sources are only listed as globular cluster candidates.

The range of source XID fluxes goes from $3.1\times10^{-15}$ erg cm$^{-2}$ s$^{-1}$ (№ 924) to $2.7\times10^{-12}$ erg cm$^{-2}$ s$^{-1}$ (№ 1 057), or in luminosity from $2.3\times10^{35}$ erg s$^{-1}$ to $2.0\times10^{38}$ erg s$^{-1}$ (Fig. 9.27). Compared to the fluxes found for the XRBs discussed in Sect. 9.4.3, 14 sources that correlate with GlCs have fluxes below the lowest flux found for field XRBs. The reason for this finding is that the classification of field XRBs is based on the variable or transient nature of the sources, which is only to be detected for brighter sources (*cf.* Sect. 7.4) and not just by positional coincidence that also is possible for faint sources.

Figure 9.28 shows the spatial distribution of the GlC sources. X-ray sources correlating with GlCs follow the distribution of the optical GlCs, which are also concentrated towards the central region of M 31.

**XMMM31 J004303.2+412121** (№ 1 118) was identified as a foreground star in PFH2005, based on the classification in the "Revised Bologna Catalogue" (Galleti et al. 2004). Galleti et al. (2004) took the classification from Dubath & Grillmair (1997), which is based on the velocity dispersion of that source. Recent '*HST images unambiguously reveal that this* [B147] *is a well resolved star cluster, as recently pointed out also by Barmby et al. (2007)*' (Galleti et al. 2007). That is why source № 1 118 is now identified as an XRB located in globular cluster B147.

#### 9.4.4.1 XMMM31 J004143.1+413420, XMMM31 J004252.0+413109, and XMMM31 J004545.8 +413941

A detailed discussion of these three sources can be found in Barnard et al. (2008). Here only the main results are presented.

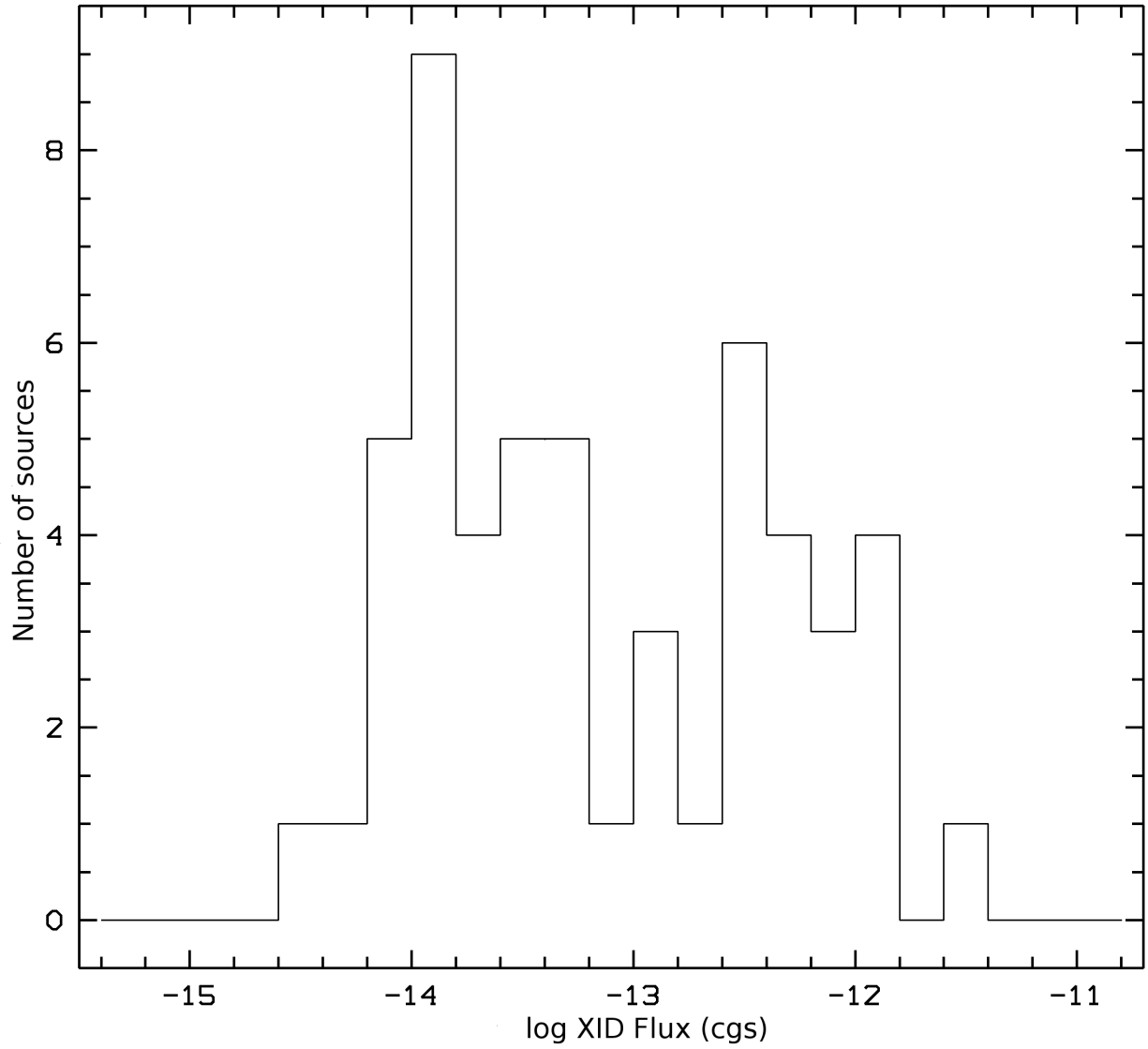


**Figure 9.27:** Distribution of the source fluxes of GlC sources in the 0.2–4.5 keV (XID) band. The diagram shows the number of identified and classified GlCs at each flux bin, plotted versus the flux.

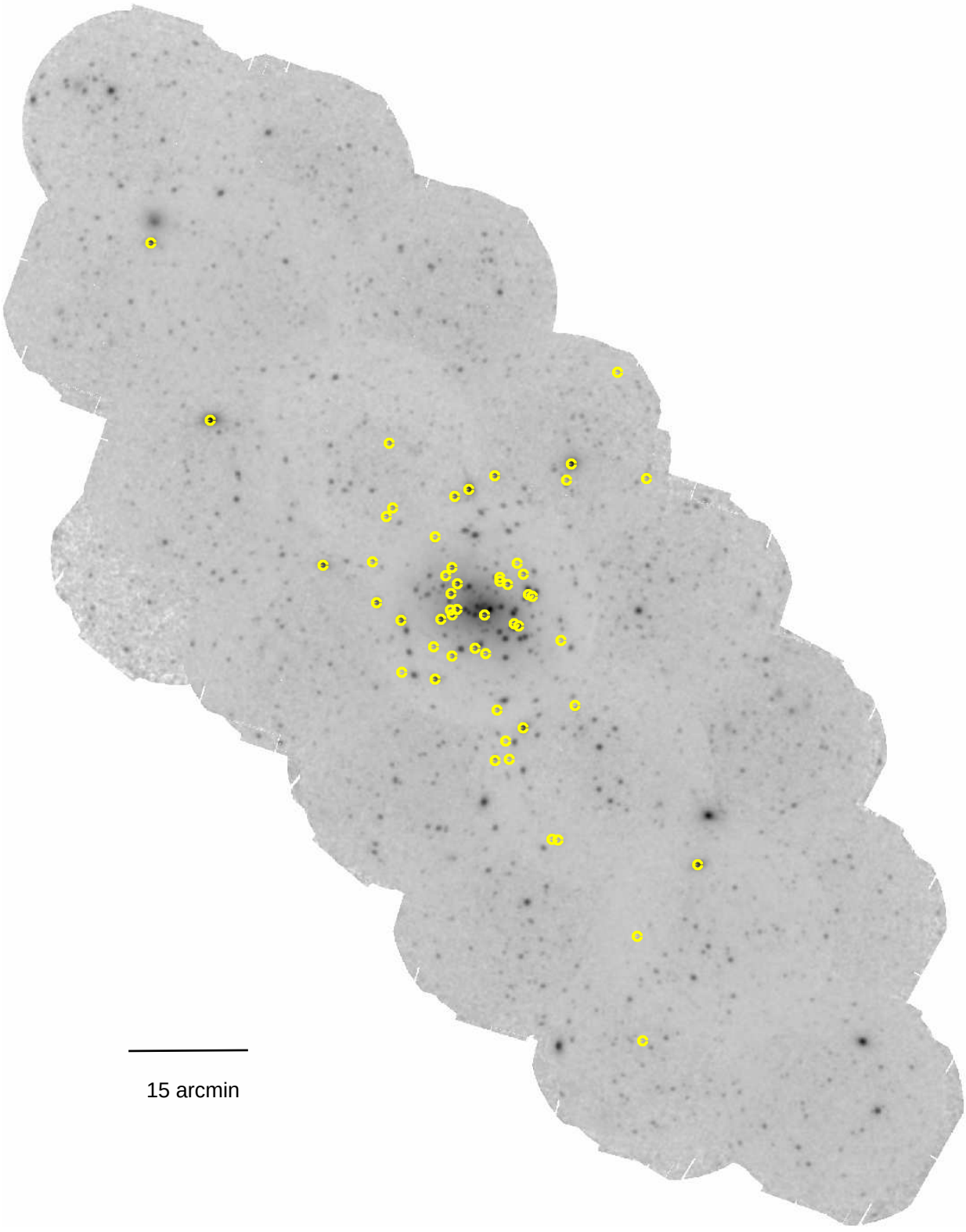


**Figure 9.28:** The spatial distribution of X-ray sources correlating with GlCs and candidates from the XMM LP-total catalogue (yellow dots). An enhancement of sources towards the central region of M 31 is clearly visible.

Bo 45, Bo 135, and Bo 375, the host clusters of the three X-ray sources, have been classified as *certain* globular clusters in the "The Revised Bologna Catalogue (RBC) of M31 globular clusters and candidates". They have been imaged with the HST and their nature has been firmly confirmed (RBC V.3.4, January 2008; Galleti et al. 2004, 2005, 2006, 2007).

The integrated magnitudes and colours of the clusters can be found in RBC V.3.4 and can be used to provide estimates of the ages and masses of the clusters, in conjunction with reddening, distance and metal abundance values. We use a reddening of $E(B-V) = 0.10 \pm 0.03$, which is the average reddening value for all M 31 clusters in Rich et al. (2005). Using these values, we have derived $M_V = -9.0, -8.74, -7.17$ and $(V-I)_o = 1.13, 1.08, 0.88$ for Bo 45, Bo 135 and Bo 375, respectively. The metal abundances of the three clusters are estimated to be $Z$ =0.002, 0.0004 and 0.0012 respectively (Bellazzini et al. 1995). According to Sarajedini et al. (2007), the above values for $(V-I)_o$, $M_V$ and $Z$ suggest that Bo 45 and Bo 135 are at least as old as $\sim 10^{10}$ yr and at least as massive as $\simeq 10^6\,M_\odot$, while the fainter optical luminosity and bluer colour of Bo 375 allow it to be as young as 1.2 Gyr and to have a mass as low as $7 \times 10^4\,M_\odot$.

In conclusion, both Bo 45 and Bo 135 seem to belong to the old massive globular cluster population of M 31. This is not an unexpected result, since low mass X-ray binaries are found preferentially in luminous (massive) and red globular clusters (Kundu et al. 2008). However, Bo 375 appears to be considerably less massive, and younger, than the other two GlCs.

Table 9.19 provides the X-ray source position, observation (with date and exposure), and the number of net source counts in each detector from each source. For our analysis we simultaneously fitted the EPIC-PN and EPIC-MOS spectra.

**XMMM31 J004143.1+413420** (№ 694) is the X-ray counterpart to Bo 45 and had not been previously observed by *XMM-Newton* or *Chandra*. However, it was observed by *Einstein* (TF91) and by *ROSAT* (SHP97, SHL2001). SHP97 found its 0.2–4.0 keV flux to have increased by a factor of $\sim$2 with respect to the *Einstein* observation. However, they reported no variability between *ROSAT* observations greater than $3\sigma$. We shall refer to this source as XBo 45.

We present the 0.3–10 keV light curve (in 400 s bins) of XBo 45 in the upper panel of Fig. 9.29(a). XBo 45 is clearly variable; the r.m.s. variability is (9.2$\pm$0.9)%, while the best fit line of constant intensity has a $\chi^2$/dof = 356/108. Such variability is expected for low-state LMXBs, with most of the power at frequencies $>$1 Hz; hence, the true variability of XBo 45 is expected to be higher than $\sim$10%. We analysed the power density spectrum of XBo 45, in search of the characteristic broken power-law PDS observed in low-state LMXBs. However, no significant power was detected in the PDS. This is likely to be due to faintness of the source.

The spectrum of XBo 45 was well described by an absorbed, hard power-law (see Table 9.20 for

**Table 9.19:** Journal of observations. For each object we give the position, *XMM-Newton* observation, good time exposure, and number of net source photons in the EPIC-PN, EPIC-MOS 1 and EPIC-MOS 2 spectra. From Barnard et al. (2008).

| Source | X-ray Position | Obs$^+$ | Date | Exp | PN cnt | MOS 1 cnt | MOS 2 cnt |
|---|---|---|---|---|---|---|---|
| XBo 45 | $00^h41^m43\overset{s}{.}19$ $+41°34\prime20\overset{\prime\prime}{.}1$ | nn1 | 2006-12-26 | 40 ks | 16894 | 7416 | 6953 |
| XBo 135 | $00^h42^m52\overset{s}{.}00$ $+41°31\prime09\overset{\prime\prime}{.}7$ | nn1 | 2006-12-26 | 40 ks | 15104 | 5560 | 6090 |
| XBo 375 | $00^h45^m45\overset{s}{.}54$ $+41°39\prime42\overset{\prime\prime}{.}6$ | ns2 | 2007-01-02 | 32 ks | 31946 | 15686 | 13798 |

Notes:

$^+$ : Name of observation as indicated in Table 5.1.

(a) XBo 45 and XBo 135 (b) XBo 375

**Figure 9.29:** Combined EPIC-PN+EPIC-MOS 0.3–10 keV light curves of (a) XBo 45 and XBo 135 and of (b) XBo 375, binned up in 400 s bins. The light curves have been background-subtracted and screened for flaring. The light curve of XBo 45 is clearly variable; its r.m.s. variability is 9.2±0.9%. However, XBo 135 shows no significant variability. The solid and dashed lines in the XBo 45 light curve indicate the intervals used for the low and high intensity spectra respectively. Even though the count rate for XBo 375 is 2–3 times higher than for XBo 45 or XBo 135, it is significantly less variable than XBo 45. From Barnard et al. (2008).

parameters). We assumed Solar abundances for our absorber (Anders & Grevesse 1989). The best fit power-law model to the PN and MOS spectra of XBo 45 is presented in Fig. 9.30(a). The quoted uncertainties correspond to 90% confidence limits. The unabsorbed 0.3–10 keV luminosity of XBo 45 was $(2.46\pm0.09)\times10^{38}$ erg s$^{-1}$, using the best fit power-law emission models.

Adding a blackbody component the fit is marginally improved. However, the blackbody contribution to the flux could not be sensibly constrained. We infer from this that there is no significant blackbody contribution to the spectrum of XBo 45.

We observed an intensity variation in XBo 45, which could be due to one of two phenomena: variation in the emission spectrum or variation in the absorbing material. To test these scenarios, we obtained two

**Table 9.20:** Best fit spectral models for fitting 0.3–7.0 keV EPIC-PN and EPIC-MOS spectra from XBo 45, XBo 135 and XBo 375. The models are an absorbed power-law (PO), and an absorbed blackbody+power-law (BB+PO). For each model we give the column density ($N_{\rm H}/10^{21}$ cm$^{-2}$), blackbody temperature ($k_{\rm B}T$/keV), photon index ($\Gamma$), constant of normalisation for EPIC-MOS 1 and EPIC-MOS 2 ($N_{\rm M1}$ and $N_{\rm M2}$), $\chi^2$/dof [good fit probability] and 0.3–10 keV unabsorbed flux. Numbers in parentheses indicate the 90% uncertainty in the final digits. From Barnard et al. (2008).

| Source | $N_{\rm H}/10^{21}$ cm$^{-2}$ | $k_{\rm B}T$/keV | $\Gamma$ | $N_{\rm M1}$ | $N_{\rm M2}$ | $\chi^2$/dof [gfp] | $F^{\dagger}_{0.3-10}$ |
|---|---|---|---|---|---|---|---|
| XBo 45 PO | 1.41(11) | ... | 1.45(4) | 1.06(4) | 1.03(4) | 517/487 [0.17] | 3.34(12) |
| XBo 45 BB+PO | 1.46(19) | 1.23(19) | 1.57(6) | 1.06(3) | 1.03(2) | 501/485 [0.30] | 3.2(2) |
| XBo 135 PO | 2.76(12) | ... | 1.56(3) | 1.12(3) | 1.06(3) | 467/435 [0.14] | 6.45(15) |
| XBo 135 BB+PO | 2.3(3) | 0.8(2) | 1.54(14) | 1.12(3) | 1.06(3) | 413/433 [0.75] | 6.0(3) |
| XBo 375 PO | 1.52(6) | ... | 1.64(2) | 1.15(2) | 1.07(2) | 1180/1032 [9E-4] | 9.17(17) |
| XBo 375 BB+PO | 1.41(11) | 0.90(10) | 1.73(18) | 1.15(2) | 1.07(2) | 1110/1030 [0.19] | 8.8(3) |

Notes:

$^{\dagger}$ : Flux in units of $10^{-12}$ erg cm$^{-2}$ s$^{-1}$.

(a) XBo 45

(b) XBo 135

(c) XBo 375

**Figure 9.30:** Best fit power-law model to simultaneously fitted 0.3–7 keV EPIC-PN (black) and EPIC-MOS (light and dark grey) spectra of (a) XBo 45 and (b) XBo 135. In Fig. (c) the best fit power-law plus blackbody model to simultaneously fitted 0.3–7 keV EPIC-PN (black) and EPIC-MOS (light and dark grey) spectra of XBo 375 is shown. For each source the upper panel shows the log-scaled spectra, while the lower panel shows the ratios of the observed to the expected flux for each energy bin. From Barnard et al. (2008).

additional EPIC-PN spectra: one from a low intensity interval, and another from an interval of high intensity, represented in Fig. 9.29(a) by a solid line and a dashed line respectively. Simultaneously fitting the low and high intensity spectra with $\Gamma$ and the normalisation linked but free to vary, and with the absorption ($N_{\rm H}$) free to vary, yielded an unacceptable fit. We then linked $N_{\rm H}$ and $\Gamma$, varying only the normalisation; this produced an acceptable fit. Finally, we freely fitted each spectrum, and found that $N_{\rm H}$ and $\Gamma$ were consistent within 90% confidence limits for the two spectra. The best fits for each of these models are presented in Table 9.21. It is clear that the variation is intrinsic to the X-ray source, rather than the absorber; such variation is characteristic of low state LMXBs (van der Klis 1994).

**XMMM31 J004252.0+413109** (N$^{\underline{o}}$ 1 057) is associated with Bo 135 and has been observed by both *XMM-Newton* and *Chandra* before. Trudolyubov & Priedhorsky (2004) found the 0.3–10 keV absorbed luminosity of Bo 135 to vary over the range (3.3–4.1)$\times 10^{38}$ erg s$^{-1}$ for power-law spectra with photon indices varying over 1.48–1.66. We name this source XBo 135.

**Table 9.21:** Results from simultaneously fitting 0.3–7 keV EPIC-PN spectra from the high and low intensity intervals in the light curve of XBo 45. For each model we present the absorption ($N_{\rm H}$ / $10^{21}$ cm$^{-2}$), the photon index ($\Gamma$), the best fit $\chi^2$/dof and the goodness of fit. Numbers in parentheses represent 90% uncertainties in the last digits. From Barnard et al. (2008).

| | Variable absorption | | | Variable normalisation | | | Free fitting | | |
|---|---|---|---|---|---|---|---|---|---|
| | $N_{\rm H}^{\dagger}$ | $\Gamma$ | $\chi^2$/dof [gfp] | $N_{\rm H}^{\dagger}$ | $\Gamma$ | $\chi^2$/dof [gfp] | $N_{\rm H}^{\dagger}$ | $\Gamma$ | $\chi^2$/dof [gfp] |
| High | 1.4(2) | 1.51(8) | 193/129 [1.9e-4] | 1.5(2) | 1.50(8) | 140/129 [0.23] | 1.5(3) | 1.45(10) | 125/127 [0.54] |
| Low | 1.5(3) | 1.51(8) | | 1.5(2) | 1.50(8) | | 1.4(4) | 1.57(15) | |

Notes:

$^{\dagger}$ : Absorption in units of $10^{21}$ cm$^{-2}$.

The light curve of XBo 135 exhibited no detectable variability (see lower panel in Fig. 9.29(a)). The best fit line of constant intensity yielded $\chi^2$/dof = 115/108, and its r.m.s. variability was found to be (1.8±1.8)%.

XBo 135 was well described by an absorbed, hard power-law (see Table 9.20 for parameters). The best fit power-law model to the PN and MOS spectra of XBo 135 is presented in Fig. 9.30(b). The quoted uncertainties correspond to 90% confidence limits. XBo 135 has an unabsorbed 0.3–10 keV luminosity of (4.76±0.11)×$10^{38}$ erg s$^{-1}$, using the best fit power-law emission models.

Adding a blackbody component to the XBo 135 emission spectrum improves the fit significantly. The best fit BB+PO model is shown in Table 9.20. The unabsorbed 0.3–10 keV luminosity for this model is (4.4±0.2) × $10^{38}$ erg s$^{-1}$; the blackbody contributes (11±5)%.

**XMMM31 J004545.8+413941** (Nº 1 692) is associated with Bo 375 and has not been previously observed with *XMM-Newton*. However, it has been observed several times since 1979, with *Einstein*, *ROSAT*, ASCA and *Chandra*. Di Stefano et al. (2002) have analysed many of these observations. We name this source XBo 375.

The EPIC-PN+EPIC-MOS 0.3–10 keV light curve of XBo 375 is shown in Fig. 9.29(b). It is significantly less variable than XBo 45 ($\chi^2$/dof = 153/86, (3.4±0.6)% variability) despite having more than twice the intensity.

For XBo 375, a pure power-law emission model must be rejected. However, adding a blackbody component yields a good fit, shown in Table 9.20. The PN and MOS spectra of XBo 375, along with this best fit model, are presented in Fig. 9.30(c). The best fit, unabsorbed 0.3–10 keV luminosity for this source is (6.5±0.2)× $10^{38}$ erg s$^{-1}$. The blackbody component contributes (14±4)%. We note that our values of $k_{\rm B}T$ and $\Gamma$ are consistent with those found by Di Stefano et al. (2002) for the ACIS-S spectrum; however, our preferred absorption is a factor ∼2 lower. We note that Di Stefano et al. (2002) found the absorption to vary by a factor of ∼3 between *ROSAT*, and *Chandra* observations, so this is likely to be real.

To compare the spectra of XBo 45 and XBo 375, we created an EPIC-PN spectrum for XBo 375 with a reduced number of source photons. As a blackbody component was still required to obtain a good fit, we verified that the emission of XBo 375 was significantly different from that of XBo 45, where no blackbody was required.

**Discussion and conclusions** We have examined the emission spectra and time variability of three X-ray sources associated with GCs in M31, using the 2006 December 26 and 2007 January 2 *XMM-Newton* observations. The emission of XBo 45 is well described by a pure power-law with photon index ∼1.4, and is highly variable. This is consistent with an NS or BH LMXB in the low state (van der Klis 1994), but is not consistent with a BH LMXB in the high state or steep power-law state (McClintock & Remillard

2006, and references within), or an NS LMXB emitting at $>10^{38}$ erg s$^{-1}$ (White et al. 1988; Church & Bałucińska-Church 2001; Barnard et al. 2003a).

Taking the distance uncertainties into account, the absorption-corrected 0.3–10 keV luminosity range for XBo 45 is $(2.5\pm0.2)\times 10^{38}$ erg s$^{-1}$, or $(140\pm10)$% of the Eddington limit for a 1.4 $M_\odot$ primary neutron star. However, several LMXBs have been found to contain neutron stars with mass as high as $\sim$2.1 $M_\odot$ (see *e. g.* Nice et al. 2005; Özel 2006); XBo 45 has an absorption-corrected 0.3–10 keV luminosity of $\sim$80% of the Eddington limit for such systems. Since Gladstone et al. (2007) showed that transitions in neutron star LMXBs occur at $\lesssim$10% of the Eddington luminosity, we consider XBo 45 to exhibit a low state behaviour at an apparent luminosity too high for a neutron star. We therefore identify the accretor in XBo 45 as a BH candidate. We note that XBo 45 has been observed several times by the *Einstein* and *ROSAT* observatories over the last $\sim$30 years, varying in luminosity by only a factor of $\sim$2. This behaviour is consistent with that predicted for a GC BH binary formed by tidal capture (Kalogera et al. 2004).

In contrast to XBo 45, the observed two component emission of XBo 375 is consistent with a bright NS LMXB, but not a low state NS or BH LMXB, nor a BH in the high or steep power-law states. Hence, we classify XBo 375 as an NS LMXB. Finally, the emission spectrum of XBo 135 is consistent with a pure power-law with photon index $\sim$1.6, but the fit is significantly improved by adding a blackbody component. Hence, XBo 135 is consistent with an NS or BH LMXB, and deeper observations are required for further classification.

In Barnard et al. (2008) we showed that the positional errors of the X-ray sources are in the range of the half-mass radius of the clusters. Therefore it is impossible to confirm whether the X-ray sources are located in the central region of the clusters. We also showed that the probability of a chance coincidence between an X-ray source and an optical globular cluster is negligible. The same is true for a correlation of a background AGN with one of the X-ray sources. Following Di Stefano et al. (2002) we find that it is very unlikely that XBo 45 combines the emission of $\sim$10 low-state neutron star LMXBs (Barnard et al. 2008). It is however possible that the emission from XBo 45 is anisotropic. Barnard et al. (2008) showed that this explanation is unlikely.

We note that the host cluster Bo 45, which contains a BH LMXB candidate, is significantly larger than the cluster Bo 375, which we think contains an NS LMXB. Di Stefano et al. (2002) describe Bo 375 as not at all unusual, with parameters close to the median of M 31 GCs. This suggests that Bo 45 (and also Bo 135) are particularly massive, and may therefore be more prone to forming BH LMXBs. Therefore we conclude that, unlike the Milky Way, at least one GC in M 31 is likely to contain a black hole binary.

#### 9.4.4.2 Comparing GlC and candidates in *XMM-Newton*, *Chandra* and *ROSAT* catalogues

The combined *ROSAT* PSPC catalogue (SHP97 and SHL2001) contains 33 sources classified as globular cluster counterparts. Of these sources one is located outside the field observed with *XMM-Newton*. Another two sources do not have counterparts in the XMM LP-total catalogue. The first one is [SHL2001] 232, which is discussed in Sect. 9.4.4.3. The second source ([SHL2001] 231) correlates with B 164 which is identified as a globular cluster in RBC V3.5. In addition [SHL2001] 231 is listed in PFH2005 as the counterpart of the source [PFH2005] 423. Due to the improved spatial position of the X-ray source in the *XMM-Newton* observations, PFH2005 rejected the correlation with B 164 and instead classified [PFH2005] 423 as foreground star candidate.

Three *ROSAT* GlC candidates have more than one counterpart in the XMM LP-total catalogue. [SHL2001] 249 correlates with sources Nº 1 262 and Nº 1 267, where the latter is the X-ray counterpart of the globular cluster B 185. [SHL2001] 254 correlates with sources Nº 1 289 and Nº 1 293, where the former is the X-ray counterpart of the globular cluster candidate mita 311 (Magnier 1993). [SHL2001] 258

has a $1\sigma$ positional error of $48''$ and thus correlates with sources Nº 1 297, Nº 1 305, and Nº 1 357.[15] The brightest of these three sources (Nº 1 305), which is also located closest to the *ROSAT* position, correlates with the globular cluster candidate SK 132C (RBC V3.5).

Table 9.22 gives the variability factors (Cols. 6, 8) and significance of variability (7, 9) for sources classified as GlC candidates in the *ROSAT* PSPC surveys. For most sources only low variability is detected. The two sources with the highest variability factors found (Nº 1262, Nº 1293) belong to *ROSAT* sources with more than one *XMM-Newton* counterpart. In these cases the *XMM-Newton* sources that correlate with the same *ROSAT* source and the optical globular cluster source show much weaker variability. Interestingly a few sources show low, but very significant variability. Among these sources is the Z-source identified in Barnard et al. (2003b, Nº 966) and two of the sources discussed in Sect. 9.4.4.1 (Nº 1 057, Nº 1 692).

The 18 X-ray sources correlating with globular clusters which were found in the *ROSAT* HRI observations (PFJ93) were all re-detected in the *XMM-Newton* data.

From the numerous studies of X-ray globular cluster counterparts in M 31 based on *Chandra* observations (Kong et al. 2002b; Di Stefano et al. 2002; Williams et al. 2004a; Trudolyubov & Priedhorsky 2004; Voss & Gilfanov 2007), only eight sources are undetected in the present study. One of them ([TP2004] 1) is located far outside the field of M 31 covered by the Deep *XMM-Newton* Survey. Source [TP2004] 35 is discussed in Sect. 9.4.4.3. The six remaining sources (r2-15, r3-51, r3-71, [VG2007] 58, [VG2007] 65, [VG2007] 82) are located in the central area of M 31 and are also not reported in PFH2005. Figure 9.31 shows the position of these six sources (in red) and the sources of the XMM LP-total catalogue (in yellow). If the brightness of the six sources had not changed between the *Chandra* and *XMM-Newton* observations, they would be bright enough to in principle be detected by *XMM-Newton* in the merged observations of the central field, which have in total an exposure $\gtrsim 100$ ks. Two sources (r2-15 and [VG2007] 65) are located next to sources detected by *XMM-Newton*. Source r2-15 is located within $13\farcs40$ of Nº 1 012 and within $16\farcs84$ of Nº 1 017 and has in the *Chandra* observation a similar luminosity as both *XMM-Newton* sources. The distance between Nº 1 012 and Nº 1 017 is $17\farcs14$, and within $19\farcs63$ of Nº 1 012 *XMM-Newton* detected source Nº 1 006, which is about a factor 4.6 fainter than Nº 1 012. Therefore, when in a bright state, source r2-15 should be detectable with *XMM-Newton*. Source [VG2007] 65 is located within $16\farcs55$ of Nº 1 100, which is at least 3.5 times brighter than [VG2007] 65. This may complicate the detection of [VG2007] 65 with *XMM-Newton*. The variability of [VG2007] 58, [VG2007] 65, and [VG2007] 82 is supported by the fact that these three sources were not detected in any *Chandra* study prior to Voss & Gilfanov (2007). Hence, these six sources are likely to be at least highly variable or even transient.

In the following paragraph I discuss sources identified with globular clusters in previous studies, which have counterparts in the XMM LP-total catalogue that are not classified as GlC sources. Source Nº 403 ([SHL2001] 74) correlates with B 007, which is now identified as a background galaxy (Caldwell et al. 2009; Kim et al. 2007b, RBC V3.5). Sources Nº 793 ([SHL2001] 136, s1-12) and Nº 796 (s1-11) are the X-ray counterparts of B 042D and B 044D, respectively, which are also suggested as background objects by Caldwell et al. (2009). Source Nº 948 (s1-83) correlates with B 063D, which is listed as a globular cluster candidate in RBC V3.5, but might be a foreground star (Caldwell et al. 2009). Due to this ambiguity in classification I classified the source as <hard>. Source Nº 966 correlates with [SHL2001] 184, which was classified as the counterpart of the globular cluster NB 21 (RBC V3.5) in the *ROSAT* PSPC survey (SHL2001). In addition, source Nº 966 also correlates with the *Chandra* source r2-26 (Kong et al. 2002b). Due to the much better spatial resolution of *Chandra* compared to *ROSAT*, Kong et al. (2002b) showed that source r2-26 does not correlate with the globular cluster NB 21. Barnard et al. (2003b) identified this source as the first Z-source in M 31. The nature of source Nº 1 078 is unclear as RBC V3.5 reported that source to be a foreground star, while Caldwell et al. (2009) classified it as an old globular cluster. Due

[15] In addition [SHL2001] 258 correlates with Nº 1 275, Nº 1 289, and Nº 1 293. However these sources have each an additional *ROSAT* counterpart.

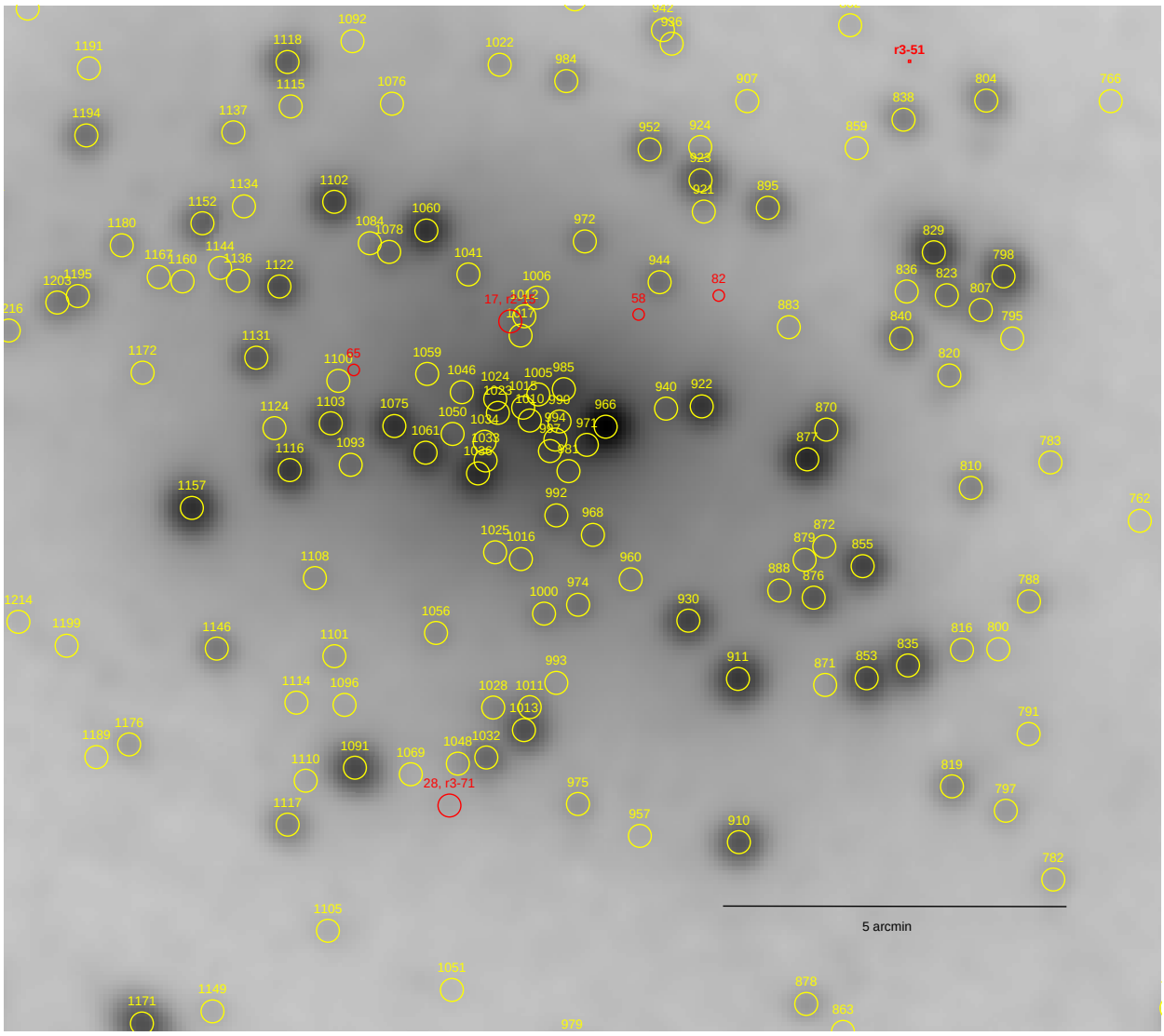


**Figure 9.31:** Image of the central field of M 31 over-plotted with the positions of six possible transient sources (red) and the sources of the XMM LP-total catalogue. Sources r2-15 and r3-71 are listed as sources #17 and #28, respectively, in Di Stefano et al. (2002). The three "red" sources that are only marked with a number (#58, #65, #82) are taken from Voss & Gilfanov (2007).

**Table 9.22:** Variability between XMM LP-total and *ROSAT* observations for sources classified as GlC candidates in the *ROSAT* PSPC surveys

| SRC (1) | SI* (2) | SII* (3) | XFLUX+ (4) | EXFLUX+ (5) | fv_SI† (6) | sv_SI† (7) | fv_SII† (8) | sv_SII† (9) | type (10) | SIf‡ (11) | SIIf‡ (12) |
|---|---|---|---|---|---|---|---|---|---|---|---|
| 383 | 73 | 68 | 1.45E-12 | 1.05E-14 | 1.26 | 11.58 | 1.23 | 9.04 | GlC | – | – |
| 403 | 79 | 74 | 2.55E-14 | 2.36E-15 | 2.61 | 2.09 | 7.57 | 4.92 | Gal | | |
| 422 | | 76 | 2.01E-14 | 1.43E-15 | | | | | <hard> | | |
| 694 | 122 | 113 | 1.52E-12 | 1.04E-14 | 1.38 | 10.56 | 1.26 | 7.46 | GlC | – | – |
| 793 | 138 | 136 | 4.76E-14 | 2.33E-15 | 1.10 | 0.55 | 1.02 | 0.14 | <Gal> | – | |
| 841 | 150 | 147 | 1.40E-12 | 1.61E-14 | 1.77 | 19.81 | 2.11 | 26.37 | GlC | – | – |
| 855 | 158 | 154 | 4.21E-13 | 3.70E-15 | 1.01 | 0.14 | 3.54 | 48.75 | GlC | – | |
| 885 | 168 | 163 | 1.56E-14 | 1.60E-15 | 1.70 | 1.54 | | | GlC | | |
| 923 | 175 | 175 | 1.47E-13 | 2.07E-15 | 1.87 | 7.68 | 1.30 | 3.44 | GlC | | |
| 933 | 178 | | 3.67E-14 | 1.64E-15 | 3.03 | 7.03 | | | GlC | | |
| 947 | 180 | 179 | 3.24E-13 | 7.46E-15 | 2.43 | 12.78 | 2.29 | 12.16 | GlC | – | – |
| 966 | 184 | 184 | 3.51E-12 | 9.21E-15 | 1.00 | 0.20 | 2.31 | 151.58 | XRB | | |
| 1 057 | 205 | 199 | 2.67E-12 | 2.05E-14 | 1.72 | 26.26 | 1.79 | 28.48 | GlC | – | – |
| 1 102 | 217 | 211 | 3.23E-13 | 2.93E-15 | 1.06 | 1.04 | 5.51 | 60.80 | GlC | – | |
| 1 109 | 218 | 212 | 3.25E-13 | 9.08E-15 | 1.91 | 9.70 | 2.10 | 10.72 | GlC | – | – |
| 1 118 | 222 | 216 | 1.16E-13 | 2.03E-15 | 1.46 | 3.63 | 1.89 | 7.46 | GlC | | |
| 1 122 | 223 | 217 | 2.48E-13 | 2.72E-15 | 2.08 | 12.02 | 7.03 | 73.27 | GlC | | |
| 1 157 | 228 | 223 | 7.59E-13 | 4.48E-15 | 1.06 | 1.68 | 1.08 | 2.75 | GlC | – | – |
| 1 171 | 229 | 227 | 4.68E-13 | 4.93E-15 | 1.82 | 12.92 | 1.75 | 12.19 | GlC | – | – |
| 1 262 | 247 | 249 | 2.94E-14 | 3.10E-15 | 14.11 | 18.40 | 14.64 | 20.24 | | | |
| 1 267 | 247 | 249 | 4.80E-13 | 4.57E-15 | 1.16 | 3.04 | 1.11 | 2.44 | GlC | – | – |
| 1 289 | 250 | 254 | 2.88E-14 | 1.91E-15 | 1.16 | 0.57 | 1.98 | 3.15 | <GlC> | – | |
| 1 293 | 250 | 254 | 6.70E-15 | 9.42E-16 | 3.73 | 2.80 | 8.53 | 5.72 | <AGN> | | |
| 1 296 | 253 | 257 | 3.89E-14 | 1.58E-15 | 4.03 | 9.38 | 1.25 | 1.17 | GlC | | |
| 1 297 | 252 | 258 | 5.59E-15 | 9.61E-16 | 4.46 | 2.69 | | | <hard> | | |
| 1 305 | | 258 | 1.69E-14 | 9.87E-16 | | | | | <GlC> | | |
| 1 340 | 261 | 266 | 6.07E-14 | 3.01E-15 | 1.77 | 4.20 | 1.30 | 1.64 | GlC | | – |
| 1 357 | | 258 | 7.04E-15 | 1.18E-15 | | | | | <hard> | | |
| 1 449 | 281 | 289 | 2.34E-14 | 1.00E-15 | 3.10 | 5.36 | 1.79 | 2.39 | fg Star | | |
| 1 463 | 282 | 290 | 7.51E-13 | 8.38E-15 | 1.13 | 3.33 | 1.33 | 7.64 | GlC | – | – |
| 1 634 | 302 | 316 | 7.70E-14 | 2.91E-15 | 3.14 | 5.60 | 1.89 | 4.33 | <hard> | – | – |
| 1 692 | 318 | 336 | 1.15E-12 | 2.00E-14 | 2.86 | 45.59 | 2.62 | 38.63 | GlC | – | |
| 1 803 | 349 | 354 | 8.72E-13 | 9.17E-15 | 1.32 | 7.87 | 1.03 | 0.93 | GlC | – | – |

Notes:

* : SI: SHP97, SII: SHL2001

+ : XID Flux and error in erg cm$^{-2}$ s$^{-1}$

† : Variability factor and significance of variability, respectively, for comparisons of *XMM-Newton* XID fluxes to *ROSAT* fluxes listed in SPH97 and SHL2001, respectively.

‡ : A minus sign indicates that the XID flux is larger than the corresponding *ROSAT* flux. *ROSAT* count rates are converted to 0.2–4.5 keV fluxes, using WebPIMMS and assuming a foreground absorption of $N_{\rm H} = 6.6{\times}10^{20}$ cm$^{-2}$ and a photon index of $\Gamma = 1.7$: $\mathrm{ECF_{SHP97}} = 2.229{\times}10^{-14}$ erg cm$^{-2}$ cts$^{-1}$ and $\mathrm{ECF_{SHL2001}} = 2.249{\times}10^{-14}$ erg cm$^{-2}$ cts$^{-1}$

to this ambiguity in the classification and due to the fact that source Nº 1 078 is resolved in two *Chandra* sources (r2-9, r2-10), I decided to classify the source as <hard>. Due to the transient nature (Kong et al. 2002b; Williams et al. 2006b) and the ambiguous classifications reported by RBC V3.5 (GlC) and Caldwell et al. (2009, HII region), I adopt the classification of PFH2005 (<XRB>) for source Nº 1 152. SBK2009 classified the source correlating with source Nº 1 293 as a globular cluster candidate. I am not able to confirm this classification, as none of the used globular cluster catalogues contains an entry at the position of source Nº 1 293. Instead I found a radio counterpart in the catalogues of Gelfand et al. (2005), Braun (1990) and NVSS. I therefore classified the source as an AGN candidate, as was done in PFH2005. For source Nº 1 449 ([SHL2001] 289) the situation is more complicated. SHL2001 report [MA94a] 380 as the globular cluster correlating with this X-ray source. Based on the same reference, Fan et al. (2005) included the optical source in their statistical study of globular cluster candidates. However the paper belonging to the acronym [MA94a] is not available. An intensive literature search of the papers by Magnier did not reveal any work relating to globular clusters in M 31, apart from Magnier (1993) which is cited in Fan et al. (2005) as "MIT". In addition the source is not included in any other globular cluster catalogues listed in Sect. 5.2.9. In the X-ray studies of Williams et al. (2004a) and PFH2005 and in Magnier et al. (1992) the source is classified as foreground star (candidate). Hence I also classified source Nº 1 449 as a foreground star candidate, but suggest optical follow-up observations of the source to clarify its true nature. A similar case is source Nº 422 ([SHL2001] 76), which is classified as globular cluster by SHL2001, based on a correlation with [MA94a] 16. Here again the source is not listed in any of the used globular cluster catalogues. I found one correlation of source Nº 422 with an object in the USNO-B1 catalogue, which has no B2 and R2 magnitude. Two faint sources (V$>22.5$ mag) of the LGS catalogue are located within the X-ray positional error circle. Thus source Nº 422 is classified as <hard>. While RBC V3.5 classified the optical counterpart of source Nº 1 634 ([SHL2001] 316) as a globular cluster candidate, Caldwell et al. (2009) regard SK 182C as being a source of unknown nature. Therefore I decided to classify source Nº 1634 as <hard>.

#### 9.4.4.3 XMMM31 J004317.5+412745: An additional source (not in the XMM LP-total catalogue)

During the study of X-ray sources in GlCs that were found with *ROSAT* and *Chandra*, and the cross-correlations to sources with the XMM LP-total catalogue, I found out, that source [TP2004] 35 (Trudolyubov & Priedhorsky 2004) has no counterpart in the XMM LP-total catalogue. The fact that the source is not visible in any *XMM-Newton* observation taken before December 2006[16] was already reported in Trudolyubov & Priedhorsky (2004). What makes this source interesting is that in the *Chandra* observation from 18 February 2001, which was taken 53 days after c2 and 131 days before c3, the source was detected. It was also detected in the *ROSAT* PSPC survey of M 31 ([SHL2001] 232, SHL2001). Hence Trudolyubov & Priedhorsky (2004) classified the source as showing recurrent transient outbursts.

To further study the outburst behaviour of that source, I examined whether the source was visible in *XMM-Newton* and *Chandra* observations of the M 31 nova monitoring project, taken between July 2006 and March 2007.

I report on the first *XMM-Newton* detection, and compare the results of the new detected outburst to the ones obtained from previous *Chandra* observations.

XMMM31 J004317.5+412745 correlates with the confirmed globular cluster B163 (RBC V.3.5) which is clearly visible in the LGS images.

The source was found in three *XMM-Newton* observations taken between 31 December 2006 and 5 February 2007 (*cf.* Table 5.2). The position of the source is $00^{\rm h}\,43^{\rm m}\,17\overset{\rm s}{.}599$ $+41°27'45\overset{''}{.}25$ with a $3\sigma$ error of $1\overset{''}{.}54$.

[16] *XMM-Newton* observations that cover the source position are c1, c2, c3, n1, c4, and b

In the last observation (c9) the source was brightest with an unabsorbed 0.2–10.0 keV luminosity of $\sim 1.45 \times 10^{38}$ erg s$^{-1}$. About a month later the central field of M 31 was observed with *Chandra* (*cf.* Table 5.3). The luminosity of the source had already decreased by a factor of $\sim$3, in that observation. The longterm light curve, given in Fig. 9.32(a), shows that the source was visible in X-ray wavelengths between 2006-10-01 and 2007-03-12. It looks like a first outburst occurred between observations c6 (9. Aug. 2006) and c8 (16. Jan. 2007), since the flux measured in each of the two *Chandra* observations 7 285 and 7 286 is higher than the flux in observations c7 and c8.

The EPIC spectra obtained from observations c7 and c9 (see Fig. 9.32(b)) are best fitted by absorbed power-law models. The differences in the absorption density and the power-law index between the two observations are consistent within the errors. Fitting absorbed bremsstrahlung models also gives formally acceptable fits, but the errors in the resulting temperatures are rather large. An absorbed disc blackbody fit might be acceptable for observation c7, but clearly gives an unacceptable $\chi^2$ value for observation c9 (see Table 9.23).

Comparing the results of the power-law fit to the values reported in Trudolyubov & Priedhorsky (2004), we found a good agreement. We have not found any significant variability on short time scales, neither in an FFT periodicity search, nor in X-ray light curves. Following Williams et al. (2006b) we created two hardness ratios based on the S: 0.5–1.0 keV, M: 1.0–2.0 keV and H: 2.0–4.5 keV energy bands: HR2 = (M−S)/(M+S) and HR5 = (H−S)/(H+S). From Fig. 9.32(b) we see that XMMM31 J004317.5+412745 does not emit any significant flux above 4.5 keV. That is why we can ignore the flux range between 4.5–7.0 keV in the definition of the H band, compared to Williams et al. (2006b), without changing the hardness ratios. The resulting hardness flux and colour-colour diagrams of XMMM31 J004317.5+412745 are shown in Fig. 9.33. From Fig. 9.33(a) we see that the source changed from a low-soft (c7, c8) to high-hard (c9) state (Williams et al. 2006b). But the nature of the primary remains an open question.

### 9.4.5 XRBs from XMM LP-hard luminosity functions and the XMM LP-total catalogue

In this section I compare the number of sources found from the log N-log S study (see Chap. 8) to the number of identified and classified XRBs (including sources in GlCs). The classified sources were taken

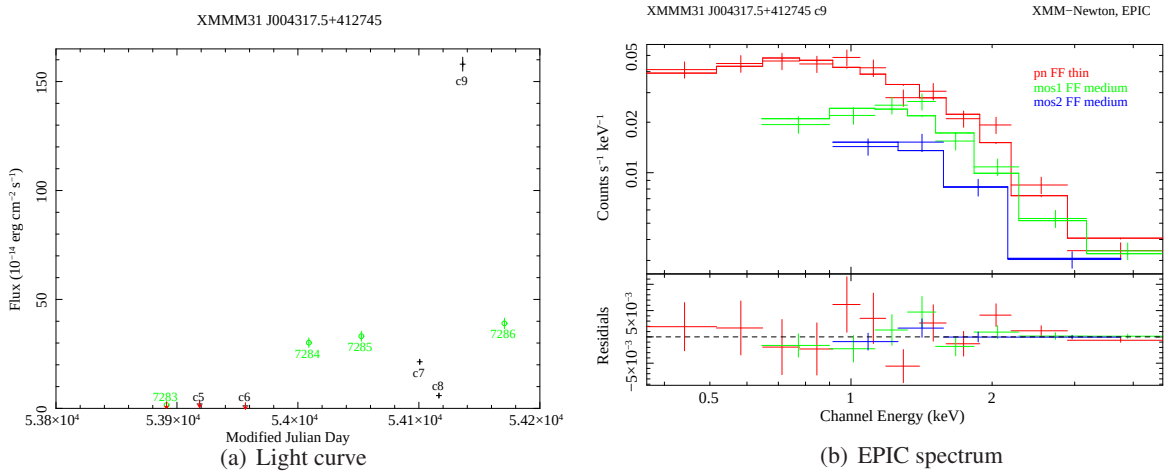


(a) Light curve (b) EPIC spectrum

**Figure 9.32:** Long-term light curve (a) and combined EPIC spectrum (b) of XMMM31 J004317.5+412745. The light curve contains data from *XMM-Newton* (black crosses) and *Chandra* (green circles) observations. 3$\sigma$ upper limits of non detections are indicated by red arrows. The spectrum was fitted with an absorbed power-law model.

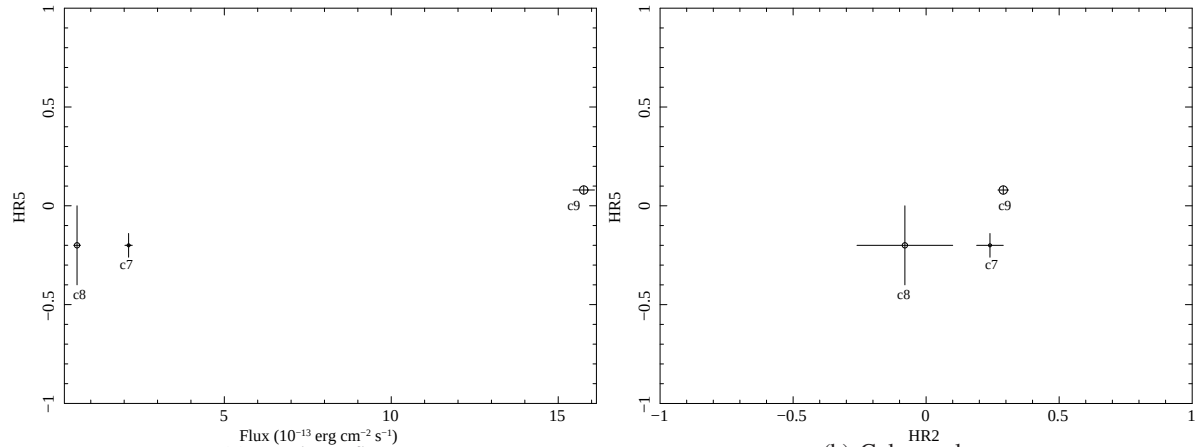


(a) Hardness flux (b) Colour colour

**Figure 9.33:** Hardness flux (a) and colour-colour (b) diagrams of XMMM31 J004317.5+412745. The sizes of the data points reflect the times of the observations. Larger data points represent later observations.

**Table 9.23:** Spectral parameters of XMMM31 J004317.5+412745.

| M 31 field | Model | $N_{\rm H}$ ($\times 10^{21}$ cm$^{-2}$) | $k_{\rm B}T$ (keV) | $R_{\rm in}\sqrt{\cos i}^{*}$ (km) | Photon Index | $\chi^2$ (d.o.f) | $L_{\rm X}^{\dagger}$ | Instrument |
|---|---|---|---|---|---|---|---|---|
| XMMM31 J004317.5+412745 | | | | | | | | |
| c7 | DISCBB | $0.15^{+0.45}_{-0.15}$ | $1.242^{+0.281}_{-0.213}$ | $6 \pm 2$ | | 26.02(22) | 0.20 | PN+M1+M2 |
| c7 | BREMSS | $0.93^{+0.55}_{-0.45}$ | $6.886^{+7.926}_{-2.762}$ | | | 20.24(22) | 0.27 | PN+M1+M2 |
| c7 | PL | $1.49^{+0.76}_{-0.70}$ | | | $1.70 \pm 0.23$ | 19.29(22) | 0.32 | PN+M1+M2 |
| c9 | DISCBB | $0.31^{+0.16}_{-0.14}$ | $1.423^{+0.138}_{-0.121}$ | $11 \pm 2$ | | 50.82(25) | 1.19 | PN+M1+M2 |
| c9 | BREMSS | $0.95^{+0.22}_{-0.19}$ | $9.494^{+4.398}_{-2.376}$ | | | 29.47(25) | 1.53 | PN+M1+M2 |
| c9 | PL | $1.29^{+0.30}_{-0.27}$ | | | $1.58^{+0.10}_{-0.09}$ | 28.57(25) | 1.45 | PN+M1+M2 |
| TP | PL | $1.1 \pm 0.4$ | | | $1.54^{+0.14}_{-0.13}$ | 30.9(23) | 1.057 | ACIS-S |

Notes:

$^{*}$ : effective inner disc radius, where $i$ is the inclination angle of the disc

$^{\dagger}$ : unabsorbed luminosity in the $0.2 - 10.0$ keV energy range in units of $10^{38}$ erg s$^{-1}$

from Table 9.4.

The examination was carried out for the five regions, which were defined to study the radial dependence of the log N-log S relations (*cf.* Fig. 8.3). The number of "missing" XRBs is the difference between the number of expected XRBs, which was derived from the log N-log S relations, and the number of identified/classified XRBs listed in Table 9.4.

Table 9.24 shows the number of sources obtained from the log N-log S relations (Cols. 3, 6), from correlations with the XMM LP-total catalogue (4, 7), and the differences between these numbers (number of missing XRBs: Cols. 5, 8) for two different limiting fluxes of $3.2\times10^{-14}$ erg cm$^{-2}$ s$^{-1}$ and $10^{-13}$ erg cm$^{-2}$ s$^{-1}$ in the 2.0 – 10.0 keV band. We see that $\sim$50% of the brighter ($10^{-13}$ erg cm$^{-2}$ s$^{-1}$) XRBs from the XMM LP-hard catalogue that are expected to be located in the dust ring region or outer disc region, and that $\sim$100% of the brighter XRBs from the XMM LP-hard catalogue that are expected to be located in the region beyond the $D_{25}$ ellipse, are classified as XRBs in the XMM LP-total catalogue. For a limiting flux of $3.2\times10^{-14}$ erg cm$^{-2}$ s$^{-1}$ about one third of the XRBs from the XMM LP-hard catalogue that are expected to be located in the dust ring region or outer disc region are classified as XRBs in the XMM LP-total catalogue. In other words, many faint XRBs from the XMM LP-hard catalogue with fluxes in the range of $3.2\times10^{-14}$ erg cm$^{-2}$ s$^{-1}$ to $10^{-13}$ erg cm$^{-2}$ s$^{-1}$ are only classified as <hard> sources in the XMM LP-total catalogue. This is not surprising, as it is more complicated to detect variability in fainter sources than in bright sources (*cf.* Sect. 7.4). This finding is also reflected in the lower flux limits of the detected XRBs and GlCs (*cf.* Sects. 9.4.3 and 9.4.4), as the classification of XRBs is based on variability (*cf.* Sect. 9.4.3).

Another result, which can be drawn from Table 9.24, is that many of the XRBs that are located in the inner disc of M 31 were not classified/identified in the XMM LP-total catalogue. The inner disc region contains large parts of the S1 and N1 fields, where each field was only covered in a single observation. Therefore it was not possible to determine the variability of sources located in these parts. Hence, the number of classified XRBs is below the expected number from the log N-log S diagram, due to there being too few sources recognised as variable.

The XMM LP-hard catalogue contains 45 sources that are listed as GlCs or GlC candidates in the XMM LP-total catalogue. Figure 9.34 shows the cumulative luminosity function of these sources. The CLF breaks at about $4.6\times10^{37}$ erg s$^{-1}$ (2.0–10.0 keV). Below that break it is well fitted by a power-law with a slope of $\sim$0.3, and above the break the slope is about 1.2. The slopes are in good agreement with the values derived in Kong et al. (2003a) for the population of LMXBs in globular clusters of M 31. The break luminosity seems to be a bit higher in the present study.

**Table 9.24:** Number of XRBs and missing XRBs in different regions for two different limiting fluxes (2.0–10.0 keV)

| | | flux$>3.2\times10^{-14}$ erg cm$^{-2}$ s$^{-1}$ | | | flux$>10^{-13}$ erg cm$^{-2}$ s$^{-1}$ | | |
|---|---|---|---|---|---|---|---|
| Region | slope | XMMLPh area$^{-1}$ | XMMLPt area$^{-1}$ | $\Delta$ area$^{-1}$ | XMMLPh area$^{-1}$ | XMMLPt area$^{-1}$ | $\Delta$ area$^{-1}$ |
| (1) | (2) | (3) | (4) | (5) | (6) | (7) | (8) |
| inner disc | 0.68±0.09 | 42±6 | 13 | 29±6 | 24.3±4.7 | 11 | 13.5±4.5 |
| dust ring | 0.56±0.11 | 22±4 | 7 | 15±4 | 9.9±2.7 | 5 | 5±3 |
| outer disc | 0.82±0.36 | 10±3 | 3 | 7±3 | 3.8±1.7 | 2 | 2±2 |
| beyond $D_{25}$ | 1.69±0.65 | 13±3 | 1 | 12±3 | 0.3±1.0 | 1 | 0 |

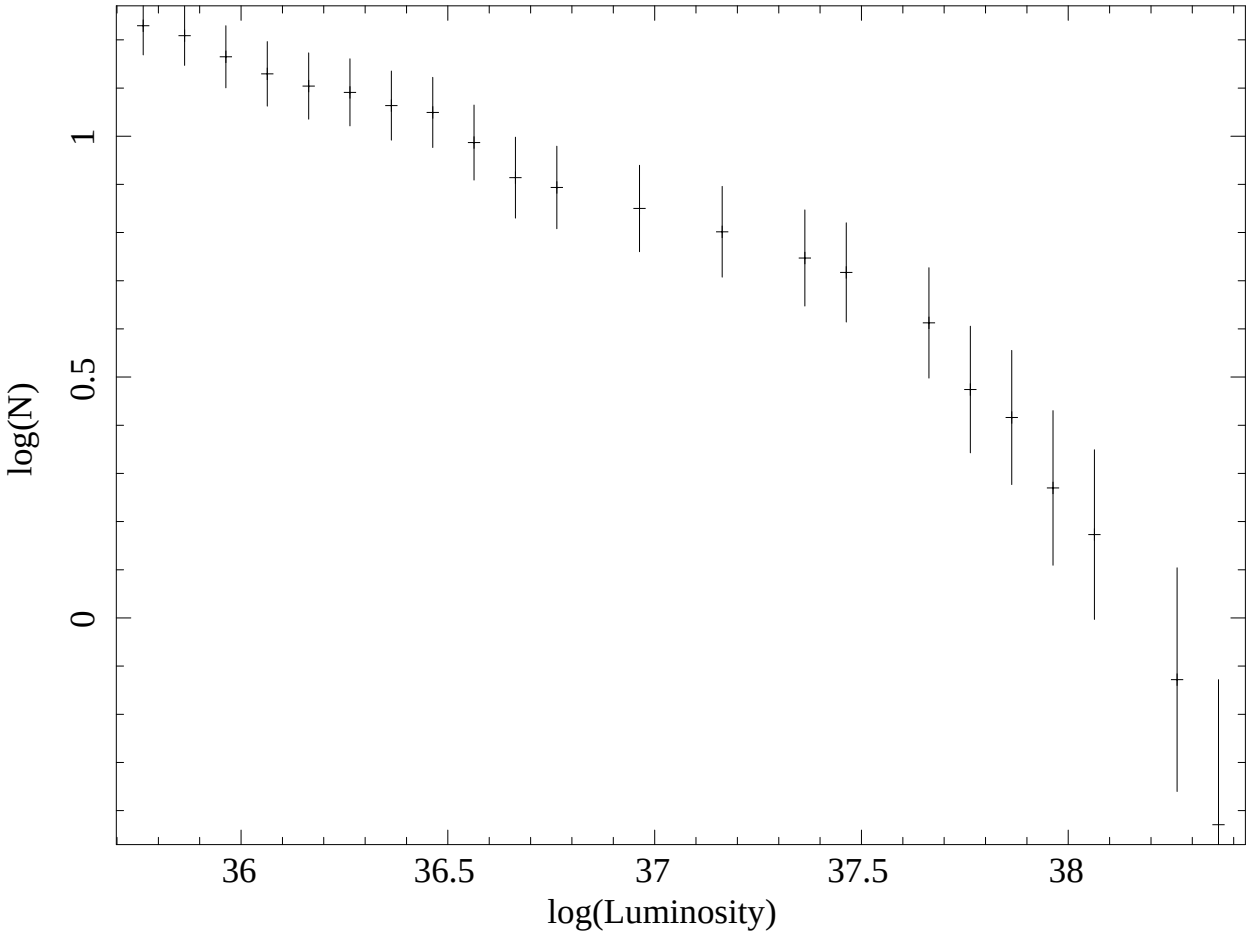


**Figure 9.34:** Cumulative luminosity function for X-ray sources located in globular clusters and globular cluster candidates.

# Chapter 10

# Conclusions and Outlook

## 10.1 Conclusions

The classification of individual sources of X-ray emission in a galaxy provides us with new insights into its structure, dynamical history and evolution. Hence, it is necessary to obtain large samples of classified X-ray sources in nearby galaxies and to establish relationships to the galactic properties. These findings then can be applied to more distant galaxies.

This dissertation presents the analysis of a large and deep *XMM-Newton* survey of the bright Local Group SA(s)b galaxy M 31. The survey observations were taken between June 2006 and February 2008. Together with re-analysed archival observations from June 2000 to July 2004 a full coverage of the whole $D_{25}$ ellipse of M 31 with *XMM-Newton*, down to luminosity of $\sim 10^{35}$ erg s$^{-1}$ in the 0.2 – 4.5 keV band, is provided, for the first time.

The analysis of combined and individual observations allowed the study of faint persistent sources as well as brighter variable sources.

Within the investigations of the long term time variability of sources in the central field of M 31 (Chap. 6), 39 sources were found in addition to the 265 reported by PFH2005 in that field. The identification and classification of these sources, which was based on properties in the X-ray wavelength regime (hardness ratios and temporal variability) and on cross correlations with source catalogues at other wavelengths, provide three SSS candidates, one SNR and six SNR candidates, one GlC candidate, three XRBs and four XRB candidates. Additionally, one foreground star candidate was identified and fifteen sources were classified as <hard>, which may either be XRBs or Crab-like SNRs in M 31, or background AGN. Five sources remained unidentified and without classification. Two sources were found to be extended. One of them was classified as <hard>. The other remain without classification. Six sources of PFH2005, which were classified as <hard>, showed distinct time variability. Based on that variability, their hardness ratios and the strong absorption in the centre of M 31, they were classified as XRB candidates. The SNR classification of the source [PFH2005] 295 was changed to foreground star due to its distinct time variability and its identification with a faint stellar object. Other SNR classifications (sources [PFH2005] 316, [PFH2005] 318) were rejected due to time variability of the sources.

The source catalogue of the Large *XMM-Newton* Survey of M 31 (Chap. 7) contains 1 948 sources in total, of which 961 sources were detected for the first time in X-rays. The XID source luminosities range from $\sim 4.4 \times 10^{34}$ erg s$^{-1}$ to $2.7 \times 10^{38}$ erg s$^{-1}$. The previously found differences in the spatial distribution of bright ($\gtrsim 10^{37}$ erg s$^{-1}$) sources between the northern and southern disc could not be confirmed. The identification and classification of the sources was based on properties in the X-ray wavelength regime: hardness ratios, extent and temporal variability. In addition, information obtained from cross correlations with M 31 catalogues in the radio, infra-red, optical and X-ray wavelength regimes were used.

The source catalogue contains 12 sources, with spatial extent between 6.″20 and 23.″03. From spectral investigation and comparison to optical images, five sources were classified as galaxy cluster candidates. 317 from 1 443 examined sources showed long term variability with a significance $>3\sigma$ between the *XMM-Newton* observations. These include 173 sources in the disc, that were not covered in the study of the central field (Chap. 6). Three sources located in the outskirts of the central field could not have been detected as variable in the study presented in Chap. 6, as they only showed variability with a significance $>3\sigma$ between the archival and the "Large Project" observations. For 69 sources the flux varied by more than a factor of five, and for ten by even more than a factor of 100 within the *XMM-Newton* observations.

To investigate the log N-log S relations of "hard" sources in the field of M 31 (Chap. 8) a catalogue of sources detected in the 2.0 – 10.0 keV energy range was created. Softer energies were excluded form this study to minimise the effects of absorption due to the interstellar medium of M 31. This catalogue contains 1 254 sources, of which seven were found to be extended. A correlation with the Large *XMM-Newton* Survey catalogue showed that, apart from 24 sources identified with foreground stars and foreground star candidates, and eight SNRs and SNR candidates, only sources identified / classified as XRBs, GlCs, background sources, <hard> sources or those without classification were included in the 2.0 – 10.0 keV catalogue. Hence, after background sources were subtracted, the log N-log S relations mainly probed the population of XRBs. The contribution of the background sources was estimated from the COSMOS field. This is an approximation, as the population of background sources in the field of M 31 has not to be the same as that observed in the COSMOS field.

The slope of the background corrected log N-log S relation for the whole galaxy is consistent with the expectation for spiral galaxies. To study the spatial dependence of the log N-log S relation the galaxy was divided on the one hand along the major axis (eastern and western part) as well as along the minor axis (northern and southern part), and on the other hand in five regions, which roughly correspond to the bulge, inner disk, dust ring, outer disk, and the area beyond the $D_{25}$ ellipse of M 31. For the western and northern part, the slopes are flatter than for the southern and eastern part. The "bump" in the $\sim$3.2–8$\times10^{-13}$ erg cm$^{-2}$ s$^{-1}$ flux range that was detected in the CNC of the whole galaxy was also present in the CNCs of the eastern and northern part, while it was not visible in the western and southern parts. It was detected in the log N-log S relation of the dust ring region, too. The slopes of the CNCs of the inner disc and dust ring regions are in the value range expected from the universal log N-log S relation of HMXBs. Furthermore, the relation between the number of sources and star formation rate for these two regions is consistent with the one presented in Grimm et al. (2003), although the number of sources is rather low. Comparing the number of sources expected for an HMXB population with the background corrected CNCs of the inner disc and dust ring region showed that the CNCs of the dust ring region only were in agreement with the expectation. However, additional refinement in the theoretical prediction of the log N-log S relation (luminosity function) for HMXBs at low star forming rates is needed to confirm this finding.

The radial dependence of the source distribution in M 31's disc could be well fitted with an exponential profile, for limiting fluxes of $\sim3.2\times10^{-14}$ erg cm$^{-2}$ s$^{-1}$ and $10^{-13}$ erg cm$^{-2}$ s$^{-1}$ ($\hat{=}2.3\times10^{36}$ erg s$^{-1}$ and $7.3\times10^{36}$ erg s$^{-1}$), respectively. The region beyond the $D_{25}$ ellipse still contains about 13 sources/deg$^2$ of M 31 with fluxes above the completeness limit of $\sim3.2\times10^{-14}$ erg cm$^{-2}$ s$^{-1}$ ($\hat{=}2.3\times10^{36}$ erg s$^{-1}$). About 60% of all sources in the XMM LP-hard catalogue with fluxes above $3.2\times10^{-14}$ erg cm$^{-2}$ s$^{-1}$ ($\hat{=}2.3\times10^{36}$ erg s$^{-1}$) were background sources. An investigation into the spatial dependence of the amount of background sources showed that in the inner disc region $\sim$20% of the sources were background objects, while this fraction increased to $\gtrsim$80% in the outer areas of M 31.

Discrepancies in source detection between the Large *XMM-Newton* Survey catalogue and previous *XMM-Newton* catalogues could be explained by different search strategies, and differences in the processing of the data, in the parameter settings of the detection runs and in the software versions used. Correlations with previous *Chandra* studies showed that those sources not detected in this study are strongly time vari-

able, transient, or unresolved. This is specifically true for sources located close to the centre of M 31, where *Chandra*'s higher spatial resolution allows us to resolve more sources. Some of the undetected sources from previous *ROSAT* studies were located outside the field covered with *XMM-Newton*. However there were several sources detected by *ROSAT* that had a *ROSAT* detection likelihood larger than 15. If these sources were still in a bright state they should have been detected with *XMM-Newton*. Thus the fact that these sources are not detected with *XMM-Newton* implies that they are transient or at least highly variable sources. On the other hand 242 <hard> *XMM-Newton* sources were found with XID fluxes larger than $10^{-14}$ erg cm$^{-2}$ s$^{-1}$, however not detected with *ROSAT*.

To study the properties of the different source populations of M 31, it was necessary to separate foreground stars (39 plus 227 candidates) and background sources (11 AGN and 49 candidates, 4 galaxies and 19 candidates, 1 galaxy cluster and 5 candidates) from the sources of M 31. 1 263 sources could only be classified as <hard>, while 139 sources remained without identification or classification.

The catalogue of the Large *XMM-Newton* survey of M 31 contains 40 SSS candidates, with unabsorbed 0.2–1.0 keV luminosities between $1.8\times10^{34}$ erg s$^{-1}$ and $2.8\times10^{37}$ erg s$^{-1}$. SSSs are concentrated to the centre of M 31, which can be explained by their correlation with optical novae, and by the overall spatial distribution of M 31 late type stars (*i. e.* enhanced density towards the centre). Of the 14 identifications made of optical novae, five were presented in more detail. Among them is the first nova/SSS detected in an M 31 globular cluster. Correlations with previous X-ray studies revealed that only three SSSs were visible for at least one decade. This is in agreement with the strong long term variability found for the class of SSSs. In addition the correlations showed that previous SSS studies of *ROSAT* and *Chandra* contain a non-negligible number of sources that were erroneously classified as SSSs. In particular *Chandra* studies had low selection power. Two sources (№ 1 034 and № 1 136) showed a transition from supersoft to hard state between the *Chandra* and *XMM-Newton* observations. This behaviour is consistent with the behaviour known to occur in BH XRBs. However, other source types like *e. g.* symbiotic stars cannot be excluded yet.

The 25 identified and 37 classified SNRs had XID luminosities between $1.1\times10^{35}$ erg s$^{-1}$ and $4.3\times10^{36}$ erg s$^{-1}$. Three of the 25 identified SNRs were detected for the first time in X-rays. For one SNR the *ROSAT* classification can be confirmed. Six of the SNR candidates were selected from correlations with sources in SNR catalogues from the literature. As these six sources had rather "hard" hardness ratios they are good candidates for "plerions". An investigation of the spatial distribution showed that most SNRs and candidates are located in regions of enhanced star formation, especially along the 10 kpc dust ring in M 31. This connection between SNRs and star forming regions, implies that most of the remnants are from type II supernovae. Most of the SNR classifications from previous studies have been confirmed. However, in five cases these classifications are doubtful.

The population of "hard" M 31 sources mainly consists of XRBs. These rather bright sources (XID luminosity range: $1.0\times10^{36}$ erg s$^{-1}$ to $2.7\times10^{38}$ erg s$^{-1}$) were selected from their transient nature or strong long term variability (variability factor >10; 10 identified, 26 classified sources). The spectral properties of three transient sources were presented in more detail.

A sub-class of LMXBs is located in globular clusters. They were selected from correlations with optical sources included in globular cluster catalogues (36 identified, 17 classified sources). The XID luminosity of GlCs ranges from $2.3\times10^{35}$ erg s$^{-1}$ to $1.0\times10^{38}$ erg s$^{-1}$. The spatial distribution of that source class also showed an enhanced concentration to the centre of M 31. From detailed spectral and time variability studies of three GlC sources, one was identified as a black hole LMXB and an other one as a neutron star candidate. Changes in source classification from previous studies were nearly always due to changes in the classifications of the optical counterpart in newer papers.

From optical and X-ray colour-colour diagrams possible HMXB candidates were selected. If the sources were bright enough, an absorbed power-law model was fitted to the source spectra. Two of the candidates had a photon index consistent with the photon index range of NS HMXBs. Hence these two sources were

suggested as new HMXB candidates.

A comparison between the number of XRBs found in the log N-log S study with the number of identified and classified XRBs (including those located in GlCs) listed in the XMM LP-total catalogue showed that many faint XRBs detected in the log N-log S study with 2.0–10.0 keV fluxes in the range of $3.2\times10^{-14}$ erg cm$^{-2}$ s$^{-1}$ to $10^{-13}$ erg cm$^{-2}$ s$^{-1}$ ($\hat{=}2.3\times10^{36}$ erg s$^{-1}$ to $7.3\times10^{36}$ erg s$^{-1}$) were not identified as XRBs or XRB candidates in the XMM LP-total catalogue and thus were only classified as <hard> sources in the XMM LP-total catalogue. This is not surprising, as variability was used to classify XRBs and it is more complicated to detect variability of fainter sources than of bright sources. Many XRBs that are located in the inner disc of M 31 were not classified/identified in the XMM LP-total catalogue. One reason is that large parts of the inner disc region are located in the S1 and N1 fields, for which no variability could have been determined, because each of them was covered in only one observation.

This work gave us deeper insights into the long-term variability, spatial and flux distribution, and log N-log S relation of the sources in the field of M 31 and thus helped us to improve our understanding of the X-ray source population of M 31.

## 10.2 Outlook

This work focused on the overall properties of the source population of individual classes. Possible future projects could for instance comprise a thorough study of the diffuse X-ray emission (like *e. g.* Bogdán & Gilfanov 2008, see also Appendix A), or a systematic study of individual, faint, "hard", point-like X-ray sources to search for bursts or dips in the light curves of these sources. Another project could be the derivation of luminosity functions in the 0.2–2.0 keV range. This requires sophisticated models to correct the number of expected background sources for absorption effects due to the M 31 interstellar medium.

Progress in the analysis software, and in the calibration of the instruments of *XMM-Newton* allowed me to reduce the number of spurious detections and to find faint sources, which were missed in previous studies. This demonstrates that the analysis of archival observations can lead to new results if improved software is available. In the near future enhanced source detection procedures should be available due to an improved modelling of EPIC's point spread functions (PSFs). This will not only help to better determine the source positions, but also advance the derivation of the encircled energy fraction for sources located (far) off-axis. In addition the implementation of a 64 bit version of the analysis software will allow us to increase the number of observations one can use simultaneously in a detection run. Related to the Large *XMM-Newton* Survey, this will make it possible to search for fainter persistent sources in the overlapping regions of the different fields by including all observations that contribute exposure to the overlapping region in one detection run. In this context, it is also worth thinking about using a larger fraction of the exposure for source detection by relaxing the selection criteria for GTIs. However, one has to verify that the numbers of false detections, due to the then enhanced background, stays low.

*XMM-Newton* and *Chandra* carry X-ray telescopes and detectors that provide high spatial and energy resolution over the $\sim$0.2–10.0 keV energy band down to low fluxes. It is, therefore possible to classify sources by their X-ray properties. However, cross-correlations with catalogues in other wavelengths are important for the classification and identification of the X-ray sources. Especially important are spectra obtained in optical follow-up observations. They allow us to strengthen the available classifications and help us to increase the number of identified X-ray sources. Both past and future optical follow-up campaigns have been led by members within our collaboration. Using telescopes of the medium size class, it is for instance possible to investigate the nature of the suggested foreground star candidates. In the near future we plan to take H$\alpha$ and SII images of the vicinity of the SNR candidates, if not already available. In addition we will take optical spectra of the found counterparts to ascertain the SNR nature of these sources. In the challenging search of HMXBs it would be helpful to have a complete sample of O and B stars, located in

M 31. Unfortunately, observations with 8–10 m class telescopes are necessary to detect these sources.

Future X-ray missions, like *eROSITA* (which will realise an all sky survey) or *IXO* (the next large X-ray mission) mainly focus on studying galaxy clusters and AGN to access cosmological questions, like the formation of large scale structures or the content of baryonic and dark matter and dark energy in the universe. The *IXO* mission will combine spatial resolution (goal $\sim 5\farcs0$) and FoV of today's instruments with significantly larger effective areas. For studies of nearby galaxies, this will give us the possibility to detect fainter sources. An ideal future X-ray mission for studies of nearby galaxies needs to combine large effective areas (like those of *IXO*) and high energy resolution with an (even improved) spatial resolution like that obtained with *Chandra*. It would also be desirable that such an instrument provides an enlarged FoV. An important task of future nearby galaxy missions will be to allow deeper monitoring of an enlarged ensemble of sources of a galaxy and thus allow us to study temporal and spectral variability of populations of X-ray sources, which is urgently needed for source classification.

# Appendix A

# First results on the diffuse emission

I adopted the method to create background and vignetting corrected images, which was developed by Bauer et al. (2008), to the *XMM-Newton* Deep Survey data. The resulting EPIC-PN colour image (Fig. A.1; red: 0.2–0.5 keV, green: 0.5–1.0 keV, blue: 1.0–2.0 keV) clearly shows the huge amount of diffuse emission from the bulge region of M 31. In addition, fainter diffuse emission from the disc, especially the northern disc, is visible. Most prominent is the linear feature located to the north-east of the bulge and following the M 31 dust ring. In Fig. A.2 X-ray contours were overlaid on a *GALEX* NUV image. This reveals that the diffuse emission of the disc is related to the star forming regions.

Future analysis will comprise an examination of the spectral properties of the diffuse emission and also a deepening study of the spatial distribution of the emission, including MOS data.

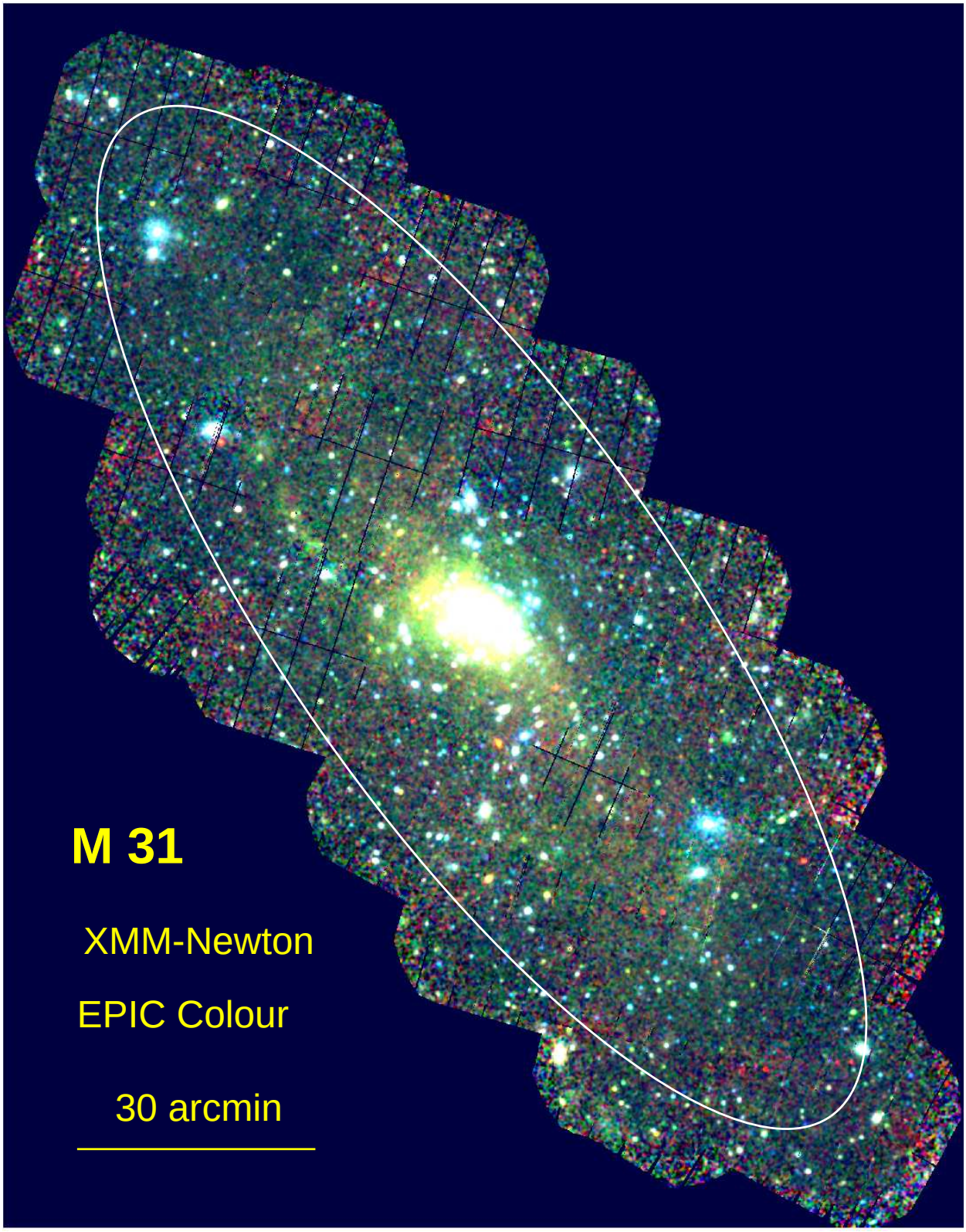


**Figure A.1:** Three-colour, background corrected EPIC PN image (red: 0.2–0.5 keV, green: 0.5–1.0 keV, blue: 1.0–2.0 keV) showing the diffuse emission of the bulge and disc of M 31.

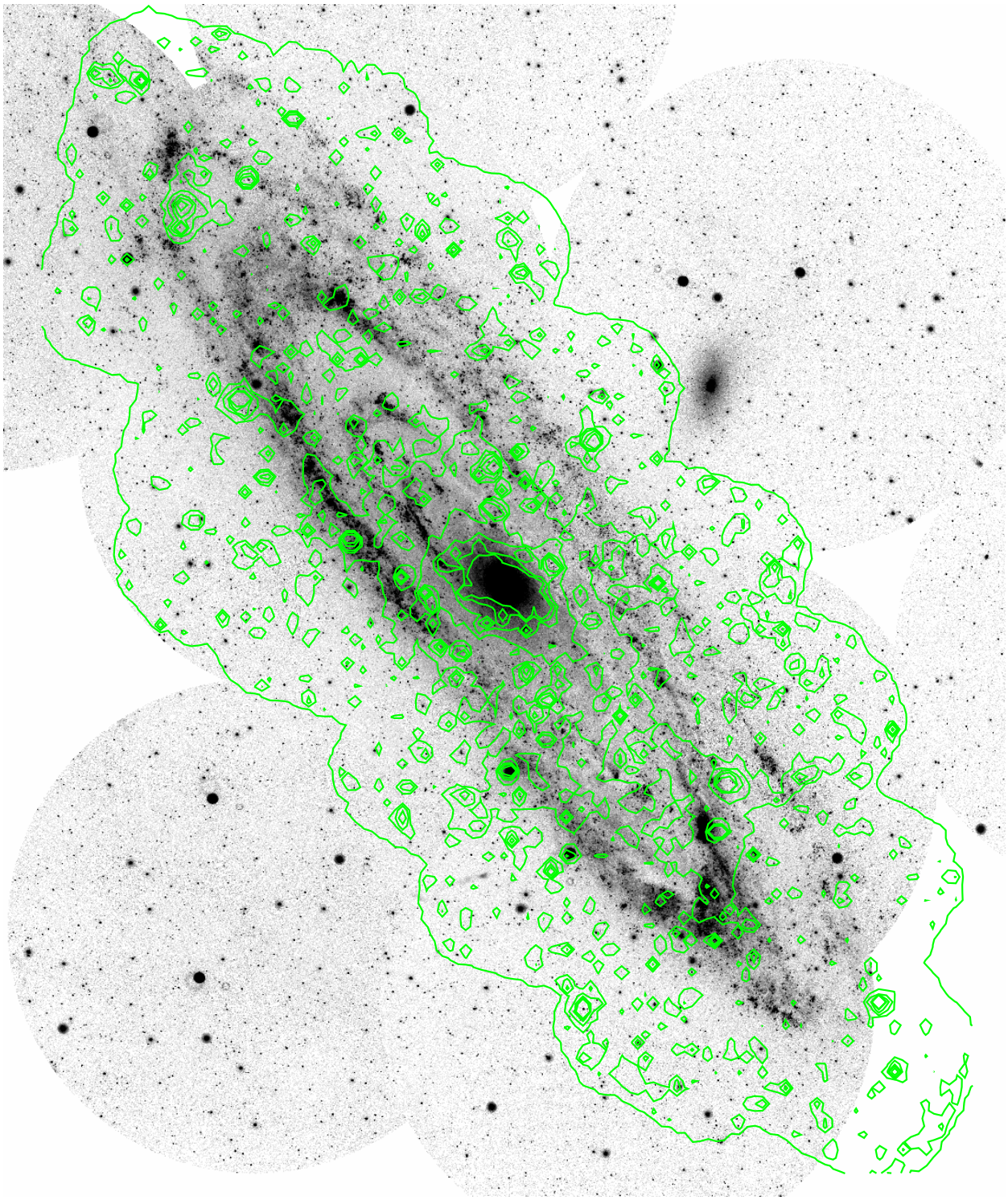

**Figure A.2:** *GALEX* NUV image with overlaid contours of the diffuse X-ray emission showing that the diffuse emission of the disc is related to star forming regions.

# Appendix B

# EPIC XID images

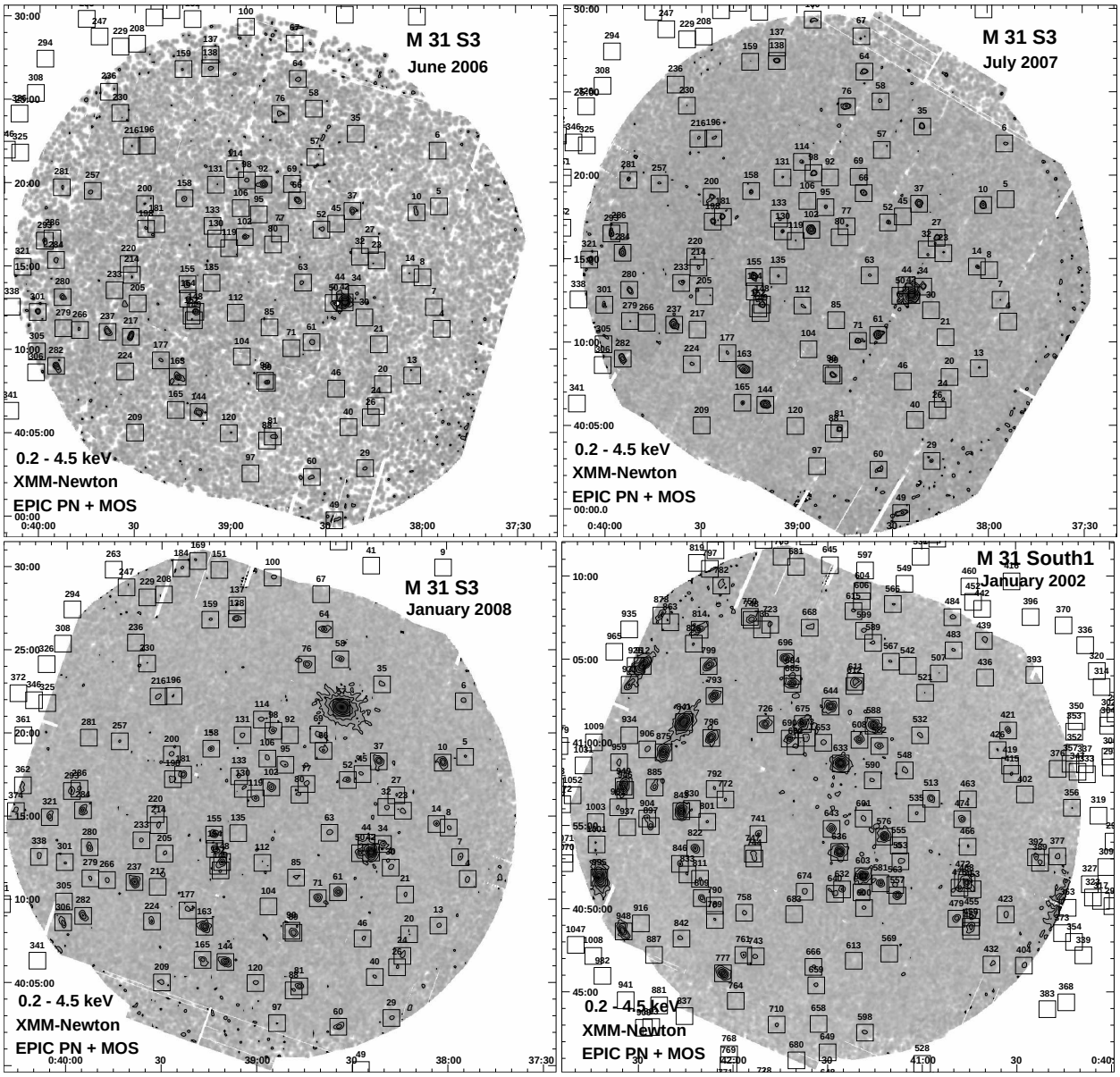


**Figure B.1:** Logarithmically scaled *XMM-Newton* EPIC low background images integrated in $2'' \times 2''$ pixels of the M 31 observations combining PN and MOS 1 and MOS 2 cameras in the (0.2–4.5) keV XID band. The data are smoothed with a 2D-Gaussian of FWHM $10''$, which corresponds to the point spread function in the centre area. The images are corrected for unvignetted exposures. Contours in units of $10^{-6}\,\mathrm{ct\,s^{-1}\,pix^{-1}}$ including a factor of two smoothing are at $(8, 16, 32, 64, 128)$ in the upper left panel, at $(6, 8, 16, 32, 64, 128)$ in the upper right panel, and at $(4, 8, 16, 32, 64, 128)$ in both lower panels. Sources from the XMM LP-total catalogue are marked as $30'' \times 30''$ squares.

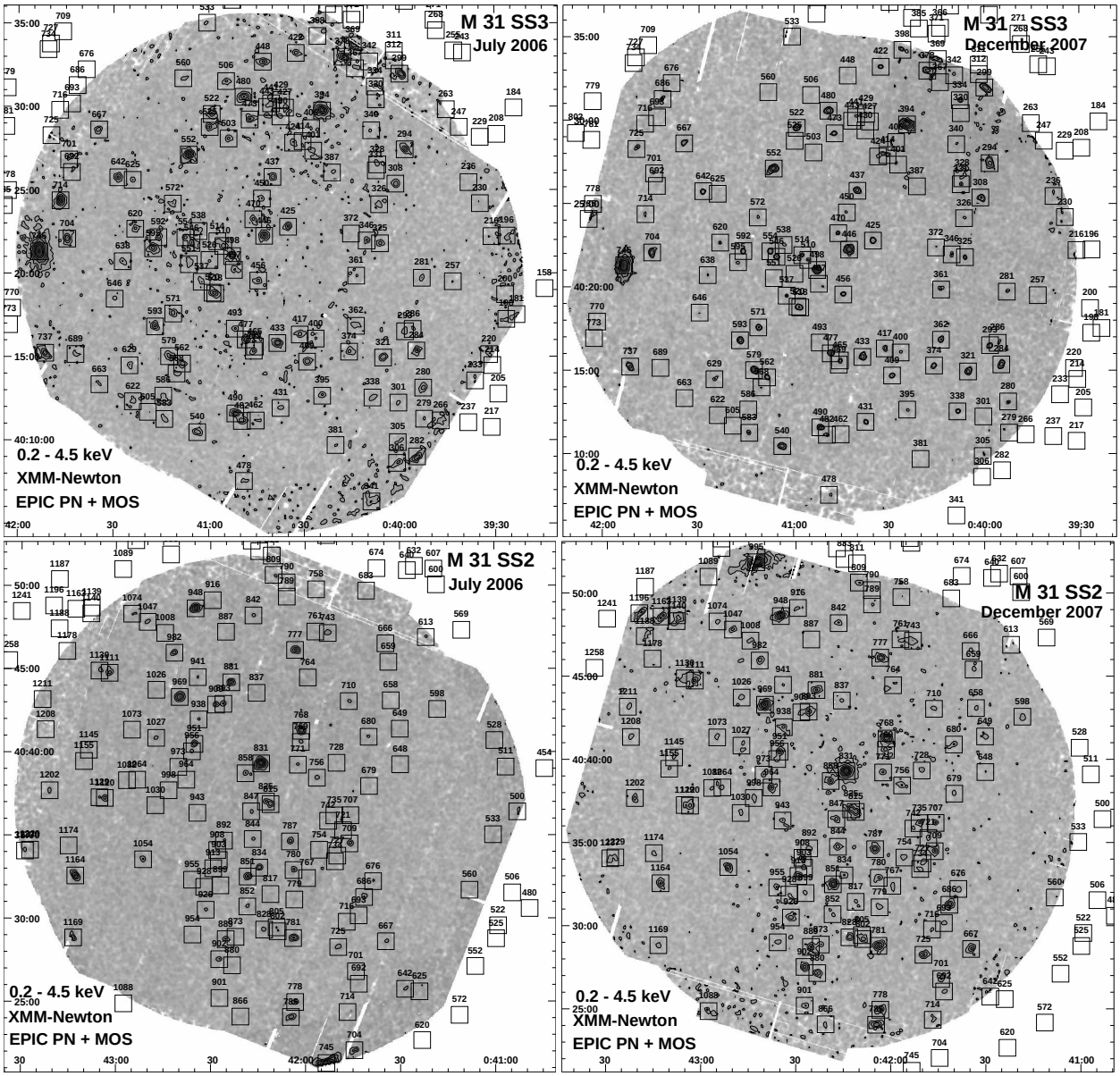


**Figure B.1:** (continued) Contours are at $(4, 8, 16, 32, 64, 128)$ in the upper left panel and lower right panel, at $(6, 8, 16, 32, 64, 128)$ in the upper right panel, and at $(8, 16, 32, 64, 128)$ in the lower left panel.

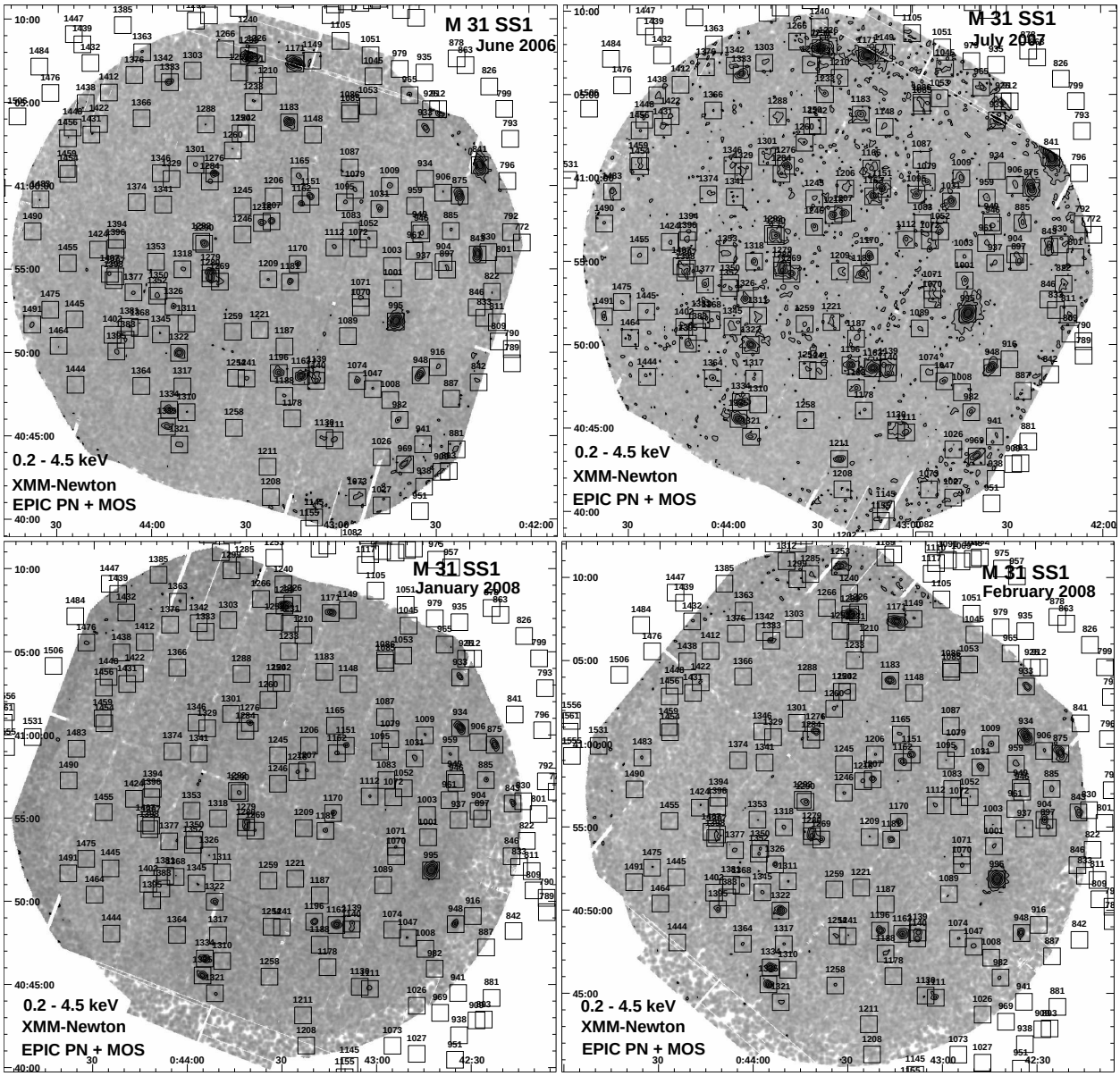


**Figure B.1:** (continued) Contours are at $(8, 16, 32, 64, 128)$ in the upper left panel and lower right panel, at $(4, 8, 16, 32, 64, 128)$ in the upper right panel, and at $(16, 32, 64, 128)$ in the lower left panel.

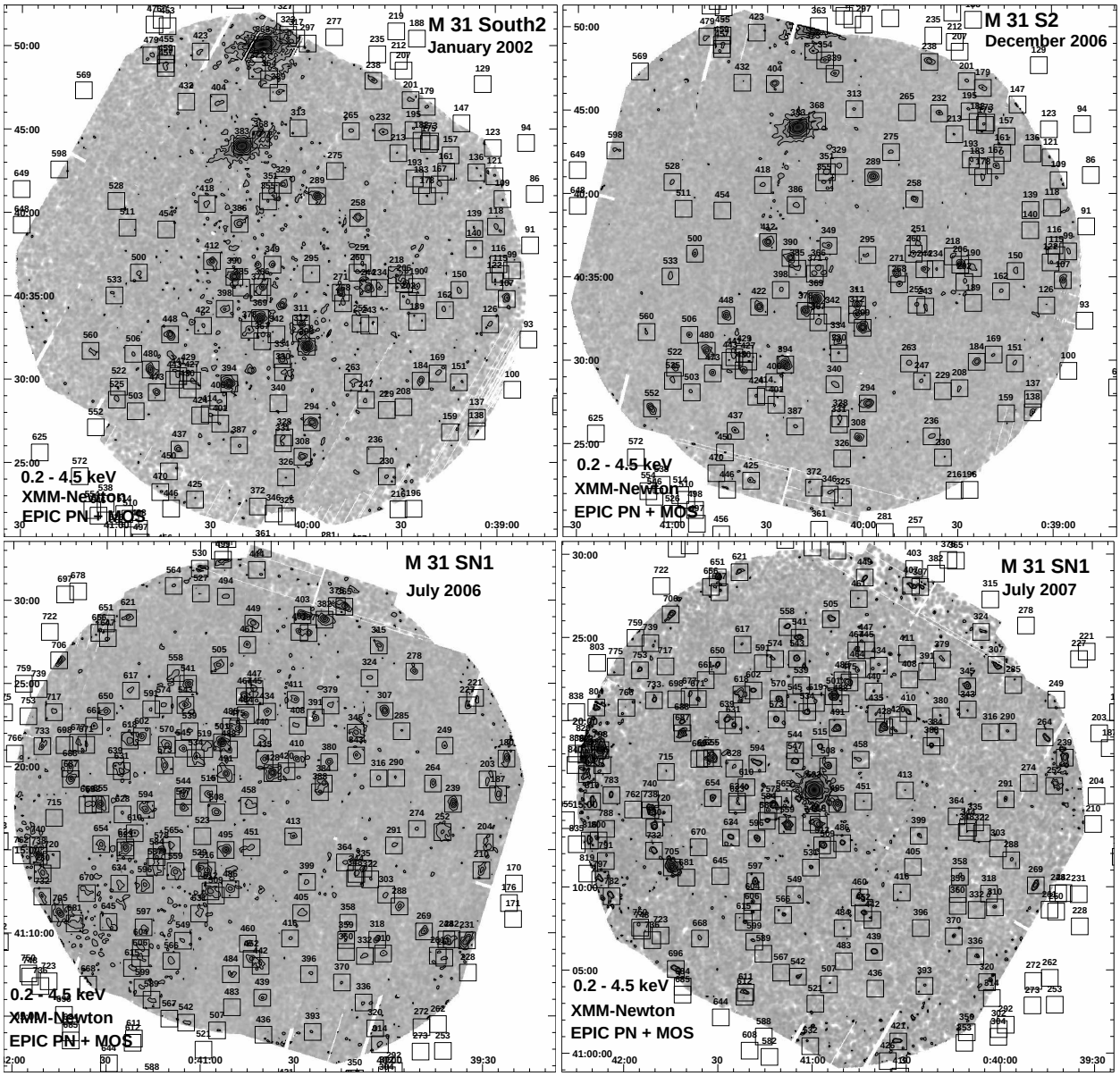


**Figure B.1:** (continued) Contours are at $(4, 8, 16, 32, 64, 128)$ in both upper panels and the lower left panel, and at $(6, 8, 16, 32, 64, 128)$ in the lower right panel.

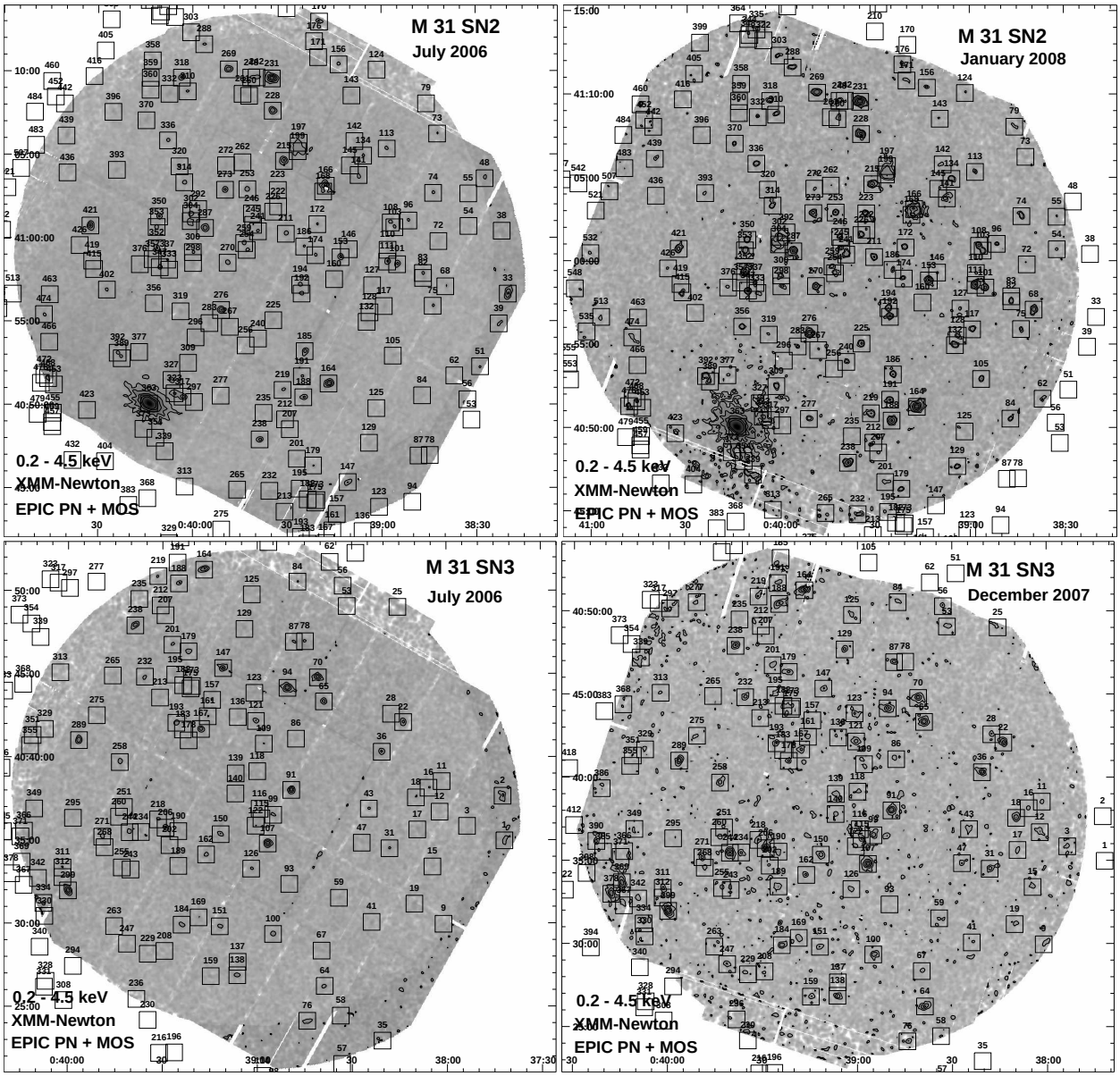


**Figure B.1:** (continued) Contours are at: $(8, 16, 32, 64, 128)$ in the upper left and lower left panels, $(6, 8, 16, 32, 64, 128)$ in the upper right panel, and at $(4, 8, 16, 32, 64, 128)$ in the lower right panel.

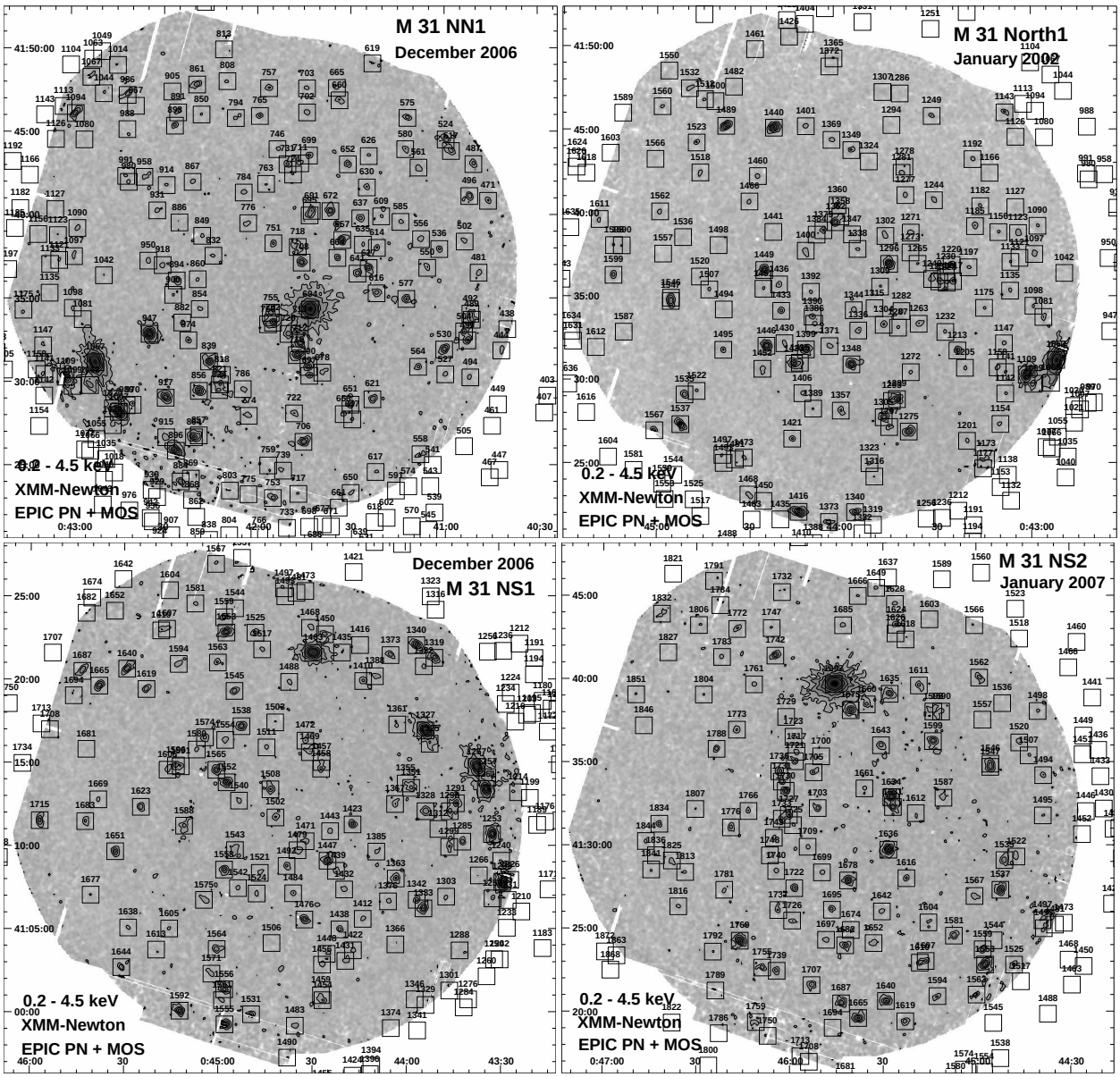


**Figure B.1:** (continued) Contours are at $(4, 8, 16, 32, 64, 128)$ in all panels.

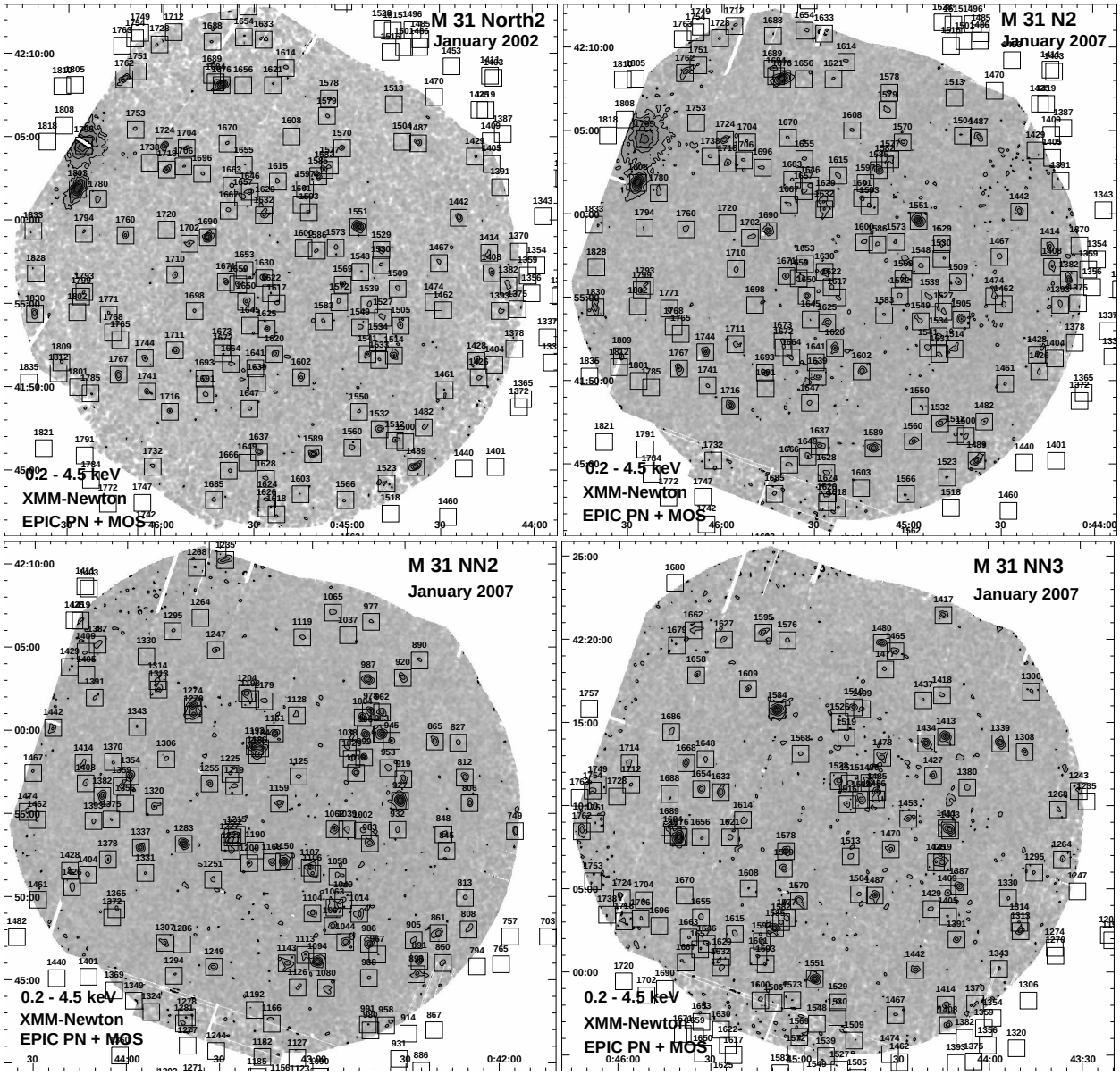


**Figure B.1:** (continued) Contours are at $(4, 8, 16, 32, 64, 128)$ in all panels.

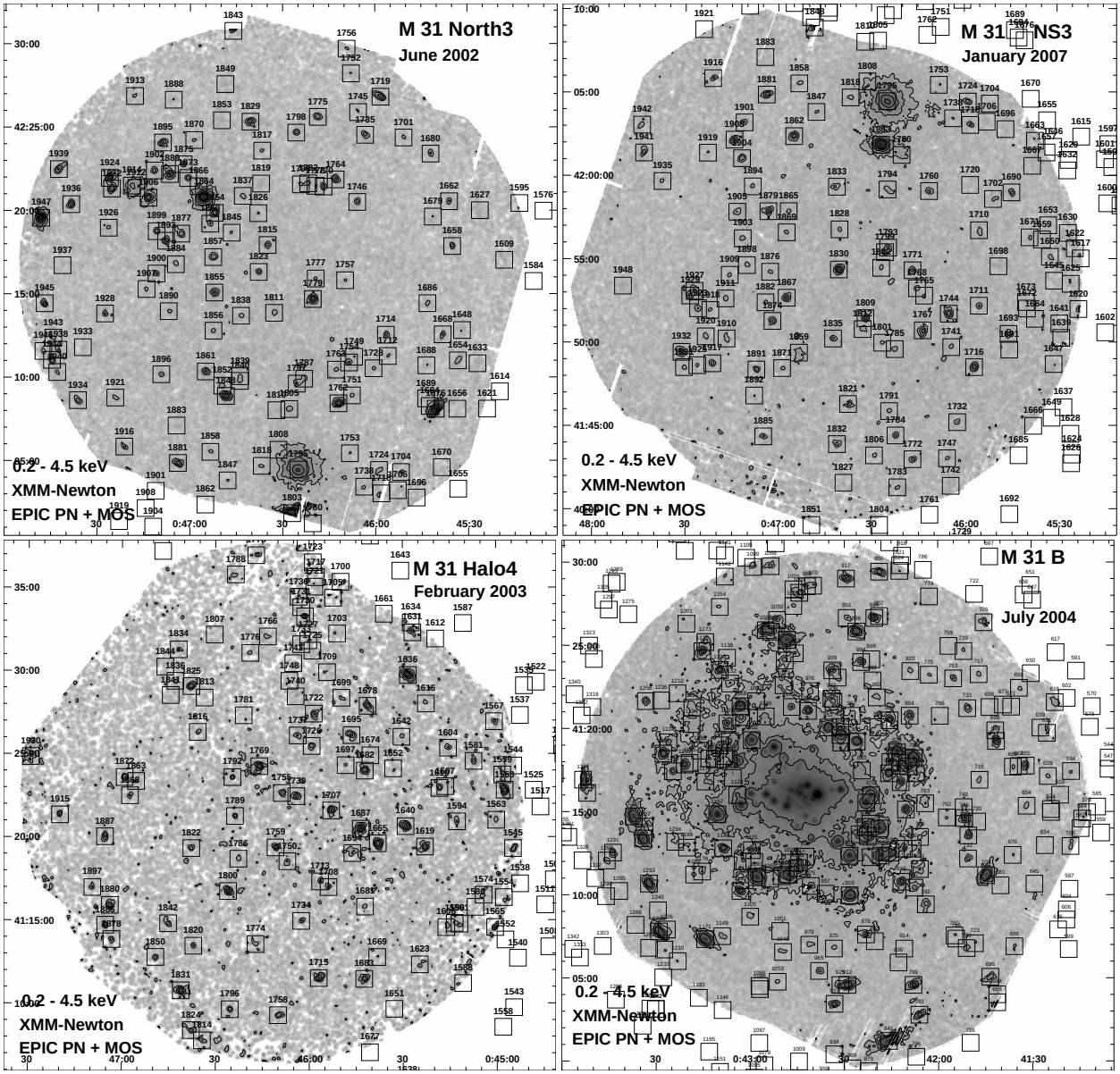


**Figure B.1:** (continued) Contours are at $(4, 8, 16, 32, 64, 128)$ in both upper panels and the lower left panel, and at $(4, 8, 16, 32)$ in the lower right panel. The inner area of the image shown in the lower right panel is shown in detail in Fig. B.2.

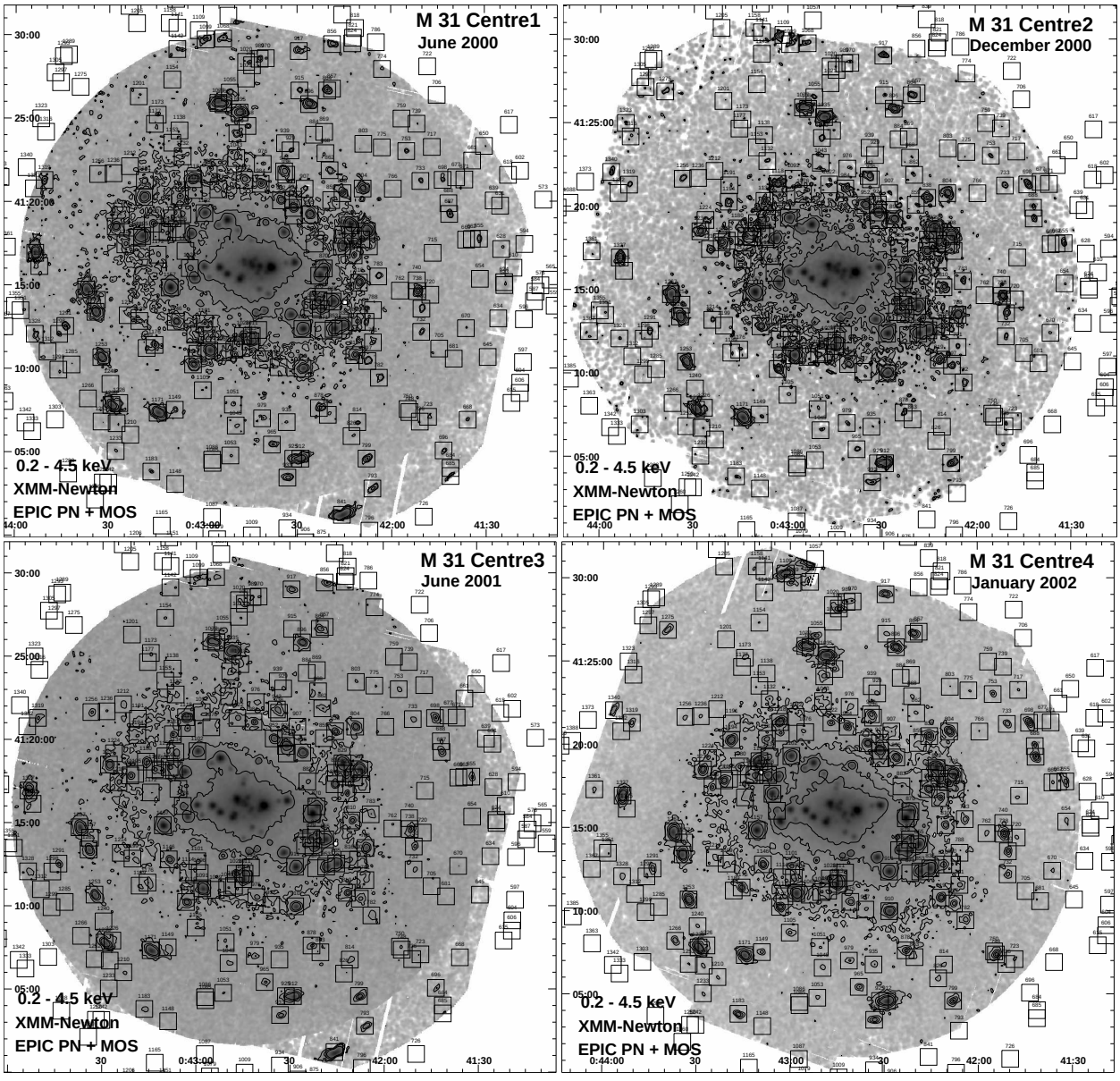


**Figure B.1:** (continued) Contours are at $(6, 8, 16, 32)$ in both upper panels, at $(8, 16, 32)$ in the lower left panel, and at $(4, 8, 16, 32)$ in the lower right panel. The inner area is shown in detail in Fig. B.2.

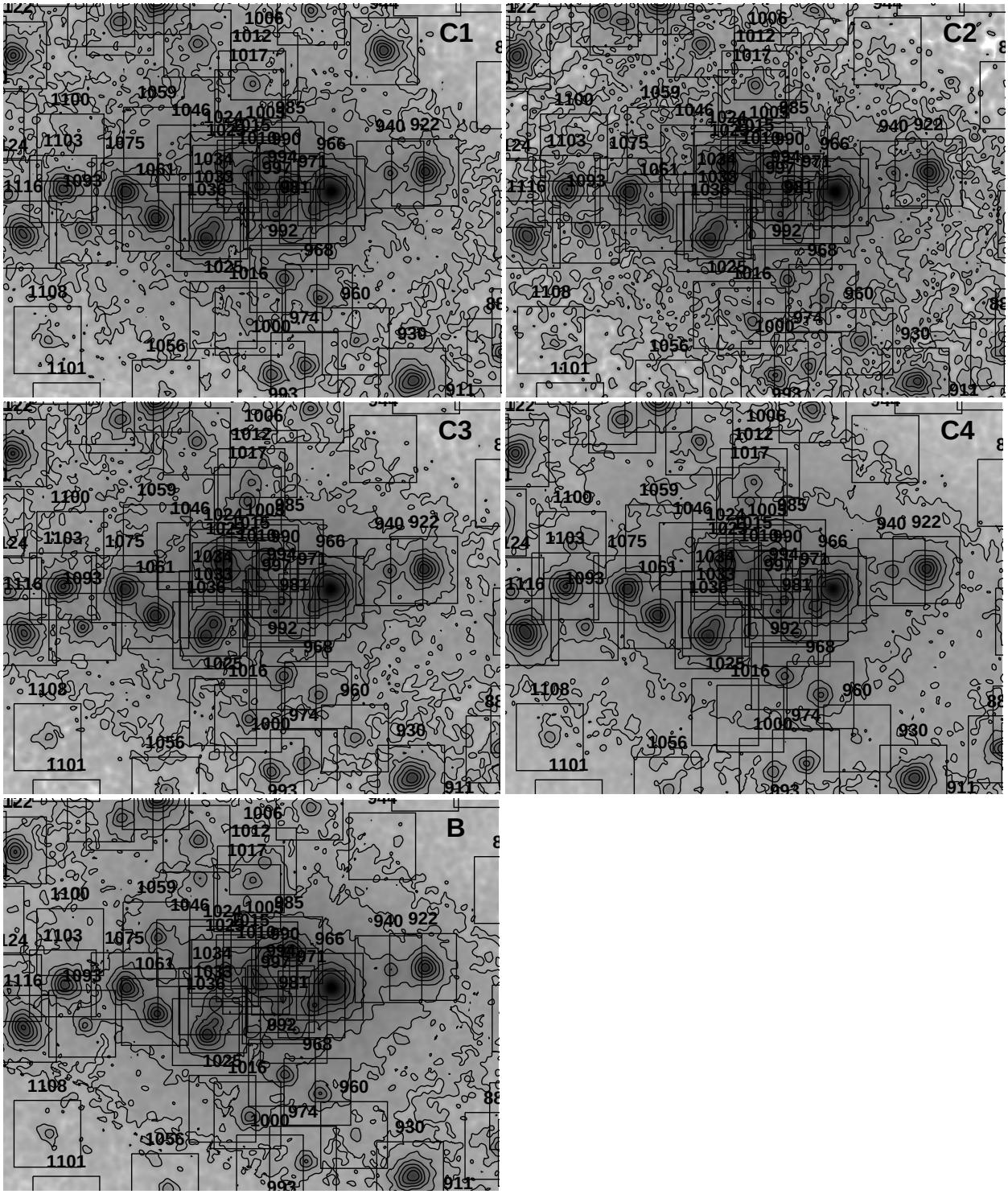


**Figure B.2:** Inner area of M 31 enlarged from Fig. B.1. Contours are at $(4, 8, 16, 32, 64, 128, 256) \times 10^{-6}$ ct s$^{-1}$ pix$^{-1}$ including a factor of one smoothing. Sources from the large catalogue are marked as $30'' \times 30''$ squares. The images are ordered as follows: Centre 1 (upper left), Centre 2 (upper right), Centre 3 (middle left), Centre 4 (middle right) and Centre B (lower left).

# Appendix C

# Description of Tables 6.3 and 6.5

Table 6.3 presents a catalogue extension of the source catalogue reported in PFH2005. It contains 39 sources, which were detected in the July 2004 *XMM-Newton* monitoring observations of the low mass X-ray binary RX J0042.6+4115 (pointed $1\farcm1$ to the west of the M 31 nucleus position), and in the re-analysed archival *XMM-Newton* observations of the central region of M 31, obtained from June 2000 to January 2002. In contrast to PFH2005 the observations were examined individually.

Table 6.5 provides all information necessary to examine time variability of sources in the central region of M 31. The sources are taken from the combined catalogue (*i. e.* PFH2005 and Table 6.3). Sources are only included in the table, if they are in the FoV for at least two observations.

**Table C.1:** Read Me file for Table 6.3

| Bytes | Format | Units | Label | Explanations |
|---|---|---|---|---|
| 1– 3 | I3 | — | [SPH2008] | Source Number |
| 5– 10 | A6 | — | M31_ID | M 31 field identification |
| 11– 12 | I2 | h | RAh | Right Ascension J2000 (hours) |
| 14– 15 | I2 | min | RAm | Right Ascension J2000 (minutes) |
| 17– 21 | F5.2 | s | RAs | Right Ascension J2000 (seconds) |
| 24 | A1 | — | DE- | Declination J2000 (sign) |
| 25– 26 | I2 | deg | DEd | Declination J2000 (degrees) |
| 28– 29 | I2 | arcmin | DEm | Declination J2000 (minutes) |
| 31– 34 | F4.1 | arcsec | DEs | Declination J2000 (seconds) |
| 36– 40 | F5.2 | arcsec | PosErr | Positional error (1) |
| 42– 49 | E8.2 | — | LH | Source detection likelihood (combined EPIC) |
| 51– 58 | E8.2 | ct/s | CRate | Combined EPIC count rate (2) |
| 60– 66 | E7.1 | ct/s | e_CRate | Error in CRate |
| 68– 75 | E8.2 | mW/m2 | CFlux | Combined EPIC flux in erg/cm2/s (2) |
| 77– 83 | E7.1 | mW/m2 | e_CFlux | Error in CFlux |
| 85– 89 | F5.2 | — | CHR1 | ? Combined EPIC hardness ratio 1 (3) |
| 91– 94 | F4.2 | — | e_CHR1 | ? Error in CHR1 |
| 96–100 | F5.2 | — | CHR2 | ? Combined EPIC hardness ratio 2 (3) |
| 102–105 | F4.2 | — | e_CHR2 | ? Error in CHR2 |

**Table C.1:** continued.

| Bytes | Format | Units | Label | Explanations |
|---|---|---|---|---|
| 107–111 | F5.2 | — | CHR3 | ? Combined EPIC hardness ratio 3 (3) |
| 113–116 | F4.2 | — | e_CHR3 | ? Error in CHR3 |
| 118–122 | F5.2 | — | CHR4 | ? Combined EPIC hardness ratio 4 (3) |
| 124–127 | F4.2 | — | e_CHR4 | ? Error in CHR4 |
| 129–131 | A3 | — | VAL | EPIC instruments contributing to source detection (4) |
| 133–137 | F5.1 | ks | PN_Expo | ? Exposure of EPIC pn instrument |
| 139–146 | E8.2 | — | PN_LH | ? EPIC pn source detection likelihood |
| 148–155 | E8.2 | ct/s | PNRate | ? EPIC pn count rate (2) |
| 157–163 | E7.1 | ct/s | e_PNRate | ? Error in PNRate |
| 165–172 | E8.2 | mW/m2 | PNFlux | ? EPIC pn flux in erg/cm2/s (2) |
| 174–180 | E7.1 | mW/m2 | e_PNFlux | ? Error in PNFlux |
| 182–186 | F5.2 | — | PNHR1 | ? EPIC pn hardness ratio 1 (3) |
| 188–191 | F4.2 | — | e_PNHR1 | ? Error in PNHR1 |
| 193–197 | F5.2 | — | PNHR2 | ? EPIC pn hardness ratio 2 (3) |
| 199–202 | F4.2 | — | e_PNHR2 | ? Error in PNHR2 |
| 204–208 | F5.2 | — | PNHR3 | ? EPIC pn hardness ratio 3 (3) |
| 210–213 | F4.2 | — | e_PNHR3 | ? Error in PNHR3 |
| 215–219 | F5.2 | — | PNHR4 | ? EPIC pn hardness ratio 4 (3) |
| 221–224 | F4.2 | — | e_PNHR4 | ? Error in PNHR4 |
| 226–230 | F5.1 | ks | M1_Expo | ? Exposure of EPIC MOS1 instrument |
| 232–239 | E8.2 | — | M1_LH | ? EPIC MOS1 source detection likelihood |
| 241–248 | E8.2 | ct/s | M1Rate | ? EPIC MOS1 count rate (2) |
| 250–256 | E7.1 | ct/s | e_M1Rate | ? Error in M1Rate |
| 258–265 | E8.2 | mW/m2 | M1Flux | ? EPIC MOS1 flux in erg/cm2/s (2) |
| 267–273 | E7.1 | mW/m2 | e_M1Flux | ? Error in M1Flux |
| 275–279 | F5.2 | — | M1HR1 | ? EPIC MOS1 hardness ratio 1 (3) |
| 281–284 | F4.2 | — | e_M1HR1 | ? Error in M1HR1 |
| 286–290 | F5.2 | — | M1HR2 | ? EPIC MOS1 hardness ratio 2 (3) |
| 292–295 | F4.2 | — | e_M1HR2 | ? Error in M1HR2 |
| 297–301 | F5.2 | — | M1HR3 | ? EPIC MOS1 hardness ratio 3 (3) |
| 303–306 | F4.2 | — | e_M1HR3 | ? Error in M1HR3 |
| 308–312 | F5.2 | — | M1HR4 | ? EPIC MOS1 hardness ratio 4 (3) |
| 314–317 | F4.2 | — | e_M1HR4 | ? Error in M1HR4 |
| 319–323 | F5.1 | ks | M2_Expo | ? Exposure of EPIC MOS2 instrument |
| 325–332 | E8.2 | — | M2_LH | ? EPIC MOS2 source detection likelihood |
| 334–341 | E8.2 | ct/s | M2Rate | ? EPIC MOS2 count rate (2) |
| 343–349 | E7.1 | ct/s | e_M2Rate | ? Error in M2Rate |
| 351–358 | E8.2 | mW/m2 | M2Flux | ? EPIC MOS2 flux in erg/cm2/s (2) |
| 360–366 | E7.1 | mW/m2 | e_M2Flux | ? Error in M2Flux |
| 368–372 | F5.2 | — | M2HR1 | ? EPIC MOS2 hardness ratio 1 (3) |
| 374–377 | F4.2 | — | e_M2HR1 | ? Error in M2HR1 |
| 379–383 | F5.2 | — | M2HR2 | ? EPIC MOS2 hardness ratio 2 (3) |

**Table C.1:** continued.

| Bytes | Format | Units | Label | Explanations |
|---|---|---|---|---|
| 385–388 | F4.2 | — | e_M2HR2 | ? Error in M2HR2 |
| 390–394 | F5.2 | — | M2HR3 | ? EPIC MOS2 hardness ratio 3 (3) |
| 396–399 | F4.2 | — | e_M2HR3 | ? Error in M2HR3 |
| 401–405 | F5.2 | — | M2HR4 | ? EPIC MOS2 hardness ratio 4 (3) |
| 407–410 | F4.2 | — | e_M2HR4 | ? Error in M2HR4 |
| 412–511 | A100 | — | XID | ? X-ray identification (5) |
| 512–523 | A12 | — | USNO_B1.0 | ? Name of brightest USNO-B1.0 source within search area |
| 525 | I1 | — | USNO_Mul | ? Number of USNO-B1.0 correlations |
| 527–529 | F3.1 | arcsec | USNO_dis | ? Distance of source USNO-B1.0 |
| 531–534 | F4.1 | mag | USNO_B2 | ? B2 magnitude of source USNO-B1.0 |
| 536–539 | F4.1 | mag | USNO_R2 | ? R2 magnitude of source USNO-B1.0 |
| 541–544 | F4.1 | mag | USNO_I | ? I magnitude of source USNO-B1.0 |
| 546–549 | F4.1 | — | log_fxo | ? Logarithm of fX/fopt |
| 551–565 | A15 | — | Class | ? Classification of X-ray source (6) |
| 567–666 | A100 | — | Remarks | ? Additional remarks (7) |
| 668–692 | A25 | — | IAU_NAME | Source Name XMMM31 Jhhmmss.s+ddmmss |

Note (1): 1 sigma statistical error, $0''.5$ to be added as 1 sigma systematic error
Note (2): Count rate and flux in XID band (0.2-4.5keV)
Note (3): HRi=(R(i+1)-R(i))/(R(i+1)+R(i)) where Ri are the count rates in the energy bands 1 to 5 and
band 1 = 0.2–0.5keV,
band 2 = 0.5–1.0keV,
band 3 = 1.0–2.0keV,
band 4 = 2.0–4.5keV,
band 5 = 4.5–12keV
Note (4): First character for EPIC PN, second for MOS1, third for MOS2;
character = T: source is in field of view of instrument
F: otherwise
Note (5): References in XID:

| | |
|---|---|
| TF91: | Trinchieri et al., 1991ApJ...382...82T |
| PFJ93: | Primini et al., 1993ApJ...410..615P |
| am-n: | Kong et al., 2002ApJ...577..738K |
| | Di Stefano et al., 2004ApJ...610..247D |
| | Williams et al., 2004ApJ...609..735W |
| | Williams et al., 2006ApJ...637..479W |
| | Williams et al., 2005ApJ...632.1086W |
| Jhhmmss.s+ddmmss: | Kaaret, 2002ApJ...578..114K |
| | Di Stefano et al., 2002ApJ...570..618D |
| | Trudolyubov et al., 2006ApJ...645..277T |
| PHS2007: | Pietsch et al., 2007A&A...465..375P |
| FMZ2005: | Fan et al., 2005PASP...117.1236F |

| | | |
|---|---|---|
| | VG2007: | Voss et al., 2007A&A...468...49V |
| | XMMU Jhhmmss.s+ddmmss: | Trudolyubov et al., 2006ApJ...645..277T |
| | TPC2006b: | Trudolyubov et al., 2006astro.ph.10809T |
| Note (6): | Classifications used (see Table 7.3) | |
| | fg Star = foreground star | |
| | <fg Star> = foreground star candidate | |
| | AGN = active galactic nucleus | |
| | <AGN> = AGN candidate | |
| | Gal = galaxy | |
| | <Gal> = galaxy candidate | |
| | GCl = galaxy cluster | |
| | <GCl> = galaxy cluster candidate | |
| | SSS = supersoft source in M 31 | |
| | <SSS> = supersoft source candidate in M 31 | |
| | SNR = supernova remnant in M 31 | |
| | <SNR> = supernova remnant candidate in M 31 | |
| | GlC = source in globular cluster | |
| | <GlC> = source in globular cluster candidate | |
| | XRB = X-ray binary in M 31 | |
| | <XRB> = X-ray binary candidate in M 31 | |
| | <hard> = HR2-e_HR2>-0.2 or only HR3 and HR4 defined, and no other classification | |
| Note (7): | References in remarks: | |
| | SIM : | SIMBAD Database |
| | NED : | NASA Extragalactic Database |
| | BHG88 : | Berkhuijsen et al., 1988A&AS...76...65B |
| | KSW2003 : | Kong et al., 2003ApJ...590L..21K |
| | JPN2003 : | Joshi et al., 2003A&A...402..113J |
| | PHS2007 : | Pietsch et al., 2007A&A...465..375P |
| | SKHV : | Sargent et al., 1977AJ.....82..947S |
| | | Holland et al., 1995AJ....109.2061H |
| | WGC2006 : | Williams et al., 2006ApJ...637..479W |
| | WGC2005 : | Williams et al., 2005ApJ...632.1086W |
| | TPC2006a : | Trudolyubov et al., 2006ApJ...645..277T |
| | GFB2004 : | Galetti et al., 2004A&A...416..917G |
| | VG2007 : | Voss et al., 2007A&A...468...49V |
| | KLG2007 : | Kim et al., 2007AJ....134..706K |
| | B : | Battistini et al., 1980A&AS...42..357B |
| | | Battistini et al., 1987A&AS...67..447B |
| | | Galleti et al., 2005A&A...436..535G |

**Table C.2:** Read Me file for Table 6.5

| Bytes | Format | Units | Label | Explanations |
|---|---|---|---|---|
| 1– 3 | I3 | — | SRC_ID | Source Number (1) |
| 5– 12 | e8.3 | mW/m2 | CFLUX | Combined EPIC flux in erg/cm2/s (2) |

**Table C.2:** continued.

| Bytes | Format | Units | Label | Explanations |
|---|---|---|---|---|
| 14– 20 | e7.2 | mW/m2 | e_CFLUX | Error in CFlux |
| 22– 26 | F5.2 | — | CHR1 | ? Combined EPIC hardness ratio 1 (3) |
| 28– 31 | F4.2 | — | e_CHR1 | ? Error in CHR1 |
| 33– 37 | F5.2 | — | CHR2 | ? Combined EPIC hardness ratio 2 (3) |
| 39– 42 | F4.2 | — | e_CHR2 | ? Error in CHR2 |
| 44– 48 | F5.2 | — | CHR3 | ? Combined EPIC hardness ratio 3 (3) |
| 50– 53 | F4.2 | — | e_CHR3 | ? Error in CHR3 |
| 55– 59 | F5.2 | — | CHR4 | ? Combined EPIC hardness ratio 4 (3) |
| 61– 64 | F4.2 | — | e_CHR4 | ? Error in CHR4 |
| 66–221 | A156 | — | XID | ? X-ray identification (5) |
| 223–237 | A15 | — | Class | ? Classification of X-ray source (6) |
| 239–338 | A100 | — | Remarks | ? Additional remarks (7) |
| 340–342 | A3 | — | c1_val | ? EPIC instruments contributing to source detection in observation c1 (4) |
| 344–351 | e8.3 | ct/s | c1_RATE | ? EPIC count rate in observation c1 (2) |
| 353–359 | e7.2 | ct/s | e_c1_RATE | ? Error in c1_Rate |
| 361–368 | e8.3 | mW/m2 | c1_FLUX | ? EPIC flux in erg/cm2/s in observation c1(2) |
| 370–376 | e7.2 | mW/m2 | e_c1_FLUX | ? Error in c1_Flux |
| 378–382 | F5.2 | — | c1_HR1 | ? EPIC hardness ratio 1 in observation c1 (3) |
| 384–387 | F4.2 | — | e_c1_HR1 | ? Error in c1_HR1 |
| 389–393 | F5.2 | — | c1_HR2 | ? EPIC hardness ratio 2 in observation c1 (3) |
| 395–398 | F4.2 | — | e_c1_HR2 | ? Error in c1_HR2 |
| 400–404 | F5.2 | — | c1_HR3 | ? EPIC hardness ratio 3 in observation c1 (3) |
| 406–409 | F4.2 | — | e_c1_HR3 | ? Error in c1_HR3 |
| 411–415 | F5.2 | — | c1_HR4 | ? EPIC hardness ratio 4 in observation c1 (3) |
| 417–420 | F4.2 | — | e_c1_HR4 | ? Error in c1_HR4 |
| 422–424 | A3 | — | c2_val | ? EPIC instruments contributing to source detection in observation c2 (4) |
| 426–433 | e8.3 | ct/s | c2_RATE | ? EPIC count rate in observation c2 (2) |
| 435–441 | e7.2 | ct/s | e_c2_RATE | ? Error in c2_Rate |
| 443–450 | e8.3 | mW/m2 | c2_FLUX | ? EPIC flux in erg/cm2/s in observation c2(2) |
| 452–458 | e7.2 | mW/m2 | e_c2_FLUX | ? Error in c2_Flux |
| 460–464 | F5.2 | — | c2_HR1 | ? EPIC hardness ratio 1 in observation c2 (3) |
| 466–469 | F4.2 | — | e_c2_HR1 | ? Error in c2_HR1 |
| 471–475 | F5.2 | — | c2_HR2 | ? EPIC hardness ratio 2 in observation c2 (3) |
| 477–480 | F4.2 | — | e_c2_HR2 | ? Error in c2_HR2 |
| 482–486 | F5.2 | — | c2_HR3 | ? EPIC hardness ratio 3 in observation c2 (3) |
| 488–491 | F4.2 | — | e_c2_HR3 | ? Error in c2_HR3 |
| 493–497 | F5.2 | — | c2_HR4 | ? EPIC hardness ratio 4 in observation c2 (3) |
| 499–502 | F4.2 | — | e_c2_HR4 | ? Error in c2_HR4 |
| 504–506 | A3 | — | c3_val | ? EPIC instruments contributing to source detection in observation c3 (4) |
| 508–515 | e8.3 | ct/s | c3_RATE | ? EPIC count rate in observation c3 (2) |

**Table C.2:** continued.

| Bytes | Format | Units | Label | Explanations |
|---|---|---|---|---|
| 517–523 | e7.2 | ct/s | e_c3_RATE | ? Error in c3_Rate |
| 525–532 | e8.3 | mW/m2 | c3_FLUX | ? EPIC flux in erg/cm2/s in observation c3(2) |
| 534–540 | e7.2 | mW/m2 | e_c3_FLUX | ? Error in c3_Flux |
| 542–546 | F5.2 | — | c3_HR1 | ? EPIC hardness ratio 1 in observation c3 (3) |
| 548–551 | F4.2 | — | e_c3_HR1 | ? Error in c3_HR1 |
| 553–557 | F5.2 | — | c3_HR2 | ? EPIC hardness ratio 2 in observation c3 (3) |
| 559–562 | F4.2 | — | e_c3_HR2 | ? Error in c3_HR2 |
| 564–568 | F5.2 | — | c3_HR3 | ? EPIC hardness ratio 3 in observation c3 (3) |
| 570–573 | F4.2 | — | e_c3_HR3 | ? Error in c3_HR3 |
| 575–579 | F5.2 | — | c3_HR4 | ? EPIC hardness ratio 4 in observation c3 (3) |
| 581–584 | F4.2 | — | e_c3_HR4 | ? Error in c3_HR4 |
| 586–588 | A3 | — | n1_val | ? EPIC instruments contributing to source detection in observation n1 (4) |
| 590–597 | e8.3 | ct/s | n1_RATE | ? EPIC count rate in observation n1 (2) |
| 599–605 | e7.2 | ct/s | e_n1_RATE | ? Error in n1_Rate |
| 607–614 | e8.3 | mW/m2 | n1_FLUX | ? EPIC flux in erg/cm2/s in observation n1(2) |
| 616–622 | e7.2 | mW/m2 | e_n1_FLUX | ? Error in n1_Flux |
| 624–628 | F5.2 | — | n1_HR1 | ? EPIC hardness ratio 1 in observation n1 (3) |
| 630–633 | F4.2 | — | e_n1_HR1 | ? Error in n1_HR1 |
| 635–639 | F5.2 | — | n1_HR2 | ? EPIC hardness ratio 2 in observation n1 (3) |
| 641–644 | F4.2 | — | e_n1_HR2 | ? Error in n1_HR2 |
| 646–650 | F5.2 | — | n1_HR3 | ? EPIC hardness ratio 3 in observation n1 (3) |
| 652–655 | F4.2 | — | e_n1_HR3 | ? Error in n1_HR3 |
| 657–661 | F5.2 | — | n1_HR4 | ? EPIC hardness ratio 4 in observation n1 (3) |
| 663–666 | F4.2 | — | e_n1_HR4 | ? Error in n1_HR4 |
| 668–670 | A3 | — | c4_val | ? EPIC instruments contributing to source detection in observation c4 (4) |
| 672–679 | e8.3 | ct/s | c4_RATE | ? EPIC count rate in observation c4 (2) |
| 681–687 | e7.2 | ct/s | e_c4_RATE | ? Error in c4_Rate |
| 689–696 | e8.3 | mW/m2 | c4_FLUX | ? EPIC flux in erg/cm2/s in observation c4(2) |
| 698–704 | e7.2 | mW/m2 | e_c4_FLUX | ? Error in c4_Flux |
| 706–710 | F5.2 | — | c4_HR1 | ? EPIC hardness ratio 1 in observation c4 (3) |
| 712–715 | F4.2 | — | e_c4_HR1 | ? Error in c4_HR1 |
| 717–721 | F5.2 | — | c4_HR2 | ? EPIC hardness ratio 2 in observation c4 (3) |
| 723–726 | F4.2 | — | e_c4_HR2 | ? Error in c4_HR2 |
| 728–732 | F5.2 | — | c4_HR3 | ? EPIC hardness ratio 3 in observation c4 (3) |
| 734–737 | F4.2 | — | e_c4_HR3 | ? Error in c4_HR3 |
| 739–743 | F5.2 | — | c4_HR4 | ? EPIC hardness ratio 4 in observation c4 (3) |
| 745–748 | F4.2 | — | e_c4_HR4 | ? Error in c4_HR4 |
| 750–752 | A3 | — | s1_val | ? EPIC instruments contributing to source detection in observation s1 (4) |
| 754–761 | e8.3 | ct/s | s1_RATE | ? EPIC count rate in observation s1 (2) |
| 763–769 | e7.2 | ct/s | e_s1_RATE | ? Error in s1_Rate |

**Table C.2:** continued.

| Bytes | Format | Units | Label | Explanations |
|---|---|---|---|---|
| 771–778 | e8.3 | mW/m2 | s1_FLUX | ? EPIC flux in erg/cm2/s in observation s1(2) |
| 780–786 | e7.2 | mW/m2 | e_s1_FLUX | ? Error in s1_Flux |
| 788–792 | F5.2 | — | s1_HR1 | ? EPIC hardness ratio 1 in observation s1 (3) |
| 794–797 | F4.2 | — | e_s1_HR1 | ? Error in s1_HR1 |
| 799–803 | F5.2 | — | s1_HR2 | ? EPIC hardness ratio 2 in observation s1 (3) |
| 805–808 | F4.2 | — | e_s1_HR2 | ? Error in s1_HR2 |
| 810–814 | F5.2 | — | s1_HR3 | ? EPIC hardness ratio 3 in observation s1 (3) |
| 816–819 | F4.2 | — | e_s1_HR3 | ? Error in s1_HR3 |
| 821–825 | F5.2 | — | s1_HR4 | ? EPIC hardness ratio 4 in observation s1 (3) |
| 827–830 | F4.2 | — | e_s1_HR4 | ? Error in s1_HR4 |
| 832–834 | A3 | — | b_val | ? EPIC instruments contributing to source detection in observation b (4) |
| 836–843 | e8.3 | ct/s | b_RATE | ? EPIC count rate in observation b (2) |
| 845–851 | e7.2 | ct/s | e_b_RATE | ? Error in b_Rate |
| 853–860 | e8.3 | mW/m2 | b_FLUX | ? EPIC flux in erg/cm2/s in observation b (2) |
| 862–868 | e7.2 | mW/m2 | e_b_FLUX | ? Error in b_Flux |
| 870–874 | F5.2 | — | b_HR1 | ? EPIC hardness ratio 1 in observation b (3) |
| 876–879 | F4.2 | — | e_b_HR1 | ? Error in b_HR1 |
| 881–885 | F5.2 | — | b_HR2 | ? EPIC hardness ratio 2 in observation b (3) |
| 887–890 | F4.2 | — | e_b_HR2 | ? Error in b_HR2 |
| 892–896 | F5.2 | — | b_HR3 | ? EPIC hardness ratio 3 in observation b (3) |
| 898–901 | F4.2 | — | e_b_HR3 | ? Error in b_HR3 |
| 903–907 | F5.2 | — | b_HR4 | ? EPIC hardness ratio 4 in observation b (3) |
| 909–912 | F4.2 | — | e_b_HR4 | ? Error in b_HR4 |
| 914 | I1 | — | ndet | Number of observations covering the source |
| 916–920 | F5.2 | — | svar_max | Maximum significance of variation |
| 922–926 | F5.2 | — | fvar_max | Maximum flux ratio |
| 928 | I1 | — | n_upper | Number of upper limits |
| 930–937 | e8.3 | mW/m2 | fmax | Maximum flux |
| 939–945 | e7.2 | mW/m2 | e_fmax | Error in fmax |
| 947–971 | A25 | — | IAU_NAME | Source Name XMMM31 Jhhmmss.s+ddmmss |

Note (1): Source numbers from Table 2 in Pietsch et al., 2005A&A...434..483P and Table 6.3 in this thesis
Note (2): Count rate and flux in XID band (0.2-4.5keV)
Note (3): HRi=(R(i+1)-R(i))/(R(i+1)+R(i)) where Ri are the count rates in the energy bands 1 to 5 and
band 1 = 0.2–0.5keV,
band 2 = 0.5–1.0keV,
band 3 = 1.0–2.0keV,
band 4 = 2.0–4.5keV,
band 5 = 4.5–12keV

Note (4): First character for EPIC PN, second for MOS1, third for MOS2;
character = T : source is in field of view of instrument
F : otherwise

Note (5): References in XID:

| | |
|---|---|
| TF91 : | Trinchieri et al., 1991ApJ...382...82T |
| CRP90 : | Collura et al., 1990ApJ...356..119C |
| PFJ93 : | Primini et al., 1993ApJ...410..615P |
| SHP97 : | Supper et al., 1997A&A...317..328S |
| CXOGMP Jhhmmss.s+ddmmss: | Garcia et al., 2000ApJ...537L..23G |
| SHL2001 : | Supper et al., 2001A&A...373...63S |
| OBT2001 : | Osborne et al., 2001A&A...378..800O |
| am-n : | Kong et al., 2002ApJ...577..738K |
| | Di Stefano et al., 2004ApJ...610..247D |
| | Williams et al., 2004ApJ...609..735W |
| | Williams et al., 2006ApJ...637..479W |
| | Williams et al., 2005ApJ...632.1086W |
| DKG2002 : | Di Stefano et al., 2002ApJ...570..618D |
| Jhhmmss.s+ddmmss : | Kaaret, 2002ApJ...578..114K |
| | Di Stefano et al., 2002ApJ...570..618D |
| | Trudolyubov et al., 2006ApJ...645..277T |
| TKP2004 : | Trudolyubov et al., 2005ApJ...634..314T |
| PHS2007 : | Pietsch et al., 2007A&A...465..375P |
| FMZ2005 : | Fan et al., 2005PASP...117.1236F |
| VG2007 : | Voss et al., 2007A&A...468...49V |
| XMMU Jhhmmss.s+ddmmss : | Trudolyubov et al., 2006ApJ...645..277T |
| TPC2006b : | Trudolyubov et al., astro-ph/0610809 |

Note (6): Classifications used (see Table 7.3)
fg Star = foreground star
<fg Star> = foreground star candidate
AGN = active galactic nucleus
<AGN> = AGN candidate
Gal = galaxy
<Gal> = galaxy candidate
GCl = galaxy cluster
<GCl> = galaxy cluster candidate
SSS = supersoft source in M 31
<SSS> = supersoft source candidate in M 31
SNR = supernova remnant in M 31
<SNR> = supernova remnant candidate in M 31
GlC = source in globular cluster
<GlC> = source in globular cluster candidate
XRB = X-ray binary in M 31
<XRB> = X-ray binary candidate in M 31
<hard> = HR2-e_HR2>-0.2 or only HR3 and HR4 defined, and no other classification

Note (7): References in remarks:

| | |
|---|---|
| SIM : | SIMBAD Database |
| NED : | NASA Extragalactic Database |
| NVSS : | Condon et al., 1998AJ....115.1693C |
| mitann : | Magnier, 1993, Ph.D. thesis, MIT |
| H29 : | Hubble, 1929ApJ....69..103H |
| R73 : | Rosino, 1973A&AS....9..347R |
| PAV78 : | Pellet et al., 1978A&AS...31..439P |
| DDB80 : | Dodorico et al., 1980A&AS...40...67D |
| WSB85 : | Wirth et al., 1985ApJ...290..140W |
| CFN87 : | Ciardullo et al., 1987ApJ...318..520C |
| BHG88 : | Berkhuijsen et al., 1988A&AS...76...65B |
| HPJ88 : | Humphreys et al., 1988AJ.....96.1884H |
| B90 : | Braun, 1990ApJS...72..761B |
| WB92a : | Walterbos & Braun, 1992A&AS...92..625W |
| BW93 : | Braun & Walterbos, 1993A&AS...98..327B |
| MLA93 : | Meyssonnier et al., 1993A&AS..102..251M |
| MPV95 : | Magnier et al., 1995A&AS..114..215M |
| HIB95 : | Hill et al., 1995ApJS...98..595H |
| TC96 : | Tomaney & Crotts, 1996AJ....112.2872T |
| M98a : | Massey, 1998ApJ...501..153M |
| SK98 : | Shokin & Kulagina, 1998PAZh...24...93S |
| KSK98 : | Kaluzny et al., 1998AJ....115.1016K |
| BBH98 : | Beck et al., 1998A&AS..129..329B |
| SKK99 : | Stanek et al., 1999AJ....117.2810S |
| OBT2001 : | Osborne et al., 2001A&A...378..800O |
| TBP2001 : | Trudolyubov et al., 2001ApJ...563L.119T |
| SI2001 : | Shafter & Irby, 2001ApJ...563..749S |
| KPM2002 : | Kraemer et al., 2002AJ....124.2990K |
| K2002 : | Kaaret, 2002ApJ...578..114K |
| TBP2002 : | Trudolyubov et al., 2002ApJ...581L..27T |
| KGP2002 : | Kong et al., 2002ApJ...580L.125K |
| TPB2002 : | Trudolyubov et al., 2002IAUC.7798....2T |
| BOK2003 : | Barnard et al., 2003A&A...405..505B |
| BKO2003 : | Barnard et al., 2003A&A...411..553B |
| KTV2003 : | Kotov et al., 2006ApJ...641..756K |
| WGK2004 : | Williams et al., 2004ApJ...609..735W |
| WSK2004 : | Williams et al., 2004ApJ...615..720W |
| BKO2004 : | Barnard et al., 2004A&A...423..147B |
| MIS2004 : | Mangano et al., 2004A&A...419.1045M |
| TKP2004 : | Trudolyubov et al., 2005ApJ...634..314T |
| GLGnnn : | Gelfand et al., 2004ApJS..155...89G |
| KSW2003 : | Kong et al., 2003ApJ...590L..21K |
| JPN2003 : | Joshi et al., 2003A&A...402..113J |
| PHS2007 : | Pietsch et al., 2007A&A...465..375P |
| SKHV : | Sargent et al., 1977AJ.....82..947S |

| | |
|---|---|
| | Holland et al., 1995AJ....109.2061H |
| WGC2006 : | Williams et al., 2006ApJ...637..479W |
| WGC2005 : | Williams et al., 2005ApJ...632.1086W |
| TPC2006a : | Trudolyubov et al., 2006ApJ...645..277T |
| GFB2004 : | Galetti et al., 2004A&A...416..917G |
| VG2007 : | Voss et al., 2007A&A...468...49V |
| KLG2007 : | Kim et al., 2007AJ....134..706K |
| B : | Battistini et al., 1980A&AS...42..357B |
| | Battistini et al., 1987A&AS...67..447B |
| | Galleti et al., 2005A&A...436..535G |

# Appendix D

# Description of Tables 7.2 and 7.5

Table 7.2 presents the source catalogue of the large *XMM-Newton* survey of M 31 (XMM LP-total catalogue). It contains 1 948 X-ray sources, of which 961 sources are detected in X-rays for the first time. 40 sources are identified as SSS candidates, 25 as SNRs, 37 as SNR candidates, 10 as XRBs, 26 as XRB candidates, 36 as X-ray sources located in globular clusters and 17 as X-ray sources in globular cluster candidates. In addition there are 266 foreground stars and candidates and 89 background objects. 1 263 sources can only be classified as <hard>, while 139 sources remain unidentified and without classification.

Table 7.5 provides all information necessary to examine time variability – in particular the flux variability factors and significance of variability – for all sources of the XMM LP-total catalogue that are observed at least twice. Out of the 1 443 examined sources, 317 sources have a significance for variability $> 3.0$. These are 182 additional sources compared with Table 6.5.

**Table D.1:** Read Me file for Table 7.2

| Bytes | Format | Units | Label | Explanations |
|---|---|---|---|---|
| 1– 4 | I4 | — | [XMMLPt] | Source Number |
| 6– 10 | A5 | — | M31_ID | M 31 field identification |
| 11– 12 | I2 | h | RAh | Right Ascension J2000 (hours) |
| 14– 15 | I2 | min | RAm | Right Ascension J2000 (minutes) |
| 17– 21 | F5.2 | s | RAs | Right Ascension J2000 (seconds) |
| 24 | A1 | — | DE- | Declination J2000 (sign) |
| 25– 26 | I2 | deg | DEd | Declination J2000 (degrees) |
| 28– 29 | I2 | arcmin | DEm | Declination J2000 (minutes) |
| 31– 34 | F4.1 | arcsec | DEs | Declination J2000 (seconds) |
| 36– 40 | F5.2 | arcsec | PosErr | Positional error (1) |
| 42– 49 | E8.2 | — | LH | Source detection likelihood (combined EPIC) |
| 51– 58 | E8.2 | ct/s | CRate | Combined EPIC count rate (2) |
| 60– 66 | E7.1 | ct/s | e_CRate | Error in CRate |
| 68– 75 | E8.2 | mW/m2 | CFlux | Combined EPIC flux in erg/cm2/s (2) |
| 77– 83 | E7.1 | mW/m2 | e_CFlux | Error in CFlux |
| 85– 89 | F5.2 | — | CHR1 | ? Combined EPIC hardness ratio 1 (3) |
| 91– 94 | F4.2 | — | e_CHR1 | ? Error in CHR1 |

**Table D.1:** continued.

| Bytes | Format | Units | Label | Explanations |
|---|---|---|---|---|
| 96–100 | F5.2 | — | CHR2 | ? Combined EPIC hardness ratio 2 (3) |
| 102–105 | F4.2 | — | e_CHR2 | ? Error in CHR2 |
| 107–111 | F5.2 | — | CHR3 | ? Combined EPIC hardness ratio 3 (3) |
| 113–116 | F4.2 | — | e_CHR3 | ? Error in CHR3 |
| 118–122 | F5.2 | — | CHR4 | ? Combined EPIC hardness ratio 4 (3) |
| 124–127 | F4.2 | — | e_CHR4 | ? Error in CHR4 |
| 129–131 | A3 | — | VAL | EPIC instruments contributing to source detection (4) |
| 133–137 | F5.1 | ks | PN_Expo | ? Exposure of EPIC pn instrument |
| 139–146 | E8.2 | — | PN_LH | ? EPIC pn source detection likelihood |
| 148–155 | E8.2 | ct/s | PNRate | ? EPIC pn count rate (2) |
| 157–163 | E7.1 | ct/s | e_PNRate | ? Error in PNRate |
| 165–172 | E8.2 | mW/m2 | PNFlux | ? EPIC pn flux in erg/cm2/s (2) |
| 174–180 | E7.1 | mW/m2 | e_PNFlux | ? Error in PNFlux |
| 182–186 | F5.2 | — | PNHR1 | ? EPIC pn hardness ratio 1 (3) |
| 188–191 | F4.2 | — | e_PNHR1 | ? Error in PNHR1 |
| 193–197 | F5.2 | — | PNHR2 | ? EPIC pn hardness ratio 2 (3) |
| 199–202 | F4.2 | — | e_PNHR2 | ? Error in PNHR2 |
| 204–208 | F5.2 | — | PNHR3 | ? EPIC pn hardness ratio 3 (3) |
| 210–213 | F4.2 | — | e_PNHR3 | ? Error in PNHR3 |
| 215–219 | F5.2 | — | PNHR4 | ? EPIC pn hardness ratio 4 (3) |
| 221–224 | F4.2 | — | e_PNHR4 | ? Error in PNHR4 |
| 226–230 | F5.1 | ks | M1_Expo | ? Exposure of EPIC MOS1 instrument |
| 232–239 | E8.2 | — | M1_LH | ? EPIC MOS1 source detection likelihood |
| 241–248 | E8.2 | ct/s | M1Rate | ? EPIC MOS1 count rate (2) |
| 250–256 | E7.1 | ct/s | e_M1Rate | ? Error in M1Rate |
| 258–265 | E8.2 | mW/m2 | M1Flux | ? EPIC MOS1 flux in erg/cm2/s (2) |
| 267–273 | E7.1 | mW/m2 | e_M1Flux | ? Error in M1Flux |
| 275–279 | F5.2 | — | M1HR1 | ? EPIC MOS1 hardness ratio 1 (3) |
| 281–284 | F4.2 | — | e_M1HR1 | ? Error in M1HR1 |
| 286–290 | F5.2 | — | M1HR2 | ? EPIC MOS1 hardness ratio 2 (3) |
| 292–295 | F4.2 | — | e_M1HR2 | ? Error in M1HR2 |
| 297–301 | F5.2 | — | M1HR3 | ? EPIC MOS1 hardness ratio 3 (3) |
| 303–306 | F4.2 | — | e_M1HR3 | ? Error in M1HR3 |
| 308–312 | F5.2 | — | M1HR4 | ? EPIC MOS1 hardness ratio 4 (3) |
| 314–317 | F4.2 | — | e_M1HR4 | ? Error in M1HR4 |
| 319–323 | F5.1 | ks | M2_Expo | ? Exposure of EPIC MOS2 instrument |
| 325–332 | E8.2 | — | M2_LH | ? EPIC MOS2 source detection likelihood |
| 334–341 | E8.2 | ct/s | M2Rate | ? EPIC MOS2 count rate (2) |
| 343–349 | E7.1 | ct/s | e_M2Rate | ? Error in M2Rate |
| 351–358 | E8.2 | mW/m2 | M2Flux | ? EPIC MOS2 flux in erg/cm2/s (2) |
| 360–366 | E7.1 | mW/m2 | e_M2Flux | ? Error in M2Flux |
| 368–372 | F5.2 | — | M2HR1 | ? EPIC MOS2 hardness ratio 1 (3) |

**Table D.1:** continued.

| Bytes | Format | Units | Label | Explanations |
|---|---|---|---|---|
| 374–377 | F4.2 | — | e_M2HR1 | ? Error in M2HR1 |
| 379–383 | F5.2 | — | M2HR2 | ? EPIC MOS2 hardness ratio 2 (3) |
| 385–388 | F4.2 | — | e_M2HR2 | ? Error in M2HR2 |
| 390–394 | F5.2 | — | M2HR3 | ? EPIC MOS2 hardness ratio 3 (3) |
| 396–399 | F4.2 | — | e_M2HR3 | ? Error in M2HR3 |
| 401–405 | F5.2 | — | M2HR4 | ? EPIC MOS2 hardness ratio 4 (3) |
| 407–410 | F4.2 | — | e_M2HR4 | ? Error in M2HR4 |
| 412–706 | A282 | — | XID | ? X-ray identification (5) |
| 708–719 | A12 | — | USNO_B1.0 | ? Name of brightest USNO-B1.0 source within search area |
| 721–722 | I2 | — | USNO_Mul | ? Number of USNO-B1.0 correlations |
| 724–727 | F3.1 | arcsec | USNO_dis | ? Distance of source USNO-B1.0 |
| 729–732 | F4.1 | mag | USNO_B2 | ? B2 magnitude of source USNO-B1.0 |
| 734–737 | F4.1 | mag | USNO_R2 | ? R2 magnitude of source USNO-B1.0 |
| 739–742 | F4.1 | mag | USNO_I | ? I magnitude of source USNO-B1.0 |
| 744–759 | A16 | — | 2MASS | ? Name of brightest 2MASS source within search area |
| 761 | I1 | — | 2MASS_Mul | ? Number of 2MASS correlations |
| 763–766 | F4.1 | arcsec | 2MASS_dis | ? Distance of source 2MASS |
| 768–786 | A19 | — | LGS | ? Name of brightest LGS source within search area |
| 788–790 | I3 | — | LGS_Mul | ? Number of LGS correlations |
| 792–794 | F3.1 | arcsec | LGS_dis | ? Distance of source LGS |
| 796–799 | F4.1 | mag | LGS_V | ? V magnitude of source LGS |
| 801–804 | F4.1 | mag | LGS_V-R | ? V-R colour of source LGS |
| 806–809 | F4.1 | mag | LGS_B-V | ? B-V colour of source LGS |
| 811–814 | F4.1 | — | log_fxo | ? Logarithm of fX/fopt |
| 816–819 | F4.1 | — | log_fxob | ? Logarithm of fX/fopt (blue) |
| 821–824 | F4.1 | — | log_fxor | ? Logarithm of fX/fopt (red) |
| 826–829 | F4.1 | — | log_fxov | ? Logarithm of fX/fopt (LGS) |
| 831–839 | A9 | — | Class | ? Classification of X-ray source (6) |
| 841–988 | A148 | — | Remarks | ? Additional remarks (6,7) |
| 990–1014 | A25 | — | IAU_NAME | Source Name XMMM31 Jhhmmss.s+ddmmss |

Note (1): 3 sigma error (99.73%; both, statistical and systematic, errors included)
Note (2): Count rate and flux in XID band (0.2–4.5 keV)
Note (3): HRi=(R(i+1)-R(i))/(R(i+1)+R(i)) where R(i) are the count rates in the energy bands 1 to 5 and
band 1 = 0.2–0.5keV,
band 2 = 0.5–1.0keV,
band 3 = 1.0–2.0keV,
band 4 = 2.0–4.5keV,
band 5 = 4.5–12keV

Note (4): First character for EPIC PN, second for MOS1, third for MOS2;
character = T: source is in field of view of instrument
F: otherwise

Note (5): References in XID:

| | |
|---|---|
| [DKG2002]: | Di Stefano et al., 2002ApJ...570..618D |
| [DKG2004]: | Di Stefano et al., 2004ApJ...610..247D |
| [GMP2000]: | Garcia et al., 2000ApJ...537L..23G |
| [K2002]: | Kaaret, 2002ApJ...578..114K |
| [KGP2002]: | Kong et al., 2002ApJ...577..738K |
| [KGPM02]: | Kong et al., 2002ApJ...580L.125K |
| [KSW2003]: | Kong et al., 2003ApJ...590L..21K |
| [O2006,i]: | Orio, 2006ApJ...643..844O; Table i |
| [OBT2001]: | Osborne et al, 2001A&A...378..800O |
| [PFH2005]: | Pietsch et al., 2005A&A...434..483P |
| [PFJ93]: | Primini et al., 1993ApJ...410..615P |
| [SBK2009]: | Shaw-Greening et al., 2009A&A...495..733S |
| [SHL2001]: | Supper et al., 2001A&A...373...63S |
| [SHP97]: | Supper et al., 1997A&A...317..328S |
| [SPH2008]: | Stiele et al., 2008A&A...480..599S |
| [TBP2001]: | Trudolyubov et al., 2001ApJ...563L.119T |
| [TF91]: | Trinchieri et al., 1991ApJ...382...82T |
| [TP2004]: | Trudolyubov et al., 2004ApJ...616..821T |
| [TPC2006]: | Trudolyubov et al., 2006astro.ph.10809T |
| [TPC2006a]: | Trudolyubov et al., 2006ApJ...645..277T |
| [VG2007]: | Voss et al., 2007A&A...468...49V |
| [WGK2004]: | Williams et al., 2004ApJ...609..735W |
| [WSK2004]: | Williams et al., 2004ApJ...615..720W |
| [WGC2005]: | Williams et al., 2005ApJ...632.1086W |
| [WNG2006]: | Williams et al., 2006ApJ...637..479W |
| v: | variable |
| sv, SV: | spectral variable |
| t, TR: | transient |
| REC: | recurrent |
| Bur: | source shows a burst/bursts |
| DIP: | source shows a dip/dips |

Note (6): Classifications used (see Table 7.3)
fg Star = foreground star
<fg Star> = foreground star candidate
AGN = active galactic nucleus
<AGN> = AGN candidate
Gal = galaxy
<Gal> = galaxy candidate
GCl = galaxy cluster
<GCl> = galaxy cluster candidate
SSS = supersoft source in M 31
<SSS> = supersoft source candidate in M 31

SNR = supernova remnant in M 31
<SNR> = supernova remnant candidate in M 31
GlC = source in globular cluster
<GlC> = source in globular cluster candidate
XRB = X-ray binary in M 31
<XRB> = X-ray binary candidate in M 31
<hard> = HR2−e_HR2>-0.2 or only HR3 and HR4 defined, and no other classification

Note (7): References in remarks:

| | |
|---|---|
| 2MASX: | Skrutskie et al., 2006AJ....131.1163S |
| 5C 3.nn: | Pooley, 1969MNRAS.144..101P |
| [B90]: | Braun, 1990ApJS...72..761B |
| [BA64] : | Baade & Arp, 1964ApJ...139.1027B |
| [BA87]: | Battistini et al., 1987A&AS...67..447B |
| BD: | Argelander, 1903BD....C.....0A |
| | Schonfeld, 1886BD....C.....0S |
| [BHG88]: | Berkhuijsen et al., 1988A&AS...76...65B |
| [BHP2009]: | Bonfini et al., 2009A&A...507..705B |
| [BKO2003]: | Barnard et al., 2003A&A...411..553B |
| [Br1992]: | Walterbos & Braun, 1992A&AS...92..625W |
| | Braun & Walterbos, 1993A&AS...98..327B |
| [BSH2008]: | Barnard et al., 2008ApJ...689.1215B |
| BW93: | Braun & Walterbos, 1993A&AS...98..327B |
| CCDM: | Dommanget, 1983BICDS..24...83D |
| | Dommanget & Nys, 1994CoORB.115....1D |
| [CHM09]: | Caldwell et al., 2009AJ....137...94C |
| DDB80: | Dodorico et al., 1980A&AS...40...67D |
| [FMZ2005]: | Fan et al., 2005PASP..117.1236F |
| [FRS2006]: | Fliri et al., 2006A&A...445..423F |
| [GFB2004]: | Galetti et al., 2004A&A...416..917G |
| [GGS2007]: | Galache et al., 2007ATel.1147....1G |
| GLG: | Gelfand et al., 2005ApJS..159..242G |
| | Gelfand et al., 2004ApJS..155...89G |
| GPM: | Rybka & Yatsenko, 1997KFNT...13e..70R |
| [H29]: | Hubble, 1929ApJ....69..103H |
| HD: | Cannon & Pickering, 1918AnHar..91....1C |
| [HIB95]: | Hill et al., 1995ApJS...98..595H |
| [HKB2009]: | Hodge et al, 2009AJ....138..770H |
| [HPJ88]: | Humphreys et al., 1988AJ.....96.1884H |
| [HPH2009]: | Henze et al., 2009A&A...500..769H |
| [HPM06]: | Hatzidimitriou et al., 2006A&A...451..835H |
| [JPN2003]: | Joshi et al., 2003A&A...402..113J |
| [K2002]: | Kaaret, 2002ApJ...578..114K |
| [KGP2002]: | Kong et al., 2002ApJ...577..738K |
| KHM31: | Krienke & Hodge, 2008PASP..120....1K |
| | Krienke & Hodge, 2007PASP..119....7K |
| [KLG2007]: | Kim et al., 2007AJ....134..706K |

| | |
|---|---|
| [KMV98]: | Kodaira et al., 1998ApJS..118..177K |
| [KPM2002]: | Kraemer et al., 2002AJ....124.2990K |
| [KSK98]: | Kaluzny et al., 1998AJ....115.1016K |
| [KTV2006]: | Kotov et al., 2006ApJ...641..756K |
| LGS, LGGS: | Local Group Survey |
| MA93, [Ma93], mita: | Magnier, 1993, 1993PhDT.....41M |
| [MBG2008,i]: | Mould et al., 2008ApJ...687..230M; Table i |
| [MIS2004]: | Mangano et al., 2004A&A...419.1045M |
| [MLA93]: | Meyssonnier et al., 1993A&AS..102..251M |
| [MLV92]: | Magnier et al., 1992A&AS...96..379M<br>Haiman et al., 1994A&A...286..725H |
| [MPV95]: | Magnier et al., 1995A&AS..114..215M |
| [MS83]: | Moffat & Shara, 1983ApJ...273..544M |
| [MSH2004]: | Mould et al., 2004ApJS..154..623M |
| MY: | Zhang et al., 1993A&AS...99..545Z |
| NED: | NASA Extragalactic Database |
| [NKS2001]: | Nowotny et al., 2001A&A...367..557N |
| [NTK96]: | Nedialkov et al., 1996IBVS.4411....1N |
| NVSS: | Condon et al., 1998AJ....115.1693C |
| [OBT2001]: | Osborne et al., 2001A&A...378..800O |
| [PAV78]: | Pellet et al., 1978A&AS...31..439P |
| [PFF2005]: | Pietsch et al., 2005A&A...442..879P |
| [PFH2005]: | Pietsch et al., 2005A&A...434..483P |
| [PH2004]: | Pietsch & Haberl, 2005A&A...430L..45P |
| [PHS2007]: | Pietsch et al., 2007A&A...465..375P |
| Pul: | Khrutskaya et al., 2004A&A...418..357K |
| [R73]: | Rosino, 1973A&AS....9..347R |
| RadioS: | Kimball & Ivezić, 2008AJ....136..684K |
| RBC3.5: | Galleti et al., 2004A&A...416..917G, 2005A&A...436..535G,<br>2006A&A...456..985G, 2007A&A...471..127G |
| [SAZ2006]: | Smirnova et al., 2006IBVS.5737....1S |
| [SD2009]: | Samus et al., 2009yCat....102025S |
| [SK98]: | Shokin & Kulagina, 1998PAZh...24...93S |
| [SKK99]: | Stanek et al., 1999AJ....117.2810S |
| SIM: | SIMBAD Database |
| [TBP2001]: | Trudolyubov et al., 2001ApJ...563L.119T |
| [TBP2002]: | Trudolyubov et al., 2002ApJ...581L..27T |
| [TKP2004]: | Trudolyubov et al., 2005ApJ...634..314T |
| [TP2008]: | Trudolyubov et al., 2008ApJ...676.1218T |
| [TPB2002]: | Trudolyubov et al., 2002IAUC.7798....2T |
| [TPC2006]: | Trudolyubov et al., 2006astro.ph.10809T |
| [TPC2006a]: | Trudolyubov et al., 2006ApJ...645..277T |
| TYC: | Høg et al., 2000A&A...355L..27H |
| USNO-B1: | United States Naval Observatory all sky catalogue |
| [WB92a]: | Walterbos & Braun, 1992A&AS...92..625W |
| [WGC2005]: | Williams et al., 2005ApJ...632.1086W |
| [WGC2006]: | Williams et al., 2006ApJ...637..479W |

| | |
|---|---|
| [WGK2004]: | Williams et al., 2004ApJ...609..735W |
| [WNG2006]: | Williams et al., 2006ApJ...643..356W |
| [WSB85]: | Wirth et al., 1985ApJ...290..140W |
| [WSK2004]: | Williams et al., 2004ApJ...615..720W |
| WSTB 36W: | Bystedt et al., 1984A&AS...56..245B |
| WSTB 37W: | Walterbos et al., 1985A&AS...61..451W |
| [V62]: | Vetešnik, 1962BAICz..13..180V |
| [VG2007]: | Voss & Gilfanov 2007A&A...468...49V |
| [VRJ2006]: | Vilardell et al., 2006A&A...459..321V |
| BH: | black hole |
| BHC: | black hole candidate |
| BKG: | background AGN |
| BL Lac: | special type of AGN where the jet points to the observer |
| cand. : | candidate |
| corr. : | correlation |
| EmO: | emission line object |
| Em*: | emission line star |
| F0, F2, F5, F6, F7, F8: | spectral stellar types |
| f, FGS: | foreground star |
| FoV: | field of view |
| FRI: | radio galaxy, whose core-dominated radio emission is powered by a central AGN |
| FRII: | radio galaxy, whose lobe-dominated radio emission is powered by a central AGN |
| G0, G2, G6, G8, G9: | spectral stellar types |
| g, GCC, Gl?: | globular cluster candidate |
| GCS: | globular cluster source |
| Ha: | H alpha |
| HFV: | high-frequency variable |
| HR: | hardness ratio |
| HzRG: | high-z radio galaxy |
| IR-S, IR: | infra-red source |
| K0, K1, K2, K3: | spectral stellar type |
| LFV: | low-frequency variable |
| LMXRB: | low mass X-ray binary |
| M1 V : | spectral stellar type |
| na: | probably a cluster, but not sure what type |
| NULL: | source without classification |
| PM star: | high proper-motion star |
| PN: | planetary nebula |
| PWN: | pulsar wind nebula |
| QSO: | quasi stellar object |
| Seyfert 1: | AGN located in spiral or irregular galaxy that show broad lines |
| src: | source |
| UV: | ultraviolet emission source |
| WeCAPP: | Wendelstein Calar Alto Pixellensing Project |
| WR star: | Wolf-Rayet star |

Z-source: Low-mass X-ray binary that is named after the pattern traced on its colour-colour diagram.

**Table D.2:** Read Me file for Table 7.5

| Bytes | Format | Units | Label | Explanations |
|---|---|---|---|---|
| 1– 4 | I4 | — | [XMMLPt] | Source Number (1) |
| 6– 13 | e8.3 | mW/m2 | CFLUX | Combined EPIC flux in erg/cm2/s (2) |
| 15– 21 | e7.2 | mW/m2 | e_CFLUX | Error in CFlux |
| 23– 27 | F5.2 | — | HR1 | ? Combined EPIC hardness ratio 1 (3) |
| 29– 32 | F4.2 | — | HR1_ERR | ? Error in CHR1 |
| 34– 38 | F5.2 | — | HR2 | ? Combined EPIC hardness ratio 2 (3) |
| 40– 43 | F4.2 | — | HR2_ERR | ? Error in CHR2 |
| 45– 49 | F5.2 | — | HR3 | ? Combined EPIC hardness ratio 3 (3) |
| 51– 54 | F4.2 | — | HR3_ERR | ? Error in CHR3 |
| 56– 60 | F5.2 | — | HR4 | ? Combined EPIC hardness ratio 4 (3) |
| 62– 65 | F4.2 | — | HR4_ERR | ? Error in CHR4 |
| 67– 85 | A19 | — | type | ? Classification of X-ray source (5) |
| 87– 91 | A5 | — | obs1 | Observation 1 |
| 93– 95 | A3 | — | obs1_val | EPIC instruments contributing to source detection in observation 1 (4) |
| 97– 104 | e8.3 | ct/s | obs1_RATE | ? EPIC count rate in observation 1 (2) |
| 106– 112 | e7.2 | ct/s | obs1_ERATE | ? Error in obs1_Rate |
| 114– 121 | e8.3 | mW/m2 | obs1_FLUX | ? EPIC flux in erg/cm2/s in observation 1(2) |
| 123– 129 | e7.2 | mW/m2 | obs1_EFLUX | ? Error in obs1_Flux |
| 131– 135 | F5.2 | — | obs1_HR1 | ? EPIC hardness ratio 1 in observation 1 (3) |
| 137– 140 | F4.2 | — | obs1_EHR1 | ? Error in obs1_HR1 |
| 142– 146 | F5.2 | — | obs1_HR2 | ? EPIC hardness ratio 2 in observation 1 (3) |
| 148– 151 | F4.2 | — | obs1_EHR2 | ? Error in obs1_HR2 |
| 153– 157 | F5.2 | — | obs1_HR3 | ? EPIC hardness ratio 3 in observation 1 (3) |
| 159– 162 | F4.2 | — | obs1_EHR3 | ? Error in obs1_HR3 |
| 164– 168 | F5.2 | — | obs1_HR4 | ? EPIC hardness ratio 4 in observation 1 (3) |
| 170– 173 | F4.2 | — | obs1_EHR4 | ? Error in obs1_HR4 |
| 175– 179 | A5 | — | obs2 | Observation 2 |
| 181– 183 | A3 | — | obs2_val | EPIC instruments contributing to source detection in observation 2 (4) |
| 185– 192 | e8.3 | ct/s | obs2_RATE | ? EPIC count rate in observation 2 (2) |
| 194– 200 | e7.2 | ct/s | obs2_ERATE | ? Error in obs2_Rate |
| 202– 209 | e8.3 | mW/m2 | obs2_FLUX | ? EPIC flux in erg/cm2/s in observation 2(2) |
| 211– 217 | e7.2 | mW/m2 | obs2_EFLUX | ? Error in obs2_Flux |
| 219– 223 | F5.2 | — | obs2_HR1 | ? EPIC hardness ratio 1 in observation 2 (3) |
| 225– 228 | F4.2 | — | obs2_EHR1 | ? Error in obs2_HR1 |
| 230– 234 | F5.2 | — | obs2_HR2 | ? EPIC hardness ratio 2 in observation 2 (3) |
| 236– 239 | F4.2 | — | obs2_EHR2 | ? Error in obs2_HR2 |
| 241– 245 | F5.2 | — | obs2_HR3 | ? EPIC hardness ratio 3 in observation 2 (3) |
| 247– 250 | F4.2 | — | obs2_EHR3 | ? Error in obs2_HR3 |

**Table D.2:** continued.

| Bytes | Format | Units | Label | Explanations |
|---|---|---|---|---|
| 252– 256 | F5.2 | — | obs2_HR4 | ? EPIC hardness ratio 4 in observation 2 (3) |
| 258– 261 | F4.2 | — | obs2_EHR4 | ? Error in obs2_HR4 |
| 263– 267 | A5 | — | obs3 | ? Observation 3 |
| 269– 271 | A3 | — | obs3_val | ? EPIC instruments contributing to source detection in observation 3 (4) |
| 273– 280 | e8.3 | ct/s | obs3_RATE | ? EPIC count rate in observation 3 (2) |
| 282– 288 | e7.2 | ct/s | obs3_ERATE | ? Error in obs3_Rate |
| 290– 297 | e8.3 | mW/m2 | obs3_FLUX | ? EPIC flux in erg/cm2/s in observation 3(2) |
| 299– 305 | e7.2 | mW/m2 | obs3_EFLUX | ? Error in obs3_Flux |
| 307– 311 | F5.2 | — | obs3_HR1 | ? EPIC hardness ratio 1 in observation 3 (3) |
| 313– 316 | F4.2 | — | obs3_EHR1 | ? Error in obs3_HR1 |
| 318– 322 | F5.2 | — | obs3_HR2 | ? EPIC hardness ratio 2 in observation 3 (3) |
| 324– 327 | F4.2 | — | obs3_EHR2 | ? Error in obs3_HR2 |
| 329– 333 | F5.2 | — | obs3_HR3 | ? EPIC hardness ratio 3 in observation 3 (3) |
| 335– 338 | F4.2 | — | obs3_EHR3 | ? Error in obs3_HR3 |
| 340– 344 | F5.2 | — | obs3_HR4 | ? EPIC hardness ratio 4 in observation 3 (3) |
| 346– 349 | F4.2 | — | obs3_EHR4 | ? Error in obs3_HR4 |
| 351– 355 | A5 | — | obs4 | ? Observation 4 |
| 357– 359 | A3 | — | obs4_val | ? EPIC instruments contributing to source detection in observation 4 (4) |
| 361– 368 | e8.3 | ct/s | obs4_RATE | ? EPIC count rate in observation 4 (2) |
| 370– 376 | e7.2 | ct/s | obs4_ERATE | ? Error in obs4_Rate |
| 378– 385 | e8.3 | mW/m2 | obs4_FLUX | ? EPIC flux in erg/cm2/s in observation 4(2) |
| 387– 393 | e7.2 | mW/m2 | obs4_EFLUX | ? Error in obs4_Flux |
| 395– 399 | F5.2 | — | obs4_HR1 | ? EPIC hardness ratio 1 in observation 4 (3) |
| 401– 404 | F4.2 | — | obs4_EHR1 | ? Error in obs4_HR1 |
| 406– 410 | F5.2 | — | obs4_HR2 | ? EPIC hardness ratio 2 in observation 4 (3) |
| 412– 415 | F4.2 | — | obs4_EHR2 | ? Error in obs4_HR2 |
| 417– 421 | F5.2 | — | obs4_HR3 | ? EPIC hardness ratio 3 in observation 4 (3) |
| 423– 426 | F4.2 | — | obs4_EHR3 | ? Error in obs4_HR3 |
| 428– 432 | F5.2 | — | obs4_HR4 | ? EPIC hardness ratio 4 in observation 4 (3) |
| 434– 437 | F4.2 | — | obs4_EHR4 | ? Error in obs4_HR4 |
| 439– 443 | A5 | — | obs5 | ? Observation 5 |
| 445– 447 | A3 | — | obs5_val | ? EPIC instruments contributing to source detection in observation 5 (4) |
| 449– 456 | e8.3 | ct/s | obs5_RATE | ? EPIC count rate in observation 5 (2) |
| 458– 464 | e7.2 | ct/s | obs5_ERATE | ? Error in obs5_Rate |
| 466– 473 | e8.3 | mW/m2 | obs5_FLUX | ? EPIC flux in erg/cm2/s in observation 5(2) |
| 475– 481 | e7.2 | mW/m2 | obs5_EFLUX | ? Error in obs5_Flux |
| 483– 487 | F5.2 | — | obs5_HR1 | ? EPIC hardness ratio 1 in observation 5 (3) |
| 489– 492 | F4.2 | — | obs5_EHR1 | ? Error in obs5_HR1 |
| 494– 498 | F5.2 | — | obs5_HR2 | ? EPIC hardness ratio 2 in observation 5 (3) |
| 500– 503 | F4.2 | — | obs5_EHR2 | ? Error in obs5_HR2 |

**Table D.2:** continued.

| Bytes | Format | Units | Label | Explanations |
|---|---|---|---|---|
| 505– 509 | F5.2 | — | obs5_HR3 | ? EPIC hardness ratio 3 in observation 5 (3) |
| 511– 514 | F4.2 | — | obs5_EHR3 | ? Error in obs5_HR3 |
| 516– 520 | F5.2 | — | obs5_HR4 | ? EPIC hardness ratio 4 in observation 5 (3) |
| 522– 525 | F4.2 | — | obs5_EHR4 | ? Error in obs5_HR4 |
| 527– 531 | A5 | — | obs6 | ? Observation 6 |
| 533– 535 | A3 | — | obs6_val | ? EPIC instruments contributing to source detection in observation 6 (4) |
| 537– 544 | e8.3 | ct/s | obs6_RATE | ? EPIC count rate in observation 6 (2) |
| 546– 552 | e7.2 | ct/s | obs6_ERATE | ? Error in obs6_Rate |
| 554– 561 | e8.3 | mW/m2 | obs6_FLUX | ? EPIC flux in erg/cm2/s in observation 6(2) |
| 563– 569 | e7.2 | mW/m2 | obs6_EFLUX | ? Error in obs6_Flux |
| 571– 575 | F5.2 | — | obs6_HR1 | ? EPIC hardness ratio 1 in observation 6 (3) |
| 577– 580 | F4.2 | — | obs6_EHR1 | ? Error in obs6_HR1 |
| 582– 586 | F5.2 | — | obs6_HR2 | ? EPIC hardness ratio 2 in observation 6 (3) |
| 588– 591 | F4.2 | — | obs6_EHR2 | ? Error in obs6_HR2 |
| 593– 597 | F5.2 | — | obs6_HR3 | ? EPIC hardness ratio 3 in observation 6 (3) |
| 599– 602 | F4.2 | — | obs6_EHR3 | ? Error in obs6_HR3 |
| 604– 608 | F5.2 | — | obs6_HR4 | ? EPIC hardness ratio 4 in observation 6 (3) |
| 610– 613 | F4.2 | — | obs6_EHR4 | ? Error in obs6_HR4 |
| 615– 619 | A5 | — | obs7 | ? Observation 7 |
| 621– 623 | A3 | — | obs7_val | ? EPIC instruments contributing to source detection in observation 7 (4) |
| 625– 632 | e8.3 | ct/s | obs7_RATE | ? EPIC count rate in observation 7 (2) |
| 634– 640 | e7.2 | ct/s | obs7_ERATE | ? Error in obs7_Rate |
| 642– 649 | e8.3 | mW/m2 | obs7_FLUX | ? EPIC flux in erg/cm2/s in observation 7(2) |
| 651– 657 | e7.2 | mW/m2 | obs7_EFLUX | ? Error in obs7_Flux |
| 659– 663 | F5.2 | — | obs7_HR1 | ? EPIC hardness ratio 1 in observation 7 (3) |
| 665– 668 | F4.2 | — | obs7_EHR1 | ? Error in obs7_HR1 |
| 670– 674 | F5.2 | — | obs7_HR2 | ? EPIC hardness ratio 2 in observation 7 (3) |
| 676– 679 | F4.2 | — | obs7_EHR2 | ? Error in obs7_HR2 |
| 681– 685 | F5.2 | — | obs7_HR3 | ? EPIC hardness ratio 3 in observation 7 (3) |
| 687– 690 | F4.2 | — | obs7_EHR3 | ? Error in obs7_HR3 |
| 692– 696 | F5.2 | — | obs7_HR4 | ? EPIC hardness ratio 4 in observation 7 (3) |
| 698– 701 | F4.2 | — | obs7_EHR4 | ? Error in obs7_HR4 |
| 703– 707 | A5 | — | obs8 | ? Observation 8 |
| 709– 711 | A3 | — | obs8_val | ? EPIC instruments contributing to source detection in observation 8 (4) |
| 713– 720 | e8.3 | ct/s | obs8_RATE | ? EPIC count rate in observation 8 (2) |
| 722– 728 | e7.2 | ct/s | obs8_ERATE | ? Error in obs8_Rate |
| 730– 737 | e8.3 | mW/m2 | obs8_FLUX | ? EPIC flux in erg/cm2/s in observation 8(2) |
| 739– 745 | e7.2 | mW/m2 | obs8_EFLUX | ? Error in obs8_Flux |
| 747– 751 | F5.2 | — | obs8_HR1 | ? EPIC hardness ratio 1 in observation 8 (3) |
| 753– 756 | F4.2 | — | obs8_EHR1 | ? Error in obs8_HR1 |

**Table D.2:** continued.

| Bytes | Format | Units | Label | Explanations |
|---|---|---|---|---|
| 758– 762 | F5.2 | — | obs8_HR2 | ? EPIC hardness ratio 2 in observation 8 (3) |
| 764– 767 | F4.2 | — | obs8_EHR2 | ? Error in obs8_HR2 |
| 769– 773 | F5.2 | — | obs8_HR3 | ? EPIC hardness ratio 3 in observation 8 (3) |
| 775– 778 | F4.2 | — | obs8_EHR3 | ? Error in obs8_HR3 |
| 780– 784 | F5.2 | — | obs8_HR4 | ? EPIC hardness ratio 4 in observation 8 (3) |
| 786– 789 | F4.2 | — | obs8_EHR4 | ? Error in obs8_HR4 |
| 791– 795 | A5 | — | obs9 | ? Observation 9 |
| 797– 799 | A3 | — | obs9_val | ? EPIC instruments contributing to source detection in observation 9 (4) |
| 801– 808 | e8.3 | ct/s | obs9_RATE | ? EPIC count rate in observation 9 (2) |
| 810– 816 | e7.2 | ct/s | obs9_ERATE | ? Error in obs9_Rate |
| 818– 825 | e8.3 | mW/m2 | obs9_FLUX | ? EPIC flux in erg/cm2/s in observation 9(2) |
| 827– 833 | e7.2 | mW/m2 | obs9_EFLUX | ? Error in obs9_Flux |
| 835– 839 | F5.2 | — | obs9_HR1 | ? EPIC hardness ratio 1 in observation 9 (3) |
| 841– 844 | F4.2 | — | obs9_EHR1 | ? Error in obs9_HR1 |
| 846– 850 | F5.2 | — | obs9_HR2 | ? EPIC hardness ratio 2 in observation 9 (3) |
| 852– 855 | F4.2 | — | obs9_EHR2 | ? Error in obs9_HR2 |
| 857– 861 | F5.2 | — | obs9_HR3 | ? EPIC hardness ratio 3 in observation 9 (3) |
| 863– 866 | F4.2 | — | obs9_EHR3 | ? Error in obs9_HR3 |
| 868– 872 | F5.2 | — | obs9_HR4 | ? EPIC hardness ratio 4 in observation 9 (3) |
| 874– 877 | F4.2 | — | obs9_EHR4 | ? Error in obs9_HR4 |
| 879– 883 | A5 | — | obs10 | ? Observation 10 |
| 885– 887 | A3 | — | obs10_val | ? EPIC instruments contributing to source detection in observation 10 (4) |
| 889– 896 | e8.3 | ct/s | obs10_RATE | ? EPIC count rate in observation 10 (2) |
| 898– 904 | e7.2 | ct/s | obs10_ERATE | ? Error in obs10_Rate |
| 906– 913 | e8.3 | mW/m2 | obs10_FLUX | ? EPIC flux in erg/cm2/s in observation10(2) |
| 915– 921 | e7.2 | mW/m2 | obs10_EFLUX | ? Error in obs10_Flux |
| 923– 927 | F5.2 | — | obs10_HR1 | ? EPIC hardness ratio 1 in observation 10(3) |
| 929– 932 | F4.2 | — | obs10_EHR1 | ? Error in obs10_HR1 |
| 934– 938 | F5.2 | — | obs10_HR2 | ? EPIC hardness ratio 2 in observation 10(3) |
| 940– 943 | F4.2 | — | obs10_EHR2 | ? Error in obs10_HR2 |
| 945– 949 | F5.2 | — | obs10_HR3 | ? EPIC hardness ratio 3 in observation 10(3) |
| 951– 954 | F4.2 | — | obs10_EHR3 | ? Error in obs10_HR3 |
| 956– 960 | F5.2 | — | obs10_HR4 | ? EPIC hardness ratio 4 in observation 10(3) |
| 962– 965 | F4.2 | — | obs10_EHR4 | ? Error in obs10_HR4 |
| 967– 968 | I2 | — | ndet | Number of observations covering the source |
| 970– 974 | F5.2 | — | svar_max | Maximum significance of variation |
| 976– 980 | F5.2 | — | fvar_max | Maximum flux ratio |
| 982– 982 | I1 | — | n_upper | Number of upper limits |
| 984– 991 | e8.3 | mW/m2 | fmax | Maximum flux |
| 993– 999 | e7.2 | mW/m2 | e_fmax | Error in fmax |

Note (1): Source numbers from Table 7.2 in this thesis
Note (2): Count rate and flux in XID band (0.2-4.5keV)
Note (3): HRi=(R(i+1)-R(i))/(R(i+1)+R(i)) where Ri are the count rates in the energy bands 1 to 5 and
band 1 = 0.2–0.5keV,
band 2 = 0.5–1.0keV,
band 3 = 1.0–2.0keV,
band 4 = 2.0–4.5keV,
band 5 = 4.5–12keV
Note (4): First character for EPIC PN, second for MOS1, third for MOS2;
character = T : source is in field of view of instrument
F : otherwise
Note (5): Classifications used (see Table 7.3)
fg Star = foreground star
<fg Star> = foreground star candidate
AGN = active galactic nucleus
<AGN> = AGN candidate
Gal = galaxy
<Gal> = galaxy candidate
GCl = galaxy cluster
<GCl> = galaxy cluster candidate
SSS = supersoft source in M 31
<SSS> = supersoft source candidate in M 31
SNR = supernova remnant in M 31
<SNR> = supernova remnant candidate in M 31
GlC = source in globular cluster
<GlC> = source in globular cluster candidate
XRB = X-ray binary in M 31
<XRB> = X-ray binary candidat in M 31
<hard> = HR2-e_HR2>-0.2 or only HR3 and HR4 defined, and no other classification

# Appendix E

# Description of Tables 8.2 and 9.4

Table 8.2 presents the catalogue of "hard" sources, which were detected in the 2.0–10.0 keV data of the large *XMM-Newton* survey of M 31 (XMM LP-hard catalogue). It contains 1 254 sources, including 24 sources flagged as foreground stars and seven extended sources.

Table 9.4 contains the results of a cross-correlation of the XMM LP-hard catalogue with the XMM LP-total catalogue. In total 1 107 sources of the XMM LP-hard catalogue have counterparts in the XMM LP-total catalogue. Five sources are identified as foreground stars, 19 as foreground star candidates, 11 as AGN, 37 as AGN candidates, 2 as background galaxies, 10 as galaxy candidates, one as a galaxy cluster, two as galaxy cluster candidates, one as an SNR, 7 as SNR candidates, 6 as XRBs, 15 as XRB candidates, 33 as GlCs and 13 as GlC candidates.

**Table E.1:** Read Me file for Table 8.2

| Bytes | Format | Units | Label | Explanations |
|---|---|---|---|---|
| 1– 4 | I4 | — | [XMMLPh] | Source Number |
| 6– 7 | I2 | h | RAh | Right Ascension J2000 (hours) |
| 9– 10 | I2 | min | RAm | Right Ascension J2000 (minutes) |
| 12– 16 | F5.2 | s | RAs | Right Ascension J2000 (seconds) |
| 18 | A1 | — | DE- | Declination J2000 (sign) |
| 20– 21 | I2 | deg | DEd | Declination J2000 (degrees) |
| 23– 24 | I2 | arcmin | DEm | Declination J2000 (minutes) |
| 26– 29 | F4.1 | arcsec | DEs | Declination J2000 (seconds) |
| 31– 35 | F5.2 | arcsec | PosErr | Positional error (1) |
| 37– 44 | E8.2 | — | LH | Source detection likelihood (combined EPIC) |
| 46– 53 | E8.2 | ct/s | CRate | Combined EPIC count rate (2) |
| 55– 61 | E7.1 | ct/s | e_CRate | Error in CRate |
| 63– 70 | E8.2 | mW/m2 | CFlux | Combined EPIC flux in erg/cm2/s (2) |
| 72– 78 | E7.1 | mW/m2 | e_CFlux | Error in CFlux |
| 80– 83 | F4.1 | ks | Exp | Exposure |
| 85 | I1 | — | flag | flag (3) |
| 87–111 | A25 | — | IAU_NAME | Source Name XMMM31 Jhhmmss.s+ddmmss |

Note (1): 3 sigma error (99.73%; both, statistical and systematic, errors included)
Note (2): Count rate and flux in 2.0-10.0 keV band
Note (3): 0: hard, point like source, used for derivation of luminosity function
4: foreground Star
8: extended source

**Table E.2:** Extented sources in the XMM LP-hard catalogue (Table 8.2)

| SRC (1) | EXT$^+$ (2) | EXT_ERR$^+$ (3) | EXT_ML (4) | SRC (1) | EXT$^+$ (2) | EXT_ERR$^+$ (3) | EXT_ML (4) |
|---|---|---|---|---|---|---|---|
| 3 | 6.48 | 0.00 | 2.02e+04 | 721 | 18.84 | 2.68 | 1.63e+01 |
| 77 | 28.40 | 0.16 | 3.47e+03 | 906 | 10.28 | 1.48 | 4.34e+00 |
| 593 | 9.68 | 1.28 | 1.44e+01 | 1212 | 10.96 | 1.68 | 1.99e+01 |
| 698 | 9.12 | 0.68 | 4.58e+01 | | | | |

Notes:
$^+$ : Extent and error of extent in units of $1''$; $1''$ corresponds to 3.8 pc at the assumed distance of M 31

**Table E.3:** Read Me file for Table 9.4

| Bytes | Format | Units | Label | Explanations |
|---|---|---|---|---|
| 1– 4 | I4 | — | [XMMLPh] | XMM LP-hard Source Number(1) |
| 6– 9 | I4 | — | [XMMLPt] | XMM LP-total Source Number(2) |
| 11– 13 | F3.1 | arcsec | Dist | Spatial Distance |
| 15– 23 | A9 | — | Class | ? Classification of X-ray source (3) |
| 25 | I1 | — | Flag | ? Flag(4) |

Note (1): Source numbers from Table 8.2 in this thesis
Note (2): Source numbers from Table 7.2 in this thesis
Note (3): Classifications used (see Table 7.3)
fg Star = foreground star
<fg Star> = foreground star candidate
AGN = active galactic nucleus
<AGN> = AGN candidate
Gal = galaxy
<Gal> = galaxy candidate
GCl = galaxy cluster
<GCl> = galaxy cluster candidate
SSS = supersoft source in M 31
<SSS> = supersoft source candidate in M 31
SNR = supernova remnant in M 31
<SNR> = supernova remnant candidate in M 31
GlC = source in globular cluster
<GlC> = source in globular cluster candidate
XRB = X-ray binary in M 31

<XRB> = X-ray binary candidate in M 31
<hard> = HR2-e_HR2>-0.2 or only HR3 and HR4 defined, and no other classification

Note (4): 2: XMM LP-hard source correlates with more than one XMM LP-total source
3: XMM LP-total source correlates with more than one XMM LP-hard source

# Appendix F

# CD with source catalogues

### Contents:

- ReadMe
- table6.3.dat
- table6.3.fit
- table6.5.dat
- table6.5.fit
- table7.2.dat
- table7.2.fit
- table7.5.dat
- table7.5.fit
- table8.2.dat
- table8.2.fit
- table9.4.dat
- table9.4.fit

# List of technical terms and acronyms

**1RXH:** Source catalogue of pointed *ROSAT* HRI observations

**2MASS:** Two Micron All-Sky Survey

**ACIS-I/ACIS-S:** Advanced CCD Imaging Spectrometer on-board *Chandra*. The CCDs are arranged in a $2\times2$ array (ACIS-I) for imaging and a $1\times6$ array (ACIS-S) for either imaging or as grating readout.

**ACS:** Advanced Camera for Surveys on-board the Hubble Space Telescope

**AGN:** Active Galactic Nuclei

**AO:** Announcement of Opportunity

**ASCA:** Advanced Satellite for Cosmology and Astrophysics (formerly named Astro-D). It was a Japanese X-ray satellite, which was in operation from 1993 to 2000.

**Bias:** An offset voltage applied to all pixels in an array detector.

**BH:** Black Hole

**BL Lac:** A special type of AGN where the jet points to the observer. Named from the first detected object of that class: BL Lacertae

**BLRG:** Broad Line Radio Galaxies

**CAL:** Calibration Access Layer

**CAL83, CAL87:** Two SSSs in the Large Magellanic Cloud

**CCD:** Charge-Coupled Device

**Chandra:** American-led X-ray observatory launched in 1999 with an on-axis spatial resolution of $0.5''$.

**CLF:** Cumulative Luminosity Function

**CNCs:** Cumulative Number Counts

**CO:** Carbon monoxide

**COSMOS:** Cosmic Evolution Survey

**CTI:** Charge Transfer Inefficiency

**CV:** Cataclysmic Variable

**CXB:** Cosmic X-ray Background

**CXOM31:** IAU-approved name for *Chandra* X-ray sources, detected in M 31.

**$D_{25}$ ellipse:** gives an elliptical representation of the dimension of a galaxy at the 25 mag/arcsec$^2$ isophote in blue light.

**DEC:** Declination

**DET ML:** Detection Maximum Likelihood

**ds9:** Astronomical Data Visualisation Application

**ECF:** Energy Conversion Factor

**Einstein:** First X-ray telescope with imaging optics

**EPIC:** European Photon Imaging Cameras on-board XMM-Newton

**eROSITA:** extended Röntgen Survey with an Imaging Telescope Array

**err:** error

**ESA:** European Space Agency

**ESO:** European Southern Observatory, with its headquarters in Garching, Germany.

**eV:** electron Volt, energy unit

**EXSAS:** Extended X-ray Scientific Analysis System to Evaluate Data from the Astronomical X-ray Satellite ROSAT

**Ext:** Extent

**EXT ML:** Extent Maximum Likelihood

**fg Star:** Foreground Star

**FITS:** Flexible Image Transport System. Standard format for astronomical images.

**FoV:** Field-of-View. Sky area that can be covered with one image of a particular instrument.

**FR I, FR II:** Fanaroff-Riley radio galaxies

**FTOOLS:** A software package to manipulate FITS files.

**FUV:** Far-UltraViolet

**FWHM:** Full-Width Half-Maximum, a measure of the width of an object in an image. The FWHM is a well-defined number obtained by fitting a 1D-Gaussian curve of the form $f(x) = 1/(\sigma\sqrt{2\pi}) \times \exp(-\frac{x^2}{2\sigma^2})$ to the intensity profile of an object. In one dimension the standard deviation $\sigma$ and the full width at half the peak intensity of the profile only differ by a constant factor of FWHM $= 2\sqrt{2\ln 2}\sigma$ (Stöcker 1998). This relation still holds for a rotationally-symmetric 2D-Gaussian with uncorrelated coordinates if the diameter of the circle around the point (0, 0, $f\,(0,0)\,/2$) is defined as the FWHM, where $f\,(x,y) = 1/(2\pi\sigma^2) \times \exp(-\frac{x^2+y^2}{2\sigma^2})$.

**Gain:** Conversion factor from detected electrons to digital counts.

**Gal:** galaxy

**GALEX:** Galaxy Evolution Explorer

**GCl:** Galaxy Cluster

**GlC:** Globular Cluster

**GTI:** Good Time Intervals

**HMXB:** High Mass X-ray Binary

**HR:** Hardness Ratio

**HRC:** High Resolution Camera on-board Chandra

**HRI:** High Resolution Imager on-board ROSAT

**HST:** Hubble Space Telescope

**IAU:** International Astronomical Union

**ICM:** Intracluster Medium

**IMBH:** Intermediate Mass Black Hole

**IR:** InfraRed

**IRAC:** InfraRed Array Camera on-board the Spitzer observatory

**ISM:** Interstellar Medium

**IXO:** International X-ray Observatory

**LF:** Luminosity Function

**LG:** Local Group

**LGS, LGGS:** Local Group (galaxy) Survey

**LINERS:** Low Ionisation Nuclear Emission Regions

**LMC:** Large Magellanic Cloud

**LMXB:** Low Mass X-ray Binary

**Log N-Log S:** Relation between the number of sources (N) and the flux (S) of these sources.

**M 31:** Andromeda Galaxy, our neighbouring large, spiral galaxy

**M31N:** IAU-approved name for optical novae detected in M 31.

**M 32:** Small satellite galaxy of M 31

**MEKAL:** Plasma emission code from MEwe, KAastra, and Liedahl

**MELH:** Maximum Extent LikeliHood

**MIDAS:** Munich Image Data Analysis System. Astronomical software package developed and maintained by the European Southern Observatory.

**ML:** Maximum Likelihood

**MOS:** Metal Oxid Semi-conductor instrument on-board XMM-Newton

**MPE:** Max-Planck-Institut für extraterrestrische Physik

**MPI:** Max-Planck-Institut

**NASA:** National Aeronautics and Space Administration

**NED:** NASA Extragalactic Database

**NGC 224:** Andromeda Galaxy

**NIR:** Near-InfraRed

**NLRG:** Narrow Line Radio Galaxies

**NRAO:** National Radio Astronomy Observatory

**NS:** Neutron Star

**NUV:** Near-UltraViolet

**NVSS:** NRAO/VLA Sky Survey

**Obs:** Observation

**Obs. id.:** Unique identification number for each *XMM-Newton* observation.

**ODF:** Observation Data File

**OoT:** Out-of-Time events

**OM:** Optical Monitor on-board XMM-Newton

**PATTERN:** The number and arrangement of pixels of the detector a photon was detected in.

**PDS:** Power Density Spectrum

**PHA:** Pulse Height Analyser, denotes the column containing the uncalibrated spectral channel in *XMM-Newton* (event) files

**PI:** Principal Investigator

**Pipeline:** Automated data reduction software requiring only minimal user interaction.

**plerion:** "Crab-like" SNR that has a power-law spectrum.

**PN:** Imaging camera on-board XMM-Newton

**POINT-AGAPE:** Pixel-lensing Observations with the Isaac Newton Telescope-Andromeda Galaxy Amplified Pixels Experiment

**Pointing:** One principal telescope position. The sum of all images with a specific target in the field of view.

**PSF:** Point-Spread Function. Intensity distribution of a point-like light source in an astronomical image.

**PSPC:** Position Sensitive Proportional Counter, main instrument of ROSAT.

**QE:** Quantum Efficiency

**QSO:** Quasi-Stellar Object

**QSS:** Quasi-Soft Source

**R.A.:** Right Ascension

**RGB image:** Three colour (Red, Green, Blue) image

**RGS:** Reflecting Grating Spectrometer on-board XMM-Newton

**r.m.s.:** root mean square, also know as quadratic mean

**ROSAT:** ROentgen SATellite, German/UK/US X-ray survey mission from 1990 to 1999.

**RX:** IAU-approved name for *ROSAT* X-ray sources.

**S And:** Supernova in the Andromeda galaxy, observed in August 1885

**SAS:** XMM-Newton Science Analysis Software

**SFR:** Star Formation Rate

**SFXT:** Super-giant Fast X-ray Transient

**SIMBAD:** Centre de Données astronomiques de Strasbourg

**SPIE:** Society of Photo-Optical Instrumentation Engineers

**Spitzer:** Mid-infrared space telescope launched in 2003.

**SMC:** Small Magellanic Cloud

**SN:** SuperNova

**SNR:** SuperNova Remnant

**SSS:** SuperSoft Source

**SWCX:** Solar Wind Charge exchange

**Swift:** Gamma-ray burst mission, lead by NASA

**ToO:** Target of Opportunity

**TSS:** Texas Supernova Search

**UHURU:** US X-ray satellite from 1970 to 1973

**ULX:** Ultra Luminous X-ray source

**USNO-B1:** All sky catalogue form the United States Naval Observatory

**UT:** Universal Time

**UV:** UltraViolet

**Vignetting:** Obscuration of parts of the primary mirror as seen by a detector pixel.

**VLA:** Very Large Array

**VSS:** Very Soft Source

**WD:** White Dwarf

**WebPIMMS:** Online Mission Count Rate Simulator powered by the Portable, Interactive Multi-Mission Simulator.

**WeCAPP:** Wendelstein Calar Alto Pixellensing Project

**XLF:** X-ray Luminosity Function

**XID:** 0.2–4.5 keV band

**XMM LP-total catalogue:** Source catalogue of the "Deep *XMM-Newton* survey of M 31" which contains all sources detected in the 0.2–12.0 keV band. The catalogue also contains cross-correlations with other catalogues in the radio, infrared, optical, ultraviolet and X-ray wavelength ranges.

**XMM LP-hard catalogue:** Source catalogue of the "Deep *XMM-Newton* survey of M 31" which contains all sources detected in the 2.0–10.0 keV band. The catalogue was created to study the log N-log S relation.

**XMM-Newton:** X-ray Spectroscopy Multi-Mirror Mission; European X-ray observatory launched in 1999.

**XMMM31:** IAU-approved name for *XMM-Newton* X-ray sources, detected in the M 31 field of the *XMM-Newton* Large Program on M 31.

**XMMU:** IAU-approved name for *XMM-Newton* X-ray sources, detected by individual researchers.

**XRB:** X-ray Binary

**XRT:** X-ray Telescope on-board the Swift satellite.

**XSA:** XMM-Newton Science Archive

**Xspec:** An X-ray Spectral Fitting Package

# List of Figures

# List of Tables

# Bibliography


Alves-Brito, A., Forbes, D. A., Mendel, J. T., Hau, G. K. T., & Murphy, M. T. 2009, MNRAS, 395, L34

An, J. H., Evans, N. W., Hewett, P., et al. 2004, MNRAS, 351, 1071

Anders, E. & Grevesse, N. 1989, Geochim. Cosmochim. Acta, 53, 197

Baganoff, F. K., Bautz, M. W., Brandt, W. N., et al. 2001, Nature, 413, 45

Bałucińska-Church, M. & McCammon, D. 1992, ApJ, 400, 699

Barmby, P., McLaughlin, D. E., Harris, W. E., Harris, G. L. H., & Forbes, D. A. 2007, AJ, 133, 2764

Barnard, R., Church, M. J., & Bałucińska-Church, M. 2003a, A&A, 405, 237

Barnard, R., Kolb, U., & Osborne, J. P. 2003b, A&A, 411, 553

Barnard, R., Kolb, U., & Osborne, J. P. 2004, A&A, 423, 147

Barnard, R., Kolb, U. C., & Osborne, J. P. 2007a, A&A, 469, 873

Barnard, R., Osborne, J. P., Kolb, U., & Borozdin, K. N. 2003c, A&A, 405, 505

Barnard, R., Stiele, H., Hatzidimitriou, D., et al. 2008, ApJ, 689, 1215

Barnard, R., Trudolyubov, S., Kolb, U. C., et al. 2007b, A&A, 469, 875

Bauer, M., Pietsch, W., Trinchieri, G., et al. 2008, A&A, 489, 1029

Beck, R., Berkhuijsen, E. M., & Hoernes, P. 1998, A&AS, 129, 329

Begelman, M. C. 2002, ApJ, 568, L97

Bellazzini, M., Pasquali, A., Federici, L., Ferraro, F. R., & Pecci, F. F. 1995, ApJ, 439, 687

Bender, R., Kormendy, J., Bower, G., et al. 2005, ApJ, 631, 280

Bildsten, L. & Deloye, C. J. 2004, ApJ, 607, L119

Biviano, A. 2000, in Constructing the Universe with Clusters of Galaxies

Blackburn, J. K. 1995, in Astronomical Society of the Pacific Conference Series, Vol. 77, Astronomical Data Analysis Software and Systems IV, ed. R. A. Shaw, H. E. Payne, & J. J. E. Hayes, 367

Blair, W. P., Kirshner, R. P., & Chevalier, R. A. 1981, ApJ, 247, 879

Block, D. L., Bournaud, F., Combes, F., et al. 2006, Nature, 443, 832

Bogdán, Á. & Gilfanov, M. 2008, MNRAS, 388, 56

Boissier, S., Gil de Paz, A., Boselli, A., et al. 2007, ApJS, 173, 524

Bonfini, P., Hatzidimitriou, D., Pietsch, W., & Reig, P. 2009, A&A, 507, 705

Bowyer, S., Margon, B., Lampton, M., & Cruddace, R. 1974, ApJ, 190, 285

Bradt, H., Levine, A. M., Remillard, R. A., & Smith, D. A. 2000, in Proceedings of the Vulcano May 1999 Workshop: Multifrequency Behaviour of High Energy Cosmic Sources: III, ed. F. Giovannelli & L. Sabau-Graziati, Vol. 71, arXiv:astro–ph/0001460

Brandt, W. N. & Hasinger, G. 2005, ARA&A, 43, 827

Braun, R. 1990, ApJS, 72, 761

Braun, R. 1991, ApJ, 372, 54

Braun, R., Thilker, D. A., Walterbos, R. A. M., & Corbelli, E. 2009, ApJ, 695, 937

Braun, R. & Walterbos, R. A. M. 1993, A&AS, 98, 327

Bregman, J. N. 1980, ApJ, 236, 577

Brinks, E. & Shane, W. W. 1984, A&AS, 55, 179

Brunner, H., Cappelluti, N., Hasinger, G., et al. 2008, A&A, 479, 283

Brusa, M., Zamorani, G., Comastri, A., et al. 2007, ApJS, 172, 353

Caballero-García, M. D. & Fabian, A. C. 2010, MNRAS, 402, 2559

Caldwell, N., Harding, P., Morrison, H., et al. 2009, AJ, 137, 94

Cappelluti, N., Brusa, M., Hasinger, G., et al. 2009, A&A, 497, 635

Cappelluti, N., Hasinger, G., Brusa, M., et al. 2007, ApJS, 172, 341

Cash, W. 1979, ApJ, 228, 939

Cavaliere, A. & Fusco-Femiano, R. 1976, A&A, 49, 137

Chapman, S. C., Ibata, R., Lewis, G. F., et al. 2006, ApJ, 653, 255

Charles, P. A. & Seward, F. D. 1995, Exploring the X-ray Universe (Cambridge University Press)

Chemin, L., Carignan, C., & Foster, T. 2009, ApJ, 705, 1395

Chen, W., Shrader, C. R., & Livio, M. 1997, ApJ, 491, 312

Chevalier, R. A. & Clegg, A. W. 1985, Nature, 317, 44

Chu, Y.-H. & Mac Low, M.-M. 1990, ApJ, 365, 510

Church, M. J. & Bałucińska-Church, M. 1995, A&A, 300, 441

Church, M. J. & Bałucińska-Church, M. 2001, A&A, 369, 915

Coddington, E. 1898, PASP, 10, 45

Colbert, E. J. M., Heckman, T. M., Ptak, A. F., Strickland, D. K., & Weaver, K. A. 2004, ApJ, 602, 231

Collura, A., Reale, F., & Peres, G. 1990, ApJ, 356, 119

Compton, A. H. 1923, Phys. Rev., 21, 483

Condon, J. J., Cotton, W. D., Greisen, E. W., et al. 1998, AJ, 115, 1693

Cotton, W. D., Condon, J. J., & Arbizzani, E. 1999, ApJS, 125, 409

Crampton, D., Hutchings, J. B., Cowley, A. P., Schade, D. J., & van Speybroeck, L. P. 1984, ApJ, 284, 663

Dame, T. M., Koper, E., Israel, F. P., & Thaddeus, P. 1993, ApJ, 418, 730

de Vaucouleurs, G. 1959, Handbuch der Physik, 53, 275

de Vaucouleurs, G. & Corwin, Jr., H. G. 1985, ApJ, 295, 287

de Vaucouleurs, G. & Corwin, Jr., H. G. 1986, ApJ, 302, 517

de Vaucouleurs, G., de Vaucouleurs, A., Corwin, H. G., et al. 1991, Third Reference Catalogue of Bright Galaxies (Volume 1-3, XII, 2069 pp. 7 figs.. Springer-Verlag Berlin Heidelberg New York)

Decourchelle, A., Sauvageot, J. L., Audard, M., et al. 2001, A&A, 365, L218

Deloye, C. J. & Bildsten, L. 2003, ApJ, 598, 1217

den Herder, J. W., Brinkman, A. C., Kahn, S. M., et al. 2001, A&A, 365, L7

Di Stefano, R. & Kong, A. K. H. 2003, arXiv:astro-ph/0311374

Di Stefano, R., Kong, A. K. H., Garcia, M. R., et al. 2002, ApJ, 570, 618

Di Stefano, R., Kong, A. K. H., Greiner, J., et al. 2004, ApJ, 610, 247 (DKG2004)

Dodds-Eden, K., Porquet, D., Trap, G., et al. 2009, ApJ, 698, 676

Dodorico, S., Dopita, M. A., & Benvenuti, P. 1980, A&AS, 40, 67

Dreyer, J. L. E. 1888, MmRAS, 49, 1

Drout, M. R., Massey, P., Meynet, G., Tokarz, S., & Caldwell, N. 2009, ApJ, 703, 441

Dubath, P. & Grillmair, C. J. 1997, A&A, 321, 379

Dubus, G., Hameury, J.-M., & Lasota, J.-P. 2001, A&A, 373, 251

Dursi, L. J. & Timmes, F. X. 2006, ApJ, 641, 1071

Eckart, A., Baganoff, F. K., Morris, M., et al. 2004, A&A, 427, 1

Eger, P. 2008, Master's thesis, TU München

Eggleton, P. P. 1983, ApJ, 268, 368

Ehle, M., de la Calle, I., Diaz Trígo, M., et al. 2008, XMM-Newton Users Handbook, Issue 2.6, http://xmm.esac.esa.int/external/xmm_user_support/documentation/uhb/index.html

Fabbiano, G. 2006, ARA&A, 44, 323

Fabbiano, G. & Trinchieri, G. 1987, ApJ, 315, 46

Fabbiano, G. & White, N. E. 2006, Compact Stellar X-ray Sources in Normal Galaxies, ed. W. H. G. Lewin & M. van der Klis (Cambridge University Press), 475

Fabbiano, G., Zezas, A., & Murray, S. S. 2001, ApJ, 554, 1035

Fabian, A. C., Zoghbi, A., Ross, R. R., et al. 2009, Nature, 459, 540

Fan, Z., Ma, J., Zhou, X., et al. 2005, PASP, 117, 1236

Feldmeier, A., Puls, J., & Pauldrach, A. W. A. 1997, A&A, 322, 878

Ferrière, K. M. 2001, Reviews of Modern Physics, 73, 1031

Filipović, M. D., Haberl, F., Winkler, P. F., et al. 2008, A&A, 485, 63

Fleming, T. A., Gioia, I. M., & Maccacaro, T. 1989, ApJ, 340, 1011

Fliri, J., Riffeser, A., Seitz, S., & Bender, R. 2006, A&A, 445, 423

Frank, J., King, A., & Raine, D. J. 2002, Accretion Power in Astrophysics: Third Edition, ed. J. Frank, A. King, & D. J. Raine (Cambridge University Press)

Freyberg, M. J., Briel, U. G., Dennerl, K., et al. 2004, in Proceedings of the SPIE, Vol. 5165, X-Ray and Gamma-Ray Instrumentation for Astronomy XIII., ed. K. A. Flanagan & O. H. W. Siegmund, 112

Gaetz, T. J., Blair, W. P., Hughes, J. P., et al. 2007, ApJ, 663, 234

Galache, J. L., Garcia, M. R., Steeghs, D., et al. 2007, The Astronomer's Telegram, 1147, 1

Galleti, S., Bellazzini, M., Federici, L., Buzzoni, A., & Fusi Pecci, F. 2007, A&A, 471, 127

Galleti, S., Bellazzini, M., Federici, L., & Fusi Pecci, F. 2005, A&A, 436, 535

Galleti, S., Federici, L., Bellazzini, M., Buzzoni, A., & Fusi Pecci, F. 2006, A&A, 456, 985

Galleti, S., Federici, L., Bellazzini, M., Fusi Pecci, F., & Macrina, S. 2004, A&A, 416, 917

Gao, Y., Wang, Q. D., Appleton, P. N., & Lucas, R. A. 2003, ApJ, 596, L171

Garcia, M. R., Murray, S. S., Primini, F. A., et al. 2000, ApJ, 537, L23

Gelfand, J. D., Lazio, T. J. W., & Gaensler, B. M. 2004, ApJS, 155, 89

Gelfand, J. D., Lazio, T. J. W., & Gaensler, B. M. 2005, ApJS, 159, 242

Giacconi, R., Branduardi, G., Briel, U., et al. 1979, ApJ, 230, 540

Giacconi, R., Gursky, H., Paolini, F. R., & Rossi, B. B. 1962, Phys. Rev. Lett., 9, 439

Giacconi, R., Gursky, H., & van Speybroeck, L. P. 1968, ARA&A, 6, 373

Giacconi, R., Murray, S., Gursky, H., et al. 1974, ApJS, 27, 37

Gilfanov, M. 2004, MNRAS, 349, 146

Gilli, R., Comastri, A., & Hasinger, G. 2007, A&A, 463, 79

Gladstone, J., Done, C., & Gierliński, M. 2007, MNRAS, 378, 13

Greiner, J. 2000, New Astronomy, 5, 137

Greiner, J. & Di Stefano, R. 2002, A&A, 387, 944

Greiner, J., Di Stefano, R., Kong, A., & Primini, F. 2004a, ApJ, 610, 261

Greiner, J., Iyudin, A., Jimenez-Garate, M., et al. 2004b, in Revista Mexicana de Astronomia y Astrofisica Conference Series, ed. G. Tovmassian & E. Sion, Vol. 20, 18

Grimm, H., McDowell, J., Zezas, A., Kim, D., & Fabbiano, G. 2005, ApJS, 161, 271

Grimm, H.-J., Gilfanov, M., & Sunyaev, R. 2003, MNRAS, 339, 793

Haberl, F. & Pietsch, W. 1999a, A&AS, 139, 277

Haberl, F. & Pietsch, W. 1999b, A&A, 344, 521

Hachisu, I. & Kato, M. 2006, ApJS, 167, 59

Haiman, Z., Magnier, E., Lewin, W. H. G., et al. 1994, A&A, 286, 725

Haisch, B., Strong, K. T., & Rodono, M. 1991, ARA&A, 29, 275

Harnden, Jr., F. R., Golub, L., Rosner, R., et al. 1979, in Bulletin of the American Astronomical Society, Vol. 11, 775

Hasinger, G., Altieri, B., Arnaud, M., et al. 2001, A&A, 365, L45

Hasinger, G., Cappelluti, N., Brunner, H., et al. 2007, ApJS, 172, 29

Hasinger, G. & van der Klis, M. 1989, A&A, 225, 79

Hatzidimitriou, D., Pietsch, W., Misanovic, Z., Reig, P., & Haberl, F. 2006, A&A, 451, 835

Henze, M., Pietsch, W., Haberl, F., et al. 2010, Astronomische Nachrichten, 331, 193

Henze, M., Pietsch, W., Haberl, F., et al. 2009, A&A, 500, 769

Hernanz, M. 2005, in Astronomical Society of the Pacific Conference Series, Vol. 330, The Astrophysics of Cataclysmic Variables and Related Objects, ed. J.-M. Hameury & J.-P. Lasota, 265

Hodge, P. W., Krienke, O. K., Bellazzini, M., et al. 2009, AJ, 138, 770

Holland, S. 1998, AJ, 115, 1916

Hubble, E. P. 1929, ApJ, 69, 103

Huchtmeier, W. K. & Richter, O.-G. 1989, A General Catalog of HI Observations of Galaxies. The Reference Catalog., ed. W. K. Huchtmeier & O.-G. Richter (Springer-Verlag Berlin Heidelberg)

Huchtmeier, W. K., Richter, O.-G., Bohnenstengel, H. D., & Hauschildt, M. 2008, VizieR Online Data Catalog, 8068, 0

Ibata, R., Irwin, M., Lewis, G., Ferguson, A. M. N., & Tanvir, N. 2001, Nature, 412, 49

Immler, S. & Lewin, W. H. G. 2003, in Lecture Notes in Physics, Berlin Springer Verlag, Vol. 598, Supernovae and Gamma-Ray Bursters, ed. K. Weiler, 91

Itoh, H., Hayakawa, S., Masai, K., & Nomoto, K. 1987a, PASJ, 39, 529

Itoh, M., Kumagai, S., Shigeyama, T., Nomoto, K., & Nishimura, J. 1987b, Nature, 330, 233

Iye, M. & Ozawa, T. 1999, in Astronomical Society of the Pacific Conference Series, Vol. 182, Galaxy Dynamics - A Rutgers Symposium, ed. D. R. Merritt, M. Valluri, & J. A. Sellwood, 255

Jansen, F., Lumb, D., Altieri, B., et al. 2001, A&A, 365, L1

Jess, D. B., Mathioudakis, M., Erdélyi, R., et al. 2009, Science, 323, 1582

Jose, J. & Hernanz, M. 1998, ApJ, 494, 680

Joye, W. A. & Mandel, E. 2003, in Astronomical Society of the Pacific Conference Series, Vol. 295, Astronomical Data Analysis Software and Systems XII, ed. H. E. Payne, R. I. Jedrzejewski, & R. N. Hook, 489

Kaaret, P. 2002, ApJ, 578, 114

Kahabka, P. 1999, A&A, 344, 459

Kahabka, P., Pietsch, W., Filipović , M. D., & Haberl, F. 1999, A&AS, 136, 81

Kahabka, P. & van den Heuvel, E. P. J. 1997, ARA&A, 35, 69

Kalirai, J. S., Gilbert, K. M., Guhathakurta, P., et al. 2006, ApJ, 648, 389

Kalogera, V., King, A. R., & Rasio, F. A. 2004, ApJ, 601, L171

Kang, Y., Bianchi, L., & Rey, S. 2009, ApJ, 703, 614

Kim, M., Wilkes, B. J., Kim, D.-W., et al. 2007a, ApJ, 659, 29

Kim, S. C., Lee, M. G., Geisler, D., et al. 2007b, AJ, 134, 706

Kimball, A. E. & Ivezić, Ž. 2008, AJ, 136, 684

King, A. R., Davies, M. B., Ward, M. J., Fabbiano, G., & Elvis, M. 2001, ApJ, 552, L109

Kitaura, F. S., Janka, H.-T., & Hillebrandt, W. 2006, A&A, 450, 345

Kong, A. K. H., DiStefano, R., Garcia, M. R., & Greiner, J. 2003a, ApJ, 585, 298

Kong, A. K. H., Garcia, M. R., Primini, F. A., & Murray, S. S. 2002a, ApJ, 580, L125

Kong, A. K. H., Garcia, M. R., Primini, F. A., et al. 2002b, ApJ, 577, 738

Kong, A. K. H., Sjouwerman, L. O., Williams, B. F., Garcia, M. R., & Dickel, J. R. 2003b, ApJ, 590, L21

Kotov, O., Trudolyubov, S., & Vestrand, W. T. 2006, ApJ, 641, 756

Krienke, O. K. & Hodge, P. W. 2007, PASP, 119, 7

Krienke, O. K. & Hodge, P. W. 2008, PASP, 120, 1

Kundu, A., Zepf, S. E., & Maccarone, T. J. 2008, in American Institute of Physics Conference Series, Vol. 1010, A Population Explosion: The Nature & Evolution of X-ray Binaries in Diverse Environments, ed. R. M. Bandyopadhyay, S. Wachter, D. Gelino, & C. R. Gelino, 313

Lasota, J.-P. 2001, New Astronomy Review, 45, 449

Lewin, W. H. G., van Paradijs, J., & Taam, R. E. 1993, Space Science Reviews, 62, 223

Maccacaro, T., Gioia, I. M., Wolter, A., Zamorani, G., & Stocke, J. T. 1988, ApJ, 326, 680

Macri, L. M., Calzetti, D., Freedman, W. L., et al. 2001, ApJ, 549, 721

Magnier, E. A. 1993, PhD thesis, Massachusetts Inst. of Tech.

Magnier, E. A., Lewin, W. H. G., van Paradijs, J., et al. 1992, A&AS, 96, 379

Magnier, E. A., Prins, S., van Paradijs, J., et al. 1995, A&AS, 114, 215

Makishima, K., Kubota, A., Mizuno, T., et al. 2000, ApJ, 535, 632

Mangano, V., Israel, G. L., & Stella, L. 2004, A&A, 419, 1045

Mason, K. O., Breeveld, A., Much, R., et al. 2001, A&A, 365, L36

Massey, P., McNeill, R. T., Olsen, K. A. G., et al. 2007, AJ, 134, 2474

Massey, P., Olsen, K. A. G., Hodge, P. W., et al. 2006, AJ, 131, 2478

Massey, P., Silva, D. R., Levesque, E. M., et al. 2009, ApJ, 703, 420

McClintock, J. E. & Remillard, R. A. 2006, Black hole binaries, ed. W. H. G. Lewin & M. van der Klis (Cambridge University Press), 157

McConnachie, A. W., Irwin, M. J., Ferguson, A. M. N., et al. 2005, MNRAS, 356, 979

Messier, C. 1781, in Connoissance des Temps for 1784, Catalogue des Nébuleuses & des amas d'Étoiles, 227

Misanovic, Z., Pietsch, W., Haberl, F., et al. 2006, A&A, 448, 1247

Monet, D. G., Levine, S. E., Canzian, B., et al. 2003, AJ, 125, 984

Mould, J., Barmby, P., Gordon, K., et al. 2008, ApJ, 687, 230

Mushotzky, R. F. 1984, Advances in Space Research, 3, 157

Mushotzky, R. F., Cowie, L. L., Barger, A. J., & Arnaud, K. A. 2000, Nature, 404, 459

Nedialkov, P., Orio, M., Birkle, K., et al. 2002, A&A, 389, 439

Negueruela, I., Smith, D. M., Reig, P., Chaty, S., & Torrejón, J. M. 2006, in ESA Special Publication, Vol. 604, The X-ray Universe 2005, ed. A. Wilson, 165

Nice, D. J., Splaver, E. M., Stairs, I. H., et al. 2005, ApJ, 634, 1242

Nieten, C., Neininger, N., Guélin, M., et al. 2006, A&A, 453, 459

Nomoto, K., Yamaoka, H., Pols, O. R., et al. 1994, Nature, 371, 227

Ofek, E. O., Muno, M., Quimby, R., et al. 2008, ApJ, 681, 1464

Orio, M. 2006, ApJ, 643, 844

Osborne, J. P., Borozdin, K. N., Trudolyubov, S. P., et al. 2001, A&A, 378, 800

Özel, F. 2006, Nature, 441, 1115

Paczyński, B. 1971, ARA&A, 9, 183

Pellet, A., Astier, N., Viale, A., et al. 1978, A&AS, 31, 439

Pickles, A. J. 1998, PASP, 110, 863

Pietsch, W. 2010, Astronomische Nachrichten, 331, 187

Pietsch, W., Burwitz, V., Greiner, J., et al. 2006, The Astronomer's Telegram, 850, 1

Pietsch, W., Fliri, J., Freyberg, M. J., et al. 2005a, A&A, 442, 879 (PFF2005)

Pietsch, W., Freyberg, M., & Haberl, F. 2005b, A&A, 434, 483 (PFH2005)

Pietsch, W. & Haberl, F. 2005, A&A, 430, L45 (PH2005)

Pietsch, W., Haberl, F., Sala, G., et al. 2007, A&A, 465, 375 (PHS2007)

Pietsch, W., Misanovic, Z., Haberl, F., et al. 2004, A&A, 426, 11

Pooley, G. G. 1969, MNRAS, 144, 101

Porquet, D., Predehl, P., Aschenbach, B., et al. 2003, A&A, 407, L17

Prestwich, A. H. 2002, in Astronomical Society of the Pacific Conference Series, Vol. 262, The High Energy Universe at Sharp Focus: Chandra Science, ed. E. M. Schlegel & S. D. Vrtilek, 127

Priedhorsky, W. C. & Holt, S. S. 1987, Space Science Reviews, 45, 291

Primini, F. A., Forman, W., & Jones, C. 1993, ApJ, 410, 615 (PFJ93)

Quimby, R., Mondol, P., Hoeflich, P., Wheeler, J. C., & Gerardy, C. 2005, The Astronomer's Telegram, 600, 1

Quimby, R. M. 2006, PhD thesis, University of Texas at Austin

Read, A. M., Sembay, S. F., Abbey, T. F., & Turner, M. J. L. 2006, in ESA Special Publication, Vol. 604, The X-ray Universe 2005, ed. A. Wilson, 925

Revnivtsev, M., Churazov, E., Sazonov, S., Forman, W., & Jones, C. 2007, A&A, 473, 783

Revnivtsev, M., Sazonov, S., Churazov, E., et al. 2009, Nature, 458, 1142

Revnivtsev, M., Sazonov, S., Gilfanov, M., Churazov, E., & Sunyaev, R. 2006, A&A, 452, 169

Rey, S.-C., Rich, R. M., Sohn, S. T., et al. 2007, ApJS, 173, 643

Reynolds, C. S., Loan, A. J., Fabian, A. C., et al. 1997, MNRAS, 286, 349

Ribas, I., Jordi, C., Vilardell, F., et al. 2005, ApJ, 635, L37

Rich, R. M., Corsi, C. E., Cacciari, C., et al. 2005, AJ, 129, 2670

Roberts, T. P. 2007, Ap&SS, 311, 203

Roberts, T. P., Warwick, R. S., Ward, M. J., & Murray, S. S. 2002, MNRAS, 337, 677

Robrade, J. & Schmitt, J. H. M. M. 2009, A&A, 497, 511

Sala, G. & Hernanz, M. 2005, A&A, 439, 1061

Sarajedini, A., Barker, M. K., Geisler, D., Harding, P., & Schommer, R. 2007, AJ, 133, 290

Sarazin, C. L. 1986, Reviews of Modern Physics, 58, 1

Schmitt, J. H. M. M. 2000, in Reviews in Modern Astronomy, ed. R. E. Schielicke, Vol. 13, 115

Schröder, C. & Schmitt, J. H. M. M. 2007, A&A, 475, 677

Scoville, N., Aussel, H., Brusa, M., et al. 2007, ApJS, 172, 1

Shafter, A. W. & Quimby, R. M. 2007, ApJ, 671, L121

Shakura, N. I. & Sunyaev, R. A. 1973, A&A, 24, 337

Shapiro, P. R. & Field, G. B. 1976, ApJ, 205, 762

Sharov, A. S. & Alksnis, A. 1998, Astronomy Letters, 24, 641

Shaw Greening, L., Barnard, R., Kolb, U., Tonkin, C., & Osborne, J. P. 2009, A&A, 495, 733 (SBK2009)

Shirey, R. 2001, IAU Circ., 7659, 1

Shirey, R., Soria, R., Borozdin, K., et al. 2001, A&A, 365, L195

Shtykovskiy, P. & Gilfanov, M. 2005, MNRAS, 362, 879

Simien, F., Pellet, A., Monnet, G., et al. 1978, A&A, 67, 73

Skrutskie, M. F., Cutri, R. M., Stiening, R., et al. 2006, AJ, 131, 1163

Smirnova, O., Alksnis, A., & Zharova, A. V. 2006, Information Bulletin on Variable Stars, 5737, 1

Snowden, S. L., Collier, M. R., & Kuntz, K. D. 2004, ApJ, 610, 1182

Soria, R. 2003, in IAU Symposium, Vol. 214, High Energy Processes and Phenomena in Astrophysics, ed. X. D. Li, V. Trimble, & Z. R. Wang, 59

Soria, R. & Wu, K. 2002, A&A, 384, 99

Stanek, K. Z. & Garnavich, P. M. 1998, ApJ, 503, L131

Stark, A. A., Gammie, C. F., Wilson, R. W., et al. 1992, ApJS, 79, 77

Starrfield, S., Sparks, W. M., & Truran, J. W. 1974, ApJS, 28, 247

Stiele, H., Pietsch, W., Haberl, F., et al. 2008a, in X-rays From Nearby Galaxies, ed. S. Carpano, M. Ehle, & W. Pietsch, 23

Stiele, H., Pietsch, W., Haberl, F., et al. 2010, Astronomische Nachrichten, 331, 212

Stiele, H., Pietsch, W., Haberl, F., & Freyberg, M. 2008b, A&A, 480, 599 (SPH2008)

Stiele, H., Pietsch, W., Haberl, F., Freyberg, M., & Trigo, M. D. 2007, The Astronomer's Telegram, 1191, 1

Stobbart, A., Roberts, T. P., & Wilms, J. 2006, MNRAS, 368, 397

Stöcker, H. 1998, Taschenbuch der Physik (Frankfurt am Main: Verlag Harri Deutsch)

Strohmayer, T. & Bildsten, L. 2006, New Views of Thermonuclear Bursts, ed. W. H. G. Lewin & M. van der Klis (Cambridge University Press), 113

Strüder, L., Briel, U., Dennerl, K., et al. 2001, A&A, 365, L18

Sunyaev, R., Kaniovsky, A., Efremov, V., et al. 1987, Nature, 330, 227

Sunyaev, R. A., Tinsley, B. M., & Meier, D. L. 1978, Comments on Astrophysics, 7, 183

Supper, R., Hasinger, G., Lewin, W. H. G., et al. 2001, A&A, 373, 63 (SHL2001)

Supper, R., Hasinger, G., Pietsch, W., et al. 1997, A&A, 317, 328 (SHP97)

Tanaka, Y. & Lewin, W. H. G. 1995, in X-ray binaries, ed. W. H. G. Lewin, J. van Paradijs, & E. P. J. van den Heuvel (Cambridge University Press), 126

Tanaka, Y. & Shibazaki, N. 1996, ARA&A, 34, 607

Thilker, D. A., Hoopes, C. G., Bianchi, L., et al. 2005, ApJ, 619, L67

Trinchieri, G. & Fabbiano, G. 1991, ApJ, 382, 82 (TF91)

Trudolyubov, S. & Priedhorsky, W. 2004, ApJ, 616, 821

Trudolyubov, S., Priedhorsky, W., Borozdin, K., Mason, K., & Cordova, F. 2002a, IAU Circ., 7798, 2

Trudolyubov, S., Priedhorsky, W., & Cordova, F. 2006a, ApJ, 645, 277 (TPC06)

Trudolyubov, S., Priedhorsky, W., & Cordova, F. 2006b, arXiv:astro-ph/0610809

Trudolyubov, S. P., Borozdin, K. N., & Priedhorsky, W. C. 2001, ApJ, 563, L119

Trudolyubov, S. P., Borozdin, K. N., Priedhorsky, W. C., Mason, K. O., & Cordova, F. A. 2002b, ApJ, 571, L17

Trudolyubov, S. P. & Priedhorsky, W. C. 2008, ApJ, 676, 1218

Trümper, J. 1982, Advances in Space Research, 2, 241

Tuchman, Y. & Truran, J. W. 1998, ApJ, 503, 381

Tully, R. B. 1988, Nearby galaxies catalog (Cambridge and New York, Cambridge University Press)

Turner, M. J. L., Abbey, A., Arnaud, M., et al. 2001, A&A, 365, L27

Urry, C. M. & Padovani, P. 1995, PASP, 107, 803

van den Heuvel, E. P. J., Bhattacharya, D., Nomoto, K., & Rappaport, S. A. 1992, A&A, 262, 97

van der Heyden, K. J., Bleeker, J. A. M., & Kaastra, J. S. 2004, A&A, 421, 1031

van der Klis, M. 1994, ApJS, 92, 511

van der Klis, M. 1995, in X-ray binaries, ed. W. H. G. Lewin, J. van Paradijs, & E. P. J. van den Heuvel (Cambridge University Press), 252

van Speybroeck, L., Epstein, A., Forman, W., et al. 1979, ApJ, 234, L45

Verbunt, F. & van den Heuvel, E. P. J. 1995, in X-ray binaries, ed. W. H. G. Lewin, J. van Paradijs, & E. P. J. van den Heuvel (Cambridge University Press), 457

Vogel, H. 1995, Gerthsen Physik (Springer-Verlag, Berlin)

Voit, G. M. 2005, Reviews of Modern Physics, 77, 207

Voss, R. & Gilfanov, M. 2007, A&A, 468, 49

Voss, R., Pietsch, W., Haberl, F., et al. 2008, A&A, 489, 707

Walterbos, R. A. M. & Braun, R. 1992, A&AS, 92, 625

Walterbos, R. A. M., Brinks, E., & Shane, W. W. 1985, A&AS, 61, 451

Warner, B. 1995, Cataclysmic variable stars, ed. B. Warner (Cambridge University Press)

Watson, M. G., Schröder, A. C., Fyfe, D., et al. 2009, A&A, 493, 339

Weisskopf, M. C., Tananbaum, H. D., Van Speybroeck, L. P., & O'Dell, S. L. 2000, in Society of Photo-Optical Instrumentation Engineers (SPIE) Conference Series, ed. J. E. Trümper & B. Aschenbach, Vol. 4012, 2

White, N. E., Nagase, F., & Parmar, A. N. 1995, in X-ray binaries, ed. W. H. G. Lewin, J. van Paradijs, & E. P. J. van den Heuvel (Cambridge University Press), 1

White, N. E., Stella, L., & Parmar, A. N. 1988, ApJ, 324, 363

Williams, B. F. 2003, AJ, 126, 1312

Williams, B. F., Garcia, M. R., Kong, A. K. H., et al. 2004a, ApJ, 609, 735

Williams, B. F., Garcia, M. R., Kong, A. K. H., Primini, F. A., & Murray, S. S. 2005a, ApJ, 620, 723

Williams, B. F., Garcia, M. R., McClintock, J. E., Primini, F. A., & Murray, S. S. 2005b, ApJ, 632, 1086

Williams, B. F., Garcia, M. R., McClintock, J. E., Primini, F. A., & Murray, S. S. 2006a, ApJ, 637, 479 (WGM06)

Williams, B. F., Naik, S., Garcia, M. R., & Callanan, P. J. 2006b, ApJ, 643, 356

Williams, B. F., Sjouwerman, L. O., Kong, A. K. H., et al. 2004b, ApJ, 615, 720

Wilms, J., Allen, A., & McCray, R. 2000, ApJ, 542, 914

Wolter, H. 1952, Annalen der Physik, 445, 94

Yan, M., Sadeghpour, H. R., & Dalgarno, A. 1998, ApJ, 496, 1044

Yaron, O., Prialnik, D., Shara, M. M., & Kovetz, A. 2005, ApJ, 623, 398

Yin, J., Hou, J. L., Prantzos, N., et al. 2009, A&A, 505, 497

# Danksagung / Acknowledgements

Nun ist es an der Zeit all jenen zu danken, die direkt oder auch indirekt zum Gelingen dieser Arbeit beigetragen haben.

Als erstes möchte ich mich bei Herr Prof. Dr. Günther Hasinger bedanken, dass er mir die einmalige Gelegenheit bot in der Hochenergie-Gruppe des Max-Planck-Instituts für extraterrestrische Physik zu arbeiten und dort meine Doktorarbeit anzufertigen.

Ebenfalls möchte ich Herr Prof. Dr. Ralf Bender danken, dass er die offizielle Vertretung der Doktorarbeit gegenüber der LMU übernommen hat.

Besonderen Dank gebührt meinem Betreuer Herr Dr. Wolfgang Pietsch, der es mir ermöglichte im Rahmen der internationalen "*XMM-Newton* M 31 large program collaboration" eigenständig zu arbeiten und zu lernen, der es verstand mich zu fördern und zu fordern und mit seinem Rat zum Gelingen dieser Arbeit beizutragen.

Auch allen Mitgliedern der Arbeitsgruppe ein herzliches Dankeschön, insbesondere Herr Dr. Frank Haberl dafür, dass er mir stets als Diskussionspartner zur Verfügung stand und mir half meine Fragen zum Erstellen, Fitten und Interpretieren von Röntgenspektren zu beantworten. Bedanken möchte ich mich bei Herr Dr. Hermann Brunner, Herr Dr. Michael Freyberg und Herr Dr. Konrad Dennerl dafür, dass Sie immer eine Antwort wussten, wenn ich eine Frage über *XMM-Newton* oder die Analysesoftware hatte. In diesem Zusammenhang möchte ich auch Herr Dr. Georg Lamer vom Astrophysikalischen Institut Potsdam für die Zusammenarbeit beim Erstellen der `emldetect` Version 4.60 danken, mit der es mir möglich war, die Zeitvariabilitätsuntersuchungen durchzuführen. Vielen Dank an Herr Dr. Vadim Burwitz für seine angenehme Gesellschaft und, dass er uns hin und wieder den Tee versüsst hat.

Herr Prof. Dr. Thomas Boller möchte ich für die Diskussion über die Variabilität von AGN auf langen Zeitskalen danken.

Bedanken möchte ich mich auch bei meinen Kollegen Herr Martin Henze, Herr Peter Eger, Herr Richard Sturm und Herr Dr. Michael Bauer. Insbesondere möchte ich Michael Bauer für seine Hilfe und Unterstützung danken die ich während meiner Anfangszeit am Insitut von ihm erfahren habe.

I also would like to thank all members of the *XMM-Newton* M 31 large program collaboration. I am grateful to Dr. Robin Barnard for giving me the chance to work with him on LMXBs in globular clusters. That way I learned a lot about studying short-term time variability of XRBs. Special thanks goes to Prof. Dr. Despina Hatzidimitriou for our discussions about optical identifications, and for her advice which helped to improve the publication about the long-term time variability study of SSSs.

Furthermore, I would like to thank Dr. Nico Cappelluti for the discussions about, as well as his advice with regard to the derivation of luminosity functions. I would also like to thank Dr. Marcella Brusa for the discussion about source identification techniques in deep fields.

I am very grateful to Dr. Patricia Schady, Dr. Robert Dunn and Dr. Lindsey Shaw Greening who read through this thesis.

Many thanks go to all IMPRS students for the great time we had, despite all the work, especially to my

office mates Dr. Pilar Esquej, Ximena Mazzalay and Valentin Fedl.

Vielen Dank an Herr Prof. Dr. Werner Becker und Frau Christa Imgram, deren Türen für IMPRS Studenten immer offen standen.

Für die schnelle und kompetente Hilfe bei sämtlichen Problemen und Fragen im Zusammenhang mit dem DV System möchte ich den Systemadministratoren Herr Harald Baumgartner und Herr Joachim Paul danken.

Ein besonderer Dank gebührt auch meinen Eltern und meinem Bruder die mich auf meinem bisherigen Lebensweg stets unterstützt und bestärkt haben.

Da es unmöglich ist alle aufzuzählen, die indirekt zum Gelingen dieser Arbeit beigetragen haben, möchte ich diesen allen auch noch danken.

This publication makes use of the USNOFS Image and Catalogue Archive operated by the United States Naval Observatory, Flagstaff Station (http://www.nofs.navy.mil/data/fchpix/), of data products from the Two Micron All Sky Survey, which is a joint project of the University of Massachusetts and the Infrared Processing and Analysis Center/California Institute of Technology, funded by the National Aeronautics and Space Administration and the National Science Foundation, of the SIMBAD database, operated at CDS, Strasbourg, France, and of the NASA/IPAC Extragalactic Database (NED) which is operated by the Jet Propulsion Laboratory, California Institute of Technology, under contract with the National Aeronautics and Space Administration. The XMM-Newton project is supported by the Bundesministerium für Wirtschaft und Technologie/Deutsches Zentrum für Luft- und Raumfahrt (BMWI/DLR, FKZ 50 OX 0001) and the Max-Planck Society. The XMM-Newton SAS is developed and maintained by the Science Operations Centre at the European Space Astronomy Centre (ESAC), Madrid, Spain and the Survey Science Centre at the University of Leicester, Leicester, UK. This research has made use of SAOImage DS9, developed by Smithsonian Astrophysical Observatory. HS acknowledges support by the Bundesministerium für Wirtschaft und Technologie/Deutsches Zentrum für Luft- und Raumfahrt (BMWI/DLR, FKZ 50 OR 0405).